

AGARD-AG-298 VOL. I

AD-A181 676

AGARD

ADVISORY GROUP FOR AEROSPACE RESEARCH & DEVELOPMENT

7 RUE ANCELLE 92200 NEUILLY SUR SEINE FRANCE

AGARDograph No. 298

AGARD Manual

on

Aeroelasticity in Axial-Flow
Turbomachines

Volume 1

Unsteady Turbomachinery
Aerodynamics

200603/4017

DTIC

ELECTE

JUN 23 1987

D

NORTH ATLANTIC TREATY ORGANIZATION



DISTRIBUTION STATEMENT A

Approved for public release
Distribution Unlimited

87 6 22 003

NORTH ATLANTIC TREATY ORGANIZATION
ADVISORY GROUP FOR AEROSPACE RESEARCH AND DEVELOPMENT
(ORGANISATION DU TRAITE DE L'ATLANTIQUE NORD)

AGARDograph No.298
AGARD MANUAL
on
AEROELASTICITY IN AXIAL-FLOW TURBOMACHINES
VOLUME 1
UNSTEADY TURBOMACHINERY AERODYNAMICS

Edited by

Max F. Platzer
Department of the Navy
Naval Postgraduate School
Monterey, CA 93953-5100, USA

and

Franklin O. Carta
United Technologies Research Center
East Hartford, CT 06108, USA



| | |
|--------------------|-------------------------------------|
| Accession For | |
| NTIS CRA&I | <input checked="" type="checkbox"/> |
| DTIC TAB | <input type="checkbox"/> |
| Unannounced | <input type="checkbox"/> |
| Justification | |
| By | |
| Distribution / | |
| Availability Codes | |
| Dist | Avail and/or Special |
| A-1 | |

Best Available Copy

This AGARDograph was prepared at the request of the Propulsion and Energetics Panel
and of the Structures and Materials Panel of AGARD.

THE MISSION OF AGARD

The mission of AGARD is to bring together the leading personalities of the NATO nations in the fields of science and technology relating to aerospace for the following purposes:

- Exchanging of scientific and technical information;
- Continuously stimulating advances in the aerospace sciences relevant to strengthening the common defence posture;
- Improving the co-operation among member nations in aerospace research and development;
- Providing scientific and technical advice and assistance to the Military Committee in the field of aerospace research and development (with particular regard to its military application);
- Rendering scientific and technical assistance, as requested, to other NATO bodies and to member nations in connection with research and development problems in the aerospace field;
- Providing assistance to member nations for the purpose of increasing their scientific and technical potential;
- Recommending effective ways for the member nations to use their research and development capabilities for the common benefit of the NATO community.

The highest authority within AGARD is the National Delegates Board consisting of officially appointed senior representatives from each member nation. The mission of AGARD is carried out through the Panels which are composed of experts appointed by the National Delegates, the Consultant and Exchange Programme and the Aerospace Applications Studies Programme. The results of AGARD work are reported to the member nations and the NATO Authorities through the AGARD series of publications of which this is one.

Participation in AGARD activities is by invitation only and is normally limited to citizens of the NATO nations.

The content of this publication has been reproduced directly from material supplied by AGARD or the authors.

Published March 1987

— Copyright © AGARD 1987
All Rights Reserved

ISBN 92-835-1543-9



*Printed by Specialised Printing Services Limited
40 Chigwell Lane, Loughton, Essex IG10 3TZ*

The state of the art in axial turbomachinery has advanced to the point where further improvements will have to come from a better understanding and eventual control of the unsteady flow phenomena which occur in turbomachines. These unsteady flows have a significant influence on efficiency, aerodynamic stability of the compression system, aeroelastic stability, forced response, and noise generation.

Over the past fifteen years, a number of workshops and symposia have been held to discuss various turbomachinery unsteady flow and aeroelastic aspects, e.g., the Project SQUID Meetings on Aeroelasticity in Turbomachines 1972 and on Unsteady Flow in Jet Engines 1974, the AGARD 46th Propulsion and Energetics Panel Meetings on Unsteady Phenomena in Turbomachinery 1975, the IUTAM Symposium on Aeroelasticity in Turbomachines 1976, the 2nd IUTAM Symposium on Aeroelasticity in Turbomachines 1980 and the Symposium on Unsteady Aerodynamics of Turbomachines and Propellers 1986.

The idea for a thorough review and assessment of the current state of the art of unsteady turbomachinery aerodynamics dates back to the 1975 AGARD Meeting. Such a review was presented by one of the editors (M. F. Platzer) at the AGARD Conference on Unsteady Aerodynamics 1977 (AGARD-CP-227). A major conclusion of this paper was that further engine performance improvements and the avoidance of expensive engine modifications due to aerodynamic/aeroelastic stability problems will not only depend on the continued systematic research in unsteady turbomachinery aerodynamics. Rather, the need to transfer highly specialized unsteady aerodynamic and aeroelastic information to the turbomachinery design community and the introduction of young engineers to this discipline suggested the compilation of a "Manual on Aeroelasticity in Turbomachines", similar to the "AGARD Manual on Aeroelasticity" for the aeroelastic design of flight vehicles, due to the lack of any textbook or other comprehensive compendium on unsteady aerodynamics and aeroelasticity in turbomachines. It is noteworthy, however, that several books on this subject have been published in Russia, i.e., Samoylovich, Unsteady Flow Around and Aeroelastic Vibration in Turbomachine Cascades, WPAFB-FTD-MC-23-242-70, February 1971, Samoylovich, Excitation of the Fluctuations of the Blades of Turbomachines, Moscow 1975, Gorelov, Kurzin, Saren, Atlas of Non-Steady Aerodynamic Characteristics of Profile Cascades, Novosibirsk 1974.

This conclusion was presented to and endorsed by the AGARD Propulsion & Energetics and Structures & Materials Panels, the U.S. Office of Naval Research, the Naval Air Systems Command, and the Air Force Office of Scientific Research. The support of these organizations is gratefully acknowledged. We are especially indebted to the late Dr. Herbert J. Mueller, Research Administrator and Chief Scientist of the Naval Air Systems Command, for his encouragement and guidance during the initial phase of the project. Thanks are also due to Dr. G. Heiche and Mr. G. Derderian (Naval Air Systems Command), Dr. A. Wood (Office of Naval Research), Dr. A. Amos (Air Force Office of Scientific Research) and Dr. E. Riester (AGARD) for their continuing interest and support.

The present first volume attempts to review the field of unsteady turbomachinery aerodynamics. The reader will notice that most methods are still limited to the two-dimensional (cascade) flow approximation, although great progress has been made in the inclusion of blade geometry and loading effects. The current status of the underlying aerodynamic theory and of the major results are described by Verdon and Whitehead. The importance of three-dimensional flow effects is still insufficiently understood. Therefore, a special effort was made to include the existing results by Namba and Salaün in order to stimulate further work on this very difficult problem. Viscous flow effects are discussed by Sisto in the chapter on stall flutter. Rigorous methods for the computation of unsteady boundary layer effects are beginning to be developed. However, its inclusion in this volume was judged to be premature. Great progress has been made in the field of computational fluid dynamics. Its application to the problem of unsteady transonic cascade flows is reviewed by Acton and Newton. A separate volume will have to be devoted in the near future to the numerical computation of unsteady flows in turbomachines because of the rapid advances in the field of computational fluid dynamics. The final four chapters by Fleeter, Jay, Szechenyi, and Gallus present the status of the unsteady aerodynamic and aeroelastic measurement techniques and of the available experimental cascade and rotor results. Whenever possible a comparison between theory and experiment was attempted in the various chapters. The need for well-controlled test cases was recognized a few years ago. This effort is currently in progress and the reader is referred to Fransson's systematic comparison of different experimental data and theoretical results for nine standard test configurations, presented at the Symposium on Unsteady Aerodynamics of Turbomachines and Propellers in 1984.

The editors are deeply indebted to the authors for their willingness to contribute their time and energies to this project in spite of other pressing demands. Our thanks also go to the authors' employers for their support. Funding limitations made it necessary to limit the number of contributors. Nevertheless, we hope that a fairly comprehensive and balanced coverage of the field of turbomachinery unsteady aerodynamics and aeroelasticity was accomplished and that the present volume on unsteady turbomachinery aerodynamics and the second volume on turbomachinery structural dynamics and aeroelasticity will be found useful as an introduction to this important special discipline and as a basis for future work.

NOTATION

The reader is alerted to the differences in notation used by different authors. The most important quantities are tabulated below. Also note that Verdon and Namba use dimensionless quantities.

Verdon uses the following reference quantities: reference length = blade chord, reference time = ratio of blade chord to upstream free-stream speed, reference density = upstream free-stream density.

Namba uses the following reference quantities: In the section "Subsonic, Supersonic, and Transonic Unsteady Annular Cascade Theory", equations (1) through (143), reference length = tip radius, reference velocity = axial velocity of the undisturbed flow, reference time = ratio of tip radius to axial velocity of the undisturbed flow, reference density = upstream free-stream density. This part of Namba's chapter is denoted "Namba 1" in the list of symbols. In the following sections, equations (144) through (239), Namba uses as reference length = blade chord, reference velocity = undisturbed flow velocity, reference time = ratio of blade chord to undisturbed flow velocity, reference density = upstream free-stream density. This part of Namba's chapter is denoted as "Namba 2".

V = Verdon W = Whitehead N1 = Namba 1 N2 = Namba 2 S = Salaun

| | V | W | N1 | N2 | S |
|-----------------------------|--------------|--------------|------------|--------------|----------------|
| Axial Coordinate | ξ | ξ | z | | z |
| Circumferential Coordinate | η | η | θ | | θ |
| Radial Coordinate | | | r | y | r |
| Chordwise Coordinate | x | x | | x | |
| Normal-to-Chord Coordinate | y | y | y | z | |
| Axial Chord Length | | | $Ca(r)$ | | $2l$ |
| Blade Chord Length | c | c | | c^* | $2c$ |
| Blade Spacing | | s | | | b |
| Gap-to-Chord Ratio | G | | | s | |
| Stagger Angle | ϕ | θ | | γ | γ |
| Hub Radius | | | r_1 | | r_1 |
| Tip Radius | | | r_T^* | | r_2 |
| Blade Number | | | N | | N |
| Time | t | t | t | t | t |
| Vibration Frequency | | ω | | | ω |
| Reduced Frequency | ω | λ | λ | ω | ω_R |
| Axial Wave Number | k_ξ | α | | | |
| Circumferential Wave Number | k_η | β | n | | |
| Interblade Phase Angle | σ | σ | δ | $2\pi\sigma$ | $\hat{\sigma}$ |
| Axial Velocity | | | w_a^* | | v_∞ |
| Speed of Sound | A | A | | $a_0(x,y)$ | a_∞ |
| Free-Stream Density | $\bar{\rho}$ | $\bar{\rho}$ | ρ_0^* | ρ_0^* | ρ_∞ |
| Angular Velocity of Rotor | | | ω^* | | Ω |
| Free-Stream Speed | | U | | U^* | |

CONTENTS

| | |
|---|------|
| PREFACE - - - - - | iii |
| NOTATION - - - - - | iv |
| TABLE OF CONTENTS - - - - - | v |
| | |
| I. INTRODUCTION AND OVERVIEW | |
| F. Sisto, Stevens Institute of Technology | |
| Introduction - - - - - | 1-1 |
| Historical Perspective - - - - - | 1-2 |
| Overview of the Manual - - - - - | 1-8 |
| | |
| II. LINEARIZED UNSTEADY AERODYNAMIC THEORY | |
| J. M. Verdon, United Technologies Research Center | |
| Introduction - - - - - | 2-1 |
| Problem Description - - - - - | 2-2 |
| The Full Time-Dependent Governing Equations - - - - - | 2-5 |
| The Small Unsteady Disturbance Approximation - - - - - | 2-8 |
| The Linearized Unsteady Flow - - - - - | 2-11 |
| Aerodynamic Response Parameters - - - - - | 2-16 |
| Numerical Examples - - - - - | 2-18 |
| Limiting Forms of the Governing Equations - - - - - | 2-25 |
| Concluding Remarks - - - - - | 2-30 |
| | |
| III. CLASSICAL TWO-DIMENSIONAL METHODS; <i>Three dimensional flows; → (to p vii)</i> | |
| D. S. Whitehead, Cambridge University | |
| Introduction - - - - - | 3-1 |
| Unsteady Thin Aerofoil Theory, Bound and Free Vorticity - - - - - | 3-2 |
| Kernel Function for Incompressible Flow - - - - - | 3-3 |
| Fundamental Acoustic Wave Solutions - - - - - | 3-4 |
| Vorticity Wave Solutions - - - - - | 3-5 |
| Kernel Function for Subsonic Cascade - - - - - | 3-6 |
| Solution for Subsonic Cascade - - - - - | 3-7 |
| Solutions for Supersonic Cascade - - - - - | 3-8 |
| Transonic Theory - - - - - | 3-12 |
| Actuator Disc Theory - - - - - | 3-14 |
| Singularity Theory - - - - - | 3-16 |
| Specimen Results for Flat Plate Cascades - - - - - | 3-18 |
| Conclusions - - - - - | 3-20 |
| Program Listing for Unsteady Two-Dimensional Linearized Subsonic Flow in Cascades - - - - - | 3-22 |

IV. THREE-DIMENSIONAL FLOWS

M. Namba, Kyushu University

| | |
|---|------|
| Introduction - - - - - | 4-1 |
| Model and Mathematical Formulation - - - - - | 4-2 |
| Finite Radial Mode Expansion - - - - - | 4-4 |
| Acoustic Field Expressed by the Finite Radial Mode System - - - - - | 4-6 |
| Disturbance Pressure Induced by Unsteady Lifting Surfaces - - - - - | 4-7 |
| Upwash Velocity Induced by Lifting Surfaces - - - - - | 4-9 |
| Integral Equation - - - - - | 4-11 |
| The Discrete Element Method - - - - - | 4-12 |
| The Mode Function Method - - - - - | 4-12 |
| The Hybrid Method - - - - - | 4-15 |
| Example Calculation and Trends of Three-Dimensional Effects - - - - - | 4-15 |
| Unsteady Cascade in Spanwise Nonuniform Mean Flow - - - - - | 4-20 |
| Model and Mathematical Formulation - - - - - | 4-20 |
| Disturbance Pressure - - - - - | 4-22 |
| Disturbance Velocities - - - - - | 4-22 |
| Integral Equation for Unsteady Loadings - - - - - | 4-23 |
| Numerical Examples and Effect of Mean Flow Shear Upon Unsteady Blade Loadings - - - - - | 4-24 |
| Effect of Wall Linings - - - - - | 4-25 |
| Model and Mathematical Formulation - - - - - | 4-25 |
| Disturbance Pressure - - - - - | 4-27 |
| Disturbance Velocities and Fluid Particle Displacement - - - - - | 4-28 |
| Determination of Unsteady Blade Loading and Mass Source - - - - - | 4-28 |
| Numerical Examples and Effect of Wall Linings upon Blade Loading - - - - - | 4-29 |

V. THREE-DIMENSIONAL FLOW

Pièrre Salaün, ONERA

| | |
|---|------|
| Subsonic and Supersonic Unsteady Annular Cascade Theory - - - - - | 5-1 |
| Formulation of the Problem - - - - - | 5-1 |
| Pressure due to N Monopoles or N Dipoles - - - - - | 5-3 |
| Pressure and Velocity Potential due to N Sheets of Pressure Dipoles - - - - - | 5-4 |
| Analysis of the Velocity Potential and its Derivatives - - - - - | 5-6 |
| Integral Equation of the Problem - - - - - | 5-6 |
| Use of Nondimensional Quantities, Method of Solution of the Integral Equation - - - - - | 5-9 |
| Generalized Forces - - - - - | 5-12 |
| Numerical Results - - - - - | 5-12 |

VI. NUMERICAL METHODS FOR UNSTEADY TRANSONIC FLOW ;

E. Acton, Topexpress Ltd and
S. G. Newton, Rolls-Royce p/c

| | |
|--|------|
| Introduction - - - - - | 6-1 |
| Solutions of the Potential Equations - - - - - | 6-3 |
| Time-Marching Solutions of the Euler Equations - - - - - | 6-8 |
| Implementation of Boundary Conditions - - - - - | 6-12 |
| Application of the Methods to Flutter Calculations - - - - - | 6-15 |
| Concluding Remarks - - - - - | 6-21 |

VII. STALL FLUTTER ;

F. Sisto, Stevens Institute of Technology

| | |
|---|------|
| Introduction - - - - - | 7-1 |
| The Role of Mach Number - - - - - | 7-2 |
| Choke Flutter and Supersonic Stall Flutter - - - - - | 7-2 |
| Nonlinear Phenomena - - - - - | 7-3 |
| Empirical Correlations - - - - - | 7-5 |
| Separated Flow Models - - - - - | 7-7 |
| Recent Trends, Modern Approach to Stall Flutter - - - - - | 7-9 |
| Concluding Remarks - - - - - | 7-11 |

VIII. UNSTEADY AERODYNAMIC MEASUREMENTS IN FLUTTER RESEARCH *and in*

S. Fleeter, Purdue University and
R. L. Jay, General Motors Corporation

| | |
|--|------|
| Introduction - - - - - | 8-1 |
| Experimental Objectives - - - - - | 8-1 |
| Experimental Facilities and Techniques - - - - - | 8-2 |
| Experimental Results - - - - - | 8-8 |
| Summary - - - - - | 8-18 |

IX. UNSTEADY AERODYNAMIC MEASUREMENTS IN FORCED VIBRATION RESEARCH; *→ (over)*

R. L. Jay, General Motors Corporation and
S. Fleeter, Purdue University

| | |
|---|------|
| Introduction - - - - - | 9-1 |
| Problem Defined - - - - - | 9-1 |
| Experimental Facility Requirements - - - - - | 9-9 |
| Experimental Research - - - - - | 9-12 |
| Calibration and Data Acquisition - - - - - | 9-15 |
| Examples of Investigations Regarding Aerodynamic Damping and Gust Loading - - - - - | 9-21 |
| Data Presentation - - - - - | 9-37 |
| Summary - - - - - | 9-37 |

X. UNDERSTANDING FAN BLADE FLUTTER THROUGH LINEAR CASCADE AEROELASTIC TESTING. and
E. Szechenyi, ONERA

| | |
|---|-------|
| Introduction - - - - - | 10-1 |
| Aeroelastic Testing - - - - - | 10-2 |
| Sub/Transonic Flow Flutter in Torsion - - - - - | 10-5 |
| Supersonic Flow Started Flow Flutter - - - - - | 10-10 |
| Some Ideas on Supersonic Unstarted Flow Flutter - - - - - | 10-14 |
| Cascade Results and Predictions - - - - - | 10-14 |
| The Future - - - - - | 10-15 |

XI. UNSTEADY AERODYNAMIC MEASUREMENTS ON ROTORS. ~~+~~
H. E. Gallus, Technical University of Aachen, FRG

| | |
|--|-------|
| Introduction - - - - - | 11-1 |
| Objectives of Experimental Rotor and Stage Unsteady Aerodynamic Research - | 11-1 |
| Measurement Techniques on Rotors of Turbomachines- - - - - | 11-3 |
| Techniques for Displacement and Vibration Measurements on Rotor Blades - - | 11-3 |
| Techniques for Unsteady Flow Measurements on Rotors - - - - - | 11-4 |
| Examples for the Application of Unsteady Flow Measuring Techniques on - - | 11-5 |
| Rotors | |
| Unsteady Blade Static Pressure Measurements - - - - - | 11-5 |
| High Response Pressure Transducers for Unsteady Pressure Field - - - - - | 11-8 |
| Measurements on the Casing Wall | |
| Rotor Flow Field and Rotor Wake Studies with the Aid of Rotating Probes- - | 11-9 |
| Measurement of the Rotor Flow by High Response Stationary Probes - - - - - | 11-11 |
| Optical Methods for Rotor Flow Investigations - - - - - | 11-13 |
| Flow Visualization - - - - - | 11-13 |
| Schlieren- and Shadowgraph Techniques - - - - - | 11-14 |
| Gas Fluorescence Technique - - - - - | 11-15 |
| Holographic Interferometry - - - - - | 11-15 |
| Laser Velocimetry - - - - - | 11-15 |
| Summary - - - - - | 11-18 |

INTRODUCTION AND OVERVIEW

F. SISTO
Department of Mechanical Engineering
Stevens Institute of Technology
Hoboken, New Jersey 07030
USA

INTRODUCTION

Definition. The engineering science of aeroelasticity has been described by Collar (1946) as the study of the mutual interaction of the inertial, elastic and aerodynamic forces on structural members exposed to an airstream and the influence of this study on design. In Collar's triangle of forces each of the three types of forces occupies a vertex of the triangle and the three sides constitute the subfields of static aeroelasticity, dynamic control and structural dynamics. This is an excellent mnemonic device for helping to characterize the field and organize the literature. The full aeroelastic self-excited instability is termed flutter; in axial turbomachines the structure is typically the bladed rotor and only infrequently the stator vanes.

Background. Aeroelasticity as an empirical field of enquiry extends back in time with accounts of flutter occurrences on the early "iron" bridges in England, ca 1818. The vibration of tall smokestacks and other bluff structures by Karman vortex excitation are further examples of dynamic aeroelastic phenomena of the type that persist to the present day, cf. the Tacoma Narrows Bridge failure in 1940.

Aircraft empennage and wing flutter became a recognized problem at the time of World War I, and analytical prediction became possible using the then-new theories for nonsteady aerodynamics. Major advances in the structural description of the aeroelastic system were not required at that time. Static aeroelasticity, as exemplified by the torsional wing divergence of the early monoplanes, was properly diagnosed contemporaneously. Subsequent development of the field as applied to the external aerodynamics of lifting and control surfaces of aircraft and missiles continued into the early 1960's. More sophisticated analysis of the structural systems became necessary as sweep, monocoque construction and other geometries, materials, and methods of fabrication were introduced.

A summary of this previous experience was documented in an earlier Manual on Aeroelasticity (Jones, ed. 1961) issued by the Advisory Group for Aeronautical Research and Development of the North Atlantic Treaty Organization. The present Manual derives a great deal of strength and continuity from that prior documentation of the then current state of the art, which subsequently has continued to mature with emphases on supersonic flow, transonic flow, missile skin panels, control surfaces, and helicopter rotors.

Axial-Flow Turbomachines. The first successful gas turbine engines were the turbojet powerplants developed in England and Germany during World War II and immediately afterwards in the U. S. and U.K. This development coincided with the

first important documentation of axial compressor blade flutter as reported by Shannon (1945).

The development of aeroelasticity in axial turbomachines has been stimulated mostly, although not exclusively, by problems related to aircraft gas turbines. Typically, the working fluid is referred to as air. The twin desiderata of light weight and high isentropic efficiency in aeronautical applications led to the design of axial-flow compressors with airfoils of fairly high aspect ratios. Moderate thickness ratios were required by the high subsonic relative Mach numbers. Under high stage loading conditions these machines experienced either severe bending or torsional vibrations of their cantilever blades, then termed "stalling flutter." This behavior was not to be tolerated since it led to fatigue failure of the blades.

It is probable, in retrospect, that dynamic aeroelastic instability had occurred earlier in compressors of more robust construction and in the latter stages of condensing steam turbines. Blade vibrations attributable to partial admission of steam in impulse turbines (Campbell 1924) were correctly treated as forced vibration, but without emphasis on the aeroelastic nature of the problem. It is interesting to note, however, that many of the fundamental concepts related to the vibration mode of bladed-disk assemblies, currently being intensively researched, have their genesis in that earlier steam turbine experience of the 1920's.

The development of axial turbomachine aeroelasticity since World War II is set out briefly in the remainder of this chapter. At the outset, however, it is important to summarize the basic differences that give rise to new phenomena not encountered with fixed lifting surfaces. Clearly, the major feature differentiating the aircraft wing and the axial flow turbomachine is the large multiplicity of evenly spaced and mutually interfering airfoils in the latter. The aerodynamic coupling amongst the airfoils in an annular row of vibrating blades is extremely complex and depends on many governing parameters, not the least of which is the interblade phase angle, σ (sigma). The structural coupling is also uniquely different in the turbomachine, being strongly affected by the twist of the airfoils, their attachment to the hub and to each other, and, in the case of rotor blades which are more prone to vibrate than stator blades, by operation in a strong rotational body force field. The importance of modeling the rotor structure as a bladed-disk assembly has already been alluded to.

These major complicating factors, attributable to the multiplicity of coupled and annularly cascaded airfoils arranged

in alternately fixed and moving rows, have characterized the development of aeroelasticity in axial turbomachines, as contrasted with that in aeronautics in general.

HISTORICAL PERSPECTIVE

Early Manifestations in Axial Compressors. In Shannon's pioneering report it was noted that axial flow compressors were prone to stall flutter vibrations in which the blade mode was usually fundamental flexure, although lesser stresses were sometimes encountered in torsion. The compressor rotor blades being unshrouded and only slightly twisted had natural modes in which either flexure or torsion predominated. (The typical predominance of the flexural mode was to be reversed at a later time in the evolution of compressor design.) These cantilever rotor blade oscillations occurred at part speed when the operating line, during oscillation or otherwise, traversed a region of the compressor map where high incidence on the first several stages was combined with moderately high relative airspeed. See Region I in the schematic compressor map, or characteristic, comprising Figure 1.

This graphical representation of compressor performance, with its aerodynamic parameters of aeroelastic significance, is explained in Chapter 6 of Dowell et al (1978). (For example, contours of the first rotor tip incidence may be plotted in Figure 1.) However, the compressor map identification of flutter regions cannot predict the type, or occurrence, of flutter with complete certitude. The map is purely an aerothermodynamic descriptor and gives no information about structural dynamics.

Forced vibrations were also observed where there was a clear coincidence of the natural frequency of the rotor blade with the frequency of encountering disturbances in the airstream, or with the rotor passing frequency in the case of a stator vane vibration. Although aerodynamically forced vibrations of blades and vanes at integral multiples of synchronous speed have continued to be important aeroelastic occurrences, the diagnosis and cure have been straightforward. (The magnitude of the excitation must be reduced and/or the coincidence of frequencies moved out of the running range.) Consequently, with few exceptions, this type of aeroelastic vibration has received relatively less

PRESSURE RATIO

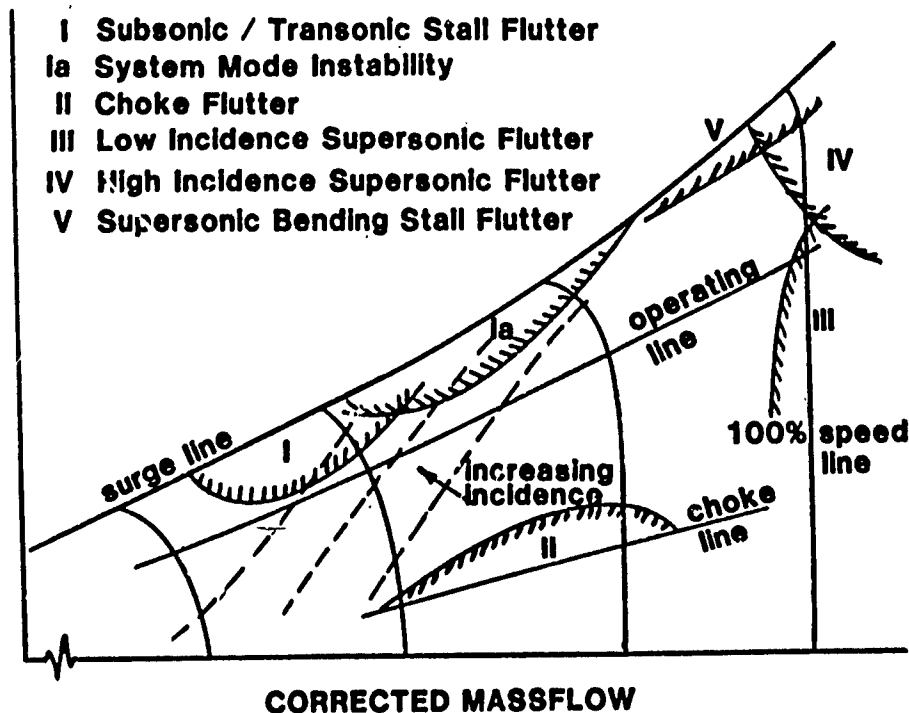


Fig. 1. Axial compressor or fan characteristic map showing principal types of flutter and regions of occurrence.

attention in the literature and in this Manual. One development has been in the application of unsteady aerodynamics to relate the magnitude, frequency, orientation, and phase of the periodic gust to the resulting unsteady blade lift and moment and hence, unsteady stress.

An exception to these observations concerning aerodynamic forcing occurs when the resonant frequency is at a non-integral engine order which is the situation when rotating (or propagating) stall is present. This is touched upon later and discussed again somewhat more fully in Chapter, "Stall Flutter." (Similarly, static aeroelasticity has only a minor exposure in the turbomachinery literature, the chief applications being to blade "untwist" and "lean" which stem from the combined effects of steady aerodynamic and centrifugal loadings. The performance of horizontal axis wind turbines, for example, is strongly affected by static aeroelastic deformations.)

The early attempts to predict and thus avoid stall flutter in practice resulted in empirical "design rules" which limited the reduced velocity* at design speed to

*Relative airspeed normalized with respect to blade frequency and semichord, a parameter of great importance in dynamic aeroelasticity.

certain critical values which were not to be exceeded in order to achieve freedom from flutter. (A rather fanciful depiction of an empirical flutter boundary appears in the artistic rendering of Figure 2; the disadvantages and advantages related to crossing or non-crossing of the boundary are graphically portrayed.) Although flutter in those subsonic compressors was not encountered at design speed, the specification of maximum allowable reduced velocity was made at design speed to assure that the critical values would not be exceeded at lower speeds in Region I. The qualitative explanation rested upon the previous single wing experience with stall flutter documented and explained by Studer (1936), Mary Victory (1943), and others. Although the design rules ignored the importance of aerodynamic coupling noted before, they were moderately successful in delineating the region between flutter and no flutter for similar designs. This was primarily due to the fact that the rules were empirical to begin with, and also, that at the inception of flutter, stresses are low and all blades vibrate at their individual "as manufactured" frequencies with disparate amplitudes. Before entrainment of frequencies occurs at higher flutter stress levels a unique interblade phase angle cannot be defined and the aerodynamic coupling, when averaged over time, is not a strong influence. The stress level for entrainment is subject to the degree of mistuning present.

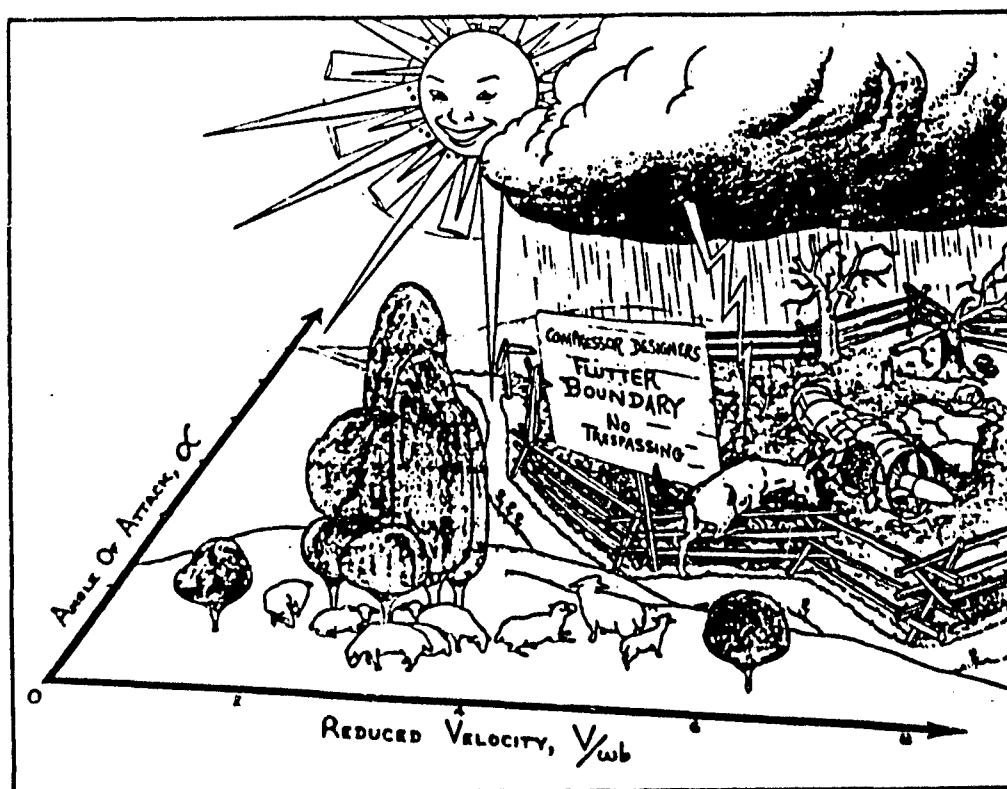


FIG. 2. An allegorical portrayal (circa 1954) of the perils encountered when a compressor operating line penetrates the stall flutter boundary. (Artist unknown.)

Second Decade Developments. Beginning in the early 1950's the research on blade flutter was advanced by Billington (1949), Lilley (1952), Pearson (1953), Carter (1955), Kilpatrick & Burrows (1958), and others in England, and Mendelson (1949), Sisto (1952), Carta (1957), and others in the United States. This work had several thrusts, not the least useful of which was the extension of the earlier design rules to include correlations for the effect of blade geometry, such as aspect ratio, thickness and aerothermodynamic quantities such as stage pressure ratio, number of stages and, most particularly, incidence. Much of this work was proprietary.

Another important thrust in the 1950's was hardware development with the objective of avoiding stall flutter, or mitigating its harmful effects. One such item was the part-span shroud, or snubber, introduced to control the vibrations of higher Mach number compressor blades and the fan components of the then nascent turbofan engines. Some controversy exists as to the reason for the effectiveness of these devices. There is an unquestioned stiffening effect on the structure, thus providing an increase in reduced frequency and modification of the vibration mode, both aeroelastically important. However, during vibration it is also true that the interfacial surfaces between butting shroud segments may introduce mechanical damping. It is possible that both benefits accrue and that one effect or the other may be optimized by the particular philosophy employed in the shroud design. It is important to observe that the turbine component has made use of tip shrouds as a viable option from the earliest gas turbine engine development, probably as a natural carry-over from prior steam turbine practice.

In this same time period the significant use of variable guide vanes in compressor components was introduced, following an intensive period of research and development. The research on the aeroelastic implications of these devices was largely experimental and improved stall flutter avoidance was one of the major practical results.

Another major thrust was the analytical formulation of the unsteady incompressible aerodynamics of two-dimensional cascades restricted to conditions of small thickness, camber and incidence. It did prove to be possible to include the important interblade phase angle as a parameter in the analysis. Although flutter was not being encountered in practice under those restrictive conditions (low incidence and subsonic flow) it was possible to study the effect of interblade phase angle analytically and observe the strong, even dominant effect of this parameter on aerodynamic work* and the related aerolastic stability. The central role of sigma (σ) in cascade aeroelasticity, firmly estab-

lished at that time, continues to the present day. Thus, for the first time, the interblade phase angle was conceived of as a variable, or a parameter, with a strong influence on the aerodynamic reactions. Before this development at MIT, σ had been considered to be roughly 180° , more or less specified in advance of any predictive calculation and denoted as "antiphase" behavior.

The entire question of the influence of interblade phase angle was put on a firm analytical basis with the publication of what might be called a "phase theorem" by Lane (1956). In this elegant analytical treatise, written at New York University, the following proposition was proved, subject to the assumptions of linearity and identical blades equally spaced about a common rotor: i) permissible values of the interblade angle are $\sigma = 2\pi n/N$, where N is the number of blades in the annular row and n is an integer, $0 < n < N$; and ii) the flutter inception point may be determined by minimizing the flutter speed of a simple equivalent blade with respect to σ , a discrete variable. Actually, when N is large, σ may be considered to be a continuous variable with slight error. These formulations put the flutter prediction of turbomachinery stages on a rational foundation upon which later developments could be firmly based.

As the second decade of turbomachine aeroelasticity drew to a close the analytical/theoretical body of knowledge and the practical/experimental developments were quite unrelated. It was not possible to use the incompressible small incidence theory to predict flutter and elimination of stall flutter relied almost exclusively on empiricism. The transonic compressor made its debut in this time period and, as supersonic tip relative Mach numbers appeared, so also did supersonic flutter. With the introduction of compressibility in the analysis (Carta 1957) (Lane & Friedman, 1958) theory and practice began to intersect. In subsequent years the treatment of subsonic, supersonic and finally transonic ($M = 1$) flows have characterized the more practically useful analyses that have appeared.

Rotating Stall. In continuing to trace the development of aeroelasticity as applied to axial turbomachines, the phenomenon known as rotating stall, or propagating stall, should be mentioned. Rotating stall was observed experimentally by the Whittle Jet Engine Group in 1938 and proceeded to be involved in an interesting and important controversy.

A row of blades does not stall uniformly as the incidence is increased. Instead, zones of low velocity or even reversed flow appear evenly spaced about the annulus. These zones are not stationary relative to the blades; the patches rotate in the annulus in the same direction as the rotor, but at lower speed. It is clear that the loading on rotor blades and stator vanes will change with a frequency that depends on the relative angular velocity of stall propagation and the number of patches. This frequency is in general non-synchronous, i.e., it does not coincide with an engine order line on the Campbell diagram.

*Flutter may be predicted by an energy method in which the work done by the aerodynamic forces on the assumed vibration mode, less the energy consumed by mechanical damping, goes from zero to a small positive quantity at the flutter point.

This diagram, a typical example of which appears as Figure 3, is now a classical device for diagnosing rotor blade vibrations. With the abscissa of rotational speed and ordinate of vibration frequency, blade natural frequencies may be plotted as a function of rotor speed. Straight lines radiating from the origin correspond to engine order lines. Forced vibration will usually occur where the natural frequency line of the resonating rotor blade crosses the integral engine order line. High vibratory stress at the natural frequency and between integral order lines may be due to rotating stall or else a self-excited instability such as flutter.

Propagating stall, identified in this manner, was researched initially by groups at NACA (Hupert & Benner 1953), CalTech (Iura and Rannie 1953) and Harvard/MIT (Ermans 1954). A strong controversy arose concerning the relative significance for blade vibration of propagating stall vis a vis stalling flutter. At one time there was a serious question whether separate mechanisms were involved and whether, in fact, there was such a distinct phenomenon as stall flutter. The controversy continued to find expression well into the following decade. General agreement now distinguishes between the two types of stall-provoked vibrations by noting that propagating stall may occur without any

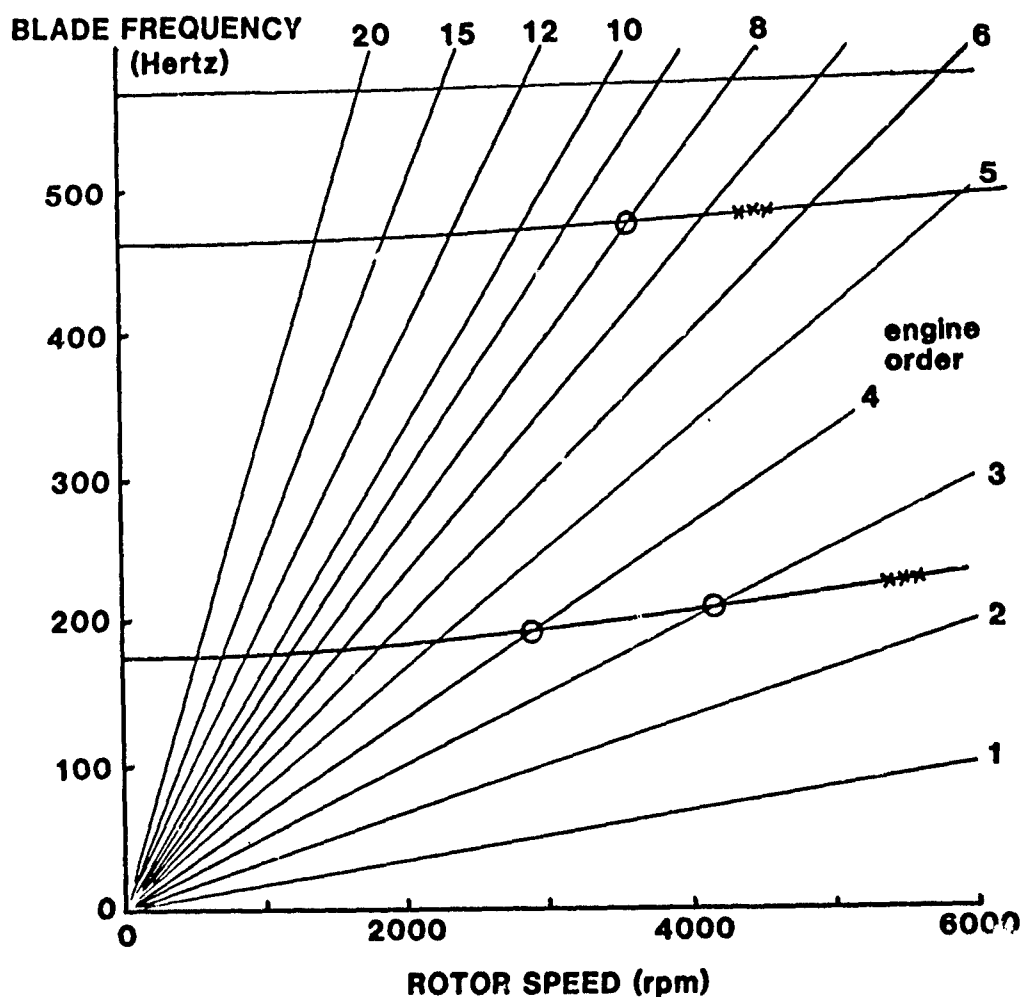


Fig. 3. Campbell diagram for a rotor blade (xxx stresses imply either propagating stall, flutter, or other nonsynchronous excitation; ooo stresses indicate forced resonance).

significant blade vibration, or may result in forced rotor blade vibration much as any other non-axisymmetric flow in the blade annulus. The vibration of the annularly cascaded blades usually exerts little or no influence on the propagating speed of the stall zones, and hence on the forcing frequency. Stalling flutter, on the other hand, is a true self-excited vibration, as is conventionally implied by the term "flutter," and may occur with steady, uniform mean flow.

This resolution of the controversy is not without its paradoxes. Since the nonstationary stalling process is nonlinear there is a small interval of frequencies bracketing blade resonance within which entrainment of frequency takes place; the stall frequency departs from its continuous dependence on rotor speed and "locks in" to the blade natural frequency. Furthermore, a stall flutter condition in a blade row, with time invariant interblade phase angles, will generate a periodic pattern of strong flow perturbations (separations) that may be viewed as a traveling wave propagating peripherally relative to the blade row.

This subject is developed more fully later in the Manual since it is the basis of a modern formulation and analysis of stall flutter.

System Mode Instabilities. The following decade of the 1960's was notable for the introduction of the turbofan engine, the supersonic transport (SST) and realization of the lift engine.

The fan component of turbofan engines and the front stages of transonic compressors have rotors of low hub/tip ratio. The rigidity of these disk structures is much lower than the drums of high radius ratio stages. Furthermore, despite the introduction of titanium alloy as a front-stage blade material, further decrease of the reduced velocity is found to be aeroelastically necessary and one or two rings of part-span shrouds are routinely applied to these front end rotor rows. The resulting structural system is one in which the vibration modes of the entire blade-disk-shroud system must be considered.

Although steam turbine designers have analyzed this type of structure, in which the modes are identified by the number of diametral and circumferential nodal lines, Carta (1967) first reported the significant application to aeroengine components. It was shown that if the intra-blade phase angle between pitching and plunging is $\pi/2$ (i.e. the torsional motion lags the bending motion by 90°), then instability is observed to occur typically with an intermediate number, say 4, of diametral nodes between 2 and 8. The particular choice of intra-blade phase angle corresponds to displacement waves relative to rotor coordinates travelling in the direction of rotor rotation, i.e. "forward" travelling waves. This initial investigation of system mode instabilities has led subsequently to a great proliferation of important investigations and results. In particular, the later and very significant aeroelastic developments associated with so-called

"mistuned" bladed-disk assemblies rests upon this prior work on system modes.

The SST was a strong stimulus to the growing concern with aerodynamic noise, which in turn gave rise to the modern field of aeroacoustics. Although this Manual is not concerned directly with aeroacoustics it is notable that the acoustic approximation (i.e. pressure and velocity changes across a sound wave are infinitesimals) can be effectively employed in the perturbation analysis of unsteady compressible flow through cascades. Virtually the same formulation that describes acoustic radiation, see Goldstein (1976), also predicts the unsteady flow field properties of cascades at small incidence. Thus the 1960's development of unsteady compressible flow in cascades was reinforced by the growing field of aeroacoustics. At a particular subsonic Mach number, the phenomenon of "cutoff" to describe frequencies below which disturbances do not propagate upstream, is an acoustical concept. So also is the phenomenon of aerodynamic resonance, where disturbances from one vibrating blade arrive in phase with the similar vibration of the neighboring blade. Both types of behavior have important consequences in the formulation of unsteady pressure distribution and hence unsteady lift and moment.

The entire lift engine development, with all its variations, peaked out during this decade. Many interesting composite blade materials and types of construction were tried; the aeroelastic benefits in the area of flutter prevention were apparently insufficient to overcome the aeroelastic disadvantages with respect to foreign object damage (FOD) and fatigue behavior in forced vibration. These lift engine developments were later abandoned (with the vectored-lift Pegasus engine an exception). Nonetheless a great deal was learned about the aeroelastic features of FOD, other transient loadings and, most particularly, the inlet distortions encountered with these special engines. Although the aeroelastic implications of operating in distorted flow were recognized in the late 1940's, probably as a consequence of earlier experience with partial admission in steam turbines, the intensive study of aeromechanical response to flow distortion took place late in the decade (Armstrong and Williams, 1966). This was due mainly to the severe distortion presented to the wing-mounted lift engine, and also in some measure, to the increased use of buried engine installations requiring bifurcated and/or tortuous inlet ducting, supersonic inlets operating off design and a trend to lower cantilever blade frequencies. Stemming from the limitations to, and deterioration of, engine performance in distorted flow, the intense research of this subject provided a stimulus for paralleling the engine performance studies with investigations of aeroelastic response.

Modern Developments. In the modern era, taken to mean from about 1970 onward, several important trends may be noted.

The aerodynamic formulations have attempted to keep pace with and explain the newly observed phenomena. In particular, a number of supersonic flutter regimes have been encountered in practice, see Regions III, IV and V in Figure 1. Only Region III flutter, in either pitching or plunging, will usually be encountered along a normal operating line, and then only at corrected overspeed conditions. Supersonic aerodynamic theories were developed that were adequate to explain and confirm Region III flutter. Low incidence formulations were reported by a number of investigators (Verdon, 1973), (Brix & Platzer, 1974), (Kurosaka, 1974), (Nagashima & Whitehead, 1974), (Adamczyk & Goldstein, 1978), and others, with greatest interest being attached to the onset flows having a subsonic axial component. The survey paper by Platzer (1977) at the Ottawa Meeting of AGARD gives an excellent summary of the aerodynamics literature and experience up to that time. The AGARD paper was preceded by a briefer survey in Platzer (1975) and updated in succeeding papers (Platzer, 1978, 1982). This group of papers provides a recent historical perspective of this modern aspect of turbomachine aeroelasticity and forms a prime bibliographic reference to the unsteady aerodynamics sections of the present Manual. It is important to point out that the summaries of relevant papers by authors in the Soviet Union are a unique contribution of the Platzer surveys. No further reference to the somewhat less voluminous Soviet literature is required here.

Regions IV and V in Figure 1 are at higher compressor pressure ratio, above the normal equilibrium operating line, and, in Region V, may involve stalling at supersonic blade relative Mach number. Unsteady aerodynamic analyses appropriate to this regime have been presented by Adamczyk (1978) and (1982). For the first time account was taken of the effect of shock waves which may appear when the surface Mach number exceeds unity. Flutter observed in these regions has been mostly flexural, although not exclusively. In Region V stalling of the flow has been implicated since the region is in the neighborhood of the surge or stall limit line. Hence Region V is provisionally termed "supersonic bending stall flutter" and it is assumed that there is a detached bow shock at each blade passage entrance; i.e., the passage is unstalled. By contrast, the flutter mechanism in Region IV is thought to involve an in-passage shock wave whose oscillatory movement is essential for the instability mechanism.

A counterclockwise continuation around Figure 1 returns one to Region I which, it now appears, should be divided into more than one subregion. The so-called system mode instability seems to be associated with the upper end of this region, and although the blade loading is high, flutter may not involve flow separation as an essential part of the mechanism. Instead it has been hypothesized (Stargardt, 1979) that even with a subsonic onset flow the surface Mach number can exceed unity locally and oscillating shocks may help explain the appearance of negative

aerodynamic damping. It seems that these instability mechanisms (separation, oscillating shocks) may both appear in this general region of the fan or compressor map, although not both at the same time in a particular machine. Thus the non-aerodynamic factors, which are not revealed by the map parameters and are discussed in Section "Introduction", may determine which, if any, of these flutter types will manifest itself in any particular instance. The clarification of this matter is still required so that Region I is now provisionally labelled Subsonic/Transonic Stall Flutter and System Mode Instability.

Region II, of relatively lesser importance, is associated with choking of the passage and is labelled Choke Flutter. As such the role of oscillatory shock waves is again indicated to be important. Hence for relatively low negative incidence and high enough relative subsonic Mach numbers, appropriate to a middle stage of a multistage compressor, the mechanism of choke flutter has many similarities to the transonic stall flutter of Region I. In addition, some authors (Fleeter, 1979) add a second sub-region at a larger negative incidence and lower relative Mach number, and term it negative incidence stall flutter. The choke flutter mechanism is still controversial and is discussed more fully later in the Manual. It may involve the type of machine (fan, compressor or turbine), type of stage (front, middle, or rear) and structural details (shrouded vs unshrouded, disk vs drum, etc.).

Three-dimensional unsteady cascade flow was first formulated in this decade (Namba, 1972), (Salaün, 1974), and this important area continues to receive significant attention. In order to apply two-dimensional theory to the aeroelastic problems of real blade systems one must either use a representative section analysis or else apply the strip hypothesis; the aerodynamics at one radius is uncoupled from the aerodynamics at any other radius. In particular, it is known that at "aerodynamic resonance" the strip theory breaks down and the acoustic modes are strongly coupled radially.

Along with aerodynamic advances the structural description of the bladed-disk assembly (Ewins, 1973), (Srinivasan ed, 1976), has received a great impetus, and the importance of forward and backward travelling waves has been firmly established. Within a particular number of nodal diameters, coupling between modes has been shown to be significant (Chi & Srinivasan, 1984) and the role of the "twin modes" (i.e. $\sin n\phi$ and $\cos n\phi$) in determining propagation has been clarified. Ford & Foord (1979) have used the twin mode concept in both analysis and flutter measurement. Furthermore, the number of nodal diameters affects the fundamental natural frequencies slightly so that they cluster together. Coupling of modes with closely spaced frequencies by aerodynamic means therefore becomes appreciable and the resulting flutter mode may contain significant content from two or three modes with consecutive numbers of diametral nodes.

Recently, the concept of mistuning introduced by Whitehead (1966) has been studied and exploited most intensively. Small geometric and structural variations from blade to blade naturally give rise to an aeroelastic system in which these multiple elements are not quite identical nor periodically disposed, and to which Lane's Theorem cannot be applied directly. The nonuniformities of spacing and setting angle in the blade flow annulus imply that mistuning also may be aerodynamic in nature. The general conclusion seems to be that mistuning is generally a favorable effect in that it raises the critical flutter speed (Whitehead, 1966) (Srinivasan, 1980) (Kaza & Kielb, 1982). Furthermore, a mistuning strategy (Crawley & Hall, 1984) has been developed to optimize the distribution and degree of mistuning of a basic set of blades under certain simplifying assumptions. The analyses have usually employed the traveling wave modal description although the standing wave approach common to propeller and helicopter rotor work has been introduced to turbomachinery by Dugundji (1983).

Practical Developments. Engine and rotating rig experiments have continued to provide important information for direct use in design and also for guiding analytical work. The output of such analysis, when codified into design procedures, thus also provides an indirect connection between experimentation and design. Stemming from the high cost of obtaining on-rotor data most of these programs have been conducted by NASA and the turbine engine manufacturers. Especially to be noted is the pioneering work of Stargardt (1979), Kurkov (1981), and Nieberding & Pollock (1977) in the use of sophisticated optical and electronic methods for gathering data from fluttering rotor blades. A smaller amount of more fundamental data has been obtained at the necessarily more modest university laboratories in the U.S., Western Europe, and Japan.

Important advances in the structural dynamics of axial-turbomachine blading have continued over the past 40 years. Stationary laboratory experiments have usually simplified the structural features of the nonrotating blade models so that these apparatuses tend to emphasize the aerodynamic information related to aeroelasticity rather than structure. However, the modal description (eigenfrequency and eigenfunction) of tapered twisted blades of thin but arbitrary cross-sections in centrifugal and gyroscopic fields (Sisto & Chang, 1981) has kept pace with the need for increasingly accurate information of this nature. The finite element method has been of great utility in most of this structural description of blades, vanes, and disks, particularly when numerical methods must be resorted to early in the analysis.

Studies of material damping and slip damping have led to increased understanding of these effects which are usually bene-

ficial in high vibratory environments. This new knowledge has resulted in the application to turbines of mechanical dampers and special high damping materials, such as chromium-based stainless steels, and to compressor/fan blades built up of laminates and composites. Although of importance when operating in regions of potential flutter, the influence of damping is most highly critical in the presence of forced vibration. In the latter case the accumulation of fatigue damage due to lightly damped resonant or near-resonant operation can occur in a very short interval of time.

Other developments not introduced in the preceding sections are dealt with in the Overview which follows. In addition, recent topics that require fuller treatment or that otherwise should be covered in future editions of the Manual, are described in the Overview.

OVERVIEW OF THE MANUAL

General Comments. Volume I of this AGARD Manual is concerned mainly with the unsteady aerodynamic aspects of aeroelasticity, one vertex of Collar's "Triangle of Forces." An overview of these topics, as they appear in Chapters 2 through 11, forms the concluding section of the present introductory chapter.

In Volume II, which deals with structural dynamics and aeroelasticity (the remaining elements of the Triangle), a separate Overview is provided for those topics, as they are set out after Chapter 11.

Chapters 2 through 11 in the current volume provide an excellent foundation for the present status of knowledge in the unsteady aerodynamics of axial blade rows. The contributors to these chapters are recognized authorities who have individually and collectively helped to lay that foundation and establish that status. From the rapid rate of growth of the field one may anticipate the need for new chapters to be commissioned for future editions of the Manual.

Subjects receiving attention very recently that have not been treated fully, if at all, include such topics as finite shock motion, variable shock strength, thick and highly cambered blades in a compressible flow, and the effects of curvilinear wakes and vorticity transport. These and other large amplitude and therefore nonlinear perturbations which prevent the linear superposition implicit in classical modal analysis have certain implications relative to the traditional solutions of the aeroelastic eigenvalue problem. Although a linearized treatment of three-dimensional unsteady flow is provided in Chapters 4 and 5, future editions of the Manual will profit from the inclusion of some of these expected refinements, presumably first to be developed for two-dimensional flow and subsequently for the annular geometry.

Unsteady Aerodynamics. The first contribution in this section is Chapter 2, Linearized Unsteady Aerodynamic Theory by Joseph Verdon. This theoretical treatise sets the stage for the unsteady aerodynamic formulations which follow it. The general importance of unsteady flow is noted, the extreme complexity of the full problem is described and the usual approximations found to be necessary are delineated. E.g. classical theory (the subject of Chapter 3) is concerned with an isolated two-dimensional cascade of unloaded flat plate airfoils in which unsteady components of the fluid velocity are small perturbations on a uniform onset flow. All of these specifications depart from the true state of affairs in an axial turbomachine to an appreciable extent.

Hence, in Chapter 2, the specifications of two-dimensionality and isolatedness are retained but the effects of blade geometry, finite mean pressure ratio across the blade row and transonic mean relative Mach number are taken into account. The unsteady disturbances are considered to be small-amplitude fluctuations about a non-uniform steady potential flow. The small disturbance unsteady flow is then governed by a set of linear partial differential equations in which the variable coefficients depend on the underlying steady flow.

The principal applications of the equations are to the aerodynamic response resulting from prescribed blade motions and from incident vortical, entropic and acoustic disturbances. The use and principles of aerodynamic work are elucidated succinctly. Also, the two special cases of classical linearized theory and transonic small disturbance theory are recovered by appropriate simplification of the general result.

Chapter 2 is thus the foundation upon which rest most of the succeeding aerodynamic formulations, particularly those parts that have proven in the past to be of direct, practical use in the applications.

Classical Theory. The second contribution in unsteady aerodynamics is Chapter 3, Classical Two-Dimensional Methods, by Denis Whitehead. This chapter deals authoritatively with the first development of two-dimensional cascade theory reduced to useful tables of coefficients (Whitehead, 1960) and the subsequent enlargement of the area of applicability to include subsonic and supersonic mean flow. The general theory developed in the previous chapter is here made explicit for the important applications to the practical systems; aeroelastic studies using two-dimensional aerodynamics via the strip hypothesis remain the predominant method of analysis up to the present time.

In addition, the actuator disk and semi-actuator disk theories are introduced by Professor Whitehead for the first time in the Manual, and their applicability in the case of small interblade phase angle

and small reduced frequency is discussed. The ability to adapt semi-actuator disk theories to stalled flutter analysis is introduced; in Chapter 7 this discussion is continued.

The compressible flow solutions (subsonic and supersonic relative Mach numbers) provide for incident acoustic and vorticity waves and thus allow for the aerodynamic responses to these types of flow disturbances in addition to the usual responses to plunging and pitching of the airfoils. Aerodynamic "resonance" is exhibited by these theoretical models and the phenomena of "cutoff" and "propagation" show the connection with the field of aeroacoustics. A very useful FORTRAN program is supplied for the subsonic case.

Finally, some basic concepts in the method of distributed singularities are introduced for modeling incompressible flow through cascades of thick, highly cambered blades. These methods are important because they relate to realistic compressor and fan blade roots, as well as turbine geometries. In addition, the concept of replacing the blade surface by a vortex sheet with a notional velocity of zero within the airfoil contour is a model that is finding further development in the so-called vortex methods for analyzing unsteady separated flows in cascades. These, and other field methods, are conceptually related to the surface singularity methods introduced at the end of this very important chapter.

Annular Cascade Effects. In Chapter 4, Three-Dimensional Flows by Masanobu Namba, the method of distributed singularities (monopoles and dipoles) is used to find the blade loadings arising from a variety of radially-varying nonuniform effects. In Chapter 5, bearing the same title, Pierre Salaün deals with a similar problem for the annular cascade, differing mainly in the particular method chosen to solve the integral equation for the unsteady blade loadings.

The full three-dimensional unsteady aerodynamics problem is extremely complex since many of the governing parameters may vary along the span: cascade geometry (profile, chordlength, pitch, stagger, sweep), degree of fixity, amplitude and phase of vibration modes, unsteady (gust) and steady incident flow velocity vectors, fluid properties, and steady blade loadings. In addition, the endwall surfaces at the hub and casing impose important boundary conditions. When casing treatment is used for sound absorption or stall margin enhancement these boundary conditions become a generalization of the classical nonpenetration condition. It is fortunate that the authors have been able to present solutions for linearized small disturbance models with many of these effects taken into account. The results demonstrate that three-dimensional treatment is essential in certain instances where a strip theory approximation is shown to be inadequate.

Three-dimensional effects on unsteady blade loadings are found by Professor Namba to be small in most cases of

supersonic flow and large in most cases of subsonic flow, although the differences in the latter are more of degree than in kind. In particular, the disturbance flow near the sonic span is quite different from quasi-two-dimensional flow and the presented three-dimensional treatment is therefore essential for analyzing the radially transonic stage. These results are confirmed by computing the flutter boundaries based on aerodynamic work. Dr. Salaün demonstrates that certain subsonic torsional flutter occurrences over narrow ranges of interblade phase angle, σ , may be missed entirely with strip theory.

Another important difference occurs near the resonant state of the predominant acoustic mode. Thus aerodynamic resonance, as predicted by quasi-two-dimensional strip-type analysis, does not properly describe the variation of unsteady blade loadings with spanwise radius.

Chapter 4 is concluded with two studies, one on the effect of a mean flow with spanwise shear, and another on the effect of sound absorbing wall liners. In the first study, with the incompressible flow velocity increasing toward the cantilever blade tip of a linear cascade, there results a decrease in overall aerodynamic work compared to a strip theory solution.

In the sound absorption study a linear cascade again is analyzed, this time with a portion of one of the endwall boundaries lined with a locally reacting sound absorbing material of uniform admittance. The remainder of the sidewalls is perfectly rigid (i.e. of zero admittance). It is found for a typical example that the acoustic treatment exerts a considerable influence on the unsteady local lift in the vicinity of the lined wall. The effect is highly localized, however, and the change in the overall blade lift is small. Similarly, the effect of nonzero acoustic wall admittance on the aerodynamic work, a discriminant of flutter, is also small for a practically reasonable extent of wall treatment.

The material presented in Chapters 4 and 5 is unique in that it presents authoritatively the most current information concerning unsteady three-dimensional flow, a field about which too little is known and which is extremely important for aeroelasticity in axial turbomachines. It is an area worthy of intense continuing effort and one which hopefully may be expected to be enlarged and reported upon in future editions of this Manual.

Field Methods. Recently a number of studies based on numerical solutions of the unsteady Navier-Stokes and Euler Equations have appeared in the literature. In Chapter 6, Numerical Methods for Transonic Flow, the authors Elizabeth Acton and Stephen Newton discuss the physical and mathematical bases for discretizing these equations and solving them using so-called field methods. Particular attention is given to the proper numerical treatment of shock waves, the uses of artificial viscosity, formulation of the unsteady boundary conditions and a comparison of the various methods with each other and with some limited experimental results. In keeping with the initial

state of development of these numerical methods for unsteady cascades, only two-dimensional inviscid flows are considered.

Based on the potential flow equations developed in Chapters 2 and 3, various mesh generation schemes are described along with the appropriate discretization of the governing equations. Both finite element and finite volume formulations are presented and also considerations concerning mesh refinement, periodicity and boundary conditions and the underlying steady flow. Only linearized unsteady flow formulations are developed and special considerations are discussed for the guarantee and acceleration of convergence to the unsteady solution. With the finite volume method no special treatment of the shock is adopted; it shows up as a region of high gradients dependent on the mesh size and the particular choice of artificial viscosity. With the finite element solution the shock is "captured" in the steady flow solution and then a different discretization and mesh, fitted about the mean shock position, is adopted for the unsteady flow. These methods are shown to be quite robust and useful design tools for application to flutter studies and are now being adapted for application with a nonsteady inflow to the cascade (the forced response problem).

In the second general class of problems an attempt is made to allow for rotational flow by solving the Euler equations by time marching techniques. The conservation form of these equations is used and the steady solution is first obtained. Either differential (finite difference) or integral (finite element) methods may be adapted to time marching. After transforming the computational mesh from the physical plane to a cartesian grid, time stepping schemes such as the predictor-corrector method are then applied to the finite difference equations in the transformed variables. Many refinements of this concept are discussed by the authors including the basic explicit scheme described, semi-explicit and implicit schemes as well. The finite volume (integral) methods using time marching have been proved successful for steady flows, including three-dimensional flows for both aircraft and cascade applications. Although the unsteady cascade solution is not yet successfully achieved, work is proceeding in that direction at many centers. Success in this area, it is felt, will lead subsequently to the eventual solution of the Navier-Stokes equations, and hence the inclusion of viscosity and turbulence in field methods.

The importance of the proper formulation of the boundary conditions cannot be overstressed. In these numerical methods they literally drive the iterated solutions toward convergence. For both the potential and Euler equations the upstream and downstream conditions, the repeat or periodicity conditions and the blade surface (the so-called internal boundary on the fluid) condition are treated carefully and exhaustively in this Chapter. Three examples are discussed. 1) Compressible fluids allow wave propagation and it is found necessary to prevent spurious reflections from the edge of the

computational domain. 2) A wake of shed vorticity is present downstream of each trailing edge and the proper jump conditions across the wake must be satisfied. 3) The vibrating blade is moving relative to inertial coordinates and either the boundary conditions must be expanded in Taylor series about the mean position or the computational grid must be formulated to move with the surface.

Chapter 6 closes with a brief comparison of results from the potential flow methods. It is shown that these methods agree quite well with each other and with experiments in general, particularly at low Mach number. The comparisons are also better in general for flat plate cascades as opposed to thick, curved blades. Precise shock positioning is also shown to be extremely important for accurate prediction of surface pressures. Finally, the importance of relying on the aerodynamic work for stability prediction, rather than the aerodynamic reactions at one blade radius, is emphasized.

In the conclusion the authors noted that the methods so far developed are limited to unsteady flows which are small linear perturbations about a nonlinear steady potential flow. This implies in turn that the shock movement is not too large. Solutions of the Euler equation, although not as well advanced, hold greater promise for less simplified modeling of the flow.

Stall and Separation. The earliest manifestation of aeroelastic instability in axial turbomachines was stall flutter. This phenomenon, in which flow separation plays a crucial role, continues to be important and the subject of analysis for application. In Chapter 7, Stall Flutter, this experience is summarized by Fred Sisto and the methods of treating periodically stalled flow are described.

The theories are somewhat heuristic, based strongly on empiricism, and there is a great observational reliance on aeroelasticity, the coupling between unsteady aerodynamics and structural dynamics, to explain stall flutter experience. Thus the older design rules for avoiding flutter are given the historical importance they have earned and physical insight into flutter behavior is provided. Emphasis is given to recognizing the nonlinear nature of the unsteady aerodynamic loads when periodic separation is present.

Chapter 7 closes with a note on the Random Vortex Method of Chorin (1973), as further developed by Spalart (1984), one of the newer field methods, as presently applied to propagating stall in cascades. With the introduction of small amplitude motion of the internal boundaries (i.e., the airfoil upper and lower cambers) the RVM holds great promise for yielding the first quantitatively reliable theory for unsteady separated flow in two dimensions, a minimal requirement for aeroelastic modeling. It is another area where considerable future growth is anticipated.

Experimental Results. Chapter 8, Unsteady Aerodynamic Measurements in Flutter Research, has been prepared by Sanford Fleeter and Robert Jay. This is the earliest chapter in Volume I devoted to the role of experimentation and some fundamental experimental flutter results are described. The emphasis here is on self-excited instability; the subject of aerodynamically forced vibration is reserved for the following Chapter 9.

Professor Fleeter properly emphasizes the important role of experimentation in guiding the development of analytical models for flutter prediction. Other objectives of experimental programs are the acquisition of a flutter boundary data bank and the verification of new concepts for flutter stability enhancement. Omitting full scale component testing, the principal experimental facilities are high speed rotating rigs, linear cascades and stationary annular cascades. Typical strain gage, optical and other instrumentation (and the data acquired therefrom) are then described. The features and importance of high speed digital data processing are discussed.

Considerable attention is given to the fundamental data acquired in a driven oscillatory airfoil cascade with imposed interblade phase angle, σ , as a primary independent variable. By contrast, the importance and limitations of free flutter testing are discussed from a research vantage point. Chapter 8 concludes with a survey of the key experimental results for stall flutter, supersonic flutter, choke flutter, and negative incidence flutter. These results may be identified with the flutter regions on the compressor characteristic map, Figure 1, and profitably compared with the analytical, or theoretical, discussion in Chapters 2, 3, 4, 5, 6, and 7.

Forced Vibration Experiments. Chapter 9, Unsteady Aerodynamic Measurement in Forced Vibration Research, is a continuation of the previous chapter on experimentation and penetrates the important area of aeroelastic forced vibration (as contrasted with the self-excited instability known as flutter). Robert Jay and Sanford Fleeter continue their collaboration as the authors.

Solution of the forced response problem requires that a balance be struck between the aerodynamic work done by the unsteady "gust" acting on the airfoil and aerodynamic damping work resulting from the subsequent vibration. Mechanical forms of damping may be added to the latter. After defining this problem and its dependence on the flow field, airfoil geometry, and mode shape, the importance is noted of key parameters such as reduced frequency and interblade phase angle. Typical facilities in which experiments are conducted are linear cascades, annular cascades, low speed rotating rigs, and high speed rotating rigs, as introduced in the previous Chapter. Nine typical investigations in linear cascades are briefly summarized, as are four in annular cascades, seven in low speed rotating rigs, and four in high speed rotating rigs.

Familiarization with various instruments and data recording components is provided, including hot wire anemometers, pressure transducers, Schlieren systems, analog-to-digital converters, tape recorders, oscilloscopes, and their dynamic calibration and assembly into useful data acquisition systems.

The Chapter closes with very detailed and useful descriptions of two specific experimental programs and the facilities in which they were conducted. For the aerodynamic damping study a linear turbine cascade tunnel is described in which the blades are oscillated electro-mechanically and the resulting pressure distribution is measured on the center blade. Dynamic calibration of the Kulite pressure sensors is critical.

For the stator vane gust loading study a single stage low speed compressor rig is instrumented with an inter-row hot wire anemometer and the stator vanes following the rotor are pressure instrumented. The data were acquired and processed to yield very useful and informative distributions of unsteady flow fields and the related unsteady aerodynamic forces.

Experimental Aeroelastic Transfer Function. In Chapter 10, Understanding Fan Flutter Through Linear Cascade Aeroelastic Testing, the author, Edmond Szechenyi, describes a unique combination of experimentation and data processing. The linear cascade simulating turbofan blades is provided with the capability of forced oscillation of two blades in any position in the cascade. One of the two blades is heavily instrumented with up to 26 pressure transducers. These measured pressures may be integrated to yield lift and moment. The outputs from the blade pressure and blade position transducers are Fourier transformed so as to output a transfer function: the pressure and phase produced by a particular oscillatory blade motion.

Using this complex transfer function parameter, an extensive study is conducted of the direct influence of the blade upon itself and the "coupling" or aerodynamic influence of one vibrating blade upon another. Assuming the validity of superposition, the local pressure coefficient, the lift coefficient, and the moment coefficient may then be synthesized for a complete (presumed infinite) cascade of fluttering blades. Stability is discriminated by the phase of the force response with respect to the motion inducing it.

An interesting, if controversial set of parametric studies are conducted with this apparatus and the associated data reduction technique. Particular concern is given to the influence of separation on flutter in Regions I, III, IV, and V of Figure 1, which correspond with Regions 1, 3, 4, and 2 of Chapter 10 (no separation in Regions III or 3). The prediction of flutter is subsumed in the statement that "propagation" (as defined by the variation along the chord of the transfer function phase angle) shifts to a direction from leading edge to trailing edge as soon as the flow on the suction

surface of the airfoil becomes separated. "But what causes this change of direction when the flow separates?" This question is posed, but remains to be answered perhaps in the future.

Other major parametric influences referring to shock structure and shock movement in supersonic flow, the role of back pressure and the influence of mode shape are addressed by this unique approach. Comparisons with cascade and rotating rig measurements, the influence of frequency (rather than reduced frequency or frequency parameter) and other interesting applications of the transfer function method of data reduction are presented in this Chapter. This new method of experimentation should prove increasingly valuable as it becomes more refined and more widely applied. For its general application the transfer function formulation relies on the principle of superposition. Although the validity of superposition in this specific application has not been proven, the practical resolution of the question seems to be that it works with acceptable accuracy for drawing qualitative conclusions.

One may also discern a possible feedback in suggesting new analytical models for unsteady cascade aerodynamics based on these ideas. Thus the placement of this Chapter near the end of Volume I is indicative of its potential for stimulating new initiatives.

Unsteady Aerodynamic Measurements on Rotors. The eleventh and final Chapter of Volume I contributed by Heinz Gallus bears the above-captioned title. The simulation of unsteady flow in axial turbomachines by linear cascades, and to a lesser extent in stationary annular cascades, is usually deficient in several important respects. Furthermore, it is difficult and expensive to attempt such experimentation on the full multistage turbomachine due to the inaccessibility of instrumentation and the inability to isolate the effects of individual parameters. For this reason the testing of rotating annular cascades, or "rigs," is extremely valuable. In particular, unsteady interaction attributable to the relative motion of rotor and stator can only be obtained experimentally in rotating rigs. This is particularly important for forced vibration experiments where it is desired to vary gust amplitude, reduced frequency, and interblade phasing in a parametric fashion. Rotating rigs also allow the immediate study of realistic three-dimensional effects associated with large aspect ratio, tapered, twisted blading. Other effects which may be studied, and which are not yet fully accessible to analysis, include tip leakage, secondary flow, fluid viscosity and separated flow.

Professor Gallus discusses briefly the types of instrumentation used in rotor testing, with principal emphasis on the aerodynamic measurement devices: pressure taps, pressure transducers, hot film gauges, hot wire anemometers and multi-element probes. Optical systems discussed include the laser doppler velocimeter, the schlieren shadowgraph, the holograph interferometer and various visualization schemes using smoke or dye injection or

gas fluorescence. Additional information is given on data conditioning and data reduction techniques.

The major portion of Chapter 11 is then given over to discussing a large representative sample of the specific applications of unsteady flow measuring techniques on rotors which appear in the literature. In addition to presenting the specifics of the instrumentation and the associated measurements, considerable attention is paid to the transfer of the signals from rotating frame to fixed frame by slip rings, scanivalves and telemetering. The subject of rotating probes, unique to the problem of on-rotor data acquisition, is covered and contrasted with the alternative of interpreting stationary probe

readings to yield time-resolved data relative to the rotor. It is noted that laser velocimetry has turned out to be the main tool for flow field research in high speed rotors.

This final Chapter of Volume I closes appropriately with some general observations concerning the methods available for determining the unsteady flow in axial turbomachines. These methods, when taken together with the structural information to be discussed more fully in Volume II, allow a complete aeroelastic description to be developed experimentally. Finally, and most importantly, the roles of experimentation as the final arbiter of design and as the method for guiding and checking theoretical analysis are once again noted.

LINEARIZED UNSTEADY AERODYNAMIC THEORY

Joseph M. Verdon
United Technologies Research Center
East Hartford, CT 06108
USA

INTRODUCTION

Overall Background

The impact of flow unsteadiness on the performance, efficiency and, in particular, on the reliability of axial-flow turbomachines has been widely recognized and documented both in the present Manual and in a number of earlier publications (e.g., see Mikolajczak 1975; Platzer 1975, 1977; Sisto 1978; Fleeter 1979; Whitehead 1980; and Greitzer 1985). Important current design concerns directly associated with unsteady phenomena include the following: the effects of aerodynamically induced and self-excited blade vibrations on aeroelastic response and stability, the effects of blade row interactions and turbulence on efficiency and noise generation, the effects of inlet flow nonuniformities on compressor and engine aerodynamic stability, and the nature and flow structure of general post-stall engine transients.

In the past very successful turbomachines have been developed by compensating for an inadequate understanding of unsteady flows with extensive empirical correlations. However, the continuing demand for increased performance has resulted in design trends such as higher tip speeds and higher loadings which aggravate dynamic problems in the various components particularly the blading. Further, requirements for increased efficiency and noise suppression will impose additional and important constraints on future designs. Thus an understanding of unsteady flow phenomena and the development and application of theoretical procedures for predicting such phenomena has become essential to the successful design process.

The development of theoretical models to predict unsteady flows in axial-flow turbomachines is a formidable task. The analyst is confronted with determining the time-dependent, three-dimensional flow of a viscous compressible fluid through a geometric configuration of enormous complexity. Phenomena of interest include potential flow interactions between closely spaced blade rows, intricate shock formations and reflections, shock/boundary layer interactions, vortex shedding at blade tips, boundary layer separations, wake formations and cuttings, and wake transport, spreading and decay. Moreover, theoretical models must be formulated so that reliable design predictions can be achieved efficiently and economically. This task clearly requires the introduc-

tion of a considerable number of simplifying assumptions to make the problem mathematically tractable and to render the resulting solutions useful to the designer.

For the most part, theoretical unsteady aerodynamic formulations have been directed toward predicting the aeroelastic or aeroacoustic response phenomena associated with self-excited or forced vibrations of the blades of an isolated array. In the former circumstance the elastic motion of the structure and the aerodynamic forces are inseparably coupled, whereas in the latter, the forces initiating the motion of the structure are independent of that motion. As noted by Whitehead (1980) to determine the unsteady response characteristics of interest for an isolated blade row, aerodynamic theories must be capable of predicting the unsteady forces acting on the blades, the entropy and vorticity fluctuations convected downstream, and the static pressure or acoustic waves radiated away from the blade row, for prescribed (self-excited) blade motions and externally induced (forced) aerodynamic excitations. Sources of forced excitation include variations in total pressure and total temperature ("entropy and vorticity waves") at entry and variations in static pressure (acoustic waves) entering the blade row from upstream or downstream. Although beyond the scope of this chapter, it should be noted that the determination of the forcing functions is a difficult but very important aspect of the overall problem. Unfortunately, because of the assumptions used in the development of unsteady aerodynamic analyses for aeroelastic or aeroacoustic applications, the foregoing response information is only available in a limited sense. In such analyses viscous effects are usually neglected at the outset, the flow is usually regarded as two-dimensional, and unsteady fluctuations are assumed to be of sufficiently small magnitude that a linearized analysis of the unsteady flow is justified.

Many of the unsteady aerodynamic analyses currently used in turbomachinery aeroelastic or aeroacoustic design applications are based on classical linearized theory. Here both steady and unsteady departures from a uniform free stream are regarded as small and of the same order of magnitude relative to the free-stream speed. Thus classical unsteady analyses are essentially restricted to unloaded, flat-plate cascades which operate in an entirely subsonic or entirely supersonic

flow environment. Very efficient semi-analytic solution procedures have been developed for two-dimensional attached subsonic (Whitehead 1970; Kaji & Okazaki 1970; Smith 1971; and others) or supersonic (Kurosaka 1974; Verdon 1977; Nagashima & Whitehead 1978; Adamczyk & Goldstein 1978; Ni 1979; and others) flows and applied in flutter (self-excited blade vibrations) and resonant stress (forced vibrations) design calculations. Moreover, the classical supersonic analyses have been found to be quite successful, when bolstered by empirical information, at predicting observed flutter behavior in the fan stages of modern high-bypass ratio engines (see Snyder & Commerford 1974; and Mikolajczak, et. al. 1975). Models based on variations or extensions of the two-dimensional classical linearization have also been developed for treating separated subsonic flows (Perumal 1976; Chi 1980), high-frequency transonic flows (Surampudi & Adamczyk 1984), supersonic flows with strong in-passage normal shocks (Goldstein, Braun & Adamczyk 1977) and three-dimensional attached flows (Salaun 1976; Namba 1977; and Namba & Ishikawa 1983), but these have received only limited application in the design process.

The classical linearization does not account for interactions between steady and unsteady disturbances and such interactions are crucial to the successful prediction of a wide variety of turbomachinery unsteady aerodynamic phenomena. It is thus important that more general unsteady aerodynamic models be developed which include the effects of realistic design features, such as blade geometry, finite mean pressure variation across a blade row, and operation at transonic Mach numbers, on unsteady aerodynamic response. The present chapter will focus on the derivation of such a model in which unsteady disturbances are regarded as small-amplitude fluctuations relative to a fully nonuniform steady (in a coordinate frame attached to the blade row) potential flow. As a result of the foregoing assumption, the small-disturbance unsteady flow is governed by a set of linear variable-coefficient equations in which the variable coefficients depend upon the velocity potential of the underlying steady flow. This type of model and its application to turbomachinery blading has received considerable attention in recent years (see Atassi & Akai 1978, 1980; Carstens 1981; Caruthers 1981; Whitehead & Grant 1981; Whitehead 1982; Caspar & Verdon 1981; and Verdon & Caspar 1980, 1982, 1984), and solution methods are gradually reaching the stage where it will be appropriate to consider them for design applications.

Scope of this Chapter

In the following presentation the equations governing the steady and linearized unsteady flow for an isolated two-

dimensional cascade will be derived in some detail. Further, the governing equations of classical linearized subsonic or supersonic theory and, for the most part, those of time-linearized transonic small-disturbance theory (see Tijdeman & Seebass 1980) will be recovered as special cases of the more general linearized formulation. In this manner the basic equations underlying the most important unsteady linearizations that have been proposed for dealing with airfoil or blade vibration problems can be determined from within a unified theoretical framework. This author's previous experience has been primarily concerned with developing unsteady aerodynamic analyses for fan or compressor blade flutter applications. Therefore, in preparing this article heavy reliance has been placed on the work of Goldstein (1978, 1979) in an effort to provide a complete linearized formulation in which forced excitations due to incident vortical, entropic and acoustic disturbances are included along with those due to prescribed blade motions.

In this chapter we are primarily concerned with the derivation of the equations governing the steady and unsteady flow phenomena associated with the blades of an isolated two-dimensional cascade. Semi-analytic solution methods for classical linearized two-dimensional cascade flows are discussed by Whitehead in the following chapter of this Manual, and extensions of the classical formulation along with the description of solution methods for three-dimensional flows are given in the chapters by Namba and Salaun. For a description of the semi-analytic surface-integral and the numerical field methods that have been proposed for solving the steady and the linearized unsteady equations, derived herein, the reader is referred to the report by McNally & Sockol (1981), the text of Gostelow (1984) and the unsteady cascade analyses cited above.

PROBLEM DESCRIPTION

We consider the time-dependent and two-dimensional adiabatic flow, with negligible body forces, of an inviscid non-heat conducting perfect gas through an infinite and isolated array of airfoils (i.e., a cascade such as the one shown in fig. 1). Although we are restricting our consideration to two-dimensional flows, with the exception of the surface and far-field conditions, most of the governing equations presented below are valid in three spatial dimensions. The time-dependent or unsteady fluctuations in the flow are assumed to be of small amplitude and to arise from one or more of the following sources (c.f. fig. 2): self-excited blade motions, upstream and/or downstream acoustic disturbances which propagate toward the blade row, and upstream vortical and entropic disturbances. It is assumed

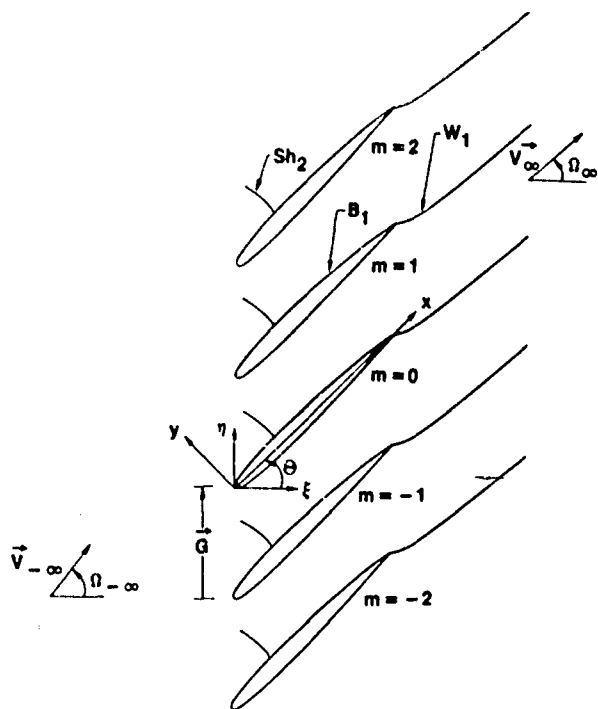


Figure 1. Two-dimensional transonic compressor cascade; $M_\infty < M_{sh} < 1$.

that, in the absence of these unsteady excitations, the blades are equally spaced, identical in shape and their chord lines are each inclined at an angle θ relative to the axial flow (or positive ξ -) direction; and that beyond some finite distances upstream (say $\xi \leq \xi_-$) and downstream ($\xi \geq \xi_+$) from the blade row, the flow is at most a small (steady) perturbation from a uniform free-stream condition. For aeroelastic investigations, the application of primary interest here, the goal is to predict the unsteady pressures and the global unsteady airloads acting on the blades and arising from various prescriptions of the foregoing excitations.

For flows of practical interest the Reynolds number (Re) is usually sufficiently high so that viscous effects are concentrated in relatively thin layers across which the flow properties vary rapidly but continuously. Provided that large scale flow separations do not occur, these layers generally appear adjacent to the blade surfaces (boundary layers), downstream of the blades (wakes) and in the vicinity of rapid compressions (shocks). In the inviscid approximation ($Re \rightarrow \infty$) their thickness becomes zero and they are modeled as surfaces across which the flow variables are discontinuous. In particular, boundary layers and wakes are regarded as thin vortex sheets which support a discontinuity in tangential velocity, and shocks are regarded as thin surfaces which support a discontinuity in normal velocity. Here we assume that the boundary layers remain attached to the blade surfaces. Hence, the vortex-sheet boundary layers coincide with the blade surfaces and support a jump in velocity

from zero at the "wall" to the inviscid value at the "edge" of the boundary layer. Further, the vortex-sheet unsteady wakes emanate from the blade trailing-edges and extend infinitely far downstream.

The description of the foregoing assumptions brings us to a convenient starting point for presenting the equations governing the flow through the cascade. As we proceed with the development of these equations, additional assumptions, for example, restrictions on shock strength and on the temporal and spatial behavior of the unsteady excitations, will be introduced to further simplify the theoretical model.

In the following discussion all variables are dimensionless. Lengths have been scaled with respect to blade chord, time with the ratio of blade chord to the upstream free-stream speed, and density with respect to the upstream free-stream density. The scalings for the remaining variables are readily determined from the equations given below which have essentially the same form as their dimensional counterparts. In anticipation of the small-unsteady-disturbance approximation, which will be introduced below, the symbol \sim is used to denote a time-dependent fluid property. With the exception of density, upper case letters are used below to represent the various nonlinear flow variables, and lower case letters will be introduced to represent their small-disturbance counterparts. Thus, for example, \bar{p} and p denote the full time-dependent and the steady-state fluid pressure respectively, and \bar{p} and p will denote the time-dependent small-disturbance unsteady pressure and its complex amplitude. The corresponding symbols for the fluid density are $\bar{\rho}$, $\bar{\rho}$, $\bar{\rho}$ and ρ , respectively. The subscripts $-\infty$ and $+\infty$ will be used to denote the uniform flow properties far upstream and far downstream from the blade row.

In addition to these notations for the fluid dynamic variables, upper-case

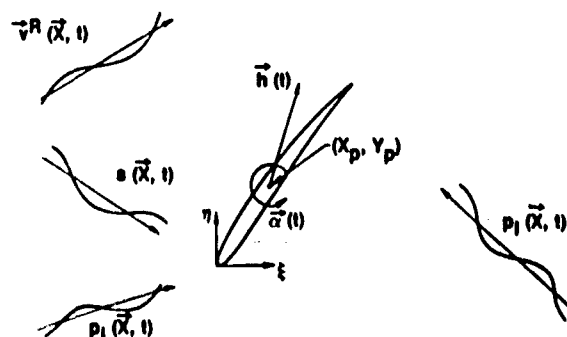


Figure 2. Unsteady excitations: blade motion (rotation and translation), incident vortical and entropic disturbances from upstream, and incident acoustic disturbances from upstream and downstream.

script letters denote instantaneous surface (blade, wake or shock) locations, while corresponding upper-case block letters refer to steady-state surface positions, and the vector, \vec{R} , measures the displacement of a point on a moving surface relative to its mean or steady-state position (see fig. 3). The unit vectors \vec{h} and \vec{t} are normal and tangent respectively to a surface and directed such that $\vec{h} \times \vec{t} = \vec{e}_z$ points out from the page. Finally, as in fig. 1, the steady-state positions of the blade chord lines are assumed to coincide with the line segments $\eta = \xi \tan \Theta + mG$, $0 < \xi < \cos \Theta$, $m = 0, \pm 1, \pm 2, \dots$, where ξ and η are the cascade axial and "circumferential" coordinates, m is a blade number index, Θ is the cascade stagger angle, and G is the cascade gap vector which is directed along the η -axis with magnitude equal to the blade spacing.

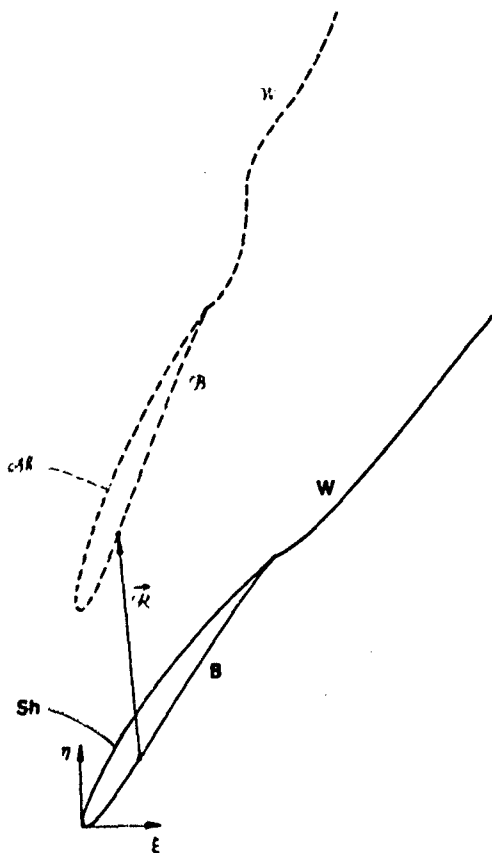


Figure 3. Steady state, —, and instantaneous, ----, blade, shock and wake positions.

Conservation Laws and Thermodynamic Relations

The equations governing the flow follow from the integral forms of the mass momentum and energy conservation laws. For an arbitrary moving control volume $\omega(t)$ bounded by a control surface $d(\vec{X}, t)$, where \vec{X} is a position vector and t is time, these laws are written as

$$\frac{d}{dt} \int_{\omega} \rho \, d\omega + \int_{d(\vec{X}, t)} \rho \left(\vec{V} - \frac{\partial \vec{R}}{\partial t} \right) \cdot \vec{h} \, d\omega = 0, \quad (1)$$

$$\begin{aligned} \frac{d}{dt} \int_{\omega} \rho \vec{V} \, d\omega + \int_{d(\vec{X}, t)} \rho \left[\vec{V} \left(\vec{V} - \frac{\partial \vec{R}}{\partial t} \right) \right] \cdot \vec{h} \, d\omega \\ = - \int_{d(\vec{X}, t)} \tilde{P} \vec{h} \, d\omega \end{aligned} \quad (2)$$

and

$$\begin{aligned} \frac{d}{dt} \int_{\omega} \rho \left(\tilde{E} + \vec{V}^2/2 \right) d\omega \\ + \int_{d(\vec{X}, t)} \rho \left(\tilde{E} + \vec{V}^2/2 \right) \left(\vec{V} - \frac{\partial \vec{R}}{\partial t} \right) \cdot \vec{h} \, d\omega \\ = - \int_{d(\vec{X}, t)} \tilde{P} \vec{V} \cdot \vec{h} \, d\omega, \end{aligned} \quad (3)$$

respectively. Here ρ , \vec{V} , \tilde{P} and \tilde{E} are the fluid density, velocity, pressure and specific internal energy, respectively, $\vec{R}(\vec{X}, t)$ defines the displacement of points on the control surface, \vec{h} is a unit outward normal vector at this surface and \otimes denotes the tensor or dyadic product of two vectors.

The first and second terms on the left-hand-sides of (1), (2) or (3) represent the time rate of increase of a quantity (i.e., mass, momentum or energy) within the control volume and the efflux of that quantity through the control surface, respectively. The terms on the right-hand-sides of (2) and (3) represent the external force acting on the fluid within the control volume and the rate at which the surface pressures do work on that fluid. Since discontinuities in the flow variables will generally occur, the integral forms of the conservation laws are required to describe the flow over the entire domain of interest. These forms provide corresponding differential equations in regions where the flow variables are continuously differentiable and "jump" conditions at surfaces across which (in the inviscid approximation) the flow variables are discontinuous.

In addition to the foregoing conservation equations, some relations from classical thermodynamics are needed to complete the specification of the fluid mechanical problem. In particular, we require the equation of state for a thermally perfect gas,

$$\tilde{P} = \gamma^{-1}(\gamma - 1) \tilde{\rho} \tilde{T}, \quad (4)$$

and the relation between the internal energy and the temperature for a calorically perfect gas,

$$\tilde{E} = \gamma^{-1} \tilde{T} = (\gamma - 1)^{-1} \tilde{P} / \tilde{\rho}. \quad (5)$$

Here \tilde{T} is the temperature and γ is the specific heat ratio of the fluid (constant pressure to constant volume).

It will also prove to be useful to introduce the fundamental thermodynamic

identity

$$\tilde{T} d\tilde{S} = d\tilde{E} + \tilde{P} d(\tilde{\rho}^{-1}), \quad (6)$$

where \tilde{S} is the specific entropy of the fluid. It then follows from (4) through (6) that the entropy is related to the pressure and density by the differential expression

$$d\tilde{S} = \gamma^{-1} d\tilde{P}/\tilde{P} - d\tilde{\rho}/\tilde{\rho}. \quad (7)$$

Equation (7) can be integrated to relate the change in entropy between any two equilibrium states to the corresponding changes in pressure and density.

THE FULL TIME-DEPENDENT GOVERNING EQUATIONS

Field Equations

The field or differential equations which govern the flow variables in continuous regions of the flow are obtained by applying Green's theorem (see Aris 1962, p. 58) to the surface integrals in (1), (2) and (3) and taking the limit as $\epsilon(t)$ approaches zero. It follows that

$$\frac{\partial \tilde{\rho}}{\partial t} + \nabla \cdot (\tilde{\rho} \tilde{\mathbf{V}}) = 0, \quad (8)$$

$$\frac{\partial}{\partial t} (\tilde{\rho} \tilde{\mathbf{V}}) + \nabla \cdot (\tilde{\rho} \tilde{\mathbf{V}} \otimes \tilde{\mathbf{V}}) + \nabla \tilde{P} = 0 \quad (9)$$

and

$$\begin{aligned} \frac{\partial}{\partial t} [\tilde{\rho} (\tilde{E} + \tilde{V}^2/2)] + \nabla \cdot [\tilde{\rho} \tilde{\mathbf{V}} (\tilde{E} + \tilde{V}^2/2)] \\ + \nabla \cdot (\tilde{P} \tilde{\mathbf{V}}) = 0. \end{aligned} \quad (10)$$

These (conservative) forms of the governing differential equations correspond to the integrated forms (eqs. (1), (2) and (3)) and are often required for the numerical treatment (i.e., shock capture) of shocks. But for other purposes the equations may be simplified. Thus the mass conservation equation can be written as

$$\frac{D\tilde{\rho}}{Dt} + \tilde{\rho} \nabla \cdot \tilde{\mathbf{V}} = 0, \quad (11)$$

where the symbol D/Dt is used in place of d/dt to emphasize that the latter is now a material or convective derivative operator; i.e., $D/Dt = d/dt = \partial/\partial t + \tilde{\mathbf{V}} \cdot \nabla$. Further, it follows from (8) and (9) that the momentum equation can be written as

$$\tilde{\rho} \frac{D\tilde{\mathbf{V}}}{Dt} + \nabla \tilde{P} = 0. \quad (12)$$

Finally, The energy equation can be written in various alternative forms. For example, it follows from (10) through (12)

and some algebra that

$$\begin{aligned} \tilde{\rho} \frac{D\tilde{E}}{Dt} &= -\tilde{\rho} \tilde{\mathbf{V}} \cdot \frac{D\tilde{\mathbf{V}}}{Dt} - \nabla \cdot (\tilde{P} \tilde{\mathbf{V}}) = -\tilde{P} \nabla \cdot \tilde{\mathbf{V}} \\ &= \tilde{P} \tilde{\rho}^{-1} \frac{D\tilde{\rho}}{Dt} = -\tilde{P} \tilde{\rho} \frac{D(\tilde{\rho}^{-1})}{Dt}, \end{aligned} \quad (13)$$

or after introducing the fundamental thermodynamic identity (6) that

$$\frac{D\tilde{S}}{Dt} = 0. \quad (14)$$

Thus the entropy of each fluid particle must remain constant in continuous regions of the flow. From (7), in such regions the pressure and density of each particle are related by the isentropic equation of state; i.e.,

$$\tilde{P} \tilde{\rho}^{-\gamma} = \text{constant}. \quad (15)$$

For turbomachinery aeroelastic applications, we require solutions of the foregoing mass (8) or (11), momentum (9) or (12) and energy (10) or (14) equations subject to boundary conditions at moving blade surfaces, jump conditions at moving wake and shock surfaces, and appropriate conditions far from the blade row. First, we consider the flow behavior in the far field by making use of the assumptions that steady and unsteady disturbances are small (i.e., of $O(\epsilon)$) relative to the uniform free-stream conditions. Thus, to within first order in ϵ , these disturbances are not coupled, and hence, they can be examined separately.

Far-Field Behavior

The character of a small-amplitude unsteady motion imposed on a uniform flow has been described by Kovaszay (1953) and more recently by Goldstein (1978). The velocity field can be decomposed into distinct vortical-, entropic- and acoustic-type modes. The vortical disturbance (often called a gust) has a divergence-free velocity field and is completely decoupled from the fluctuations in pressure or any other thermodynamic property. The entropic disturbance is decoupled from the velocity and pressure fluctuations, but is directly related to the density fluctuation (c.f., eq. (7)). Both the vortical and the entropic disturbance are convected without distortion by the uniform mean flow. Finally, the acoustic disturbance produces no entropy fluctuation and is therefore directly related to an irrotational velocity fluctuation, which implies that its kinematic behavior is quite different from that of the vortical and entropic disturbances. Each of these modes of unsteady motion is a solution of the governing equations and can

therefore be super-imposed on a uniform flow independently of the others.

It follows from the foregoing discussion that the velocity field far upstream ($\xi \leq \xi_-$) of an isolated blade row must be of the form

$$\vec{V}(\vec{X}, t) = \vec{V}(\vec{X}) + \vec{v}^R(\vec{X} - \vec{V}_\infty t) + \vec{v}^\phi(\vec{X}, t) + \dots, \quad (16)$$

where

$$\nabla \cdot \vec{v}^R = 0, \quad (17)$$

$\vec{V}(\vec{X})$ is the steady velocity, \vec{V}_∞ is the upstream free-stream velocity, \vec{v}^R is the rotational velocity associated with the imposed vortical or gust disturbance, and \vec{v}^ϕ is the irrotational unsteady velocity associated with the acoustic disturbance. That part of the irrotational disturbance velocity which is associated with inward propagating acoustic waves is known (or prescribed), but the portion of \vec{v}^ϕ associated with outward propagating waves must be determined as part of the overall solution. Similarly, the entropy far upstream of the blade row must be of the form

$$\tilde{S}(\vec{X}, t) = S(\vec{X}) + \tilde{s}(\vec{X} - \vec{V}_\infty t) + \dots, \quad (18)$$

where S is the entropy of the steady flow and \tilde{s} is the imposed unsteady entropic disturbance. Expressions for the time-dependent velocity and entropy fields far downstream of the blade row are of similar form. However, it is to be emphasized that the downstream rotational velocity and entropy fluctuations are not prescribed, but must be determined as part of the unsteady solution. Finally, the pressure far upstream $\xi \leq \xi_-$ or far downstream $\xi \geq \xi_+$ from the blade row is given by

$$\tilde{P}(\vec{X}, t) = P(\vec{X}) + \tilde{p}(\vec{X}, t) + \dots = P(\vec{X}) - \bar{\rho}_{\infty} \left(\frac{\partial}{\partial t} + \vec{V}_\infty \cdot \nabla \right) \tilde{\chi}(\vec{X}, t) + \dots, \quad (19)$$

where P is the steady pressure, $\bar{\rho}_{\infty}$ is the uniform density far upstream or downstream, and \tilde{p} and $\tilde{\chi}$ are the pressure and the velocity potential fluctuations associated with the small-amplitude acoustic disturbances.

By assumption, steady disturbances in the far field must originate at the cascade. Therefore such disturbances will be isentropic and irrotational far upstream; i.e., $S(\vec{X}) = S_\infty$ and $\vec{V}(\vec{X}) = \vec{V}_\infty + \nabla \phi(\vec{X})$, where ϕ is a steady disturbance potential. However, in general, steady rotational velocity and entropic disturbances may also be present in the far-downstream flow.

The foregoing results, which have been determined on the basis of a small-disturbance approximation, indicate the far-field conditions that must be imposed in the nonlinear time-dependent problem. In particular, information on the far-upstream and far-downstream uniform flows and the incident acoustic disturbances, along with information on the far-upstream rotational velocity and entropic disturbances, must be given. Far-field disturbances caused by the blades and their motions, i.e., irrotational disturbances which propagate away from the blade row and vortical and entropic disturbances which are convected downstream, must be determined as part of the nonlinear time-dependent solution.

Surface Conditions

Conditions at vortex sheet boundary layer and wake surfaces and at shock surfaces are obtained from the integral conservation laws by considering a control volume which contains an element of such a surface and taking the limit as the length normal to this surface element approaches zero. The resulting jump conditions for conserving mass momentum and energy at a surface, across which the flow variables are discontinuous, are

$$[\tilde{M}_f] = 0, \quad (20)$$

$$\tilde{M}_f [\tilde{V}] + [\tilde{P}] \hat{n} = 0 \quad (21)$$

and

$$\tilde{M}_f [\tilde{E} + \tilde{V}^2/2] + [\tilde{P} \tilde{V}] \cdot \hat{n} = 0 \quad (22)$$

respectively. Here $[\]$ denotes the jump in a flow quantity experienced by an observer when moving across the surface of discontinuity in the \hat{n} -direction and

$$\tilde{M}_f = \bar{\rho} \left(\tilde{V} - \frac{\partial \chi}{\partial t} \right) \cdot \hat{n} \quad (23)$$

is the mass flux through the surface.

Although the viscous displacement and curvature effects associated with actual boundary layers, wakes and shocks are neglected in the present analysis, since by assumption $Re \rightarrow \infty$, changes could be made in the foregoing jump conditions to accommodate them. If so, it would then be necessary to match the inviscid or "outer" solution sought here to "inner" viscous solutions in order to provide a solution for the complete flow field. We refer the reader to the articles by Melnik (1980), Lock and Firmin (1982), and LeBalleur (1984) for comprehensive reviews on the application of such viscous/inviscid interaction concepts in steady-state aerodynamics.

Since the vortex sheets, which represent the boundary layers and wakes, support a jump in tangential velocity (i.e.,

$\vec{V} \cdot \vec{r} = 0$), it follows from (21) that \vec{M}_f must equal zero. Hence, the conditions

$$\vec{M}_f = 0, \quad (24)$$

$$[\vec{P}] = 0 \quad (25)$$

and

$$[\vec{V}] \cdot \vec{n} = 0 \quad (26)$$

prevail at vortex sheet boundary-layer and wake surfaces. In the inviscid attached-flow approximation the vortex-sheet boundary layers coincide with the blade surfaces. Thus it follows from (23) and (24) that the flow tangency condition

$$\left(\vec{V} - \frac{\partial \vec{R}}{\partial t}\right) \cdot \vec{n} = 0, \quad (27)$$

which applies at the "outer edges" of the viscous layers, must also apply at the solid blade surfaces, \mathcal{B}_m , and on the upper and lower sides of the thin vortex wakes, \mathcal{W}_m . In the present application the surface displacement vector $\vec{R}(\vec{X}, t)$ is prescribed at blade surfaces, but at wake surfaces it must be determined as part of the overall time-dependent solution.

At shocks, $\mathcal{S}_{m,n}$, where the subscripts refer to the n th shock associated with the m th blade, the mass flux is generally nonzero (i.e., $\vec{M}_f \neq 0$). Hence, it follows from (21) that the component of fluid velocity tangent to a shock surface must be continuous across the shock. The remaining jump conditions, along with the thermodynamic equations of state, are then required to determine the shock velocity, $\partial \vec{R} / \partial t$, and the changes in the normal component of the fluid velocity and in the thermodynamic properties of the fluid as it passes through the shock. In the usual situation the flow ahead of the shock is known, and the Rankine-Hugoniot conditions, i.e., (20), (21) and (22), are used to determine the flow behind in terms of the shock velocity, or to determine the shock velocity and the remaining flow quantities in terms of one of the flow quantities behind.

Discussion

Our derivation of the equations governing the time-dependent inviscid flow produced by prescribed blade motions and small-amplitude incident vortical, entropic and acoustic disturbances is now complete. The problem posed is a formidable one, consisting of nonlinear time-dependent field equations along with conditions imposed on moving blade, wake and shock surfaces in which the instantaneous positions of the wake and shock surfaces must, in principle, be determined as part of the

solution. There has been, as yet, little attempt to solve the resulting nonlinear time-dependent equation set for blade vibration or noise applications, not only because of the associated numerical complexities, but primarily because the computing time requirements of such solutions would prohibit their use in detailed aeroelastic or aeroacoustic investigations. Thus, in the next section we will make use of additional simplifying assumptions with the intention of providing a useful analytical model for turbomachinery aeroelastic applications.

In particular, the small unsteady-disturbance approximation, which at this point has been invoked only to specify the flow behavior in the far field, will be applied throughout the fluid domain to provide a linearized unsteady boundary-value problem. In addition, we will restrict our consideration to temporally and spatially periodic unsteady excitations. That is, we will consider blade motions of the form

$$\vec{R}(\vec{X} + m\vec{G}, t) = \text{Re} \{ \vec{r}(\vec{X}) \exp[i(\omega t + m\sigma)] \} \quad (28)$$

for \vec{X} on B ,

where $\vec{r}(\vec{X})$ is a complex displacement-amplitude vector, ω is the (reduced) frequency of the blade motion, σ is the phase angle between the motions of adjacent blades and $\text{Re} \{ \}$ denotes the real part of $\{ \}$; and incident disturbances of the form

$$\vec{v}^R(\vec{X} - \vec{V}_\infty t) = \text{Re} \{ \vec{v}_\infty^R \exp[i \vec{k}_\infty \cdot (\vec{X} - \vec{V}_\infty t)] \}, \quad (29)$$

where \vec{v}_∞^R and \vec{k}_∞ are the amplitude and wave number vectors of the incident rotational velocity disturbance. Finally, we will restrict our consideration to flows in which any shocks that might occur remain weak, and we will neglect changes in vorticity across these shocks. In general, the discontinuous changes in the flow quantities across shocks are proportional to the shock strength, but the increase in entropy across a shock is proportional only to the third power of the shock strength (Whitham 1974). Thus it is a reasonable approximation to neglect the changes in entropy across a shock of weak to moderate strength; i.e., one for which the Mach number of the normal velocity component on its upstream face is less than about 1.3. With the foregoing shock approximations and in the absence of unsteady excitations the (steady) flow through the cascade will be isentropic and irrotational. In this case $\vec{V}(\vec{X}, t) = \vec{v}(\vec{X}, t)$, where ϕ is the velocity potential of the nonlinear time-independent flow.

The isentropic and irrotational mean flow assumptions preclude the possibility of simultaneously conserving mass, momentum and energy across a shock. Therefore, we will require only that mass and the tangential component of momentum be conserved across shocks; i.e.,

$$\left[\bar{p} \left(\vec{V} - \frac{\partial \vec{R}}{\partial t} \right) \right] \cdot \vec{n} = 0 \quad (30)$$

and

$$\left[\vec{V} \right] \cdot \vec{t} = 0. \quad (31)$$

In principle, an Euler-equation description of the mean flow would be required to analyze inviscid flows in which strong shocks are present (but see Hafez & Lovell 1983 and Klopfer & Nixon 1984 on methods for approximating strong shock phenomena within a potential flow analysis). However, the weak shock assumption should suffice for most aeroelastic applications. Therefore, we shall follow the usual practice in deriving unsteady aerodynamic equations and limit our consideration to flows containing, at most, weak shocks.

THE SMALL UNSTEADY-DISTURBANCE APPROXIMATION

Mathematical Preliminaries

We now seek an approximation to the foregoing nonlinear, time-dependent, boundary-value problem which is appropriate for small-amplitude unsteady excitations; i.e., $|\vec{t}|$, $|\vec{V}^R|$, etc., $\sim O(\epsilon) \ll 1$. For this purpose the flow variables are each expanded in an asymptotic series in ϵ ; e.g.,

$$\vec{P}(\vec{X}, t) = \vec{P}(\vec{X}) + \vec{p}(\vec{X}, t) + \dots, \quad (32)$$

where \vec{P} and \vec{p} are of order ϵ^0 and ϵ^1 , respectively, and the dots refer to the remaining terms which are of higher than first order in ϵ . In addition, Taylor series expansions, e.g.,

$$\vec{p}_{\vec{S}} = (\vec{p} + \vec{R} \cdot \nabla \vec{p} + \dots) \Big|_{\vec{S}}, \quad (33)$$

are applied to refer information at a moving blade, wake or shock surface to the mean position of this surface. In (33) the subscripts \vec{S} and \vec{S} refer to the instantaneous and mean surface locations respectively, and, as illustrated in fig. 3, \vec{R} measures the displacement of a point on the moving surface relative to its mean position. The unit tangent and normal vectors at a point on a moving surface are related to the unit tangent and normal vectors at the location of this point on the mean surface as follows:

$$\vec{t}_{\vec{S}} = \vec{t}_{\vec{S}} [1 - \vec{t}_{\vec{S}} \cdot \nabla \otimes \vec{R} \cdot \vec{t}_{\vec{S}} + ((\vec{t}_{\vec{S}} \cdot \nabla) \vec{R}) \times \vec{t}_{\vec{S}} + \dots], \quad (34)$$

and

$$\vec{n}_{\vec{S}} = \vec{t}_{\vec{S}} \times \vec{t}_{\vec{S}} = \vec{n}_{\vec{S}} [1 - \vec{t}_{\vec{S}} \cdot \nabla \otimes \vec{R} \cdot \vec{t}_{\vec{S}} + ((\vec{t}_{\vec{S}} \cdot \nabla) \vec{R}) \times \vec{t}_{\vec{S}} + \dots]. \quad (35)$$

After substituting the foregoing series expansions and surface vector relations into the full time-dependent governing equations, equating terms of like power in ϵ and neglecting terms of higher than first order in ϵ , nonlinear and linear variable-coefficient boundary-value problems are obtained respectively for the zeroth- and first-order flows.

A significant advantage offered by this linearization is that unsteady effects arising from self-excited blade motions and from the various incident disturbances are not coupled and hence can be determined separately. Indeed, it is sufficient to develop solution procedures only for a single harmonic component of a given disturbance (c.f. (28) and (29)). Solutions for arbitrary disturbances and arbitrary combinations of the various disturbances can then be obtained by Fourier superposition. Note, however, that the present linearization does limit the unsteady response phenomena that can be analyzed since nonlinear unsteady phenomena, such as the influence of inlet distortion on blade flutter, are neglected.

As $\epsilon \rightarrow 0$ the blade surfaces collapse to their mean positions and the incident vortical entropic and acoustic disturbances vanish. Hence, the zeroth-order terms of the asymptotic expansions (32) are the fluid properties corresponding to the steady flow past a stationary cascade. Since the equations governing the first-order or unsteady properties will be linear, the fluctuations in these properties induced by a harmonic unsteady excitation must have harmonic time dependence. We can take advantage of this feature by introducing a complex representation, e.g., $\vec{p}(\vec{X}, t) = \text{Re}[\vec{p}(\vec{X}) e^{i\omega t}]$, for all first-order flow properties and adopting the convention that the real parts of the various complex parameters represent the actual time-dependent physical quantities. Here ω is the temporal frequency of the blade motion or of an incident disturbance; i.e., $\omega = -\vec{k}_{\infty} \cdot \vec{V}_{\infty}$ (c.f. (29)). The complex representation serves to remove explicit time dependence from the linearized unsteady boundary value problem thereby facilitating the determination of a solution. In addition, the cascade geometry, the prescribed form of the unsteady excitations (c.f. (28) and (29)), and the linearity of the first-order equations require that both the steady and unsteady flows exhibit blade-to-blade periodicity. Thus, for example,

$$\vec{P}(\vec{X} + m\vec{G}) = \vec{P}(\vec{X}) \quad (36)$$

and

$$p(\vec{X} + m\vec{G}) = p(\vec{X})e^{im\sigma}, \quad (37)$$

where σ is the phase angle between the motions of adjacent blades or the scalar product of the far-field circumferential wave number and the cascade gap-vector \vec{G} (i.e., $\sigma = \vec{k}_{\infty} \cdot \vec{G}$) for an incident disturbance. Conditions (36) and (37) allow a numerical resolution of the steady and the linearized unsteady flows to be limited to a single extended blade-passage region of the cascade and permit fluid properties at the m th blade or wake surface or the m th shock surface to be evaluated in terms of information available at the corresponding reference ($m = 0$) surface. For simplicity the subscript m will be omitted in the following discussion when referring to a reference surface.

Solutions based on the foregoing linearization must be interpreted carefully to provide the correct response information in the neighborhood of a moving shock (see Hounjet 1981). The zeroth and first-order solutions will be discontinuous at the mean shock location; therefore, they do not account for the fact that an observer situated between the extreme shock positions will experience large-amplitude jumps in the flow variables as the shock passes by. Such local anharmonic effects can be accommodated by analytically continuing the zeroth and first-order solutions from the upstream and downstream sides of the mean shock locus to the upstream and downstream sides, respectively, of the instantaneous shock locus (see Williams 1979). This procedure essentially transfers the discontinuities in the flow variables from the mean to the instantaneous shock locations. Thus, local anharmonic effects have no impact on the solutions to the nonlinear steady and the linearized unsteady boundary-value problems but only on the physical interpretation of the resulting unsteady solution. Hence, we defer a more detailed discussion of the analytical continuation procedure to the subsequent section on unsteady aerodynamic response.

The Steady Base Flow

The field equations governing the zeroth-order or steady background flow follow from the nonlinear field equations given in the previous section after replacing the time-dependent flow variables, \vec{V} , \vec{P} , $\vec{\rho}$, \vec{S} , etc., by their zeroth-order counterparts, \vec{V} , \vec{P} , $\vec{\rho}$, \vec{S} , etc., and setting local temporal derivatives equal to zero. Thus, the differential mass momentum and energy or entropy transport equations for the mean flow are

$$\vec{V} \cdot (\vec{\rho} \vec{V}) = 0, \quad (38)$$

$$\vec{\rho}(\vec{V} \cdot \vec{V})\vec{V} + \vec{V} \cdot \vec{P} = 0 \quad (39)$$

and

$$\vec{V} \cdot \vec{\nabla} S = 0, \quad (40)$$

where in view of the weak-shock assumption the conservation form has been retained only for the mass equation (38). Since we are restricting our consideration to weak shocks and, as a consequence, neglecting changes in entropy and vorticity across shocks, the uniform free-stream conditions far upstream of the blade row will give rise to an isentropic ($\vec{\nabla} S = 0$) and hence, an irrotational ($\vec{V} = \vec{\nabla} \phi$ and $(\vec{V} \cdot \vec{\nabla})\vec{V} = \vec{\nabla}(\vec{\nabla} \phi)^2/2$) steady flow through the cascade. Therefore (38) and, after integrating, (39) and (40) reduce to

$$\vec{V} \cdot (\vec{\rho} \vec{\nabla} \phi) = 0, \quad (41)$$

$$\begin{aligned} V^2/2 + A^2/(\gamma-1) &= A_0^2/(\gamma-1) \\ &= V_{\infty}^2/2 + A_{\infty}^2/(\gamma-1) \end{aligned} \quad (42)$$

and

$$S = S_{\infty} = 0, \quad (43)$$

where ϕ and $A = [(\gamma-1)T]^{1/2} = (\gamma P/\vec{\rho})^{1/2}$ are the mean-flow velocity potential and speed of sound propagation respectively, the subscript 0 denotes the stagnation condition and we have, without loss in generality, set the mean entropy equal to zero.

Convenient relations between the mean-flow variables can be determined from Bernoulli's equation (42), the isentropic relation (15) and the conditions $\vec{\rho}_{\infty} = \vec{V}_{\infty} = 1$. Thus after some algebra, it follows that

$$\begin{aligned} (M_{\infty} V/M)^2 &= (M_{\infty} A)^2 = \vec{\rho}(\gamma-1) \\ &= (\gamma M_{\infty}^2 P)(\gamma-1)/\gamma \\ &= 1 - \frac{\gamma-1}{2} M_{\infty}^2 [(\vec{\nabla} \phi)^2 - 1] \\ &= \frac{2 + (\gamma-1) M_{\infty}^2}{2 + (\gamma-1) M^2}, \end{aligned} \quad (44)$$

where $M = V/A$ is the local steady Mach number. Equation (44) can be applied to eliminate the density from (41) and obtain a differential equation containing the steady velocity potential as the only dependent variable; i.e.,

$$\begin{aligned} \left[1 - \frac{\gamma-1}{2} M_{\infty}^2 [(\vec{\nabla} \phi)^2 - 1]\right] \vec{\nabla}^2 \phi \\ - M_{\infty}^2 \vec{\nabla} \phi \cdot \vec{\nabla}(\vec{\nabla} \phi)^2/2 = 0. \end{aligned} \quad (45)$$

However, the conservation form (i.e., (41)) of the governing differential equation is the one usually preferred for a

numerical resolution of a flow containing shocks because it is more convenient to "capture" shock phenomena rather than to "fit" shocks into the nonlinear steady solution.

Surface conditions for the zeroth-order or steady flow follow from eqs. (20) through (27) and are imposed at the mean positions of the blade (B_m), wake (W_m) and shock ($Sh_{m,n}$) surfaces. Blade mean positions are prescribed, but the mean shock and wake locations must be determined as part of the steady solution. In the present development it is assumed that the mean wake locations coincide with the steady-flow stagnation streamlines downstream of the blade row.

Since the steady flow remains attached to the mean blade surfaces, it follows that

$$\vec{v} \cdot \vec{n} = v_\phi \cdot \vec{n} = 0 \quad \text{on } B_m. \quad (46)$$

In addition, the steady pressure and normal velocity component must be continuous across blade wakes. Hence, the conditions

$$[p] = [v_\phi] \cdot \vec{n} = 0 \quad \text{on } W_m \quad (47)$$

apply at the mean wake locations. For two-dimensional mean flows the tangential component of the mean velocity must also be continuous across blade wakes since no vorticity is generated in the mean flow. Therefore, it follows from (44) and (47) that

$$[\phi] = [\phi]_{TE} \quad \text{on } W_m, \quad (48)$$

where the subscript TE refers to the trailing-edge point of the m th blade.

Finally, the requirements of mass conservation and continuity of tangential velocity across shocks provide the following conditions at the mean shock locations

$$[\bar{\rho} \vec{v}] \cdot \vec{n} = [\bar{\rho} v_\phi] \cdot \vec{n} = 0 \quad \text{on } Sh_{m,n} \quad (49)$$

and

$$[\vec{v}] \cdot \vec{t} = [v_\phi] \cdot \vec{t} = 0 \quad \text{on } Sh_{m,n}. \quad (50)$$

Equation (50) can be integrated to yield

$$[\phi] = [\phi]_{Ref} \quad \text{on } Sh_{m,n}, \quad (51)$$

where $[\phi]_{Ref} = 0$ if the shock terminates in a continuous region of the flow.

In addition to the foregoing surface conditions, constraints must be placed on the steady solution far from the blade row. For the cascade flows of practical interest the axial components of the inlet

and exit free-stream velocities will be subsonic; i.e., $V_{\xi, \infty} = V_{\infty} \cos \alpha_{\infty} < A_{\infty}$. Thus the steady velocity far upstream and far downstream from the blade row will be of the form

$$\lim_{\xi \rightarrow \pm \infty} \vec{V}(\vec{X}) = \vec{V}_{\infty} + \nabla \bar{\phi}(\vec{X}), \quad (52)$$

where $\bar{\phi}(\vec{X})$ is the velocity potential associated with small steady perturbations of the upstream and downstream free-stream flows and must be determined as part of the overall steady solution. Although the steady disturbances described by $\bar{\phi}(\vec{X})$ originate at the blade row, their behavior in the far field depends largely upon whether the relative free-stream velocity V_{∞} is subsonic or supersonic. In the former case steady disturbances attenuate exponentially with increasing axial distance from the blade row (and hence $\bar{\phi} \rightarrow 0$ as $|\xi| \rightarrow \infty$); in the latter, they are small but persist as $|\xi| \rightarrow \infty$. In general, three of the uniform velocity components in (52), or their equivalents (e.g., Mach number M_{∞} , flow angle α_{∞} , etc.), must be prescribed to specify completely the steady boundary-value problem. The fourth or remaining component is determined in terms of the three prescribed by using (44) and the integral form of the mass conservation law, c.f., (1). Since $\bar{\rho}_{\infty} = V_{\infty} = 1$, the latter provides the following relation between the inlet and exit flow variables:

$$\begin{aligned} \bar{\rho}_{\infty} V_{\xi, \infty} &= \bar{\rho}_{\infty} V_{\infty} \cos \alpha_{\infty} \\ &= \frac{M_{\infty}}{M_{\infty}} \frac{2 + (\gamma - 1) M_{\infty}^2}{2 + (\gamma - 1) M_{\infty}^2} \frac{\gamma + 1}{2(\gamma - 1)} \cos \alpha_{\infty} \\ &= \bar{\rho}_{\infty} V_{\xi, \infty} = \cos \alpha_{\infty}. \end{aligned} \quad (53)$$

Numerical solution procedures for determining two-dimensional steady potential flows through cascades have been developed extensively, particularly for flows with subsonic relative inlet and exit Mach numbers (i.e., $M_{\infty} < 1$). For more complete information we refer the reader to the report by McNally and Sockol (1981), the text by Gostelow (1984) and the recent papers by Caspar (1983), Whitehead & Newton (1985) and Habashi, Hafez & Kotliuga (1985). In such calculations far-field boundary conditions are imposed at axial stations placed at finite distances upstream (say at $\xi = \xi_-$) and downstream (at $\xi = \xi_+$) from the blade row where linearized solutions describing the behavior of the disturbance potential $\bar{\phi}$ in the far field (i.e., for $\xi \gtrless \xi_{\pm}$) can be matched to nonlinear near-field solutions. In addition, conditions are often imposed at the blade surfaces (e.g., a unique incidence condition at a sharp leading edge and/or a Kutta condition at a sharp trailing edge) in lieu of prescribing an inlet and/or an exit free-stream flow property. Finally, the usual practice is

to express the mass-balance equation in conservative form (c.f. (41)) and to solve this equation throughout the entire fluid domain, while allowing for a discontinuity in the velocity potential at blade trailing edge points and along arbitrary periodic lines (c.f. (36)) which emanate from these points and extend downstream. Thus in steady potential-flow calculations, shock-jump conditions are usually not imposed; rather shock phenomena are captured through the use of special differencing techniques. It appears that such procedures can lead to reasonably accurate predictions of mean shock locations and of mean flow behavior in the vicinity of a shock. The mean wake locations W_m , i.e., the downstream stagnation streamlines, are determined a posteriori from the resulting steady solution.

THE LINEARIZED UNSTEADY FLOW

Field Equations

The differential equations governing the first-order or linearized unsteady flow in continuous regions are determined by substituting the asymptotic expansions for the flow variables (e.g., (32)) into the full time-dependent equations derived from the mass momentum and energy conservation laws (i.e., (8), (12) and (14)), subtracting out the corresponding equations for the steady background flow ((38) through (40)) and neglecting terms of higher than first order in ϵ . This procedure provides the following system of linearized (Euler) equations:

$$i\omega\rho + \nabla \cdot (\bar{\rho} \hat{v} + \rho \hat{V}) = 0, \quad (54)$$

$$\bar{\rho} \left(\frac{D\hat{v}}{Dt} + (\hat{v} \cdot \nabla) \hat{v} \right) + \rho (\hat{V} \cdot \nabla) \hat{V} + \nabla p = 0 \quad (55)$$

and

$$\frac{D\hat{s}}{Dt} + \hat{v} \cdot \nabla s = 0. \quad (56)$$

Here ρ , \hat{v} , p and s are the complex amplitudes of the first-order density, velocity, pressure and entropy respectively, and $D/Dt = i\omega + \hat{V} \cdot \nabla$ is a mean-flow convective derivative operator. To complete this system we require an additional equation for the first-order flow properties. This is obtained by integrating the thermodynamic relation (7) from the state occupied by the steady background flow at the point \hat{x} to the actual state of the fluid at that point. It follows that the first-order entropy, pressure and density must satisfy the relation

$$s = \gamma^{-1} p/p - \rho/\bar{\rho}. \quad (57)$$

In the present development the steady background flow is assumed to be isentropic ($s = 0$) and irrotational ($\hat{V} = \nabla\phi$ and hence $(\hat{V} \cdot \nabla) \hat{V} = \nabla(\nabla\phi)^2/2$). These condi-

tions can be applied to simplify the differential equations (54) through (56). In addition, the thermodynamic relation (57) can be used to eliminate the density ρ from the linearized momentum (55) and continuity (54) equations. First, the linearized energy or entropy transport equation can be reduced to

$$\frac{D\hat{s}}{Dt} = 0. \quad (58)$$

Further, it follows from (57), the mean-flow Bernoulli relations (44) and some algebra that the linearized momentum equation can be written as

$$\frac{D\hat{v}}{Dt} + (\hat{v} \cdot \nabla) \hat{v} - s \nabla(\nabla\phi)^2/2 = -\nabla(p/\bar{\rho}). \quad (59)$$

After we combine (58) and (59) and rearrange terms, the latter equation can be expressed in the form

$$\frac{D}{Dt} (\hat{v} - s \nabla\phi/2) + [(\hat{v} - s \nabla\phi/2) \cdot \nabla] \hat{v} = -\nabla(p/\bar{\rho}). \quad (60)$$

Finally, after we combine the steady continuity equation (38) with the corresponding first-order equation (54), it follows that

$$\frac{D}{Dt} (\rho/\bar{\rho}) + \bar{\rho}^{-1} \nabla \cdot (\bar{\rho} \hat{v}) = 0 \quad (61)$$

and, after combining this result with (57) and (58), we find that the linearized continuity equation can be expressed in the form

$$\frac{D}{Dt} [p/(\bar{\rho} A^2)] + \bar{\rho}^{-1} \nabla \cdot (\bar{\rho} \hat{v}) = 0, \quad (62)$$

where $A = (\gamma p/\bar{\rho})^{1/2}$ is the speed of sound propagation in the steady background flow.

Thus the linearized unsteady flow can be determined by solving the system of equations (58), (60) and (62), subject to the appropriate surface and far-field conditions, for the complex amplitudes of the first-order unsteady entropy, velocity and pressure. If the only source of unsteady excitation is a prescribed blade motion (i.e., the flutter problem), then the linearized unsteady flow will be isentropic ($s = 0$) and irrotational ($\hat{v} = \nabla\phi$), and it follows from the momentum equation (60) and the far-field condition (19) that

$$p = -\bar{\rho} \frac{D\phi}{Dt}. \quad (63)$$

In this case the continuity equation (62) reduces to

$$\frac{\bar{D}}{Dt} (A^{-2} \frac{\bar{D}\phi}{Dt}) - \bar{\rho}^{-1} \nabla \cdot (\bar{\rho} \nabla \phi) = 0, \quad (64)$$

and it is only necessary to solve (64) subject to conditions on the mean blade, wake and shock surfaces and an outgoing acoustic wave requirement for $\xi + \tau = \infty$ to completely determine the linearized unsteady flow. A similar conclusion holds if incident acoustic waves are included as a source of unsteady excitation, but in this case the far-field condition on $\phi(\bar{X})$ must account for such incident waves. The general unsteady problem ($s, \nabla \times \bar{v} \neq 0$) is more complicated since, as presently formulated, the linearized momentum and continuity equations must be solved simultaneously. However, it is still possible to simplify this general problem by introducing a suitable velocity decomposition as discussed below.

The unsteady perturbation velocity can be represented as the sum of an irrotational part and a rotational part; i.e.,

$$\bar{v} = \bar{v}_\phi + \bar{v}^R. \quad (65)$$

Hence $\bar{\zeta} = \nabla \times \bar{v}^R$, where $\bar{\zeta}$ is the complex-amplitude of the perturbation vorticity. Since this velocity decomposition involves the introduction of the additional dependent variable \bar{v}^R , an additional constraint is required to close the linearized unsteady problem. One possibility is to impose the zero-divergence condition, i.e.,

$$\nabla \cdot \bar{v}^R = 0 \quad (66)$$

on the rotational part of the perturbation velocity. This leads to a compressible unsteady analysis (see Caruthers 1981) which is a natural extension of earlier incompressible analyses (e.g., see Adamczyk 1975) but one which entails rather complicated numerical and analytical solution procedures. Although it has not yet been used in detailed unsteady cascade calculations, it appears that a more natural and convenient velocity decomposition is the one suggested by Goldstein (1978, 1979). Here, the rotational velocity \bar{v}^R is taken to be independent of the pressure fluctuations and dependent only on the prescribed upstream rotational velocity and entropy distortions and on the mean velocity field. In addition, the irrotational velocity \bar{v}_ϕ is related directly to the pressure fluctuations by (63). This is accomplished by requiring that the rotational part of the unsteady velocity be a solution of the equation

$$\frac{\bar{D}}{Dt} (\bar{v}^R - s\bar{v}_\phi/2) + [(\bar{v}^R - s\bar{v}_\phi/2) \cdot \nabla] \bar{v}_\phi = 0. \quad (67)$$

It then follows from the linearized momen-

tum equation (60) and the far-field condition (19) that the pressure and velocity potential fluctuations are related according to (63). Further, upon substituting this pressure-potential relation along with the velocity decomposition (65) into the continuity equation (62) we find that

$$\frac{\bar{D}}{Dt} (A^{-2} \frac{\bar{D}\phi}{Dt}) - \bar{\rho}^{-1} \nabla \cdot (\bar{\rho} \nabla \phi) = \bar{\rho}^{-1} \nabla \cdot (\bar{\rho} \bar{v}^R). \quad (68)$$

Except for the source term on the right-hand-side, (68) is identical to the field equation (64) which governs the flutter problem. Thus the introduction of the Goldstein velocity decomposition has led to a system of field equations, i.e., (58), (67) and (68), which describe the general linearized unsteady flow in continuous regions and which can be solved sequentially to determine the complex amplitudes of the entropy, rotational velocity and velocity potential fluctuations, respectively.

Surface Conditions

Conditions on the unsteady perturbation at the mean positions of blade, wake and shock surfaces are obtained by substituting the asymptotic (e.g., (32)) and Taylor (e.g., (33)) series expansions and the surface vector relations, (34) and (35), into the full time-dependent surface conditions, subtracting out the corresponding steady conditions and neglecting terms of higher than first order in ϵ . Thus it follows from (27) and (46) that the linearized flow tangency condition can be expressed in the form

$$\bar{v} \cdot \bar{n} = [i\omega \bar{f} + (\bar{v} \cdot \bar{f})(\bar{f} \cdot \nabla) \bar{f} - (\bar{f} \cdot \nabla) \bar{v}] \cdot \bar{n} \quad \text{on } B_m, \quad (69)$$

where $\bar{r}(\bar{X}) = \bar{r}(\bar{X} - m\bar{G})e^{i\omega s}$ is the complex-amplitude of the m th blade displacement vector (c.f. (28)). Further, it follows from the irrotationality of the mean flow and the decomposition of the fluctuating velocity according to (65) that the foregoing condition can be written as

$$\bar{v}_\phi \cdot \bar{n} = [-\bar{v}^R + i\omega \bar{f} + (\bar{v}_\phi \cdot \bar{f})(\bar{f} \cdot \nabla) \bar{f} - (\bar{f} \cdot \nabla) \bar{v}_\phi] \cdot \bar{n} \quad \text{on } B_m. \quad (70)$$

Equation (70) provides a relation for the normal component of the irrotational part of the unsteady velocity fluctuation at the mean blade surface. The first term on the right-hand-side of this equation is the normal velocity (directed inward) at the blade surface due to the convected rotational gust; the second term is the

normal velocity of the moving blade surface; and the third and fourth terms account for the effects of a variation in blade-displacement along the blade surface and of blade motion through a spatially varying mean velocity field respectively. Note that the blade displacement vector is prescribed and that for rigid motions (c.f. (102)) $(\nabla \phi \cdot \hat{r}) (\hat{r} \cdot \nabla) \hat{r} = \hat{a} \times \nabla \phi$ where $\hat{a} = a \hat{e}_z$ is the complex amplitude of the angular displacement vector.

The linearized wake-jump conditions follow from (25), (26) and (47) and are given by

$$[\hat{v}] \cdot \hat{n} = -(\hat{r} \cdot \hat{n}) [\nabla(\hat{v} \cdot \hat{n})] \cdot \hat{n} \text{ on } W_m \quad (71)$$

and

$$[\hat{p}] = -(\hat{r} \cdot \hat{n}) [\nabla \hat{p}] \cdot \hat{n} \text{ on } W_m, \quad (72)$$

where \hat{r} is the complex-amplitude of the wake displacement vector and the mean positions of the unsteady wakes, W_m , are assumed to coincide with the mean flow stagnation streamlines. Since mean flow properties and their derivatives are continuous downstream of the blade row, the right-hand-sides of (71) and (72) are identically zero. Thus the two-dimensional unsteady solution will be independent of the actual form of the wake displacement. It then follows from the irrotationality of the mean flow, the velocity decomposition (65) and the linearized pressure-potential relation (63) that

$$[\nabla \phi] \cdot \hat{n} = -[\hat{v}^R] \cdot \hat{n} \text{ on } W_m \quad (73)$$

and

$$\left[\frac{D\phi}{Dt} \right] = [1\omega + (\nabla \phi \cdot \hat{r}) \hat{r} \cdot \nabla] [\phi] = 0 \text{ on } W_m. \quad (74)$$

Equation (74) can be integrated along the wake to yield a condition on the jump in the potential across the wake; i.e.,

$$[\phi] = [\phi]_{TE} \exp \left[- \int_{TE}^x 1\omega (\nabla \phi \cdot \hat{r})^{-1} d\tau \right] \text{ on } W_m. \quad (75)$$

Thus (73) and (75) provide two relations for determining the jump in the normal component of the irrotational part of the unsteady velocity and the jump in the unsteady velocity potential across each wake. These quantities depend upon the jump in the normal component of the rotational part of the unsteady velocity across the wake and upon the mean velocity along the mean-flow stagnation streamlines respectively.

At shock mean positions it follows from (30), (31), (49) and (50) that the

linearized mass and tangential momentum conservation conditions have the form

$$[\bar{\rho} \hat{v} + \rho \hat{V} + (\hat{r} \cdot \nabla) \bar{\rho} \hat{V} - 1\omega \hat{r} \bar{\rho}] \cdot \hat{n} + [\bar{\rho} \hat{V}] \cdot [(\hat{r} \cdot \nabla) \hat{r} \times \hat{e}_z] = 0 \text{ on } Sh_{m,n} \quad (76)$$

and

$$[\hat{v} + (\hat{r} \cdot \nabla) \hat{V}] \cdot \hat{r} + [\hat{V}] \cdot (\hat{r} \cdot \nabla) \hat{r} = 0 \text{ on } Sh_{m,n} \quad (77)$$

respectively, where \hat{r} is now the complex-amplitude of the shock-displacement; i.e., $\hat{r}(\hat{X}, t) = \text{Re}[\hat{r}(\hat{X} - m\hat{G}) e^{i(\omega t + m\sigma)}]$ for \hat{X} on $Sh_{m,n}$. After performing some vector algebra and making use of the steady continuity equation (38) and the shock-jump conditions (49) and (50), we can reduce the foregoing expressions to

$$[\bar{\rho} \hat{v} + \rho \hat{V}] \cdot \hat{n} = [\bar{\rho}] (1\omega + (\hat{v} \cdot \hat{r}) \hat{r} \cdot \nabla) (\hat{r} \cdot \hat{n}) + (\hat{r} \cdot \hat{n}) \hat{r} \cdot \nabla ([\bar{\rho}] \hat{V} \cdot \hat{r}) \text{ on } Sh_{m,n} \quad (78)$$

and

$$[\hat{v}] \cdot \hat{r} = -\hat{r} \cdot \hat{n} [\nabla(\hat{v} \cdot \hat{r})] \cdot \hat{n} - [\hat{v} \cdot \hat{n}] \hat{r} \cdot \nabla(\hat{r} \cdot \hat{n}) \text{ on } Sh_{m,n}. \quad (79)$$

Finally, after combining $\hat{V} = \nabla \phi$, $\hat{v} = \nabla \phi + \hat{v}^R$, $A = (\gamma P / \bar{\rho})^{1/2}$, the thermodynamic relation (57) and the pressure-potential relation (63) with equations (78) and (79), and neglecting changes in the unsteady entropy and rotational velocity perturbations across weak shocks, we find that

$$[\bar{\rho} (\nabla \phi - A^{-2} \frac{D\phi}{Dt} \nabla \phi)] \cdot \hat{n} = -[\bar{\rho}] \hat{v}^R \cdot \hat{n} + [\bar{\rho}] (1\omega + (\nabla \phi \cdot \hat{r}) \hat{r} \cdot \nabla) (\hat{r} \cdot \hat{n}) + (\hat{r} \cdot \hat{n}) \hat{r} \cdot \nabla ([\bar{\rho}] \nabla \phi \cdot \hat{r}) \text{ on } Sh_{m,n} \quad (80)$$

and

$$[\nabla \phi] \cdot \hat{r} = -\hat{r} \cdot \nabla (\hat{r} \cdot \hat{n} [\nabla \phi] \cdot \hat{n}) \text{ on } Sh_{m,n} \quad (81)$$

Note that for a normal shock $\nabla \phi \cdot \hat{r} = 0$ along the mean shock surface, so that (80) can be simplified, and for a shock which terminates in the fluid, (81) can be integrated along the shock to yield

$$[\phi] = -\hat{r} \cdot \hat{n} [\nabla \phi] \cdot \hat{n} \text{ on } Sh_{m,n}. \quad (82)$$

Equations (80) and either (81) or (82) provide two relations for determining the discontinuity in the unsteady potential $[\phi]$ at the mean position of a shock and the shock displacement normal to the mean shock locus $\hat{r} \cdot \hat{n}$. Moreover, these equa-

tions illustrate that $[\phi]$ and $\hat{t} \cdot \hat{n}$ depend on the mean flow properties and the first-order rotational velocity fluctuation at the mean shock location. Shock mean positions are determined by the zeroth-order or steady-flow solution and, whereas blade displacements are prescribed, shock displacements must be determined as part of the unsteady solution.

Unsteady Far-Field Behavior

We have assumed that in the far-field, i.e., beyond some finite distance upstream ($\xi \leq \xi_-$) and downstream ($\xi \geq \xi_+$) from the blade row, the irrotational steady flow is at most a small perturbation (i.e., of $O(\epsilon)$) from a uniform flow. Therefore, far from the blade row and to within the first-order unsteady approximation considered here, the linearized unsteady equations can be reduced to constant coefficient equations for which analytical far-field solutions can be determined. In particular, for $\xi \lesssim \xi_+$, the differential equations (58) and (67) governing the entropy and rotational velocity fluctuations reduce to

$$\frac{\bar{D}s}{Dt} = (i\omega + \hat{V}_{\infty} \cdot \nabla) s(\hat{X}) = 0 \quad (83)$$

and

$$\frac{\bar{D}\hat{v}^R}{Dt} = (i\omega + \hat{V}_{\infty} \cdot \nabla) \hat{v}^R(\hat{X}) = 0. \quad (84)$$

Equations (83) and (84) have solutions of the form

$$s(\hat{X}) = s_{\infty} \exp[ik_{\infty}(\hat{X} - \hat{X}_+)] \quad (85)$$

and

$$\hat{v}^R(\hat{X}) = \hat{v}_{\infty}^R \exp[ik_{\infty}(\hat{X} - \hat{X}_+)], \quad (86)$$

where s_{∞} , \hat{v}_{∞}^R and k_{∞} are the complex amplitudes and wave numbers of the far-field entropic and rotational velocity fluctuations and $\hat{X}_+ = (\xi_+, n)$. By definition, $k_{\infty} \cdot \hat{V}_{\infty} = -\omega$ and $k_{n,\infty} = \sigma G^{-1}$; therefore the far upstream and far downstream axial gust wave numbers are given by

$$k_{\xi,\infty} = -(\omega + \sigma G^{-1} V_{\infty} \sin \alpha_{\infty}) / (V_{\infty} \cos \alpha_{\infty}), \quad (87)$$

The foregoing equations illustrate that the small-amplitude entropic and vortical gusts are convected without distortion by the mean flow in both the far-upstream ($\xi < \xi_-$) and far-downstream ($\xi > \xi_+$) regions of the flow. Recall that the entropic and vortical gusts and hence, the wave number k_{∞} and the complex amplitudes

s_{∞} and \hat{v}_{∞}^R are prescribed quantities and that, by prescription, the rotational velocity fluctuation is divergence-free far upstream; i.e.,

$$\hat{k}_{\infty} \cdot \hat{v}_{\infty}^R = 0. \quad (88)$$

The far-downstream entropy and rotational velocity perturbations, s_{∞} and \hat{v}_{∞}^R , must be determined as part of the overall unsteady solution. We suspect that the rotational velocity fluctuation will have zero-divergence far-downstream and also that this velocity fluctuation will be continuous across blade wakes. But since these conjectures have not been demonstrated, the constraints $\hat{k}_{\infty} \cdot \hat{v}_{\infty}^R = 0$ and $[\hat{v}_{\infty}^R] \cdot \hat{n} = 0$ on W_m will not be imposed in the present formulation.

Similarly, in the far-field ($\xi \gtrsim \xi_+$) the linearized continuity equation (68) can be written as

$$M_{\infty}^2 \frac{\bar{D}^2 \phi}{Dt^2} - \nabla^2 \phi = \nabla \cdot \hat{v}^R, \quad (89)$$

where

$$\nabla \cdot \hat{v}^R = \begin{cases} 0 & \text{for } \xi < \xi_-, \\ i\hat{k}_{\infty} \cdot \hat{v}_{\infty}^R \exp[ik_{\infty}(\hat{X} - \hat{X}_+)] & \text{for } \xi > \xi_+. \end{cases} \quad (90)$$

We seek a solution to (89) subject to the blade-to-blade periodicity condition (37), the wake-jump conditions (73) and (75) and the requirement that acoustic responses either attenuate or propagate away from or parallel to the blade row. Note that in the far-downstream region (75) reduces to

$$[\phi(\tau)] = [\phi(\tau_+)] \exp[i\omega(\tau - \tau_+)/V_{\infty}] \quad \text{on } W_m \text{ for } \tau > \tau_+, \quad (91)$$

where $\tau(\xi)$ is a coordinate measuring distance downstream along the wake and $\tau_+ = \tau(\xi_+)$. For the present purpose it is convenient to set

$$\phi(\hat{X}) = \begin{cases} \phi^H(\hat{X}) & \text{for } \xi < \xi_-, \\ \phi^H(\hat{X}) + \phi^P(\hat{X}) & \text{for } \xi > \xi_+, \end{cases} \quad (92)$$

where $\phi^H(\hat{X})$ is a continuous function which accounts for the fluctuations in velocity potential due to acoustic or pressure waves, and $\phi^P(\hat{X})$ is discontinuous at blade wakes and accounts for the fluctuations in the potential due to rotational velocity fluctuations and counter-vorticity convected along the blade wakes. The latter disturbances do not give rise to pressure fluctuations, and therefore

$$\frac{\partial \phi^P}{\partial t} = 0 \text{ for } \xi \leq \xi_+ \quad (93)$$

The continuous component of the potential, i.e., the solution to the homogeneous equation corresponding to (89), can be determined conveniently in terms of the cascade axial (ξ) and circumferential (n) coordinates using Fourier methods. We refer the reader to Verdon, Adamczyk & Caspar (1975), Verdon & Caspar (1980), Caruthers (1981) or Whitehead (1982) for more complete details. The homogeneous solution has the form

$$\begin{aligned} \phi^H(\vec{X}) = & a_{j,\tau_m} \exp [ik_{j,\tau_m} \cdot (\vec{X} - \vec{X}_\tau)] \\ & + \sum_{j=-\infty}^{\infty} b_{j,\tau_m} \exp [\pm \beta_{j,\tau_m} (\xi - \xi_\tau) \\ & - ik_{j,\tau_m} \cdot (\vec{X} - \vec{X}_\tau)] \text{ for } \xi \geq \xi_\tau \end{aligned} \quad (94)$$

The first term in (94) accounts for a prescribed incident wave coming from far upstream and/or far downstream of the blade row, and the infinite series accounts for acoustic waves which originate at the blade row. The constants β_{j,τ_m} and k_{j,τ_m} depend upon the far-upstream or far-downstream uniform mean-flow conditions, the blade spacing and the frequency and interblade phase angle of the unsteady motion. The complex amplitudes a_{j,τ_m} and the wave numbers k_{j,τ_m} of the incident waves are prescribed, and the Fourier coefficients b_{j,τ_m} are determined by matching the analytical far-field solutions to a numerical near-field solution for $\phi(\vec{X})$ at the inlet $\xi = \xi_-$ and exit $\xi = \xi_+$ axial stations.

The particular solution $\phi^P(\vec{X})$ of (89) can be determined conveniently in terms of Cartesian coordinates r_m and n_m , where the r_m axis is parallel to the far-downstream uniform flow direction, and the origin of the r_m, n_m -axes coincides with the intersection of the axial line $\xi = \xi_+$ and the mean position of the m th wake. It then follows from (93) that, for $r_m > 0$ and $0 < n_m < G \cos \alpha_m$, ϕ^P must be of the form

$$\phi^P(\vec{X}) = P(n_m) e^{-i\omega r_m/V_\infty} \quad (95)$$

The function $P(n_m)$ is determined to within an arbitrary constant by substituting this expression into (89) and solving the resulting ordinary differential equation subject to the wake conditions (73) and (91). Once $P(n_m)$ is determined in this manner, the arbitrary constant is determined by matching to the near-field numerical solution.

Discussion

The derivation of the equations gov-

erning the small-disturbance unsteady flow is now complete. These equations account for the effects of blade geometry and mean blade loading on the unsteady fluctuations arising from small-amplitude harmonic excitations. The unsteady equations are linear and contain variable coefficients which depend on a fully nonlinear isentropic and irrotational steady background flow. Because of the assumed form of the excitations (c.f. (28) and (29)), a numerical resolution of the time-independent linearized unsteady equations is required only over a single extended blade-passage region. In addition, since analytical far-field unsteady solutions have been determined, the numerical solution domain can be further restricted to a single extended blade-passage region of finite extent as shown in fig. 4.

The linearized unsteady boundary-value problem has been reduced to a system of three field equations, i.e., (58), (67) and (68), which can be solved sequentially to determine the complex amplitudes of the entropy $s(\vec{X})$, rotational velocity $\vec{v}^R(\vec{X})$ and velocity potential $\phi(\vec{X})$ fluctuations. It has been assumed that the entropy and the rotational part of the fluid velocity are continuous across weak shocks. Therefore, the entropy fluctuation $s(\vec{X})$ is determined as a solution of (58) for a prescribed upstream entropy distribution, i.e., $s(\xi_-, n)$, and the rotational velocity

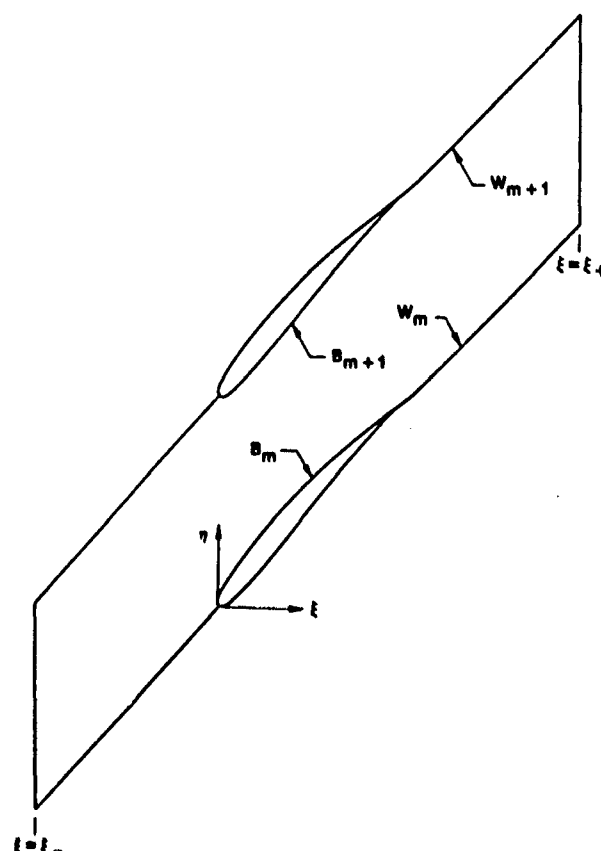


Figure 4. Numerical solution domain - extended blade passage region of finite extent.

fluctuation $\delta R(X)$ is determined as a solution of eq. (67) for this entropy fluctuation and a prescribed upstream rotational velocity distribution, i.e., $\bar{v}^R(t, n)$. Convenient formal solutions for the linearized entropic and rotational velocity fluctuations have been determined by Goldstein (1978), and it should be possible to apply these results to reduce the computational effort associated with the unsteady cascade problem. Finally, the velocity potential fluctuation $\phi(X)$ is determined as a solution of (68) subject to conditions imposed at the mean blade, wake and shock surfaces and the far-field behavior indicated by (94) and (95). The flow tangency condition (70) applies at blade surfaces; the jump conditions (73) and (75) apply at wake surfaces; and the jump conditions (80) and either (81) or (82) apply at shock surfaces.

For the general linearized unsteady problem, the rotational velocity appears as a source term in the differential equation (68) and in the various surface conditions. If self-excited blade motions are the only source of unsteady disturbance, i.e., there are no incident rotational velocity or entropy fluctuations and no incident acoustic waves ($a_{\infty} = 0$ in (94)), then the unsteady problem is simplified considerably since only a single field equation must be solved. In any event, a numerical resolution of the linearized unsteady flow is required to determine the response parameters of interest for aeroelastic or aeroacoustic design applications.

AERODYNAMIC RESPONSE PARAMETERS

Surface Pressure

The unsteady pressures and the global unsteady airloads acting on the moving blade surfaces are the important results of an aerodynamic analysis intended for blade aeroelastic response predictions. In particular, for flutter applications, a knowledge of the unsteady airloads permits the evaluation of aerodynamic work per cycle and/or aerodynamic damping; either of which can be used to determine whether the airstream tends to support or suppress a prescribed blade motion. The pressure acting at the instantaneous position of the m th blade surface is given by

$$\tilde{p}_{\mathcal{B}m}(\tau, t) = p_B(\tau) + \operatorname{Re} \left[p_{\mathcal{B}}(\tau) e^{i(\omega t + m\sigma)} \right] + \sum_n p_{\mathcal{B}m,n}(\tau, t) + \dots, \quad (96)$$

where τ is a coordinate measuring distance in the counterclockwise (or \hat{i} -) direction along the mean blade surface. The first two terms on the right-hand-side of (96) are the steady and first-harmonic components of the pressure acting at the m th

moving blade surface and outside of the small intervals bounded by the mean and instantaneous shock locations. These components of the pressure acting at the moving blade surface, \mathcal{B}_m , are evaluated in terms of steady and first-harmonic unsteady information supplied at the mean position, B , of the reference blade. The third term represents the anharmonic contribution to the unsteady surface pressure caused by the motions of shocks along the surface of the m th blade.

After expanding the pressure \tilde{P} in the manner indicated by (32) and (33) and making use of the unsteady pressure-potential relation (63), we find that

$$p_{\mathcal{B}} = \left[-\bar{p} \frac{\partial \tilde{\psi}}{\partial t} + (\hat{f}_B \cdot \nabla) P \right]_{\mathcal{B}}, \quad (97)$$

where \bar{p} and P are determined from the steady solution (c.f. (44)) and \hat{f}_B is the complex amplitude of the reference blade displacement. The first term on the right-hand-side of (97) represents the harmonic unsteady pressure acting at the mean position of the reference blade, and the second term represents the harmonic pressure produced by motion through a spatially varying steady pressure field.

The local anharmonic effect caused by the motion of a shock is determined by an analytic continuation of the solutions to the steady and the linearized unsteady boundary-value problems (see Williams 1979). Thus, for example,

$$p_{\mathcal{B}h}(\tau, t) = - \frac{\operatorname{Re} \{ r_{\mathcal{S}h, B} \}}{|\operatorname{Re} \{ r_{\mathcal{S}h, B} \}|} \times H[(\tau - \tau_{\mathcal{S}h})(\tau_{\mathcal{S}h} - \tau)] Q(\tau, t), \quad (98)$$

where $r_{\mathcal{S}h, B} = (\hat{f}_{\mathcal{S}h} - \hat{f}_B) \cdot \hat{i}$ is the complex amplitude of the displacement of the shock foot in the counterclockwise or \hat{i} -direction along the moving blade surface; the subscripts $\mathcal{B}h$ and $\mathcal{S}h$ refer to the instantaneous and mean shock locations respectively; H is the unit-step function; i.e.,

$$H(\tau) = \begin{cases} 0, & \tau < 0 \\ 1, & \tau > 0 \end{cases} \quad (99)$$

and

$$Q(\tau, t) = [p_B]_{\mathcal{S}h} + (\tau - \tau_{\mathcal{S}h}) \left[\partial p_B / \partial \tau \right]_{\mathcal{S}h} + \operatorname{Re} \left\{ [p_{\mathcal{B}}]_{\mathcal{S}h} e^{i(\omega t + m\sigma)} \right\}. \quad (100)$$

The discontinuous terms on the right-hand side of (100) are evaluated at the mean position of the shock foot and by moving across the shock in the \hat{i} -direction; i.e., $[p_B]_{\mathcal{S}h} = p_B(\tau_{\mathcal{S}h}^+) - p_B(\tau_{\mathcal{S}h}^-)$. The

first two terms on the right-hand-side of (96) are discontinuous at the undisturbed shock locations. The third term cancels these discontinuities and transfers them to the instantaneous shock locations. This can be seen if we set $r = r_{sh}$ in the foregoing relations to determine that

$$\begin{aligned} [\tilde{P}_B]_{sh} &= [P_B]_{sh} + (r_{sh} - r_{sh}) [\partial P_B / \partial r]_{sh} \\ &+ \operatorname{Re} \left\{ [P_B]_{sh} e^{i(\omega t + m\sigma)} \right\} + \dots \end{aligned} \quad (101)$$

It should be noted that the relative displacement of a normal shock along a blade surface is readily determined in terms of the prescribed blade motion and the linearized unsteady solution for the shock displacement (c.f. (80) and (81) or (82)). However, the steps required to determine $r_{sh,B}$ for an oblique shock must still be determined. Finally, although the unsteady pressure disturbance is not everywhere harmonic, its regions of anharmonicity are small. Consequently (see Tijdeman 1977 and Ehlers & Weatherill 1982), the first-order global aerodynamic coefficients are harmonic in time.

Unsteady Force and Moment, Aerodynamic Work per Cycle

Up to this point we have placed no restriction on the mode of the blade motion. But we will now limit our consideration to the condition usually considered in turbomachinery aeroelastic applications wherein each incremental blade section undergoes a rigid-body motion. In this case only the unsteady force and moment must be determined to analyze the stability of a prescribed blade motion or the response of the blade to external aerodynamic excitations. For rigid blade motions the first-order displacement-amplitude vector is given by

$$\dot{\tilde{X}} = \dot{h} + \dot{a} \times \tilde{R}_p \quad \text{for } \tilde{X} \text{ on } B, \quad (102)$$

where \dot{h} defines the amplitude and direction of blade translations (positive in the positive coordinate directions), \dot{a} defines the amplitude and direction of blade rotations (positive counterclockwise), and \tilde{R}_p is a position vector extending from the mean position of the reference blade axis of rotation (i.e., from the point x_p, y_p) to points on the mean position of the reference blade surface. These rigid two-dimensional motions model bending and torsional vibrations of actual rotor blades. The components h_x, h_y and a are, in general, complex to permit phase differences between the translations in the x - and y -directions and the rotation. Here the Cartesian x, y -coordinate axes are taken to coincide with and lie normal to, respectively, the mean position of the

reference blade chord line (Fig. 1) with x increasing from the leading to the trailing edge of this blade.

The force and moment acting on the m th blade are given by

$$\tilde{F}_m = - \oint_{B_m} \tilde{P} \hat{n} d\tau = \tilde{F} + \operatorname{Re} \{ \tilde{f} e^{i(\omega t + m\sigma)} \} + \dots \quad (103)$$

and

$$\tilde{M}_m = \oint_{B_m} \tilde{P} \tilde{R}_p \cdot d\tilde{r} = \tilde{M} + \operatorname{Re} \{ m e^{i(\omega t + m\sigma)} \} + \dots \quad (104)$$

The components of the force vector \tilde{F}_m are taken as positive in the positive coordinate directions, and the moment \tilde{M}_m is taken about the moving pitching axis of the m th blade and as positive in the counterclockwise direction. The vector \tilde{R}_p in (104) extends from this pitching axis to points on the moving m th blade surface. After some algebra, it follows that

$$\tilde{f} = \dot{a} \times \tilde{F} - \oint_B p_B \hat{n} d\tau + \int r_{sh,B} [P_B]_{sh} \hat{n}_B \quad (105)$$

and

$$m = \oint_B p_B \tilde{R}_p \cdot d\tilde{r} - \int r_{sh,B} [P_B]_{sh} (\tilde{R}_p \cdot \hat{r}), \quad (106)$$

where \tilde{f} and m are the complex amplitudes of the unsteady force and moment respectively. Recall that p_B is the complex amplitude of the harmonic component of the unsteady surface pressure, the subscript B refers to the mean blade surface, $r_{sh,B}$ is the relative shock displacement in the counterclockwise or \hat{r} -direction along this surface, and $[P_B]_{sh}$ is the jump in the steady pressure in moving across the shock in the \hat{r} -direction. The summations in (105) and (106) account for the concentrated loads due to shock motion and consist of terms that are evaluated at the mean positions of the shock roots.

A useful parameter for blade flutter investigations is the aerodynamic work per cycle, $\tilde{W}_{\text{per cycle}}$, which is the work done by the fluid on a given blade over one period of its motion. By definition

$$\tilde{W}_{\text{per cycle}} = \oint \frac{d\tilde{W}}{dt} dt = \omega^{-1} \int_0^{2\pi} \frac{d\tilde{W}}{dt} d(\omega t), \quad (107)$$

where

$$\frac{dW}{dt} = - \oint_{SB} \tilde{p} \tilde{V} \cdot \tilde{h} \, dt \quad (108)$$

is the rate at which this work is done (see (3)). A prescribed blade motion is classified as stable, neutrally stable or unstable, according to linearized theory, depending upon whether the aerodynamic work per cycle is less than, equal to or greater than zero, respectively.

At the instantaneous position of a blade surface

$$\tilde{V} \cdot \tilde{h}_B = \operatorname{Re} \left\{ \frac{\partial \tilde{R}}{\partial t} \right\} \cdot \tilde{h}_B + \dots \quad (109)$$

Therefore for a rigid motion, it follows from the definitions for the aerodynamic force and moment that the rate at which work is done on say the reference blade is given by

$$\frac{dW}{dt} = \operatorname{Re} \{ i \omega e^{i \omega t} \} \cdot \tilde{F} + \operatorname{Re} \{ i \omega a e^{i \omega t} \} \tilde{M} \quad (110)$$

After we substitute this expression along with the expansions (103) and (104) into (107) and carry out the integration, it follows that

$$\begin{aligned} \tilde{W}_{\text{per cycle}} = \pi [& |h_x| |f_x| \sin \phi_{f_x h_x} \\ & + |h_y| |f_y| \sin \phi_{f_y h_y} \\ & + |a| |m| \sin \phi_{ma}], \end{aligned} \quad (111)$$

where $| |$ denotes the magnitude of a complex quantity and ϕ_{re} denotes the angle by which a complex response quantity r leads the corresponding complex excitation quantity e . Equation (111) illustrates that, if a complex response term lags its corresponding excitation, the effect is a stabilizing one, since this phase-lag provides a negative contribution to the aerodynamic work per cycle, thereby indicating that the airstream is removing energy from the vibratory motion.

For single-degree-of-freedom bending or torsional vibrations — usually only bending normal to the blade chord is considered — stability is determined by the phase angle between the lift force f_y and the normal displacement h_y or between the moment m and the angular displacement a . In particular, for pure (normal) bending with h_y taken as a positive real quantity,

$$W_{\text{per cycle}} = \pi h_y \operatorname{Im} \{ f_y \}; \quad (112)$$

while for pure torsion with a real and positive,

$$W_{\text{per cycle}} = \pi a \operatorname{Im} \{ m \}. \quad (113)$$

Thus, if the out-of-phase (with blade displacement) component of the lift for a pure bending motion, or the moment for a pure torsional motion, is less than zero, this motion will be stable according to linearized theory. For the foregoing single-degree-of-freedom motions the aerodynamic work per cycle is often expressed in normalized form as an aerodynamic damping parameter Ξ (see Carta 1983); i.e.,

$$\Xi_h = - \frac{W_{\text{per cycle}}}{\pi h_y} = -\operatorname{Im} \{ f_y \} \quad (114)$$

and

$$\Xi_a = - \frac{W_{\text{per cycle}}}{\pi a} = -\operatorname{Im} \{ m \}. \quad (115)$$

Hence, the aerodynamic damping is positive for a stable motion.

NUMERICAL EXAMPLES

As a consequence of the linearization introduced in this chapter, the nonlinear time-dependent unsteady aerodynamic problem has been reduced to two time-independent boundary-value problems — a nonlinear one for the zeroth-order or steady flow and a linear one for the first-order or unsteady flow. Moreover, numerical resolutions of the zeroth- and first-order flows are required only over a single extended blade-passage region of finite extent (fig. 4) to provide the type of response information needed for turbomachinery aeroelastic or aeroacoustic design applications. Thus the restriction to small-amplitude harmonic unsteady excitations has permitted a substantial simplification of the original unsteady problem. However, the resulting steady and linearized unsteady problems still pose severe challenges to numerical analysts.

A detailed discussion on the numerical field methods that have been proposed for solving the compressible steady and linearized unsteady problems is beyond the scope of this chapter. However, limited numerical results will be presented for subsonic compressor-type ($M_u < M_{\infty} < 1$) cascades to partially reflect the current status of such solution methods and to illustrate several important effects on unsteady aerodynamic response associated with features of nonuniform steady flows. For a description of the field methods used to obtain these results we refer the reader to Caspar (1983) and to Verdon & Caspar (1982, 1984). In addition, for a description of some alternative numerical field methods along with their applications to unsteady cascade flows involving forced aerodynamic excitations, turbine cascades and supersonic inlet and/or exit Mach numbers see Caruthers (1981), Whitehead & Grant (1981) and Whitehead (1982) respectively. Finally, for a description of the semi-analytic surface-integral methods used for analyzing incom-

pressible steady and unsteady cascade flows see Atassi & Akai (1978, 1980) and Carstens (1981).

We will consider three simple cascade configurations each with blades undergoing prescribed self-excited motions and operating under uniform subsonic mean inlet and exit conditions. In each case the cascade stagger angle is 45° and the gap/chord ratio is unity. The first cascade consists of modified NACA 0012 airfoils and will be used primarily to illustrate effects of a relatively thick blunt-nosed blade geometry and mean blade loading on unsteady response. The second consists of sharp-edged double-circular-arc airfoils and will be used to illustrate the effects of shock phenomena and mean blade loading on the unsteady response at high subsonic inlet Mach number. Finally, for purposes of comparison, results will also be presented for a flat-plate cascade in which the blade mean positions and the mean inlet and exit flow directions are aligned. In this case the steady flow is uniform throughout the field and hence, there is no coupling between steady and unsteady disturbances.

Numerical results for steady Mach number M , first-harmonic unsteady pressure p_1 and pressure-difference (i.e., $\Delta p = p_{1B} - p_{1A}$) distributions along the reference blade surface, unsteady aerodynamic moments m and unsteady shock displacements $r_{sh,B}$ will be presented for blades undergoing single-degree-of-freedom torsional vibrations about their midchords (i.e., $X_p, Y_p = 0.5, 0$). The unsteady results have been determined by setting the complex torsional amplitude α in (102) equal to one. Hence, the real or imaginary parts of a complex response parameter represent the response component that is in- or out-of-phase, respectively, with the reference blade displacement. It is also important to note that the aerodynamic response to a prescribed blade motion depends, to a large extent, on the behavior in the far field of the acoustic waves generated by that motion (see (94)). For subsonic mean inlet and exit conditions blade motions are classified as subresonant if all acoustic waves attenuate with increasing axial distance ($|\xi| \rightarrow \infty$) from the blade row, or as superresonant if at least one such wave persists far upstream or far downstream and carries energy away from the blade row. At the boundaries between the different regions an acoustic resonance occurs; i.e., at least one wave persists in the far field and carries energy only in the circumferential or n -direction (see fig. 1).

NACA 0012 Cascade

Steady and unsteady flows through the staggered cascade (with $\Theta = 45^\circ$ and $G = 1$) of modified NACA 0012 airfoils have been determined for a prescribed inlet Mach number (M_∞) of 0.6 and four prescribed

inlet flow angles (α_∞). In each case a Kutta condition, i.e.,

$$\vec{v} \cdot d\vec{r} \Big|_{B_-} = -\vec{v} \cdot d\vec{r} \Big|_{B_+}, \quad (116)$$

has been imposed at blade trailing edges in the steady calculation, and hence, exit mean-flow conditions (M_∞ , α_∞) are determined as part of the steady solution. The mean position of the reference blade is defined by

$$y_\pm(x) = \pm 5T [0.2969x^{1/2} - 0.1260x - 0.3516x^2 + 0.2843x^3 - 0.1036x^4] \quad \text{for } 0 \leq x \leq 1, \quad (117)$$

where $T = 0.12$ is the nominal blade thickness and $1.1019T^2 = 0.015867$ is the leading edge radius. Note that the coefficient of the x^4 term in eq. (117) has been changed from the coefficient (i.e., -0.1015) used in the standard definition of a NACA 0012 airfoil (see Abbott and Von Doenhoff, 1959) so that the example blade profile will close in a wedge-shaped trailing edge.

Steady Mach number distributions along the reference NACA 0012 blade surface for prescribed inlet flow angles of 48° , 50° , 52° and 54° are shown in fig. 5. The calculated exit Mach numbers are respectively 0.595, 0.557, 0.522 and

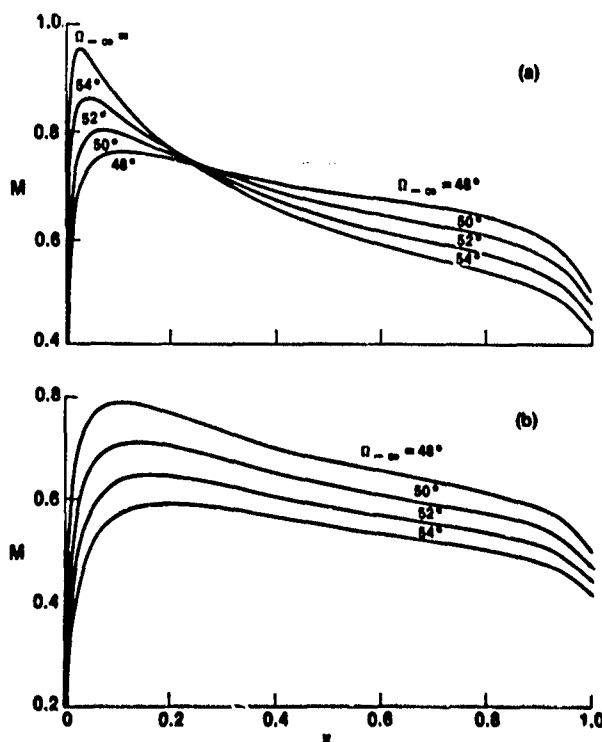


Figure 5. Steady surface Mach-number distributions for the example NACA 0012 cascade; $M_\infty = 0.6$; (a) suction surface; (b) pressure surface.

0.490, and in each case the calculated exit flow angle is approximately 47.7° . These steady flows are entirely subsonic with a peak Mach number of 0.789 occurring at $x = 0.113$ on the pressure surface of the blade for $\alpha_\infty = 48^\circ$, and 0.8, 0.86 and 0.96 occurring at $x = 0.07, 0.05$ and 0.03 on the suction surface for $\alpha_\infty = 50^\circ, 52^\circ$ and 54° respectively. In each case the mean flow stagnation point occurs within 0.2% of blade chord downstream from the leading edge.

Unsteady response predictions for the NACA 0012 cascade are shown in figs. 6 through 9. Corresponding results are also given in figs. 6, 8 and 9 for the flat-plate cascade operating in a uniform steady background flow with $M_\infty = 0.6$, and are indicated by the dashed lines in these figures. Unsteady pressure difference distributions and aerodynamic moments for the NACA 0012 and flat-plate blades undergoing unit-frequency ($\omega = 1$) torsional motions at $\sigma = 90^\circ$ are shown in fig. 6. In addition, the unsteady surface pressures acting on the reference NACA 0012 airfoil for $\omega = 1$ and $\sigma = 90^\circ$ are plotted in fig. 7 versus the square-root of the distance along the chord to emphasize the surface pressure behavior near the leading edge. The unsteady pressure is singular and behaves like a multiple of $x^{-1/2}$ near the leading edge of the flat plate airfoil (see fig. 6). In contrast, the unsteady pressure is analytic in the vicinity of the NACA 0012 leading edge (figs. 6 and 7). In this case both the real and imaginary components of the unsteady pressure difference are zero at the leading edge and reach local extrema very close to the leading edge. The results in figs. 6 and 7 also indicate that for $\omega = 1$ and $\sigma = 90^\circ$ the coupling between the steady and unsteady flows, because of blade geometry and mean loading, leads to a reduction in the out-of-phase pressure differences ($\text{Im}\{\Delta p(x)\}$) over the forward part of the blade and therefore a reduction in the moment opposing the blade motion.

Unsteady moments acting on the reference blades of the NACA 0012 and flat-plate cascades undergoing unit-frequency torsional vibrations are shown in fig. 8 for the entire range of interblade phase angles, i.e., $-180^\circ \leq \sigma \leq 180^\circ$. The abrupt changes in the moment curves are indicative of an acoustic resonance at the inlet and/or exit. The blade motions are superresonant at phase angles lying between the lowest and the highest resonant phase angles and subresonant at phase angles outside this range. The extent of the superresonant region will increase with increasing frequency and/or inlet Mach number. The motions considered in fig. 8 are stable; i.e., the out-of-phase component of the unsteady moment, $\text{Im}\{m\}$, is less than zero and therefore opposes the blade motion for all values of σ . However, the results in fig. 8 indicate that for a given σ the effect of an in-

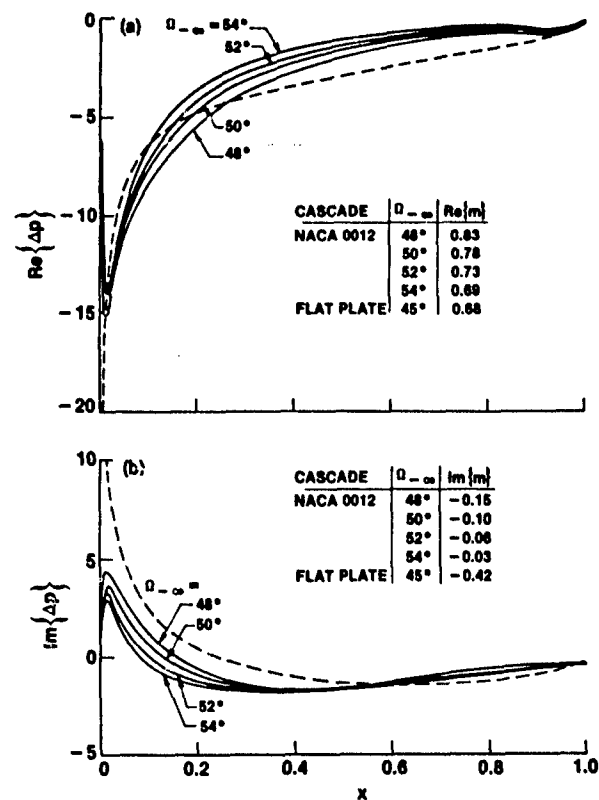


Figure 6. Unsteady response to torsional blade vibrations; $M_\infty = 0.6$, $\omega = 1.0$, $\sigma = 90^\circ$; (a) in-phase component; (b) out-of-phase component. — NACA 0012 cascade; ---- flat-plate cascade.

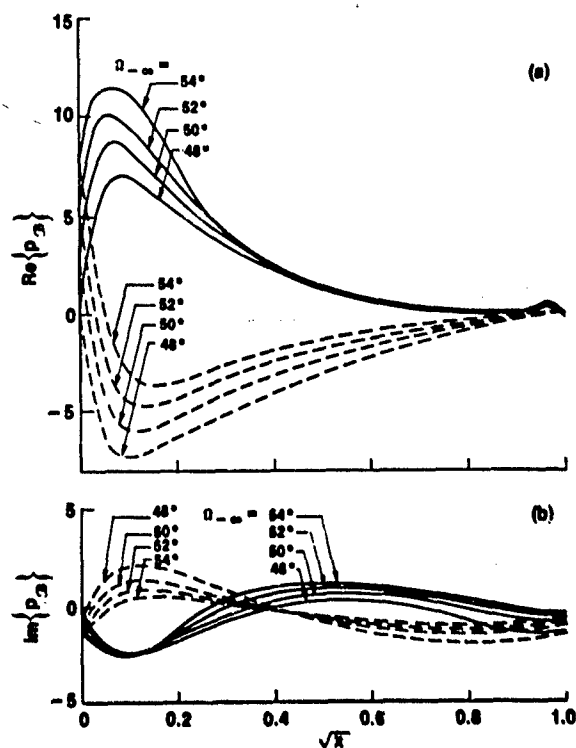


Figure 7. Unsteady surface pressures due to torsional vibrations of the NACA 0012 blades; $M_\infty = 0.6$, $\omega = 1.0$, $\sigma = 90^\circ$; (a) in-phase component; (b) out-of-phase component. — suction surface; ---- pressure surface.

crease in mean blade loading (i.e., \bar{m}_{∞}) is usually destabilizing for the NACA 0012 cascade, since the out-of-phase moment curves move closer to the stability boundary as the inlet flow angle α_{∞} is increased. In addition, the stability margin at $\omega = 1$ is greater for the unloaded flat-plate cascade with $\alpha_{\infty} = 45^\circ$ than it is for the NACA 0012 cascade operating at the inlet flow angles reported in fig. 8.

The effect of frequency on the out-of-phase unsteady moment due to torsion about midchord for the NACA 0012 cascade operating at $\alpha_{\infty} = 54^\circ$ and for the flat-plate cascade with $\alpha_{\infty} = 45^\circ$ is illustrated in fig. 9. It can be seen that the NACA 0012 blades experience a region of subresonant torsional instability at $\omega = 0.25, 0.5$ and 0.75 and that the extent of this region decreases with increasing frequency. The subresonant torsional motions of the flat-plate cascade are unstable only at the lowest frequency considered, $\omega = 0.25$.

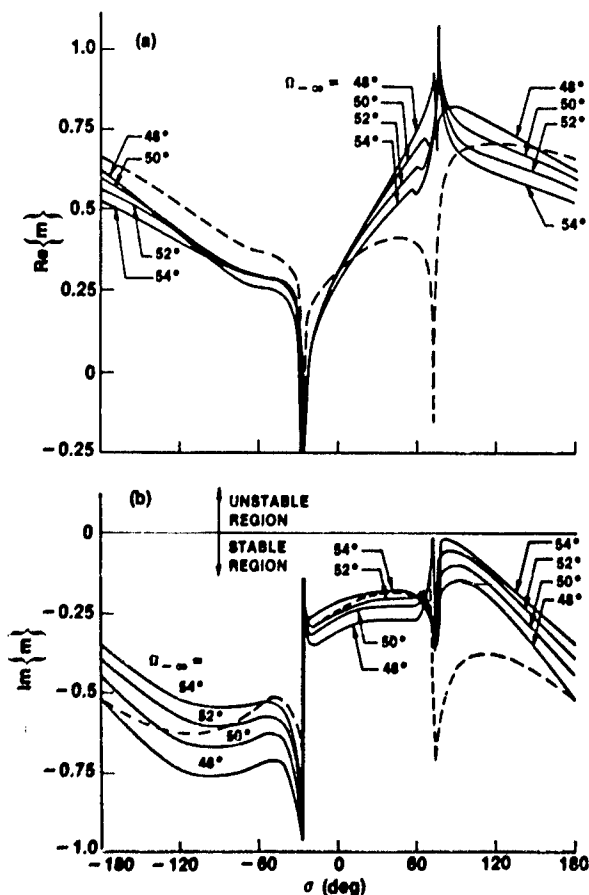


Figure 8. Unsteady moments due to torsional blade vibrations at $M_{\infty} = 0.6$ and $\omega = 1.0$: (a) in-phase component; (b) out-of-phase component. — NACA 0012 cascade; ---- flat-plate cascade.

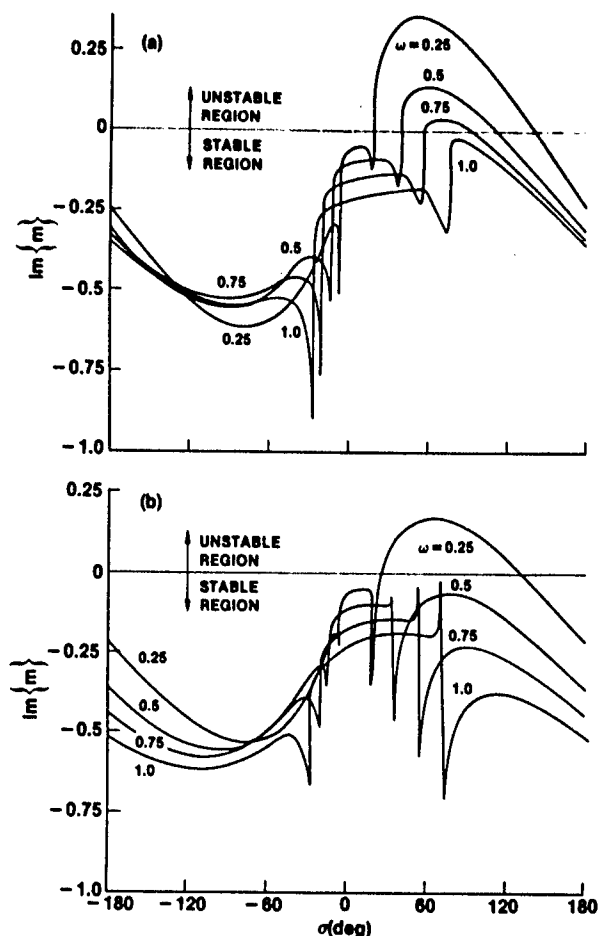


Figure 9. Effect of frequency on the out-of-phase component of the unsteady moment due to torsional blade vibrations at $M_{\infty} = 0.6$: (a) NACA 0012 cascade, $\alpha_{\infty} = 54^\circ$; (b) flat-plate cascade, $\alpha_{\infty} = 45^\circ$.

DCA Cascade

For a cascade of sharp-edged double-circular-arc airfoils the mean position of the reference blade surface is defined by

$$y_{\pm}(x) = \begin{cases} \text{sgn}(H_{\pm}) \{ |H_{\pm}| - R_{\pm} + [R_{\pm}^2 - (x-0.5)^2]^{1/2} \}, & \text{for } H_{\pm} \neq 0 \\ 0, & \text{for } H_{\pm} = 0, \end{cases} \quad (118)$$

where $0 \leq x \leq 1$, H is the y -coordinate of the surface at midchord, $R = |H|^{-1} (H^2 + 0.25)/2$ is the radius of curvature of the surface, $\text{sgn}(H) = \pm 1$ for $H \gtrless 0$ and the subscripts $+$ or $-$ refer to the upper or lower surfaces of the blade. Here we consider a cascade (with $\Theta = 45^\circ$ and $G = 1$) of 5% thick, flat-bottomed DCA airfoils (i.e., $H_+ = 0.05$ and $H_- = 0$). Full-potential steady and linearized unsteady flows through this example configuration have been determined for prescribed inlet Mach numbers (M_{∞}) of 0.5, 0.7, 0.8 and 0.9. In each case the requirement (116) has been imposed at blade leading (zero load-

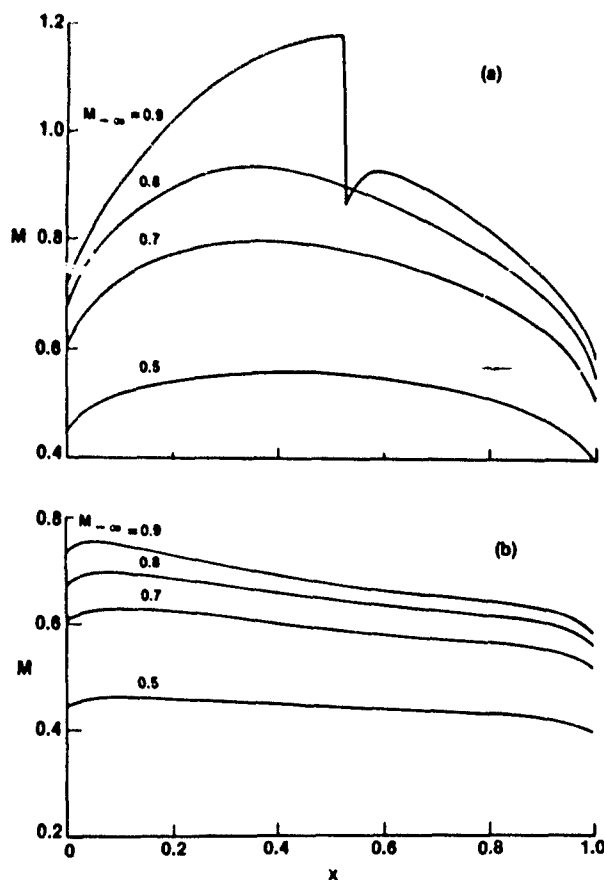


Figure 10. Steady surface Mach-number distributions for the example DCA cascade: (a) suction surface; (b) pressure surface.

ing condition) and trailing (Kutta condition) edges in lieu of prescribing an inlet flow angle and an exit Mach number or flow angle, respectively. Numerical results for this configuration and for a corresponding flat-plate ($H_1 = 0$) configuration are given in figs. 10 through 16. Those depicted in figs. 10 through 14 have been taken from Verdon & Caspar (1984).

The predicted surface Mach number distributions for the DCA cascade are shown in fig. 10. For the prescribed inlet Mach numbers stated above the calculated exit Mach numbers M_{∞} are 0.43, 0.57, 0.62 and 0.64, respectively. In addition, the calculated inlet flow angles α_{∞} are 49.0° , 49.2° , 49.4° and 49.6° , respectively, and in each case the calculated exit flow angle is approximately 43.0° . The steady flows at $M_{\infty} = 0.5$, $M_{\infty} = 0.7$ and $M_{\infty} = 0.8$ are entirely subsonic with peak suction-surface Mach numbers of 0.561, 0.804 and 0.941 occurring at respectively 40.8, 38.5 and 36.5% of blade chord downstream from the leading edge. The steady flow is transonic for $M_{\infty} = 0.9$ with a supersonic region extending from 18.5 to 52.5% of blade chord along the suction surface and terminating at a shock discontinuity. The Mach numbers at the foot of the shock are 1.193 on the

upstream or supersonic side and 0.871 on the downstream or subsonic side.

First harmonic pressure difference distributions and aerodynamic moments for the example DCA and flat-plate cascades operating at an inlet Mach number of 0.9 are presented in figs. 11 and 12, respec-

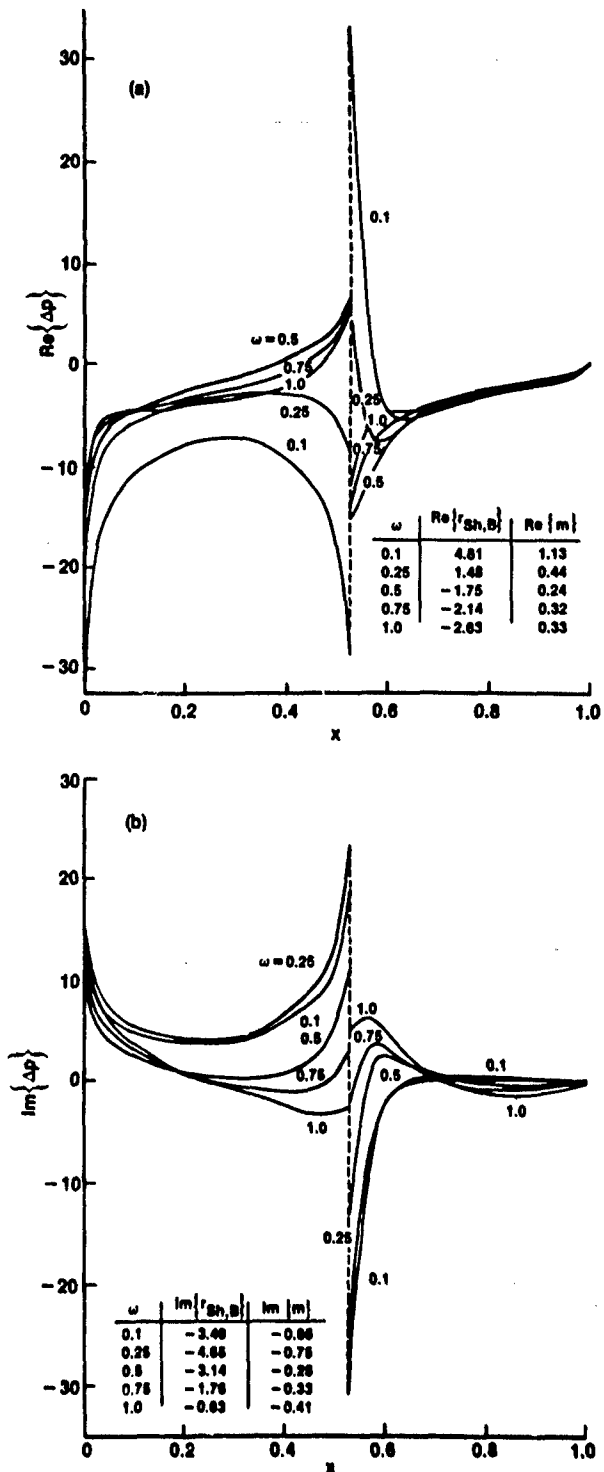


Figure 11. Effect of frequency on the unsteady response to torsional blade vibrations for the DCA cascade; $M_{\infty} = 0.9$, $\alpha = 180^\circ$: (a) in-phase component (real part) of the unsteady response; (b) out-of-phase component (imaginary part) of the unsteady response.

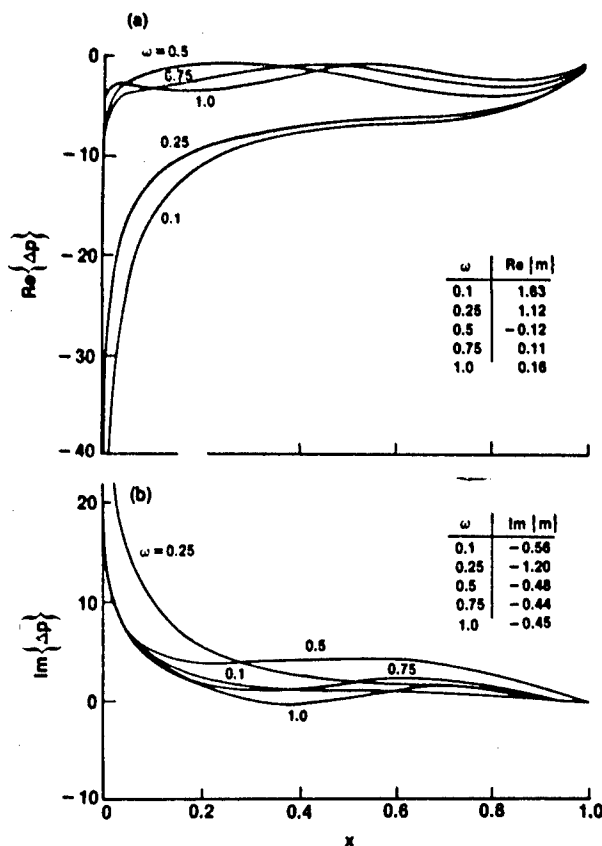


Figure 12. Effect of frequency on the unsteady response to torsional blade vibrations for the flat-plate cascade; $M_\infty = 0.9$, $\sigma = 180^\circ$: (a) and (b) as in figure 11.

tively. Here the blades are undergoing out-of-phase ($\sigma = 180^\circ$) torsional vibrations at different prescribed frequencies. As mentioned previously, in a discontinuous flow there are two contributions to the unsteady moment: one arising from the harmonic unsteady surface-pressure response and the other from the anharmonic surface pressures produced by shock motion. However, for the example DCA cascade with $M_\infty = 0.9$, the mean shock location is only slightly aft of blade midchord, and in this case, therefore, the anharmonic surface pressures produce relatively small contributions to the unsteady moments.

A comparison of the DCA and flat-plate results depicted in figs. 11 and 12 clearly demonstrates a dramatic impact of nonuniform steady flow phenomena on the unsteady response at transonic speeds; in that, the amplitudes of the harmonic pressure fluctuations on the DCA blade surface become quite large near the shock discontinuity. A second interesting feature, illustrated by these results, is the change in the character of the pressure difference curves and in the magnitude of the unsteady moments as the blade vibration frequency increases from 0.25 to 0.5. These changes occur because the out-of-phase blade motions of the example DCA and flat-plate cascades are subresonant for ω

$= 0.1$ and 0.25 and superresonant for $\omega = 0.5, 0.75$ and 1.0 . The resulting difference in far-field acoustic-wave behavior has a significant impact on the unsteady response at the blade surface.

The effect of Mach number on the response to unit-frequency in-phase ($\sigma = 0^\circ$) torsional vibrations of the DCA and flat-plate blades is illustrated in figs. 13 and 14. These motions are superresonant, and hence, acoustic waves persist in the far field and propagate away from the blade row. For the flows at $M_\infty = 0.5, 0.7$ and 0.8 two such waves persist — one upstream and one downstream. For the DCA cascade operating at $M_\infty = 0.9$ three waves persist — two upstream and one downstream. Finally, for the flat-plate cascade operating at $M_\infty = 0.9$ there are four such waves — two upstream and two downstream.

The pressure difference distributions and moments reported for the DCA (fig. 13) and flat-plate (fig. 14) blades reflect this change in character of the unsteady flow in the far field; in that, the trends indicated by the results for $M_\infty = 0.5, 0.7$ and 0.8 are not maintained at $M_\infty = 0.9$. Also, a comparison of the DCA and flat-plate pressure-difference curves for in-phase motions suggests that the influence of mean-flow gradients on the unsteady response becomes more pronounced

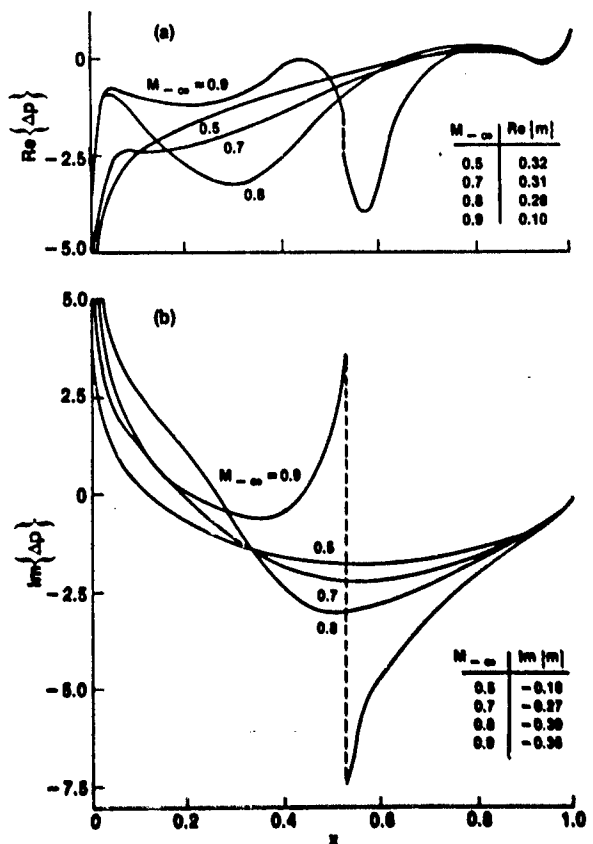


Figure 13. Effect of Mach number on the unit-frequency response to in-phase ($\sigma = 0^\circ$) torsional blade vibrations for the DCA cascade: (a) and (b) as in figure 11.

with increasing inlet Mach number. The pressure-difference distributions for the DCA and flat-plate blades are very similar for $M_{\infty} = 0.5$ and 0.7 , differ somewhat for $M_{\infty} = 0.8$ and differ substantially for $M_{\infty} = 0.9$. The differences at $M_{\infty} = 0.8$ can be attributed partially to the relatively large gradients in the subsonic mean flow that occur along the suction surface of each DCA blade, while the substantial differences at $M_{\infty} = 0.9$ are caused by the transonic effects associated with the DCA cascade.

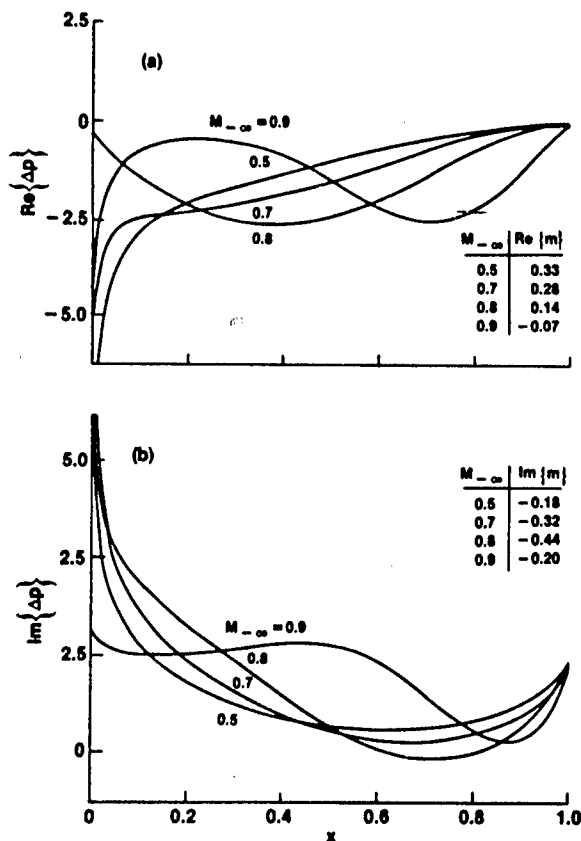


Figure 14. Effect of Mach number on the unit-frequency response to in-phase torsional blade vibrations for the flat-plate cascade: (a) and (b) as in figure 11.

Predictions of aerodynamic moment versus interblade phase angle for torsional motions of the flat-plate and DCA cascades are shown in figs. 15 and 16. The results in fig. 15 are for a prescribed inlet Mach number of 0.7 and those in fig. 16 are for an inlet Mach number of 0.9 . The unit-frequency torsional motions of the two cascades are stable (i.e., $Im[m] < 0$) at both inlet Mach numbers. Those angles at which an acoustic resonance occurs are indicated by the arrows at the top of each figure. For the unloaded flat-plate cascade the same resonance conditions apply at inlet and exit; however, quite different conditions apply for the DCA cascade because of the differences between the inlet and exit mean-flow properties. Thus, for example, for the flat-plate blades operating at $M_{\infty} = 0.7$

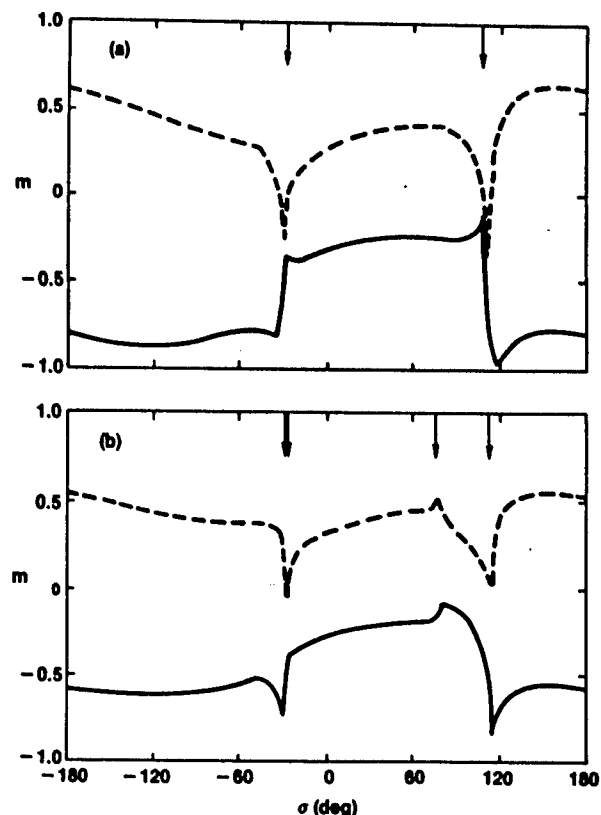


Figure 15. Unsteady moments due to unit-frequency torsional blade vibrations at $M_{\infty} = 0.7$: (a) flat-plate cascade; (b) DCA cascade. ---- in-phase component; — out-of-phase component.

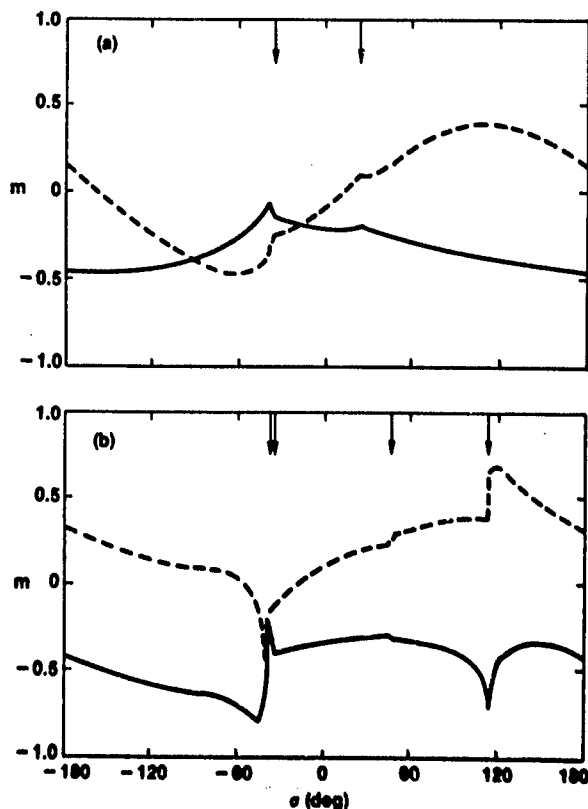


Figure 16. Unsteady moments due to unit-frequency torsional blade vibrations at $M_{\infty} = 0.9$: (a) flat-plate cascade; (b) DCA cascade. ---- in-phase component; — out-of-phase component.

and $\alpha_{in} = 45^\circ$ one acoustic wave propagates away from the blade row in both the up-stream and downstream regions when $-29.4^\circ < \sigma < 107.3^\circ$. The situation for the DCA cascade is slightly more complicated. Here $M_{in} = 0.7$, $\alpha_{in} = 49.2^\circ$, $M_{out} = 0.57$ and $\alpha_{out} = 43^\circ$, and one acoustic wave propagates away from the blade row in the far-upstream region if $-28.2^\circ < \sigma < 111.6^\circ$, and one such wave exists in the far-downstream region if $-29.7^\circ < \sigma < 74.8^\circ$. The moment curves for the two cascades in fig. 15 show similar trends with interblade phase angle except over range in which different far-downstream acoustic-wave-propagation characteristics exist, i.e., in the approximate range $74.8^\circ < \sigma < 107.3^\circ$. At the higher inlet Mach number the trends exhibited by the flat-plate and DCA moment response curves are quite different over the entire range of interblade phase angles. These differences occur because the mean flow through the flat-plate cascade is purely subsonic while that through the DCA cascade is transonic with a shock discontinuity, and also because of the substantial difference between the exit Mach numbers for the two cascades. Recall that M_{out} is 0.9 for the flat-plate cascade and 0.65 for the DCA cascade which implies that the two cascades operate in very different far-downstream acoustic environments over almost the entire interblade phase angle range.

The foregoing numerical results have been presented to demonstrate several important features associated with unsteady linearizations relative to nonuniform mean flows. These include the ability to predict: (1) unsteady pressures in the vicinity of a blunt leading edge and the effects of mean incidence on unsteady aerodynamic response; (2) steady and unsteady properties in the vicinity of a normal shock and the displacement of this shock along the blade surface; and (3) the effect of blade loading, i.e., a difference between the inlet and exit free-stream conditions, on the unsteady response at high subsonic inlet Mach number. These results are indicative of the progress that has been achieved during the past decade on the numerical resolution of two-dimensional steady and linearized unsteady cascade flows as well as the limitations of current numerical-solution methods.

Important advances in numerical field methods are still required to meet the goal of providing engine designers with reliable and efficient unsteady-aerodynamic prediction schemes which can be applied over a wide range of operating conditions. In particular, such schemes should be applicable to fan, compressor and turbine cascades operating in low subsonic through low supersonic flow regimes and subjected to various types of unsteady excitations occurring over a broad frequency range.

LIMITING FORMS OF THE GOVERNING EQUATIONS

In this section limiting forms of the foregoing aerodynamic equations will be determined for cascade flows in which steady departures from a uniform upstream condition can be regarded as small. One purpose here is to demonstrate that the steady and unsteady equations derived above can, for the most part, be reduced to the familiar small-disturbance equations of inviscid aerodynamic theory (see Miles 1959; Landahl 1961; Ashley & Landahl 1965; and Tijdeman & Seebass 1980). This demonstration will also provide a convenient opportunity to discuss several of the important theoretical analyses that have been developed for turbomachinery aeroelastic applications. We assume that the blades and their motions produce only small and very small disturbances respectively in an otherwise uniform flow and, for simplicity, that self-excited blade motions are the only source of unsteady excitation. The equations governing the steady and unsteady disturbances are usually derived by starting from the full, time-dependent governing equations; but here we proceed from the steady and linearized unsteady equations which have been provided in the previous sections of this chapter.

Preliminaries

Consider two-dimensional flow through a cascade of thin airfoils (fig. 17) undergoing identical small-amplitude harmonic motions at frequency ω but with constant phase angle σ between the motion of adjacent blades (c.f. (28)). The uniform inlet flow velocity $\vec{V}_{in} = \vec{e}_x$ is directed along the positive x -axis. Further, blade mean positions lie mainly along and are defined relative to chord

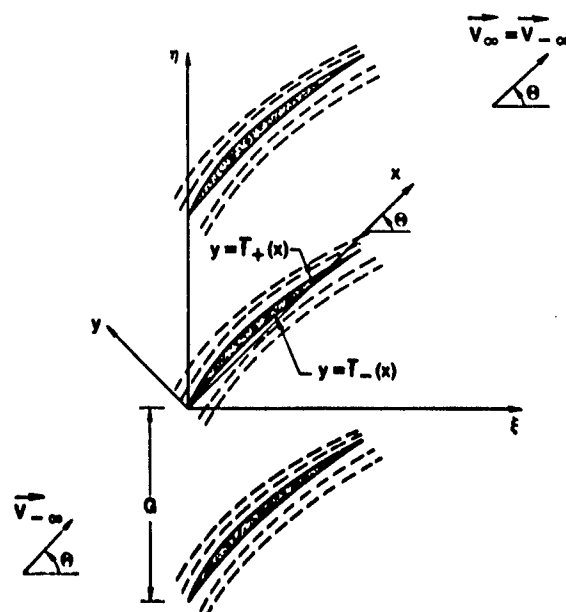


Figure 17. Cascade of thin-airfoils undergoing small-amplitude motions normal to the free-stream (or x -) direction.

lines which are parallel to this axis, and their unsteady displacements are normal to it. Thus (see fig. 17), the instantaneous location of the reference ($m = 0$) blade is given by

$$\begin{aligned} \mathcal{B}(x, y, t) &= y_{\pm}(x, t) - \bar{f}_{\pm}(x) \\ &- \operatorname{Re}[f_{\pm}(x)e^{i\omega t}] = 0 \\ &\text{for } 0 \leq x \leq 1, \quad (119) \end{aligned}$$

where the subscripts + and - refer to the upper and lower surfaces of the blade. We set $\bar{f}_{\pm}(x) = \delta \bar{g}_{\pm}(x)$ and $f_{\pm}(x) = \delta g_{\pm}(x)$, where $0 \leq \delta \ll 1$ and $0 \leq \delta \ll \bar{\delta}$ are characteristic lengths measuring the projection of the mean airfoil surface on the y-axis and the amplitude of the unsteady displacement, respectively, and the shape functions $\bar{g}_{\pm}(x)$ and $g_{\pm}(x)$ are smooth with x-derivatives of order unity everywhere along the chord.

Under the foregoing assumptions it is reasonable to expect that the flow, except in small regions near the leading and trailing edges of each blade and near shocks, can be described by a velocity potential of the form

$$\tilde{\phi}(x, y, t) = \phi(x, y) + \operatorname{Re}[\phi(x, y)e^{i\omega t}] + \dots, \quad (120)$$

where

$$\phi(x, y) = x + \bar{\phi}(x, y) = x + \bar{c}\bar{\phi}_1(x, \hat{y}), \quad (121)$$

$$\phi(x, y) = c\phi_1(x, \hat{y}) \quad (122)$$

and $\bar{\epsilon} \ll 1$ and $\epsilon \ll \bar{\epsilon}$ are positive functions of δ and $\bar{\delta}$, respectively, such that $\epsilon \rightarrow 0$ as $\delta \rightarrow 0$ and $\bar{\epsilon} \rightarrow 0$ as $\bar{\delta} \rightarrow 0$. In addition, the coordinate scaling $\hat{y} = \lambda y$ has been introduced and it is assumed that ϕ_1 and $\bar{\phi}_1$ and their derivatives with respect to x and \hat{y} are of order unity. The relative magnitudes of the parameters λ , δ , $\bar{\epsilon}$, $\bar{\delta}$ and ϵ will be determined from the boundary conditions at the reference blade surface and the differential equations governing ϕ_1 and $\bar{\phi}_1$.

Equations governing the steady and the linearized unsteady potentials have already been derived for a fully nonuniform mean flow. We now seek consistent approximations to these equations for flows in which the steady and unsteady departures from the uniform stream \hat{V}_{∞} are regarded as small and very small, respectively. In this case the unit tangent and normal vectors to the mean reference blade surface are given by

$$\hat{t}_{B_{\pm}}(x) = \pm \hat{e}_x + \delta \bar{g}'_{\pm} \hat{e}_y + \dots \quad (123)$$

and

$$\hat{n}_{B_{\pm}}(x) = \mp \delta \bar{g}'_{\pm} \hat{e}_x \pm \hat{e}_y + \dots, \quad (124)$$

where \hat{e}_x and \hat{e}_y are unit vectors directed in the positive x- and y-directions and the prime signifies differentiation with respect to x . In addition, the complex-amplitude of the reference blade displacement vector has the form

$$\hat{n}_{B_{\pm}}(x) = \delta g_{\pm}(x) \hat{e}_y. \quad (125)$$

After substituting (121) through (125) into the steady (46) and unsteady (70) flow tangency conditions for the reference blade ($m = 0$) and referring the resulting conditions to the x-axis, we obtain

$$\begin{aligned} \hat{\phi}_{1\hat{y}} &= \frac{\delta}{\lambda \bar{\epsilon}} \bar{g}'_{\pm} + \dots, \\ &\text{for } y = \pm 0, 0 \leq x \leq 1 \quad (126) \end{aligned}$$

and

$$\begin{aligned} \hat{\phi}_{1\hat{y}} &= \frac{\delta}{\lambda \epsilon} [i\omega g_{\pm} + g'_{\pm}] + \dots, \\ &\text{for } y = \pm 0, 0 \leq x \leq 1, \quad (127) \end{aligned}$$

where the subscript \hat{y} indicates partial differentiation with respect to \hat{y} and ± 0 denotes the limit $y \rightarrow 0$ from above or below. It follows that

$$\lambda \sim O(\bar{\delta}/\bar{\epsilon}) \sim O(\delta/\epsilon) \quad (128)$$

for the expansion (120-122) to be meaningful.

Similarly, upon substituting (121) and (122) into the steady, (44) and (45), and the linearized unsteady, (63) and (68), field equations and neglecting terms that are definitely small, as $\delta \ll \bar{\delta} \rightarrow 0$, compared to those retained, we are able to determine the following approximate equations for the small-disturbance steady and unsteady flows:

$$\begin{aligned} (M_{\infty} A)^2 &= \bar{\rho}(\gamma - 1) = (\gamma M_{\infty}^2 P)(\gamma - 1)/\gamma \\ &= 1 - \bar{\epsilon}(\gamma - 1)M_{\infty}^2 \bar{\phi}_{1x}, \quad (129) \end{aligned}$$

$$\begin{aligned} (\bar{\epsilon}/\delta)^2 [1 - M_{\infty}^2 - \bar{\epsilon}(\gamma + 1)M_{\infty}^2 \bar{\phi}_{1x}] \bar{\phi}_{1xx} \\ + \bar{\phi}_{1\hat{y}\hat{y}} = 0, \quad (130) \end{aligned}$$

$$P = -\epsilon(1 + \frac{1}{\delta x})\phi_1 \quad (131)$$

and

$$\begin{aligned}
& (\bar{c}/\bar{\delta})^2 [1 - M_\infty^2 - \bar{c}(\gamma+1)M_\infty^2 \bar{\phi}_{1x}] \bar{\phi}_{1xx} \\
& + \bar{\phi}_{1yy} - 2i\omega M_\infty^2 \bar{\phi}_{1x} \\
& - (\bar{c}^3/\bar{\delta}^2) M_\infty^2 [2i\omega \bar{\phi}_{1x} + (\gamma+1)\bar{\phi}_{1xx}] \bar{\phi}_{1x} \\
& + \omega^2 M_\infty^2 \bar{\phi}_1 \\
& - (\bar{c}^3/\bar{\delta}^2) i\omega M_\infty^2 (\gamma-1) \bar{\phi}_{1xx} \bar{\phi}_1 = 0. \quad (132)
\end{aligned}$$

The important nondegenerate forms of the differential equations (130) and (132) are obtained if either $(\bar{c}/\bar{\delta})^2 |1 - M_\infty^2|$ and ω are all of order 1; or $(\bar{c}^3/\bar{\delta}^2)$ is of order 1 and $|1 - M_\infty^2|$ and ω are both of order $\bar{\epsilon}$. In the first case the equations of classical linearized subsonic or supersonic flow theory are recovered; in the second, those of time-linearized transonic flow theory.

The resulting equations are given below in terms of the original variables \bar{f} , f , $\bar{\phi}$, ϕ and y . The differential equations (DE) and flow tangency conditions (FT) follow from (130), (132), (126) and (127); the wake-and shock-jump conditions (WJ) and (ShJ) and the surface pressure relations (SP) follow after the foregoing small-disturbance scalings are introduced into the corresponding nonlinear steady and linearized unsteady relations derived in this chapter. Note that steady and unsteady fluid properties must satisfy the periodicity conditions (36) and (37), and thus it is sufficient to state surface conditions only for those surfaces associated with the reference blade. Also, to within the order of approximation used here, the flow tangency, surface-pressure and wake-jump relations can be transferred to a flat-mean surface representation (i.e., the x -axis) of the steady-state and instantaneous reference blade and wake positions. Thus the flow tangency conditions and surface-pressure relations apply on the line segments $y = \pm 0$, $0 \leq x \leq 1$, and the wake-jump conditions apply on $y = 0$ for $x > 1$. The shock-jump conditions apply at the mean positions of the shock(s) and shock reflection(s) that originate at the reference blade. In each case below the first shock-jump relation follows after relations based on the mass conservation and irrotationality conditions are combined, while the second relation follows from the irrotationality condition alone. In addition to the surface conditions, the small-disturbance equations must be solved subject to the requirements that disturbances must either attenuate or propagate away from or parallel to the blade row in the far field.

Classical Linearized Theory

The classical linearized equations apply at subsonic ($M_\infty < 1$) or supersonic ($M_\infty > 1$) inlet Mach numbers and at the vibration frequencies of interest (i.e., $\omega \sim O(1)$) for turbomachinery flutter appli-

cations. In this approximation first-order steady and unsteady disturbances are independent of each other and can be regarded as being of the same order of magnitude (i.e., $\delta \sim O(\bar{\epsilon})$). Thus the linearized unsteady flow is identical to that produced by a vibrating flat-plate cascade in which the blade and wake mean positions are aligned with the free-stream flow. The following equations govern the harmonic unsteady disturbance:

$$\begin{aligned}
\text{(DE)} \quad & (1 - M_\infty^2) \bar{\phi}_{xx} + \bar{\phi}_{yy} - 2i\omega M_\infty^2 \bar{\phi}_x \\
& + \omega^2 M_\infty^2 \bar{\phi} = 0; \quad (133)
\end{aligned}$$

$$\text{(FT)} \quad \bar{\phi}_y = f_x^* + i\omega f_x^*; \quad (134)$$

$$\text{(WJ)} \quad [\bar{\phi}_y] = 0 \quad (135)$$

and

$$\begin{aligned}
& [p] = 0 \text{ or} \\
& [\bar{\phi}] = [\bar{\phi}]_{TE} \exp[i\omega(x-1)]; \quad (136)
\end{aligned}$$

$$\begin{aligned}
\text{(ShJ)} \quad & (1 - M_\infty^2) [\bar{\phi}_x] \\
& + (dx/dy)_{Sh} [\bar{\phi}_y] = 0 \quad (137)
\end{aligned}$$

and

$$(dx/dy)_{Sh} [\bar{\phi}_x] + [\bar{\phi}_y] = 0; \quad (138)$$

and

$$\text{(SP)} \quad p = -(\bar{\phi}_x + i\omega \bar{\phi}). \quad (139)$$

The corresponding steady-disturbance equations can be obtained from (133) through (139) by simply setting $\omega = 0$ and replacing $\bar{\phi}$, f and p by $\bar{\phi}$, \bar{f} and $\bar{p} = P - P_\infty = P - (\gamma M_\infty^2)^{-1}$.

Weak oblique shock (or Mach) waves occur if $M_\infty > 1$. These shocks, which emanate from blade leading and trailing edges, and their reflections off neighboring blades, lie on the characteristic lines $x \mp (M_\infty^2 - 1)^{1/2} y = \text{constant}$, and therefore they remain stationary in the classical linearized approximation. Because of this, and if we exclude the physically unrealistic situation of an impulsive change in velocity along a blade surface, the steady and unsteady disturbance potentials will be continuous across the shocks. Finally, it is worth noting that response phenomena associated with incident vortical and acoustic excitations are easily incorporated into the classical formulation (133) through (139). In particular, it is only necessary to add terms to the right-hand-sides of the flow-tangency equation (134) and pressure-potential relation (139), which cancel the normal velocities induced at the reference blade surface by the incident waves and account for the pressures due to incident

acoustic waves, respectively (see Whitehead 1970 or Smith 1971).

Over a period extending from the late 1960s through the 1970s, a significant level of research activity was focused on the development of semi-analytic solution procedures for the classical linearized equations. This work (see the introduction to this chapter for a partial list of references) has resulted in the availability of very efficient solutions which are now used extensively in turbomachinery flutter and resonant stress design prediction systems. The development of supersonic methods was motivated by the occurrence of so-called "supersonic unstalled torsional flutter" in the fan stages of modern high-bypass ratio jet engines. This type of flutter occurs at design operating conditions and therefore imposes a limit on the high speed operation of the machine. Unsteady supersonic solutions for unloaded flat-plate cascades operating at supersonic relative but subsonic axial inlet velocities have been found to give conservative estimates for the onset of supersonic unstalled torsional flutter, and have therefore provided engine designers with an effective means for predicting and controlling its occurrence. This capability has proved to be one of the most significant practical benefits gained from the use of theoretical unsteady aerodynamic prediction methods.

Related Theories

Modifications to the foregoing classical formulation have been proposed to treat separated subsonic flows, high frequency transonic flows and transonic (i.e., supersonic inlet/subsonic exit) flows containing strong in-passage shocks. In the flow-separation model (Perumal 1976; Chi 1980) the flow is assumed to separate at a prescribed point on each blade suction surface. The only change required in the foregoing unsteady formulation to accommodate this separation is the imposition of a constant surface-pressure condition, in lieu of the flow tangency condition (134), on the suction surface of the reference blade from the point of separation to the trailing edge (i.e., on $y = +0$ for $x_{sep} \leq x \leq 1$). Solutions based on this model (see Chi 1980) have been found to be in qualitative agreement with experimental measurements of unsteady lift and moment and they tend to predict observed flutter in fans in cases where subsonic attached-flow analyses indicate stability. Thus, although this simple flow-separation model ignores many of the complicated features of unsteady separated flow, it may contain an essential mechanism for the occurrence of subsonic flutter in cascades of thin highly-loaded blades.

For free-stream Mach numbers close to one (i.e., $|1-M_\infty^2| \sim O(\epsilon) \ll 1$) the first term in the differential equation (133) is

small compared to those remaining. Hence, this term can be formally neglected to recover the linearized equation of high-frequency unsteady transonic flow theory (see Landahl 1961). Surampudi & Adamczyk (1984) have recently developed a Wiener-Hopf solution technique for the resulting unsteady cascade boundary-value problem. With this procedure they have determined analytical results that are in agreement with classical subsonic results for $M_\infty = 0.9$ and classical supersonic results for $M_\infty = 1.1$. Hence, their unsteady transonic analysis may bridge the gap near $M_\infty = 1$ between separate subsonic and supersonic unsteady cascade analyses.

Finally, Goldstein, Braun and Adamczyk (1977) have provided an analysis of unsteady flow through a supersonic cascade in which a strong normal shock appears in each blade passage. These shocks extend from the lower surface and near the leading edge of each blade to the upper surface of the adjacent blade below. The resulting flow configuration approximates that observed in the tip region of a loaded supersonic fan rotor.

The free-stream flow upstream of the normal shocks is supersonic, with subsonic axial velocity component, while that downstream is subsonic. Away from the shocks, the steady and unsteady disturbances produced by the blades and their motions are regarded as small, relative to the uniform supersonic and subsonic free-stream flows, and independent of each other. The flow upstream of the strong normal shocks is irrotational, while the unsteady flow downstream contains both a rotational as well as an irrotational component. The upstream supersonic and the downstream irrotational subsonic unsteady flows are determined as solutions of the classical linearized supersonic and subsonic equations respectively, and the unsteady irrotational and rotational solutions in the subsonic region are connected to the unsteady solution in the supersonic region through jump conditions which are applied at the normal shocks.

Analytical predictions based on this strong-shock model indicate a greater torsional stability margin than those based on the completely supersonic model. This result is consistent with experimental observations of an increased supersonic torsional stability margin when back pressure is increased. In addition, the analytical results indicate the occurrence of pure bending flutter at lower frequencies. This flutter is partially attributed to the destabilizing effect of the concentrated shock loads, and it has not been revealed by purely supersonic analyses.

Time-Linearized Transonic Flow Theory

The time-linearized transonic small-disturbance approximation applies formally

at free-stream Mach numbers close to one and at low vibration frequencies. Here steady and unsteady disturbances are assumed to be small and very small respectively relative to the free-stream flow. The steady disturbance potential is determined by a nonlinear field equation, and the harmonic unsteady disturbance potential is determined by a linear equation with variable coefficients which depend on the underlying steady disturbance field. The following equations govern the steady and unsteady transonic disturbances:

Steady equations

$$(DE) \quad [1 - M_\infty^2 - (\gamma + 1)M_\infty^2 \bar{\phi}_x] \bar{\phi}_{xx} + \bar{\phi}_{yy} = 0; \quad (140)$$

$$(FT) \quad \bar{\phi}_y = \bar{f}_z'; \quad (141)$$

$$(WJ) \quad [\bar{\phi}_y] = 0 \quad (142)$$

and

$$[\bar{\phi}] = [\bar{\phi}]_{TE}; \quad (143)$$

$$(ShJ) \quad [1 - M_\infty^2 - 2M_\infty^2 \langle \bar{\phi}_x \rangle] [\bar{\phi}_x] - [\bar{\phi}_y] (dx/dy)_{Sh} = 0 \quad (144)$$

and

$$[\bar{\phi}_x] (dx/dy)_{Sh} + [\bar{\phi}_y] = 0 \quad \text{or} \quad [\bar{\phi}] = 0; \quad (145)$$

and

$$(SP) \quad \bar{p} = P - P_\infty = -\bar{\phi}_x. \quad (146)$$

Unsteady Equations

$$(DE) \quad [1 - M_\infty^2 - (\gamma + 1)M_\infty^2 \bar{\phi}_x] \phi_{xx} + \phi_{yy} - 2i\omega M_\infty^2 \phi_x - (\gamma + 1)M_\infty^2 \bar{\phi}_{xx} \phi_x = i\omega M_\infty^2 [2\bar{\phi}_x \phi_x - (\gamma - 1)\bar{\phi}_{xx} \phi] - \omega^2 M_\infty^2 \phi; \quad (147)$$

$$(FT) \quad \phi_y - f_z' = i\omega f_z; \quad (148)$$

$$(WJ) \quad [\phi_y] = 0 \quad (149)$$

and

$$[\phi_x] = -i\omega [\phi]; \quad (150)$$

$$(ShJ) [1 - M_\infty^2 + (dx/dy)_{Sh}^2] [\phi_x] - (\gamma + 1)M_\infty^2 [\bar{\phi}_x \phi_x] - 2i\omega M_\infty^2 [\phi] = 0 \quad (151)$$

and

$$[\phi] = -r_x [\bar{\phi}_x]; \quad (152)$$

and

$$(SP) \quad p + \phi_x - \langle \bar{p}_{sh} \rangle (x, t) = -i\omega \phi. \quad (153)$$

Here the symbol $\langle \rangle$ denotes the average value of a quantity at the shock, r_x is the shock displacement in the free-stream direction and the anharmonic shock load \bar{p}_{sh} is evaluated in the manner indicated by equations (98) through (100).

Two features of the foregoing transonic equations require further comment. First, the terms on the right-hand-sides of (147), (148), (150) and (153) are formally of higher order than those on the left. Hence, the former should be eliminated for a strict observance of the transonic order-of-magnitude analysis. However, these terms are often retained in time-linearized transonic approximations in an attempt to extend their range of application to include moderate vibration frequencies (see Fung, Yu & Seebass 1978).

Second, the jump conditions (144) and (151) have been derived by enforcing the mass conservation law at shocks. However, these conditions differ from those usually imposed in time-linearized transonic analyses because the latter are derived from a different conservation requirement. In particular, the steady and time-linearized unsteady shock jump conditions are usually derived from a conservation law based on the nonlinear transonic small-disturbance equation; i.e.,

$$[1 - M_\infty^2 - (\gamma + 1)M_\infty^2 \bar{\phi}_x] \bar{\phi}_{xx} + \bar{\phi}_{yy} - 2M_\infty^2 \bar{\phi}_{xx} = M_\infty^2 [\bar{\phi}_{tt} + 2\bar{\phi}_x \bar{\phi}_{xt} + (\gamma - 1)\bar{\phi}_t \bar{\phi}_{xx}], \quad (154)$$

where $\bar{\phi}(x, y, t)$ is the time-dependent disturbance potential. The resulting jump conditions (see Hafez, Rizk & Murman 1977 and Ehlers & Weatherill 1982) are

$$[1 - M_\infty^2 - (\gamma + 1)M_\infty^2 \langle \bar{\phi}_x \rangle] [\bar{\phi}_x] - [\bar{\phi}_y] (dx/dy)_{Sh} = 0 \quad (155)$$

and

$$[1 - M_\infty^2 + (dx/dy)_{Sh}^2] [\phi_x + r_x \bar{\phi}_{xx}] - (\gamma + 1)M_\infty^2 [\bar{\phi}_x (\phi_x + r_x \bar{\phi}_{xx})] + 2 [\bar{\phi}_x] (dx/dy)_{Sh} dr_x/dy = 2i\omega M_\infty^2 [\phi], \quad (156)$$

respectively. Equations (152) and (156) are the ones usually imposed in the time-linearized transonic approximation to determine the jump in the unsteady potential at the mean shock location and the shock displacement in the streamwise direction.

Numerical field methods for solving the transonic small-disturbance equations have received extensive development since the early 1970s. In particular, time (Fung & Yu & Seebass 1978) and frequency (Ehlers & Weatherill 1982) domain finite-difference methods have been determined for time-linearized transonic flows, with moving shocks, around isolated airfoils. Unfortunately, such developments have been directed primarily toward external aeronautical applications and solution methods for cascade flows are only beginning to appear (see Kerlick & Nixon 1982; Vogeler 1984; He & Zhou 1984). It should be noted, however, that the large mean-flow gradients and high-frequency unsteady fluctuations typical of transonic flows in turbomachines may limit the usefulness of the time-linearized transonic approximation for turbomachinery aeroelastic applications.

CONCLUDING REMARKS

In this chapter we have outlined the importance, complexity and variety of the unsteady flow phenomena occurring in axial-flow turbomachines, the major assumptions used in theoretical aerodynamic formulations intended for aeroelastic investigations, and the requirements placed on such formulations. Because of their extensive development for aeroelastic applications, the emphasis here has been placed on the description of linearized two-dimensional unsteady aerodynamic theories and, in particular, on the derivation of a rather general linearization which fully accounts for the effects of blade geometry, mean blade loading and shocks and their motions on the aerodynamic response to prescribed structural and aerodynamic excitations. The equations of classical linearized subsonic or supersonic flow theory and, for the most part, those of time-linearized transonic flow theory have been recovered as special cases of this general linearization.

In the more general theory, the unsteady flow is regarded as a small-amplitude harmonic perturbation of a nonuniform isentropic and irrotational steady flow. Thus steady-state values of the fluid properties are determined from the solution of a nonlinear boundary-value problem containing only a single differential field equation (i.e., the full-potential equation). The boundary-value problem for the linearized unsteady flow contains a system of three differential field equations. In both problems boundary conditions are imposed at the mean positions of

blade, shock and wake surfaces and along axial stations placed at finite distances upstream and downstream from the blade row. The unsteady equations are linear, time-independent and contain variable coefficients which depend on the underlying steady flow. These equations can be solved sequentially to determine the entropic, vortical and velocity potential fluctuations throughout a single extended blade-passage solution domain. This solution then provides the necessary information to predict the unsteady responses at a blade surface (surface pressures, relative shock displacements and global unsteady airloads) and in the far field (outgoing acoustic waves and convected entropic and vortical disturbances) which arise from prescribed unsteady excitations (self-excited blade motions and incident entropic, vortical and acoustic disturbances).

The intention here has been to provide a relatively complete linearized inviscid unsteady aerodynamic formulation for isolated two-dimensional blade rows which could serve as a basis for future research on the development of numerical solution methods and more comprehensive linearized aerodynamic formulations. However, a number of issues still persist relative to the two-dimensional inviscid problem, which require further study and clarification. A partial list includes: the approximation of strong shock behavior within a potential mean-flow formulation; the prediction of oblique shock motions; the inclusion of closed form expressions for the linearized entropy and rotational velocity fluctuations in the unsteady formulation, and the determination of useful analytical representations for the unsteady potential in the far field at transonic ($M \sim 1$) and supersonic free-stream Mach numbers.

Numerical results have been presented in this chapter to demonstrate several important effects, associated with nonuniform steady flow phenomena, on the linearized unsteady response at a moving blade surface and, to some extent, the current status of numerical solution methods for steady and linearized unsteady cascade flows. It is again to be emphasized that significant improvements in such methods are required before reliable and efficient linearized unsteady response information can be provided for the wide range of geometric configurations and flow conditions of interest to turbomachinery designers. Some needed capabilities include the ability to predict transonic flows (i.e., subsonic flows with embedded supersonic regions) through fan and compressor cascades operating at high mean incidence, supersonic flows with complex moving shock patterns, and the high-frequency unsteady flows associated with incident vortical, entropic and acoustic disturbances.

An important step has been taken

recently to assist in the validation of the results of future theoretical and experimental unsteady aerodynamic research programs. This concerns the establishment of a theoretical and experimental data base for a series of nine two-dimensional and quasi three-dimensional standard cascade configurations. The reader is referred to the reports by Fransson & Suter (1983) and Fransson (1984) for detailed information on this effort. Hopefully, it will be continued and expanded upon in the future.

The considerable advances made over the past two decades in computing nonlinear aerodynamic flows suggest that complete and reliable time-accurate solutions for nonlinear unsteady flows through two- and three-dimensional cascades may become available in the near future. However, the computing expense associated with such simulations and the numerous combinations of geometric, aerodynamic and structural parameters that must be analyzed will continue to prohibit their use in detailed aeroelastic applications. There will, therefore, be an ongoing need to develop more complete linearized formulations and solution methods. Major advances in our

ability to predict turbomachinery aeroelastic behavior should result if future research is directed toward including, in a rational manner, the effects of viscous/inviscid interactions and large-scale flow-separations within a linearized unsteady aerodynamic framework. Ultimately, linearized analyses, which account for nonuniform steady flow and, perhaps, viscous/inviscid interaction phenomena should be extended to treat three-dimensional unsteady flows.

ACKNOWLEDGEMENTS

The author expresses his sincere appreciation to Professors E. M. Greitzer (Massachusetts Institute of Technology) and D. S. Whitehead (Cambridge University) for carefully reviewing draft versions of this article and offering many helpful suggestions for improvement. Financial support for preparing this article was provided by the U. S. Naval Air Systems Command, the U. S. Air Force Office of Scientific Research and the United Technologies Research Center. This support is also gratefully acknowledged.

CLASSICAL TWO-DIMENSIONAL METHODS

by

D.S. Whitehead
Whittle Laboratory
Engineering Department
Cambridge University
Adingley Road
Cambridge CB3 0EL
UK

INTRODUCTION

This chapter presents some solutions of the basic equations derived in the previous chapter using methods which have become rather widely used and accepted. The flow is assumed to be two-dimensional, reversible, and isentropic. The methods rely on being able to build up the required flow from simple analytical solutions, and this can be done if either the fluid is incompressible or if the flow contains only small perturbations of a uniform flow. In the latter case the blades are assumed to be flat plates operating at zero incidence, so that the effects of camber and thickness cannot be treated.

The notation used is essentially the same as was used in the chapter "Linearized Unsteady Aerodynamic Theory" by J. Verdon. But the technique of making all variables dimensionless, by scaling with respect to the blade chord (c) and the far upstream velocity (V_∞), will not be used in this chapter because it is felt that in this context there is a gain of physical understanding by working with the dimensional variables. ω is therefore the angular frequency of vibration in radians per second, and a non-dimensional frequency parameter λ will be used, given by $\lambda = \omega c / V_\infty$. In the linearized theory the symbol U will be used as an alternative to V_∞ .

In this chapter no attempt is made to show how the theory has been built up by many authors over several decades. Here, only references to primary sources will be quoted. During the earlier part of the chapter many of these references are to the work of the author of this chapter and his students, and this calls for some apology. But it was felt that only in this way could this author give a reasonably connected account of the theory. There are many other equally valid ways of presenting the material, and the literature is substantial.

UNSTEADY THIN AEROFOIL THEORY, BOUND AND FREE VORTICITY

Consider a cascade of flat plates operating at zero incidence (Figure 1) so that the unsteady effects are small perturbations of a uniform flow. There is a jump in v_x across each blade, and the blades are therefore equivalent to vortex sheets. If γ_t is the total strength of the vortex sheet

$$\gamma_t = v_{x-} - v_{x+} \quad (1)$$

where the $-$ and $+$ suffices refer to lower and upper surfaces of the blade.

The total circulation round the blade is $\int_0^c \gamma_t dx$, and since this

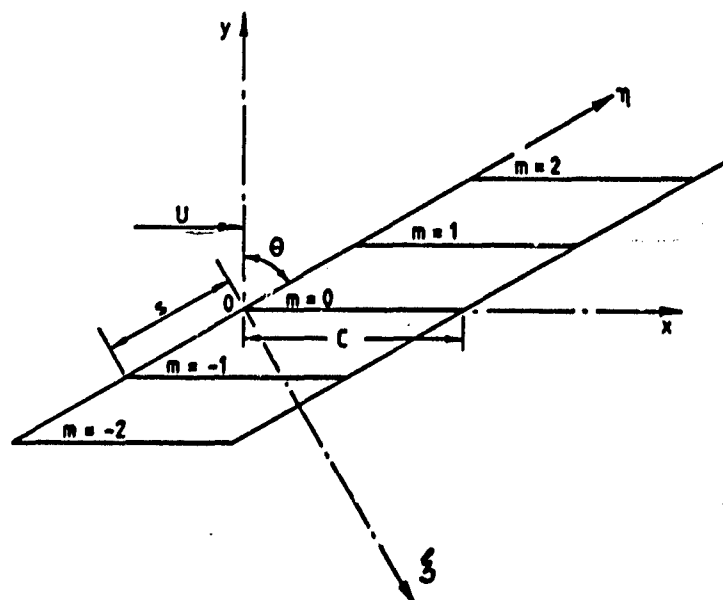


Fig. 1. Notation.

varies sinusoidally with time there will be a vortex sheet shed from the trailing edge which is convected downstream at the mainstream velocity, U .

The whole flow may be considered as being due to the vorticity which replaces the blades and their wakes. The essence of the thin aerofoil theory is to find what vorticity distribution will give the correct upwash velocity so as to satisfy the boundary conditions at the aerofoil surface and in the wake.

Although it is perfectly legitimate to regard the total strength of the vortex sheet γ_t as the primary variable, there is another way which is in practice more convenient. Consider an element of bound vorticity $\gamma(x) \delta x e^{i\omega t}$ at a point $(x, 0)$ on the reference aerofoil. Since the strength varies sinusoidally with time, there will be a sheet of free vorticity $\epsilon e^{i\omega t}$ shed from the element and extending far downstream. During a small time interval δt the strength of the element of bound vorticity changes by an amount

$$\gamma(x) \delta x e^{i\omega t} i\omega \delta t.$$

This is equal in magnitude and opposite in sign to the free vorticity appearing in the time δt , during which the shed sheet moves back a distance $U \delta t$. Hence just behind the element of bound vorticity, the strength of the sheet of free vorticity is

$$-\frac{\gamma(x) \delta x e^{i\omega t} i\omega \delta t}{U \delta t}.$$

Since the whole sheet of free vorticity moves back at the speed, U , the strength at $(x_1, 0)$ is

$$\begin{aligned} \epsilon(x_1) e^{i\omega t} = & \\ & - \gamma(x) \delta x \frac{i\omega}{U} e^{i\omega(t + (x-x_1)/U)}. \end{aligned} \quad (2)$$

At the point $(x_1, 0)$ the sheet of free vorticity gets contributions from all the elements of bound vorticity up to that point. Hence

$$\epsilon(x_1) = -\frac{i\omega}{U} \int_0^{x_1} \gamma(x) e^{i\omega(x-x_1)/U} dx. \quad (3)$$

Multiplying by $e^{i\omega x_1}$, differentiating with respect to x_1 and simplifying gives

$$\frac{d\epsilon}{dx} + \frac{i\omega}{U} (\gamma + \epsilon) = 0, \quad (4)$$

or

$$\frac{d\epsilon}{dx} + \frac{i\omega}{U} \gamma_t = 0,$$

since the total vorticity γ_t is given by

$$\gamma_t = \gamma + \epsilon. \quad (5)$$

Writing the linearized x momentum equation for a point just below the blade, and for a point just above the blade and subtracting gives

$$\begin{aligned} & \left(\frac{\partial}{\partial t} + U \frac{\partial}{\partial x} \right) ((v_{x-} - v_{x+}) e^{i\omega t}) \\ & = -\frac{1}{\rho} \frac{\partial}{\partial x} (p_- - p_+) e^{i\omega t} \\ & = (i\omega(\gamma + \epsilon) + U \frac{d\gamma}{dx} + U \frac{d\epsilon}{dx}) e^{i\omega t} \\ & = U \frac{d\gamma}{dx} e^{i\omega t} \end{aligned}$$

from Equation (4).

Integrating, and noting that the constant of integration is zero since both γ and $(p_- - p_+)$ are zero off the blade

$$(p_- - p_+) = -\rho U \gamma. \quad (6)$$

It can now be seen why bound vorticity, γ , is a more convenient primary variable than total vorticity γ_t . In the wake γ is zero whereas γ_t is not. Also, in subsonic flow a Kutta condition is applied so that $(p_- - p_+)$ is zero at the trailing edge, and therefore γ is also zero there. In addition, the force and moment on the blade are readily obtained from γ .

$$f_y = \int_0^c (p_- - p_+) dx = -\rho U \int_0^c \gamma dx, \quad (7)$$

and

$$m = \int_0^c (p_- - p_+) x dx = -\rho U \int_0^c \gamma x dx. \quad (8)$$

Since bound vorticity is equivalent to pressure jump across the blade, theories presented in terms of pressure dipoles, or dipoles of acceleration potential, are formally equivalent to theories presented in terms of bound vorticity.

If an element of bound vorticity $\gamma(x) dx$ at the point $(x, 0)$ on the reference blade is considered, together with corresponding elements on all other blades, and also the sheets of free vorticity shed from all these elements, then the velocity in the y direction induced at the point $(x', 0)$ may be written

$$v_y(x') = \frac{1}{c} K \left(\frac{x' - x}{c} \right) \gamma(x) dx. \quad (9)$$

Integrating for all elements along the chord

$$v_y(x') = \frac{1}{c} \int_0^c K \left(\frac{x' - x}{c} \right) \gamma(x) dx. \quad (10)$$

The evaluation of the kernel function K will be the main concern of the next six sections, but for the present it may be assumed to be known.

The upwash velocity $v_y(x')$ is also known. There are two cases of main interest.

For bending vibration normal to the chord, if the blade displacement is $h e^{i\omega t}$ then velocity must match the upwash velocity, so that

$$v_y(x') = i\omega h_y = \dot{h}_y. \quad (11)$$

Bending vibration parallel to the chord has no effect in thin aerofoil theory.

For torsional vibration of the blades about the origin at the leading edge, if the angular displacement is $\alpha e^{i\omega t}$ (anticlockwise positive), then the velocity normal to the blade at a distance x' from the axis is

$$(v_y(x') - \alpha U) e^{i\omega t} = \frac{d}{dt} (x' \alpha e^{i\omega t}).$$

Hence

$$v_y(x') = \alpha (U + i\omega x'). \quad (12)$$

There are other upwash velocity distributions which are often of interest, due to incoming acoustic waves and incoming vorticity waves. These waves are considered in the sections "Fundamental Acoustic Wave Solutions" and "Vorticity Wave Solutions".

In Equation (10) therefore the v_y function and the K function are known. Equation (10) is therefore an integral equation for the unknown bound vorticity distribution γ . It will be solved numerically by specifying γ at N suitably chosen points along the chord, and then making the upwash velocities match at N other suitably chosen points. More particulars of a solution procedure will be given in the sections "Solution for Subsonic Cascade" and "Solutions for Supersonic Cascade", but first the calculation of the kernel function will be considered.

KERNEL FUNCTION FOR INCOMPRESSIBLE FLOW

If the fluid is assumed to be incompressible, the velocities induced by vortices may be calculated by the Biot-Savart law. The v_y velocity induced at the point $(x', 0)$ by a vortex of strength $\Gamma_m e^{i\omega t}$ at the point (x_m, y_m) is

$$v_y = \frac{\Gamma_m}{2\pi} \frac{(x' - x_m)}{(x' - x_m)^2 + y_m^2}.$$

If the vortex on the reference blade at $(x, 0)$ has strength Γ_0 , then the strength of the corresponding vortex on the m th blade is given by

$$\Gamma_m = \Gamma_0 e^{i\omega \sigma},$$

where σ is the inter-blade phase angle. The position of this vortex is given by

$$x_m = ms \sin \theta + x,$$

$$y_m = ms \cos \theta.$$

Summing the effect for all blades gives

$$v_y = \frac{\Gamma_0}{2\pi} \sum_{m=-\infty}^{+\infty} \frac{e^{i\omega \sigma} (x' - x - ms \sin \theta)}{(x' - x - ms \sin \theta)^2 + (ms \cos \theta)^2}.$$

This may be written

$$v_y = \frac{\Gamma_0}{c} V\left(\frac{x' - x}{c}\right) \quad (13)$$

where

$$V(z) = \frac{1}{2\pi} \sum_{m=-\infty}^{+\infty} \frac{e^{i\omega \sigma} (z - m \sin \theta s/c)}{(z - m \sin \theta s/c)^2 + (m \cos \theta s/c)^2}.$$

This series can be summed analytically. The result for $0 < \sigma < 2\pi$ is

$$V(z) = \quad (14)$$

$$\frac{c}{4s} \frac{\exp\{-(\pi - \sigma)(\cos \theta + i \sin \theta)zc/s + i\theta\}}{\sinh\{\pi(\cos \theta + i \sin \theta)zc/s\}} + \frac{c}{4s} \frac{\exp\{+(\pi - \sigma)(\cos \theta - i \sin \theta)zc/s - i\theta\}}{\sinh\{\pi(\cos \theta - i \sin \theta)zc/s\}}.$$

The case of zero phase angle is special because a row of unsteady vortices produces non-zero induced velocities far upstream and downstream. In order to deal with this case, and have zero induced velocity far upstream of the row of vortices, it is necessary to replace $V(z)$ by $\{V(z) - V(-\infty)\}$.

Equation (13) may be used to evaluate the upwash velocity induced by both the elements of bound velocity γdx , and also the corresponding sheets of free vorticity given by equation (2)

$$v_y(x') = \frac{\gamma dx}{c} V\left(\frac{x' - x}{c}\right) - \frac{i\omega y dx}{Uc} \int_x^\infty e^{i\omega(x-x_1)/U} V\left(\frac{x' - x_1}{c}\right) dx_1.$$

Comparing this with equation (9) and rearranging gives

$$K(z) = V(z) - i\lambda e^{-i\lambda z} \int_{-\infty}^z e^{i\lambda z_1} V(z_1) dz_1 \quad (15)$$

where $\lambda = \omega c/U$ is the frequency parameter. This is the required expression for the kernel function in equation (10). The first term gives the effect of the bound vorticity, and the second term gives the effect of the shed sheets of free vorticity.

This is as far as the incompressible solution will be taken, since it is regarded as having been superceded by the methods for subsonic compressible flow. Techniques for solving the integral equation will be discussed in the section "Solution for Subsonic Cascade". A series method for evaluating the infinite integral in equation (15) has been given by Whitehead (1960).

FUNDAMENTAL ACOUSTIC WAVE SOLUTIONS

The equation governing the unsteady velocity potential for small deviations from a uniform mean flow has been derived in the previous chapter by Verdon (equation 133) and is

$$(1 - M^2) \frac{\partial^2 \phi}{\partial x^2} + \frac{\partial^2 \phi}{\partial y^2} - \frac{2i\omega}{A} M \frac{\partial \phi}{\partial x} + \frac{\omega^2}{A^2} \phi = 0,$$

where x and y are measured parallel and perpendicular to the mean flow. Referred to the axial and circumferential axes, coordinates ξ and η , this equation becomes

$$(1 - M_\xi^2) \frac{\partial^2 \phi}{\partial \xi^2} + (1 - M_\eta^2) \frac{\partial^2 \phi}{\partial \eta^2} - 2M_\xi M_\eta \frac{\partial^2 \phi}{\partial \xi \partial \eta} - 2 \frac{i\omega}{A} (M_\xi \frac{\partial \phi}{\partial \xi} + M_\eta \frac{\partial \phi}{\partial \eta}) + \frac{\omega^2}{A^2} \phi = 0 \quad (16)$$

where

$$M_\xi = M \cos \theta,$$

and

$$M_\eta = M \sin \theta.$$

The required solution is of the form

$$\phi = \phi e^{i(\alpha\xi + \beta\eta)} \quad (17)$$

where α and β are the wave numbers in the axial and circumferential directions.

Substituting this in equation (16) gives

$$\alpha^2 + \beta^2 - (\alpha M_\xi + \beta M_\eta + \omega/A)^2 = 0. \quad (18)$$

The solution being looked for has a phase angle σ between any blade and its next above neighbour, so that all variables are multiplied by $\exp(i\sigma)$ on going a distance s in the circumferential direction. Hence β is always real and is given by

$$\beta = (\sigma - 2\pi r)/s \quad (19)$$

where r is any integer.

Equation (18) is then a quadratic equation for α , and the solution for α is

$$\alpha = [M_\xi(\beta M_\eta + \omega/A) \pm \{(\beta M_\eta + \omega/A)^2 - (1 - M_\xi^2)\beta^2}^{1/2}] / (1 - M_\xi^2). \quad (20)$$

$$\text{If } (\beta M_\eta + \omega/A)^2 - (1 - M_\xi^2)\beta^2 > 0 \quad (21)$$

there are two real roots for α . This corresponds to waves propagating with constant amplitude, and it will be shown that one root corresponds to waves travelling upstream and the other root corresponds to waves travelling downstream (provided $M_\xi < 1$).

$$\text{If } (\beta M_\eta + \omega/A)^2 - (1 - M_\xi^2)\beta^2 < 0 \quad (22)$$

there are two complex roots for α . One root corresponds to a disturbance which grows exponentially in the axial (positive ξ) direction, and the other root corresponds to a disturbance which decays exponentially in the axial direction.

$$\text{If } (\beta M_\eta + \omega/A)^2 - (1 - M_\xi^2)\beta^2 = 0 \quad (23)$$

or

$$\frac{\omega}{A} = (M_\eta \pm (1 - M_\xi^2)^{1/2}) / (1 - M^2) \quad (24)$$

then the waves are just on the verge of propagating. This is known as the "cut-off" or "resonance" condition.

In order to apply the boundary conditions correctly it is necessary to determine the direction in which the propagating acoustic waves carry energy. To do this it is convenient to consider axes $O\xi'\eta'$, which are parallel to the $O\xi\eta$ axes, but which move with the mean velocity of the fluid. Relative to these axes, the wave propagates at a speed A and at an angle ψ as shown in Figure 2. The velocity potential is therefore of the form

$$\phi e^{i\omega'(t - \xi' \cos\psi/A - \eta' \sin\psi/A)} \quad (25)$$

where ω' is the intrinsic frequency, the frequency seen by an observer moving with the fluid. Note that the angle ψ gives the inclination of the wavefronts, and is not the direction of energy propagation relative to fixed coordinates.

On switching to fixed axes, $\xi = \xi' + M_\xi A t$, $\eta = \eta' + M_\eta A t$, so that the potential is

$$\phi e^{i\omega t} = \phi e^{i(\omega t + \alpha\xi + \beta\eta)}$$

$$= \phi e^{i\{(\omega + \alpha M_\xi A + \beta M_\eta A)t + \alpha\xi' + \beta\eta'\}}.$$

Comparing this with equation (25) gives

$$\omega' = \omega + \alpha M_\xi A + \beta M_\eta A, \quad (26)$$

$$\alpha = -\omega' \cos\psi / A, \quad (27)$$

$$\beta = -\omega' \sin\psi / A. \quad (28)$$

If α and β are eliminated from these equations the result is

$$\omega' = \omega / \{1 + M \cos(\theta - \psi)\}. \quad (29)$$

This equation shows that in subsonic flow ω' is always positive, but that in supersonic flow there are some directions of wave propagation (for instance $\psi = \theta + \pi$) for which ω' becomes negative.

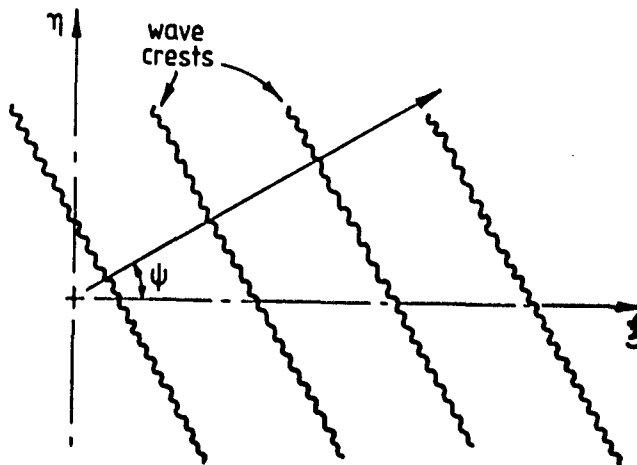


Fig. 2. Wave Propagation.

The group velocity in the axial direction, which is also the rate of axial transfer of wave energy, is then given by the sum of the convection velocity and the axial propagation velocity, and is

$$c_{\xi} = M_{\xi}A + A \cos \psi \quad (30)$$

$$= M_{\xi}A - A^2 \alpha / \omega' \quad (31)$$

$$= \mp ((\omega + \beta M_{\eta}A)^2 - (1 - M_{\xi}^2) \beta^2 A^2)^{1/2} / \omega',$$

where equations (26) and (20) have been used.

At the resonance or cut-off condition given by equation (23)

$$M_{\xi} + \cos \psi = 0$$

so that equation (30) shows that $c_{\xi} = 0$, and the waves carry energy in a purely circumferential direction, so that in a machine the energy propagates round the machine but none is lost by radiation in an axial direction. It will be found that at this point the acoustic waves can reach large amplitudes and the solutions become singular.

In subsonic flow, propagating acoustic waves occur over the range of β given by

$$\frac{M_{\eta} - (1 - M_{\xi}^2)^{1/2}}{1 - M^2} < \frac{A\beta}{\omega} < \frac{M_{\eta} + (1 - M_{\xi}^2)^{1/2}}{1 - M^2} \quad (32)$$

Outside this range decaying waves occur. Within this range, since ω' is always positive, equation (31) shows that the upper sign in equations (20) and (31) corresponds to waves carrying energy upstream, with negative c_x .

If the flow is supersonic ($M > 1$), but with subsonic axial velocity ($M_{\xi} < 1$), then propagating acoustic waves occur over the ranges of β given by

$$\frac{A\beta}{\omega} < \frac{-M_{\eta} - (1 - M_{\xi}^2)^{1/2}}{M^2 - 1} \quad (33)$$

$$\text{and } \frac{A\beta}{\omega} > \frac{-M_{\eta} + (1 - M_{\xi}^2)^{1/2}}{M^2 - 1} \quad (34)$$

Between these two regimes a range of decaying waves occurs. Assuming that $M_{\eta} > 0$, within the range given by equation (33) some analysis shows that ω' is negative for both waves, so that the lower sign in equations (20) and (31) corresponds to waves carrying energy upstream with negative c_x . Within the range given by equation (34), ω' is positive for both waves and the upper sign in equations (20) and (31) corresponds to waves carrying energy upstream.

If the axial velocity is supersonic ($M_{\xi} > 1$) the waves always propagate, and since c_x is always positive they always carry energy downstream and there is no resonance condition.

For these acoustic waves the velocity perturbations are given by

$$v_{\xi} = \frac{\partial \phi}{\partial \xi} = i\beta \phi, \quad (35)$$

$$v_{\eta} = \frac{\partial \phi}{\partial \eta} = i\beta \phi \quad (36)$$

The pressure perturbation may be obtained from the momentum equation

$$\left(\frac{\partial}{\partial t} + V_{\xi} \frac{\partial}{\partial \xi} + V_{\eta} \frac{\partial}{\partial \eta} \right) v_{\xi} + \frac{1}{\rho} \frac{\partial p}{\partial \xi} = 0 \quad (37)$$

and is

$$\frac{p}{\rho} = - \frac{\omega' v_{\xi}}{\alpha} = - \frac{\omega' v_{\eta}}{\beta} \quad (38)$$

Since the fluctuations are isentropic the density perturbation is given by

$$\rho = p/A^2 \quad (39)$$

If the effects of incoming acoustic waves are to be calculated, then the sum of the upwash velocities normal to the chord due to the bound and free vorticity, $v_y(x')$ and due to the incoming wave must be zero. Hence

$$v_y(x') - v_{\xi i} \sin \theta + v_{\eta i} \cos \theta = 0$$

where the suffix i refers to the incoming wave. Using equation (38)

$$v_y(x') = \frac{p_i}{\rho U} \frac{\beta c \cos \theta - \alpha c \sin \theta}{\lambda + \alpha c \cos \theta + \beta c \sin \theta}$$

This can be evaluated for each of the pair of the waves corresponding to a given value of β . For unit value of $p_i/\rho U$ at the origin

$$v_y(x') = \frac{\beta c \cos \theta - \alpha c \sin \theta}{\lambda + \alpha c \cos \theta + \beta c \sin \theta} \exp i(\alpha \cos \theta + \beta \sin \theta)x' \quad (40)$$

VORTICITY WAVE SOLUTIONS

In addition to the acoustic wave solutions discussed in the last section, the continuity and momentum equations also admit of solutions which include vorticity, but have no pressure or density perturbation. For these solutions the velocity potential does not exist and the disturbances are convected downstream at the mean fluid velocity. These solutions therefore have

$$p = 0, \quad \rho = 0 \quad (41)$$

The required solution is of the form

$$v_{\xi} e^{i\omega t} = \text{const } e^{i(\omega t + \alpha \xi + \beta \eta)}$$

Putting these in the momentum equation (37) gives

$$\omega + V_{\xi} \alpha + V_{\eta} \beta = 0,$$

so that

$$\alpha = -(\omega + V_{\eta} \beta)/V_{\xi} \quad (42)$$

Since there is no density perturbation, the continuity equation can be used in its incompressible form

$$\frac{\partial v_{\xi}}{\partial \xi} + \frac{\partial v_{\eta}}{\partial \eta} = 0,$$

to give

$$\alpha v_{\xi} + \beta v_{\eta} = 0 \quad (43)$$

Since these vorticity wave solutions have no pressure or density perturbations, they are unaffected by compressibility effects and apply at all Mach numbers.

The force and moment on the blades, due to wakes from some obstructions upstream which are in motion relative to the blades, are often required in order to calculate the forced vibration. A Fourier analysis of the wake profile in the η direction may be carried out, and each term corresponds to a vorticity wave of the type considered in this section. The sum of the upwash velocities normal to the chord due to the bound and free vorticity, $v_v(x')$ and due to the incoming vorticity wave must be zero.

Hence

$$v_v(x') - v_{\xi 1} \sin \theta + v_{\eta 1} \cos \theta = 0,$$

where the suffix i refers to the incoming wave.

Using equations (42) and (43) this gives for a velocity v_w normal to the chord at the origin

$$\begin{aligned} v_v(x') &= -v_w \exp(-i\omega x'/U) \\ &= -v_w \exp(-i\lambda x'/c), \end{aligned} \quad (44)$$

showing how the waves are convected along the chord at the mainstream velocity.

KERNEL FUNCTION FOR SUBSONIC CASCADE

The incompressible kernel function which was derived in the section "Kernel Function for Incompressible Flow" of this chapter was based on the replacement of the aerofoils of the cascade by a number of bound vortices. In that case the effect of a row of bound vortices, with the spacing and stagger corresponding to the cascade in question, could be obtained by summing the series analytically. The corresponding solution in subsonic compressible flow for a single bound vortex involves Hankel functions, and when the series for a row of such vortices is written down it appears that it cannot be summed analytically, and if numerical evaluation of the series is attempted the series is found to converge very badly. The approach that will be used is therefore to build up the solution for the row of vortices from the acoustic and vorticity wave solutions given in the sections "Fundamental Acoustic Wave Solutions" and "Vorticity Wave Solutions". The presentation largely follows the paper by Smith (1972).

Consider therefore a row of vortices spread along the η axis with spacing s and phase angle σ . This may be considered as a distribution of bound vorticity along the η axis given by

$$\gamma = \sum_{m=-\infty}^{+\infty} \Gamma_0 e^{im\sigma/s} \delta(\eta - ms). \quad (45)$$

This series of delta functions may be transformed to a Fourier series as follows

$$\gamma = \Gamma_0 e^{i\eta\sigma/s} \sum_{m=-\infty}^{+\infty} e^{-i(n-ms)\sigma/s} \delta(\eta - ms)$$

$$= \Gamma_0 e^{i\eta\sigma/s} \sum_{m=-\infty}^{+\infty} \delta(\eta - ms)$$

since the delta function is only non-zero when $\eta - ms = 0$. Hence

$$\gamma = \Gamma_0 e^{i\eta\sigma/s} (1/s) \sum_{r=-\infty}^{+\infty} e^{-i2\pi r\eta/s}$$

by example 38 of Lighthill (1958). Hence

$$\gamma = \frac{\Gamma_0}{s} \sum_{r=-\infty}^{+\infty} e^{i(\sigma - 2\pi r)\eta/s}. \quad (46)$$

Each term of this series is sinusoidal in the η direction, and therefore the solutions of the sections "Fundamental Acoustic Wave Solutions" and "Vorticity Wave Solutions" may be matched to it. Upstream of the row of vortices only the upstream going acoustic wave, or alternatively the wave which decays exponentially upstream, can exist, and this will be distinguished by the suffix 1. Downstream of the row, only the downstream going acoustic wave, or alternatively the wave which decays exponentially downstream, can exist, and this will be distinguished by the suffix 2. In addition, downstream of the row there will be a vorticity wave, and this will be distinguished by the suffix 3.

Considering then just one term of the series in equation (46) three conditions are necessary to find these waves. Firstly, continuity may be applied across the vortex sheet at $\xi = 0$, so that

$$\begin{aligned} (V_{\xi} + \tilde{V}_{\xi 1}) (\bar{p} + \tilde{p}_1) &= \\ (V_{\xi} + \tilde{V}_{\xi 2} + \tilde{V}_{\xi 3}) (\bar{p} + \tilde{p}_2), \end{aligned}$$

or, to first order in the perturbations,

$$\bar{p} V_{\xi 1} + V_{\xi} \tilde{p}_1 = \bar{p} V_{\xi 2} + \bar{p} V_{\xi 3} + V_{\xi} \tilde{p}_2. \quad (47)$$

Secondly, the velocity jump across the row in the η direction must be equal to the strength of the sheet of bound vorticity, so that, for a sheet of unit amplitude

$$v_{\eta 2} + v_{\eta 3} - v_{\eta 1} = 1. \quad (48)$$

Thirdly, the strength of the vorticity wave may be related to the strength of the sheet of bound vorticity from which it is shed. In a time interval δt , the circulation shed from an element of bound vorticity $\gamma d\eta$ is

$$- \frac{d}{dt} (\gamma d\eta) \delta t = \zeta_3 d\eta (V_{\xi} \delta t)$$

where ζ_3 is the vorticity just downstream, and this is spread over an area $d\eta$ in the η direction and $(V_{\xi} \delta t)$ in the ξ direction. Hence

$$\zeta_3 = -i\omega\gamma/V_{\xi}.$$

But

$$\begin{aligned} \zeta &= \frac{\partial v_{\eta}}{\partial \xi} - \frac{\partial v_{\xi}}{\partial \eta} \\ &= i\omega v_{\eta} - i\omega v_{\xi}. \end{aligned}$$

Hence, for a sheet of unit amplitude,

$$\alpha_3 v_{n3} - \beta v_{\xi 3} = -\omega/V_{\xi} \quad (49)$$

Equations (47), (48) and (49) may now be solved to give the velocity perturbations for the acoustic waves and the vorticity wave just upstream and downstream of the $\xi = 0$ axis. Equations (38) and (39) are used to relate the acoustic perturbations, and equation (43) is used for the vorticity wave. The wave numbers in the axial direction are given by equations (20) and (42). The results are

$$v_{n3} = (\lambda^2 + \lambda\beta c \sin\theta)/A', \quad (50)$$

$$v_{n1} = (\beta c/2A') \{-(\beta c + \lambda \sin\theta) + \lambda\beta c \cos\theta(-E)^{-1/2}\} \quad (51)$$

$$v_{n2} = (\beta c/2A') \{+(\beta c + \lambda \sin\theta) + \lambda\beta c \cos\theta(-E)^{-1/2}\} \quad (52)$$

where

$$A' = \lambda^2 + \beta^2 c^2 + 2\lambda\beta c \sin\theta \quad (53)$$

and

$$E = \beta^2 c^2 - M^2 A' \quad (54)$$

Equations (51) and (52) are written for propagating waves ($E < 0$). For decaying waves ($E > 0$) $(-E)^{-1/2}$ is replaced by $i(E)^{-1/2}$. The corresponding v_{ξ} velocity perturbations are obtained from equations (38) and (43).

The velocities induced in the y direction normal to the blade chord at the point $\xi = x' \cos\theta$, $\eta = x' \sin\theta$, by the row of bound vortices at $\xi = 0$ may therefore be written, for $x' < 0$ (upstream of the row)

$$v_y = \frac{\Gamma_0}{s} \int_{-\infty}^{\infty} (v_{n1} \cos\theta - v_{\xi 1} \sin\theta) e^{i(\alpha_1 \cos\theta + \beta \sin\theta)x'} \quad (55)$$

Comparing this with equation (10) shows that the kernel function is given by

$$K(z) = \frac{c}{s} \int_{-\infty}^{\infty} (v_{n1} \cos\theta - v_{\xi 1} \sin\theta) e^{i(\alpha_1 \cos\theta + \beta \sin\theta)cz} \quad (56)$$

for $z < 0$.

The corresponding expression for downstream of the row of vortices includes the effect of the vorticity waves, so that

$$K(z) = \frac{c}{s} \int_{-\infty}^{\infty} (v_{n2} \cos\theta - v_{\xi 2} \sin\theta) e^{i(\alpha_2 \cos\theta + \beta \sin\theta)cz} + \frac{c}{s} \int_{-\infty}^{\infty} (v_{n3} \cos\theta - v_{\xi 3} \sin\theta) e^{i(\alpha_3 \cos\theta + \beta \sin\theta)cz} \quad (57)$$

for $z > 0$.

It has been shown that propagating waves only occur for a limited range of β , and that outside this range the waves decay. Hence large values of r (positive or negative) give large value of $|\beta|$, and the effect decays very rapidly on going away from the row of vortices. The two series for the acoustic waves therefore show good convergence, with terms decaying exponentially as $|r|$ increases. However, the convergence is less good when z is small, but still very satisfactory.

The second series for the vorticity waves in equation (56) does not show satisfactory convergence. However, Smith (1972) shows that this series may be summed analytically. The result for the kernel function may then be written

$$K(z) = \frac{c}{s} \int_{-\infty}^{\infty} (v_{n2} \cos\theta - v_{\xi 2} \sin\theta) e^{i(\alpha_2 \cos\theta + \beta \sin\theta)cz} + \frac{\lambda}{2} \frac{\sinh(\lambda \cos\theta s/c) \exp(-i\lambda z)}{\cosh(\lambda \cos\theta s/c) - \cos(\sigma + \lambda \sin\theta s/c)} \quad (58)$$

for $z > 0$.

SOLUTION FOR SUBSONIC CASCADE

In order to complete the analysis it is necessary to solve numerically the integral equation (10). In subsonic flow this has to be done subject to the Kutta condition at the trailing edge, which says that the pressure difference across the blade must tend to zero as the trailing edge is approached.

The bound vorticity, γ , will be specified at N points and perhaps the obvious way to do this would be to take these points equally spaced along the chord. But it has been found that a great increase in accuracy, using a modest value of N , can be obtained using the transformation (as in the classical thin-aerofoil theory of isolated aerofoils).

$$x = \frac{1}{2} c (1 - \cos \psi) \quad (59)$$

Then γ is specified at points given by

$$\psi = \pi l/N \quad (60)$$

where l is an integer $0 \leq l \leq (N-1)$. It will be noted that this does not include the point at the trailing edge ($x = c$, $\psi = \pi$, $l = N$), since, by the Kutta condition, γ is zero there.

The upwash velocities will then be matched at points given by

$$x' = \frac{1}{2} c (1 - \cos \epsilon) \quad (61)$$

where

$$\epsilon = \pi(2m+1)/(2N) \quad (62)$$

and m is an integer $0 \leq m \leq (N-1)$.

These points have values of ϵ halfway between the values of ψ at which the bound vorticity is specified.

Making these substitutions in equation (10) gives

$$v_y(c) = \quad (62)$$

$$\frac{1}{2} \int_0^\pi K \left(\frac{1}{2} (\cos \psi - \cos \epsilon) \right) \gamma(\psi) \sin \psi \, d\psi.$$

These substitutions remove a difficulty at the leading edge ($x = 0, \psi = 0$), since in the solution γ becomes infinite at that point. But by regarding $\gamma \sin \psi$ as the fundamental variable this product remains finite at the leading edge and causes no numerical difficulty. These substitutions also remove the singularity at the leading edge in integrals for the blade force and moment in equations (7) and (8), which were

$$f_y = -\frac{1}{2} \bar{\rho} U c \int_0^\pi \gamma(\psi) \sin \psi \, d\psi \quad (63)$$

$$m = -\frac{1}{4} \bar{\rho} U c^2 \int_0^\pi \gamma(\psi) \sin \psi (1 - \cos \psi) \, d\psi. \quad (64)$$

With the reservation to be made shortly the integrals in equations (62), (63) and (64) may be evaluated by the trapezoidal rule. Expressing the results in matrix form, equation (62) becomes

$$\underline{U} = \underline{K} \underline{I} \quad (65)$$

where \underline{U} is an upwash matrix having N rows and 2 columns. The first column gives the upwash velocity due to bending for unit (h_y/U) and the second column gives the upwash velocity due to torsion for unit a . According to equations (11) and (12)

$$\underline{U} = [1, (1 + i\lambda x'/c)] \quad (66)$$

Further columns may be added for incoming acoustic waves from upstream or downstream, and for incoming vorticity waves, if these results are required.

\underline{K} is a kernel matrix ($N \times N$) where elements are given by $K(1/2(\cos \psi - \cos \epsilon))$.

\underline{I} is a bound vorticity matrix having N rows and two (or more) columns whose elements are given by

$$\underline{I} = [(\pi/2N)(\gamma/U) \sin \psi] \quad (67)$$

except for the first row which has half weight.

Equations (63) and (64) may similarly be written in matrix form

$$\underline{C} = \underline{X} \underline{I} \quad (68)$$

where

$$\underline{C} = \begin{bmatrix} (f_y/\bar{\rho} U c h_y) & (f_y/\bar{\rho} U^2 c a) \\ (m/\bar{\rho} U c^2 h_y) & (m/\bar{\rho} U^2 c^2 a) \end{bmatrix} \quad (69)$$

and

$$\underline{X} = [-1 \quad -\frac{1}{2}(1 - \cos \psi)] \quad (70)$$

Further columns may be added to \underline{C} for additional input waves, and further rows may be added to \underline{X} and \underline{C} to give additional outputs, such as the strength

of the vortex sheets shed from the blades, and outgoing acoustic waves.

Equation (65) may be formally solved for \underline{I} , and substituted into equation (68) to give the final result

$$\underline{C} = \underline{X} \underline{K}^{-1} \underline{U} \quad (71)$$

One important complication concerns the singularities of the kernel function $K(z)$ at $z = 0$. Smith (1972) shows that these are of the form

$$\frac{b^2}{2\pi z} - \frac{\lambda}{2\pi b} (1 + a_1 \lambda z - i a_2 \lambda^2 z^2 - a_3 \lambda^3 z^3 + \dots) \text{Log}|z|$$

where

$$a_1 = 1 - M^2/2b^2$$

$$a_2 = 1 - 1/2b^2 + M^2/4b^4$$

$$a_3 = \frac{1}{2} (1 - 1/b^2 + M^2/6b^2 + 1/3b^4 - 3M^4/8b^6 + M^6/6b^6)$$

and

$$b^2 = 1 - M^2.$$

Whitehead (1960) has shown that integration of the $1/z$ singularity is accurately handled by the trapezoidal rule, but that a correction is required for the $\text{Log}|z|$ singularity if accurate results are to be obtained with modest values of N . Reference may be made to the original papers for the details of this correction.

A Fortran computer program for the implementation of this subsonic solution is given in Appendix A.

SOLUTIONS FOR SUPERSONIC CASCADE

When the mainstream is supersonic, the same general approach may be used as in the subsonic case, but there are a number of features which make the solution very different. There are also fundamental differences between the case when the axial velocity is subsonic and when the axial velocity is supersonic. If the axial velocity is supersonic the effects of an element of bound vorticity or pressure dipole introduced at any point are entirely downstream of that point. There is no effect upstream of the leading edge plane, and the flow can in principle be calculated by the method of characteristics. But if the axial velocity is subsonic, then a pressure dipole introduced on one blade implies other pressure dipoles on the blades below it, and the effects of these dipoles go upstream of the original dipole. The flow is therefore one in which upstream effects are possible and it has some of the features of a subsonic flow. There is an effect upstream of the leading edge plane, and the flow cannot be calculated in a straightforward way by the method of characteristics since there is no region of known flow from which to start. The supersonic axial velocity case very seldom occurs in real turbomachines, and is therefore of mainly academic interest. Attention will therefore be concentrated here on the subsonic axial velocity case.

Another difference between the subsonic and supersonic cases is that in the supersonic case the Kutta condition is applicable. The pressures across the wake are equalized by waves emanating from the trailing edge, and just upstream of the trailing edge there is a finite pressure jump across the blade. Conversely, at the leading edge the pressure jump is finite, and not infinite as it is in subsonic flow.

Waves of finite strength originate from the leading and trailing edges of the blades. These waves may be reflected from the surfaces of adjacent blades, and some of the patterns which result are illustrated in Figure 3. Diagrams (a) to (d) apply for the subsonic axial velocity case, and diagrams (e) to (h) apply for the supersonic axial velocity case. In Figure 3a all the waves from one blade go ahead of the blade above it and behind the blade below it, so there are no reflections. In steady flow there is no interference between blades, but in unsteady flow each blade can influence the flow over the blades above it. Figure 3b shows a trailing edge wave reflected once. Figure 3c shows a trailing edge wave reflected once and a leading edge wave reflected twice: this is the usual design case for a fan tip section. Figure 3d shows four reflections of a leading edge wave, and by extending the blade chord the number of reflections can be increased indefinitely, but these cases are not of much practical importance.

Figures 3(e) to (h) show the supersonic axial velocity cases, and the trailing edge waves always go downstream of all other blades. In Figure 3(e) the leading edge waves also go downstream and

there is no interference between blades which all behave like isolated aerofoils. Figure 3(f) shows one reflection of a leading edge wave, and Figure 3(g) shows one reflection of both of the leading edge waves, and Figure 3(h) shows two reflections of both of the leading edge waves. Again there are theoretical possibilities with large numbers of reflections.

In order to illuminate the most important features of the flow we shall start with a simple quasi-steady analysis. Torsional vibration is considered, and it is supposed that the blades have moved to a position consistent with a prescribed phase angle σ between blades and are then frozen in that position.

Standard supersonic thin aerofoil theory will be used, so that the relationship between the pressure change (Δp) across a weak wave and the corresponding deflection ($\Delta \theta$) of the flow is

$$\frac{\Delta p}{\rho U^2} = \pm \frac{\Delta \theta}{B} \quad (72)$$

where $B^2 = (M^2 - 1)$ and the positive sign applies to an upward going wave and the negative sign to a downward going wave.

Since the blades are flat plates, waves originate only from the leading and trailing edges of the blades. They may then be reflected from the adjacent blades, as already discussed and illustrated in Figure 3.

A wave starting downwards from the leading edge of one blade hits the next blade below at a point distant d_1 downstream from its leading edge, where

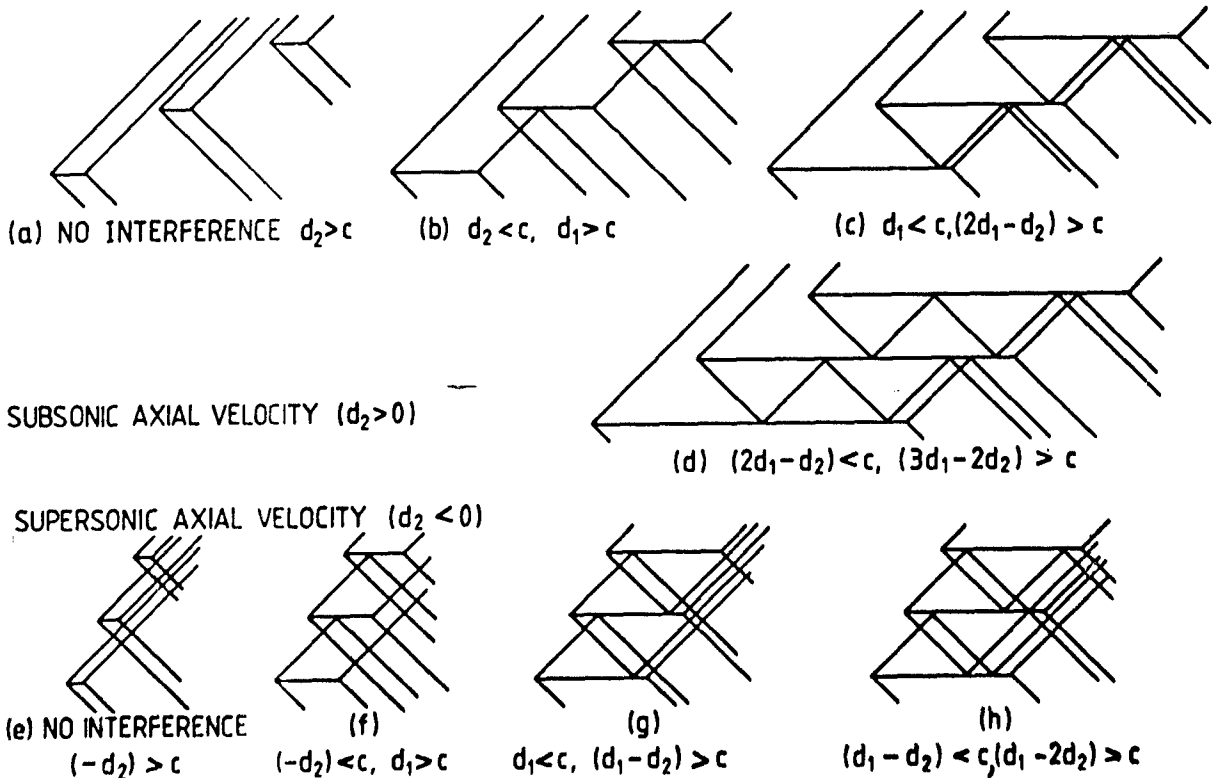


Fig. 3. Wave Reflection Patterns.

$$d_1 = s(\sin \theta + B \cos \theta) . \quad (73)$$

Similarly a wave starting upwards from the leading edge of one blade reaches the y position of the next blade above at a point distant d_2 upstream of its leading edge, where

$$d_2 = g(\sin \theta - B \cos \theta) . \quad (74)$$

If the axial velocity is supersonic, d_2 is negative.

We consider first cases with a subsonic axial velocity, such as (b) and (c) in Figure 3, but exclude case (a). Case (c) is illustrated on a larger \bar{s} scale in Figure 4. Let L be the strength, measured by the increase in pressure, of the wave going upwards from the leading edge of blade $m = 0$, and let T be the strength of the wave going upwards from the trailing edge. Then waves of strength $-L$ and $-T$ go downwards from the leading and trailing edges respectively.

Just ahead of the blade $m = 0$, the flow angle must match the angle of blade $m = -1$, just below, and is $\exp(-i\sigma)$. Just behind the wave of strength L going upward from the leading edge blade $m = 0$, the flow angle must match the angle of blade $m = 0$, and is α . Hence from equation (72),

$$\frac{L}{\beta U^2} = + \frac{a - a \exp(-i\sigma)}{B} = \frac{a}{B}(1 - \exp(-i\sigma)). \quad (75)$$

This determines the strength of the leading edge wave. It is zero if $\sigma = 0$. It does not depend on the number of internal wave reflections.

Bearing in mind that a wave is reflected from a solid surface as a wave of the same strength, the pressure in each area between waves may now be written down, and these are shown in square boxes on Figure 4 relative to the pressure ahead of the blade $m = 0$. It will be noted that the pressure jump across each blade has three discontinuities along the chord.

The strength of the trailing edge wave, T , may now be determined from the condition that the pressures on each side of the wake behind the blade must be equal. This gives

$$L - 2L e^{i\sigma} + T = -3L + 2 T e^{-i\sigma} - T .$$

Hence

$$T = - \frac{2 - e^{i\sigma}}{1 - e^{-i\sigma}} L. \quad (76)$$

If $\sigma = 0$, then $L = 0$ and T becomes indeterminate. The case $\sigma = 0$ must therefore be excluded from the present analysis. It will be handled by actuator disc methods in section "Actuator Disk Theory."

Apart from this case equations (75) and (76) give

$$\frac{T}{\partial U^2} = -\frac{a}{8} (2 - e^{i\sigma}) \quad (77)$$

The force on the blade $m = 0$ may now be determined, and is

$$f_y = -L(d_1 - d_2) - 3L(c - d_1) + (-3L + 2Te^{-i\sigma})d_2 - Ld_1 - (L - 2Le^{i\sigma})(c - d_1).$$

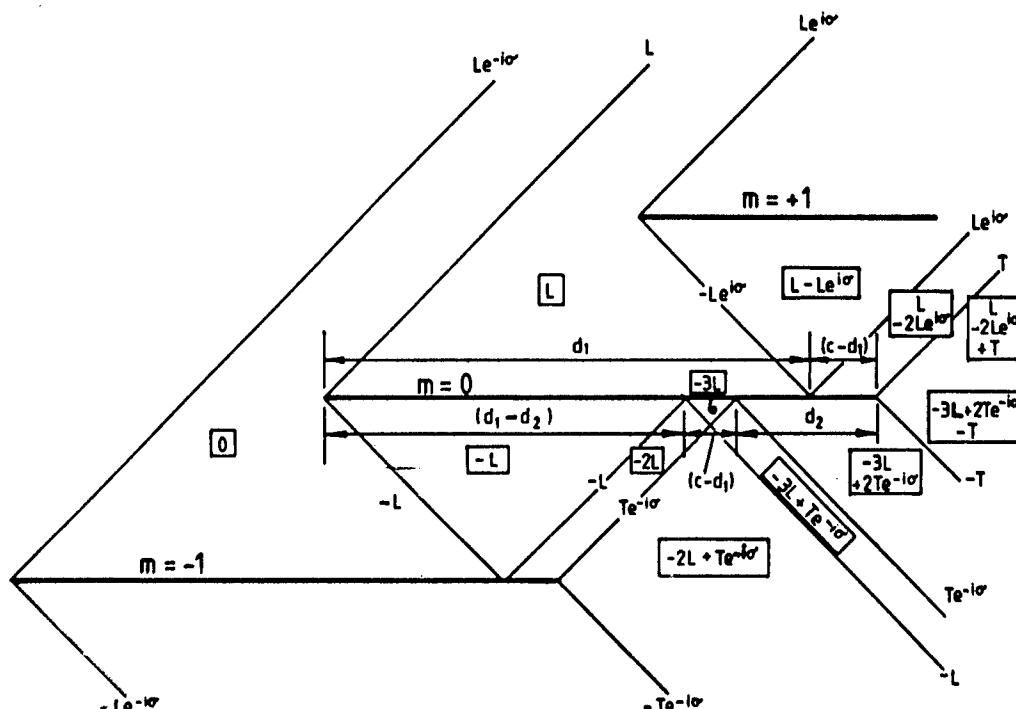


Fig. 4. Detail of Pressure Field for Case (c).

This gives for case (c)

$$f_y/\bar{\rho}U^2c\alpha = -\frac{2}{B} \{1 - e^{-i\sigma}(1-d_2/c) + 2(1-\cos\sigma)(1-d_1/c)\} \quad (78)$$

and the moment about the leading edge is similarly given by

$$m/\bar{\rho}U^2c^2\alpha = -\frac{1}{B} \{1 - e^{-i\sigma}(1-d_2/c)^2 + 2(1-\cos\sigma)(1-d_1/c)(1+d_1/c-d_2/c) - 2i \sin\sigma(1-d_1/c)(d_2/c)\} \quad (79)$$

Results for other cases of wave reflections may be obtained in a similar way. For cases (a) and (e) in Figure 3, when there is no inter-blade effect,

$$f_y/\bar{\rho}U^2c\alpha = -\frac{2}{B} \quad (80)$$

and

$$m/\bar{\rho}U^2c^2\alpha = -\frac{1}{B} \quad (81)$$

For subsonic axial velocity and for the general case when a wave starting downwards is reflected R times from the blade below and R times by the original blade, R is an integer given by

$$(R-1) < \frac{c-d_1}{d_1-d_2} < R \quad (82)$$

$R = 0$ corresponds to case (b) (Figure 3), $R = 1$ corresponds to case (c) and $R = 2$ to case (d).

The strength of the leading edge waves is given by equation (75), and the strength of the trailing edge waves is

$$T/\bar{\rho}U^2 = -\frac{\sigma}{B} \{1 + R(1 + e^{i\sigma})\} \quad (83)$$

The blade force is given by

$$f_y/\bar{\rho}U^2c\alpha = -\frac{2}{B} [1 - e^{-i\sigma}(1-d_2/c) + (1-\cos\sigma)R(2(1-d_2/c) - (R+1)(d_1-d_2)/c)] \quad (84)$$

and the moment about the leading edge is

$$m/\bar{\rho}U^2c^2\alpha = -\frac{1}{B} [1 - e^{-i\sigma}(1-d_2/c)^2 + (1-\cos\sigma)R(2(1-d_2/c)-d_2(d_1-d_2)(R+1)/c^2 - (d_1-d_2)^2(R+1)(2R+1)/(3c^2)) - (i \sin\sigma)R(2(1-d_2/c)(d_2/c) - d_2(d_1-d_2)(R+1)/c^2)] \quad (85)$$

These results have been written for torsion, but they also apply, to bending with U_α replaced by h_y , since equations (11) and (12) show that when $\omega = 0$ the upwash velocities are then identical. They also apply to the effect of wakes from upstream obstructions, since equation (44) shows that when $\omega = 0$ the upwash velocity is also uniform.

The results are essentially those derived by Kurosaka (1973) and by Strada, Chadwick, and Platzer (1979) and by Nagashima and Whitehead (1977), using different methods. These papers also give formulae valid when the frequency is small, but not zero, and correct to first order in ω . However, it appears that some of the terms in these formulae are not entirely in agreement between the three papers.

Nagashima and Whitehead (1977) also give formulae for force and moment in the case of $\omega = 0$ for supersonic axial velocity.

Turning to the full unsteady case with a frequency which is not small, all the available theories are complicated. Therefore, only a brief qualitative introduction to these methods will be given here. The most straightforward approach is to use a semi-infinite cascade, assuming that there is no perturbation upstream of a first blade. The flow may then be solved by the method of characteristics, (Brix and Platzer, 1974), or by finite difference methods (Verdon, 1973). The number of blades in the cascade must be chosen sufficiently large for the blade force and moment to approach limiting values. This involves large computation times, since the convergence with increasing blade number is slow. Also it appears that the results for the unsteady pressures on the surface of the blades converge much more slowly than the results for the blade loadings (Strada, Chadwick, and Platzer, 1979).

Calculations for an infinite cascade at realistic frequencies must include two physical effects. The first of these is the reflections of the leading and trailing edge waves from the adjacent surfaces, as already discussed in the case of steady flow. The second is the acoustic resonance effect, as discussed in the section "Fundamental Acoustic Wave Solutions." For a certain range of phase angles, all possible acoustic waves will propagate, and this regime is sometimes called the "subresonant" regime. The range of the phase angles where one or more of the possible acoustic waves are of exponentially decaying type is then called the "super-resonant" regime. This regime normally occurs for negative interblade phase angles, when the wave of elastic vibration of a fan rotor travels in the opposite direction to the direction of rotation, and is therefore classified as a "backward-travelling" wave.

A calculation in a single blade passage, with the correct blade-to-blade periodicity condition, has been given by Verdon and McCune (1975). The solution is formulated in terms of the velocity potential, and the kernel function is evaluated as a series of Bessel functions. The internal reflections are treated explicitly, and iteration is necessary to deal with the influence of the wake from one blade on the rear part of the lower surface of the blade above. This convergence fails in the "super-resonant" region. This limitation has been removed by Verdon (1977) by using a formulation in terms of pressure to find

the unsteady loading on the lower surface behind the point at which the Mach wave from the trailing edge of the next blade below hits the lower surface.

Formulations in terms of pressure, which relate more closely to the subsonic solution given in the previous section, have been given by Nagashima and Whitehead (1977) and by Ni ('979). If an attempt is made to calculate the kernel function by the series given in (55) it is found that the series does not converge. This behaviour is related to the jump changes in pressure across the waves propagated from the sources. The technique used is therefore to subtract out the steady and quasi-steady terms from the series in (55), to leave a series which does converge, and this is done in two different ways in these two papers. It is also necessary to allow for the reflections of the waves within the blade passage explicitly. In supersonic flow there is no point in using the transformations given in (58) and (60), and uniform spacing along the chord seems to be best for the points at which the bound vorticity is specified and for the points at which the upwash velocities are matched.

A quite different approach has been used by Adamczyk and Goldstein (1978). The problem is split into two parts. The first part consists of the inlet region, followed by a cascade of plates having the same spacing and stagger angle as the actual cascade, but with the chord extending to $x = +\infty$. The second part consists of the exit region, preceded by a cascade of flat plates with the chord extended back to $x = -\infty$. These two parts are then solved by two separate applications of the Wiener-Hopf technique. The solutions are then combined to give a solution of the complete problem.

Computer programs based on these last four very different methods have been shown to give identical results. Some specimen results will be presented in the section "Specimen Results for Flat Plate Cascades."

TRANSONIC THEORY

The equation governing small deviations from a uniform flow has been given by Verdon, equation (133). If the mainstream Mach number is near unity the term

$$(1-M^2) \frac{\partial^2 \phi}{\partial x^2}$$

is negligible compared to the term

$$\frac{2i\omega M}{A} \frac{\partial \phi}{\partial x}$$

This is true provided

$$|1-M| \ll \omega c/U$$

so the approximation is valid provided the frequency is high enough. The transonic small perturbation equation is therefore

$$\frac{\partial^2 \phi}{\partial y^2} - \frac{2i\omega M}{A} \frac{\partial \phi}{\partial x} + \frac{\omega^2}{A^2} \phi = 0. \quad (86)$$

This equation is also valid for blades of small thickness, provided $(\partial \phi / \partial x)_{\text{steady}} \ll \omega c/U$ which leads to $\omega c/U \gg \delta^{2/3}$.

This argument shows that the transonic equation is at least as good an approximation as the original acoustic equation. In fact Landahl (1961) has argued in detail that for isolated aerofoils in the transonic range the acoustic equation leads to physically inadmissible solutions, whereas the transonic equation gives the correct small perturbation solution. These arguments will be summarized here.

The one-dimensional solution of the acoustic equation, Verdon, equation (133), for flow in the chordwise direction shows two waves, one, the 'advancing wave', traveling forward at a speed of $A(M+1)$, and the other, the 'receding wave', traveling at a speed of $A(M-1)$. The transonic equation (86) on the other hand just shows the advancing wave traveling at a speed of $2AM$, and no receding wave. Disturbances do not propagate upstream in the transonic solution.

Looking at the solution of the acoustic equation near $M=1$ one sees that the receding wave has a low velocity, and therefore a short wavelength. If there is a smooth distribution of sources along the chord, the effects of the receding wave will tend to cancel, as $M \rightarrow 1$, but this cancellation will not operate at the leading and trailing edges where there are discontinuities in the source distribution. If the Mach number is just above 1, the solution of the acoustic equation will show large short-wavelength oscillations propagating back from the leading edge. If the Mach number is just below 1, the solution will show large short wavelength oscillations propagating upstream from the trailing edge. These oscillations are not present in the solution of the transonic equation.

Now consider the actual steady flow over an aerofoil with small but finite thickness just below $M=1$. The flow will be subsonic near the leading edge, sonic near the maximum thickness point, and supersonic up to the trailing edge where there will be attached shock waves. Unsteady receding waves generated at the leading edge will go upstream, and receding waves generated at the trailing edge cannot go upstream, so no receding wave effects appear on the aerofoil from the leading and trailing edges. This behavior is quite different from the solution of the acoustic equation, but is matched by the behavior of the transonic equation. If the freestream Mach number is slightly above one, there will be a shock wave ahead of the leading edge, but the flow over the aerofoil will be the same, and the argument is unaffected (Mach number freeze).

At a somewhat lower Mach number the trailing edge shock will move upstream onto the aerofoil, and its position will oscillate due to the effect of the unsteady flow. This situation will not be well modeled by either the acoustic equation or the transonic equation.

Landahl (1961) also shows that due to a variation of Mach number along the chord, the amplitude of the receding wave varies strongly, growing in a flow decelerating through $M=1$, and decaying in an accelerating flow. This is in contrast to the solution of the acoustic equation which shows a wave of constant amplitude. The transonic equation, which shows no receding wave should be a better model.

Finally Landahl (1961) considers nonlinear unsteady effects, and concludes that these will prevent the amplitude of the receding waves from becoming large and will cause them to damp out within a few wavelengths.

In cascade geometry the acoustic equation becomes unusable between Mach numbers of approximately 0.9 and 1.1. If the Mach number is raised from 0.9, maintaining the phase angle constant, an infinite series of resonances is passed on approaching $M=1$, and another infinite series is found just above $M=1$. Also, in the supersonic range, the number of wave reflections becomes infinite as M approaches 1 from above. These features make the programs discussed in the previous two sections unusable in the transonic range.

It is concluded that the transonic theory should be used for thin blades of small camber between Mach numbers of about 0.9 and 1.1, but that its use should be confined to cases when there are no significant shock waves on the blade surfaces.

The effect of Mach number in the transonic equation (86) can be removed by a transformation similar to the Prandtl-Glauert transformation used in subsonic flow. All dimensions in the y direction are scaled by the factor M . The transformed cascade therefore has a different spacing and stagger angle, but frequency parameter and phase angle are unaffected. The transonic equation then becomes

$$\frac{\partial^2 \phi}{\partial y^2} - \frac{2i\omega}{U} \frac{\partial \phi}{\partial x} + \frac{\omega^2 \phi}{U^2} = 0. \quad (87)$$

It is therefore only necessary to consider the case $M=1$ in the following discussion.

Switching to axial and tangential axes ξ and η , the transonic equation becomes

$$\sin^2 \theta \frac{\partial^2 \phi}{\partial \xi^2} - 2 \sin \theta \cos \theta \frac{\partial^2 \phi}{\partial \xi \partial \eta} + \cos^2 \theta \frac{\partial^2 \phi}{\partial \eta^2} - \frac{2i\omega}{U} \left(\frac{\partial \phi}{\partial \xi} \cos \theta + \frac{\partial \phi}{\partial \eta} \sin \theta \right) + \frac{\omega^2}{U^2} \phi = 0.$$

If we now look for a solution of the form $\phi = \phi \exp i(\alpha \xi + \beta \eta)$, we find that the wave numbers are related by

$$\alpha^2 \sin^2 \theta - 2\alpha\beta \sin \theta \cos \theta + \beta^2 \cos^2 \theta - \frac{2\omega}{U}(\alpha \cos \theta + \beta \sin \theta) - \frac{\omega^2}{U^2} = 0.$$

Since β is determined by the phase angle, this is a quadratic equation for α , and may be solved to give

$$(U\alpha/\omega) = (\cos \theta [(U\beta/\omega) \sin \theta + 1]) \pm [2(U\beta/\omega) \sin \theta + 1]^{1/2} / \sin^2 \theta$$

and resonance occurs when $(U\beta/\omega) = -1/(2 \sin \theta)$.

There is therefore only one value of phase angle for resonance. If β exceeds this value, (assuming positive stagger angle), α is real and propagating waves occur. If β is less than this value, α is complex and decaying waves occur. This resonance is associated with the advancing wave. The multiple resonances associated with the receding wave have been suppressed.

The transonic solution for zero stagger angle and 180° phase angle has been given by Savkar (1976) using Laplace transform methods. This is the case of a single aerofoil vibrating in a wind tunnel. He concludes that the degree of interference from the tunnel walls is weaker than would be thought of at first.

A transonic solution for general stagger angle and phase angle has been given by Surampudi and Adamczyk (1984, 1985) using the Wiener-Hopf procedure. It is shown that the transonic solution joins on smoothly to the subsonic and supersonic solutions at Mach numbers of 0.9 and 1.1. It is found that bending vibration is always stable, but that torsional flutter is predicted. It is found that increasing the frequency parameter and decreasing the stagger angle and solidity have a stabilizing effect on torsional flutter.

The transonic solution therefore fills in the gap between the subsonic and supersonic solutions. It is however likely that real effects such as shock waves and boundary layers will have a much larger effect than in the subsonic and supersonic regimes.

A transonic solution for zero stagger and arbitrary phase angle was developed by Schlein (1975) and Platzer et al (1976). This approach was based on the time-linearized transonic flow theory delineated by Verdon in this volume. Neglecting the product terms on the right-hand side of Verdon's equation (147) and introducing the approximations

$$\bar{\phi}_x = 0 \quad \text{and} \quad (\gamma+1) \bar{\phi}_{xx} = \text{Const} = \lambda > 0$$

a linear parabolic equation is obtained, following Oswatitsch and Keune (1955) and Teipel (1964).

Three different methods of solution were developed using Laplace and Fourier-transform techniques as well as a collocation technique. The inversion technique due to Hamamoto (1960) proved to be the computationally most efficient procedure. The collocation technique was based on previous work by Gorelov (1966) for supersonic oscillating cascades. Computed stability boundaries showed increased regions of instability with decreasing blade spacing.

ACTUATOR DISC THEORY

Actuator disc theory applies to certain special cases of the more general theory discussed in previous sections, and in these cases it will be found possible to derive analytic results in closed form. There are two fundamental limitations.

The first of these is that the time taken for the fluid to flow through the cascade must be small compared with the time for one oscillation of the flow. This is equivalent to assuming that the frequency parameter λ must be small,

$$\lambda = \omega c/U \ll 1.$$

The second fundamental limitation is that the interblade phase angle must be small,

$$|\sigma| \ll 1.$$

In general λ and σ will be of the same order of magnitude. The wavelength of the disturbance in the chordwise (x) direction is $2\pi c/\lambda$ and the wavelength in the tangential (η) direction is $2\pi s/\sigma$, so that these wavelengths are comparable.

These assumptions enable the flow to be considered from two viewpoints. First there is a picture (Figure 5), drawn to a scale comparable with the wavelength of the disturbance, in which the blades are very small, and the cascade is equivalent to an actuator disc. A second picture, similar to Figure 1, may be drawn to a scale comparable to the blade chord, and this just shows a few of the blades near the origin of Figure 5. In this second picture the flow may be regarded as quasi-steady, and any kind of steady flow cascade data can be used.

In the actuator disc plane, and upstream of the actuator disc, the perturbations consist of just one of the acoustic wave solutions discussed in "Fundamental Acoustic Wave Solutions," with $r = 0$ in equation (19). The solution carrying acoustic energy upstream is required. Downstream of the actuator disc, the corresponding solution carrying energy downstream is required, plus a vorticity wave as discussed in the section "Vorticity Wave Solutions."

The solution for incompressible unstalled flow through a cascade of flat plates at zero incidence has been given by Whitehead (1959), and for subsonic flow by Whitehead (1986). Three conditions from the cascade plane are required. These are for continuity, deviation, and zero stagnation pressure loss.

The continuity equation is

$$\frac{\rho_2}{\rho} + \frac{V_r \xi_2}{V_\xi} = \frac{\rho_1}{\rho} + \frac{V_r \xi_1}{V_\xi} \quad (88)$$

where the suffix r refers to conditions relative to the blades, and suffixes 1 and 2 refer to conditions just upstream and downstream of the cascade, but very near the origin in the actuator disc plane.

The condition for deviation in subsonic flow is obtained by applying the Prandtl-Glauert transformation to get an equivalent cascade in incompressible flow, and then using the known analytical result for incompressible flow in cascades of flat plates given by Durand (1934). In the Prandtl-Glauert transformation all distances parallel to the chord are unchanged, but all distances normal to the chord are reduced by a factor B , where $B^2 = 1 - M^2$. Using a $*$ to indicate quantities in the transformed plane, the stagger and space/chord ratio are given by

$$\tan(\theta^*) = \tan(\theta)/B, \text{ and} \quad (89)$$

$$(s^*/c) = B (s/c) \cos(\theta)/\cos(\theta^*).$$

The deviation is then given by

$$v_{ry_2} = b v_{ry_1}. \quad (90)$$

This equation holds in both the original and the transformed planes. The constant b is related to the space/chord ratio and the stagger angle in the transformed plane as follows

$$\pi c/s^* = -\cos \theta^* \ln b + 2 \sin \theta^* \tan^{-1} \{ (1-b) \tan \theta^* / (1+b) \} \quad (91)$$

For closely spaced blades, $b = 0$ is a good approximation.

The condition for zero stagnation pressure loss is

$$P_{r02} = P_{r01} \quad (92)$$

where the suffix zero means a stagnation pressure.

Equations (88), (89) and (91) apply for the flow relative to the blades in the cascade plane. When these equations are combined with the actuator disc plane equations, the whole set may be solved.

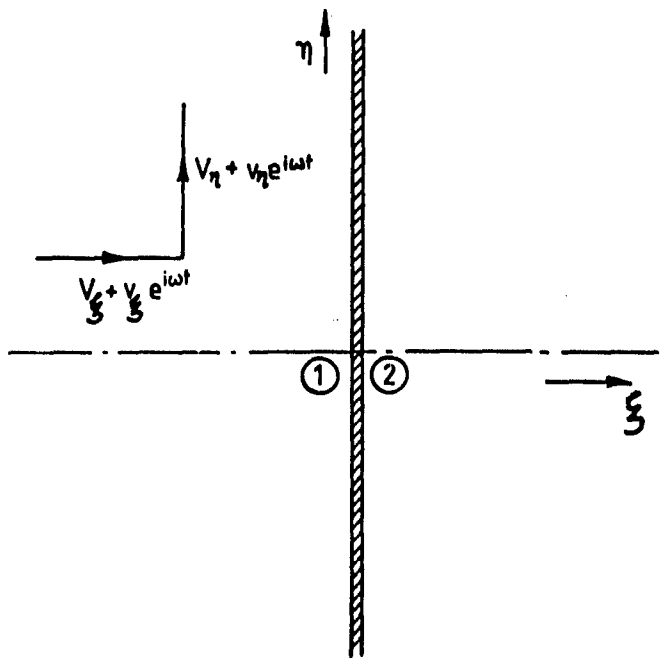


Fig. 5. Actuator Disc Plane.

Results from actuator disc theory depend on the ratio of phase angle to frequency, although both of these quantities are individually small. It is therefore convenient to write

$$\mu = \omega U / \omega_s = \omega c / \lambda s. \quad (93)$$

The result for the blade force, due to blade vibration with velocity h_y in the y direction is then

$$f_y / \rho U c h_y = \frac{-2T E (1-b)}{-b H + I + K} \quad (94)$$

where

$$E = (\mu^2 + 2\mu \sin \theta + 1)(1 - M^2 \cos^2 \theta)$$

$$H = (P - T \sin \theta)(-R + \mu \cos \theta)$$

$$I = (P + T \sin \theta)(R + \mu \cos \theta)$$

$$K = 2T \cos \theta (1 - M^2 \cos^2 \theta)$$

$$P = \mu \cos \theta (1 - M^2 \cos^2 \theta) - \sin \theta \cos \theta M^2 (1 + \mu \sin \theta)$$

$$R = T(\mu + \sin \theta)$$

and

$$T = \{(\mu^2 + 2\mu \sin \theta + 1)M^2 - \mu^2\}^{1/2}$$

for propagating waves,

$$T = -i\{-(\mu^2 + 2\mu \sin \theta + 1)M^2 + \mu^2\}^{1/2}$$

for decaying waves.

The corresponding result for supersonic flow, with a subsonic axial velocity, has been given by Whitehead and Davies (1983).

In supersonic flow the continuity equation (87) is unchanged and there is no Kutta condition at the trailing edge. But provided the axial velocity is subsonic, and that case (a) in Figure 3 is excluded the incidence angle of relative flow into the cascade is zero (Kantrowitz, 1946). This condition is used instead of the deviation-condition (90), and gives

$$v_{y1} = h_y \quad (95)$$

The result of the elimination is

$$f_y / \rho U c h_y = \frac{2sTE}{cFG} \quad (96)$$

$$\begin{aligned} E &= (\mu^2 + 2\mu \sin \theta + 1)(1 - M^2 \cos^2 \theta) \\ P &= [M^2 \cos \theta (\sin \theta + \mu) - \mu \cos \theta + T \sin \theta] \\ G &= [\mu \cos \theta - (\mu + \sin \theta)T] \end{aligned}$$

where

$$T = -\{(\mu^2 + 2\mu \sin \theta + 1)M^2 - \mu^2\}^{1/2}$$

if

$$\mu < M / \{-M \sin \theta + (1 - M^2 \cos^2 \theta)^{1/2}\}$$

case of propagating waves,

$$T = -i\{(\mu^2 + 2\mu \sin \theta + 1)M^2 + \mu^2\}^{1/2}$$

if

$$M / \{-M \sin \theta + (1 - M^2 \cos^2 \theta)^{1/2}\} < \mu$$

$$< M / \{-M \sin \theta - (1 - M^2 \cos^2 \theta)^{1/2}\}$$

case of decaying waves,

$$T = +\{(\mu^2 + 2\mu \sin \theta + 1)M^2 - \mu^2\}^{1/2}$$

if

$$M / \{-M \sin \theta - (1 - M^2 \cos^2 \theta)^{1/2}\} < \mu,$$

case of propagating waves.

The force is zero at the cut-off or resonance points, where $T = 0$. The force is also zero when the axial velocity is sonic, $M \cos \theta = 1$.

These results also apply to torsional motion of the blades, with h_y replaced by U_a , and to the effect of wakes being convected into the cascade. This is because at zero frequency the upwash velocities given by equations (11), (12) and (44) are all uniform.

These results can also be used to find the moment acting on the blades. Since the cascade operates in quasi-steady flow, the force acts at the centre of pressure for steady flow in the cascade. In subsonic flow this point can be found by using thin aerofoil theory for cascades (Pistoletti, 1937). In supersonic flow the centre of pressure is a distance $(c - d/2)$ downstream of the leading edge, as in the section "Solutions for Supersonic Cascade."

Actuator disc theory can be extended in a number of ways. For instance, results have been obtained for incompressible flow through cascades of closely spaced blades having large amounts of turning of the mean flow. (The results given in the paper by Whitehead (1959) are wrong in this respect. The correct results are given in an appendix to the paper by Whitehead (1962). Results have also been obtained for incompressible flow through cascades of closely spaced blades having a stagnation pressure loss which varies with incidence.

The most important extension of actuator disc theory is when the restriction to small frequencies is relaxed, but the restriction to small phase angles is maintained. This is now called semi-actuator-disc theory. This method was developed by Sohngen (1953) and by Tanida and Okazaki (1963) for incompressible flow and for translational motion of the blades.

The equations for the actuator disc plane are the same as in actuator disc theory. The three equations required from the cascade plane are obtained by considering the control surface shown in Figure 6. The control surface is the space between two blades, 13'34'21, and moves at a constant speed equal to that at which the blade 12 travels at that instant. The sides of the control surface 33' and 44' are the displacement of blade 34 relative to the blade 12, and are given by

$s' = h_y e^{i(\omega t + \sigma)} - h_y e^{i\omega t} = i c h_y e^{i\omega t}$
 since σ is small.

Applying continuity to this control surface gives the result

$$v_{\xi 1} - v_{\xi 2} + (v_{n1} - v_{n2})(\sigma/\omega s) h_y \sin \theta - i(c/s) \omega h_y = 0. \quad (97)$$

Here $v_{\xi 1}$ and $v_{\xi 2}$ are the absolute unsteady axial velocities. The third term arises from the change of steady tangential velocity giving a net flow through the sides of length s' , and is an actuator disc term. The last term arises from the change in gap between the blades and is a semi-actuator-disc term.

The second equation from the cascade plane is for the relative flow exit angle, and equation (90) for the relative velocity normal to the blades is unchanged. The usual approximation is $b = 0$.

The third equation relates the pressure at outlet from the cascade to the pressure at inlet. This relationship is derived in two stages. It is presumed that a loss of relative stagnation pressure occurs at the inlet to the cascade, so that

$$Pr_1 - Pr_3 = \frac{1}{2} \rho V r_{\xi 1}^2 Z \quad (98)$$

where the suffix 3 refers to a plane just behind the leading edges of the blades, and Z is a stagnation pressure loss coefficient which is a function of the inlet angle of flow relative to the cascade or $v_{r n1}/v_{r \xi 1}$.

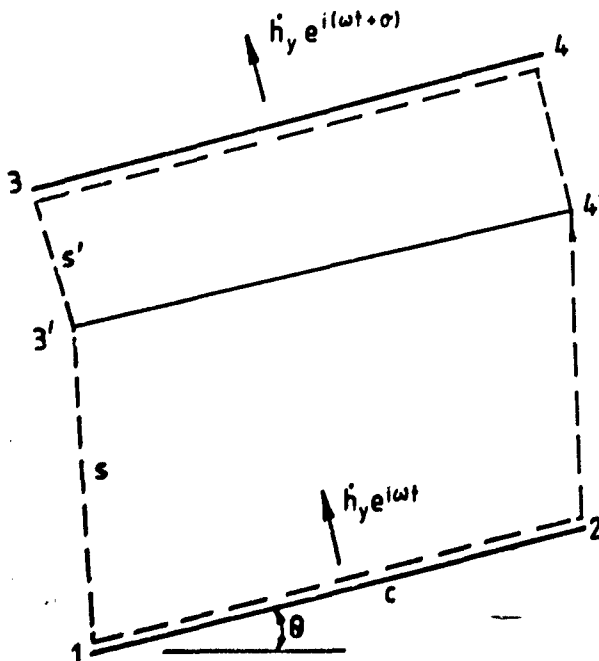


Fig. 6. Control Surface for Semi-Actuator-Disc Theory.

The relationship between the relative stagnation pressure at cascade outlet (plane 2) and at plane 3 is obtained by integrating the equation of motion in the x direction along the passage between two adjacent blades to give

$$Pr_3 - Pr_2 = i \omega \rho c v_{rx}. \quad (99)$$

With the addition of a momentum equation in the n direction, which relates the blade force to the flow variables, a complete set of linear equations is available and may be solved. The result is too lengthy to give here, but may be found in the paper by Tanida and Okazaki (1963).

Semi-actuator-disc theory has been extended to compressible subsonic flow. The case of transmission and reflection of sound waves by a cascade, and the generation of sound waves due to an incoming vorticity wave, have been treated by Kaji and Okazaki (1970). The effects of compressibility on flutter in subsonic flow have been considered by Kaji and Okazaki (1972).

Semi-actuator-disc theory has been extended to supersonic flow by Kaji (1980), and in a somewhat different way by Adamczyk (1978).

The semi-actuator-disc theories are probably the most useful available for stalled flow. But they do require experimental or empirical input giving the nature of the loss function Z . Actual stalling processes take a finite time to develop. The theories can be extended to allow for a time lag, but again experimental or empirical information must be provided to determine the time constant.

SINGULARITY THEORY

We now turn to a quite different way of building up solutions for the unsteady flow through cascades by the superposition of simple analytical solutions. In this case, the solutions are restricted to lossless incompressible flow, but they apply to blades with large amounts of thickness and camber. The particular method which will be sketched in the following is largely taken from a paper by Atassi and Akai (1980).

The potential flow past any number of two-dimensional bodies of arbitrary shape may be represented as being due to a distribution of singularities placed around the boundaries of the bodies. The singularities may be either a distribution of sources and sinks (plus at least one vortex for each body if that body has circulation) or a distribution of vortices (plus at least one source or sink if the body has a net flow out or in from the surface). A further alternative is to use doublets. A distribution of doublets placed around the boundary and directed along the boundary is equivalent to a distribution of sources and sinks, and a distribution of doublets directed normal to the boundary is equivalent to a distribution of vortices (provided there is no net flow out or in from the surface and no net circulation). The well-known Martensen (1959) method for steady flow

in cascades uses a distribution of vortices round the surfaces of the blades. In this case the notional flow inside the contours of the surfaces has zero velocity, so that the strength of the vortices can be arranged to make the tangential velocity just inside the contour equal to zero. For the unsteady case however, the velocity normal to the surface just outside the surface is used as a boundary condition. Also, since in the unsteady case there is vorticity shed from the blades into the wake, it is necessary to use an additional distribution of vortices along the wakes of the blades.

In order to handle singularity theory it is convenient to work in a complex z plane where $z = x + iy$. It is then necessary to change the notation slightly and make all the unsteady variables proportional to $\exp(j\omega t)$. The unsteady variables are then hypercomplex numbers, which have four components, a real component, an i component, a j component, and an ij component. ($i^2 = -1$, $j^2 = -1$, but we must not write $ij = -1$).

If there is a source density distribution m on the surface at the point z , so that the source strength for a length of surface $\delta\tau$ is $m\delta\tau$, then the velocities induced at a point z^1 not on the surface are given by

$$v_x - iv_y = \frac{1}{2\pi} \int \frac{m d\tau}{z^1 - z} \quad (100)$$

where the integral is taken over the surfaces of all blades and their wakes.

Similarly for a vorticity distribution γ_t , the induced velocities at z^1 are given by

$$v_x - iv_y = \frac{1}{2\pi i} \int \frac{\gamma_t d\tau}{z^1 - z} \quad (101)$$

In general any combination of source and vorticity distribution may be used. Equations (100) and (101) may therefore be combined to give

$$v_x - iv_y = \frac{1}{2\pi i} \int \frac{(\gamma_t + im)d\tau}{z^1 - z} = \frac{1}{2\pi i} \oint \frac{\mu_m dz}{z^1 - z} \quad (102)$$

where the integral is now a contour integral taken anticlockwise round the blade surface. μ_m is a complex singularity strength. If $\mu_m dz$ is real it corresponds to pure vorticity, and if $\mu_m dz$ is imaginary it corresponds to a pure source-sink distribution.

Equation (102) gives the induced velocities at a point z^1 which is not on the surface. If z is on the surface the integral is singular and the induced velocities just outside the surface are given by

$$v_x - iv_y = \frac{1}{2\pi i} \oint \frac{\mu_m(z) dz}{z - z^1} - \frac{1}{2} \mu_m(z^1) \quad (103)$$

and the induced velocities just inside the surface are given by

$$v_x - iv_y = \frac{1}{2\pi i} \oint \frac{\mu_m(z) dz}{z - z^1} + \frac{1}{2} \mu_m(z^1) \quad (104)$$

The extra terms on the right hand side of these equations give a jump in tangential velocity across the surface equal to the strength of the vortex sheet at the surface and a jump in normal velocity across the surface equal to the strength of the source-sink distribution along the surface.

Since the cascade is assumed to be vibrating with an inter-blade phase angle σ , the singularity strength on the m th blade at $z + m\epsilon i\theta$ is given by

$$\mu_m = \mu_0 e^{jm\sigma}$$

Hence the velocities induced just outside a point z^1 on the reference blade are

$$v_x - iv_y = \frac{1}{2\pi i} \oint_{m=-\infty}^{\infty} \frac{\mu_0(z) e^{jm\sigma} dz}{z + m\epsilon i\theta - z^1} - \frac{1}{2} \mu_0(z^1) \quad (105)$$

where the contour integral is now taken round the reference blade $m = 0$.

The series can be summed analytically to give the induced velocities just outside z^1 as

$$v_x - iv_y = \frac{1}{2\pi i} \oint K(z - z^1) \mu_0(z) dz - \frac{1}{2} \mu_0(z^1) \quad (106)$$

where

$$K(z^*) = \frac{\pi e^{j(\pi - \sigma)z^*}}{\epsilon i\theta \sin(\pi z^*)} \quad 0 < \sigma < 2\pi \quad (107)$$

This is a more general form of equation (14). The integral in equation (106) is taken round the reference blade and its wake.

The contour integral of μ_0 round the reference blade is

$$\oint \mu_0 dz = \oint (\gamma_t + im)d\tau = \Gamma_0 \quad (108)$$

where Γ_0 is the circulation round the reference blade, and the integral of the source term is zero since there is no net flow out of the blade surface.

Verdon's equation (75) gives the jump in potential across the wake as

$$[\phi] = [\phi]_{TE} e^{-j\omega(\Delta - \Delta_{TE})} \quad (109)$$

where Δ is the drift function, defined so that the difference in Δ between any two points on the same mean streamline is equal to the time for a particle to move from one point to the other under the influence of the mean flow. In this case

$$\Delta - \Delta_{TE} = \int_{TE}^T V_t^{-1} dt \quad (110)$$

which gives the time taken for fluid to flow from the trailing edge to the point in question on the wake, and the integral is taken along the wake line.

The jump in potential across the wake at the trailing edge is just the circulation, so that

$$\left[\oint \right]_{TE} = \Gamma_0. \quad (111)$$

Differentiating equation (109) with respect to distance along the wake then gives

$$\left[\frac{\partial \phi}{\partial \tau} \right] = \left[v_t \right] = \gamma_t = -j\omega \Gamma_0 \frac{\partial \Delta}{\partial \tau} \quad (112)$$

$$e^{-j\omega(\Delta - \Delta_{TE})} = -j\omega \Gamma_0 v_t^{-1} e^{-j\omega(\Delta - \Delta_{TE})}.$$

This equation gives the strength of the vortex sheet at any point in the wake.

The boundary condition to be satisfied just outside the blade surface is given by Verdon's equation (69). For rigid body motion of the blades, the displacement vector is given by Verdon's equation (102) and the normal velocity just outside the blade surface reduces to

$$v_n = j\omega \vec{r} \cdot \vec{n} + \alpha v_t - (\vec{r} \cdot \nabla \vec{V}) \cdot \vec{n}, \quad (113)$$

where

$$\vec{r} = \vec{h} + \vec{\alpha} \times \vec{R}_p. \quad (114)$$

The integral equation for μ_0 is therefore

$$\left[\frac{1}{2\pi i} \oint K(z-z^1) \mu_0(z) dz - \frac{j\omega \Gamma_0}{2\pi i} \int K(z-z^1) v_t^{-1} e^{-j\omega(\Delta - \Delta_{TE})} d\tau - \frac{1}{2} \mu_0(z^1) \right] \cdot \vec{n} = j\omega \vec{r} \cdot \vec{n} + \alpha v_t - (\vec{r} \cdot \nabla \vec{V}) \cdot \vec{n} \quad (115)$$

where the first integral is taken anti-clockwise around the reference blade, and the second integral is taken along the wake of the reference blade from the trailing edge to downstream infinity. Γ_0 is related to μ_0 by equation (108). This equation has to be solved, subject to the additional Kutta condition at the trailing edge, which specifies that μ_0 must not be infinite at that point.

Details of a solution method are given in the paper by Atassi and Akai (1980). The first move is to solve for the steady flow. Then for the unsteady flow equation (115) is solved numerically. The last term on the right hand side of equation (115), which arises from the translation of a point on the blade surface through the mean velocity field, may be singular at the trailing edge and exhibits large values round the leading edge. This is a source of numerical difficulty. Atassi and Akai (1980) overcame the difficulty essentially by writing

$$\mu_0^1(z) = \mu_0(z) + \vec{r} \cdot \nabla \vec{V}. \quad (116)$$

By using μ_0^1 as the primary measure of the unknown singularity strength instead of μ_0 , the awkward last term on the righthand side of equation (115) may be cancelled.

The complex singularity strength μ_0 may in principle be any combination of source and vorticity strengths. This arbitrariness corresponds to the idea that whereas the flow outside the blade surfaces is fixed by the physics of the problem, the notional flow inside the blade surfaces may be chosen in any convenient way. Atassi and Akai (1980) therefore choose to make μ_0^1 real with respect to the space variables. The singularity therefore corresponds to pure vorticity when the surface is parallel to the x (chordwise) axis, and to pure source or sinks when the surface is parallel to the y axis.

The integral equation (115) is solved numerically by matching the normal velocities at N points round the blade surface, where N must correspond to the number of points at which the singularity strength is specified. Once the singularity strength has been found, the velocity and pressure distributions just outside the blade surface may be found. The pressure distributions are then integrated to give the aerodynamic forces and moment.

Due to a programming error, the results for the real part of the pressure distributions given in the paper by Atassi and Akai (1980) are not correct. Results for which the error has been corrected are given by Akai and Atassi (1981).

SPECIMEN RESULTS FOR FLAT PLATE CASCADES

In order to specify the unsteady performance of cascades of flat plates, five independent non-dimensional variables are necessary. These are the space to chord ratio, the stagger angle, the Mach number, the frequency parameter, and the interblade phase angle. Excluding the acoustic information, and the detail of the pressure distributions, there are twelve dependent variables of interest. These are the real and imaginary components of the force and moment for bending, torsion, and wakes. This number of variables makes any general presentation of the results totally impractical, and it is only possible to present specimen results. It is therefore necessary to have computer programs available so that any particular cases of interest can be calculated.

For incompressible flow, tables of specimen results have been made by Whitehead (1960). Figure 7 illustrates the force coefficient due to bending for a space to chord ratio of unity and a stagger angle of 60° . In this and the following figures the axes are the real and imaginary parts of the force coefficient, and lines of constant frequency parameter and phase angle are shown. In general the lines of constant frequency parameter form closed loops as the phase angle is varied. However, the line of zero frequency parameter is not closed for finite phase angles. In order to close the loop actuator disc theory, with various values of σ/λ in the limit $\sigma \rightarrow 0$ and $\lambda \rightarrow 0$, must be used, and the result for this is shown on Figure 7.

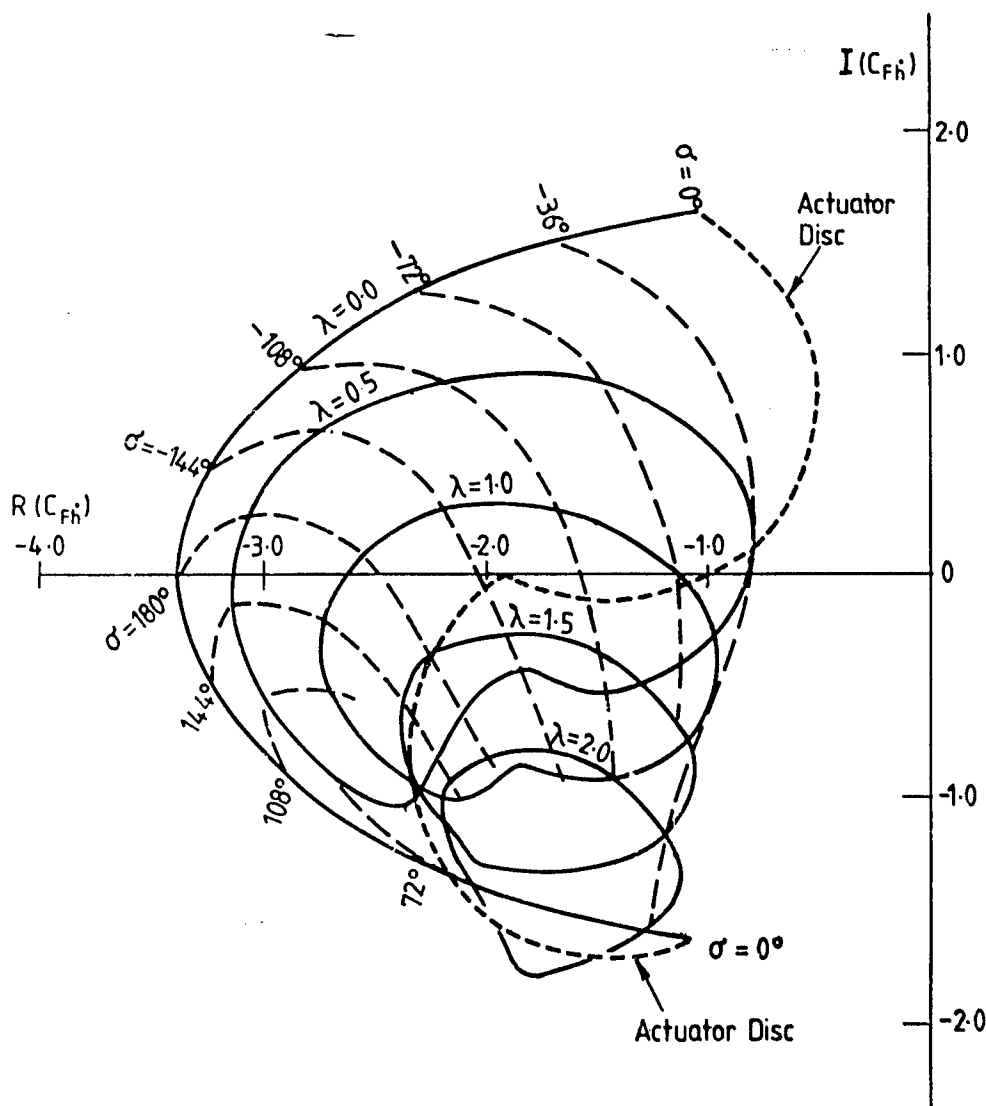


Fig. 7. Force Coefficient due to Bending. C_{Fh}
 $s/c=1.0$, $\theta=60^\circ$, $M=0.0$.

Similar results for the same cascade in subsonic compressible flow are shown in Figure 8 (for a Mach number of 0.5) and on Figure 9 (for a Mach number of 0.8). The presentation of results for compressible flow is made difficult by the very wild behaviour of the coefficients which occurs near the acoustic resonances. For this reason the real and imaginary parts of the force coefficient are plotted separately against phase angle on figures 9a and 9b. One resonance on these figures at $\lambda = 0.5$ and $\sigma = 102.45^\circ$ is shown in detail. The other resonances are merely indicated as discontinuities in the curves. Only the parts of the loops of constant frequency parameter which are in the well-behaved sub-resonant region are shown on the figures. Figure 8 also shows the actuator disc cases: there is also a range of values of σ/λ for which C_{Fh} is purely real, so that the line lies along the real axis. Figure 9 at the higher Mach number of 0.8 illustrates the wild fluctuations which occur near the resonance point at the frequency parameter of 0.5, but at the higher frequency parameters the results steady down and become much less dependent on frequency parameter and phase angle.

Specimen results for two supersonic cascades are shown in Figures 10 and 11. These cascades are examples used by Verdon and McCune (1975) which have been rather widely used as test cases. Cascade A (Figure 10) has the wave pattern illustrated in figure 3b, whereas Cascade B (Figure 11) has the additional internal wave reflections illustrated in Figure 3c. On these figures the wild behaviour near the acoustic resonance has been largely suppressed, but on Figure 10 the complete loop for a frequency parameter of 0.602 is shown and illustrates typical behaviour.

Pure bending flutter of a system with no mechanical damping is predicted if the real part of the force coefficient due to bending is positive. Figures 7 to 11 show that the real part of this coefficient is always negative, so that pure bending vibration is damped. This behaviour has always been found for flat plate cascades at zero incidence. However, actuator-disc and semi-actuator-disc analyses allowing for steady deflection of the steady flow through the cascade do show the possibility of pure bending flutter.

Pure torsional flutter depends on a further parameter, which is the position along the chord of the torsional axis. Torsional flutter is predicted by these theories if the frequency parameter is sufficiently low. The effect of compressibility of the fluids is generally found to be stabilizing as the Mach number increases in the subsonic range. But there is also a theoretical possibility of "resonance flutter", over a very narrow range of interblade phase angle close to the acoustic resonance condition at comparatively high frequency parameters (Whitehead 1973). Whether this is a real danger on practical machines is not known.

CONCLUSIONS

This chapter has presented what are regarded as the most important two-dimensional solutions which can be ob-

tained by the superposition of elementary analytical solutions. This has enabled cascades of flat plates to be treated up to Mach numbers at which the axial velocity becomes sonic. Also, singularity theory, valid for incompressible flow through cascades of thick cambered blades, has been discussed in the section "Singularity Theory" and actuator disc theory, valid at low frequencies and for small phase angles, in the section "Actuator Disc Theory." These methods enable useful predictions to be made for the vibration characteristics of real blades. But for turbine blade sections with a lot of turning and with high Mach numbers or for compressor blades having strong shock waves in the flow, these methods are hardly adequate, and it is necessary to go to field methods. These will be discussed in the Chapter, "Numerical Methods for Unsteady Transonic Flow."

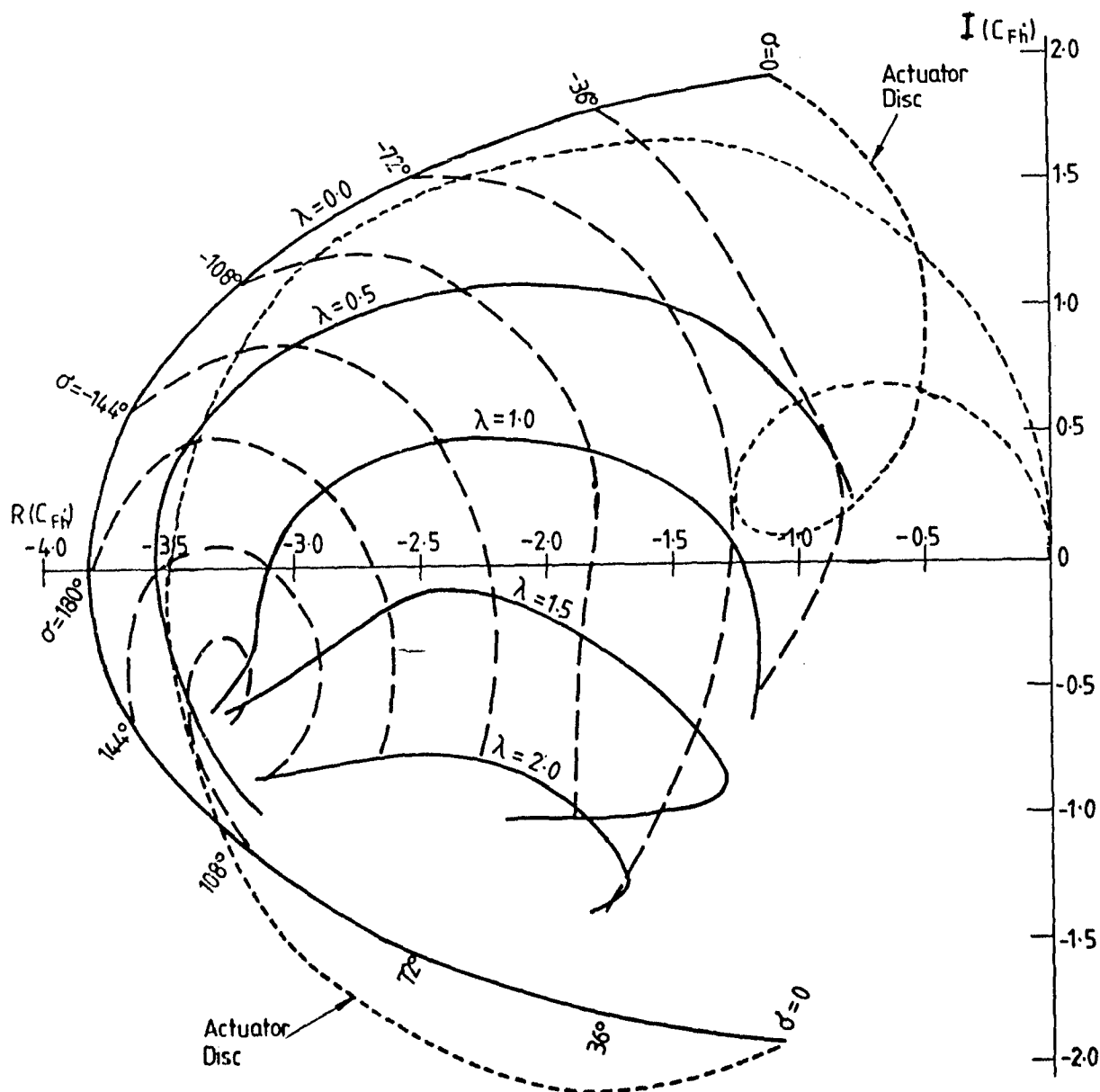


Fig. 8. Force Coefficient due to Bending. C_{FH}
 $s/c=1.0$, $\theta=60^\circ$, $M=0.5$.

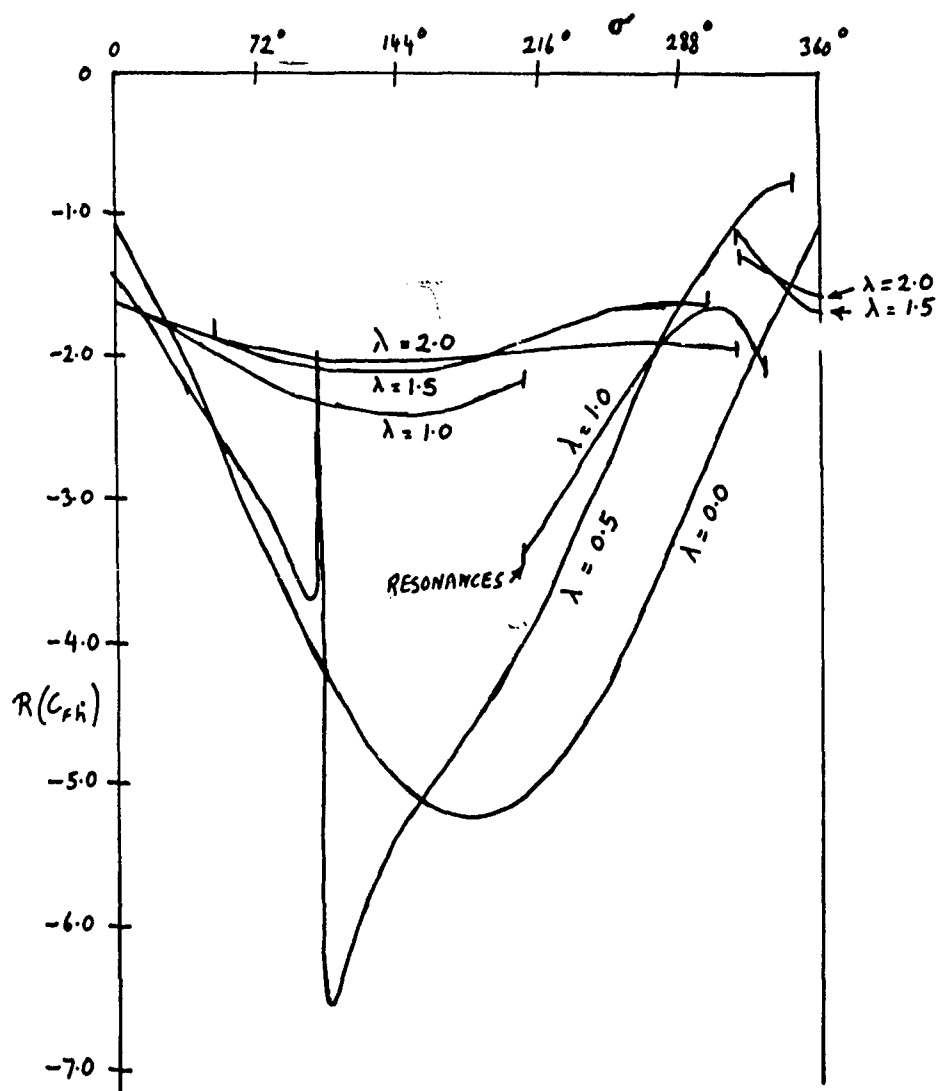


Fig. 9a. Force Coefficient due to Bending. C_{Fh} Real Part.
 $s/c=1.0$, $\theta=60^\circ$, $M=0.8$.

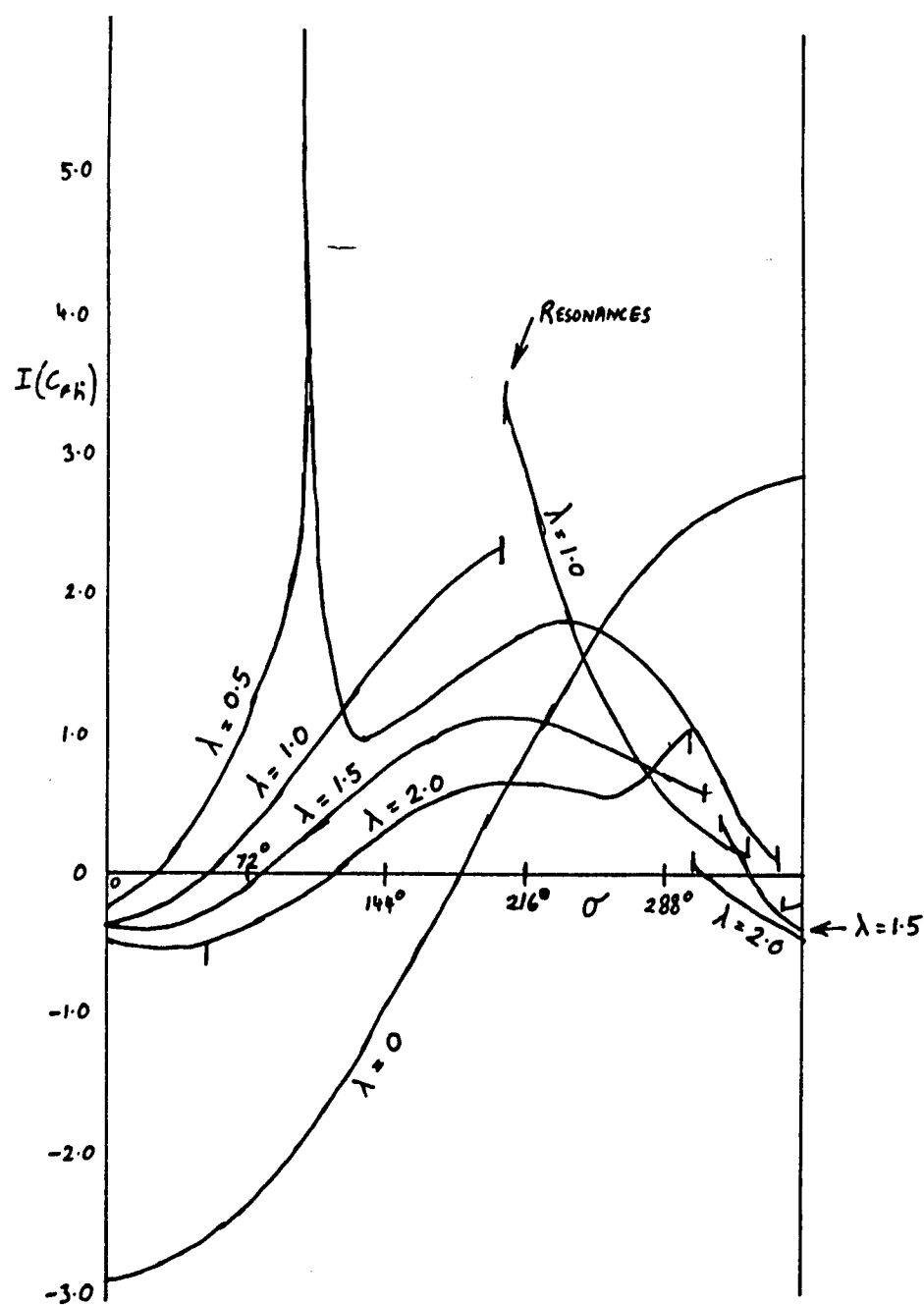


Fig. 9b. Force Coefficient due to Bending. $C_F h$ Imaginary Part.
 $a/c=1.0$, $\theta=60^\circ$, $M=0.8$.

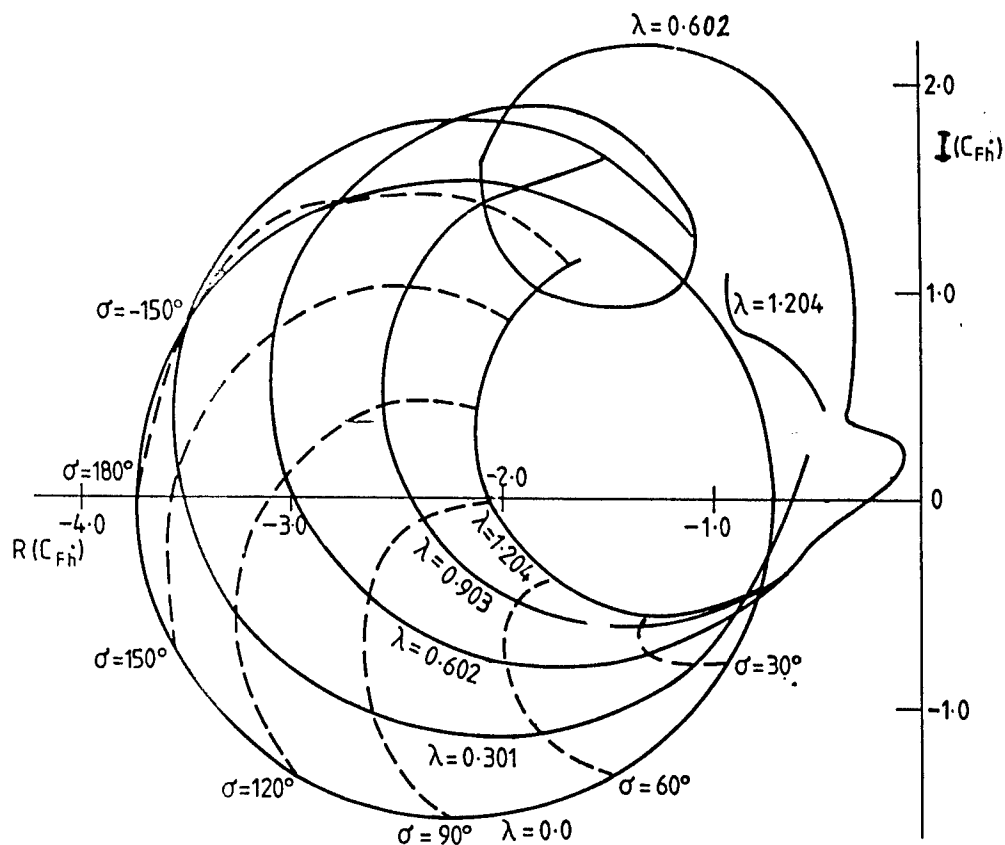


Fig. 10. Force Coefficient due to Bending. C_{Fh}
 $s/c=0.7889$, $\alpha=59.53^\circ$, $M=1.3454$.

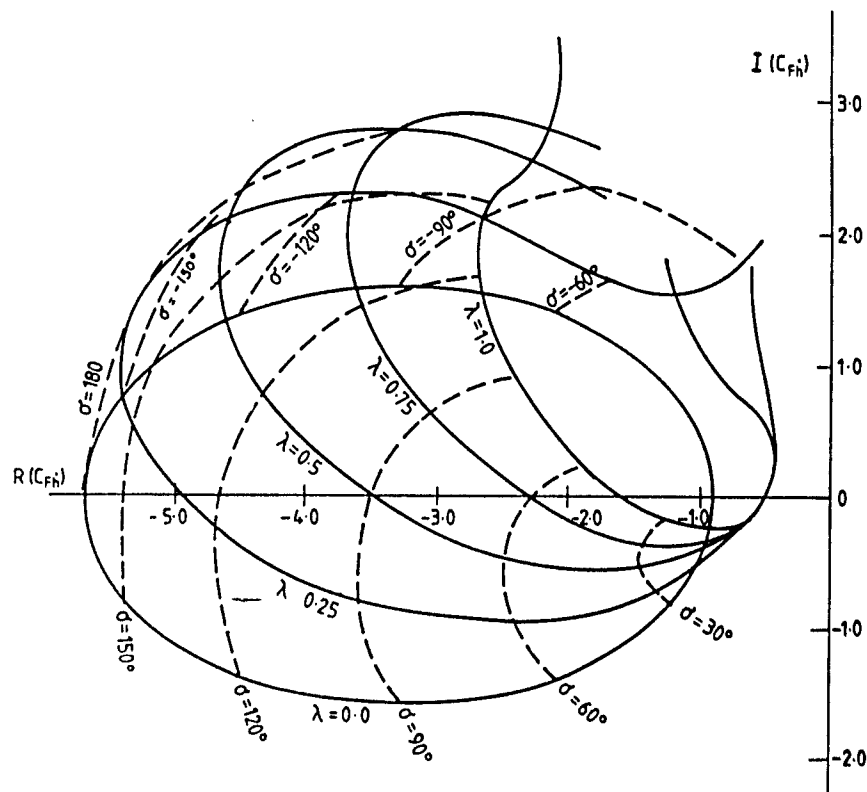


Fig. 11. Force Coefficient due to Bending. C_{Fh}
 $s/c=0.6708$, $\alpha=63.43^\circ$, $M=1.2806$.


```

      TITLE='LINSUB.FOR'
      $STORAGE=2
      $NODEBUG
      C
      C PROGRAM LINSUB
      C
      C LINEARISED SUBSONIC UNSTEADY FLOW IN CASCADE
      C
      C
      REAL MACH, LAM, MACH2, KR(15,15), KI(15,15)
      CHARACTER PRNOPT*1, REPEAT*1, CRET*1, LF*1, LINE(5)*10
      COMMON SC, STAG, MACH, LAM, PHASE, DEG, PI, COSST, SINST, MACH2, B, B2, BC,
      1BC2
      DIMENSION UR(15,5), UI(15,5), XR(5,15), XI(5,15), CR(5,5), CI(5,5)
      DATA LINE(1) / ' Force' /, LINE(2) / ' Moment' /, LINE(3) / ' Wake' /
      DATA LINE(4) / ' Up Wave' /, LINE(5) / ' Down Wave' /
      C
      C INITIAL SET-UP
      C
      C
      DEG=57.29578
      PI=3.141593
      OPEN(1, FILE='PRN')
      WRITE(*, '(A)') ' Print Pressure Jump? Y or N'
      READ(*, '(A)') PRNOPT
      WRITE(*, '(A)') ' Number of Points on Blade?'
      READ(*, '(B, I3)') NP
      IF(NP.GT.15) GO TO 2
      WRITE(1,3) NP
      FORMAT(' Number of Points on Blade=', I3)
      C
      C READ AND PRINT DATA
      C
      C
      10 WRITE(*, '(A)') ' Space/Chord ?'
      READ(*, '(F10.5)') SC
      WRITE(*, '(A)') ' Stagger Angle, Degrees?'
      READ(*, '(F10.5)') STAG
      WRITE(*, '(A)') ' Mach Number?'
      READ(*, '(F10.5)') MACH
      IF(MACH.GE.1.0) GO TO 12
      WRITE(*, '(A)') ' Frequency Parameter?'
      READ(*, '(F10.5)') LAM
      WRITE(1,14) SC, STAG
      FORMAT(' SCspace/Chord=', F10.5, ' Stagger Angle= ', F10.5,
      1' Degrees')
      14 WRITE(1,16) MACH, LAM
      FORMAT(' Mach Number=', F10.5, ' Frequency Parameter=', F10.5)
      STAG=STAG/DEG
      C
      C CONSTANTS INDEPENDENT OF PHASE
      C
      C
      COSST=COS(STAG)
      SINST=SIN(STAG)
      C
      MACH2=MACH*MACH
      B2=1.0-MACH2
      B=SQRT(B2)
      BC2=1.0-MACH2*COSST*COSST
      BC=SQRT(BC2)
      C
      C CALCULATE PHASE ANGLES FOR RESONANCE
      C
      C
      Z=MACH*LAM*SC/B2
      PHASE1=(SINST*MACH-BC)*Z
      PHASE2=(SINST*MACH+BC)*Z
      X=PHASE1*DEG
      Y=PHASE2*DEG
      WRITE(*, 21) X, Y
      WRITE(1, 21) X, Y
      FORMAT(' Phase angles for resonance', 2F12.5, ' Degrees')
      21
      C
      C READ AND PRINT PHASE
      C
      C
      30 WRITE(*, '(A)') ' Phase Angle, Degrees?'
      READ(*, '(F10.5)') PHASE
      WRITE(1, 31) PHASE
      FORMAT(' OPhase Angle=', F10.5, ' Degrees')
      PHASE=PHASE/DEG
      NR=3
      IF(PHASE.GT.PHASE1.AND.PHASE.LT.PHASE2) NR=5
      C
      C MATRIX GENERATION AND ALGEBRA
      C
      C
      40 CALL DSWK('R, KI, NP, IV')
      IF(IV.EQ.1) GO TO 60
      CALL DSWU(UR, UI, NP, NR)
      CALL DSVX(XR, XI, NP, NR)
      CALL CHDIV(KR, KI, UR, UI, NP, NR, 15, 15)
      CALL CHPRD(XR, XI, UR, UI, CR, CI, NR, NR, 5, 15, 5)
      C
      C PRINT RESULTS
      C
      C
      WRITE(1, '(18X, A, 13X, A, 13X, A)') ' Bending', 'Torsion', 'Vakes'
      DO 51 I=1, NR
      WRITE(1, 52) LINE(1), (CR(I, J), CI(I, J), J=1, 3)
      FORMAT(A, 6F10.5)
      IF(NR.NE.5) GO TO 54
      WRITE(1, '(18X, A, 13X, A)') 'Wave Up', 'Wave Down'
      DO 53 I=1, NR
      WRITE(1, 52) LINE(1), (CR(I, J), CI(I, J), J=4, 5)
      53
      C
      C PRINT PRESSURE JUMP
      C
      C
      54 IF(PRNOPT.NE.'Y') GO TO 60
      WRITE(1, '(A)') ' Pressure Jumps'
      AN=FLOAT(NP)

```

```

31  FORMAT(' Resonance at IR=',I4)
    IV=1
    GO TO 60
32  F=SQRT(ABS(E))
    FB=F/BC2
    H=(BETAH+LAM*SINST)/(2.0*A)
    P=BETAH*LAM*COSST/(P*2.0*A)
    IF(E.GT.0.0) GO TO 50
C
C  WAVE NUMBERS, PROPAGATING CASE
C
    ACUI=D+PB
    ACUI=D-PB
    APD=ACUI*COSST+BETAH*SINST
    APD=ACUI*COSST+BETAH*SINST
    ANU=BETAH*COSST-ACUI*SINST
    AND=BETAH*COSST-ACUI*SINST
    PUR=ANU*(P-H)
    PDR=AND*(P+H)
    PUI=0.0
    XU=0.0
    VU=(P-H)*(LAM+APU)/SC
    WU=(P+H)*(LAM+APD)/SC
    GO TO 60
C
C  WAVE NUMBERS, DECAYING CASE
C
    APU=D+COSST*BETAH*SINST
    APD=APU
    ANU=BETAH*COSST-D*SINST
    AND=ANU
    PUR=ANU*H-PB*SINST*P
    PDR=--PUR
    PUI=ANU*P-PB*SINST*H
    XU=PB+COSST
    RETURN
    END
    $TITLE:'LINSUB'
    $SUBTITLE:'DSVU.FOR'
    $STORAGE:2
    $NODEBUG
C
C  CALCULATION OF UPVASH MATRIX
C
    SUBROUTINE DSVU(UR,UI,NP,NR)
    REAL MACH,LAM,MACH2
    COMMON SC,STAG,MACH,LAM,PHASE,DEG,PI,COSST,SINST,MACH2,B,B2,BC,
1BC2
    COMMON/VAVEG/ XU,APU,APD,ANU,AND,PUR,PDR,PUI,VU,VD
    DIMENSION UR(15,5),UI(15,5)
C
    AK=AN*2.0/PI
    DO 58 I=2,NP
    Y=PI*FLOAT(I-1)/AN
    X=(1.0-COS(Y))/2.0
    AN=AK/SIN(Y)
    DO 57 J=1,NR
    UR(I,J)=UR(I,J)*AM
    UI(I,J)=UI(I,J)*AM
    WRITE(1,59) X,(UR(I,J),UI(I,J),J=1,3)
    PFMAT(1X,7F10.5)
    IF(NR.NE.5) GO TO 58
    WRITE(1,56) (UR(I,J),UI(I,J),J=4,5)
    PFMAT(1X,4F10.5)
    CONTINUE
C
C  OTHER CASES?
C
60  WRITE(*,'(A\)' ) ' Another Phase Angle? Y or N'
    READ(*,'(A\)' ) REPEAT
    IF(REPEAT.EQ.'Y') GO TO 30
    WRITE(*,'(A\)' ) ' Another Whole Set Of Data? Y or N'
    READ(*,'(A\)' ) REPEAT
    IF(REPEAT.EQ.'Y') GO TO 10
C
C  EMPTY PRINTER BUFFER
C
    CRET=CHAR(13)
    LF=CHAR(10)
    WRITE(1,'(2A)' ) CRET,LF
    STOP
    END
    $TITLE:'LINSUB'
    $SUBTITLE:'VAVE.FOR'
    $STORAGE:2
    $NODEBUG
C
C  CALCULATION OF ACOUSTIC WAVE PROPERTIES
C
    SUBROUTINE WAVE(IR,IV)
    REAL MACH,LAM,MACH2
    COMMON SC,STAG,MACH,LAM,PHASE,DEG,PI,COSST,SINST,MACH2,B,B2,BC,
1BC2
    COMMON/VAVEG/ XU,APU,APD,ANU,AND,PUR,PDR,PUI,VU,VD
    BETAH=(PHASE-2.0*PI*FLOAT(IR))/SC
    BETAH2=BETAH*BETAH
    A=LAM+LAM*BETAH2-2.0*LAM*BETAH*SINST
    D=MACH2*(LAM+BETAH*SINST)*COSST/BC2
    E=BETAH2-MACH2*A
    IF(E.NE.0.0) GO TO 32
    WRITE(*,31) IR

```

```

C WAVE PROPERTIES
C
  IF(NR.NE.5) GO TO 1
  CALL WAVE(0,IV)
  WAVU=ANU/(LAM+APU)
  WADV=AND/(LAM+APD)

C BENDING TORSION AND WAKES
C
  DO 12 I=1,NP
    EPSIL=PI*FLOAT(2*I-1)/FLOAT(2*NP)
    Z=0.5*(1.0-COS(EPSIL))
    X=Z*LAM
    UR(1,1)=1.0
    UI(1,1)=0.0
    UR(1,2)=1.0
    UI(1,2)=X
    UR(1,3)=-COS(X)
    UI(1,3)=SIN(X)
    IF(NR.NE.5) GO TO 12
  12 CONTINUE
  RETURN
  END

C UPSTREAM AND DOWNSTREAM WAVES
C
  X=Z*APU
  UR(1,4)=WAVU*COS(X)
  UI(1,4)=WAVU*SIN(X)
  X=Z*APD
  UR(1,5)=WADV*COS(X)
  UI(1,5)=WADV*SIN(X)
  12 CONTINUE
  RETURN
  END

$TITLE:'LINSUB'
$SUBTITLE:'DSVK.FOR'
$STORAGE:2
$NODEBUG

C CALCULATION OF LIFT,MOMENT, SHEED VORTEX SHEET, AND WAVES OUT
C
  SUBROUTINE DSVK(XR,XI,NP,NR)
  REAL MACH,LAM,MACH2,MACH4,MACH6,KR(15,15),KI(15,15)
  COMMON SC,STAG,MACH,LAM,PHASE,DEG,PI,COSST,SINST,MACH2,B,B2,BC,
  1BC2
  COMMON/WAVEC/ XU,APU,APD,ANU,AND,PUR,PDR,PUI,VU,VD
  DIMENSION ICHECK(15,15),ZE(15),ZP(15)
  C CONSTANTS FOR VORTEX SHEET CALCULATION
  C
  X=LAM*SC+COSST
  Y=LAM*SC*SINST+PHASE
  VORT=0.5*LAM*SINH(X)/(COSH(X)-COS(Y))

  C CONSTANTS FOR LOG SINGULARITY CORRECTION
  C
  MACH4=MACH2*MACH2
  MACH6=MACH2*MACH4
  B4=B2*B2
  B6=B2*B4
  A1=1.0-0.5*MACH2/B2
  A2=1.0-0.5/B2+0.25*MACH2/B4
  A3=0.5*(1.0-1.0/B2*MACH2/(6.0*B4)+1.0/(3.0*B4)
  1-0.375*MACH4/B6+MACH6/(6.0*B6))

  C
  IF(NR.NE.5) GO TO 12
  12 CONTINUE
  RETURN
  END

$TITLE:'LINSUB'
$SUBTITLE:'DSVK.FOR'
$STORAGE:2
$NODEBUG

C CALCULATION OF LIFT,MOMENT, AND WAVES
C
  DO 12 I=1,NP
    PSI=PI*FLOAT(I-1)/FLOAT(NP)
    Z=0.5*(1.0-COS(PSI))
  12 CONTINUE
  RETURN
  END

```

```

C MATCHING AND VORTEX POINTS
C
DO 11 I=1,NP
  EPSIL=PI*FLOAT(2*I-1)/FLOAT(2*NP)
  ZE(I)=0.5*(1.0-COS(EPSIL))
  PSI=PI*FLOAT(I-1)/FLOAT(NP)
  ZP(I)=0.5*(1.0-COS(PSI))
11
C
C ZERO COUNTS AND ARRAYS
C
IR=0
ICOUNT=0
IV=0
NP2=NP*NP
DO 21 I=1,NP
  DO 21 J=1,NP
    ICHECK(I,J)=0
    KR(I,J)=0.0
    KI(I,J)=0.0
21
C
C ASSEMBLE MATRIX
C
C I(=1 IN PAPER) GIVES VORTEX POSITION
C J(=1 IN PAPER) GIVES MATCHING POINT
C
CALL WAVE(IR,IV)
IF(IV.EQ.1) GO TO 142
DO 131 I=1,NP
  DO 131 J=1,NP
    IF(ICHECK(I,J).EQ.1) GO TO 131
    POS=ZE(I)-ZP(J)
    IF(POS.GT.0.0) GO TO 90
C
C UPSTREAM POINT
C
XP=EXP(XU*POS)
YP=APU*POS
QR=XP*COS(YP)
QI=XP*SIN(YP)
TERMI=(PUR*QR-PUI*QI)/SC
TERMI=(PUR*QI-PUI*QR)/SC
GO TO 100
C
C DOWNSTREAM POINT
C
XP=EXP(-XU*POS)
YP=APD*POS
QR=XP*COS(YP)
QI=XP*SIN(YP)
TERMI=(PUR*QR-PUI*QI)/SC
TERMI=(PUR*QI-PUI*QR)/SC
GO TO 100
C
C ADD TO MATRIX
C
DO 11 I=1,NP
  EPSIL=PI*FLOAT(2*I-1)/FLOAT(2*NP)
  ZE(I)=0.5*(1.0-COS(EPSIL))
  PSI=PI*FLOAT(I-1)/FLOAT(NP)
  ZP(I)=0.5*(1.0-COS(PSI))
11
C
C CHECK CONVERGENCE OF SERIES
C
X=TERMR*TERMR+TERMI*TERMI
Y=KR(I,J)*KR(I,J)+KI(I,J)*KI(I,J)
IF((X/Y).GT.1.0E-10) GO TO 131
ICHECK(I,J)=1
ICOUNT=ICOUNT+1
C
C CORRECT FOR LOG SINGULARITY (LAST TIME THROUGH)
C
SUM=0.0
EPSIL=PI*FLOAT(2*I)/FLOAT(2*NP)
PSI=PI*FLOAT(J-1)/FL. T(NP)
NPM1=NP-1
DO 121 JR=1,NPM1
  FJR=FLOAT(JR)
  SUM=SUM+COS(FJR*EPSIL)*COS(FJR*PSI)/FJR
  SUM=2.0*SUM+ALOG(4.0*ABS(POS))
  SUM=SUM*LAM/(2.0*PI*B)
  PLAN=LAM*POS
  PLAN2=PLAN*PLAN
  PLAN3=PLAN2*PLAN
  KR(I,J)=KR(I,J)+SUM*(A1*PLAN-A3*PLAN3)
  KI(I,J)=KI(I,J)+SUM*(1.0-A2*PLAN2)
121
C
C ADD VORTICITY WAVE
C
IF(POS.LE.0.0) GO TO 131
KR(I,J)=KR(I,J)+VORT*COS(PLAN)
KI(I,J)=KI(I,J)-VORT*SIN(PLAN)
WRITE(*,132) I,J,IR,KR(I,J),KI(I,J),ICOUNT
132
131
C
C CHECK FOR COMPLETION
C
IF(ICOUNT.EQ.NP2) GO TO 142
IF(IR.GT.0) GO TO 141
IR=IR+1
GO TO 30
141
IR=IR
GO TO 30
142
RETURN
END
$TITLE:'CNDIV'
$STORAGE:2
$NODEBUG
C

```

```

C      SUBROUTINE CNDIV(AR, AI, BR, BI, IRA, ICB, IRAD, IRBD)
C
C      Complex Matrix Division
C
C      DIMENSION AR(IRAD, IRA), AI(IRAD, IRA), BR(IRBD, ICB), BI(IRBD, ICB)
C
C      Loop for pivot row
C
C      DO 8 I=1, IRA
C
C      Choose largest pivot for pivot column
C
C      Z=0.
C      DO 1 I=1, IRA
C      X=AR(I, IP)*AR(I, IP)+AI(I, IP)*AI(I, IP)
C      IF(X.LT.Z) GO TO 1
C      Z=X
C      IE=I
C
C      CONTINUE
C      IF(Z.EQ.0.) GO TO 9
C
C      Exchange rows, scaling new pivot row
C
C      ZR=AR(IE, IP)/Z
C      ZI=AI(IE, IP)/Z
C      IF(IP.EQ.IRA) GO TO 3
C      AR(IE, IP)=AR(IP, IP)
C      AI(IE, IP)=AI(IP, IP)
C      K=IP+1
C      DO 2 J=K, IRA
C      XB=AR(IE, J)*ZR-AI(IE, J)*ZI
C      XI=AR(IE, J)*ZI+AI(IE, J)*ZR
C      AR(IE, J)=XB
C      AI(IE, J)=XI
C      AR(IP, J)=XR
C      AI(IP, J)=XI
C      DO 4 J=1, ICB
C      XR=BR(IE, J)*ZR-BI(IE, J)*ZI
C      XI=BR(IE, J)*ZI+BI(IE, J)*ZR
C      BR(IE, J)=XR
C      BI(IE, J)=XI
C      BR(IP, J)=XR
C      BI(IP, J)=XI
C
C      Multiply rows by multiple of pivot row
C
C      DO 8 I=1, IRA
C      IF(I.EQ.IP) GO TO 8
C      IF(IP.EQ.IRA) GO TO 6
C      DO 5 J=K, IRA
C      AR(I, J)=AR(I, J)-AR(IP, J)*AR(I, IP)+AI(IP, J)*AI(I, IP)

```

```

5      AI(I, J)=AI(I, J)-AR(IP, J)*AI(I, IP)+AI(IP, J)*AR(I, IP)
6      DO 7 J=1, ICB
7      BR(I, J)=BR(I, J)-BR(IP, J)*AR(I, IP)+BI(IP, J)*AI(I, IP)
8      BI(I, J)=BI(I, J)-BR(IP, J)*AI(I, IP)+BI(IP, J)*AR(I, IP)
9      CONTINUE
10     RETURN
C      Error message
C
C      WRITE(*, 10) IP
10     FORMAT(' Zero pivot at line', I4)
C      STOP
C      END
C
C      SUBROUTINE CHPRD(AR, AI, BR, BI, CR, CI, IRA, ICARB, ICB, IRAD, IRBD, IRCD)
C
C      DIMENSION AR(IRAD, ICARB), AI(IRAD, ICARB), BR(IRBD, ICB),
1BI(IRBD, ICB), CR(IRCD, ICB), CI(IRCD, ICB)
C      DO 1 I=1, IRA
C      DO 1 J=1, ICB
C      CR(I, J)=0.
C      CI(I, J)=0.
C      DO 1 K=1, ICARB
C      CR(I, J)=CR(I, J)+AR(I, K)*BR(K, J)-AI(I, K)*BI(K, J)
C      CI(I, J)=CI(I, J)+AR(I, K)*BI(K, J)+AI(I, K)*BR(K, J)
1      RETURN
C      END
C
C      PROGRAM LINSUB
C
C      Description
C
C      -----

```

This program calculates the unsteady two-dimensional linearized subsonic flow in cascades, using the theory published by Smith (1971). The blades are assumed to be flat plates operating at zero incidence. Five different kinds of input are treated. These are

- (a) Translational vibration of the blades normal to their chord.
- (b) Torsional vibration of the blades about the origin at the leading edge.
- (c) Sinusoidal wakes shed from some obstructions upstream, which move relative to the cascade in question.
- (d) Incoming acoustic waves, coming from downstream.
- (e) Incoming acoustic waves, coming from upstream.

The program calculates five quantities for each of these kinds of input. These are

- (a) Lift force on the blades.
- (b) Moment on the blades, about the leading edge.
- (c) Strength of the vortex sheet shed from the trailing edge.
- (d) Strength of the outgoing acoustic wave going upstream.
- (e) Strength of the outgoing acoustic wave going downstream.

If required, the distribution of pressure jump across the blade along the chord is also output.

If the input data is such that no acoustic waves can propagate, then the acoustic information is suppressed.

The marginal condition when the waves are just on the verge of propagation, also referred to as a resonance condition, is singular, and there is no solution. The program moves on to the next case.

The program is written in FORTRAN and runs on an IBM Personal Computer. It can easily be transferred to run on any computer having a FORTRAN compiler.

Input

The program asks for the following inputs.

- (a) Is the pressure jump across the blade to be printed?
- (b) Number of points to be used on blade? $NP \leq 15$. $NP=6$ is often sufficient, and $NP=8$ is usually safe, but if the stagger angle or the frequency parameter is high, larger values may be required. This may be checked by running a few test cases with two different values of NP . If $NP > 15$ is asked for, the program asks for a new value.
- (c) Space/Chord ratio? $SC > 0.0$ (No check for positive values.)
- (d) Stagger Angle, Degrees? $-90.0 < STAG < 90.0$. (Unchecked.)
- (e) Mach number? $0.0 < MACH < 1.0$. The results from the program may be unreliable if $MACH > 0.9$. If $MACH > 1.0$ is asked for, the program asks for a new value.
- (f) Frequency parameter? $LAM = \omega c / U$, where ω is the angular frequency, radians/sec.

c is the blade chord,

U is the steady mainstream velocity.

$LAM > 0.0$ (Unchecked.)

(g) Phase angle between any blade and the next blade above, Degrees, PHASE ?

The optimum range is $-180.0 < PHASE < 180.0$, but the range $-360.0 < PHASE < 360.0$ is acceptable. Outside this range there may be some loss of accuracy or increase of computation time.

After a case has been calculated, the program asks whether another case with a new phase angle, or another case with a whole new set of data is to be calculated.

Printed Output

This consists of

- (a) The input values of NP , SC , $STAG$, $MACH$, and LAM .
- (b) The phase angles at which resonance occurs. Phase angles between these two values allow acoustic waves to propagate.
- (c) The input value of $PHASE$.
- (d) Non-dimensional coefficients giving the five output quantities for each of the five input quantities, as follows

$$f_y / \rho U c h_y \quad f_y / \rho U^2 c \alpha \quad f_y / \rho U c w \quad f_y / c p_{i+} \quad f_y / c p_{i-}$$

$$m / \rho U c^2 h_y \quad m / \rho U^2 c^2 \alpha \quad m / \rho U c^2 w \quad m / c^2 p_{i+} \quad m / c^2 p_{i-}$$

$$\epsilon / h_y \quad \epsilon / U \alpha \quad \epsilon / w \quad \rho U \epsilon / p_{i+} \quad \rho U \epsilon / p_{i-}$$

$$P_{O+} / \rho U h_y \quad P_{O+} / \rho U^2 \alpha \quad P_{O+} / \rho U w \quad P_{O+} / p_{i+} \quad P_{O+} / p_{i-}$$

$$P_{O-} / \rho U h_y \quad P_{O-} / \rho U^2 \alpha \quad P_{O-} / \rho U w \quad P_{O-} / p_{i+} \quad P_{O-} / p_{i-}$$

where

ρ = Mean fluid density.

h_y = Velocity of blade due to translational vibration, positive up.

α = Angular displacement of blade due to torsional vibration, positive anticlockwise about the leading edge.

w = Velocity which would be induced at the leading edge of the blade, if the cascade were removed, by the inlet wakes, positive up.

p_i = Pressure fluctuation which would occur at the position of the leading edge of the blade, if the cascade were removed, due to the incoming acoustic wave coming upstream from far downstream.

p_{i+} = Pressure fluctuation which would occur at the position of the leading edge of the blade, if the cascade were removed, due to the incoming acoustic wave coming downstream from far upstream.

f_y = Lift force on blade, positive up.

m = Moment on blade, positive anticlockwise about the leading edge.

ϵ = Strength of the vortex sheet shed from the trailing edge, positive anticlockwise, which would occur at the leading edge if the wake were extended back to this point.

P_{O+} = Pressure fluctuation at the leading edge due to the outgoing acoustic wave going upstream.

P_{O-} = Pressure fluctuation at the leading edge due to the outgoing acoustic wave going downstream.

(e) Non-dimensional coefficients for the pressure jump across the blade (if requested) in the form

$$z/c \quad \Delta p/\rho U_\infty^2 \quad \Delta p/\rho U_\infty^2 \alpha \quad \Delta p/\rho U_\infty^2 \alpha^2 \quad \Delta p/p_1 \quad \Delta p/p_1 -$$

where

z = Distance from leading edge.

Δp = (Pressure on top surface) - (Pressure on bottom surface).

All these coefficients are complex numbers. First the real part and then the imaginary part is printed.

Running the Program.

The program is called by the command
LINSUB

D.S.Whitehead.
25 Jan. 1984.

THREE-DIMENSIONAL FLOWS

by

Masanobu Namba

Department of Aeronautical Engineering

Kyushu University

Hakosaki, Higashiku, Fukuoka 812, Japan

INTRODUCTION

Unsteady aerodynamic and aeroelastic phenomena in axial turbomachines are more or less three-dimensional. Fortunately, however, many of the essential features of the phenomena can be accounted for on the basis of two-dimensional cascade models, and many useful papers on two-dimensional cascade theories and experiments are available. Then what we should do when we apply them to axial flow turbomachines is to correct for three-dimensional effects. There are, however, some types of three-dimensional effects which give rise to very large deviations from predictions by two-dimensional cascade models, and hence the three-dimensional correction concept cannot be justified.

The three-dimensional effects on unsteady blade loadings in turbomachines result from the following causes:

- A) Annular geometry of cascades.
- B) Spanwise nonuniform amplitude of blade vibration.
- C) Spanwise nonuniformity in the unsteady component of the incident flow velocity (spanwise nonuniform gust).
- D) Spanwise nonuniformity in the steady component of the incident flow velocity.
- E) Spanwise variation of the blade geometry, e.g., swept blades.
- F) Spanwise nonuniformity in the steady component of blade loadings.
- G) Presence of sound absorbing walls.

It is a formidable task to theoretically deal with all of these three-dimensional effects in a general form. As the first stage in the process of research we have to develop particular theoretical methods based on simplified models which can exclusively deal with some types of the three-dimensional effects. As the second stage we should proceed to more realistic models taking into account various effects such as shock waves, boundary layers and blade profiles. Our goal is to establish practical rules of correction for the three-dimensional effects or practical methods of predicting the three-dimensional effects which are far beyond the concept of correction. At present we are still at the first stage, and some types of three-dimensional effects remain to be studied.

The objective of the present article is to outline the available theoretical methods which can predict various three-dimensional effects upon unsteady blade loadings. It is also attempted to describe typical features of the three-dimensional effects revealed by those theoretical methods.

The effect of the annular geometry has been studied by Namba (1976, 1977), Namba and Ishikawa (1983) and Salaun (1979, 1976). Their theories are essen-

tially extensions of the linearized small disturbance compressible flow theories for a rotating annular cascade of lifting surfaces with steady loadings, which originated from the work of McCune (1958, 1958) and have been developed by Namba (1972) and Okurounmu and McCune (1974).

The theories given by Salaun (1979, 1976) and Namba (1976, 1977) or Namba and Ishikawa (1983) deal with exactly the same model. However, there exists an important difference between both theories in mathematical treatment of the kernel function in the integral equation for unsteady blade loadings. Salaun (1976, 1979) computes the kernel function in its exact form. On the other hand, Namba (1976, 1977) and Namba and Ishikawa (1983) compute the kernel function by applying the method of finite radial mode expansion which has been developed by Namba (1972). This method enables us to extract singular terms quite easily. Owing to this advantage it proves to be a powerful tool for dealing with a rotating transonic annular cascade in which flows relative to moving blades are subsonic at radii near the hub and supersonic at radii near the tip.

The unsteady three-dimensional flow in a rotating transonic annular cascade is not only of practical importance but also of great aerodynamic interest. Namba and Ishikawa (1983) have shown that the disturbance flow features near the sonic span are far from quasi-two-dimensional. Another important finding by Namba is that the three-dimensional effect on unsteady loadings is quite small if the predominant acoustic modes generated by blades are of cut-on state.

In the following chapters Salaun's and Namba's and his colleague's theories are described in some detail.

It should be noted that Namba's and Salaun's annular cascade model also includes the effect of type B), and further the effect of type D) in a special form since the resultant velocity of the approach flow relative to rotating blades is naturally non-uniform along the span.

As far as a linearized small disturbance theory is concerned, it is merely a matter of substitution to transform the formulation for the vibration problem into that for the gust problem. In fact, Namba (1977) and Namba and Ahe (1984) deal with interaction of an annular cascade with nonuniform gusts, i.e., the effect of type C).

The simplest model to exclusively deal with the effect B) or C) will be a linear cascade between parallel walls. As to this model papers by Nishiyama and Kobayashi (1977) for subsonic flows and Kikuchi (1980, 1981) for supersonic flows are available. Description of this model, however, is omitted, since it can be regarded as a special case of the model described in "EFFECT OF WALL

LININGS".

In order to study the effect D) excluding all other types of the three-dimensional effects, we have to deal with a linear cascade in shear flows. In this case the time mean flow is rotational. Then solving the governing wave equation becomes very difficult. Kurosaka (1978) conducted a preliminary study on a vibrating single airfoil in supersonic shear flow. Kaji et. al., (1981) studied the cascade flutter in incompressible shear flow on the basis of the semi-actuator disk model. Recently, Yamasaki and Namba (1982) developed a lifting surface theory for a cascade of oscillating blades in incompressible shear flow. This work is outlined in the section "UNSTEADY CASCADE IN SPANWISE NONUNIFORM MEAN FLOW".

Current turbofan engines are equipped with sound absorbing liners on engine duct walls in order to attenuate sounds. The principal part of disturbances generated by blade vibration propagates as sound waves and interacts with the sound absorbing liners. It is then needed to know how this interaction with the liners will influence unsteady blade loadings. Especially, our interest is whether the wall liner can be an efficient suppressor of the cascade flutter or not.

A preliminary research on this problem also has been given by Kurosaka and Edelfelt (1978). A more extensive study has recently been conducted by Yamasaki and Namba (1982). They developed a lifting surface theory for a cascade of oscillating blades in a parallel walled channel treated with sound absorbing linings. The section "EFFECT OF WALL LININGS" deals with the effect of type D) by describing Yamasaki and Namba's theory with some new findings.

Recently, swept-back blades have become attractive in the development of advanced turbopropellers. Application of swept-back blades to turbofans, however, remains unexplored. The effect of the blade design E) will deserve to be investigated, especially from the standpoint of suppressing noise generation.

It is now widely accepted that the steady component of blade loadings has an important effect on the cascade flutter. Then the nonuniformity in steady blade loadings, i.e., the effect of type F), will give rise to modification of unsteady blade loadings. Some recent works on the effects of types E) and F) are reported by Namba and Fan (1985) and Namba, Yamasaki, and Kurihara (1984).

SUBSONIC, SUPERSONIC AND TRANSONIC UNSTEADY ANNULAR CASCADE THEORY BASED ON THE FINITE RADIAL MODE EXPANSION METHOD

MODEL AND MATHEMATICAL FORMULATION

We consider a single annular cascade composed of N blades rotating at a constant angular speed ω^* in an inviscid perfect gas flowing in a rigid walled annular duct of infinite axial extent with the outer radius r_T^* and the hub-to-tip ratio h as shown in Fig. 1. The undisturbed state of the fluid is assumed

to be a uniform axial flow with velocity W_a^* and density ρ_0^* . Hereafter we use dimensionless quantities with the reference length r_T^* , velocity W_a^* , density ρ_0^* , pressure $\rho_0^* W_a^{*2}$ and time r_T^*/W_a^* . Let us assume that the angle of attack, camber and thickness of blades and amplitudes of blade motions or incident disturbance flow velocities are small so that disturbances induced by blades are small and isentropic. Let (r, θ, z) be a cylindrical coordinate system fixed to the rotor and t be a time coordinate. Then the position of blade surfaces can be represented by

$$\theta - \omega z - 2\pi m/N = f_m(r, z, t)/r \quad (1)$$

$$b_L(r) \leq z \leq b_T(r), \quad h \leq r \leq 1;$$

$$m = 0, 1, \dots, N-1$$

Hence $\theta' = \theta - \omega z = \text{constant}$ gives an undisturbed helical streamsurface, $f_m(r, z, t)$ denotes a circumferential distance of the m -th blade surface from the helical surface $\theta' = 2\pi m/N$, and $b_L(r)$ and $b_T(r)$ denote axial positions of leading and trailing edges of blades respectively. Furthermore, $\omega = \omega^* r_T^*/W_a^*$ denotes the dimensionless rotational speed of the rotor, i.e., the ratio of the circumferential rotor tip speed to the axial flow velocity.

Now the presence of blades can be described by body forces acting on the fluid as counter action of aerodynamic forces on blades and mass sources representing the displacement effect of the blade thickness. Then the linearized equations of continuity and motion are given by

$$\frac{D\tilde{P}}{Dt} + \nabla \cdot \tilde{q} = \sum_{m=0}^{N-1} \int_h^1 \frac{1}{r} \delta(r-r_0) dr_0 \int_{b_L(r_0)}^{b_T(r_0)} \tilde{T}_m(r_0, z_0, t) \quad (2)$$

$$\times \delta(\theta - \omega z_0 - 2\pi m/N) \delta(z - z_0) \sqrt{1 + \omega^2 r_0^2} dz_0,$$

$$\frac{D\tilde{q}}{Dt} = -\nabla \tilde{P} \quad (3)$$

$$-e_r \sum_{m=0}^{N-1} \int_h^1 \frac{1}{r} \delta(r-r_0) dr_0 \int_{b_L(r_0)}^{b_T(r_0)} \tilde{\Delta P}_{Bm}(r_0, z_0, t) \times \delta(\theta - \omega z_0 - 2\pi m/N) \delta(z - z_0) \sqrt{1 + \omega^2 r_0^2} dz_0.$$

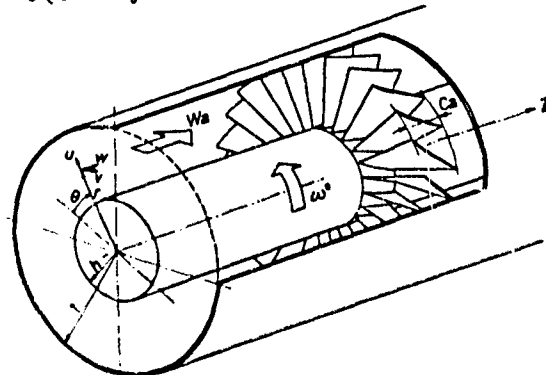


FIG. 1. ANNULAR CASCADE AND DUCT GEOMETRY

Here $\tilde{\rho}$ and \tilde{q} denote the disturbance fluid density and the disturbance fluid velocity respectively, and \mathbf{e}_r denotes the unit vector normal to the helical surface $\theta' = \text{constant}$, i.e.,

$$\mathbf{e}_z = \frac{1}{\sqrt{1+\omega^2 r^2}} (-\omega r \mathbf{e}_\theta + \mathbf{e}_0). \quad (4)$$

Further

$$\nabla = \mathbf{e}_r \frac{\partial}{\partial r} + \mathbf{e}_\theta \frac{1}{r} \frac{\partial}{\partial \theta} + \mathbf{e}_z \frac{\partial}{\partial z}, \quad (5)$$

$$\frac{D}{Dt} = \frac{\partial}{\partial t} + \frac{\partial}{\partial z} + \omega \frac{\partial}{\partial \theta}, \quad (6)$$

where \mathbf{e}_r , \mathbf{e}_θ and \mathbf{e}_z denote unit vectors in r , θ and z directions respectively. In Eqs. (2) and (3)

$$\tilde{T}_m(r_0, z_0, t) \quad \text{and} \quad \Delta \tilde{p}_{Bm}(r_0, z_0, t)$$

denote respectively the mass source density and the pressure difference across the m -th blade surface. The relation of isentropic flow is given by

$$\frac{D\tilde{p}}{Dt} - M_a^2 \frac{D\tilde{\rho}}{Dt} = 0, \quad (7)$$

where M_a is the axial flow Mach number. Eliminating $\tilde{\rho}$ and \tilde{q} from Eqs. (2), (3) and (7), we obtain the equation for \tilde{p} as follows

$$\begin{aligned} & (\nabla^2 - M_a^2 \frac{D^2}{Dt^2}) \tilde{p} \\ &= - \frac{D}{Dt} \sum_{m=0}^{N-1} \int_{b_L(r_0)}^{b_T(r_0)} \frac{1}{r} \delta(r-r_0) dr_0 \int_{b_L(r_0)}^{b_T(r_0)} \tilde{T}_m(r_0, z_0, t) \\ & \times \delta(z-z_0) \delta(\theta-\omega z-2\pi m/N) \sqrt{1+\omega^2 r_0^2} dz_0 \quad (8) \\ & - \frac{1}{\sqrt{1+\omega^2 r^2}} \left(-\omega r \frac{\partial}{\partial z} + \frac{1}{r} \frac{\partial}{\partial \theta} \right) \sum_{m=0}^{N-1} \int_{b_L(r_0)}^{b_T(r_0)} \frac{1}{r} \delta(r-r_0) dr_0 \\ & \times \int_{b_L(r_0)}^{b_T(r_0)} \Delta \tilde{p}_{Bm}(r_0, z_0, t) \delta(z-z_0) \\ & \times \delta(\theta-\omega z-2\pi m/N) \sqrt{1+\omega^2 r_0^2} dz_0. \end{aligned}$$

The boundary condition at the duct walls is

$$\partial \tilde{p} / \partial r = 0 \quad \text{at } r = 1 \text{ and } h. \quad (9)$$

Now let us assume the unsteady state of the flow to be of harmonic time dependence with a constant interblade phase angle. Then we can put

$$\tilde{T}_m(r_0, z_0, t) = T(r_0, z_0) e^{i\lambda t + i\delta m}, \quad (10)$$

$$\Delta \tilde{p}_{Bm}(r_0, z_0, t) = \Delta p_B(r_0, z_0) e^{i\lambda t + i\delta m}, \quad (11)$$

where λ denotes the reduced frequency, and $\delta = 2\pi\sigma/N$ is the interblade phase angle. We should note σ is an integer between $-N/2$ and $N/2$. Substituting Eqs. (10) and (11) into (8), we can easily find that the disturbance pressure can be expressed in the form

$$\tilde{p}(r, \theta, z, t) = p_T(r, \theta, z) e^{i\lambda t} + p_L(r, \theta, z) e^{i\lambda t}, \quad (12)$$

where

$$p_T(r, \theta, z) = \quad (13)$$

$$\int_{b_L(r_0)}^{b_T(r_0)} dr_0 \int_{b_L(r_0)}^{b_T(r_0)} T(r_0, z_0) K_{pT}(r, \theta', z-z_0 | r_0) dz_0,$$

$$p_L(r, \theta, z) = \quad (14)$$

$$\int_{b_L(r_0)}^{b_T(r_0)} dr_0 \int_{b_L(r_0)}^{b_T(r_0)} \Delta p_B(r_0, z_0) K_{pL}(r, \theta', z-z_0 | r_0) dz_0.$$

Here kernel functions $K_{pT}(r, \theta', z-z_0 | r_0)$ and $K_{pL}(r, \theta', z-z_0 | r_0)$ are given by

$$\begin{aligned} & K_{pT}(r, \theta', z-z_0 | r_0) \\ &= - \left[\left(i\lambda + \frac{\partial}{\partial z} \right) G(r, \theta-\theta_0, z-z_0 | r_0) \sqrt{1+\omega^2 r_0^2} \right]_{\theta_0=\omega z_0} \quad (15) \end{aligned}$$

$$\begin{aligned} & K_{pL}(r, \theta', z-z_0 | r_0) \\ &= - \left[\frac{1}{\sqrt{1+\omega^2 r^2}} \left(-\omega r \frac{\partial}{\partial z} + \frac{1}{r} \frac{\partial}{\partial \theta} \right) G(r, \theta-\theta_0, z-z_0 | r_0) \sqrt{1+\omega^2 r_0^2} \right]_{\theta_0=\omega z_0} \\ &= \left[\left(-\omega r_0 \frac{\partial}{\partial z_0} + \frac{1}{r_0} \frac{\partial}{\partial \theta_0} \right) G(r, \theta-\theta_0, z-z_0 | r_0) \right]_{\theta_0=\omega z_0}, \end{aligned} \quad (16)$$

where $G(r, \theta-\theta_0, z-z_0 | r_0) e^{i\lambda t}$ denotes the pressure field induced by a row of monopoles located at $(r_0, z_0, \theta_0 + 2\pi m/N)$ with the strength $e^{i\lambda t + i\delta m}$ ($m = 0, 1, \dots, N-1$).

It is the solution to the following equations:

$$\left\{ \nabla^2 - M_a^2 \left(i\lambda + \frac{\partial}{\partial z} \right)^2 \right\} G(r, \theta-\theta_0, z-z_0 | r_0) \quad (17)$$

$$= \frac{1}{r} \delta(r-r_0) \delta(z-z_0) \sum_{m=0}^{N-1} e^{i\delta m} \delta(\theta-\theta_0-2\pi m/N),$$

$$\partial G / \partial r = 0 \quad \text{at } r = 1 \text{ and } h. \quad (18)$$

As shown by Namba (1972) the solution is expressed as follows:

1) For subsonic axial flows, i.e., $M_a < 1$,

$$\begin{aligned} G(r, \theta, z | r_0) &= - \frac{N}{4\pi A^2} \sum_{\gamma=-\infty}^{\infty} \sum_{\mu=0}^{\infty} \frac{1}{\Omega_\mu^{(\gamma)}} R_\mu^{(\gamma)}(r) R_\mu^{(\gamma)}(r_0) \\ & \times \exp[i\pi\gamma + i(\pi\omega + \lambda)z M_a^2 / A^2 - \Omega_\mu^{(\gamma)} |z|]. \end{aligned} \quad (19)$$

- ii) For supersonic axial flows, i.e., $M_a > 1$,

$$G(r, \theta, z | r_0) \quad (20)$$

$$= H(z) \frac{N}{2\beta_a^2} \sum_{\nu=-\infty}^{\infty} \sum_{l=0}^{\infty} \frac{1}{|\Omega_l^{(\nu)}|} R_l^{(\nu)}(r) R_l^{(\nu)}(r_0) \times \sin(|\Omega_l^{(\nu)}| z) \exp[i n \theta + i(\nu \omega + \lambda) z M_a^2 / \beta_a^2],$$

where

$$n = \nu N + 0 \quad (21)$$

$$\beta_a^2 = 1 - M_a^2 \quad (22)$$

and $H(z)$ denotes the Heaviside step function. Furthermore, the axial wave factor $\Omega_l^{(\nu)}$ is defined by

$$\Omega_l^{(\nu)} = \begin{cases} \sqrt{A} & : A > 0, \\ i\sqrt{-A} & : A < 0 \end{cases} \quad (23)$$

$$\text{and } k_l^{(\nu)2} - \omega^2 n^2 M_a^2 / \beta_a^2 > 0, \\ i \operatorname{sgn}(\nu \omega + \lambda) \sqrt{-A} : A < 0 \\ \text{and } k_l^{(\nu)2} - \omega^2 n^2 M_a^2 / \beta_a^2 < 0,$$

$$A = \{ k_l^{(\nu)2} - (\nu \omega + \lambda)^2 M_a^2 / \beta_a^2 \} / \beta_a^2.$$

Further $R_l(n)(r)$ and $k_l(n)(l = 0, 1, \dots)$ are orthogonal radial eigenfunctions and eigenvalues respectively of the following Sturm-Liouville boundary value problem:

$$\frac{1}{r} \frac{d}{dr} \left\{ r \frac{dR_l^{(n)}}{dr} \right\} + \left(k_l^{(n)2} - \frac{n^2}{r^2} \right) R_l^{(n)} = 0 \quad (24)$$

$$dR_l^{(n)} / dr = 0 \text{ at } r = 1, h.$$

The eigenfunctions are normalized as follows:

$$\int_h^1 r R_l^{(n)}(r) R_m^{(n)}(r) dr = \delta_{lm}, \quad (25)$$

where δ_{lm} denotes the Kronecker delta. The eigenfunctions $R_l(n)(r)$ are equivalent to the symbol $R_n(k_l(n)r)$ used by McCune (1958) and they are constructed by combining the Bessel functions of the first and second kinds of order n . Note that for $n = l = 0$

$$k_0^{(0)} = 0, \quad R_0^{(0)} = \sqrt{2/(1-h^2)}.$$

therefore each set of orthogonal functions $R_l(n)(r)$ ($l = 0, 1, \dots$) is complete.

Among various properties of $R_l(n)(r)$ and $k_l(n)$, mention should be made of

$$\delta(r-r_0) = r \sum_{l=0}^{\infty} R_l^{(n)}(r) R_l^{(n)}(r_0), \quad (26)$$

and

$$\lim_{n \rightarrow \infty} (k_l^{(n)} / n) = 1 \text{ if } l \text{ is fixed.} \quad (27)$$

Furthermore as l increases with n fixed, radial changes in $R_l(n)(r)$ are confined to an increasingly narrow region near the inner wall. On the other hand, as n increases with l fixed, radial variation in $R_l(n)(r)$ becomes larger near the outer wall.

As Eqs. (19) and (20) show, the pressure field induced by a row of monopoles is composed of an infinite number of acoustic modes, which are specified by the circumferential wave number n and the radial order, i.e., radial node l . The circumferential wave form given by $e^{in\theta}$ is sinusoidal and independent of the radial order, while the radial wave form described by $R_l(n)(r)$ is heavily dependent upon the circumferential wave number n as pointed out above.

FINITE RADIAL MODE EXPANSION

The pressure fields induced by rows of discrete monopoles and dipoles given by Eqs. (15, 16, 19, 20) are singular at monopoles and dipole positions, and hence acoustic modes of large n and l play an important role, especially near the singular points. We should note, however, that the radial variations of the pressure fields induced by sheets of dipoles and monopoles representing the cascade of blades are no longer singular, and hence the contribution of acoustic modes of large radial orders is expected to be small. This suggests that the pressure fields given by Eqs. (13) and (14) can be approximated by a sum of acoustic modes with finite radial orders from $l = 0$ up to $l = L-1$, say.

We should note, however, that simply to truncate the series while keeping the exact values for $R_l(n)(r)$ and $k_l(n)$ fails to reproduce proper behaviors of the field. Therefore, truncation of the l series must be accompanied by modification in $R_l(n)(r)$ and $k_l(n)$ so that the contribution of large circumferential wave numbers is properly realized over the whole radial position. This is accomplished by the following method.

Let $R_l(n)(r)$ be approximated by a finite series expansion in the form

$$R_l^{(n)}(r) = \sum_{m=0}^{L-1} B_{lm}^{(n)} R_m^{(0)}(r), \quad (28)$$

where $R_m^{(0)}(r)$ ($m = 0, 1, \dots$) are exact solutions for $n = 0$. Substituting Eq. (28) into Eq. (24), multiplying the resulting equation by $r R_k^{(0)}(r)$ and integrating with respect to r from $r = h$ to 1, we obtain

$$\sum_{m=0}^{L-1} B_{lm}^{(n)} [\{ \kappa_l^{(n)2} - (k_m^{(0)}/n)^2 \} \delta_{km} - R_{km}] = 0, \\ k = 0, 1, \dots, L-1, \quad (29)$$

where

$$R_{km} = \int_h^1 \frac{1}{r} R_k^{(0)}(r) R_m^{(0)}(r) dr, \quad (30)$$

$$\kappa_l^{(n)} = k_l^{(n)} / n. \quad (31)$$

Eq. (29) implies that $\kappa_l(n)^2$ and $B_{lm}(n)$ ($l, m = 0, 1, \dots, L-1$) are respectively eigenvalues and eigenvectors of the symmetric real matrix

$$\left[R_{lk} + (\kappa_m^{(0)}/n)^2 \delta_{lk} \right] \quad (32)$$

$(m, k = 0, 1, \dots, L-1).$

Furthermore Eq. (28) implies that

$$B_{lm}^{(n)} = \int_0^1 r R_m^{(0)}(r) R_l^{(n)}(r) dr. \quad (33)$$

Then it holds that

$$R_m^{(0)}(r) = \sum_{l=0}^{L-1} B_{lm}^{(n)} R_l^{(n)}(r), \quad (34)$$

and hence

$$\left. \begin{aligned} \sum_{l=0}^{L-1} B_{lm}^{(n)} B_{lk}^{(n)} &= \delta_{mk}, \\ \sum_{l=0}^{L-1} B_{ml}^{(n)} B_{kl}^{(n)} &= \delta_{mk}. \end{aligned} \right\} \quad (35)$$

A remarkable advantage of the finite radial mode expansion is that we can obtain limit eigenfunctions $R_l^{(*)}(r)$ and limit eigenvalues $\kappa_l^{(*)}$ by applying $n \rightarrow \infty$ to Eq. (29). Furthermore, asymptotic behaviors for $n \rightarrow \infty$ are

$$R_l^{(n)}(r) = R_l^{(*)}(r) + O(n^{-2}), \quad (36)$$

$$\kappa_l^{(n)} = \kappa_l^{(*)} + O(n^{-2}).$$

This fact enables us to extract the singular parts of the kernel functions very easily. Figs. 2 and 3 show $\kappa_l^{(*)}$ and $R_l^{(*)}(r)$ computed by the present method.

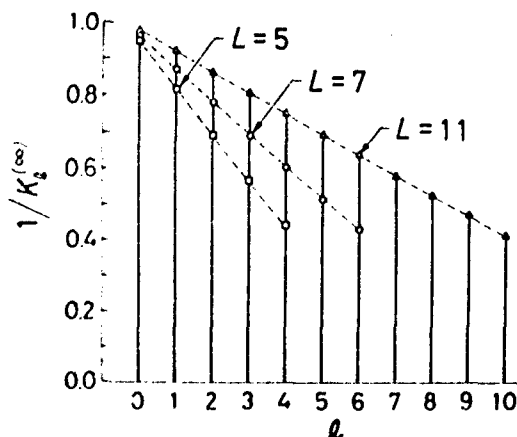


FIG. 2. LIMIT EIGENVALUES $\kappa_l^{(*)}$ FOR $h=0.4$ AND VARIOUS L (number of retained radial orders)

We should note that $\kappa_l^{(*)}$ are no longer equal to unity contrary to (27). Furthermore, $1/\kappa_l^{(*)}$ ($l = 0, 1, \dots, L-1$) constitute a finite sequence of numbers which are equally spaced between 1 and h . We should note further that each of $R_l^{(*)}(r)$ shows a highest extremum at $r=1/\kappa_l^{(*)}$.

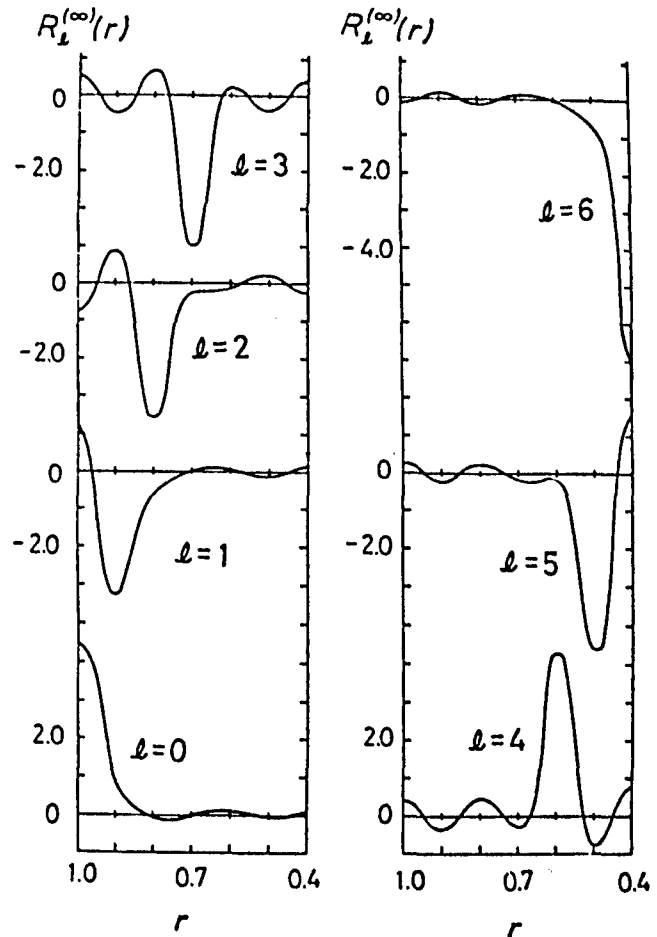


FIG. 3. LIMIT EIGENFUNCTIONS $R_l^{(*)}(r)$ FOR $h=0.4$ AND $L=7$

The behavior of $R_l^{(*)}(r)$ shown above suggests to use a set of $R_l^{(*)}(r)$ ($l = 0, 1, \dots, L-1$) as the basis function system. In this respect the following relations are useful.

$$R_l^{(n)}(r) = \sum_{k=0}^{L-1} B_{lk}^{(n)} R_k^{(*)}(r), \quad (37)$$

$$\frac{1}{r^2} R_l^{(n)}(r) = \sum_{k=0}^{L-1} C_{lk}^{(n)} R_k^{(*)}(r), \quad (38)$$

where

$$B_{lk}^{(n)} = \sum_{m=0}^{L-1} B_{lm}^{(n)} B_{km}^{(*)}, \quad (39)$$

$$\begin{aligned} C_{lk}^{(n)} &= \int_0^1 \frac{1}{r} R_l^{(n)}(r) R_k^{(*)}(r) dr \\ &= \sum_{m=0}^{L-1} C_{lm}^{(n)} B_{km}^{(*)}, \end{aligned} \quad (40)$$

$$\begin{aligned} C_{lm}^{(n)} &= \sum_{k=0}^{L-1} B_{lk}^{(n)} R_{mk}^{(*)} \\ &= B_{lm}^{(n)} \{ \kappa_l^{(*)2} - (\kappa_m^{(0)}/n)^2 \}. \end{aligned} \quad (41)$$

Furthermore, it holds that

$$BB_{lk}^{(\infty)} = \delta_{lk}, \quad (42)$$

$$C_{lm}^{(0)} = R_{lm}, \quad (43)$$

$$CB_{lk}^{(\infty)} = \kappa_l^{(\infty)2} \delta_{lk}, \quad (44)$$

$$B_{lm}^{(0)} = \delta_{lm}, \quad (45)$$

$$\sum_{l=0}^{L-1} BB_{lj}^{(n)} BB_{lk}^{(n)} = \delta_{jk}. \quad (46)$$

ACOUSTIC FIELD EXPRESSED BY THE FINITE RADIAL MODE SYSTEM

The concept of the finite radial mode system given in the previous section lies in condensing all acoustic modes into a finite number of families with radial orders from $l = 0$ to $l = L-1$ rather than in simply omitting modes of radial orders higher than L . This 'rearrangement' of acoustic modes allows us to classify the acoustic mode families into supersonic and subsonic types as follows.

Let $\hat{\Omega}_l^{(n)}$ be defined by

$$\hat{\Omega}_l^{(n)} = \Omega_l^{(n)} / |n|. \quad (47)$$

Then

$$\hat{\Omega}_l^{(\infty)2} = (\kappa_l^{(\infty)2} - 1/r_s^2) / \beta_a^2 \quad (48)$$

where

$$r_s = \{\beta_a^2 / (M_a \omega)^2\}^{1/2} \quad (49)$$

is the sonic radius at which the resultant Mach number $M = M_a(1+\omega^2 r^2)$ is unity. Then we can state that a mode family of the radial order l is of subsonic type

if $\hat{\Omega}_l^{(\infty)2} > 0$, i.e., $1/\kappa_l^{(\infty)2} < r_s^2$, while

a mode family is of supersonic type if

$$\hat{\Omega}_l^{(\infty)2} < 0 \quad \text{i.e.,} \quad 1/\kappa_l^{(\infty)2} > r_s^2.$$

The rationality of this statement is supported by the following demonstration.

When the relative Mach number is less than unity at the tip, i.e., $M_a(1+\omega^2) < 1$, the cut-off boundaries $\Omega_l^{(n)} = 0$ of each mode family become as shown in Fig. 4. In this case all mode families satisfy $1/\kappa_l^{(\infty)2} < r_s^2$, since $r_s > 1$. We can see that there exist only a finite number of cut-on modes for a given frequency λ . Denoting the roots of $\Omega_l^{(n)} = 0$ by $n = n_-(l, \lambda)$ and $n_+(l, \lambda)$, we can state that a mode (n, l) is of cut-on state if $n_-(l, \lambda) < n < n_+(l, \lambda)$. The critical circumferential wave numbers $n_{\pm}(l, \lambda)$ decrease as λ decreases and/or l increases.

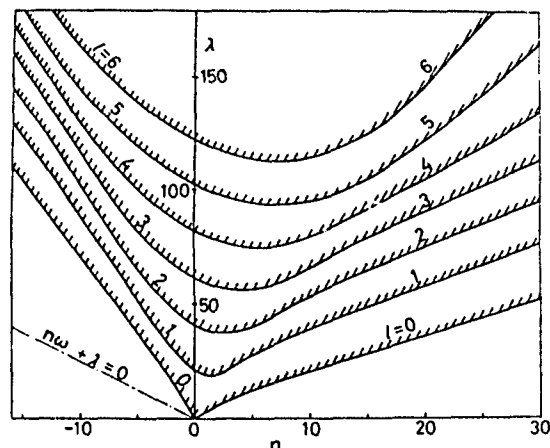


FIG. 4. CUT-OFF BOUNDARIES OF ACOUSTIC MODES IN A SUBSONIC FLOW
 $M_a=0.25$, $h=0.4$, $\omega=2.4744$, $L=7$
Hatched regions denote cut-on state.

When the relative Mach number at the hub is larger than unity, i.e.,

$M_a(1+\omega^2 h^2)^{1/2} > 1$ all mode families satisfy

$1/\kappa_l^{(\infty)2} > r_s^2$, since $r_s^2 < h^2$. Then as

shown in Fig. 5 a mode (n, l) is cut-on if $n > n_+(l, \lambda)$ or $n < n_-(l, \lambda)$. Therefore, in this case there exists an infinite number of cut-on modes for a given frequency λ .

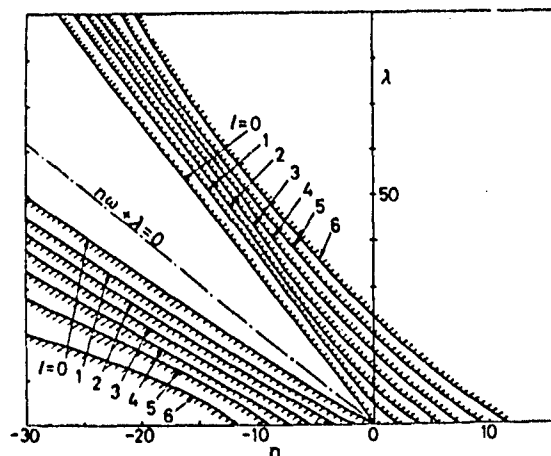


FIG. 5. CUT-OFF BOUNDARIES OF ACOUSTIC MODES IN A SUPERSONIC FLOW
 $M_a=0.8$. Other conditions as in FIG. 4.

When the relative Mach number is larger than unity at the tip and less than unity at the hub, i.e., $M_a(1+\omega^2 h^2)^{1/2} < 1 < M_a(1+\omega^2)^{1/2}$, mode families of subsonic and supersonic types coexist. In fact, as shown in Fig. 6, cut-off boundary curves for families of $1/\kappa_l^{(\infty)2} < r_s^2$ are of subsonic type, while those for families of $1/\kappa_l^{(\infty)2} > r_s^2$ are of supersonic type.

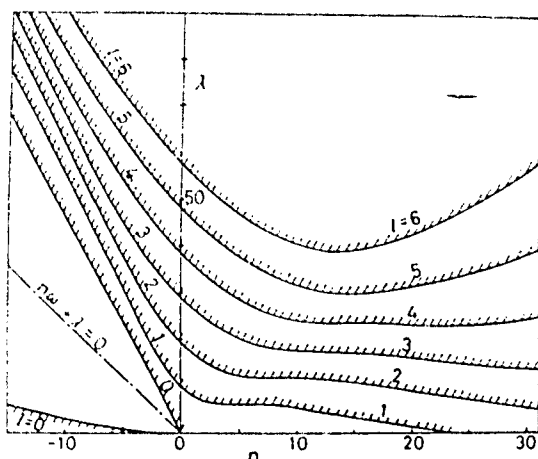


FIG. 6. CUT-OFF BOUNDARIES OF ACOUSTIC MODES IN A TRANSONIC FLOW:
 $M_a = 0.48$
 Other conditions as in FIG. 4.

We can define a critical radial order l_c such that $1/\kappa_{l_c}^{(n)2} < r_s^2 < 1/\kappa_{l_c-1}^{(n)2}$. Thus mode families of $l = 0, 1, \dots, l_c-1$ are of supersonic type, while those of $l = l_c, \dots, L-1$ are of subsonic type. It is noteworthy that a basis function $R_l^{(n)}(r)$ of the subsonic family possesses a highest peak at a subsonic radius $r = 1/\kappa_l^{(n)} < r_s$, while that of the supersonic family possesses a highest peak at a supersonic radius $r = 1/\kappa_l^{(n)} > r_s$.

DISTURBANCE PRESSURE INDUCED BY UNSTEADY LIFTING SURFACES

Hereafter we limit ourselves to the case of blades with zero thickness in subsonic axial flows ($M_a < 1$). Substituting Eq. (19) into Eq. (16), we obtain

$$K_{PL}(r, \theta', z-z_0 | r_0) = -\frac{N}{4\pi\beta_a^2} \sum_{\nu=-\infty}^{\infty} \sum_{l=0}^{\infty} R_l^{(\nu)}(r) R_l^{(\nu)}(r_0) \times (-i\omega r_0 \gamma_l^{(\nu)} - i\nu/r_0) \frac{1}{\Omega_l^{(\nu)}} \times \exp\{i(\gamma_l^{(\nu)} + n\omega)(z-z_0) + i\nu\theta'\}, \quad (50)$$

where

$$\gamma_l^{(\nu)} = (\nu\omega + \lambda) M_a^2 / \beta_a^2 - \text{sgn}(z-z_0) \Omega_l^{(\nu)} / i \quad (51)$$

Applying the finite radial mode expansion to Eq. (50), we obtain

$$K_{PL}(r, \theta', z-z_0 | r_0) = -\frac{N}{4\pi\beta_a^2} \sum_{\nu=-\infty}^{\infty} \sum_{l=0}^{L-1} R_l^{(\nu)}(r) e^{i\nu\theta'} \times \exp\{i(\gamma_l^{(\nu)} + n\omega)(z-z_0)\} r_0 \sum_{k=0}^{L-1} R_k^{(\nu)}(r_0) DB_{lk}^{(\nu)}, \quad (52)$$

where

$$DB_{lk}^{(\nu)} = \frac{i}{\Omega_l^{(\nu)}} \left\{ BB_{lk}^{(\nu)} \frac{M_a^2}{\beta_a^2} \omega (\nu\omega + \lambda) - \nu CB_{lk}^{(\nu)} \right\} - BB_{lk}^{(\nu)} \omega \text{sgn}(z-z_0).$$

The expression of K_{PL} given in Eq. (52) is convenient for modal analysis of the acoustic pressure field. In fact, substitution of Eq. (52) into Eq. (14) leads to

$$p_L(r, \theta, z) = \quad (53)$$

$$= \sum_{\nu=-\infty}^{\infty} \sum_{l=0}^{L-1} R_l^{(\nu)}(r) \exp\{i\gamma_l^{(\nu)} z + i\nu\theta\} FP_{(\pm)}(n, l),$$

for axial stations downstream or upstream of the cascade. Here $FP_{(+)}(n, l)$ and $FP_{(-)}(n, l)$ denote pressure amplitudes of (n, l) acoustic mode at downstream and upstream stations respectively, and they are given by

$$FP_{(\pm)}(n, l) = -\frac{N}{4\pi\beta_a^2} \int_{r_0}^1 r_0 \sum_{k=0}^{L-1} R_k^{(\nu)}(r_0) DB_{lk}^{(\nu)} \times \int_{b(r_0)}^{b(r)} \Delta p_B(r_0, z_0) \exp\{-i(\gamma_l^{(\nu)} + n\omega)z_0\} dz_0. \quad (54)$$

The subscript (+) or (-) of $DB_{lk}^{(\nu)}$

and $\gamma_l^{(\nu)}$ implies the values for $\text{sgn}(z-z_0) = +1$ or -1 respectively.

In the case of transonic or supersonic flows the infinite series with respect to ν in Eq. (53) is divergent, since $\Omega_l^{(\nu)}$ for $l < l_c$ becomes imaginary for large ν . Furthermore, even in the case of subsonic flow, the ν -series is of non-uniform convergence, since the kernel function is singular at dipole locations. To extract the singular parts we can rewrite Eq. (52) into

$$K_{PL}(r, \theta', z-z_0 | r_0) = -\frac{N}{4\pi\beta_a^2} e^{i(M_a^2 \lambda / \beta_a^2)(z-z_0)} r_0 \sum_{j=0}^{L-1} R_j^{(\nu)}(r) \sum_{k=0}^{L-1} R_k^{(\nu)}(r_0) \times \sum_{\nu=-\infty}^{\infty} e^{i\nu(\theta' + (z-z_0)\omega/\beta_a^2)} \sum_{l=0}^{L-1} e^{-\Omega_l^{(\nu)}|z-z_0|} BB_{lj}^{(\nu)} DB_{lk}^{(\nu)}. \quad (55)$$

Noting that

$$\Omega_l^{(\nu)} = i\nu(\Omega_l^{(\nu)} - \frac{M_a^2}{\beta_a^2} \omega \lambda \frac{1}{\Omega_l^{(\nu)}} \text{sgn}(n) + O(n^{-1})),$$

$$BB_{lk}^{(\nu)} = \delta_{lk} + O(n^2), \quad (56)$$

$$DB_{lk}^{(\nu)} = -\{i \text{sgn}(n) \Omega_l^{(\nu)} \beta_a^2 + \omega \text{sgn}(z-z_0)\} \delta_{lk} + O(n^2),$$

for large $|n|$, we can write

$$K_{PL} = K_{PL}^{(B)} + K_{PL}^{(S)} + K_{PL}^{(R)}, \quad (57)$$

where $K_{pLb}^{(s)}(r, \theta', z-z_0|r_0) =$

$$\begin{aligned} & -\frac{N}{4\pi\beta_a^2} r_0 \sum_{l=0}^{L-1} R_l^{(s)}(r_0) R_l^{(s)}(r) e^{i(M_a^2\lambda/\beta_a^2)(z-z_0)} \\ & \times \left[-\{i\beta_a^2 \hat{\Omega}_l^{(s)} + \omega \operatorname{sgn}(z-z_0)\} e^{V_l\lambda|z-z_0|} \right. \\ & \times H^{(N,0)}(\hat{\Omega}_l^{(s)}|z-z_0-i\phi) \\ & - \left. \{-i\beta_a^2 \hat{\Omega}_l^{(s)} + \omega \operatorname{sgn}(z-z_0)\} e^{-V_l\lambda|z-z_0|} \right. \\ & \times \left. H^{(N,-\sigma)}(\hat{\Omega}_l^{(s)}|z-z_0+i\phi) \right], \end{aligned} \quad (58)$$

$$\begin{aligned} & K_{pLp}^{(s)}(r, \theta', z-z_0|r_0) \\ & = -\frac{1}{2} r_0 \sum_{l=0}^{L-1} R_l^{(s)}(r_0) R_l^{(s)}(r) \sum_{m=-\infty}^{\infty} \operatorname{sgn}(\theta' - 2\pi m/N) \\ & \times \exp\{i(m\hat{\sigma} - \beta_l\lambda|\theta' - 2\pi m/N|)\} \\ & \times \delta(z-z_0 + [\theta' - 2\pi m/N]/A_l), \end{aligned} \quad (59)$$

$$\begin{aligned} & K_{pL}^{(R)}(r, \theta', z-z_0|r_0) \\ & = -\frac{N}{4\pi\beta_a^2} \sum_{j=0}^{L-1} R_j^{(s)}(r) \sum_{k=0}^{L-1} r_0 R_k^{(s)}(r_0) e^{i(M_a^2\lambda/\beta_a^2)(z-z_0)} \\ & \times \sum_{\gamma=-\infty}^{\infty} e^{i\pi\gamma} \sum_{l=0}^{L-1} [BB_{lj}^{(x)} DB_{lk}^{(x)} e^{-Q_l^{(x)}|z-z_0|} \\ & + \delta_{lj} \delta_{lk} \varepsilon_{lv} \{i \operatorname{sgn}(\gamma) \hat{\Omega}_l^{(s)} \beta_a^2 + \omega \operatorname{sgn}(z-z_0)\} e^{-V_l^{(x)}|z-z_0|}], \end{aligned} \quad (60)$$

and

$$H^{(N,\sigma)}(x) = e^{-\sigma x} / (e^{Nx} - 1), \quad (61)$$

$$A_l = \omega / \beta_a^2 - \operatorname{sgn}\{\omega(z-z_0)\} |\hat{\Omega}_l^{(s)}|, \quad (62)$$

$$\varepsilon_{lv} = \begin{cases} 0 & : \gamma = 0 \text{ and } l \geq L_m, \\ 1 & : \text{otherwise,} \end{cases} \quad (63)$$

$$\phi = \theta' + (z-z_0)\omega/\beta_a^2,$$

$$V_l^{(x)} = \operatorname{sgn}(\gamma) (n \hat{\Omega}_l^{(s)} - V_l\lambda),$$

$$V_l = M_a^2 \omega / (\beta_a^2 \hat{\Omega}_l^{(s)}), \quad (64)$$

$$\beta_l = M_a^2 / (\beta_a^2 |\hat{\Omega}_l^{(s)}|).$$

The components $K_{pLb}^{(s)}$ and $K_{pLp}^{(s)}$ denote singular parts of subsonic and supersonic types respectively. We should note that the special function $H^{(N,\sigma)}(x)$ defined by Eq. (61) behaves

$$H^{(N,\sigma)}(x) = 1/(Nx) + O(1)$$

as $x \rightarrow 0$. Therefore

$$\begin{aligned} & K_{pLb}^{(s)}(r, \theta', z-z_0|r_0) \\ & = \mp \frac{1}{2} e^{i\hat{\sigma}m} \delta(z-z_0) r_0 \sum_{l=0}^{L-1} R_l^{(s)}(r_0) R_l^{(s)}(r) + O(1) \end{aligned} \quad (65)$$

as $\theta' \rightarrow 2\pi m/N \pm 0$.

On the other hand $K_{pLp}^{(s)}$ possesses the delta function singularity along characteristic lines

$$\begin{aligned} & z-z_0 + (\theta' - 2\pi m/N)/A_l = 0, \\ & (m = 0, 1, \dots, N-1). \end{aligned} \quad (66)$$

These characteristic lines can be interpreted as Mach waves of the l -th radial mode family. In fact, as Fig. 7 shows, they emanate from dipole points on the (θ, z) plane, and the Mach angle μ_l^{\pm} i.e., the angle between the Mach line and a streamline $\theta - \omega z = 0$, is given by

$$\begin{aligned} & \cot \mu_l^{\pm} = \pm \frac{1 - K_l^{(s)2}}{\omega^2 + K_l^{(s)2}} \omega \\ & + \frac{\omega^2 + 1}{\omega^2 + K_l^{(s)2}} \sqrt{M_a^2(\omega^2 + K_l^{(s)2}) - K_l^{(s)2}}. \end{aligned} \quad (67)$$

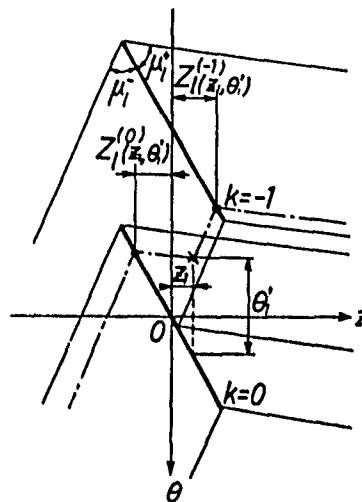


FIG. 7. MACH LINES OF THE l -th RADIAL MODE FAMILY AND DEFINITION OF $Z_l^{(m)}(z, \theta')$

We easily see that

$$\cot \mu_l^{\pm} \rightarrow \sqrt{M_T^2 - 1}$$

as $h \rightarrow 1$, where $M_T = M_a(1 + \omega^2)^{1/2}$ is the tip Mach number. In Table 1 the modal Mach angles are compared with the quasi-two-dimensional local Mach angle $\mu(r)$ defined by

$$\cot \mu(r) = \sqrt{M_a^2(1 + \omega^2 r^2) - 1}. \quad (68)$$

Table 1. Mach angles of each radial mode family μ_l^+ and μ_l^- , and quasi-two-dimensional local Mach angle $\mu(r)$.

(a) $M_a = 0.8$, $h = 0.4$, $\omega = 2.4744$, $L = 7$.

| l | μ_l^+ | μ_l^- | r | $\mu(r)$ |
|-----|-----------|-----------|-----|----------|
| 0 | 28.58° | 27.94° | 1.0 | 27.93° |
| 1 | 30.83° | 27.98° | 0.9 | 30.79° |
| 2 | 34.13° | 28.03° | 0.8 | 34.32° |
| 3 | 39.32° | 28.11° | 0.7 | 38.68° |
| 4 | 48.20° | 28.24° | 0.6 | 44.29° |
| 5 | 64.72° | 28.45° | 0.5 | 51.77° |
| 6 | 94.11° | 28.87° | 0.4 | 62.66° |

(b) $M_a = 0.48$, $h = 0.4$, $\omega = 2.4744$, $L = 7$.

| l | μ_l^+ | μ_l^- | r | $\mu(r)$ |
|-----|-----------|-----------|-----|----------|
| 0 | 53.78° | 51.97° | 1.0 | 51.38° |
| 1 | 63.27° | 54.60° | 0.9 | 58.57° |
| 2 | 80.86° | 60.60° | 0.8 | 69.87° |

In general, the inward Mach angle μ_l^+ is larger than the outward one μ_l^- . The difference between μ_l^+ and μ_l^- as well as the deviation of μ_l^+ or μ_l^- from $\mu(r)$ at $r = 1/\kappa_l^{(-)}$ increases as $1/\kappa_l^{(-)}$ approaches r_0 .

It should be emphasized that the subsonic singular part $K_{plb}^{(S)}$ and the supersonic singular part $K_{plp}^{(S)}$ are dominant at subsonic and supersonic radial stations respectively.

Finally $K_{pl}^{(R)}$ denotes the regular part, which is composed of v series of uniform convergence, as shown in Eq. (60).

UPWASH VELOCITY INDUCED BY LIFTING SURFACES

The disturbance velocities are obtained by integrating the equation of motion (2). Let $\hat{q}_L = q_L(r, \theta', z)e^{i\lambda t}$

be the disturbance velocity associated with the disturbance pressure $p_L(r, \theta, z)e^{i\lambda t}$ and let $q_{Ll}(r, \theta', z)$ be the component of q_L normal to the helical lifting-surfaces. Then

$$q_{Ll}(r, \theta', z) = -\frac{1}{\sqrt{1+\omega^2 r^2}} e^{-i\lambda z} \quad (69)$$

$$\times \int_{-\infty}^z e^{i\lambda z} \left[\left(\frac{1}{r} \frac{\partial}{\partial \theta} - \omega r \frac{\partial}{\partial z} \right) p_L(r, \theta, z) \right]_{\theta=\theta'+\omega z} dz.$$

Substituting Eq. (14) into Eq. (69), we obtain

$$q_{Ll}(r, \theta', z) = \quad (70)$$

$$\frac{1}{\sqrt{1+\omega^2 r^2}} \int_{b_L(r_0)}^{b_T(r_0)} \Delta p_B(r_0, z_0) K_{Ll}(r, \theta', z-z_0|r_0) dz_0,$$

where the upwash kernel function K_{Ll} is obtained from

$$K_{Ll}(r, \theta', z-z_0|r_0) = -e^{-i\lambda z} \quad (71)$$

$$\times \int_{-\infty}^z e^{i\lambda z} \left[\left(\frac{1}{r} \frac{\partial}{\partial \theta} - \omega r \frac{\partial}{\partial z} \right) K_{pl}(r, \theta-\omega z, z-z_0|r_0) \right]_{\theta=\theta'+\omega z} dz.$$

Substitution of Eq. (55) into (71) and integration give

$$K_{Ll}(r, \theta', z-z_0|r_0) = -\frac{N}{4\pi\beta_a^2} r r_0 \sum_{j=0}^{L-1} R_j^{(\omega)}(r) \sum_{k=0}^{L-1} R_k^{(\omega)}(r_0) \quad (72)$$

$$\times \left[-H(z-z_0) e^{-i\lambda(z-z_0)} \sum_{\nu=-\infty}^{\infty} e^{i\nu\theta'} \sum_{l=0}^{L-1} (BM_{ljk}^{(n)} - B_{ljk}^{(n)} + 2\omega^2) \right. \\ \left. - e^{i(M_a^2\lambda/\beta_a^2)(z-z_0)} \sum_{\nu=-\infty}^{\infty} e^{i\nu\phi} \sum_{l=0}^{L-1} BM_{ljk}^{(n)} e^{-\Omega_l^{(n)}|z-z_0|} \right],$$

where

$$BM_{ljk}^{(n)} = DB_{ljk}^{(n)} DB_{ljk}^{(n)} M_l^{(n)}, \quad (73)$$

$$M_l^{(n)} = \Omega_l^{(n)} / \{ \operatorname{sgn}(z-z_0) \Omega_l^{(n)} - i(\pi\omega + \lambda/\beta_a^2) \}.$$

The asymptotic behavior of $BM_{ljk}^{(n)}$ for large n is found to be

$$BM_{ljk}^{(n)} = \delta_{lj} \delta_{lk} \beta_a^2 \hat{\Omega}_l^{(n)} \{ i \operatorname{sgn}(n\omega) - \operatorname{sgn}(z-z_0) \beta_a^2 \hat{\Omega}_l^{(n)} \} \\ - \frac{1}{|\pi|} \delta_{lj} \delta_{lk} \frac{i\lambda \kappa_l^{(n)2}}{\hat{\Omega}_l^{(n)}} + O(n^{-2}). \quad (74)$$

Then separating singular parts, we can rewrite Eq. (72) into

$$K_{Ll} = K_{Ll}^{(Sw)} + K_{Ll}^{(S)} + K_{Ll}^{(B)} + K_{Ll}^{(R)}, \quad (75)$$

where

$$\begin{bmatrix} K_{\tau L}^{(sw)}(r, \theta', z-z_0 | r_0) \\ K_{\tau L}^{(s)}(r, \theta', z-z_0 | r_0) \\ K_{\tau L}^{(s)}(r, \theta', z-z_0 | r_0) \end{bmatrix} =$$

$$-\frac{N}{4\pi\beta_a^2} r_0 \sum_{l=0}^{L-1} R_l^{(w)}(r) R_l^{(w)}(r_0) \begin{bmatrix} KQ_L^{(sw)}(z-z_0, \theta') \\ KQP_L^{(s)}(z-z_0, \theta') \\ KQB_L^{(s)}(z-z_0, \theta') \end{bmatrix}, \quad (76)$$

$$K_{\tau L}^{(R)}(r, \theta', z-z_0 | r_0) =$$

$$-\frac{N}{4\pi\beta_a^2} r_0 \sum_{j=0}^{L-1} R_j^{(w)}(r) \sum_{k=0}^{L-1} R_k^{(w)}(r_0) KQ_{jk}^{(R)}(z-z_0, \theta'), \quad (77)$$

$$KQ_L^{(sw)}(z-z_0, \theta')$$

$$= 2H(z-z_0) e^{-i\lambda(z-z_0) + i\sigma\theta'} \beta_a^4 \hat{\Omega}_L^{(w)2} \quad (78)$$

$$- 2H(z-z_0) e^{-i\lambda(z-z_0) + i\sigma\theta'} (\beta_a^4 \hat{\Omega}_L^{(w)2} + \omega^2)$$

$$\times \frac{2\pi}{N} \sum_{m=-\infty}^{\infty} \delta(\theta' - \frac{2\pi m}{N}),$$

$$KQP_L^{(s)}(z-z_0, \theta')$$

$$= \beta_a^4 |\hat{\Omega}_L^{(w)}| \frac{2\pi}{N} \sum_{m=-\infty}^{\infty} \delta(z-z_0 + [\theta' - 2\pi m/N]/A_L)$$

$$\times e^{i(m\hat{\sigma} - S_L \lambda | \theta' - 2\pi m/N |)} \quad (79)$$

$$+ e^{-iS_L \lambda |A_L| |z-z_0| + i\sigma\{\theta' + (z-z_0)A_L\}}$$

$$\times \left[-\beta_a^4 |\hat{\Omega}_L^{(w)}| A_L - \frac{\lambda \chi_L^{(w)}}{|\hat{\Omega}_L^{(w)}|} \operatorname{sgn}(\omega) \left\{ \frac{i\pi}{N} ST^{(N)}(\theta' + (z-z_0)A_L) \right. \right.$$

$$\left. \left. + ER^{(N)}(\theta' + (z-z_0)A_L) \right\} \right],$$

$$KQB_L^{(s)}(z-z_0, \theta') = -e^{i(M\lambda/\beta_a^2)(z-z_0)}$$

$$\times \left[\beta_a^2 \hat{\Omega}_L^{(w)} \{ i\omega - \operatorname{sgn}(z-z_0) \beta_a^2 \hat{\Omega}_L^{(w)} \} \right.$$

$$\times e^{i\lambda |z-z_0|} H^{(N, \sigma)}(\hat{\Omega}_L^{(w)} |z-z_0| - i\phi)$$

$$+ \beta_a^2 \hat{\Omega}_L^{(w)} \{ -i\omega - \operatorname{sgn}(z-z_0) \beta_a^2 \hat{\Omega}_L^{(w)} \}$$

$$\times e^{-i\lambda |z-z_0|} H^{(N, -\sigma)}(\hat{\Omega}_L^{(w)} |z-z_0| + i\phi)$$

$$- \frac{i\lambda \chi_L^{(w)}}{\hat{\Omega}_L^{(w)}} \left\{ e^{i\lambda |z-z_0|} K^{(N, \sigma)}(\hat{\Omega}_L^{(w)} |z-z_0| - i\phi) \right.$$

$$\left. + e^{-i\lambda |z-z_0|} K^{(N, -\sigma)}(\hat{\Omega}_L^{(w)} |z-z_0| + i\phi) \right\}, \quad (80)$$

$$KQ_{jk}^{(R)}(z-z_0, \theta') = -H(z-z_0) e^{-i\lambda(z-z_0)} \sum_{\gamma=-\infty}^{\infty} e^{i\gamma\theta'}$$

$$\times \sum_{l=0}^{L-1} \{ BM_{lj\gamma}^{(w)} - BM_{lj\gamma}^{(w)} - 2\delta_{lj} \delta_{\gamma k} (1-\delta_{\gamma 0}) \beta_a^2 \hat{\Omega}_l^{(w)2} \}$$

$$- e^{i(M\lambda/\beta_a^2)(z-z_0)} \sum_{\gamma=-\infty}^{\infty} e^{i\gamma\theta'} \sum_{l=0}^{L-1} [BM_{lj\gamma}^{(w)} e^{-\Omega_l^{(w)} |z-z_0|}$$

$$- \delta_{lj} \delta_{\gamma k} (1-\delta_{\gamma 0}) \beta_a^2 \{ i \operatorname{sgn}(\omega) \hat{\Omega}_l^{(w)} - \operatorname{sgn}(z-z_0) \beta_a^2 \hat{\Omega}_l^{(w)2} \}$$

$$- \frac{i\lambda}{|\gamma|} \frac{\chi_L^{(w)2}}{\beta_a^2 \hat{\Omega}_l^{(w)}} \} e^{-\gamma_L^{(w)} |z-z_0|}. \quad (81)$$

Furthermore, special functions $ST(N)(x)$, $ER(N, \sigma)(x)$ and $K(N, \sigma)(x)$ are defined as follows:

$$ST^{(N)}(x) = \begin{cases} 1 - \frac{N}{\pi} (x - \frac{2\pi m}{N}) : \frac{2\pi m}{N} < x < \frac{2\pi(m+1)}{N} \\ 0 : x = \frac{2\pi m}{N} \end{cases}$$

$$m = 0, \pm 1, \dots \quad (82)$$

$$ER^{(N, \sigma)}(x) = -\frac{2\sigma}{N^2} \sum_{n=1}^{\infty} \left\{ \frac{\cos(nNx)}{n^2 - \sigma^2/N^2} - \frac{i\sigma}{N} \frac{\sin(nNx)}{n(n^2 - \sigma^2/N^2)} \right\} \quad (83)$$

$$K^{(N, \sigma)}(x) = -\frac{e^{-\sigma x}}{N} \log(1 - e^{-Nx})$$

$$- \sigma e^{-\sigma x} \sum_{n=1}^{\infty} \frac{e^{-nNx}}{n(n + \sigma/N)}. \quad (84)$$

The first component $K_{\tau L}^{(sw)}$ defined by Eqs. (76) and (78) denotes the main part of the nonacoustic disturbance which is not accompanied by pressure fluctuation. The second term on the right-hand side of Eq. (78) possesses the delta function singularity at wake surfaces. We can omit this term, since the state at a wake surface should be evaluated by a limiting process $\theta' \rightarrow 2\pi m/N \pm 0$.

The second component $K_{\tau L}^{(s)}$ defined by Eqs. (76) and (79) is the singular part of supersonic type. We should note that the special function $ST(N)(x)$ defined by Eq. (82) is the so-called sawtooth function. Therefore, we see that the supersonic singular part $K_{\tau L}^{(s)}$ shows singularities of the delta function and finite discontinuity across Mach lines given by Eq. (66).

The third component $K_{\tau L}^{(s)}$ defined by Eqs. (76) and (80) is the singular part of subsonic type. In fact, noting the properties of the special functions $H(N, \sigma)(x)$ and $K(N, \sigma)(x)$ such that $H(N, \sigma)(x) \sim 1/x$ and $K(N, \sigma)(x) \sim \log x$ as $x \rightarrow 0$, we easily see that

$$KQB_L^{(s)}(z-z_0, 0) \quad (85)$$

$$= \frac{2\beta_a^2}{N} \left(\beta_a^2 \hat{\Omega}_L^{(s)} \frac{1}{z-z_0} - i\lambda \frac{K_L^{(s)2}}{\beta_a^2 \hat{\Omega}_L^{(s)}} \log|z-z_0| \right) + O(1)$$

as $z-z_0 \rightarrow 0$.

The last component $K_{TL}^{(R)}$ defined by Eqs. (77) and (81) denotes the regular part. The first and second terms on the right-hand side of Eq. (81) give non-acoustic and acoustic disturbances respectively. Both v-series are uniformly convergent.

As the supersonic singular part $K_{TL}^{(s)}$ involves the delta function term, we can partially intergrate with respect to z_0 in Eq. (70), obtaining

$$q_{TL}(r, \theta, z) = \frac{1}{\sqrt{1+\omega^2 r^2}} \int_A dr_0 \int_{b_L(r_0)}^{b_T(r_0)} \Delta p_B(r_0, z_0) K_{TL}^*(r, \theta, z-z_0|r_0) dz_0 \quad (86)$$

$$+ \frac{1}{\sqrt{1+\omega^2 r^2}} \int_A r r_0 \sum_{l=0}^{L-1} R_L^{(s)}(r) R_L^{(s)}(r) \sum_{m=m^-}^{m^+} T_L^{(m)}(\theta)$$

$$\times \Delta p_B(r_0, Z_L^{(m)}(z, \theta')) dr_0,$$

where K_{TL}^* implies K_{TL} without the delta function term of Eq. (79), i.e.,

$$K_{TL}^* = K_{TL}^{(SW)} + K_{TL}^{(S)*} + K_{TL}^{(S)} + K_{TL}^{(R)},$$

$$K_{TL}^{(S)*}(r, \theta', z-z_0|r_0) = \quad (87)$$

$$- \frac{N}{4\pi\beta_a^2} r r_0 \sum_{l=0}^{L-1} R_L^{(s)}(r) R_L^{(s)}(r_0) KQP_L^{(S)*}(z-z_0|\theta'),$$

$$KQP_L^{(S)*}(z-z_0, \theta') = \quad (88)$$

$$\exp[-iS_L \lambda |A_L(z-z_0)| + i\sigma\{\theta' + (z-z_0)A_L\}]$$

$$\times [-\beta_a^4 |\hat{\Omega}_L^{(s)} A_L| - \frac{\lambda K_L^{(s)}}{|\hat{\Omega}_L^{(s)}|} \operatorname{sgn}(\omega)]$$

$$\times \left\{ i \frac{2\pi}{N} ST^{(N)}(\theta' + [z-z_0]A_L) + ER^{(N)}(\theta' + [z-z_0]A_L) \right\}.$$

Further (89)

$$T_L^{(m)}(\theta') = -\frac{1}{2} \beta_a^2 |\hat{\Omega}_L^{(m)}| \exp\{i(\hat{\sigma}m - S_L \lambda |\theta' - 2\pi m/N|)\},$$

$$Z_L^{(m)}(z, \theta') = z + (\theta' - 2\pi m/N)/A_L^{(m)}, \quad (90)$$

$$A_L^{(m)} = \omega/\beta_a^2 + \operatorname{sgn}(\theta' - 2\pi m/N) |\hat{\Omega}_L^{(m)}|.$$

As shown in Fig. 7, the function $Z_L^{(m)}(z, \theta')$ implies that the Mach line of the l -th mode family passing through a field point $z=z_1$ and $\theta = \theta'_1 + \omega z_1$ in the (θ, z) plane starts from a point of $z = Z_L^{(m)}(z_1, \theta'_1)$ on the m -th blade. Moreover, m^+ and m^- denote, respectively, the upper and lower limits of the blade number m that satisfies

$$b_L(r_0) \leq Z_L^{(m)}(z, \theta') \leq b_T(r_0). \quad (91)$$

Other components of the disturbance velocity q_L are obtainable in the same way as q_{TL} . The resulting expressions are given by Namba (1986).

INTEGRAL EQUATION

Here we confine ourselves to the blade vibration problem. It is required to evaluate unsteady loadings on blades whose circumferential displacement is given by

$$\tilde{f}_m(r, z, t) = f(r, z) e^{i\lambda t + i\hat{\sigma}m}. \quad (92)$$

Then the boundary condition on the blade surfaces can be described by

$$q_{TL}(r, 0, z) = b(r, z)/\sqrt{1+\omega^2 r^2}, \quad (93)$$

where

$$b(r, z) = (i\lambda + \frac{\partial}{\partial z}) f(r, z). \quad (94)$$

Substituting Eq. (86) into Eq. (93), we obtain an integral equation for the unsteady loading function $\Delta p_B(r_0, z_0)$ as follows:

$$\int_A dr_0 \int_{b_L(r_0)}^{b_T(r_0)} \Delta p_B(r_0, z_0) K_{TL}^*(r, 0, z-z_0|r_0) dz_0$$

$$+ \int_A r r_0 \sum_{l=0}^{L-1} R_L^{(s)}(r) R_L^{(s)}(r_0)$$

$$\times \sum_{m=m^-}^{m^+} T_L^{(m)}(0) \Delta p_B(r_0, Z_L^{(m)}(z, 0)) dr_0$$

$$= b(r, z). \quad (95)$$

Analytical inversion of the integral equation is generally impossible, and hence we have to solve it numerically. For convenient numerical treatment let us use a locally normalized axial coordinate \bar{z} defined by

$$\bar{z} = \{z - c_M(r)\}/c_A(r), \quad (96)$$

where $c_M(r)$ denotes the mid-chord axial position and $c_A(r)$ denotes the axial chord length, i.e.,

$$c_M(r) = \{b_T(r) + b_L(r)\}/2, \quad (97)$$

$$c_A(r) = b_T(r) - b_L(r).$$

Then Eq. (95) can be rewritten into

$$\int_A c_A(r_0) dr_0 \int_{-1/2}^{1/2} \Delta p_B(r_0, \bar{z}_0) K_{TL}(r, 0, g(r, \bar{z})$$

$$- g(r, \bar{z}_0)|r_0) d\bar{z}_0$$

$$\begin{aligned}
& + \int_k^1 r_0 \sum_{l=0}^{l_m-1} R_l^{(m)}(r) R_l^{(m)}(r_0) \\
& \times \sum_{m=m^-}^{m^+} T_l^{(m)}(0) \Delta p_B(r_0, \bar{z}_l^{(m)}(r, \bar{z})) dr_0 \\
& = b(r, \bar{z}),
\end{aligned} \quad (98)$$

where

$$g(r, \bar{z}) = C_a(r) \bar{z} + C_M(r), \quad (99)$$

$$\bar{z}_l^{(m)}(r, \bar{z}) = \{ Z_l^{(m)}(g(r, \bar{z}), 0) - C_M(r) \} / C_a(r) \quad (100)$$

Furthermore, $\Delta p_B(r_0, z_0)$ and $b(r, z)$ are replaced by $\Delta p_B(r_0, \bar{z}_0)$ and $b(r, \bar{z})$ respectively.

Various numerical methods developed for solving the integral equation for a single airfoil will be applied to the present problem. These methods are classified into three categories; the discrete element method, the mode function method and the hybrid method.

THE DISCRETE ELEMENT METHOD

The method consists of determining $\Delta p_B(r_0, z_0)$ at a finite number of load points (r_{0i}, z_{0j}) ($i = 1, 2, \dots, I; j = 1, 2, \dots, J$) by making Eq. (98) satisfied at the same number of control points (r_{α}, z_{β}) ($\alpha = 1, 2, \dots, I; \beta = 1, 2, \dots, J$). We should note here that the load function $\Delta p_B(r_0, z_0)$ has the singularity of inverse square root at the subsonic leading edge. Thus

$$\Delta p_B(r, z) = \begin{cases} O(1/\sqrt{1/2 + \bar{z}}) & \text{at the subsonic leading edge, (101)} \\ O(1/\sqrt{1/2 - \bar{z}}) & \text{at the subsonic trailing edge,} \\ O(1) & \text{at the super-sonic edges.} \end{cases}$$

Therefore it is better to put

$$\Delta p_B(r, \bar{z}) = P(r_0, \bar{z}_0) / \sqrt{1/4 - \bar{z}_0^2}, \quad (102)$$

and determine numerical values of which is bounded everywhere. Furthermore since

$$P(r_0, \bar{z}_0) = \begin{cases} O(1) & \text{at the subsonic l.e. (103)} \\ O(1/2 - \bar{z}_0) & \text{at the subsonic t.e.} \\ O(\sqrt{1/2 - \bar{z}_0}) & \text{at the super-sonic t.e.} \\ O(\sqrt{1/2 + \bar{z}_0}) & \text{at the super-sonic l.e.} \end{cases}$$

we can assume the Kutta condition

$$P(r_0, 1/2) = 0 \quad (104)$$

over the whole span irrespective of whether the local flow velocity is subsonic or supersonic.

Now substituting Eq. (102) into Eq. (98) and approximating the integrals by numerical integrations, we obtain a set of algebraic equations for $P(r_{0i}, \bar{z}_{0j})$ ($i = 1, 2, \dots, I; j = 1, 2, \dots, J$):

$$\begin{aligned}
& \sum_{i=1}^I \Delta r_{0i} C_a(r_{0i}) \sum_{j=1}^J \Delta \bar{z}_{0j} P(r_{0i}, \bar{z}_{0j}) / \sqrt{1/4 - \bar{z}_{0j}^2} \\
& \times K_{CL}^*(r_{\alpha}, 0, g(r_{\alpha}, \bar{z}_{\beta}) - g(r_{0i}, \bar{z}_{0j}) | r_{0i}) \\
& + r_{\alpha} \sum_{i=1}^I \Delta r_{0i} r_{0i} \sum_{l=0}^{l_m-1} R_l^{(m)}(r_{\alpha}) R_l^{(m)}(r_{0i}) \\
& \times \sum_{m=m^-}^{m^+} T_l^{(m)}(0) \left[\frac{1}{4} - \{ Z_l^{(m)}(r_{\alpha}, \bar{z}_{\beta}) \}^2 \right]^{-1/2} \\
& \times \sum_{j=1}^J E_j(\bar{z}_l^{(m)}(r_0, \bar{z}_{\beta}) P(r_{0i}, \bar{z}_{0j}) \\
& = b(r_{\alpha}, \bar{z}_{\beta}), \\
& \alpha = 1, 2, \dots, I; \beta = 1, 2, \dots, J.
\end{aligned} \quad (105)$$

Here $E_j(\bar{z})$ is an interpolation function such that

$$P(r_{0i}, \bar{z}) = \sum_{j=1}^J E_j(\bar{z}) P(r_{0i}, \bar{z}_{0j}), \quad (106)$$

and $\Delta \bar{z}_{0j}$ and Δr_{0i} are weights of related numerical formulae. The Kutta condition (104) should be taken into account in determination of $\Delta \bar{z}_{0j}$.

The formulation of the discrete element method is simple, but in order to attain high accuracy in the numerical evaluation of integrals a large number of control points is needed.

THE MODE FUNCTION METHOD

In this method $\Delta p_B(r_0, \bar{z}_0)$ is expanded with appropriate mode functions. In the present system the most suitable radial mode functions will be $R_l^{(m)}(r)$.

$$\text{Let us put } \Delta p_B(r_0, \bar{z}_0) = \sum_{k=0}^{L-1} G_k(\bar{z}_0) R_k^{(m)}(r_0) \quad (107)$$

Substitution of Eq. (107) into Eq. (98) gives

$$\begin{aligned}
& \int_{-1/2}^{1/2} \sum_{k=0}^{L-1} G_k(\bar{z}_0) IRKT_k(r, g(r, \bar{z}) | \bar{z}_0) d\bar{z}_0 \\
& + \sum_{k=0}^{L-1} \sum_{l=0}^{l_m-1} \sum_{m=m^-}^{m^+} G_k(\bar{z}_0^{(m)}(r, \bar{z})) IR T_{lk}^{(m)}(r, \bar{z}) \\
& = b(r, \bar{z}),
\end{aligned} \quad (108)$$

where

$$\begin{aligned}
IRKT_k(r, g(r, \bar{z}) | \bar{z}_0) &= \int_{r_0}^1 R_k^{(m)}(r) \\
&\times K_{CL}^*(r, 0, g(r, \bar{z}) - g(r_0, \bar{z}_0) | r_0) C_a(r_0) dr_0,
\end{aligned} \quad (109)$$

$$ITR_{\ell k}^{(m)}(r, \bar{z}) = \quad (110)$$

$$r R_{\ell}^{(m)}(r) \int_{r_0}^1 R_{\ell}^{(m)}(r_0) R_{\ell}^{(m)}(r_0) \alpha_{\ell}^{(m)}(r, \bar{z} | r_0) dr_0,$$

and $\alpha_{\ell}^{(m)}(r, \bar{z})$ is defined by

$$\alpha_{\ell}^{(m)}(r, \bar{z}) = \begin{cases} T_{\ell}^{(m)}(0) : m^- \leq m \leq m^+, \\ 0 : m < m^- \text{ or } m > m^+. \end{cases} \quad (111)$$

Eq. (108) is the integral equation for $G_k(\bar{z}_0)$. We can further expand the unknown functions $G_k(\bar{z}_0)$ with suitable chordwise mode functions. However, special attention should be paid to the fact that chordwise pressure distributions at subsonic spans are of different form from those at supersonic spans. In this regard we should recall that the radial mode function $R_k^{(m)}(r)$ of the k -th order is dominant near the radial station $r = 1/\chi_k^{(m)}$. Consequently $G_k(\bar{z}_0)$ for $0 < k < \ell_m - 1$ should be of supersonic profile, while $G_k(\bar{z}_0)$ for $\ell_m < k < L-1$ should be of subsonic profile.

Another difficulty with respect to the chordwise mode function expansion arises from the fact that the chordwise variation of $\Delta p_B(r_0, \bar{z}_0)$ is in general discontinuous at supersonic spans because of reflection of Mach waves emanating from leading and trailing edges of adjacent blades. One of the ways to overcome this difficulty is to apply Nagashima and Whitehead's technique (1977). Application of this technique to the case of unswept blades is described below.

In the case of unswept blades, i.e.,

$$\begin{aligned} b_T(r) &= b_T = \text{constant}, \\ b_L(r) &= b_L = \text{constant}, \\ c_M(r) &= 0, \text{ and } c_a(r) = c_a = \text{constant}, \end{aligned} \quad (112)$$

the function $g(r, \bar{z})$ defined by Eq. (99) becomes independent of r , i.e.,

$$g(r, \bar{z}) = c_a \bar{z} \quad (113)$$

Furthermore m^+ and m^- which are respectively upper and lower limits of integer m that satisfies

$$b_L \leq Z_{\ell}^{(m)}(c_a \bar{z}, 0) \leq b_U \quad (114)$$

are no longer dependent upon r and r_0 . Then integration with respect to r_0 in Eqs. (109) and (110) is easily carried out, giving

$$\begin{aligned} K T_{\ell k}(r, \bar{z} - \bar{z}_0) &= I R K T_{\ell k}(r, c_a \bar{z} | \bar{z}_0) \\ &= -\frac{N}{4\pi B_k^2} r \left[\int_{r_0}^1 R_{\ell}^{(m)}(r) K Q_{\ell k}^{(m)}(c_a \bar{z} - c_a \bar{z}_0, 0) \right. \end{aligned}$$

$$+ R_{\ell k}^{(m)}(r) K Q_{\ell k}^{(SM)}(c_a \bar{z} - c_a \bar{z}_0, 0) \quad (115)$$

$$+ R_{\ell k}^{(m)}(r) \left\{ \begin{aligned} &K Q P_{\ell k}^{(S)*}(c_a \bar{z} - c_a \bar{z}_0, 0) : 0 \leq k \leq \ell_m - 1 \\ &K Q B_{\ell k}^{(S)}(c_a \bar{z} - c_a \bar{z}_0, 0) : \ell_m \leq k \leq L-1 \end{aligned} \right\}$$

$$ITR_{\ell k}^{(m)}(r, \bar{z}) = \delta_{\ell k} r R_{\ell k}^{(m)}(r) T_{\ell k}^{(m)}(0). \quad (116)$$

Therefore Eq. (108) becomes

$$\int_{-1/2}^{1/2} \sum_{k=0}^{L-1} G_k(\bar{z}_0) K T_{\ell k}(r, \bar{z} - \bar{z}_0) d\bar{z}_0 \quad (117)$$

$$- \frac{1}{2} \beta_a^2 r \sum_{k=0}^{\ell_m-1} R_{\ell k}^{(m)}(r) |\hat{D}_k^{(m)}| \sum_{m=m^-}^{m^+} e^{im\tau_k} G_k(Z_k^{(m)}(r, \bar{z})) = b(r, \bar{z}),$$

where

$$\tau_k = \frac{2\pi}{N} \{ \sigma - \text{sgn}(m) S_k \lambda \} = \begin{cases} \tau_k^+ : m > 0 \\ \tau_k^- : m < 0 \end{cases} \quad (118)$$

The functions $G_k(\bar{z})$ of subsonic radial mode families ($k = \ell_m, \dots, L-1$) are expected to be of subsonic profile. On the other hand each $G_k(\bar{z})$ of supersonic radial mode families ($k = 0, 1, \dots, \ell_m - 1$) will be of supersonic profile with discontinuous variation at reflection points of the k -th mode Mach waves coming from the leading and trailing edges of adjacent blades. The \bar{z} coordinates of the reflection points shown in Fig. 8 are given by

$$\begin{aligned} \bar{z}_{T1}^{(k)} &= 1/2 - \bar{z}_x^{(k)}, \\ \bar{z}_{LDm}^{(k)} &= -1/2 + m \bar{z}_x^{(k)} - (m-1) \bar{z}_x^{(k)} : m = 1, 2, \dots \\ \bar{z}_{LUm}^{(k)} &= -1/2 + m \bar{z}_x^{(k)} : m = 1, 2, \dots \end{aligned} \quad (119)$$

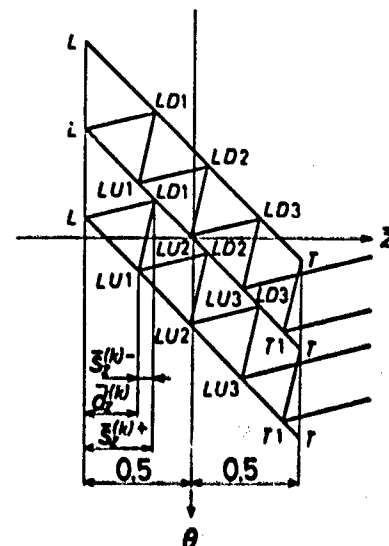


FIG. 8. REFLECTION PATTERN OF MACH LINES OF THE k -th RADIAL MODE FAMILY

where

$$\left. \begin{aligned} \bar{S}_z^{(k)\pm} &= \frac{2\pi}{N} / \left(\frac{\omega}{\beta_z^2} \mp |\hat{\Omega}_k^{(\omega)}| \right), \\ \bar{d}_z^{(k)} &= \bar{S}_z^{(k)+} - \bar{S}_z^{(k)-}, \end{aligned} \right\} \quad (120)$$

Their physical meanings are indicated in Fig. 8.

Now applying Nagashima and Whitehead's technique (1977), we express $G_k(\bar{z})$ of supersonic mode families as a superposition of continuous functions, putting

$$G_k(\bar{z}) = g_b^{(k)}(\bar{z}) \quad \text{for } l_0 \leq k \leq L-1, \quad (121)$$

$$G_k(\bar{z}) \quad (122)$$

$$\begin{aligned} &= \sum_{\alpha=1}^{\alpha_U^{(k)}} G U_{\alpha}^{(k)} D(\bar{z}; Z U_{\alpha}^{(k)-}, Z U_{\alpha}^{(k)+}) g_p^{(k)}(\bar{z} + Z U_{\alpha}^{(k)}) \\ &+ \sum_{\alpha=1}^{\alpha_D^{(k)}} G D_{\alpha}^{(k)} D(\bar{z}; Z D_{\alpha}^{(k)-}, Z D_{\alpha}^{(k)+}) g_p^{(k)}(\bar{z} + Z D_{\alpha}^{(k)}) \\ &+ g_p^{(k)}(\bar{z}) \quad \text{for } 0 < k < l_0 - 1, \end{aligned}$$

where the special function $D(z; z_1, z_2)$ is defined by

$$D(z; z_1, z_2) = \begin{cases} 1 & : z_1 \leq z \leq z_2 \\ 0 & : z < z_1 \text{ or } z > z_2 \end{cases} \quad (123)$$

Definitions of $GU_{\alpha}^{(k)}$, $GD_{\alpha}^{(k)}$, $ZU_{\alpha}^{(k)}$, $ZD_{\alpha}^{(k)}$, $ZU_{\alpha}^{(k)\pm}$ and $ZD_{\alpha}^{(k)\pm}$ are shown in Table 2. Furthermore, integral numbers $\alpha_U^{(k)}$ and $\alpha_D^{(k)}$ are defined in Table 3.

It is easy to see that Eq. (122) leads to

$$\sum_{m=-\infty}^{m^+} e^{im\tau_k} G_k(\bar{z}_k^{(m)}(r, \bar{z})) = g_p^{(k)}(\bar{z}). \quad (124)$$

Therefore Eq. (117) becomes

$$\begin{aligned} &\int_{-1/2}^{1/2} \left\{ \sum_{k=0}^{l_0-1} g_p^{(k)}(\bar{z}_0) K T_k^*(r, \bar{z} - \bar{z}_0) \right. \\ &\quad \left. + \sum_{k=l_0}^{L-1} g_b^{(k)}(\bar{z}_0) K T_k(r, \bar{z} - \bar{z}_0) \right\} d\bar{z}_0 \\ &- \frac{1}{2} \beta_z^2 r \sum_{k=0}^{l_0-1} R_k^{(\omega)}(r) |\hat{\Omega}_k^{(\omega)}| g_p^{(k)}(\bar{z}) \\ &= b(r, \bar{z}), \end{aligned} \quad (125)$$

where

$$\begin{aligned} &K T_k^*(r, \bar{z} - \bar{z}_0) = K T_k(r, \bar{z} - \bar{z}_0) \\ &+ \sum_{\alpha=1}^{\alpha_U^{(k)}} G U_{\alpha}^{(k)} D(\bar{z}_0; Z U_{\alpha}^{(k)-}, Z U_{\alpha}^{(k)+}) K T_k(r, \bar{z} - \bar{z}_0 + Z U_{\alpha}^{(k)}) \\ &+ \sum_{\alpha=1}^{\alpha_D^{(k)}} G D_{\alpha}^{(k)} D(\bar{z}_0; Z D_{\alpha}^{(k)-}, Z D_{\alpha}^{(k)+}) K T_k(r, \bar{z} - \bar{z}_0 + Z D_{\alpha}^{(k)}), \end{aligned}$$

Table 2. Definitions of factors related to Mach wave reflection.

| α | $GU_{\alpha}^{(k)}$ | $ZU_{\alpha}^{(k)}$ |
|----------|---|---|
| 2m-1 | $\begin{smallmatrix} m & m-1 \\ U & D \\ k & K \end{smallmatrix}$ | $\begin{smallmatrix} -(k)- \\ s_z \end{smallmatrix} - (m-1) \bar{d}_z^{(k)}$ |
| 2m | $\begin{smallmatrix} m & m1 \\ U_k & D_k \end{smallmatrix}$ | $-m \bar{d}_z^{(k)}$ |
| α | $GD_{\alpha}^{(k)}$ | $ZD_{\alpha}^{(k)}$ |
| 2m-1 | $\begin{smallmatrix} m & m-1 \\ D & U \\ k & k \end{smallmatrix}$ | $\begin{smallmatrix} -(k)+ \\ -s_z \end{smallmatrix} - (m-1) \bar{d}_z^{(k)}$ |
| 2m | $\begin{smallmatrix} m & m \\ D_k & U_k \end{smallmatrix}$ | $-m \bar{d}_z^{(k)}$ |
| α | $ZU_{\alpha}^{(k)-}$ | $ZU_{\alpha}^{(k)+}$ |
| 2m-1 | $-1/2 + (m-1) \bar{d}_z^{(k)}$ | $1/2 - \bar{s}_z^{(k)-}$ |
| 2m | $-1/2 + \bar{s}_z^{(k)+} + (m-1) \bar{d}_z^{(k)}$ | $1/2$ |
| α | $ZD_{\alpha}^{(k)-}$ | $ZD_{\alpha}^{(k)+}$ |
| 2m-1 | $-1/2 + \bar{s}_z^{(k)+} + (m-1) \bar{d}_z^{(k)}$ | $1/2$ |
| 2m | $-1/2 + m \bar{d}_z^{(k)}$ | $1/2 - \bar{s}_z^{(k)-}$ |

$$U_k = -\exp(-i\tau_k), \quad D_k = -\exp(i\tau_k),$$

$m = 1, 2, \dots$

Table 3. Definitions of α_U and α_D .

| CONDITION | $\alpha_U^{(k)}$ | $\alpha_D^{(k)}$ |
|--|------------------|------------------|
| $\begin{smallmatrix} -(k)- \\ s_z \end{smallmatrix} > 1$ | 0 | 0 |
| $1 > \begin{smallmatrix} -(k)- \\ s_z \end{smallmatrix} > 0$ and $\begin{smallmatrix} -(k)+ \\ s_z \end{smallmatrix} > 1$ | 1 | 0 |
| ----- | | |
| $\begin{smallmatrix} -(k)+ \\ s_z \end{smallmatrix} > m \begin{smallmatrix} -(k)+ \\ s_z \end{smallmatrix} - (m-1) \begin{smallmatrix} -(k)- \\ s_z \end{smallmatrix} > 0$ and $\begin{smallmatrix} (m+1) \begin{smallmatrix} -(k)+ \\ s_z \end{smallmatrix} - m \begin{smallmatrix} -(k)- \\ s_z \end{smallmatrix} > 1 \end{smallmatrix}$ | 2m+1 | 2m |
| $m = 0, 1, 2, \dots$ | | |

$$ZU_{\alpha}^{(k)\pm} = ZU_{\alpha}^{(k)\pm} + ZU_{\alpha}^{(k)}, \quad (127)$$

$$ZD_{\alpha}^{(k)\pm} = ZD_{\alpha}^{(k)\pm} + ZD_{\alpha}^{(k)}$$

Eq. (125) is an integral equation for

continuous functions $g_b^{(k)}(\bar{z})$ and $g_p^{(k)}(\bar{z})$. We can further expand them into chordwise mode function series, e.g.,

$$g_p^{(k)}(\bar{z}) = \sum_{m=0}^{L-1} P_m^{(k)} \cos m\bar{x} : 0 \leq k \leq L-1$$

$$g_b^{(k)}(\bar{z}) = P_0^{(k)} \cot \frac{\bar{x}}{2} + \sum_{m=1}^{L-1} P_m^{(k)} \sin m\bar{x} : \quad (128)$$

where $l_0 \leq k \leq L-1$

$$x = \text{Arccos}(-2\bar{z}) : 0 \leq x \leq \pi. \quad (129)$$

Then Eq. (125) becomes

$$\sum_{k=0}^{L-1} \sum_{m=0}^{L-1} P_m^{(k)} IT_{k,m}(r, \bar{z}) = b(r, \bar{z}) \quad (130)$$

$$IT_{k,m}(r, \bar{z}) = \frac{1}{2} \int_0^\pi KT_k^*(r, \bar{z} + \frac{1}{2} \cos \xi) \cos m\xi \sin \xi d\xi$$

$$- \frac{1}{2} \beta_a^2 r R_k^{(0)}(r) |\hat{\Omega}_k^{(0)}| \cos m\bar{x} : 0 \leq k \leq l_0-1, \quad (131)$$

$$IT_{k,m}(r, \bar{z}) =$$

$$\frac{1}{2} \int_0^\pi KT_k(r, \bar{z} + \frac{1}{2} \cos \xi) \left\{ \begin{array}{l} (1 + \cos \xi) : m=0 \\ \sin m\xi \sin \xi : m \geq 1 \end{array} \right\} d\xi$$

$$l_0 \leq k \leq L-1$$

Making (130) satisfied at $L \times I$ control points $(r_\alpha, \bar{z}_\beta)$ ($\alpha = 1, 2, \dots, L$; $\beta = 1, 2, \dots, I$), we can determine coefficients $P_m^{(k)}$ ($k = 0, 1, \dots, L-1$; $m = 0, 1, \dots, I-1$).

THE HYBRID METHOD

We can determine $G_k(\bar{z}_0)$ ($k = 0, 1, \dots, L-1$) of Eq. (107) at a finite number of chord points $\bar{z}_0 = \bar{z}_{0i}$ ($i = 1, 2, \dots, I$) by making Eq. (108) satisfied at $L \times I$ control points $(r_\alpha, \bar{z}_\beta)$ ($\alpha = 1, 2, \dots, L$; $\beta = 1, 2, \dots, I$). This may well be called the hybrid method.

EXAMPLE CALCULATION AND TRENDS OF THREE-DIMENSIONAL EFFECTS

Here we limit ourselves to unswept blades and two types of vibrations: pure bending vibration and pure torsional vibration about mid-chord axis, for which the normal displacement of a blade

$$f(r, \bar{z}) e^{i\lambda t / \sqrt{1+\omega^2 r^2}} \text{ is specified by}$$

$$f(r, \bar{z}) / \sqrt{1+\omega^2 r^2} = H C_n a_j^{(b)}(r) / \sqrt{1+\omega^2 r^2} \quad (133)$$

$$f(r, \bar{z}) / \sqrt{1+\omega^2 r^2} = \Theta a_k^{(t)}(r) (1+\omega^2 r^2)^{1/2} \bar{z} \quad (134)$$

respectively. Here $a_j^{(b)}(r)$ and $a_k^{(t)}(r)$

denote the spanwise mode shapes of the j -th order bending and k -th order torsional vibrations respectively, and H and Θ denote the circumferential displacement amplitude and twist angle amplitude at the tip respectively. As to

$a_j^{(b)}(r)$ and $a_k^{(t)}(r)$, the natural mode shapes of a uniform cantilever beam are assumed.

This problem has been treated by Namba and Ishikawa (1983) and Namba (1976), where $R_k^{(0)}(r)$ are used as basis functions instead of $R_k^{(0)}(r)$. Furthermore, Namba (1976) employed the mode function method with $L \times I = 7 \times 6$ control points to treat the subsonic blade row, while Namba and Ishikawa (1983) used the hybrid method with $L \times I = 7 \times 8$ control points to treat transonic and supersonic blade rows.

Recently, calculations using basis functions $R_k^{(0)}(r)$ as described here and the mode function method have been performed by the author and his colleague. From the mathematical point of view the present method is expected to give more reliable results than previous ones. It has been revealed that the numerical results of Namba and Ishikawa (1983) and Namba (1976) are all in good agreement with those obtained by the present method except the local load distributions $\Delta p_b(r, z)$ in the case of transonic flows. Disagreement in this case, however, has been found to give no fatal difference in the integrated total load on a blade. Therefore, all examples except Fig. 11 are quoted from Namba and Ishikawa (1983) and Namba (1976). In general, for the cascade geometries of practical interest, e.g., the hub/tip ratio $h = 0.4$, the number of blades $N = 30$, the axial chord to blade height ratio $c_a/(1-h) = 0.1$ and the circumferential tip speed to axial flow velocity ratio $\omega = 2.5$, the mode function method described in the previous section will give results of reasonable accuracy with 7×8 control points as long as the frequency parameter λC_a is at most of order 1.

As a measure of the three-dimensional effect we adopt the difference between prediction by the present lifting surface theory and that by the strip theory.

At this stage particular mention should be made of predominant acoustic modes. As shown by Eq. (53), blade vibrations give rise to disturbance pressure fields composed of an infinite number of acoustic modes (n, i) , where n and i denote the circumferential wave number and radial mode number respectively. We should note that allowed n are such that $n = vN + \sigma$ ($v = 0, \pm 1, \pm 2, \dots$), where N denotes the number of blades and $2\sigma/N$ denotes the inter-blade phase angle. In general, $(0, 0)$ is the most dominant mode and $(0, 1)$ is the second most for the first order of

bending or torsional vibration. On the other hand $(0,1)$ is the most dominant and $(0,0)$ is the second most for the second second order bending or torsional vibration. As shown below the blade loading becomes very sensitive to change in parameters near the resonances of the predominant acoustic modes. Furthermore, the magnitude of the three-dimensional effect largely depends upon whether the predominant acoustic modes are of cut-on state or not.

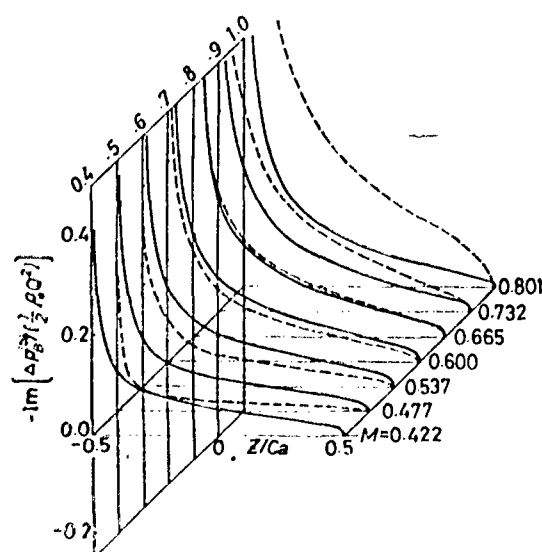
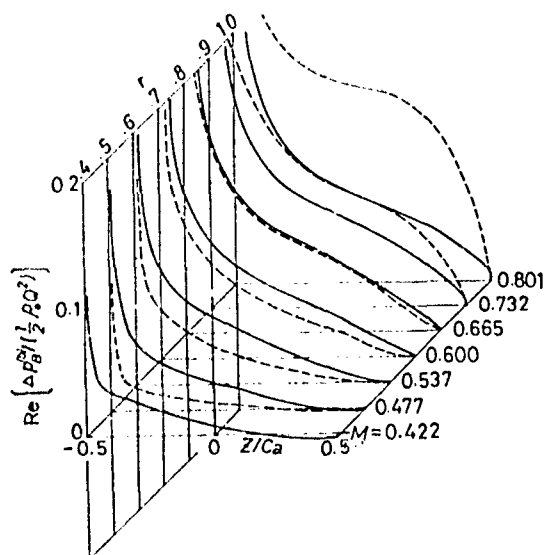


FIG. 9. UNSTEADY BLADE LOADING DISTRIBUTION FOR THE FIRST ORDER BENDING VIBRATION IN A SUBSONIC FLOW: $h=0.4$, $\omega=2.4744$, $\lambda c_a=0.2$, $\sigma/N=0.2$, $N=30$, $Nc_a=2$, $M_a=0.3$. M denotes the local relative Mach number.
 — lifting surface theory,
 - - - strip theory

Figs. 9, 10, and 11 show the distributions of the blade loading $\Delta p_B(r,z)$ in subsonic, supersonic and transonic flows respectively. For comparison the strip theory predictions are also shown by dotted lines. In these figures $\text{Re}[\]$ and $\text{Im}[\]$ imply real and imaginary parts respectively. Furthermore ρ_0 and Q denote the fluid density and relative flow velocity at the undisturbed state, and hence $\rho_0 = 1$ and $Q = \sqrt{1+\omega^2 r^2}$ according to the present nondimensionalization.

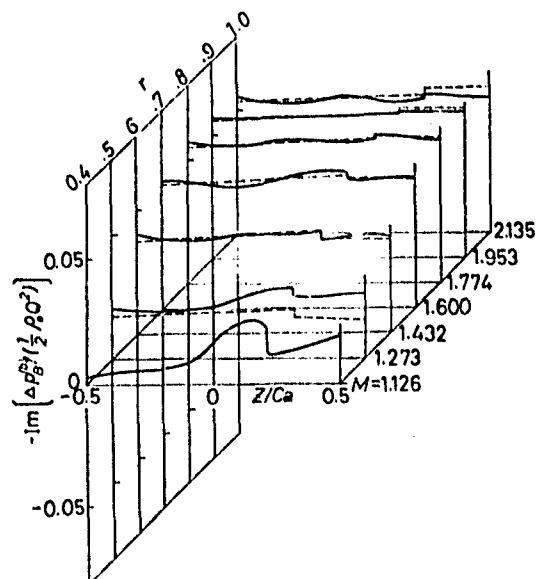
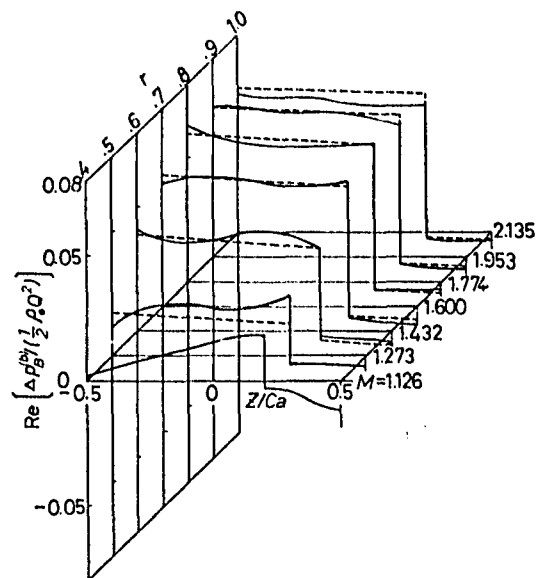


FIG. 10. UNSTEADY BLADE LOADING DISTRIBUTION FOR THE FIRST ORDER BENDING VIBRATION IN A SUPERSONIC FLOW: $M_a=0.8$. Other conditions as in FIG. 9.

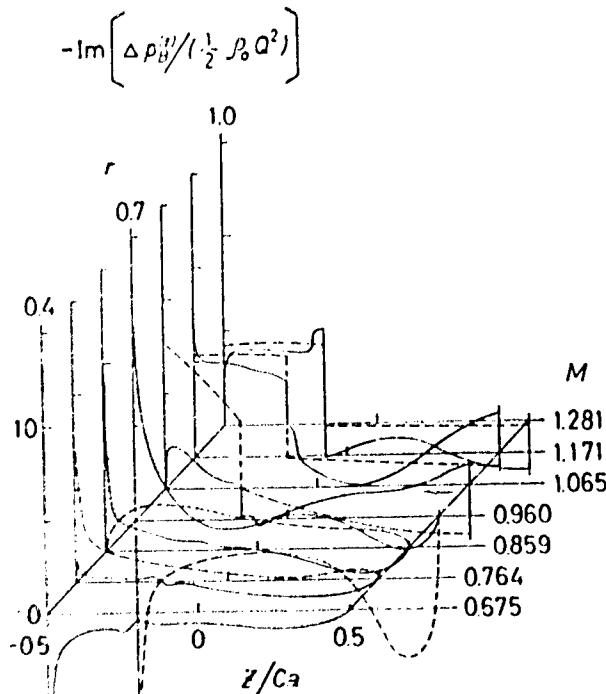
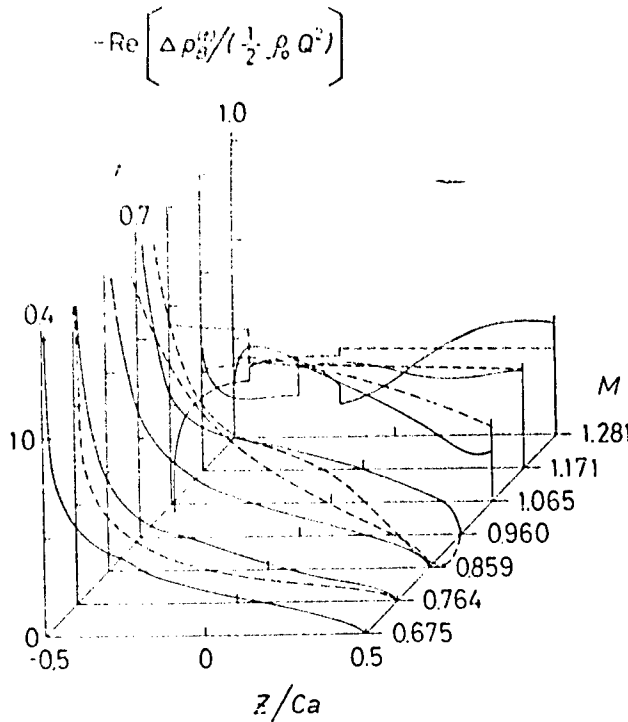


FIG. 11. UNSTEADY BLADE LOADING DISTRIBUTION FOR THE FIRST ORDER TORSIONAL VIBRATION IN A TRANSONIC FLOW: $Nc_a=2.2$, $N=35$, $M_a=0.48$. Other conditions as in FIG. 9.

First it must be noted that the difference between the lifting surface theory and strip theory predictions is remarkably small in the case of the supersonic flow (Fig. 10) except near the root $r = 0.4$, where the strip theory gives $\Delta p_B(r, z) = 0$ because of zero blade displacement.

In the case of the subsonic flow (Fig. 9), the three-dimensional effect appears in the same fashion as in the steady flow, Namba (1972). Thus the three-dimensional effect reduces the spanwise gradient of the blade loading distribution, decreasing the loadings near the tip and increasing those near the hub.

This phenomenon can be attributed to the effect of upwash velocity induced by the streamwise component of trailing vorticities, as is well known in the steady three-dimensional wing theory. Furthermore, this effect generally decreases as the frequency increases. To prove it, let us consider a lifting line placed along the y axis in an incompressible flow with velocity U as shown in Fig. 12. Let the circulation of the lifting line be $\Gamma(\eta)e^{i\omega t}$ at $y = \eta$. Then the streamwise component of the trailing vorticity at $(\xi, \eta, 0)$ is $(d\Gamma/d\eta)e^{i\omega(t-\xi/U)}$. Then the upwash velocity d^2v at $(0, y, 0)$ induced by a vortex line $y = \eta$ is given by

$$d^2v = -\frac{d\Gamma}{d\eta} e^{i\omega t} (y-\eta) \frac{1}{4\pi} A(y-\eta, \lambda) \quad (135)$$

where $\lambda = \omega/U$ and

$$A(x, \lambda) = \int_0^\infty \frac{e^{-i\lambda\xi}}{(x^2 + \xi^2)^{3/2}} d\xi. \quad (136)$$

We easily find that

$$A(x, \lambda) \sim \sqrt{\frac{\pi}{2}} \frac{1}{x^{3/2}} \sqrt{\lambda} e^{-\lambda x} - i \frac{2}{\pi} \frac{1}{x^3} \frac{1}{\lambda} + O(\lambda^{-3}), \quad (137)$$

as $\lambda \rightarrow \infty$, whereas

$$A(x, \lambda) \sim \frac{1}{x^2} + \frac{\lambda^2}{2} \log \frac{\lambda x}{2} + i \left(-\frac{2}{\pi} \frac{\lambda}{x} + \frac{\lambda^2}{2} \right) + O(\lambda^3), \quad (138)$$

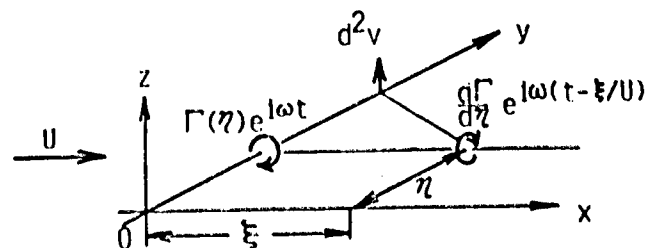


FIG. 12. A LIFTING LINE AND A TRAILING VORTEX LINE

as $\lambda \rightarrow 0$. Thus d^2v decreases exponentially as $\lambda \rightarrow \infty$, while it increases and approaches the steady value as $\lambda \rightarrow 0$.

In the case of the transonic flow, (Fig. 11), the local blade loadings predicted by the lifting surface theory markedly deviate from those by the strip theory especially near the sonic span and at subsonic spans.

At this stage it must be pointed out that both of the acoustic modes $(\sigma, 0)$ and $(\sigma, 1)$ are of cut-off state in the case of Fig. 9, but are of cut-on state in the case of Fig. 10. On the other hand, only $(\sigma, 0)$ is of cut-off state in the case of Fig. 11. Next let us make an attempt to correlate the magnitude of the three-dimensional effect to the state of the predominant acoustic modes.

Figs. 13-16 show spanwise distributions of the unsteady aerodynamic moment in torsional vibrations, where the moment coefficient $C_M^{(t)}(r)$ is defined by

$$C_M^{(t)}(r) = \int_{-V/2}^{V/2} \Delta p_B(r, \bar{z}) \bar{z} d\bar{z} / \{ \pi a_k^{(t)}(r) \}. \quad (139)$$

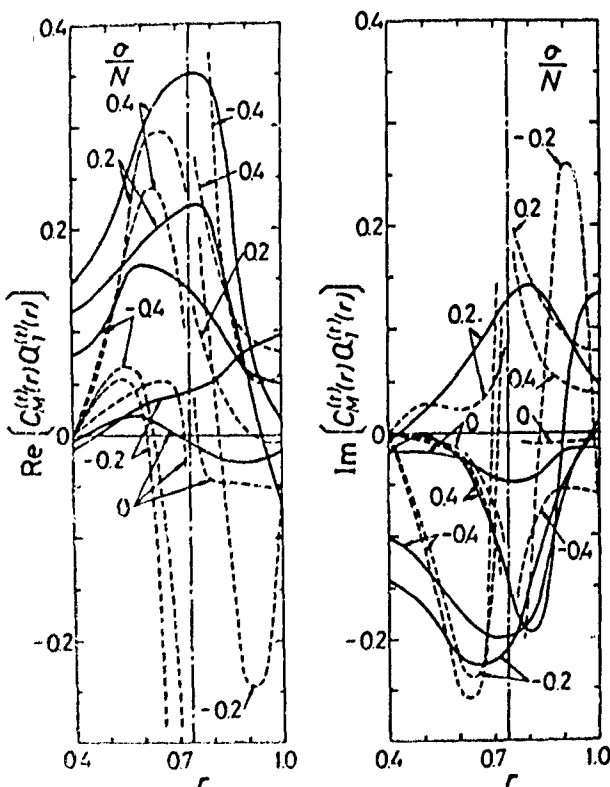


FIG. 16. SPANWISE DISTRIBUTIONS OF UNSTEADY MOMENT COEFFICIENT FOR THE FIRST ORDER TORSIONAL VIBRATION IN A TRANSONIC FLOW. $M_a=0.48$, $Nc_a=2.2$. Other conditions as in FIG. 15.

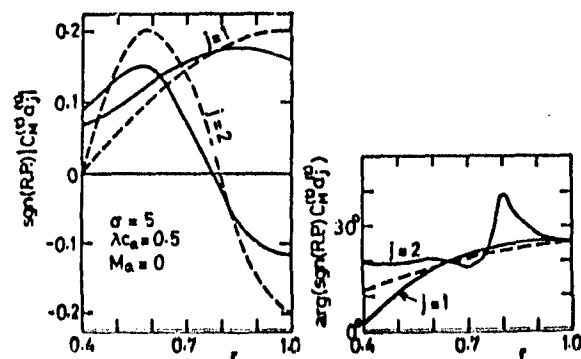


FIG. 13. SPANWISE DISTRIBUTIONS OF THE UNSTEADY MOMENT COEFFICIENT FOR THE FIRST AND SECOND ORDER TORSIONAL VIBRATIONS IN AN INCOMPRESSIBLE FLOW. $M_a=0$, $\sigma=5$, $\lambda c_a=0.5$, $h=0.4$, $\omega=2.4744$, $N=40$, $Nc_a=2.2$.
—— lifting surface theory,
----- strip theory.
 $\text{sgn(R.P.)} = \text{sgn}(\text{Re}[\quad])$

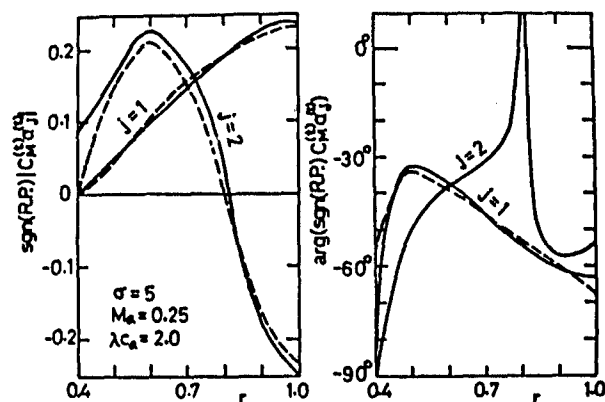


FIG. 14. SPANWISE DISTRIBUTIONS OF UNSTEADY MOMENT COEFFICIENT FOR THE FIRST AND SECOND ORDER TORSIONAL VIBRATIONS IN A SUBSONIC FLOW. $M_a=0.25$, $\lambda c_a=2.0$, $(\sigma, 0)$ AND $(\sigma, 1)$ MODES ARE CUT-ON. Other conditions as in FIG. 13.

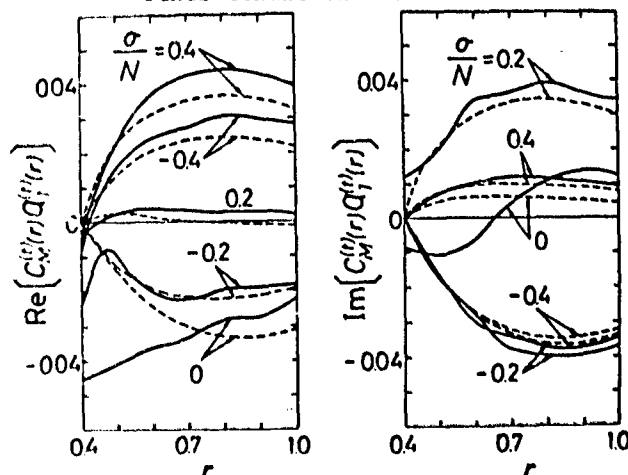


FIG. 15. SPANWISE DISTRIBUTIONS OF UNSTEADY MOMENT COEFFICIENT FOR THE FIRST ORDER TORSIONAL VIBRATION IN A SUPersonic FLOW. $M_a=0.8$, $Nc_a=1.8$, $\lambda c_a=2$, $h=0.4$, $\omega=2.4744$, $N=35$.
—— lifting surface theory,
----- strip theory

Fig. 13 shows the case of an incompressible flow where, of course, all the acoustic modes are of cut-off state, while Fig. 14 is the case of a subsonic flow, where both of the pre-dominant acoustic modes $(\sigma, 0)$ and $(\sigma, 1)$ are of cut-on state. It is evident that even in the case of subsonic flows the three-dimensional effect becomes small if the predominant acoustic modes are of cut-on state.

We can extend this rule to the case of supersonic flows as is seen from Fig. 15. In this figure the differences between the lifting surface theory and strip theory predictions are generally small except the case of $\sigma = 0$, where the $(\sigma, 1)$ mode is of cut-off state.

In general, the region of σ where both of $(\sigma, 0)$ and $(\sigma, 1)$ modes can be of cut-off state is quite small in the case of supersonic flows, whereas the possibility of $(\sigma, 0)$ and $(\sigma, 1)$ both being of cut-on state is confined to a small region of $-\sigma$ in the case of subsonic flows, as seen from Figs. 4 and 5. Consequently, the three-dimensional effect is small in most cases of supersonic flows, whereas it is large in most cases of subsonic flows.

Before proceeding to the case of transonic flows, mention should be made of the behavior of the unsteady blade loading near the resonance state of the predominant acoustic modes. Fig. 17 shows the variation of the local moment distribution for the first order torsional vibration in a subsonic flow with a change in the reduced frequency from below to above the resonance point $\lambda_{ca} = 0.683$ of the $(\sigma, 0)$ mode. As it shows, the aerodynamic moment predicted by the lifting surface theory is subject to a large decrease over the whole span as λ_{ca} changes from 0.65 to 0.693. This behavior, however, cannot be predicted by the strip theory.

According to the strip theory, which assumes a two-dimensional flow at each cylindrical surface $r = \text{constant}$, an acoustic mode of circumferential wave number $vN + \sigma$ in the corresponding quasi-two-dimensional acoustic field at radius r is of resonance state if it satisfies

$$r = |vN + \sigma| / |vN + \sigma + \lambda/\omega|, \quad (140)$$

where $r_s = \beta a / (M_\infty \omega)$ denotes the sonic radius. Consequently, the local blade loading predicted by the strip theory gives a sharp drop at the 'resonance radius' as seen in Fig. 17. Furthermore, a change in λ_{ca} from 0.65 to 0.693 only gives rise to a shift of the resonance radius, resulting in no substantial change in the overall aerodynamic force predicted by the strip theory. Thus the strip theory approximation is far from reality around the resonance state of the predominant acoustic modes.

It can easily be found that the resonance radii at which any of $vN + \sigma$ modes satisfies Eq. (140) are concentrated around the sonic radius r_s . In fact in the case of Fig. 16 in which $r_s = 0.738$, all modes of $v + \sigma/N > 0.6$ or $v + \sigma/N < -0.4$ satisfy Eq. (140) in the range $0.7 < r < 0.8$. Consequently, the

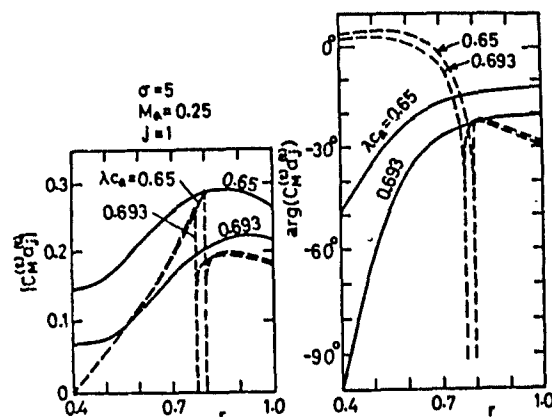


FIG. 17. SPANWISE DISTRIBUTIONS OF UNSTEADY MOMENT COEFFICIENT FOR THE FIRST ORDER TORSIONAL VIBRATION NEAR RESONANCE POINT ($\lambda_{ca} = 0.683$) OF THE $(\sigma, 0)$ MODE. Other conditions as in Fig. 14.

unsteady flow field predicted by the strip theory gives discontinuous variations with change in r near the sonic radius. This is the reason for not plotting the strip theory results near the sonic radius $r = 0.738$ in Fig. 16. Contrary to the quasi-two-dimensional aerodynamic moment predicted by the strip theory, the aerodynamic moment predicted by the lifting surface theory shows a smooth variation across the sonic radius.

It is noteworthy that all resonance radii which satisfy Eq. (140) tend to r_s as $\lambda \rightarrow 0$. As a result the linearized quasi-two-dimensional theory breaks down at the sonic radius.

Finally, let us investigate how the flutter boundaries can be affected by the three-dimensional effect. In Figs. 18 and 19 the aerodynamic work per cycle

$\bar{W}_j^{(b)}$ and $\bar{W}_k^{(t)}$ are plotted against the frequency parameter λ_{ca} . Here $\bar{W}_j^{(b)}$ and $\bar{W}_k^{(t)}$ denote the dimensionless aerodynamic work for the j -th order bending and k -th order torsional vibrations, defined by

$$\bar{W}_j^{(b)} = \bar{W} / (\pi H^2 \lambda / N), \quad (141)$$

$$\text{and} \quad \bar{W}_k^{(t)} = \bar{W} / (\pi \Theta^2), \quad (142)$$

respectively, where \bar{W} is given by

$$\bar{W} = \frac{\pi}{2\lambda} \int_{r_s}^1 dr \int_{-c/2}^{c/2} [\Delta \bar{p}_B(r, z) \{-i\lambda \bar{f}(r, z)\} + \Delta \bar{p}_B(r, z) i\lambda \bar{f}(r, z)] dz \quad (143)$$

Here $\Delta \bar{p}_B(r, z)$ and $\bar{f}(r, z)$ denote the complex conjugates of $\Delta p_B(r, z)$ and $f(r, z)$ respectively.

In the case of the supersonic flow shown in Fig. 18 the predominant acoustic modes $(\sigma, 0)$ and $(\sigma, 1)$ are of cut-on state for the whole frequency range. Although the strip theory slightly underestimates the aerodynamic work, it turns out to be an excellent approximation, giving no substantial error in estimation of the flutter boundaries. It should also be pointed out that the aerodynamic work is quite insensitive to change in the state of higher order acoustic modes such as $(\sigma, 5)$ and $(\sigma, 6)$.

On the other hand, the difference between the strip theory and the lifting surface theory predictions can become fatal in the case of transonic flows as shown in Fig. 19. The total aerodynamic work on a blade shows a sharp variation near the resonance state of a predominant acoustic mode. This phenomenon cannot be predicted by the strip theory.

It should be noted further that the state of the acoustic mode $(\sigma, 1)$ gives a greater influence on the aerodynamic work for the second order vibrations than that for the first order vibrations. Especially a sharp decrease in $\bar{W}_2^{(t)}$ at the resonance frequency of the $(\sigma, 1)$ mode results in the stability boundary of $\lambda Ca = 0.35$, whereas the strip theory predicts the stability boundary as high as $\lambda Ca = 1.2$.

UNSTEADY CASCADE IN SPANWISE NONUNIFORM MEAN FLOW

MODEL AND MATHEMATICAL FORMULATION

A linear cascade of thin blades exposed to incompressible flow sheared along the spanwise direction is considered in this chapter. First, however, let us derive fundamental equations from a more general point of view.

In the following, velocities, lengths and time t are made dimensionless using a reference velocity U_0^* , the blade chord c^* and c^*/U_0^* respectively. The fluid density and pressure also are made dimensionless using a reference density ρ_0^* and $\rho_0^* U_0^{*2}$ respectively.

Now let the undisturbed flow be a sheared unidirectional flow with non-uniform velocity $U(x, y)$, nonuniform density $\rho_0(x, y)$ and uniform pressure p_0 . Here the Cartesian coordinate system (x, y, z) is taken so that the x and y axes are oriented in the undisturbed flow direction and the spanwise direction respectively. Let us consider that the disturbance velocity $\mathbf{q} = (u, v, w)$, disturbance pressure p and disturbance density ρ are caused by disturbance sources composed of distributed body forces $\mathbf{F}(x, y, z, t)$ and mass sources $Q(x, y, z, t)$. Assuming that the disturbances are small and isentropic, we obtain linearized equations of continuity, motion and energy as follows

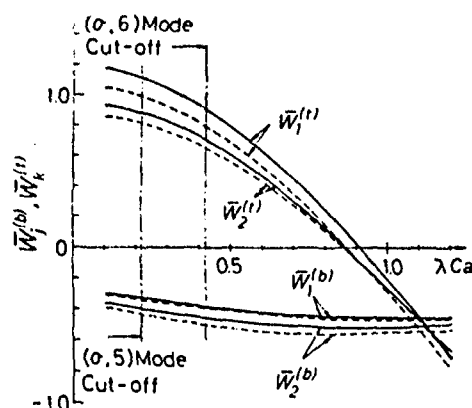


FIG. 18. VARIATION OF THE TOTAL AERO-DYNAMIC WORK WITH THE REDUCED FREQUENCY IN A SUPERSONIC FLOW. $h=0.4$, $\omega=2.4744$, $N=35$, $\sigma/N=0.2$, $Nc_a=1.8$, $M_a=0.8$. — lifting surface theory, - - - strip theory

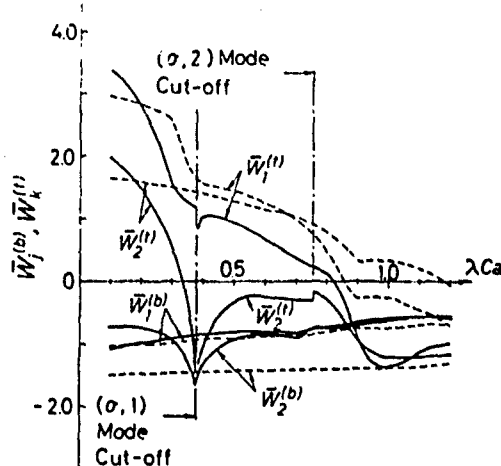


FIG. 19. VARIATION OF THE TOTAL AERO-DYNAMIC WORK WITH THE REDUCED FREQUENCY IN A TRANSONIC FLOW. $Nc_a=2.2$, $M_a=0.48$. Other conditions as in FIG. 18.

$$\rho_0 \nabla \cdot \mathbf{q} + (\mathbf{q} \cdot \nabla) \rho_0 + \frac{D_0 \rho}{D_0 t} = Q \quad (144)$$

$$\frac{D_0 \mathbf{q}}{D_0 t} + \mathbf{e}_x (\mathbf{q} \cdot \nabla) U = - \frac{1}{\rho_0} \nabla p + \frac{1}{\rho_0} \mathbf{F} \quad (145)$$

$$\frac{D_0 p}{D_0 t} - a_0^2 \frac{D_0 \rho}{D_0 t} - a_0^2 (\mathbf{q} \cdot \nabla) \rho_0 = 0, \quad (146)$$

where

$$D_0/D_0 t = \partial/\partial t + U \partial/\partial x, \quad (147)$$

and $a_0(y, z)$ denotes the dimensionless local speed of sound at the undisturbed state, i.e.,

$$a_0(y, z) = \sqrt{\kappa p_0 / \rho_0(y, z)}. \quad (148)$$

Here κ denotes the ratio of specific heats. Furthermore e_x denotes the unit vector in the x -direction.

Elimination of ρ and Q from Eqs. (144 - 146) gives an equation for p as follows:

$$\begin{aligned} & \left[\frac{D_0}{D_0 t} \left(\nabla^2 - \frac{1}{a_0^2} \frac{D_0^2}{D_0 t^2} \right) - 2 \frac{\partial}{\partial x} \left(\frac{\partial U}{\partial y} \frac{\partial}{\partial y} + \frac{\partial U}{\partial z} \frac{\partial}{\partial z} \right) \right. \\ & \quad \left. - \frac{D_0}{D_0 t} \left\{ \frac{1}{\rho_0} \left(\frac{\partial \rho_0}{\partial y} \frac{\partial}{\partial y} + \frac{\partial \rho_0}{\partial z} \frac{\partial}{\partial z} \right) \right\} \right] p \\ & = \frac{D_0}{D_0 t} \left\{ \rho_0 \nabla \left(\frac{F}{\rho_0} \right) \right\} - 2 \left(\frac{\partial U}{\partial y} \frac{\partial F_y}{\partial x} + \frac{\partial U}{\partial z} \frac{\partial F_z}{\partial x} \right) - \frac{D_0^2 Q}{D_0 t^2} \end{aligned} \quad (149)$$

where F_x , F_y and F_z denote the x , y and z components of \mathbf{F} .

Eq. (149) is an equation of acoustic waves propagating in a flowing nonuniform medium. To solve Eq. (149) in this general form is a formidable task, and until now only some special cases have been treated successfully.

In the case of steady flows, $D_0/D_0 t = U \partial / \partial x$, and hence Eq. (149) degenerates to a second order differential equation as follows:

$$\begin{aligned} & \left[(1 - M_0^2) \frac{\partial^2}{\partial x^2} + \frac{\partial^2}{\partial y^2} + \frac{\partial^2}{\partial z^2} \right. \\ & \quad \left. - \frac{2}{M_0} \left(\frac{\partial M_0}{\partial y} \frac{\partial}{\partial y} + \frac{\partial M_0}{\partial z} \frac{\partial}{\partial z} \right) \right] p \\ & = \rho_0 \nabla \cdot \left(\frac{\mathbf{F}}{\rho_0} \right) - \frac{2}{U} \left(\frac{\partial U}{\partial y} F_y + \frac{\partial U}{\partial z} F_z \right) - U \frac{\partial Q}{\partial x}, \end{aligned} \quad (150)$$

where $M_0(y, z) = U(y, z)/a_0(y, z)$ denotes the local Mach number of the undisturbed flow. As one of the earliest studies related to Eq. (150), we should refer to von Karman and Tsien (1945) who treated a lifting line in an incompressible flow sheared in a spanwise direction with a uniform fluid density. In this case Eq. (150) further reduces to

$$\left(\nabla^2 - \frac{2}{U} \frac{dU}{dy} \frac{\partial}{\partial y} \right) p = \frac{\partial F_x}{\partial x}. \quad (151)$$

Honda (1960, 1961) solved problems of three-dimensional steady disturbance flows caused by a single airfoil and a cascade of blades in an incompressible shear flow in the spanwise direction with a uniform density. His single airfoil theory includes the thickness effect, i.e., the last term in Eq. (150).

Extension to compressible shear flows was made by Namba (1969, 1969) who solved

$$\begin{aligned} & \left[\{1 - M_0^2(y)\} \frac{\partial^2}{\partial x^2} + \frac{\partial^2}{\partial y^2} + \frac{\partial^2}{\partial z^2} \right. \\ & \quad \left. - \frac{2}{M_0} \frac{dM_0}{dy} \frac{\partial}{\partial y} \right] p = \frac{\partial F_x}{\partial x}, \end{aligned} \quad (152)$$

for a cascade of blades and a single airfoil. In his theory the undisturbed flow is allowed to be transonic, i.e., $M_0(y)$ is allowed to be unity at a span under the restriction of $dM_0/dy \neq 0$ at the sonic span.

To deal with unsteady flow problems is much more difficult, since the differential equation to solve is of the third order. This difficulty originates from the fact that acoustically propagating disturbances and convected vortical disturbances are locally coupled in sheared flows. Available papers dealing with an unsteady cascade in a shear flow is restricted to incompressible fluid. Kaji et. al., (1980) treated cascade flutter in an incompressible shear flow with a uniform density using a semi-actuator disk model, while Yamasaki and Namba (1982) treated the same problem by a lifting surface method. Hereafter in this chapter we outline the theory developed by Yamasaki and Namba (1982).

Let us consider a cascade of thin blades between two parallel rigid walls with a wall-to-wall distance h as shown in Fig. 20. Further let the undisturbed flow be an incompressible flow sheared in the spanwise direction with velocity $U(y)$, which is disturbed by blades vibrating with a common reduced frequency ω , a constant interblade phase angle $2\pi\sigma$ and zero steady loading. In this case Eq. (149) becomes

$$\left[\frac{D_0}{D_0 t} \nabla^2 - 2 \frac{dU}{dy} \frac{\partial^2}{\partial x \partial y} \right] p = \frac{D_0}{D_0 t} \left(\frac{\partial F_x}{\partial x} \right). \quad (153)$$

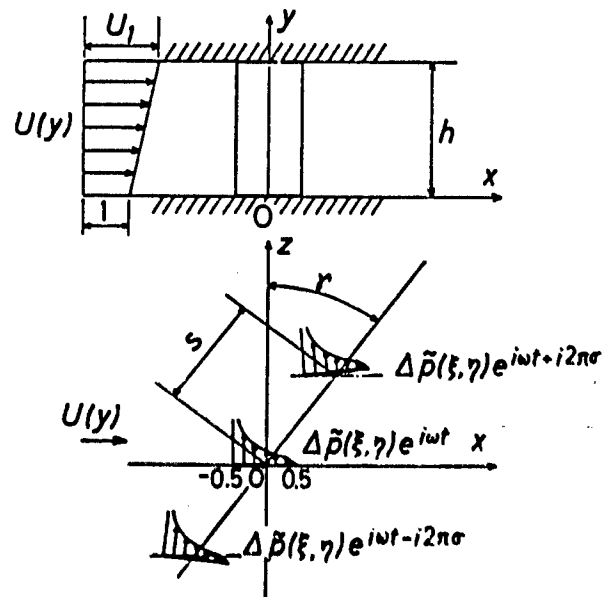


FIG. 20. THE CASCADE MODEL IN A SHEAR FLOW

Further the unsteady loading distribution on the m -th blade can be denoted by $\Delta \tilde{p}(\xi, \eta) e^{i\omega t + i2\pi m}$, where ξ and η denote local chordwise and spanwise coordinates respectively. Then denoting the pitch/chord ratio and angle of stagger by s and γ respectively, we can express the body force $F_z = \tilde{F}_z(x, y, z) e^{i\omega t}$ by

$$\tilde{F}_z(x, y, z) = \sum_{m=-\infty}^{\infty} \int_{-1/2}^{1/2} \int_0^h \Delta \tilde{p}(\xi, \eta) \delta(x - \xi - ms \sin \gamma) \delta(y - \eta) \times \delta(z - ms \cos \gamma) e^{i2\pi m} d\eta d\xi. \quad (154)$$

Here $\delta(\cdot)$ denotes the Dirac delta function.

DISTURBANCE PRESSURE

Let the disturbance pressure

$$p = \tilde{p}(x, y, z) e^{i\omega t} \text{ be represented by an integral form of } \tilde{p}(x, y, z) = \int_{-1/2}^{1/2} \int_0^h \Delta \tilde{p}(\xi, \eta) K_p(x - \xi, y, z | \eta) d\eta d\xi \quad (155)$$

Substitution of Eqs. (154) and (155) into (153) yields a differential equation for the pressure kernel function $K_p(x, y, z | \eta)$ in the form

$$\left[(\omega + U \frac{\partial}{\partial x}) \nabla^2 - 2 \frac{dU}{dy} \frac{\partial^2}{\partial x \partial y} \right] K_p(x, y, z | \eta) = -(\omega + U \frac{\partial}{\partial x}) \quad (156)$$

$$\times \sum_{m=-\infty}^{\infty} \delta(x - ms \sin \gamma) \delta(y - \eta) \delta(z - ms \cos \gamma) e^{i2\pi m}$$

In addition the boundary condition at the wall surface is given by

$$\partial K_p(x, y, z | \eta) / \partial y = 0 \text{ at } y = 0 \text{ and } h. \quad (157)$$

In order to make the problem mathematically tractable, we further assume a uniform shear flow and put

$$U(y) = 1 + (U_1 - 1)y/h. \quad (158)$$

Then applying the Fourier integral method (Namba 1986) we obtain the solution to Eqs. (156) and (157) in the form

$$K_p(x, y, z | \eta) = \frac{i}{2sh} \sum_{\mu=-\infty}^{\infty} e^{i\mu z} \sum_{\mu=0}^{\infty} \frac{Y_\mu(y; \alpha_{\nu\mu}) Y_\mu(\eta; \alpha_{\nu\mu})}{\{\omega + U(\eta) \alpha_{\nu\mu}\}^2} \times (q_\nu \cos \gamma / \sqrt{q_\nu^2 + k_\mu^2} - i \sin \gamma \operatorname{sgn} x) e^{i\alpha_{\nu\mu} x} + \frac{1}{2sh U^2(\eta)} (1 + \operatorname{sgn} x) \sum_{\nu=-\infty}^{\infty} e^{i\nu z} \times \sum_{\mu=0}^{\infty} \left[\frac{\partial}{\partial \alpha} \left\{ Y_\mu(y; \alpha) Y_\mu(\eta; \alpha) e^{i\alpha x} \right. \right. \\ \left. \left. \times \frac{\alpha \sin \gamma - q_\nu}{(\omega^2 - 2\alpha q_\nu \sin \gamma + q_\nu^2 + k_\mu^2 \cos^2 \gamma)^{3/2}} \right\} \right]_{\alpha = -\lambda(\eta)}. \quad (159)$$

where $Y_\mu(y; \alpha)$ and $k_\mu (\mu = 0, 1, \dots)$ are orthogonal eigenfunctions and eigenvalues defined by Namba (1986). In the case of Eq. (158) they are given by

$$Y_0(y; \alpha) = \sqrt{(\omega + \alpha)(\omega + U_1 \alpha)}, \quad (160)$$

$$Y_\mu(y; \alpha) = \sqrt{2} \left[\{\omega + U(y) \alpha\} \cos(k_\mu y) - (U_1 - 1) \alpha \sin(k_\mu y) / (k_\mu h) \right] \quad (161)$$

$$\mu = 1, 2, \dots \quad k_\mu = \mu \pi / h.$$

Furthermore

$$\lambda(y) = \omega / U(y), \quad (162)$$

$$X = x - z \tan \gamma, \quad Z = z / \cos \gamma, \quad (163)$$

$$q_\nu = 2\pi(\nu + \sigma) / s, \quad (164)$$

$$\alpha_{\nu\mu} = q_\nu \sin \gamma + i \operatorname{sgn} X \sqrt{q_\nu^2 + k_\mu^2} \cos \gamma. \quad (165)$$

Note that $\lambda(y)$ denotes the local reduced frequency at each span.

One of the special characteristics of unsteady disturbances in shear flows is local coupling of acoustically propagating disturbances with convected vortical disturbances. It is due to this phenomenon that the pressure kernel function possesses the second term on the right-hand side of Eq. (159) in the form of convected disturbances. In fact this term is absent in the case of uniform flow ($U_1 = 1$) or steady flow ($\omega = 0$), as seen from Namba (1986).

DISTURBANCE VELOCITIES

The disturbance velocity $\tilde{q} = \tilde{q}(x, y, z) e^{i\omega t}$ can be obtained by substituting Eq. (155) into Eq. (145) and integrating it. The result is expressed in the form

$$\tilde{q}(x, y, z) = \int_{-1/2}^{1/2} \int_0^h \Delta \tilde{p}(\xi, \eta) K_q(x - \xi, y, z | \eta) d\eta d\xi \quad (166)$$

where the velocity kernel function is given by

$$K_q(x, y, z | \eta) = -\frac{1}{U(y)} e^{-i\lambda(y)x} \left\{ \int_{-\infty}^x e^{i\lambda(y)x'} \nabla K_p(x', y, z | \eta) dx' - \operatorname{sgn} x \frac{1}{U(y)} \frac{dU}{dy} \int_{-\infty}^x \int_{-\infty}^{x'} e^{i\lambda(y)x''} \times \frac{\partial}{\partial y} K_p(x'', y, z | \eta) dx'' dx' \right\} \quad (167)$$

The second term in () of Eq. (167) stands for the streamwise acceleration of flow caused by transverse displacement of streamlines.

The upwash velocity $\tilde{w}(x, y, z) e^{i\omega t}$,

i.e., the z -component of the disturbance velocity, which is of most interest in this problem, is given by

$$\tilde{w}(x, y, z) = \int_{-1/2}^{1/2} \int_0^h \Delta \tilde{p}(\xi, \eta) K_w(x - \xi, y, z | \eta) d\eta d\xi \quad (168)$$

where

$$K_w(x, y, z | \eta) = -\frac{1}{U(y)} e^{-i\lambda(y)x} \int_{-\infty}^x e^{i\lambda(y)x'} \frac{\partial}{\partial z} K_p(x, y, z | \eta) dx' \quad (169)$$

Substituting Eq. (159) into Eq. (167) and carrying out integration with respect to x' , we obtain

$$\begin{aligned} K_w(x, y, z | \eta) = & -\frac{1}{2s\beta U(y)} \sum_{\mu=0}^{\infty} \sum_{\nu=-\infty}^{\infty} e^{i\beta_\nu z} \frac{Y_\mu(y; \alpha_{y\mu}) Y_\nu(\eta; \alpha_{y\mu})}{\{\omega + U(\eta) \alpha_{y\mu}\}^2} \\ & \times [(1 + \alpha_{y\mu} x) e^{-i\lambda(y)x} \{I_{y\mu}(y) - \sin r \tan r\} \\ & + \{i \alpha_{y\mu} x \cdot I_{y\mu}(y) + J_{y\mu}(y)\} e^{i\beta_\nu x \sin r - |x| \sqrt{\beta_\nu^2 + \beta_\mu^2} \cos r}] \\ & + \frac{1 + \alpha_{y\mu} x}{2} \frac{1}{\eta - y} \frac{\sin r}{s U^2(\eta)} \sum_{\nu=-\infty}^{\infty} e^{i\beta_\nu z} \\ & \times \sum_{\mu=0}^{\infty} \frac{1}{\{\lambda^2(\eta) + 2\lambda(\eta) \beta_\nu \sin r + \beta_\nu^2 + \beta_\mu^2 \cos^2 r\}^2} \\ & \times \left[\left\{ \lambda(\eta) e^{-i\lambda(\eta)x} - \lambda(y) e^{-i\lambda(y)x} \right\} \tan r \right. \\ & + \frac{\beta_\nu}{\cos r} \{e^{-i\lambda(\eta)x} - e^{-i\lambda(y)x}\} R_{y\mu}(y | \eta) \\ & + \left[-\frac{\omega(U-1)}{U(\eta)} \tan r \{e^{-i\lambda(\eta)x} - e^{-i\lambda(y)x}\} \right. \\ & + \frac{U(y)}{y - \eta} \left\{ \lambda(\eta) \tan r + \frac{\beta_\nu}{\cos r} \right\} \{i(\lambda(\eta) - \lambda(y))x e^{-i\lambda(\eta)x} \\ & \left. \left. + (e^{-i\lambda(\eta)x} - e^{-i\lambda(y)x})\} \right] S_{y\mu}(y | \eta) \right], \end{aligned} \quad (170)$$

where $I_{y\mu}(y)$, $J_{y\mu}(y)$, $R_{y\mu}(y | \eta)$ and $S_{y\mu}(y | \eta)$ are defined by Namba (1986). The second term on the right-hand side of Eq. (170) originates from the second term on the right-hand side of Eq. (159). We can recognize that this term stands for the effect of nonuniform convection velocity of unsteady free vortices.

INTEGRAL EQUATION FOR UNSTEADY LOADINGS

Let the z -wise displacement of the zero-th blade be denoted by $\tilde{a}(x, y) e^{i\omega t}$. Then the boundary condition at the blade surface is given by

$$\tilde{w}(x, y, 0) = (i\omega + U \frac{\partial}{\partial x}) \tilde{a}(x, y). \quad (171)$$

Substitution of Eq. (168) into Eq. (171) gives an integral equation for the unsteady loading function $\Delta p(\xi, \eta)$ in the form

$$\begin{aligned} \int_{-1/2}^{1/2} \int_0^h \Delta \tilde{p}(\xi, \eta) K_w(x - \xi, y, 0 | \eta) d\xi d\eta \\ = (i\omega + U \frac{\partial}{\partial x}) \tilde{a}(x, y). \end{aligned} \quad (172)$$

The best method to solve Eq. (172) will be the mode function method, which consists in expanding $\Delta \tilde{p}(x, y)$ in terms of appropriate chordwise and spanwise mode functions like

$$\Delta \tilde{p}(x, y) = \sum_{m=0}^{\infty} \sum_{n=0}^{\infty} A_{mn} \gamma_n(x) \phi_m(y), \quad (173)$$

and determining coefficients A_{mn} . Applying the Glauert series expansion form, we set

$$\gamma_0(x) = \cot(\theta/2), \quad (174)$$

$$\gamma_n(x) = \sin n\theta \quad (n \neq 0)$$

where

$$\theta = \arccos(-2x). \quad (175)$$

On the other hand there are various choices of spanwise mode functions $\phi_m(y)$. A guide line is that $\phi_m(y)$ should be closely related to characters of the flow field. Here we adopt orthogonal functions associated with the eigenfunctions $Y_\mu(y; \alpha)$ and set

$$\phi_m(y) = \lim_{\alpha \rightarrow \infty} \{Y_\mu(y; \alpha)/\alpha\}, \quad (176)$$

which in the case of Eq. (158) becomes

$$\phi_m(y) = \begin{cases} \sqrt{U_1} & : m = 0 \\ \sqrt{2} \{U(y) \cos(m\pi y/R) - (U_1 - 1) \sin(m\pi y/R)/(\pi n)\} & : m \neq 0 \end{cases}$$

Substitution of Eq. (173) into Eq. (168) gives an expression of the upwash velocity in terms of A_{mn} as follows:

$$\begin{aligned} \tilde{w}(x, y, z) = \sum_{m=0}^{\infty} \sum_{n=0}^{\infty} A_{mn} \int_{-1/2}^{1/2} \gamma_n(\xi) W_m(x - \xi, y, z) d\xi \end{aligned} \quad (177)$$

where

$$W_m(x, y, z) = \int_0^h \phi_m(\eta) K_w(x, y, z | \eta) d\eta \quad (178)$$

The detailed expression of $W_m(x, y, z)$ is given by Namba (1986).

As shown there, $W_m(x, y, z)$ can be divided into three parts: $W_{mI}(x, y, z)$, $W_{mII}(x, y, z)$ and $W_{mIII}(x, y, z)$. The first part W_{mI} gives the quasi-two-dimensional disturbance field which neglects interference between different span stations. The second part W_{mII} stands for the 'primary' three-dimensional effect. It takes the form such that the three-dimensional effect at a spanstation y in the shear flow $U(y)$ caused by dipoles and free vortices at other spanstations appears as if the flow is uniform with a velocity equal to $U(y)$ over the whole span. The third part W_{mIII} gives an additional three-dimensional effect which accounts for the nonuniformity in the convection velocity of free vortices. It has been revealed that the numerical

contribution of W_{mIII} is generally small compared with those of W_{mI} and W_{mII} .

We should note that $K_w(x-\xi, y, 0 | \eta)$ possesses singularities due to dipoles and free vortices, which can be extracted from the quasi-two-dimensional part W_{mI} in the form of $(x-\xi)^{-1}$ and $\log|x-\xi|$. Chordwise integration in Eq. (177) for these parts can be analytically performed. Furthermore $K_w(x-\xi, y, 0 | \eta)$ possesses also the horse-shoe vortex singularity in the form of $(y-\eta)^{-2}$ which is included in the first term on the right-hand side of Eq. (170). As to this singularity, the expression of W_{mII} in the form of Eq. (A.15) given by Namba (1986) implies that the spanwise integration for this part is automatically performed. It is required to numerically evaluate the integrals in the expression of W_{mIII} given by Namba's (1986) Eq. (A.16) and the chordwise integration for the regular parts in Eq. (177).

NUMERICAL EXAMPLES AND EFFECT OF MEAN FLOW SHEAR UPON UNSTEADY BLADE LOADING

Numerical examples shown below have been obtained by truncating the series in Eq. (173) or (177) into a finite series with 6 spanwise and 4 chordwise mode functions. The coefficients are determined by making Eq. (173) satisfied at 6×4 control points. The control points are selected at the mid points of six equally divided spanwise subsections and at the three-quarter points of four equally divided chordwise sub-sections.

We consider bending and torsional vibrations for which $\tilde{a}(x, y)$ is given by

$$\tilde{a}(x, y) = -S^{(B, k)}(y), \quad (179)$$

and

$$\tilde{a}(x, y) = \chi S^{(T, k)}(y), \quad (180)$$

respectively. Here $S^{(B, k)}(y)$ and $S^{(T, k)}(y)$ denote the k -th order bending and torsional modes of a uniform cantilever beam, which are normalized by

$$\left. \begin{aligned} \frac{1}{h} \int_0^h \{S^{(B, k)}(y)\}^2 dy &= 1 \\ \frac{1}{h} \int_0^h \{S^{(T, k)}(y)\}^2 dy &= 1 \end{aligned} \right\} \quad (181)$$

Furthermore let $S^{(B, 0)}(y) = 1$ and $S^{(T, 0)}(y) = 1$ mean translational and pitching motions respectively.

Fig. 21 shows spanwise distributions of the local lift coefficient for translational motions ($k = 0$), where $C_L^{(B, k)}(y)$ is defined by

$$C_L^{(B, k)}(y) = \frac{1}{\pi U(y) \omega} \int_{-1/2}^{1/2} \Delta \tilde{p}^{(B, k)}(x, y) dx \quad (182)$$

The results are compared with those of the strip theory prediction which are shown with broken lines. The effect of nonuniformity of the mean flow upon the magnitude of the unsteady local lift force appears essentially in the same manner as in the case of steady flows, i.e., the magnitude of the local lift at a higher velocity span is decreased, while that at a lower velocity span is increased. Furthermore, the phase of the

local lift advances at a higher velocity span, but lags at a lower velocity span compared with the strip theory prediction.

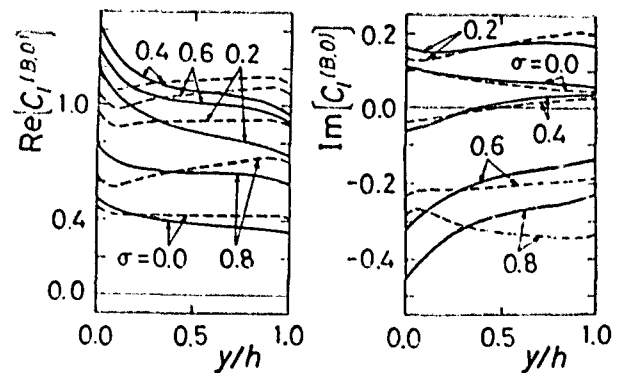


FIG. 21. SPANWISE DISTRIBUTIONS OF UNSTEADY LIFT COEFFICIENT FOR TRANSLATIONAL OSCILLATIONS.

$U_1=2.5$, $\omega=0.5$, $h=3$, $\gamma=45^\circ$, $s=1.0$.

—— lifting surface theory
----- strip theory

We should note that the effect of spanwise nonuniformity in the vibration amplitude $\tilde{a}(x, y)$ also appears in the same fashion as the effect of nonuniform mean velocity. Thus the local lift forces at large amplitude spans are reduced, while those at small amplitude spans are increased compared with quasi-two-dimensional values. Consequently, quite large deviation from the strip theory predictions takes place in the case of the first order bending vibration ($k = 1$) of blades which are fixed at the lower velocity side wall, since effects of non-uniform velocity and amplitude are superposed as shown in Fig. 22.

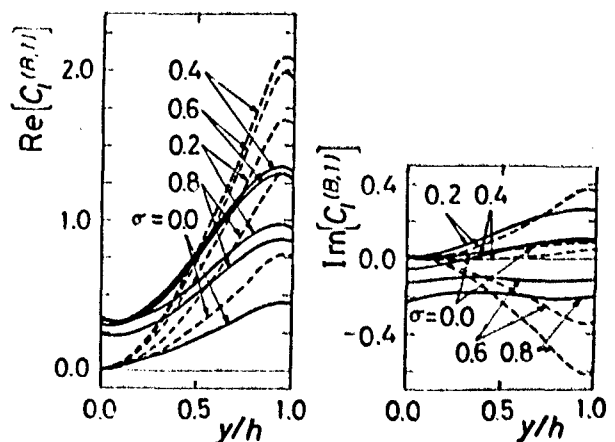


FIG. 22. SPANWISE DISTRIBUTIONS OF UNSTEADY LIFT COEFFICIENT FOR THE FIRST ORDER BENDING OSCILLATIONS WITH THE BLADE ROOT AT $y=0$. Other conditions as in FIG. 21.

Fig. 23 shows the dimensionless aerodynamic work per cycle on a blade in torsional vibrations. Here $W(T,k)$ is given by

$$W(T,k) = \frac{1}{\pi^2 h} \int_0^{2\pi/\omega} \int_{-1/2}^{1/2} \int_0^h \operatorname{Re}[\Delta \tilde{p}^{(T,k)}(x,y) e^{i\omega t}] \times \operatorname{Re}[i\omega x S^{(T,k)}(y) e^{i\omega t}] dy dx dt. \quad (183)$$

No change in the sign of $W(T,k)$, e.g., from negative to positive or vice versa is brought about by the spanwise nonuniformity of the mean flow velocity. However, it can generally be stated that the spanwise nonuniformity in the mean flow velocity reduces the absolute value of the aerodynamic work. Furthermore, the spanwise nonuniformity of the vibration amplitude adds a great deal to this effect.

EFFECT OF WALL LININGS

MODEL AND MATHEMATICAL FORMULATION

As a model that can clearly account for the three-dimensional effect due to the presence of sound absorbing wall linings, we consider a linear cascade of blades spanning between parallel walls. The time mean flow is uniform and blade geometries are uniform in the spanwise direction too, but a part of a side wall is lined with acoustically admittive materials, while the remaining part of the wall and another side wall are rigid everywhere. Hereafter using the undisturbed flow velocity U^* , the undisturbed fluid density ρ_0^* and the blade chord c^* as reference quantities, we use nondimensional velocity, density, length, pressure and time which are scaled with respect to U^* , ρ_0^* , c^* , $\rho_0^* U^{*2}$ and c^*/U^* respectively.

We take the Cartesian coordinate system (x,y,z) with x and y axes oriented in the undisturbed flow and span directions respectively, as shown in Fig. 24. Furthermore, we use the inclined coordinate system (X,Y,Z) where

$$X = x - z \tan \gamma, \quad Z = z / \cos \gamma, \quad (184)$$

and γ denotes the angle of stagger. We assume that the cascade of blades with the angle of stagger γ , the pitch/chord ratio s and the aspect ratio h which is equal to the wall-to-wall distance is vibrating with a common reduced frequency ω and a constant interblade phase angle $2\pi\sigma$. Consequently, the unsteady blade loading on the m -th blade can be denoted by $\Delta \tilde{p}(x',y') e^{i\omega t + i2\pi\sigma m}$, where x' and y' denote local chordwise and spanwise coordinates respectively. The wall at $y = 0$ is rigid everywhere. On the other hand, another side wall at $y = h$ is rigid except a strip section $d_1 < x < d_2$ where it is lined with a locally reacting sound absorbing material of a uniform admittance B_w . Note that the wall admittance B_w is scaled with respect to $1/(\rho_0^* U^*)$.

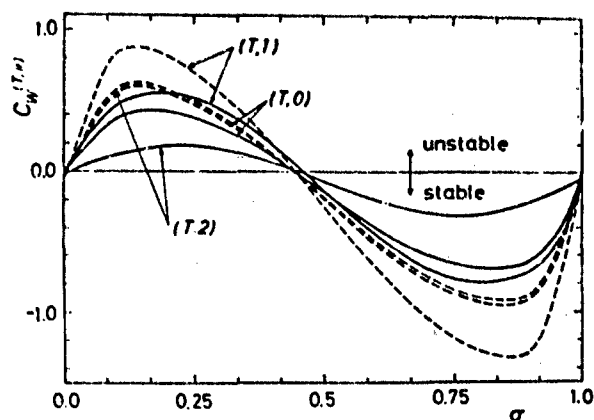


FIG. 23. VARIATION OF AERODYNAMIC WORK COEFFICIENTS WITH THE INTER-BLADE PHASE ANGLE FOR PITCHING (T,0), FIRST (T,1) AND SECOND (T,2) ORDER TORSIONAL VIBRATIONS ABOUT THE MID-CHORD. $U_1=4.0$, $\omega=0.5$, $h=3.0$, $\gamma=45^\circ$, $s=1.0$.
—— lifting surface theory
----- strip theory

We further assume that the blade thickness and the steady blade loading are zero. Then the presence of blades in the flow field can be represented by body forces $F(x,y,z,t)$ given by

$$F(x,y,z,t) = -e_z e^{i\omega t} \sum_{m=-\infty}^{\infty} \int_{-1/2}^{1/2} \int_0^h \Delta \tilde{p}(x',y') \delta(x - ms \sin \gamma - x') \times \delta(y - y') \delta(z - ms \cos \gamma) dy' dx', \quad (185)$$

where e_z denotes the unit vector in the z -direction.

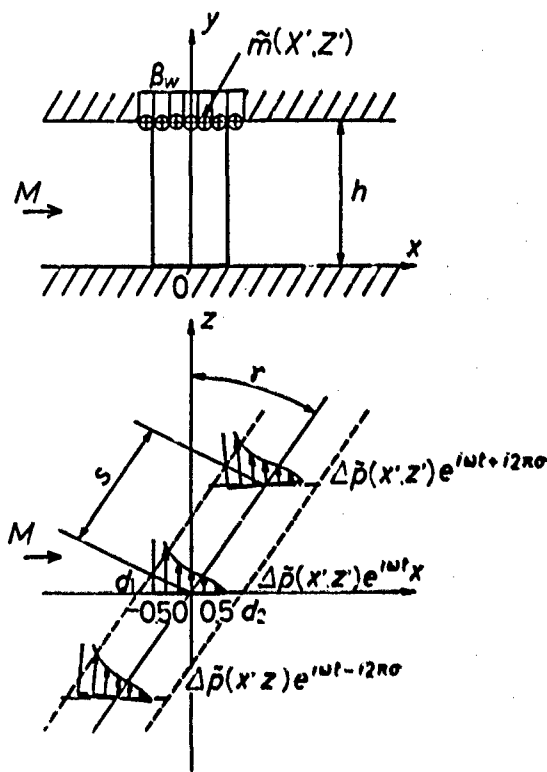


FIG. 24. THE CASCADE MODEL IN A CHANNEL WITH A PARTIALLY LINED WALL

On the other hand, the presence of the lined wall surface at which the normal fluid particle displacement is not zero can be represented by surface mass sources. This concept has been applied successfully to the duct acoustic analysis by Namba and Fukushima (1980). In the present system the flow disturbances originate from the blade vibration. Therefore, the mass sources reacting to the disturbances are periodically distributed in the blade-to-blade direction, and we can represent the mass source strength in the region $d_1 < X < d_2$ as $Z < (m+1)s$ by $\tilde{m}(X, Z - ms)e^{i\omega t + i2\pi\omega m}$. Then the mass source distribution $Q(x, y, z, t)$ in the flow field can be given by

$$Q(x, y, z, t) = e^{i\omega t} \sum_{m=-\infty}^{\infty} \int_{d_1}^{d_2} \int_0^s \tilde{m}(x', z') \delta(x - x') \delta(y - R) \times \delta(Z - ms - z') e^{i2\pi\omega m} dz' dx' \quad (186)$$

Now we can consider that the disturbance sources in the present flow field consist of the body force F and the mass source Q . Assuming disturbances to be small and isentropic, we can express the linearized acoustic wave equation for the disturbance pressure p by

$$(\nabla^2 - M^2 D^2/Dt^2)p = \nabla \cdot F - DQ/Dt, \quad (187)$$

where

$$D/Dt = \partial/\partial t + \partial/\partial x \quad (188)$$

and M denotes the Mach number of the undisturbed flow. The disturbance fluid velocity q is related to p by the equation of motion

$$Dq/Dt = -\nabla p + F. \quad (189)$$

Furthermore, the disturbance fluid particle displacement χ is related to q by

$$D\chi/Dt = q. \quad (190)$$

The above differential equations should be solved under the boundary conditions at the blade and wall surfaces. Let the z -wise displacement of the zeroth blade be denoted by $\tilde{\chi}(x, y)e^{i\omega t}$. Then the boundary condition at the blade surface is expressed as

$$w(x, y, 0, t) = (D/Dt)(\tilde{\chi}(x, y)e^{i\omega t}), \quad (191)$$

where $w(x, y, z, t)$ denotes the z -component of the disturbance velocity q .

On the other hand, the boundary condition at the wall surfaces is described as

$$\chi(x, 0, z, t) = 0, \quad (192)$$

$$\chi(x, h, z, t) = 0 \text{ for } X < d_1 \text{ and } X > d_2$$

$$\text{and } \beta_w p(x, h, z, t) = \frac{\partial}{\partial t} \chi(x, h, z, t) \text{ for } d_1 < X < d_2 \quad (193)$$

where $\eta(x, y, z, t)$ denotes the y -component of χ . Special attention should be paid to the parametric dependence of the wall admittance β_w . Here we neglect the non-linear effect and hence β_w is independent of the sound pressure level. However, β_w is generally a function of the sound frequency. Therefore it is necessary to decompose Eq. (193) into frequency components. In this regard discrimination between stator and rotor cascades is needed.

In the (x, y, z) coordinate system which is relatively fixed to the time mean position of the cascade, the disturbance quantities induced by a simple harmonic oscillation of blades can be expressed as $p(x, y, z, t) = \tilde{p}(x, y, z)e^{i\omega t}$ and $\eta(x, y, z, t) = \tilde{\eta}(x, y, z)e^{i\omega t}$. Furthermore, because of the z -wise periodical variation, the disturbance flow field can be expressed in the (x, y, z) system as

$$\begin{bmatrix} \tilde{p}(x, y, z) \\ \tilde{\eta}(x, y, z) \end{bmatrix} e^{i\omega t} = e^{i\omega t} \sum_{\gamma=-\infty}^{\infty} e^{i\gamma_z z} \begin{bmatrix} \tilde{p}^{(\gamma)}(x, y) \\ \tilde{\eta}^{(\gamma)}(x, y) \end{bmatrix} \quad (194)$$

where

$$q_\gamma = 2\pi(\gamma + \sigma)/s. \quad (195)$$

Therefore, in the case of the stator cascade where the lined wall is stationary with respect to the (x, y, z) coordinate system, Eq. (193) is rewritten as

$$\beta_w(\omega) \tilde{p}^{(\gamma)}(x, h) = i\omega \tilde{\eta}^{(\gamma)}(x, h) \quad (196)$$

$$d_1 < X < d_2, \quad \gamma = 0, \pm 1, \dots$$

On the other hand, in the case of the rotor cascade where the lined wall is relatively moving in the (x, y, z) system, disturbances sensed by an observer stationary with respect to the lined wall are no longer of a simple harmonic time variation, but are generally composed of an infinite number of frequency components. In fact, let the lined wall be moving in the negative z direction with a constant speed V , and define a coordinate system (x_s, y_s, z_s) which is stationary with respect to the moving wall by

$$X_s = X, \quad Y_s = Y, \quad Z_s = Z - Vt. \quad (197)$$

Then we can write

$$\begin{bmatrix} \tilde{p}(x, y, z) \\ \tilde{\eta}(x, y, z) \end{bmatrix} e^{i\omega t} = \sum_{\gamma=-\infty}^{\infty} e^{i\lambda_\gamma t + i\gamma_z z_s} \begin{bmatrix} \tilde{p}^{(\gamma)}(x_s, y_s) \\ \tilde{\eta}^{(\gamma)}(x_s, y_s) \end{bmatrix}, \quad (198)$$

where

$$\lambda_\gamma = \omega + \gamma_z V. \quad (199)$$

Therefore Eq. (193) should be rewritten as

$$\beta_w(\lambda) \tilde{p}^{(v)}(x_s, k) = i\lambda \tilde{\eta}^{(v)}(x_s, k); \quad (200)$$

$$d_1 < x_s < d_2, \quad v = 0, \pm 1, \dots$$

Our ultimate purpose is to determine the blade loading $\Delta \tilde{p}(x, y)$ for specified blade vibration mode $\tilde{a}(x, y)$ and wall admittance β_w . For this purpose we first solve Eqs. (187), (189) and (190) to express p , w and η in terms of $\Delta p(x, y)$ and $m(x, z)$, which then are determined by Eqs. (191) and (196) or (200). Hereafter we confine ourselves to subsonic flows $0 < M < 1$.

DISTURBANCE PRESSURE

Expressions of F and Q given by Eqs. (185) and (187) suggest to represent the disturbance pressure $\tilde{p}(x, y, z)$ in the integral form

$$\begin{aligned} \tilde{p}(x, y, z) = & \int_{-1/2}^{1/2} \int_0^k \Delta \tilde{p}(x', y') K_{pd}(x-x', y, z | y') dy' dx' \\ & + \int_{d_1}^{d_2} \int_0^s \tilde{m}(x', z') K_{pm}(x-x', y, z-z') dz' dx'. \end{aligned} \quad (201)$$

Substitution of Eq. (201) into Eq. (187) gives equations for the kernel functions K_{pd} and K_{pm} as follows:

$$\begin{aligned} \{ \nabla^2 - (i\omega + \frac{\partial}{\partial x})^2 \} K_{pd}(x-x', y, z | y') \\ = - \sum_{m=-\infty}^{\infty} \delta(x-ms \sin \gamma - x') \delta(y-y') \\ \times \delta'(z-ms \cos \gamma) e^{i2\pi m}, \end{aligned} \quad (202)$$

$$\begin{aligned} \{ \nabla^2 - (i\omega + \frac{\partial}{\partial x})^2 \} K_{pm}(x-x', y, z-z') \\ = -(i\omega + \frac{\partial}{\partial x}) \sum_{m=-\infty}^{\infty} \delta(x-x') \delta(y-k) \\ \times \delta(z-ms-z') e^{i2\pi m}. \end{aligned} \quad (203)$$

Applying the Fourier integral method employed in "UNSTEADY CASCADE IN SPANWISE NONUNIFORM MEAN FLOW", we can derive the solutions in the form of Fourier double series as follows:

$$K_{pd}(x-x', y, z | y') = \quad (204)$$

$$\sum_{v=-\infty}^{\infty} e^{i\gamma_v z} \sum_{\mu=0}^{\infty} K_{pd}^{(v, \mu)}(x-x') \phi_{\mu}(y) \phi_{\mu}(y'),$$

$$K_{pm}(x-x', y, z-z') = \quad (205)$$

$$\sum_{v=-\infty}^{\infty} e^{i\gamma_v(z-z')} \sum_{\mu=0}^{\infty} K_{pm}^{(v, \mu)}(x-x') \phi_{\mu}(y) \phi_{\mu}(k),$$

where $\phi_0 = 1$, $\phi_{\mu}(y) = \sqrt{2} \cos(k_{\mu} y)$, $(\mu = 1, 2, \dots)$

$$k_{\mu} = \mu\pi/k, \quad (\mu = 0, 1, \dots), \quad (206)$$

and expressions of $K_{pd}^{(v, \mu)}(x-x')$ and $K_{pm}^{(v, \mu)}(x-x')$ are given by Namba (1986).

From the standpoint of numerical work it is convenient to expand the loading function $\Delta \tilde{p}(x, y)$ and mass source function $\tilde{m}(x, z)$ into the double series forms

$$\Delta \tilde{p}(x, y) = \sum_{\mu=0}^{\infty} \sum_{n=0}^{\infty} A_{\mu n} \psi_n(x) \phi_{\mu}(y), \quad (207)$$

$$\tilde{m}(x, z) = \sum_{N=1}^{\infty} \sum_{v=-\infty}^{\infty} B_{vN} Q_N(x) e^{i\gamma_v z}. \quad (208)$$

In the case of subsonic flows the chordwise mode functions $\psi_n(x)$ defined by

$$\psi_0(x) = \cot(\theta/2), \quad (209)$$

$$\psi_n(x) = \sin n\theta \quad (n = 1, 2, \dots),$$

$$x = -(1/2) \cos \theta, \quad 0 \leq \theta \leq \pi,$$

are recommended. On the other hand, the suitable form of the streamwise mode functions $Q_N(x)$ for the mass source is still the subject of controversy, see Koch and Mohring (1983). The point at issue is singularities at edges $X = d_1$ and d_2 . Here we assume the fluid particle displacement to be continuous across the edge lines $X = d_1$ and d_2 , and put

$$Q_N(x) = (i\omega + \frac{\partial}{\partial x}) Y_N(x), \quad (210)$$

$$Y_N(x) = \sin N\theta,$$

$$X = (d_1 + d_2)/2 - [(d_2 - d_1)/2] \cos \theta, \quad (211)$$

$$0 \leq \theta \leq \pi,$$

as adopted by Namba and Fukushima (1980).

Substitution of Eqs. (204), (205), (207, and (208) into (201) gives

$$\tilde{p}(x, y, z) = \quad (212)$$

$$\begin{aligned} & k \sum_{\mu=0}^{\infty} \sum_{n=0}^{\infty} A_{\mu n} \phi_{\mu}(y) \int_{-1/2}^{1/2} \psi_n(x') K_{pd}^{(\mu)}(x-x', z) dx' \\ & + s \sum_{v=-\infty}^{\infty} \sum_{N=1}^{\infty} B_{vN} e^{i\gamma_v z} \int_{d_1}^{d_2} Q_N(x') K_{pm}^{(v)}(x-x', y) dx', \end{aligned}$$

where

$$K_{pd}^{(\mu)}(x-x', z) = \sum_{v=-\infty}^{\infty} e^{i\gamma_v z} K_{pd}^{(v, \mu)}(x-x'), \quad (213)$$

$$K_{pm}^{(v)}(x-x', y) = \sum_{\mu=0}^{\infty} K_{pm}^{(v, \mu)}(x-x') \phi_{\mu}(y) \phi_{\mu}(k) \quad (214)$$

DISTURBANCE VELOCITIES AND FLUID PARTICLE DISPLACEMENT

Once the disturbance pressure is given in the form of Eq. (201), we can formally integrate Eq. (189) and further Eq. (190), obtaining explicit expressions

of q and χ . Here we limit ourselves to showing expressions of $w = \tilde{w}(x, y, z)e^{i\omega t}$ and $\eta = \tilde{\eta}(x, y, z)e^{i\omega t}$ which are given as follows:

$$\tilde{w}(x, y, z) = \quad (215)$$

$$\int_{-1/2}^{1/2} \int_0^h \Delta \tilde{p}(x', y') K_{wd}(x-x', y, z | y') dy' dx' + \int_{d_1}^{d_2} \int_0^S \tilde{m}(x', z') K_{wm}(x-x', y, z-z') dz' dx', \quad (216)$$

$$\tilde{\eta}(x, y, z) = \int_{-1/2}^{1/2} \int_0^h \Delta \tilde{p}(x', y') K_{\eta d}(x-x', y, z | y') dy' dx' + \int_{d_1}^{d_2} \int_0^S \tilde{m}(x', z') K_{\eta m}(x-x', y, z-z') dz' dx'.$$

Here kernel functions can be expressed in Fourier double series form as follows:

$$K_{wd}(x-x', y, z | y') = \sum_{\nu=-\infty}^{\infty} e^{i\delta_{\nu} z} \sum_{\mu=0}^{\infty} K_{wd}^{(\nu, \mu)}(x-x') \phi_{\mu}(y) \phi_{\mu}(y'), \quad (217)$$

$$K_{wm}(x-x', y, z-z') = \sum_{\nu=-\infty}^{\infty} e^{i\delta_{\nu}(z-z')} \sum_{\mu=0}^{\infty} K_{wm}^{(\nu, \mu)}(x-x') \phi_{\mu}(y) \phi_{\mu}(h), \quad (218)$$

$$K_{\eta d}(x-x', y, z | y') = \sum_{\nu=-\infty}^{\infty} e^{i\delta_{\nu} z} \sum_{\mu=1}^{\infty} K_{\eta d}^{(\nu, \mu)}(x-x') \phi'_{\mu}(y) \phi_{\mu}(y'), \quad (219)$$

$$K_{\eta m}(x-x', y, z-z') = \sum_{\nu=-\infty}^{\infty} e^{i\delta_{\nu}(z-z')} \sum_{\mu=1}^{\infty} K_{\eta m}^{(\nu, \mu)}(x-x') \phi'_{\mu}(y) \phi_{\mu}(h). \quad (220)$$

Expressions of $K_{wd}^{(\nu, \mu)}(x-x')$, $K_{wm}^{(\nu, \mu)}(x-x')$, $K_{\eta d}^{(\nu, \mu)}(x-x')$ and $K_{\eta m}^{(\nu, \mu)}(x-x')$ are given by Namba (1986).

Substitution of Eqs. (207), (208), (217)–(220) into (215) and (216) leads us to

$$\tilde{w}(x, y, z) = h \sum_{\mu=0}^{\infty} \sum_{n=0}^{\infty} A_{\mu n} \phi_{\mu}(y) \int_{-1/2}^{1/2} \psi_n(x') K_{wd}^{(\mu)}(x-x', z) dx' \quad (221)$$

$$+ S \sum_{\nu=-\infty}^{\infty} \sum_{N=1}^{\infty} B_{\nu N} e^{i\delta_{\nu} z} \int_{d_1}^{d_2} Q_N(x') K_{wm}^{(\nu)}(x-x', y) dx'.$$

$$\tilde{\eta}(x, y, z) = \quad (222)$$

$$h \sum_{\mu=1}^{\infty} \sum_{n=0}^{\infty} A_{\mu n} \phi'_{\mu}(y) \int_{-1/2}^{1/2} \psi_n(x') K_{\eta d}^{(\mu)}(x-x', z) dx' + S \sum_{\nu=-\infty}^{\infty} \sum_{N=1}^{\infty} B_{\nu N} e^{i\delta_{\nu} z} \int_{d_1}^{d_2} Q_N(x') K_{\eta m}^{(\nu)}(x-x', y) dx',$$

where

$$K_{wd}^{(\mu)}(x-x', z) = \sum_{\nu=-\infty}^{\infty} e^{i\delta_{\nu} z} K_{wd}^{(\nu, \mu)}(x-x'), \quad (223)$$

$$K_{wm}^{(\nu)}(x-x', y) = \sum_{\mu=0}^{\infty} K_{wm}^{(\nu, \mu)}(x-x') \phi_{\mu}(y) \phi_{\mu}(h) \quad (224)$$

$$K_{\eta d}^{(\mu)}(x-x', z) = \sum_{\nu=-\infty}^{\infty} e^{i\delta_{\nu} z} K_{\eta d}^{(\nu, \mu)}(x-x'), \quad (225)$$

$$K_{\eta m}^{(\nu)}(x-x', y) = \sum_{\mu=1}^{\infty} K_{\eta m}^{(\nu, \mu)}(x-x') \phi'_{\mu}(y) \phi_{\mu}(h) \quad (226)$$

DETERMINATION OF UNSTEADY BLADE LOADING AND MASS SOURCE

Now we are in a position to determine $\Delta \tilde{p}(x, y)$ and $\tilde{m}(x, z)$, or in other words, the coefficients $A_{\mu n}$ and $B_{\nu N}$ so that the boundary conditions (191), (192), and (193) should be satisfied.

First it is easy to see that the first term on the right-hand side of Eq. (222) vanishes at $y = 0$ and h . In other words, the transverse component of the fluid particle displacement induced by pressure dipoles representing blades becomes zero at both side walls including the lined section. On the other hand, as shown by Namba (1986)

$$K_{\eta m}^{(\nu)}(x-x', 0) = 0, \quad (227)$$

$$K_{\eta m}^{(\nu)}(x-x', h) = -\frac{1}{2S} \{1 + \operatorname{sgn}(x-x')\} e^{-i\omega(x-x')}.$$

Consequently, it holds that

$$\tilde{\eta}(x, h, z) = \begin{cases} 0 : x < d_1, \\ \sum_{\nu=-\infty}^{\infty} \sum_{N=1}^{\infty} B_{\nu N} e^{i\delta_{\nu} z} [Y_N(x) - e^{i\omega(d_1-x)} Y_N(d_1)] : d_1 \leq x \leq d_2, \\ e^{-i\omega x} \sum_{\nu=-\infty}^{\infty} \sum_{N=1}^{\infty} B_{\nu N} e^{i\delta_{\nu} z} [Y_N(d_2) e^{i\omega d_2} - Y_N(d_1) e^{i\omega d_1}] : d_2 < x, \end{cases} \quad (228)$$

Then it is evident that the boundary condition (192) is satisfied, since $Y_N(X)$ defined by Eq. (211) satisfies

$$Y_N(d_1) = Y_N(d_2) = 0 \quad (229)$$

Next, substitution of Eq. (221) into Eq. (191) gives

$$\begin{aligned} & h \sum_{\mu=0}^{\infty} \sum_{n=0}^{\infty} A_{\mu n} \phi_{\mu}(y) \int_{-1/2}^{1/2} \psi_n(x') K_{wd}^{(\mu)}(x-x', 0) dx' \\ & + S \sum_{\nu=-\infty}^{\infty} \sum_{N=1}^{\infty} B_{\nu N} \int_{d_1}^{d_2} Q_N(x') K_{wm}^{(\nu)}(x-x', y) dx' \\ & = (i\omega + \partial/\partial x) \tilde{a}(x, y). \end{aligned} \quad (230)$$

With regard to functions $K_{wd}^{(\mu)}(x-x', 0)$

and $K_{wm}^{(\nu)}(x-x', y)$ involved in Eq. (230),

we should note that the Fourier series given by Eqs. (223) and (224) are nonuniformly convergent, since $K_{wd}^{(\mu)}(x-x', 0)$

and $K_{wm}^{(\nu)}(0, y)$ are singular at $x-x' = 0$

and $y = h$ respectively. Therefore, in numerical work it is necessary to separate singular parts as shown by Namba (1986).

Finally, inspection of Eqs. (212) and (222) enables us to find that $\tilde{p}^{(\nu)}(x, y)$ and $\tilde{\eta}^{(\nu)}(x, y)$ defined by Eq. (194) are expressed as

$$\tilde{p}^{(\nu)}(x, y) = \quad (231)$$

$$\begin{aligned} & h \sum_{\mu=0}^{\infty} \sum_{n=0}^{\infty} A_{\mu n} \phi_{\mu}(y) \int_{-1/2}^{1/2} \psi_n(x') K_{pd}^{(\nu, \mu)}(x-x') dx' \\ & + S \sum_{N=1}^{\infty} B_{\nu N} \int_{d_1}^{d_2} Q_N(x') K_{pm}^{(\nu)}(x-x', y) dx', \end{aligned}$$

$$\tilde{\eta}^{(\nu)}(x, y) = \quad (232)$$

$$\begin{aligned} & h \sum_{\mu=0}^{\infty} \sum_{n=0}^{\infty} A_{\mu n} \phi'_{\mu}(y) \int_{-1/2}^{1/2} \psi_n(x') K_{\eta d}^{(\nu, \mu)}(x-x') dx' \\ & + S \sum_{N=1}^{\infty} B_{\nu N} \int_{d_1}^{d_2} Q_N(x') K_{\eta m}^{(\nu)}(x-x', y) dx'. \end{aligned}$$

Further, Eqs. (228) and (229) give

$$\tilde{\eta}^{(\nu)}(x, h) = \sum_{N=1}^{\infty} B_{\nu N} Y_N(x) : d_1 \leq x \leq d_2 \quad (233)$$

Then the boundary condition at the lined wall surface for the stator cascade given by Eq. (196) becomes

$$\begin{aligned} & \beta_w(\omega) \left[h \sum_{\mu=0}^{\infty} \sum_{n=0}^{\infty} A_{\mu n} \phi_{\mu}(h) \int_{-1/2}^{1/2} \psi_n(x') K_{pd}^{(\nu, \mu)}(x-x') dx' \right. \\ & \left. + S \sum_{N=1}^{\infty} B_{\nu N} \int_{d_1}^{d_2} Q_N(x') K_{pm}^{(\nu)}(x-x', h) dx' \right] \\ & - i\omega \sum_{N=1}^{\infty} B_{\nu N} Y_N(x) = 0 : \nu = 0, \pm 1, \pm 2, \dots \end{aligned} \quad (234)$$

On the other hand, in the case of the rotor cascade, we should use Eq. (200), which becomes

$$\begin{aligned} & \beta_w(\lambda, \nu) \left[h \sum_{\mu=0}^{\infty} \sum_{n=0}^{\infty} A_{\mu n} \phi_{\mu}(h) \int_{-1/2}^{1/2} \psi_n(x') K_{pd}^{(\nu, \mu)}(x-x') dx' \right. \\ & \left. + S \sum_{N=1}^{\infty} B_{\nu N} \int_{d_1}^{d_2} Q_N(x') K_{pm}^{(\nu)}(x-x', h) dx' \right] \\ & - i\lambda \nu \sum_{N=1}^{\infty} B_{\nu N} Y_N(x) = 0 : \nu = 0, \pm 1, \pm 2, \dots \end{aligned} \quad (235)$$

Again we note that the series expression of $K_{pm}^{(\nu)}(x-x', y)$ given by Eq. (214) is of nonuniform convergence, and hence we should separate the singular part, as shown by Namba (1986), before performing the integration involved in Eqs. (234) and (235).

Eqs. (230) and (234) or (235) give a set of linear algebraic equations for an infinite number of unknowns $A_{\mu n}$ and $B_{\nu N}$. Actually, we should truncate the series into finite ones by taking up to $\mu = L-1$, $n = I-1$, $\nu = \pm (K-1)/2$ and $N = J$, say, where K is an odd number, and determine a finite number of $A_{\mu n}$ and $B_{\nu N}$ by making Eqs. (230) and (234) or (235) satisfied at a finite number of control points (x_i, y_i) ($i = 1, 2, \dots, I$; $i = 1, 2, \dots, L$) and X_j ($j = 1, 2, \dots, J$).

NUMERICAL EXAMPLES AND EFFECT OF WALL LININGS UPON UNSTEADY BLADE LOADING

Here we limit ourselves to the case of the stator cascade, i.e., Eq. (234), with the lined section confined to the cascade region, i.e., $d_1 = -1/2$ and $d_2 = 1/2$. All examples are quoted from Yamasaki and Namba (1982).

The dependence of the admittance β_w of currently used lining materials upon the sound frequency is well investigated. However, in the present study we specify β_w independently of ω . We should note that β_w is a complex number in the possible range $0 < |\beta_w| < \infty$ and $-\pi/2 < \arg(\beta_w) < \pi/2$.

Fig. 25 shows how the spanwise distribution of the local lift force for the translational vibration $\tilde{a}(x, y) = -1$ can be modified by the presence of the wall liner, where the local lift coefficient $C_l^{(B, 0)}(y)$ is defined by

$$C_l^{(B, 0)}(y) = \int_{-1/2}^{1/2} \Delta \tilde{p}(x, y) dx / (\pi i \omega). \quad (236)$$

Note that $\beta_w = 0$ implies a rigid wall. As Fig. 25 shows, the wall liner has a large influence on the unsteady local lift force in the vicinity of the lined wall, but the influence upon the overall lift force seems rather small. Attention should be paid to the scale of the ordinate.

Next, in order to see whether the presence of the wall liner can be beneficial for suppressing the cascade flutter, let us investigate how the aerodynamic work on a vibrating blade given by

$$W = \int_0^{2\pi/\omega} \int_{-1/2}^{1/2} \int_0^h \operatorname{Re} [\Delta \hat{p}(x, y) e^{i\omega t}] \times \operatorname{Re} [i\omega \tilde{a}(x, y) e^{i\omega t}] dy dx dt, \quad (237)$$

depends upon β_w . Here we define the dimensionless work for translational oscillation $\tilde{a}(x, y) = -1$ and pitching oscillation $\tilde{a}(x, y) = x$ by

$$C_w^{(B,0)} = W/(\pi^2 \omega h) \quad (238)$$

and

$$C_w^{(T,0)} = W/(\pi^2 h) \quad (239)$$

respectively. Figs. 26 and 27 show that $|C_w^{(B,0)}|$ or $|C_w^{(T,0)}|$ monotonously decrease as $|\beta_w|$ increases if $\arg(\beta_w)$ is negative. For positive $\arg(\beta_w)$, however, $|C_w^{(B,0)}|$ or $|C_w^{(T,0)}|$ increase, decrease and again increase with increase of $|\beta_w|$, asymptotically tending to the values for $|\beta_w| = \infty$. Increasing $|\beta_w|$ over 1 no longer give significant changes in the aerodynamic work, at least for small reduced frequencies relevant to flutter.

Generally speaking, the effect of the wall liners on the aerodynamic work is small, and we can hardly expect the wall liner to play a decisive role in suppressing the cascade flutter, at least if the wall liner is confined to a short section as in the present examples.

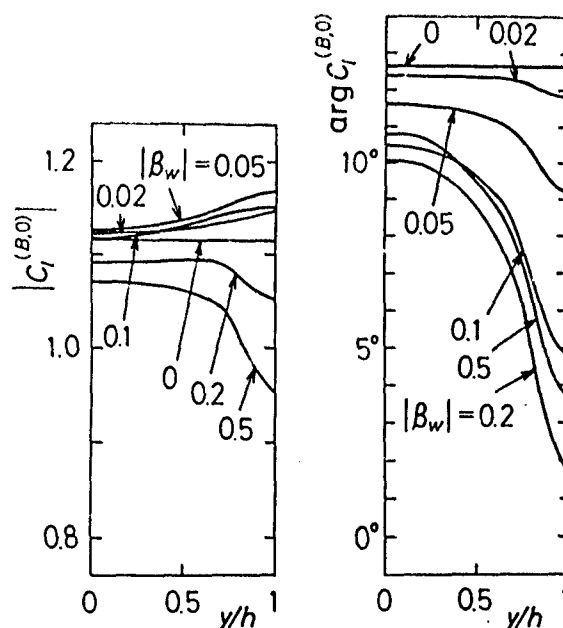


FIG. 25. EFFECT OF THE WALL LINER ADMITTANCE β_w ON THE SPANWISE DISTRIBUTION OF THE UNSTEADY LIFT COEFFICIENT FOR THE TRANSLATIONAL VIBRATION. $M = 0.6$, $\omega = 0.2$, $h = 2.0$, $S = 1.0$, $\gamma = 45^\circ$, $2\pi\sigma = 60^\circ$, $\arg(\beta_w) = 30^\circ$.

FIG. 26. DEPENDENCE OF THE TOTAL AERODYNAMIC WORK FOR THE TRANSLATIONAL VIBRATION UPON THE WALL LINER ADMITTANCE β_w . $M = 0.6$, $\omega = 0.2$, $h = 2.0$, $S = 1.0$, $\gamma = 45^\circ$, $2\pi\sigma = 60^\circ$.

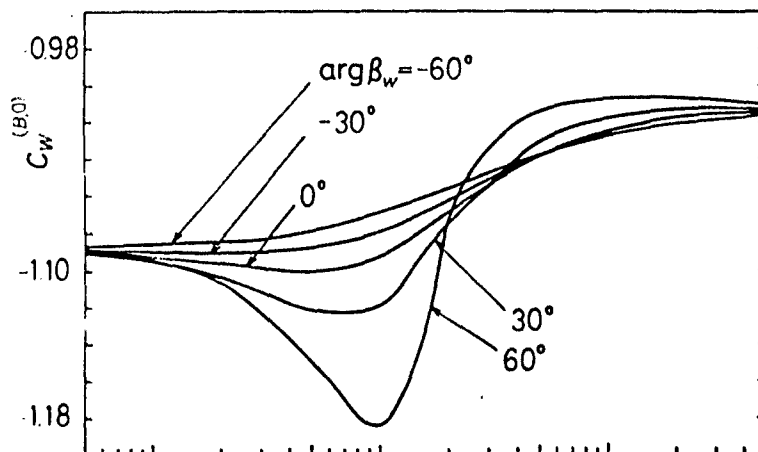
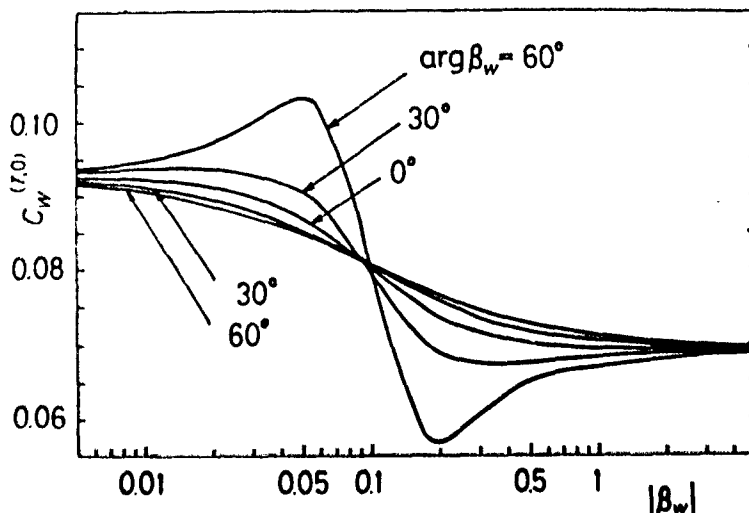


FIG. 27. DEPENDENCE OF THE TOTAL AERODYNAMIC WORK FOR THE PITCHING VIBRATION ABOUT MID-CHORD UPON THE WALL LINER ADMITTANCE β_w . OTHER CONDITIONS ARE SAME AS IN FIG. 26.



THREE-DIMENSIONAL FLOW

by

Pierre Salaün

Office National d'Etudes et de Recherches Aéronautiques (ONERA)
 29 Avenue de la Division Leclerc
 92320 Châtillon-sous-Bagneux
 France

SUBSONIC AND SUPERSONIC UNSTEADY ANNULAR CASCADE THEORY

FORMULATION OF THE PROBLEM

Consider a single annular blade row with a finite number N of vibrating blades which are rotating at a constant angular velocity Ω in an infinitely long cylindrical duct of radii r_1 and r_2 ($r_1 < r_2$).

The fluid inside the duct is an inviscid perfect gas.

The undisturbed flow is a uniform axial flow with a subsonic velocity V_∞ and density ρ_∞ . This means that the blades are parts of helicoids whose equations are, in cylindrical coordinates (r, θ, z) fixed to the rotor, α' being a constant (Figure 1).

$$\theta + \frac{\Omega}{V_\infty} z = \alpha' + \frac{j-1}{N} 2\pi \quad (j=1, 2, \dots, N) \quad (1)$$

$$r_1 < r < r_2 \quad z_1 < z < z_2$$

z_1 and z_2 denote the axial positions of leading and trailing edges.

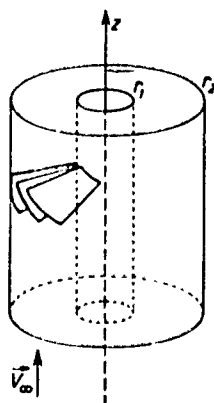


Fig. 1 Geometry of Blades

The arc s on a helix defined by a constant value of r is, s_1 being the value of s corresponding to z_1

$$s = s_1 + \left[1 + \frac{\Omega^2 r^2}{V_\infty^2} \right]^{\frac{1}{2}} (z - z_1) \quad (2)$$

The blade spacing b and the stagger angle γ , which is the angle between the tangent to the helix and the z -axis, are defined as follows:

$$b = \frac{2\pi r}{N} \quad \tan(\gamma) = \frac{\Omega r}{V_\infty} \quad (3)$$

The axial chord length $2l$ of the blade is:

$$2l = z_2 - z_1$$

and the blade chord $2c$ is

$$2c = 2l \left[1 + \frac{\Omega^2 r^2}{V_\infty^2} \right]^{\frac{1}{2}} - \frac{2l}{\cos(\gamma)} \quad (4)$$

The relative Mach number M is expressed in term of the axial Mach number M_∞ as

$$M = \frac{M_\infty}{\cos(\gamma)} \quad (5)$$

The only cases considered here are those where the relative velocity is either subsonic or supersonic all over the blades.

The equations of the vibrating blades are taken in the form:

$$\theta + \frac{\Omega}{V_\infty} z = \alpha' + \frac{j-1}{N} 2\pi + \sigma_j(r, z, t) \quad (j=1, 2, \dots, N) \quad (6)$$

where $\sigma_j(r, z, t)$ is a function of the normal deflection $f_j(r, z, t)$ of the j th blade; $f_j(r, z, t)$ is supposed to be so small that the theory can be linearized about the undisturbed flow previously defined; in this case, $f_j(r, z, t)$ is related to $\sigma_j(r, z, t)$ by the approximate expression

$$f_j(r, z, t) = \frac{r \sigma_j(r, z, t)}{\left[1 + \frac{\Omega^2 r^2}{V_\infty^2}\right]^{\frac{1}{2}}} \quad (j=1, 2, \dots, N) \quad (7)$$

A perturbation velocity potential $\varphi(r, \theta, z, t)$ is supposed to exist; if a_∞ denotes the velocity of sound in undisturbed flow, φ satisfies the wave equation, where

$$M_\infty = \frac{V_\infty}{a_\infty} \quad \beta^2 = 1 - M_\infty^2 \quad (8)$$

$$\frac{\partial^2 \varphi}{\partial r^2} + \frac{1}{r} \frac{\partial \varphi}{\partial r} + \left[\frac{1}{r^2} - \frac{\Omega^2}{V_\infty^2}\right] \frac{\partial^2 \varphi}{\partial \theta^2} + 2 \frac{\Omega V_\infty}{a_\infty^2} \frac{\partial^2 \varphi}{\partial \theta \partial z} + \beta^2 \frac{\partial^2 \varphi}{\partial z^2} + 2 \frac{\Omega}{a_\infty^2} \frac{\partial^2 \varphi}{\partial \theta \partial t} - 2 \frac{V_\infty}{a_\infty^2} \frac{\partial^2 \varphi}{\partial z \partial t} - \frac{1}{a_\infty^2} \frac{\partial^2 \varphi}{\partial t^2} = 0$$

The perturbation pressure p is

$$p = -\rho_\infty \left[\frac{\partial \varphi}{\partial t} - \Omega \frac{\partial \varphi}{\partial \theta} + V_\infty \frac{\partial \varphi}{\partial z} \right] \quad (9)$$

The boundary condition on the blades is:

$$\frac{1}{r^2} \frac{\partial \varphi}{\partial \theta} + \frac{\Omega}{V_\infty} \frac{\partial \varphi}{\partial z} = \frac{\partial \sigma_j}{\partial t} + V_\infty \frac{\partial \sigma_j}{\partial z} \quad (10)$$

Furthermore, the normal derivatives of φ must vanish on the two cylinders:

$$\frac{\partial \varphi}{\partial r}(r_1, \theta, z, t) = 0 \quad (i=1, 2) \quad (11)$$

It should be noted that p satisfies the same equation as φ , and the same boundary conditions on the cylinders. The new variable defined by

$$\alpha = \theta + \frac{\Omega}{V_\infty} z \quad (12)$$

allows the boundary condition on the blades to be written for constant values of α ; the equations of the problem are now:

$$\frac{\partial^2 \varphi}{\partial r^2} + \frac{1}{r} \frac{\partial \varphi}{\partial r} + \left[\frac{1}{r^2} + \frac{\Omega^2}{V_\infty^2}\right] \frac{\partial^2 \varphi}{\partial \alpha^2} + 2 \frac{\Omega}{V_\infty} \frac{\partial^2 \varphi}{\partial \alpha \partial z} + (1-M_\infty^2) \frac{\partial^2 \varphi}{\partial z^2} - 2 \frac{V_\infty}{a_\infty^2} \frac{\partial^2 \varphi}{\partial z \partial t} - \frac{1}{a_\infty^2} \frac{\partial^2 \varphi}{\partial t^2} = 0$$

$$p = -\rho_\infty \left[\frac{\partial \varphi}{\partial t} + V_\infty \frac{\partial \varphi}{\partial z} \right] \quad \frac{\partial \varphi}{\partial r}(r_1, \alpha, z, t) = 0 \quad (i=1, 2) \quad (13)$$

$$\left[\frac{1}{r^2} + \frac{\Omega^2}{V_\infty^2}\right] \frac{\partial \varphi}{\partial \alpha} + \frac{\Omega}{V_\infty} \frac{\partial \varphi}{\partial z} = \frac{\partial \sigma_j}{\partial t} + V_\infty \frac{\partial \sigma_j}{\partial z} \quad \text{on the } j\text{-th blade}$$

The motion of the blades is supposed to be time harmonic dependent, with frequency $\frac{\omega}{2\pi}$ and constant interblade phase angle $\frac{2K\pi}{N}$ ($K=1, 2, \dots, N$). $\sigma_j(r, z, t)$ is then written as

$$\sigma_j(r, z, t) = \sigma(r, z) \operatorname{Re} \left[\exp[i\omega t - i(j-1)\frac{2K\pi}{N}] \right] \quad (j=1, 2, \dots, N) \quad (14)$$

φ and p are then of the form $\operatorname{Re}(\varphi_0 e^{i\omega t})$ and $\operatorname{Re}(p_0 e^{i\omega t})$ and, omitting the subscript 0, the formulation of the problem is now:

$$\frac{\partial^2 \varphi}{\partial r^2} + \frac{1}{r} \frac{\partial \varphi}{\partial r} + \left[\frac{1}{r^2} + \frac{\Omega^2}{V_\infty^2}\right] \frac{\partial^2 \varphi}{\partial \alpha^2} + 2 \frac{\Omega}{V_\infty} \frac{\partial^2 \varphi}{\partial \alpha \partial z} + \beta^2 \frac{\partial^2 \varphi}{\partial z^2} - 2i \frac{\omega V_\infty}{a_\infty^2} \frac{\partial \varphi}{\partial z} + \frac{\omega^2}{a_\infty^2} \varphi = 0$$

$$p = -\rho_\infty \left[i\omega \varphi + V_\infty \frac{\partial \varphi}{\partial z} \right] \quad (15)$$

$$\frac{\partial \varphi}{\partial r}(r_1, \alpha, z) = 0 \quad (i=1, 2)$$

$$\left[\frac{1}{r^2} + \frac{\Omega^2}{V_\infty^2}\right] \frac{\partial \varphi}{\partial \alpha} + \frac{\Omega}{V_\infty} \frac{\partial \varphi}{\partial z} = \left[i\omega \varphi + V_\infty \frac{\partial \varphi}{\partial z} \right] \exp[-i(j-1)\frac{2K\pi}{N}] \quad \text{on the } j\text{-th blade}$$

The blades are equivalent to N sheets of pressure dipoles satisfying the boundary conditions on the cylinders. The velocity potential is then computed in terms of an integral over the blade number one, and the boundary conditions on the blades give an integral equation where the unknown function is the pressure difference δp between the two sides of the blade number one, the right hand side being a known function of σ .

PRESSURE DUE TO N MONOPOLES OR N DIPOLES

If L denotes the partial differential operator of the problem, the pressure p due to N monopoles vibrating with a phase shift $\frac{2K\pi}{N}$, whose coordinates are $r', z', \alpha' + \frac{2\pi}{N}(j-1)$ ($j=1, 2, \dots, N$) satisfies the equation

$$L[p_s] = \frac{1}{r} \delta(r-r') \delta(z-z') \sum_{j=1}^N \exp[-i \frac{2K\pi}{N} (j-1)] \delta[\alpha - \alpha' - \frac{2\pi}{N}(j-1)] \quad (16)$$

$$\frac{\partial p_s}{\partial r}(r_1, \alpha, z) = 0 \quad (i=1, 2)$$

The right hand side being periodic in α with period 2π , is expanded in a Fourier series:

$$L[p_s] = \frac{1}{r} \delta(r-r') \delta(z-z') \frac{N}{2\pi} \sum_{n=-\infty}^{+\infty} \exp[-in'(\alpha-\alpha')] \quad (17)$$

where $n' = nN + K$

This form shows that p can be represented by a Fourier series whose coefficients are Fourier-Bessel series of the radial eigenfunctions $R_{n'm}(\lambda_{n'm} r)$ ($m=1, 2, \dots$) associated with eigenvalues $\lambda_{n'm}$ ($m=1, 2, \dots$) defined by:

$$R_{n'm}'' + \frac{1}{r} R_{n'm}' + (\lambda_{n'm}^2 - \frac{n'^2}{r^2}) R_{n'm} = 0 \quad (18)$$

$$R_{n'm}'(\lambda_{n'm} r_1) = 0 \quad (i=1, 2)$$

These eigenfunctions are normalized as follows (Salaun 1986)

$$\int_{r_1}^{r_2} r R_{n'm_1}(\lambda_{n'm_1} r) R_{n'm_2}(\lambda_{n'm_2} r) dr = r_2^2 \delta_{m_1 m_2} \quad (19)$$

so that $R_{n'm}(\lambda_{n'm} r)$ is given by

$$R_{n'm} = A_{n'm} \left[Y_{n'}'(\lambda_{n'm} r_1) J_{n'}(\lambda_{n'm} r) - J_{n'}'(\lambda_{n'm} r_1) Y_{n'}(\lambda_{n'm} r) \right] \quad (20)$$

where

$$A_{n'm} = \frac{\sqrt{2} \lambda_{n'm} r_2}{\left[\left[\lambda_{n'm}^2 r_2^2 - n'^2 \right] \left[Y_{n'}'(\lambda_{n'm} r_1) J_{n'}(\lambda_{n'm} r_1) - J_{n'}'(\lambda_{n'm} r_1) Y_{n'}(\lambda_{n'm} r_1) \right] \right]^{1/2}} \quad (21)$$

The coefficients $Z_{n'm}(z)$ in p_s

$$p_s = \sum_{n=-\infty}^{+\infty} \sum_{m=1}^{+\infty} Z_{n'm}(z) R_{n'm}(\lambda_{n'm} r) \exp[-in'(\alpha-\alpha')] \quad (22)$$

are solutions to the ordinary differential equation

$$Z_{n'm}'' - \frac{21}{\beta^2} \left[\frac{\partial n'}{\partial z} + \frac{\omega V_\infty}{a_\infty^2} \right] Z_{n'm}' + \frac{1}{\beta^2} \left[\frac{\omega^2}{a_\infty^2} - \lambda_{n'm}^2 - \frac{\Omega^2 n'^2}{V_\infty^2} \right] Z_{n'm} = \frac{N}{2\pi \beta^2 r_2^2} \delta(z-z') R_{n'm}(\lambda_{n'm} r') \quad (23)$$

It is equivalent to find the solutions $Z_{n'm}^{(1)}$ and $Z_{n'm}^{(2)}$ to the homogeneous equation for $z < z'$ and $z > z'$ respectively, with the two conditions

$$Z_{n'm}^{(1)}(z') = Z_{n'm}^{(2)}(z') \quad (24)$$

$$Z_{n'm}^{(2)'}(z') - Z_{n'm}^{(1)'}(z') = \frac{N}{2\pi \beta^2 r_2^2} R_{n'm}(\lambda_{n'm} r')$$

The nature of these solutions depends on D^2 defined as

$$D^2 = \frac{1}{\beta^2} \left[\beta^2 \lambda_{n'm}^2 - \left[\frac{\omega + n' \Omega}{a_\infty} \right]^2 \right] \quad (25)$$

if D^2 is positive, the solutions which increase infinitely with $|z|$ do not occur.

If D^2 is negative, $z_{n'm}^{(1)}$ and $z_{n'm}^{(2)}$ are both linear combinations of two waves which remain undamped at infinity, and a choice must be made such that one wave only occurs both upstream and downstream. The complexity of the waves makes it difficult to select them by the Sommerfeld condition. It is better to use an alternative approach: the time dependence in $e^{i\omega t}$ is replaced by $e^{(a+i\omega)t}$ ($a>0$); all the functions of time are zero for $t=-\infty$ and increase in absolute value, when t increases and the condition to apply to the new waves is that they remain zero at infinity both upstream and downstream. After that, a is made equal to zero.

The case where D^2 is equal to zero is not examined here.

Finally, after some developments given by Salaün (1974), p_g is given by:

$$p_g(r, r', \alpha_0, z_0) = -\frac{N}{4\pi r^2} \sum_{n=-\infty}^{+\infty} \sum_{m=1}^{+\infty} R_{n'm}(\lambda_{n'm} r) R_{n'm}(\lambda_{n'm} r') \frac{\exp(-in'\alpha_0 + i \frac{\Gamma}{\beta^2} z_0 - \frac{\Delta}{\beta^2} |z_0|)}{\Delta} \quad (26)$$

$$\text{where } \alpha_0 = \alpha - \alpha' \quad \text{and} \quad z_0 = z - z'$$

$$\Gamma = \frac{n'\Omega}{V_\infty} + \frac{\omega V_\infty}{a_\infty^2}$$

$$\Delta = \left[\beta^2 \lambda_{n'm}^2 - \left[\frac{\omega + n'\Omega}{a_\infty} \right]^2 \right]^{\frac{1}{2}} \quad \beta^2 \lambda_{n'm}^2 > \left[\frac{\omega + n'\Omega}{a_\infty} \right]^2 \quad (27)$$

$$\Delta = i \operatorname{sgn}(\omega + n'\Omega) \left[\left[\frac{\omega + n'\Omega}{a_\infty} \right]^2 - \beta^2 \lambda_{n'm}^2 \right]^{\frac{1}{2}} \quad \beta^2 \lambda_{n'm}^2 < \left[\frac{\omega + n'\Omega}{a_\infty} \right]^2$$

The possible existence of undamped waves at infinity both upstream and downstream is one of the features of the problem.

The pressure due to N dipoles vibrating with a phase shift $\frac{2K\pi}{N}$ located at the same points as the preceding monopoles, and having their axes normal to the blades, is

$$p_D(r, r', \alpha_0, z_0) = \left[\frac{1}{r'^2} + \frac{\Omega^2}{V_\infty^2} \right]^{\frac{1}{2}} \frac{\partial p_g}{\partial \alpha'} + \frac{\frac{\Omega}{V_\infty}}{\left[\frac{1}{r'^2} + \frac{\Omega^2}{V_\infty^2} \right]^{\frac{1}{2}}} \frac{\partial p_g}{\partial z'}$$

that is to say:

$$p_D(r, r', \alpha_0, z_0) = -\frac{N}{4\pi r^2} \sum_{n=-\infty}^{+\infty} \sum_{m=1}^{+\infty} R_{n'm}(\lambda_{n'm} r) R_{n'm}(\lambda_{n'm} r') \exp(-in'\alpha_0) \times \\ \times \frac{1}{\Delta} \left\{ in' \left[\frac{1}{r'^2} + \frac{\Omega^2}{V_\infty^2} \right]^{\frac{1}{2}} + \frac{1}{\beta^2} [-i\Gamma + \Delta \operatorname{sgn}(z_0)] \frac{\frac{\Omega}{V_\infty}}{\left[\frac{1}{r'^2} + \frac{\Omega^2}{V_\infty^2} \right]^{\frac{1}{2}}} \right\} \exp(i \frac{\Gamma}{\beta^2} z_0 - \frac{\Delta}{\beta^2} |z_0|) \quad (28)$$

PRESSURE AND VELOCITY POTENTIAL DUE TO N SHEETS OF PRESSURE DIPOLES

The pressure discontinuities across the blades are taken into account by distributing over the blades N sheets of pressure dipoles having an intensity proportional to $H(r, z)$ on blade number one. The pressure obtained is expressed as

$$p(r, \alpha_0, z) = \int_{r_1}^{r_2} \int_{z_1}^{z_2} H(r', z') p_D(r, r', \alpha_0, z_0) \left[\frac{1}{r'^2} + \frac{\Omega^2}{V_\infty^2} \right]^{\frac{1}{2}} r' dr' dz' \quad (29)$$

and it can be shown that $H(r, z)$ is equal to the pressure difference between the two sides of the blade number one.

The method used for this is useful in the next paragraph; it consists of analyzing the Fourier series in the neighbourhood of the blades ($\alpha_0 = \frac{j-1}{N} 2\pi$, $j=1, 2, \dots, N$), by the knowledge of the first term of the asymptotic expansion of its coefficients for large values of n' . This term can be obtained when summations and integrations are made in the following order: z' -integration, m -summation, r' -integration, n' -summation. n' being fixed, the first term of the asymptotic expansion of the z' -integral for large values of m is first computed. Thereafter, the first term of the asymptotic expansion of the m -integral for large values of n' is computed; then, the first term of the asymptotic expansion of the r' -integral for large values of n' is computed.

It can be shown, Salaün (1986), that

$$\int_{z_1}^{z_2} H(r', z') \frac{\ln' \left[\frac{1}{r'^2} + \frac{\Omega^2}{V_\infty^2} \right] + \frac{1}{\beta^2} [-i\Gamma + \Delta \operatorname{sgn}(z_0)] \frac{\Omega}{V_\infty}}{\Delta} \exp(i \frac{\Gamma}{\beta^2} z_0 - \frac{\Delta}{\beta^2} |z_0|) dz' \approx$$

$$\approx \left[\frac{1}{r'^2} + \frac{\Omega^2}{V_\infty^2} \right] \frac{2i\Omega'}{\lambda_{n'm}^2 + \frac{\Omega^2 n'^2}{V_\infty^2}} H(r', z) \quad (30)$$

in both subsonic and supersonic relative velocity.

Also, it can be shown, Salaün (1986), that

$$\int_{r_1}^{r_2} r' H(r', z) \left[\frac{1}{r'^2} + \frac{\Omega^2}{V_\infty^2} \right] 2i\Omega' \sum_{m=1}^{+\infty} \frac{R_{n'm}(\lambda_{n'm} r) R_{n'm}(\lambda_{n'm} r')}{\lambda_{n'm}^2 + \frac{\Omega^2 n'^2}{V_\infty^2}} dr' \approx \frac{2ir_2^2}{n'} H(r, z) \quad (31)$$

Therefore, $p(r, \alpha_0, z)$ can be written

$$p(r, \alpha_0, z) = -\frac{iN}{2\pi} H(r, z) \sum_{n=-\infty}^{+\infty} \frac{\exp(-in'\alpha_0)}{n'} + \text{regular terms} =$$

$$= -\frac{iN}{2\pi} H(r, z) \exp(-i\pi\alpha_0) \frac{2i\pi}{\exp(2i\frac{K\pi}{N}) - 1} \exp(iK\alpha_0) + \text{regular terms}$$

where the notation $\{F\}$ means the periodic function of period $\frac{2\pi}{N}$ whose value between 0 and $\frac{2\pi}{N}$ is F . This expression has a jump equal to the pressure difference δp between the two sides of the blade number one:

$$H(r, z) = \delta p = p(r, 2\pi, z) - p(r, 0, z)$$

The pressure p due to the N sheets of pressure dipoles is then:

$$p(r, \alpha_0, z) = \int_{r_1}^{r_2} \int_{z_1}^z \delta p(r', z') p_D(r, r', \alpha_0, z_0) \left[1 + \frac{\Omega^2 r'^2}{V_\infty^2} \right]^{\frac{1}{2}} dr' dz' \quad (33)$$

It is to be noted that, due to the possible existence of undamped waves, p may not vanish at infinity ($z = \pm \infty$); so, the velocity potential which is a solution to the equation

$$i\omega\varphi + V_\infty \frac{\partial \varphi}{\partial z} = -\frac{1}{\rho_\infty} p \quad (34)$$

cannot be expressed as an integral taken from $-\infty$ to z , as it can be done in the classical wing theory. The z -integration constant $C(r, \alpha)$ is determined so that φ is a solution to the partial differential equation of the problem. φ can be written as

$$\varphi = -\frac{1}{\rho_\infty V_\infty} \int_{r_1}^{r_2} \int_{z_1}^z dr' dz' \left[1 + \frac{\Omega^2 r'^2}{V_\infty^2} \right]^{\frac{1}{2}} \delta p(r', z') \exp(-i\frac{\Omega}{V_\infty} z_0) \int_{z_1-z'}^{z_0} \exp(i\frac{\Omega}{V_\infty} \mu) p_D(r, r', \alpha_0, \mu) d\mu +$$

$$+ C(r, \alpha) \exp(-i\frac{\Omega}{V_\infty} z) \quad (35)$$

The term arising from the lower limit in the μ -integral provides in φ a term proportional to $\exp(-i\omega z/V_\infty)$, which is not a solution to the partial differential equation, but is it possible to choose $C(r, \alpha)$ such that this term disappears.

Then, denoting by $F_1(r, r', \alpha_0, \mu)$ an indefinite integral in μ of $\exp(i\omega\mu/V_\infty) p_D(r, r', \alpha_0, \mu)$ for $\mu < 0$ and $F_2(r, r', \alpha_0, \mu)$ an indefinite integral of the same expression for $\mu > 0$, φ can be expressed as

$$\varphi = \frac{-1}{\rho_\infty V_\infty} \int_{r_1}^{r_2} \int_{z_1}^{z_2} \delta p(r', z') \exp(-i \frac{\omega}{V_\infty} z_0) G(r, r', \alpha_0, z_0) \left[1 + \frac{\Omega^2 r'^2}{V_\infty^2} \right]^{1/2} dr' dz' \quad (36)$$

where:

$$G(r, r', \alpha_0, \mu) = \begin{cases} F_1(r, r', \alpha_0, \mu) & (z_0 < 0) \\ F_1(r, r', \alpha_0, 0) + F_2(r, r', \alpha_0, z_0) - F_2(r, r', \alpha_0, 0) & (z_0 > 0) \end{cases} \quad (37)$$

These long but easy calculations give, denoting by E the unit step function:

$$\begin{aligned} \varphi = & \frac{N}{4\pi r_2^2 \rho_\infty V_\infty} \int_{r_1}^{r_2} \int_{z_1}^{z_2} \delta p(r', z') \sum_{n=-\infty}^{+\infty} \sum_{m=1}^{+\infty} R_{n'm}(\lambda_{n'm} r) R_{n'm}(\lambda_{n'm} r') \exp(-in'\alpha_0) \times \\ & \times \left\{ - \frac{\frac{n'}{r'} \frac{\omega+n'\Omega}{V_\infty} + \frac{\Omega r'}{V_\infty} \lambda_{n'm}^2 + i \operatorname{sgn}(z_0) \Delta \left[\frac{n'}{r'} + \frac{\Omega r'}{V_\infty} \frac{\omega+n'\Omega}{V_\infty} \right]}{\Delta \left[\lambda_{n'm}^2 + \left(\frac{\omega+n'\Omega}{V_\infty} \right)^2 \right]} \exp(i \frac{\Gamma}{\beta^2} z_0 - \frac{\Delta}{\beta^2} |z_0|) + \right. \\ & \left. + 2i \frac{\left[\frac{1}{r'} + \frac{\Omega^2}{V_\infty^2} r' \right] n' + \frac{\omega\Omega}{V_\infty^2} r'}{\lambda_{n'm}^2 + \left(\frac{\omega+n'\Omega}{V_\infty} \right)^2} \exp(-i \frac{\omega}{V_\infty} z_0) E(z_0) \right\} dr' dz' \quad (38) \end{aligned}$$

ANALYSIS OF φ AND ITS DERIVATIVES $\frac{\partial \varphi}{\partial \alpha'}, \frac{\partial \varphi}{\partial z}$
INTEGRAL EQUATION OF THE PROBLEM.

The application of the boundary condition on the blade number one implies that α_0 is given the value of zero in $\frac{\partial \varphi}{\partial \alpha'}$ and $\frac{\partial \varphi}{\partial z}$. It is then necessary to know the nature of the Fourier series which appears in φ . The method of analysis is the same as in the preceding paragraph.

The z' - integral in the first term in the parenthesis in φ gives

$$- \int_{z_1}^{z_2} \delta p(r', z') \frac{- \frac{n'}{r'} \frac{\omega+n'\Omega}{V_\infty} + \frac{\Omega r'}{V_\infty} \lambda_{n'm}^2 + i \operatorname{sgn}(z_0) \Delta \left[\frac{n'}{r'} + \frac{\Omega r'}{V_\infty} \frac{\omega+n'\Omega}{V_\infty} \right]}{\Delta \left[\lambda_{n'm}^2 + \left(\frac{\omega+n'\Omega}{V_\infty} \right)^2 \right]} \exp(i \frac{\Gamma}{\beta^2} z_0 - \frac{\Delta}{\beta^2} |z_0|) dz' \quad (39)$$

$$\omega = 2\delta p(r', z) \frac{\Omega r'}{V_\infty} \frac{1}{\lambda_{n'm}^2 + \frac{\Omega^2 r'^2}{V_\infty^2}} + 4\delta p(r', z) \left[\frac{1}{r'} + \frac{\Omega^2 r'}{V_\infty^2} \right] \frac{\Omega}{V_\infty} \frac{n'^2}{\left[\lambda_{n'm}^2 + \frac{\Omega^2 n'^2}{V_\infty^2} \right]^2} + \dots$$

Furthermore, it can be shown, Salaün (1986), that

$$\begin{aligned} \int_{r_1}^{r_2} \sum_{m=1}^{+\infty} R_{n'm}(\lambda_{n'm} r) R_{n'm}(\lambda_{n'm} r') \left\{ - 2\delta p(r', z) \frac{\Omega r'}{V_\infty} \frac{1}{\lambda_{n'm}^2 + \frac{\Omega^2 r'^2}{V_\infty^2}} + \right. \\ \left. + 4\delta p(r', z) \left[\frac{1}{r'} + \frac{\Omega^2 r'}{V_\infty^2} \right] \frac{\Omega}{V_\infty} \frac{n'^2}{\left[\lambda_{n'm}^2 + \frac{\Omega^2 n'^2}{V_\infty^2} \right]^2} \right\} dr' = 2 r_2^2 \delta p(r, z) \frac{\frac{\Omega^2 r^2}{V_\infty^2}}{1 + \frac{\Omega^2 r^2}{V_\infty^2}} \frac{1}{n'^2} + \dots \quad (40) \end{aligned}$$

The series containing $E(z_0)$ in φ gives:

$$\begin{aligned}
 & 2i \int_{r_1}^{r_2} \left\{ \left[\frac{1}{r'} + \frac{\Omega^2}{V_\infty^2} r' \right] n' + \frac{\omega \Omega}{V_\infty^2} r' \right\} \times \\
 & \times \sum_{m=1}^{+\infty} \frac{R_{n',m}(\lambda_{n',m} r) R_{n',m}(\lambda_{n',m} r')}{V_{n',m}^2 + \left[\frac{\omega + n' \Omega}{V_\infty} \right]^2} \int_{z_1}^{z_2} \delta p(r', z') \exp(-i \frac{\omega}{V_\infty} z_0) E(z_0) dz' dr' \\
 & = 2i \left\{ \frac{r_2^2}{n'} - \frac{\frac{\omega \Omega r^2}{V_\infty^2}}{1 + \frac{\Omega^2 r^2}{V_\infty^2}} \frac{1}{n'^2} + \dots \right\} \int_{z_1}^{z_2} \delta p(r, z') \exp(-i \frac{\omega}{V_\infty} z_0) E(z_0) dz'
 \end{aligned} \quad (41)$$

Keeping the term in $\frac{1}{n'^2}$ in φ , in view of the analysis of $\frac{\partial \varphi}{\partial \alpha}$, the following result is obtained:

$$\begin{aligned}
 \varphi = & \frac{N}{2\pi \rho_\infty V_\infty} \delta p(r, z) \frac{\frac{\Omega r^2}{V_\infty}}{1 + \frac{\Omega^2 r^2}{V_\infty^2}} \sum_{n=-\infty}^{+\infty} \frac{\exp(-in' \alpha_0)}{n'^2} + \\
 & + \frac{iN}{2\pi \rho_\infty V_\infty} \int_{z_1}^z \delta p(r, z') \exp(-i \frac{\omega}{V_\infty} z_0) dz' \sum_{n=-\infty}^{+\infty} \left\{ \frac{1}{n'} - \frac{\frac{\omega \Omega r^2}{V_\infty^2}}{1 + \frac{\Omega^2 r^2}{V_\infty^2}} \frac{1}{n'^2} \right\} \exp(-in' \alpha_0) + \text{regular terms}
 \end{aligned} \quad (42)$$

Incidentally, this shows that the discontinuity $\delta \varphi$ across the blade number one is given by

$$\delta \varphi = \varphi(r, 2\pi, z) - \varphi(r, 0, z) = - \frac{1}{\rho_\infty V_\infty} \int_{z_1}^z \delta p(r, z') \exp(-i \frac{\omega}{V_\infty} z_0) dz' \quad (43)$$

The term in $\frac{1}{n'}$ makes impossible the term-by-term derivation with respect to α in φ ; to avoid this trouble, this term, whose sum is known, is written in the form of a double m, n -series which is subtracted term-by-term from the series in φ :

$$\begin{aligned}
 & \frac{iN}{2\pi \rho_\infty V_\infty} \int_{z_1}^z \delta p(r, z') \exp(-i \frac{\omega}{V_\infty} z_0) E(z_0) dz' \sum_{n=-\infty}^{+\infty} \frac{\exp(-in' \alpha_0)}{n'} \\
 & = \frac{iN}{2\pi \rho_\infty V_\infty} \int_{r_1}^{r_2} \int_{z_1}^{z_2} \delta p(r', z') \exp(-i \frac{\omega}{V_\infty} z_0) E(z_0) \delta(r' - r) dr' dz' \sum_{n=-\infty}^{+\infty} \frac{\exp(-in' \alpha_0)}{n'} \\
 & = \frac{iN}{2\pi \rho_\infty V_\infty r_2^2} \int_{r_1}^{r_2} \int_{z_1}^{z_2} \delta p(r', z') \exp(-i \frac{\omega}{V_\infty} z_0) \times \\
 & \times \sum_{n=-\infty}^{+\infty} \sum_{m=1}^{+\infty} \frac{R_{n',m}(\lambda_{n',m} r) R_{n',m}(\lambda_{n',m} r')}{V_{n',m}^2 + \left[\frac{\omega + n' \Omega}{V_\infty} \right]^2} \frac{\exp(-in' \alpha_0)}{n'} E(z_0) r' dr' dz'
 \end{aligned} \quad (44)$$

This is obtained by applying the relation (100) of Salaün (1986). φ then is written in the following form:

$$\varphi = \frac{N}{4\pi\rho_\infty V_\infty r_2^2} \int_{r_1}^{r_2} \int_{z_1}^{z_2} \delta p(r', z') \sum_{n=-\infty}^{+\infty} \sum_{m=1}^{+\infty} R_{n'm}(\lambda_{n'm} r) R_{n'm}(\lambda_{n'm} r') \exp(-in'\alpha_0) \times$$

$$\left\{ -\frac{\frac{n'}{r'} \frac{\omega+n'\Omega}{V_\infty} + \frac{\Omega r'}{V_\infty} \lambda_{n'm}^2 + i \operatorname{sgn}(z_0) \Delta \left[\frac{n'}{r'} + \frac{\Omega r'}{V_\infty} \frac{\omega+n'\Omega}{V_\infty} \right]}{\Delta \left[\lambda_{n'm}^2 + \left(\frac{\omega+n'\Omega}{V_\infty} \right)^2 \right]} \exp\left(i \frac{\Gamma}{\beta^2} z_0 - \frac{\Delta}{\beta^2} |z_0|\right) + \right.$$

$$\left. + 2i \left[\frac{\left(\frac{1}{r'} + \frac{\Omega^2}{V_\infty^2} r' \right) n' + \frac{\omega\Omega}{V_\infty^2} r'}{\lambda_{n'm}^2 + \left(\frac{\omega+n'\Omega}{V_\infty} \right)^2} - \frac{r'}{n'} \right] \exp(-i \frac{\omega}{V_\infty} z_0) E(z_0) \right\} dr' dz' +$$

$$+ \frac{1}{\rho_\infty V_\infty} \frac{\exp(-iK\alpha_0) (\exp(iK\alpha_0))}{1 - \exp(i \frac{2K\pi}{N})} \int_{z_1}^{z_2} \delta p(r, z') \exp(-i \frac{\omega}{V_\infty} z_0) E(z_0) dz' \quad (45)$$

$\frac{\partial \varphi}{\partial z}$ is calculated starting from the expression (38) of φ , and it is easy to see that the terms arising from the derivatives of $\operatorname{sgn}(z_0)$ and $E(z_0)$ cancel each other; $\frac{\partial \varphi}{\partial z}$ thus takes the following form:

$$\frac{\partial \varphi}{\partial z} = \frac{N}{4\pi r_2^2 \rho_\infty V_\infty} \int_{r_1}^{r_2} \int_z^{z_2} \delta p(r', z') \sum_{n=-\infty}^{+\infty} \sum_{m=1}^{+\infty} R_{n'm}(\lambda_{n'm} r) R_{n'm}(\lambda_{n'm} r') \exp(-in'\alpha_0) \times$$

$$\times \left\{ -\frac{\frac{n'}{r'} \frac{\omega+n'\Omega}{V_\infty} + \frac{\Omega r'}{V_\infty} \lambda_{n'm}^2 + i \operatorname{sgn}(z_0) \Delta \left[\frac{n'}{r'} + \frac{\Omega r'}{V_\infty} \frac{\omega+n'\Omega}{V_\infty} \right]}{\Delta \left[\lambda_{n'm}^2 + \left(\frac{\omega+n'\Omega}{V_\infty} \right)^2 \right]} \left[i \frac{\Gamma}{\beta^2} - \operatorname{sgn}(z_0) \frac{\Delta}{\beta^2} \right] \times \right.$$

$$\left. \times \exp\left(i \frac{\Gamma}{\beta^2} z_0 - \frac{\Delta}{\beta^2} |z_0|\right) + 2 \frac{\omega}{V_\infty} \frac{\left[\frac{1}{r'} + \frac{\Omega^2}{V_\infty^2} r' \right] n' + \frac{\omega\Omega}{V_\infty^2} r'}{\lambda_{n'm}^2 + \left(\frac{\omega+n'\Omega}{V_\infty} \right)^2} \exp(-i \frac{\omega}{V_\infty} z_0) E(z_0) \right\} dr' dz' \quad (46)$$

An analysis similar to that of φ shows, after some calculations, that

$$\frac{\partial \varphi}{\partial z} = \frac{iN}{2\pi\rho_\infty V_\infty} \left[\delta p(r, z) - \frac{i\omega}{V_\infty} \int_{z_1}^z \delta p(r, z') \exp(-i \frac{\omega}{V_\infty} z_0) dz' \right] \sum_{n=-\infty}^{+\infty} \frac{\exp(-in'\alpha_0)}{n'} +$$

$$+ \text{regular terms}$$

$\frac{\partial \varphi}{\partial \alpha}$ is calculated from the expression (45) of φ , which gives:

$$\frac{\partial \varphi}{\partial \alpha} = \frac{N}{4\pi r_2^2 \rho_\infty V_\infty} \int_{r_1}^{r_2} \int_{z_1}^{z_2} \delta p(r', z') \sum_{n=-\infty}^{+\infty} \sum_{m=1}^{+\infty} R_{n'm}(\lambda_{n'm} r) R_{n'm}(\lambda_{n'm} r') \exp(-in'\alpha_0) \times$$

$$\times \left\{ in' \frac{-\frac{n'}{r'} \frac{\omega+n'\Omega}{V_\infty} + \frac{\Omega r'}{V_\infty} \lambda_{n'm}^2 + i \operatorname{sgn}(z_0) \Delta \left[\frac{n'}{r'} + \frac{\Omega r'}{V_\infty} \frac{\omega+n'\Omega}{V_\infty} \right]}{\Delta \left[\lambda_{n'm}^2 + \left(\frac{\omega+n'\Omega}{V_\infty} \right)^2 \right]} \exp\left(i \frac{\Gamma}{\beta^2} z_0 - \frac{\Delta}{\beta^2} |z_0|\right) + \right.$$

$$\left. + 2in' \left[\frac{\left[\frac{1}{r'} + \frac{\Omega^2}{V_\infty^2} r' \right] n' + \frac{\omega\Omega}{V_\infty^2} r'}{\lambda_{n'm}^2 + \left(\frac{\omega+n'\Omega}{V_\infty} \right)^2} - \frac{r'}{n'} \right] \exp(-i \frac{\omega}{V_\infty} z_0) E(z_0) \right\} dr' dz' \quad (47)$$

The nature of the n -series in $\frac{\partial \varphi}{\partial \alpha}$ is immediately deduced from the analysis of φ and it is seen that the series

$$\sum_{n=-\infty}^{+\infty} \frac{\exp(-in'a_0)}{n'} \quad \text{in} \quad \left[\frac{1}{r^2} + \frac{\Omega^2}{V_\infty^2} \right] \frac{\partial g}{\partial \alpha} \quad \text{and in} \quad \frac{\Omega}{V_\infty} \frac{\partial g}{\partial z}$$

cancel each other. The normal derivative is continuous on the blades and a_0 can be given the value zero to apply the boundary condition on the blade number one; this gives the integral equation of the problem which takes the following form after some manipulation and rearrangement of terms:

$$\begin{aligned} & \int_{r_1}^{r_2} \int_{z_1}^{z_2} \delta p(r', z') \sum_{n=-\infty}^{+\infty} \sum_{m=1}^{+\infty} \frac{R_{n'm}(\lambda_{n'm} r) R_{n'm}(\lambda_{n'm} r')}{\lambda_{n'm}^2 + \left(\frac{\omega + n'\Omega}{V_\infty} \right)^2} \times \\ & \times \left\{ \exp\left(i \frac{\Gamma}{\beta^2} z_0 - \frac{\Delta}{\beta^2} |z_0|\right) \left[-i \frac{n'}{r'} \frac{n'}{r} \left[\frac{1}{\Delta} \frac{\omega + n'\Omega}{V_\infty} - i \operatorname{sgn}(z_0) \right] + \right. \right. \\ & + i \frac{n'}{r'} \frac{\Omega r}{V_\infty} \left[\frac{\lambda_{n'm}^2}{\Delta} + i \operatorname{sgn}(z_0) \frac{\omega + n'\Omega}{V_\infty} \right] - \frac{\Omega r'}{V_\infty} \frac{n'}{r} \left[-i \frac{\lambda_{n'm}^2}{\Delta} + \operatorname{sgn}(z_0) \frac{\omega + n'\Omega}{V_\infty} \right] + \\ & + \frac{\Omega r'}{V_\infty} \frac{\Omega r}{V_\infty \beta^2} \left[\operatorname{sgn}(z_0) \left[\lambda_{n'm}^2 + M^2 \left(\frac{\omega + n'\Omega}{V_\infty} \right)^2 \right] - i \frac{\omega + n'\Omega}{V_\infty} \left[(2M^2 - 1) \lambda_{n'm}^2 + M^2 \left(\frac{\omega + n'\Omega}{V_\infty} \right)^2 \right] \frac{1}{\Delta} \right] \Bigg\} + \\ & + 2 \exp\left(-i \frac{\omega}{V_\infty} z_0\right) E(z_0) \left\{ \frac{\Omega r}{V_\infty} \frac{n'}{r'} \frac{\omega + n'\Omega}{V_\infty} - \frac{r'}{r} \left[\lambda_{n'm}^2 + \frac{\omega}{V_\infty} \frac{\omega + n'\Omega}{V_\infty} \right] \right. \\ & \left. - \frac{\Omega r}{V_\infty} \frac{\Omega r'}{V_\infty} \lambda_{n'm}^2 + \frac{n'}{r} \frac{n'}{r'} \right\} dr' dz' - \\ & = \frac{4\pi r_2^2 \rho_\infty V_\infty}{N} r (i\omega + V_\infty \frac{\partial g}{\partial z}) \end{aligned} \quad (48)$$

USE OF NONDIMENSIONAL QUANTITIES—METHOD OF SOLUTION OF THE INTEGRAL EQUATION

Nondimensional quantities are defined by the equations:

$$\begin{aligned} z &= \frac{z_2 - z_1}{2} z^* + \frac{z_1 + z_2}{2} & -1 \leq z^* \leq +1 \\ r &= r_2 r^* & r_1^* \leq r^* \leq 1 \end{aligned} \quad (49)$$

$$\begin{aligned} r_1 &= r_2 r_1^* \\ \omega_R &= \frac{\omega l}{V_\infty} & \Omega_R &= \frac{\Omega l}{V_\infty} & r &= \frac{l}{r_2} \end{aligned} \quad (50)$$

$$\delta p = \frac{\rho_\infty V_\infty^2}{2} C_p(r^*, z^*) \quad (51)$$

$$\begin{aligned} \lambda_{n'm} r_2 &= \lambda_{n'm}^* \\ H &= \left[\beta^2 r^2 \lambda_{n'm}^{*2} - M^2 (\omega_R + n' \Omega_R)^2 \right]^{1/2} = \Delta^* \quad (\Delta^* \text{ real}) \\ H &= i \operatorname{sgn}(\omega_R + n' \Omega_R) \left[M^2 (\omega_R + n' \Omega_R)^2 - \beta^2 r^2 \lambda_{n'm}^{*2} \right]^{1/2} = \Delta^* \quad (\Delta^* \text{ imaginary}) \\ H' &= n' \Omega_R + M^2 \omega_R - \Gamma^* \end{aligned} \quad (52)$$

Then the integral equation takes the following form:

$$\begin{aligned}
& \int_{-1}^{+1} \int_{r_1^*}^{+1} c_p(r^*, z^*) \sum_{n=-\infty}^{+\infty} \sum_{m=1}^{+\infty} \frac{R_{n'm}(\lambda_{n'm}^* r^*) R_{n'm}(\lambda_{n'm}^* r'^*)}{\lambda_{n'm}^{*2} r^2 + (\omega_{R+n'\Omega_R})^2} \left\{ \exp(i \frac{\Gamma^*}{\beta^2} z_0^* - \frac{\Delta^*}{\beta^2} |z_0^*|) \times \right. \\
& \times \left[\frac{n'^2 r^2}{r^* r'^*} \left[-1 - \frac{\omega_{R+n'\Omega_R}}{\Delta^*} \operatorname{sgn}(z_0^*) \right] + n' \Omega_R \left[\frac{\Gamma^*}{r^*} + \frac{\Gamma'^*}{r'^*} \right] \left[1 - \frac{\lambda_{n'm}^{*2} r^2}{\Delta^*} - \operatorname{sgn}(z_0^*) (\omega_{R+n'\Omega_R}) \right] + \right. \\
& + \frac{\Omega_R^2}{\beta^2 r^2} r^* r'^* \left[\operatorname{sgn}(z_0^*) \left[\lambda_{n'm}^{*2} r^2 + M^2 (\omega_{R+n'\Omega_R})^2 \right] - 1 (\omega_{R+n'\Omega_R}) \left[\lambda_{n'm}^{*2} r^2 (2M^2 - 1) + M^2 (\omega_{R+n'\Omega_R})^2 \right] \frac{1}{\Delta^*} \right] \Bigg\} + \\
& + 2 \exp(-i \omega_R z_0^*) E(z_0^*) \left[\Omega_R \frac{\Gamma^*}{r^*} n' (\omega_{R+n'\Omega_R}) - \frac{\Gamma'^*}{r'^*} \left[\lambda_{n'm}^{*2} r^2 + \omega_R (\omega_{R+n'\Omega_R}) \right] + \right. \\
& \left. - \Omega_R^2 r^* r'^* \lambda_{n'm}^{*2} + \frac{\Omega_R^2 r^2}{r^* r'^*} \right] \Bigg\} dr'^* dz'^* \\
& - \frac{1}{2} \left(\frac{1}{r^*} + \frac{1}{r'^*} \right) r^* r'^*
\end{aligned} \tag{53}$$

set of orthogonal functions of r^* and z^* , and the Galerkin method gives a linear system whose unknowns are the coefficients in C_p .

In the subsonic case, C_p is expanded in series of $R_{ok}(\lambda_{ok}^* r^*)$ and polynomials $G_\mu(z^*)$ defined by

$$\int_{-1}^{+1} \frac{[1-z^*]^{1/2}}{[1+z^*]} G_{\mu_1}(z^*) G_{\mu_2}(z^*) dz^* = \delta_{\mu_1 \mu_2} \tag{54}$$

The expansion of the right hand side uses $G_\mu(-z^*)$ ($\mu=1,2,\dots$). It is known that these polynomials are well suited for an isolated airfoil and therefore they are used here.

In the supersonic case, the Mach waves emanating from the leading and trailing edge of a blade reflect on adjacent blades, such that C_p has simple discontinuities. To take into account these discontinuities in the pressure representation is a difficult task in a three-dimensional analysis (see Namba's analysis in the present volume). Here C_p is approximated by continuous functions. Comparisons between the results obtained with these two C_p -representations have been made by Salaün (1978) in the two-dimensional analysis, and it is shown that the generalized forces are in good agreement.

In the supersonic case, C_p and the right hand side are thus expanded in a series of Legendre polynomials P_μ defined by

$$\int_{-1}^{+1} P_{\mu_1} P_{\mu_2} dz^* = \frac{2}{2\mu_1 - 1} \delta_{\mu_1 \mu_2} \tag{55}$$

Let $Y_{\mu k}$ ($\mu=1,2,\dots$; $k=1,2,\dots$) be the coefficients of the C_p expansion:

$$C_p = \frac{[1-z^*]^{1/2}}{[1+z^*]} \sum_{\mu} \sum_k Y_{\mu k} G_{\mu}(z^*) R_{ok}(\lambda_{ok}^* r^*) \tag{56}$$

in the subsonic case;

$$C_p = \sum_{\mu} \sum_k Y_{\mu k} P_{\mu}(z^*) R_{ok}(\lambda_{ok}^* r^*)$$

in the supersonic case.

Let $X_{\nu l}$ ($\nu=1,2,\dots; l=1,2,\dots$) be the coefficients of the right hand side expansion:

$$i\omega_R \sigma + \frac{\partial \sigma}{\partial z^*} = \sum_{\nu} \sum_l X_{\nu l} G_{\mu}(-z^*) R_{ok}(\lambda_{ok}^* r^*)$$

in the subsonic case

(57)

$$i\omega_R \sigma + \frac{\partial \sigma}{\partial z^*} = \sum_{\nu} \sum_l X_{\nu l} P_{\mu}(z^*) R_{ok}(\lambda_{ok}^* r^*)$$

in the supersonic case.

The Fourier and Fourier-Bessel series are integrated term by term, in order to avoid the treatment of the kernel singularities.

The following integrals then appear:

$$P_{kn'm} = \int_{r_1}^{+1} r^* R_{ok}(\lambda_{ok}^* r^*) R_{n'm}(\lambda_{n'm}^* r^*) dr^*$$

$$Q_{kn'm} = \int_{r_1}^{+1} \frac{1}{r^*} R_{ok}(\lambda_{ok}^* r^*) R_{n'm}(\lambda_{n'm}^* r^*) dr^*$$
(58)

$$U_{\mu\nu n'm} = \int_{-1}^{+1} dz^* \left[\frac{1+z^*}{1-z^*} \right]^{1/2} G_{\nu}(-z^*) \int_{-1}^{z^*} \left[\frac{1-z'^*}{1+z'^*} \right]^{1/2} G_{\mu}(z'^*) \exp(i \frac{\Gamma^*}{\beta^2} z_0^* - \frac{\Delta^*}{\beta^2} z_0^*) dz'^*$$

in the subsonic case

$$U_{\mu\nu n'm} = \int_{-1}^{+1} dz^* P_{\nu}(z^*) \int_{-1}^{z^*} P_{\mu}(z'^*) \exp(i \frac{\Gamma^*}{\beta^2} z_0^* - \frac{\Delta^*}{\beta^2} z_0^*) dz'^*$$
(59)

in the supersonic case

$$V_{\mu\nu n'm} = \int_{-1}^{+1} dz^* \left[\frac{1+z^*}{1-z^*} \right]^{1/2} G_{\nu}(-z^*) \int_{z^*}^{+1} \left[\frac{1-z'^*}{1+z'^*} \right]^{1/2} G_{\mu}(z'^*) \exp(i \frac{\Gamma^*}{\beta^2} z_0^* + \frac{\Delta^*}{\beta^2} z_0^*) dz'^*$$
(60)

in the subsonic case

$$V_{\mu\nu n'm} = \int_{-1}^{+1} dz^* P_{\nu}(z^*) \int_{z^*}^{+1} P_{\mu}(z'^*) \exp(i \frac{\Gamma^*}{\beta^2} z_0^* + \frac{\Delta^*}{\beta^2} z_0^*) dz'^*$$

in the supersonic case

$$W_{\mu\nu} = \int_{-1}^{+1} dz^* \left[\frac{1+z^*}{1-z^*} \right]^{1/2} G_{\nu}(-z^*) \int_{-1}^{z^*} \left[\frac{1-z'^*}{1+z'^*} \right]^{1/2} G_{\mu}(z'^*) \exp(-i\omega_R z_0^*) dz'^*$$

in the subsonic case;

(61)

$$W_{\mu\nu} = \int_{-1}^{+1} dz^* P_{\nu}(z^*) \int_{-1}^{z^*} P_{\mu}(z'^*) \exp(-i\omega_R z_0^*) dz'^*$$

in the supersonic case

The linear system of equations takes then the following form:

$$\begin{aligned}
 & \sum_{\mu} \sum_k Y_{\mu k} \sum_{n=-\infty}^{+\infty} \sum_{m=1}^{+\infty} \left\{ \frac{1}{\lambda_{n,m}^{*2} r^2 + (\omega_R + n' \Omega_R)^2} \times \right. \\
 & \times \left\{ n'^2 r^2 Q_{kn'm} Q_{ln'm} \left[- (U_{\mu\nu n'm} - V_{\mu\nu n'm}) - i \frac{\omega_R + n' \Omega_R}{\Delta^*} (U_{\mu\nu n'm} + V_{\mu\nu n'm}) \right] + \right. \\
 & + n' \Omega_R (P_{kn'm} Q_{ln'm} + P_{ln'm} Q_{kn'm}) \left[- (\omega_R + n' \Omega_R) (U_{\mu\nu n'm} - V_{\mu\nu n'm}) + i \frac{\lambda_{n,m}^{*2} r^2}{\Delta^*} (U_{\mu\nu n'm} + V_{\mu\nu n'm}) \right] + \\
 & + \frac{\Omega_R^2}{\beta^2 r^2} P_{kn'm} P_{ln'm} \left[\left[\lambda_{n,m}^{*2} r^2 + M^2 (\omega_R + n' \Omega_R)^2 \right] (U_{\mu\nu n'm} - V_{\mu\nu n'm}) + \right. \\
 & \left. \left. - i \frac{(\omega_R + n' \Omega_R) [\lambda_{n,m}^{*2} r^2 (2M^2 - 1) + M^2 (\omega_R + n' \Omega_R)^2]}{\Delta^*} (U_{\mu\nu n'm} + V_{\mu\nu n'm}) \right] \right\} + \\
 & + \frac{2}{\lambda_{n,m}^{*2} r^2 + (\omega_R + n' \Omega_R)^2} \left\{ Q_{kn'm} P_{ln'm} n' \Omega_R (\omega_R + n' \Omega_R) - P_{kn'm} Q_{ln'm} \left[\lambda_{n,m}^{*2} r^2 + \omega_R (\omega_R + n' \Omega_R) \right] - \right. \\
 & \left. - P_{kn'm} P_{ln'm} \lambda_{n,m}^{*2} \Omega_R^2 + Q_{kn'm} Q_{ln'm} n'^2 r^2 \right\} W_{\mu\nu} \left. \right\} = \frac{8\pi}{N r^2} X_{\nu l}
 \end{aligned} \quad (62)$$

GENERALIZED FORCES

The flutter mode which is examined is only one degree of freedom flutter, and the generalized force on blade number one is

$$G = \int_{r_1}^{r_2} \int_{z_1}^{z_2} \delta p \frac{\sigma r}{[1 + \frac{\Omega^2 r^2}{V_\infty^2}]^{1/2}} [1 + \frac{\Omega^2 r^2}{V_\infty^2}]^{1/2} dr dz - l r_2^2 \int_{r_1}^{+1} \int_{-1}^{+1} \delta p \sigma r^* dr^* dz^* \quad (63)$$

that is to say, when δp is replaced by its expression,

$$G = \frac{1}{2} \rho_\infty V_\infty^2 l r_2^2 \sum_{\mu} \sum_k Y_{\mu k} A_{\mu k} \quad (64)$$

where $A_{\mu k}$ are the components of the expansion of σ in the orthogonal sets $R_{ok}(\lambda_{ok}^* r^*)$, $G_\mu(z^*)$ in subsonic flow, $P_\mu(z^*)$ in supersonic flow.

$$A_{\mu k} = \int_{-1}^{+1} dz^* \left[\frac{1-z^*}{1+z^*} \right]^{1/2} G_\mu(z^*) \int_{r_1}^{+1} r^* R_{ok}(\lambda_{ok}^* r^*) \sigma dr^* \quad (\text{subsonic}) \quad (65)$$

$$A_{\mu k} = \int_{-1}^{+1} dz^* P_\mu(z^*) \int_{r_1}^{+1} r^* R_{ok}(\lambda_{ok}^* r^*) \sigma dr^* \quad (\text{supersonic})$$

Details of the numerical evaluation are given by Salaun (1986).

NUMERICAL RESULTS

The motions examined here are bending and torsion, with the nodal line defined by constant value of z . Let $th^*(r^*)$ be the normal deflection of the mid-chord point and $\delta(r^*)$ the angle of rotation of the chord; $f(r, z)$ is taken in the form

$$f(r, z) = \delta(r^*) s + \ell h^*(r^*) - \delta(r^*) \left[1 + \frac{\Omega^2 r^{*2}}{v^2} \right]^{1/2} z + \ell h^*(r^*) \quad (66)$$

is given by

$$v = r \left[1 + \frac{\Omega^2 r^{*2}}{r^2} \right] \delta \frac{z^*}{r^*} + r \left[1 + \frac{\Omega^2 r^{*2}}{r^2} \right]^{1/2} \frac{1}{r^*} h^* \quad (67)$$

It is easily shown that $X_{\nu\ell}$ and $A_{\mu k}$ have the following expressions in the subsonic case:

$$X_{1\ell} = r\sqrt{\pi} \int_{r_1^*}^{+1} R_{01}(\lambda_{01}^* r^*) \left\{ \left[1 + \frac{\omega_R}{2} \right] \left[1 + \frac{\Omega^2 r^{*2}}{r^2} \right] \delta + i\omega_R \left[1 + \frac{\Omega^2 r^{*2}}{r^2} \right]^{1/2} h^* \right\} dr^* \quad (68)$$

$$X_{2\ell} = r\sqrt{\pi} i \frac{\omega_R}{2} \int_{r_1^*}^{+1} \left[1 + \frac{\Omega^2 r^{*2}}{r^2} \right] \delta dr^*$$

$$X_{\nu\ell} = 0 \quad \nu > 2$$

$$A_{1k} = r\sqrt{\pi} \int_{r_1^*}^{+1} R_{0k}(\lambda_{0k}^* r^*) \left\{ -\frac{1}{2} \left[1 + \frac{\Omega^2 r^{*2}}{r^2} \right] \delta + \left[1 + \frac{\Omega^2 r^{*2}}{r^2} \right]^{1/2} h^* \right\} dr^* \quad (69)$$

$$A_{2k} = -\frac{r\sqrt{\pi}}{2} \int_{r_1^*}^{+1} R_{0k}(\lambda_{0k}^* r^*) \left[1 + \frac{\Omega^2 r^{*2}}{r^2} \right] \delta dr^*$$

$$A_{\mu k} = 0 \quad \mu > 2$$

In the supersonic case, they take the following form:

$$X_{1\ell} = 2r \int_{r_1^*}^{+1} R_{0\ell}(\lambda_{0\ell}^* r^*) \left\{ \left[1 + \frac{\Omega^2 r^{*2}}{r^2} \right] \delta + i\omega_R \left[1 + \frac{\Omega^2 r^{*2}}{r^2} \right]^{1/2} h^* \right\} dr^* \quad (70)$$

$$X_{2\ell} = \frac{2}{3} i\omega_R r \int_{r_1^*}^{+1} R_{0\ell}(\lambda_{0\ell}^* r^*) \left[1 + \frac{\Omega^2 r^{*2}}{r^2} \right] \delta dr^*$$

$$X_{\nu\ell} = 0 \quad \nu > 2$$

$$A_{1k} = \frac{2r}{3} \int_{r_1^*}^{+1} R_{0k}(\lambda_{0k}^* r^*) \left[1 + \frac{\Omega^2 r^{*2}}{r^2} \right]^{1/2} h^* dr^* \quad (71)$$

$$A_{2k} = \frac{2r}{3} \int_{r_1^*}^{+1} R_{0k}(\lambda_{0k}^* r^*) \left[1 + \frac{\Omega^2 r^{*2}}{r^2} \right] \delta dr^*$$

$$A_{\mu k} = 0 \quad \mu > 2$$

In the case of a bending motion, $zh^*(1)$ is taken equal to $c(r_2)$ and in the case of a torsional motion $\delta(1)$ is taken equal to 1. S being the area of the blade, the non-dimensionalized generalized force G^* is defined by

$$G^* = \frac{Q}{\frac{1}{2} \rho_\infty v_\infty^2 S c(r_2)} \quad (72)$$

There is flutter when $\text{Im}(G^*)$ is positive.

The numerical results presented here refer to a cascade having a hub to tip ratio equal to 0.398.

No flutter has been found in the pure bending motion in both subsonic and supersonic relative velocity.

In the pure torsional motion about the mid-chord axis, it is difficult to find flutter in the subsonic case. However, Figures 2 and 3 give two examples of torsional flutter, for reasonable values of the parameters. The cascade has 21 blades; the Figures 2 and 3 differ by the values of $\gamma(r_2)$, respectively equal to 50° and 55° , but the value of the axial Mach number is kept constant, equal to 0.459.

The reduced blade spacing, defined by

$$b^*(r_2) = \frac{2\pi r_2}{Nc(r_2)} \quad (73)$$

is equal to 1.728. The other parameters are indicated on the figures. The points are joined by solid lines, which is meaningless, but gives more clarity. The flutter occurs occurs for values of the interblade phase angle such that there is no undamped wave at infinity. In each case, one interblade phase angle only gives instability.

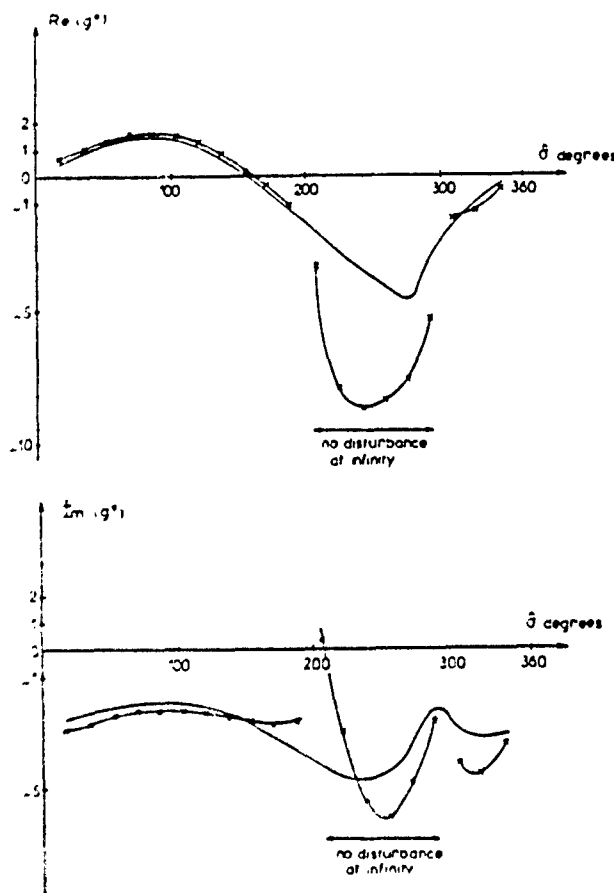


Fig. 2 Dimensionless Generalized Force as Function of Interblade Phase Angle (Torsional Motion)

$r_1^* = 0.398$ $r = 0.111$ $\gamma(r_2) = 50^\circ$ $N = 21$ $\omega R = 1.375$ $M_\infty = 0.459$ $M(r_2) = 0.714$ $f^*(r_2) = 1.728$

— x — x — x — Three dimensional theory
 ————— Strip theory

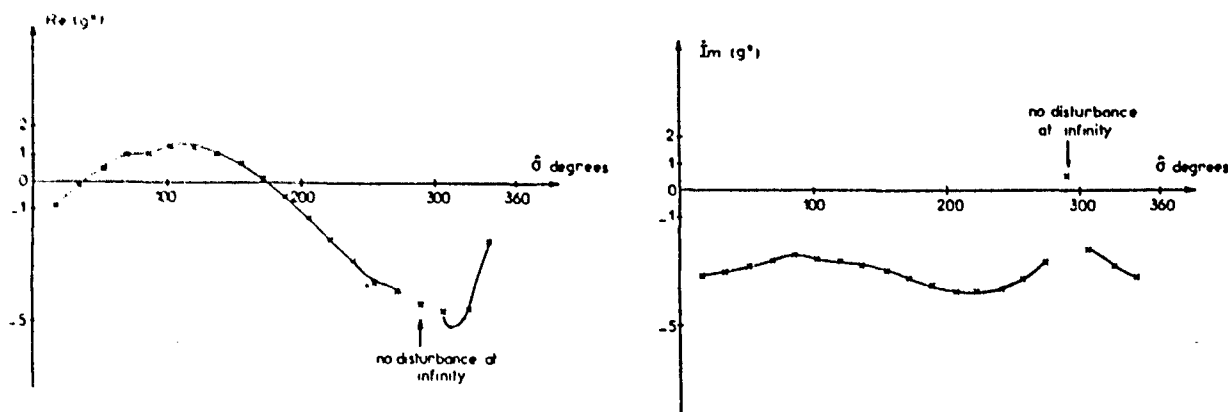


Fig. 3. Dimensionless Generalized Force as Function of Interblade Phase Angle (Torsional Motion)

$$r_1^* = 0.398 \quad \tau = 0.099 \quad \gamma(r_2) = 55^\circ \quad N = 21 \quad f^*(r_2) = 1.728 \quad \omega_R = 1.227 \quad M_\infty = 0.459 \quad M(r_2) = 0.8$$

This flutter disappears when $\gamma(r_2)$ increases to 60° , as shown in Fig. 4.

In the case where $\gamma(r_2)$ is equal to 55° , the flutter disappears also when the number of blades decreases to 20 or increases to 22, the reduced blade spacing and the reduced thickness being kept constant, this latter constraint is obtained giving a convenient thickness to the blade and using a finite element program for the determination of the new frequency (Fig. 5 and 6).

It should be noted that the strip theory gives no flutter in this case, and this fact shows the importance of the three-dimensional effects (Fig. 2).

Similar results have been found by Salaün (1974), in a case which was not so close to the actual fans.

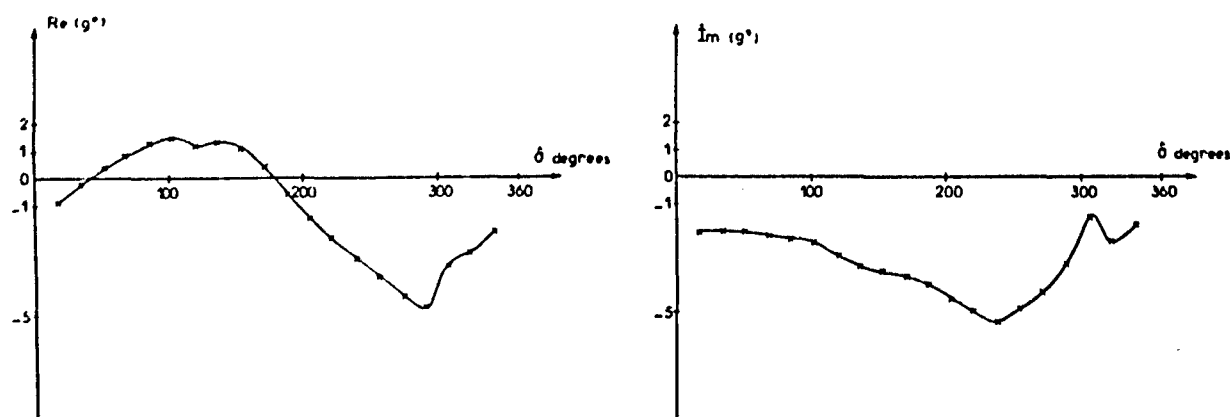


Fig. 4. Dimensionless Generalized Force as Function of Interblade Phase Angle (Torsional Motion)

$$r_1^* = 0.398 \quad \tau = 0.086 \quad \gamma(r_2) = 60^\circ \quad N = 21 \quad f^*(r_2) = 1.728 \quad \omega_R = 1.070 \quad M_\infty = 0.459 \quad M(r_2) = 0.918$$

A quite different situation is encountered in the supersonic case where torsional flutter is easily found for many interblade phase angles, as shown by Salaün (1979). The difficulty seems to make it disappear and this can be achieved, in the particular example of Fig. 7, by shortening the number of blades, the reduced blade spacing and the reduced blade thickness being kept constant. It is seen that this gives a spectacular effect.

The number of blades seems thus to be a very important parameter in the study of supersonic instabilities.

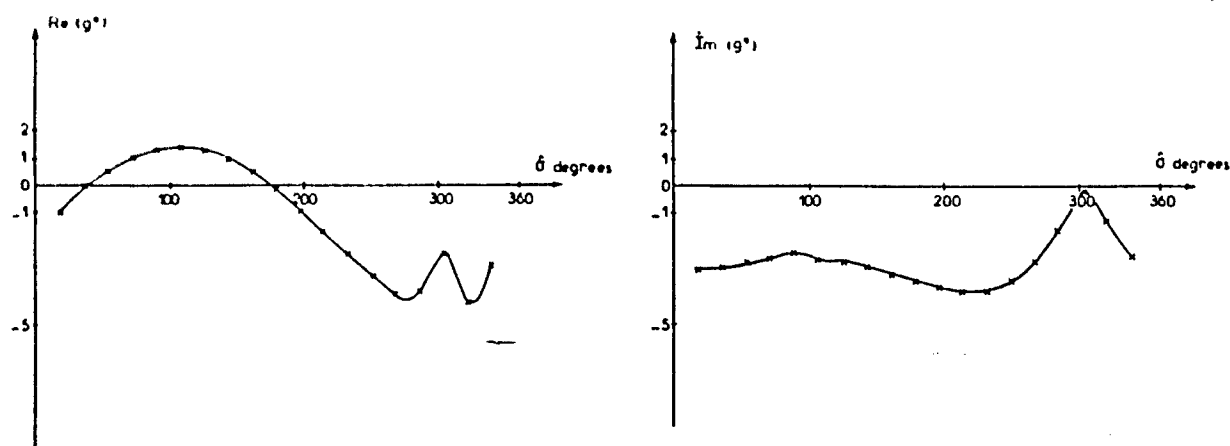


Fig. 5. Dimensionless Generalized Force as Function of Interblade Phase Angle (Torsional Motion)

$$r_1^* = 0.398 \quad r = 0.104 \quad \gamma(r_2) = 55^\circ \quad N = 20 \quad f^*(r_2) = 1.728 \quad \omega_R = 1.305 \quad M_\infty = 0.459 \quad M(r_2) = 0.8$$

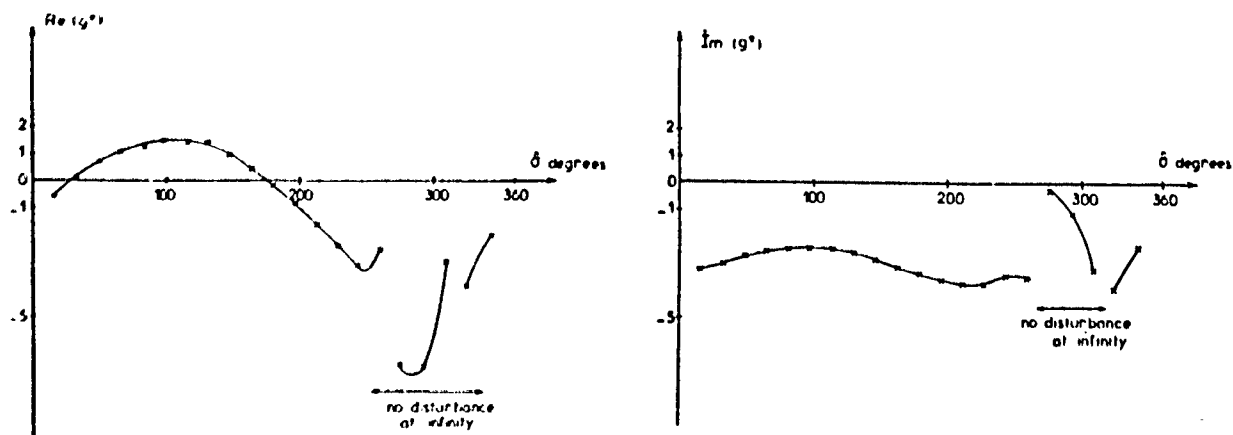


Fig. 6. Dimensionless Generalized Force as Function of Interblade Phase Angle (Torsional Motion)

$$r_1^* = 0.398 \quad r = 0.095 \quad \gamma(r_2) = 55^\circ \quad N = 22 \quad f^*(r_2) = 1.728 \quad \omega_R = 1.152 \quad M_\infty = 0.459 \quad M(r_2) = 0.8$$

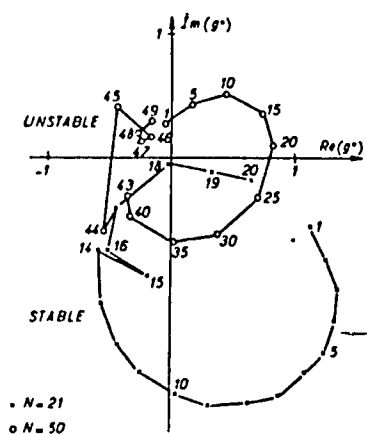


Fig. 7. Dimensionless Generalized Force as Function of Interblade Phase Angle $\frac{2K\pi}{N}$ ($K=1,2,\dots$)

$$r_1^* = 0.398 \quad \tau = 0.099 \quad \gamma(r_2) = 55^\circ$$

$$f^*(r_2) = 1.728 \quad M_\infty = 0.917 \quad M(r_2) = 1.6$$

$$\omega_R = \begin{matrix} 0.613 & \text{if } N=21 \\ 0.221 & \text{if } N=50 \end{matrix}$$

NUMERICAL METHODS FOR UNSTEADY TRANSONIC FLOW

E Acton
Topexpress Ltd., Cambridge, CB5 8AD, UK.

S G Newton
Rolls-Royce plc., Derby, DE2 8BJ, UK.

INTRODUCTION

In this chapter, we review some of the numerical methods used in aeroelastic problems to calculate unsteady transonic flow. We have restricted our attention to two major aeroelastic problems - blade flutter and what is known as forced response. In both problems, the purpose of the calculation is the prediction of unsteady loading on the blades so that the unsteady lift and moments may form the forcing terms of a separate analysis of structural vibration. It is usual in turbomachine calculations to assume that structural and aerodynamic behaviour can be decoupled; that is the unsteady aerodynamic forces have an insignificant effect on the blade vibration characteristics. Although this is certainly justified for conventional turbomachinery designs it could possibly be less well satisfied by future propeller blading.

In forced response, the unsteady loading arises from incoming unsteadiness in the flow, usually due to the wakes of upstream blade rows. Some engine vibration is then observed at frequencies corresponding to each engine order. In response to a given periodic forcing of this type, away from resonance the blade amplitude will be fairly small and depend little on the aerodynamic and mechanical damping. Flutter, on the other hand, is an instability arising when the aerodynamic response to blade motion causes resonant self-excitation, so that the amplitude of the motion increases. This is illustrated in Figure 1 which shows a Campbell diagram for a model rotor. The intensity of shading on the diagram corresponds to vibration of the rotor. The odd engine orders are shown as dashed lines and at the lower orders these are accompanied by the vibration that is termed forced response. The lines at nearly constant frequency which cross the engine order lines correspond to structural modes excited in flutter. Resonances occur where the engine order lines and the structural modes cross. Considerably more blade vibration can occur in flutter; this is shown more clearly in Figure 2.

The onset of flutter may be determined by evaluating a work integral, and flutter is said to occur when energy is being transferred from the flow to the blade motion rather than vice versa. This is often referred to as negative aerodynamic damping. At resonances, where forcing frequency coincides with a blade natural frequency, the response will also depend on the aerodynamic (and structural) damping. Thus to predict the amplitude at resonance aerodynamic solutions of both

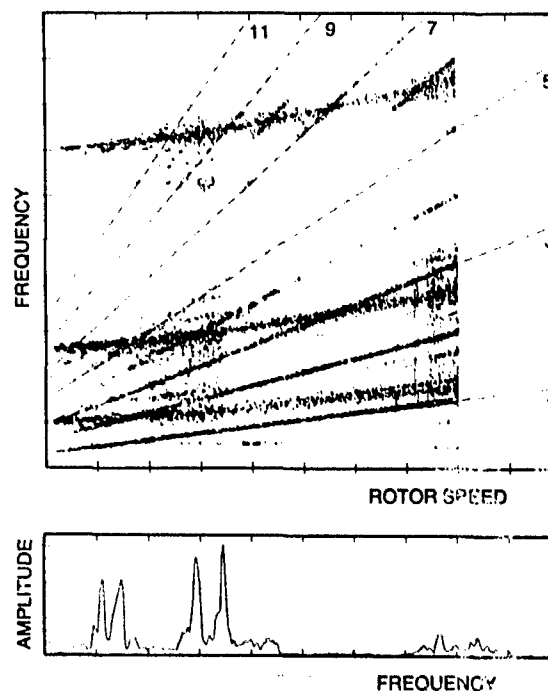


Figure 1 Campbell diagram for a model rotor

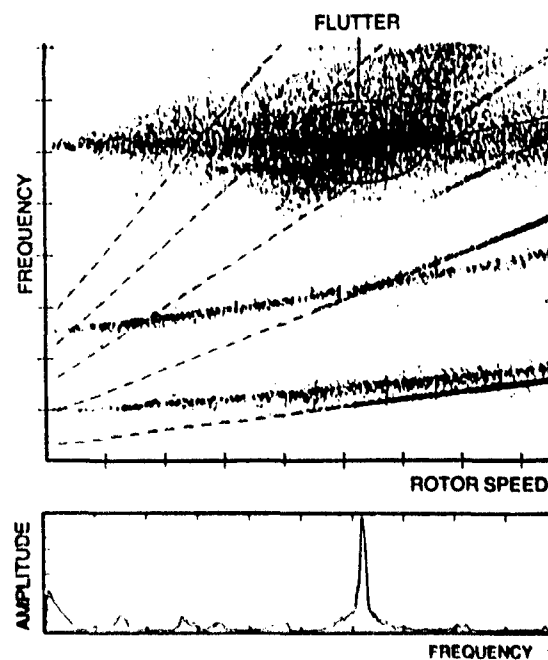


Figure 2 Campbell diagram for a model rotor showing strong flutter

the forced response and flutter problems are needed.

These physical differences between the two problems of forced response and flutter give rise to corresponding differences in the model problem attempted in each case. In both problems, the flow through the blade rows is unsteady and periodic, but only in calculating aerodynamic damping is it necessary to allow for any interaction between the blade motion and the flow. Away from resonance in forced response calculations, aerodynamic damping is unimportant and the blades may be assumed to be stationary. The unsteadiness in the flow arising from incoming wakes may be large, whereas for flutter, initially at least, this will not be so. During flutter the blade amplitude will be limited eventually by non-linear structural damping, but this is not usually of interest: flutter calculation methods are required simply to predict the onset of flutter (and so determine the flutter boundaries in an engine operating map as shown in Figure 3). For this reason the unsteady flow during flutter may be assumed to be a small, linear perturbation of the steady flow through the blade rows. Consequently, the flutter problem in some guises is amenable to analytical techniques, and these have been described in earlier chapters of this volume. The analytical problem is not easy, particularly when shocks are present, and is only tractable when further simplifying assumptions are made concerning the steady flow through the blade rows, in particular that the flow is uniform and the blades themselves are represented as flat plates. Numerical methods become necessary when these assumptions are relaxed. Similarly analytical calculations of forced response have been made by Nagashima & Whitehead (1978), and Smith (1971) but field methods have been developed for the usual case where the aerodynamic fluctuations are large. These methods are not usually applicable to the resonance problem since for non-linear incoming perturbations, the blade motion and forced response problems cannot be decoupled.

In this review we shall describe attempts to predict both flutter and forced response, although the majority of the work reviewed is concerned with flutter; few successful attempts at calculating forced response have been made. As mentioned earlier, although numerical methods have been used when the steady flow is non-uniform, many restrictive assumptions remain necessary. The development of numerical methods to calculate unsteady flow in turbomachines has followed on from calculation methods available for steady flow, but in both cases are perhaps less developed than the corresponding methods used in external aerodynamics. A useful account detailing many numerical methods for computing steady and unsteady flow in a wide range of applications is given by Peyret & Taylor (1985). In turbomachine applications most methods to date have assumed a two-dimensional unsteady flow through a linear cascade, and furthermore

that the flow is inviscid. An important aerodynamic assumption being made is that both the steady and unsteady flows are attached. The solution is usually obtained for a two-dimensional strip of the blade where each section is assumed to move as a rigid body; although it may be reasonable to model steady flow as two-dimensional between stream surfaces there is less justification for assuming that the unsteady flow is also two-dimensional. The most commonly-used methods for unsteady flow assume potential flow through the cascade, and these methods are described in detail in the next section.

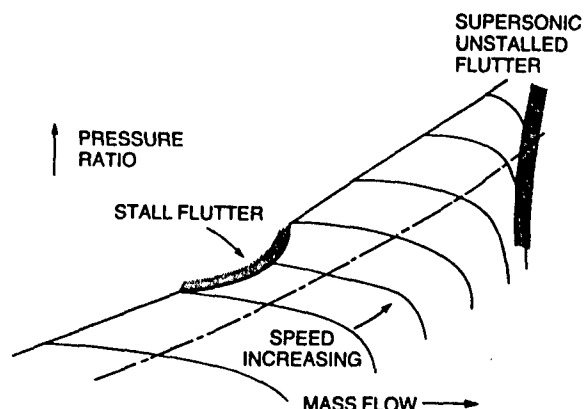


Figure 3 Typical engine operating map

We consider only field methods here and do not describe those methods that produce series or closed form solutions which are then computed numerically (for example Atassi & Akai (1978), Goldstein, Braun & Adamczyk (1977), et alia). The two major contributions to field methods for potential flow are due to Whitehead (1982) and Caspar & Verdon (1981, 1982). Both these methods solve the potential flow equations and yet are capable of treating transonic flow. An outline of the two methods is given in the next section where their differences and similarities are identified and discussed. Both methods adopt a linearized approach in which the flow is decomposed into a steady component and a small unsteady perturbation which is linear in the blade motion amplitude. This allows a simple harmonic time dependence to be assumed for the unsteady flow and the time derivatives to be eliminated from the governing equations.

If wake vorticity and unsteady shock waves are to be treated, then the inclusion of rotationality even in an otherwise inviscid flow is necessary. In this case numerical solutions of the Euler equations are required. Methods for solving these equations have now been developed for steady flow and have been extended to include unsteady flow. These methods are described in the third section of this chapter. With time dependent terms included, the Euler equations are hyperbolic and provided that the equations are written in terms of conserved quantities (mass, momentum and energy) shock waves

may be found in the numerical solution. These appear in the flow solution and are said to be 'captured'. The presence of a shock wave does however require some viscous dissipation and so it is necessary either that the difference scheme is constructed so that the truncation error is predominantly dissipative or some form of artificial dissipation must be added to the scheme. (In calculations where the conservation form of the equations is not used, it is necessary to treat the shocks as internal boundaries across which the Rankine-Hugoniot conditions hold: this is known as shock 'fitting' (de Neef & Moretti, 1980)).

Time marching solutions of the Euler equations by finite difference methods have followed two computationally distinct approaches. The first is a differential approach where the physical region in which the equations are to be solved is mapped into a rectangular region in the computational domain using a suitable transformation. Both steady and unsteady solutions have been obtained, using explicit differencing schemes such as MacCormack (1976) or Lax Wendroff, or implicit schemes such as the factored algorithm methods described by Warming & Beam (1978). Alternatively the Euler equations are solved in integral form in the physical domain on a grid of elementary control volumes. These 'finite volume' schemes for steady flow have been the subject of considerable development in recent years; in external aerodynamics most notably by Jameson and co-workers (for example Jameson, Schmidt & Turkel (1981)) and in turbomachine applications by Denton (1975, 1983). The method is such that there is no difficulty in principle in treating unsteady problems, and these methods are under active development. With the Euler equations written in conservation form both the differential and integral approaches should produce the same flux-conserving steady state solutions; a detailed comparison of the methods and the relevant spatial differencing for steady flows in turbomachine cascades is given by Thompson, Tong, Bush, Usab & Norton (1983).

The boundary conditions necessary for the computation of unsteady flows are discussed in detail in this chapter. It is necessary to apply boundary conditions to prevent spurious wave reflections at the inlet and exit planes of the computational domain. These unsteady boundary conditions are necessary in time marching methods even in calculating steady flow, but may require more careful implementation in the genuinely unsteady case. In cascade aerodynamics it is necessary to apply conditions on the repeating boundaries of the flow upstream and downstream of the leading and trailing edges. For steady flow the flow conditions are identical from blade to blade but this is modified in the unsteady flows to include the changes in phase from blade to blade. These are usually formulated in a way that is particularly convenient for the application to tuned rotors, but is not limited to this and combinations of the resulting unsteady aerodynamic coef-

ficients can be applied to mistuned assemblies.

Finally, there are boundary conditions on the blade surfaces; these conditions must be modified in the flutter problem to take account of the blade motion. In a linearized approach, the perturbed conditions are applied about the mean position of the blade and although this is not without its problems as will be discussed later, it has the advantage that it is not then necessary to incorporate moving grids.

In the final section we show some examples of the solutions obtained for unsteady flows using numerical methods. These results are unfortunately restricted to the potential methods readily available to us, and where applicable the results are compared with analytic solutions obtained for flat plate cascades. Some comparisons are also made with experimental measurements.

SOLUTIONS OF THE POTENTIAL FLOW EQUATIONS

In this section, we first review some of the methods for calculating flutter thresholds by numerical solution of the equations for potential flow. We concentrate on the methods developed by Caspar (1983), Caspar & Verdon (1981), Verdon & Caspar (1982, 1984) and the finite element method of Whitehead and co-workers (Whitehead & Grant (1980), Whitehead (1982), Whitehead & Newton (1985)); both approaches have led to programs that are now mature and have been well tested in different configurations. For this reason we discuss them in some detail. In common with most numerical methods described here, both methods are applicable to flows that are subsonic relative to the blades at inlet. Whitehead however uses a flexible, although somewhat indirect, set of inlet boundary conditions to allow also the solution of supersonic inlet flows.

Discretization and solutions of the steady flow

The equations governing the mean steady two-dimensional flow are used in the form of the mass conservation equation given by Verdon, Chapter II, equation (41)

$\nabla \cdot (\bar{\rho} \nabla \phi) = 0$. In Whitehead's formulation this is written for quasi-three dimensional flow along a stream-surface (where variation in streamtube height is accounted for, but variation in radius is not) as:

$$\nabla \cdot (\bar{\rho} h \nabla \phi) = 0 \quad (1)$$

where $\bar{\rho}$ is the density, ϕ the steady velocity potential and h is the streamtube height ratio. The relationship between density and local sound speed A is given by (Verdon, equation 42):

$$\left(\frac{\bar{\rho}}{\rho_0}\right)^{\gamma-1} = 1 - \left(\frac{\gamma-1}{2}\right) \frac{|\nabla \phi|^2}{A_0^2} = \frac{A^2}{A_0^2} \quad (2)$$

where ρ_0 , A_0 are stagnation quantities.

This pair of non-linear equations for the two scalar functions \bar{p} , Φ is solved in the blade to blade domain on a suitable grid. An example of the mesh used by Whitehead for a compressor cascade is shown in Figure 4. The mesh covers an area one blade spacing in height, with one blade profile in the middle, and extends one or two chord lengths upstream and downstream of the leading and trailing edge planes. Lines are drawn from specified points on the blade profile, which may be clustered in regions of greater interest, to the outer boundary. The space between the rays is filled with triangular elements built up in layers round the blade profile, as shown in the figure.

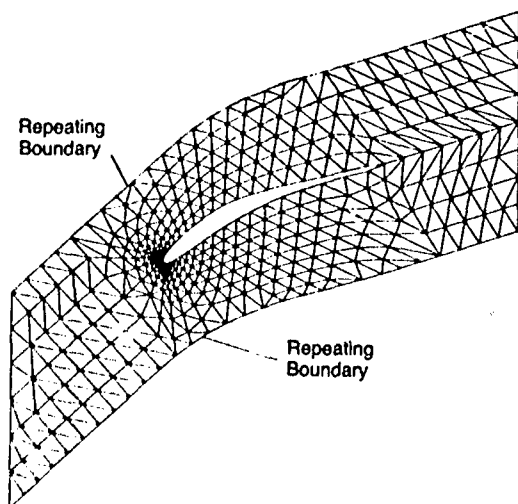


Figure 4 Typical finite element mesh

Caspar & Verdon, however, use two meshes for the steady flow: a global mesh which allows the implementation of repeat, inlet and exit boundary conditions, and a local mesh to allow more detailed resolution, as illustrated in Figure 5. The global mesh might be described as quasi-streamline; the local as a C-type grid. An important feature which the global mesh has in common with Whitehead's approach is that points are identically reproduced on repeat boundaries. This means that no interpolation is required for the repeat boundary condition. Although matching between the global and local meshes would in principle be an iterative procedure, it is in practice only a one-step process (the global solution imposing boundary conditions for the local solution). A further feature of Caspar & Verdon's local grid is the ability to provide finer step lengths in the vicinity of a shock. However, it may be noted that when artificial viscosity is implemented so that its effect diminishes with step size, mesh refinement can then lead to shock overshoots.

Both methods solve the governing differential equation for mass flow in conservation form. Caspar & Verdon use a finite volume method, whereas Whitehead applies a Galerkin finite element approach.

- Calculation points
- Neighbours

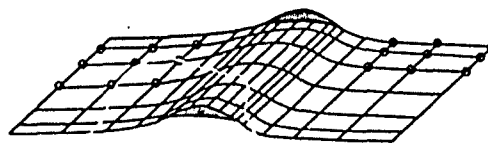


Figure 5(a) Global mesh

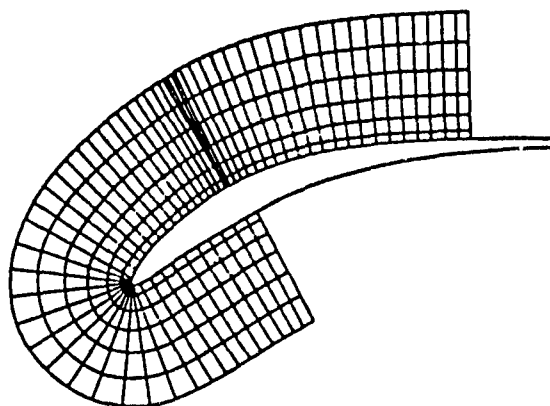


Figure 5(b) Local mesh with attraction at shock

The differences are best identified by describing the two numerical approximations to the mass conservation equation for internal points. Figure 6 shows part of the local mesh in Caspar's method: the flow equation is approximated as follows

$$0 = \int_D r \frac{\partial \Phi}{\partial n} ds = \sum_m \bar{r}_m \frac{\Phi_m - \Phi_o}{|P_m - P_o|} |\bar{Q}_m - \bar{Q}_{m-1}| \quad (3)$$

where r is the modified isentropic density ratio, $(\bar{p}/\rho_o)^{\gamma-1}$, and $|P_m - P_o|$ and $|\bar{Q}_m - \bar{Q}_{m-1}|$ are the distances between the corresponding points marked in figure 6.

Equation (3) may be written

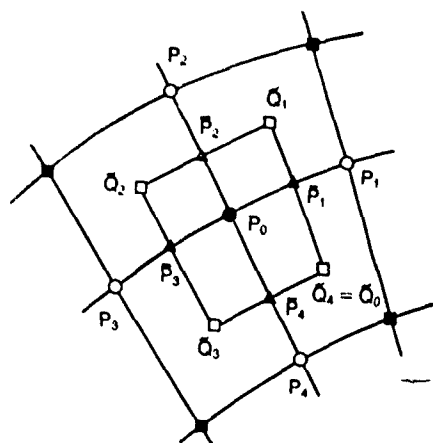
$$0 = \sum_m \tau_m \bar{r}_m (\Phi_m - \Phi_o) \quad (4)$$

$$\text{where } \bar{r}_m = (r_m + r_o)/2 \quad (5)$$

$$\text{or } \bar{r}_m = (\bar{r}_{m-1} + \bar{r}_m)/2 \quad (6)$$

$$\text{and } \tau_m = \frac{|\bar{Q}_m - \bar{Q}_{m-1}|}{|P_m - P_o|}.$$

Quantities carrying a tilde denote values at the cell centre and those with an overbar denote neighbour mid points. The approximations (5), (6) are termed "neighbour averaged" and "cell centre averaged" respectively. The latter produces a more compact difference scheme and is found to



- CENTRE MESH POINT
- NEIGHBOURING MESH POINT
- CELL CENTRES
- △ NEIGHBOUR LINE MID POINTS
- CORNER NEIGHBOURS

Figure 6 Local mesh polygon

give more sharply defined shocks in supersonic flow.

In Whitehead's method on the other hand, a linear variation of potential Φ is assumed over each triangular element:

$$\Phi(\underline{x}) = \sum_i \Phi_i Z_i \quad (7)$$

where $Z_i(\underline{x}) = Y_i(\underline{x})/Y$ are the shape functions or area co-ordinates as indicated in Figure 7.

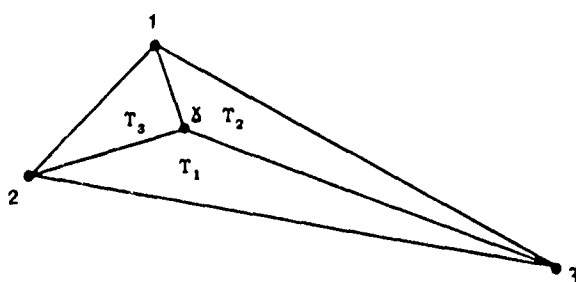


Figure 7 Area co-ordinates

In the Galerkin approach, the mass conservation equation is multiplied by the shape functions - giving three equations - and integrated over the element. Integration by parts transfers the derivative to the well-behaved (bilinear) shape functions, and summation over the elements surrounding a node leads to

$$\sum_{\text{elements}} Y(Q \cdot \underline{\nabla}) Z_i = 0 \quad (\text{for internal nodes}) \quad (8)$$

where the mass flow rate $Q = \bar{\rho} \bar{v} Y$ is defined in terms of Z_i by equation (7) and $\underline{v} = \nabla \Phi$.

An obvious similarity between the two methods is that they both lead to basic numerical schemes which are elliptic in character (i.e. offer no preferred direction). This is strictly applicable only to subsonic flows and is unsuitable for supersonic flows, where the equations are hyperbolic in nature, if the supersonic region extends over more than a few mesh points. To overcome this problem and bias the information in favour of the upstream direction, both Caspar and Whitehead employ upwind densities using an artificial viscosity.

Although the grid elements are of different shape, both methods apply a bilinear variation of velocity potential. However whereas Caspar has interpreted the mass conservation equation directly, Whitehead in applying the Galerkin method has a weighted integration placing higher dependence of the mass flow on its values at the 'centre' node being considered. Caspar solves the non-linear difference equation by a direct iterative scheme:

$$\sum_m \bar{\rho}_m^n (\Delta \Phi_m^{n+1} - \Delta \Phi_0^{n+1}) = - \sum_m \bar{\rho}_m^n (\Phi_m^n - \Phi_0^n) \quad (9)$$

where $\Delta \Phi$ is the iterative difference

$$\Delta \Phi^{n+1} = \Phi^{n+1} - \Phi^n,$$

(where Φ^n is the nth approximation to Φ) is used instead of Φ^{n+1} directly to minimise the effect of rounding errors. By reference to a model problem he identifies two possible difficulties with this numerical solution: non-uniqueness of the solution and non-convergence of the Taylor iteration (9). The former arises from the use of centred difference approximations in regions of supersonic flow, and the latter from the explicit treatment of the density. The non-uniqueness is cured by artificial viscosity, whereas non-convergence is treated by the introduction of an "implicit artificial time" term.

Whitehead solves the set of non-linear equations (8) by the Newton-Raphson method, expressing each variable as the current value plus a small correction and solving the linear equations for the correction terms. Setting $\Phi = \bar{\Phi} + \Phi'$, $\rho = \bar{\rho} + \rho'$, $Q_i = \bar{Q}_i + Q'_i$ where the primed quantities refer to correction terms (and the overbar to denote steady flow has been dropped), we may linearize in primed quantities, and equation (8) may be written

$$\sum_{\text{elements}} (K_{im} \Phi'_m + F_i) = 0 \quad (10)$$

where

$$K_{im} = \left\{ \bar{\rho} \frac{\partial Z_i}{\partial x_1} \frac{\partial Z_m}{\partial x_1} - \frac{\bar{\rho}}{\bar{A}_2} \bar{v}_1 \bar{v}_1 \frac{\partial Z_i}{\partial x_1} \frac{\partial Z_m}{\partial x_j} \right\} Y h$$

and

$$F_i = \bar{\rho} \bar{v}_1 \frac{\partial Z_i}{\partial x_1} Y h$$

is the error term at each step of the iteration. In some cases the Newton-Raphson scheme is relaxed in order to improve stability:

$$\phi^{n+1} = \phi^n + \Lambda \phi'^n, \quad 0 < \Lambda < 1. \quad (11)$$

It is found that values of the relaxation coefficient Λ of the order of 0.2 are required for supersonic inlet flows with shocks. This relaxation is equivalent to Caspar's "implicit artificial time" treatment.

As mentioned earlier, both methods modify the essentially elliptic schemes by the use of an upwinded density in which ρ is replaced in the conservation equation by $(\nu \rho^* + (1 - \nu)\rho)$, where ν , an artificial viscosity, is a function of Mach number, and ρ^* is the density of the element upstream of that under consideration. Caspar has $\nu = \chi \mu$ where χ is a constant whose magnitude is greater than 0.5 and $\mu = \max(0, 1 - 1/M^2)$. Whitehead defines the artificial viscosity to be

$$\nu = \nu_0 + \nu_1(1 - 1/M^2), \quad M > 1 \quad (12)$$

$$\text{and } \nu = \nu_0 M^{2\nu_1/\nu_0} \exp[-\lambda(M - 1)^2] \quad M < 1 \quad (13)$$

which gives continuity of ν and $d\nu/dM$ at $M = 1$. This continuity is necessary because the introduction of $\nu(M)$ leads to additional terms in the Newton-Raphson solution. Clearly in the supersonic region the two forms are similar although the constant ν_0 term means that Whitehead's artificial viscosity is non-zero at $M = 1$ (and indeed non-zero for high subsonic Mach number).

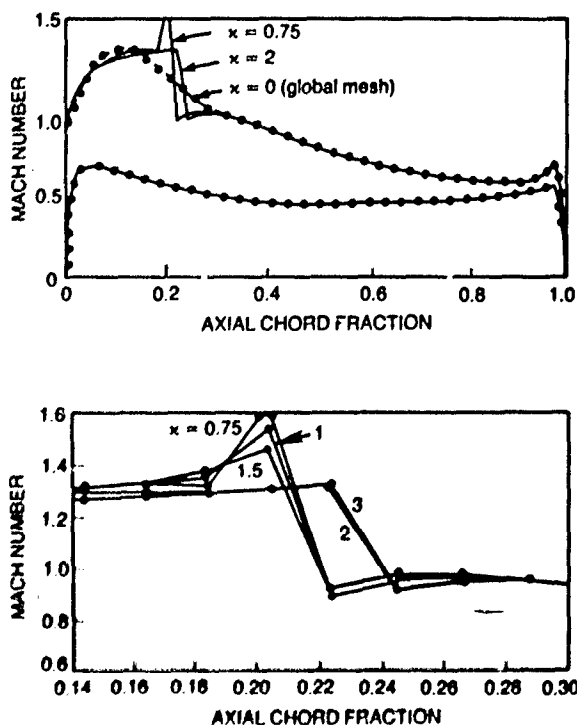


Figure 8 Effect of artificial compressibility (including shock detail)

Figure 8 shows how the shock shape depends on χ in Caspar's solution. The larger χ , the less overshoot is achieved, but the shock does not appear to become smeared as χ is increased. This is due to the introduction of the locally finer mesh in the shock region which causes the effective truncation error (or damping) to be reduced in proportion to the grid size. Figure 9 shows how Whitehead's approach approximates the shock (isentropic jump) from a similar moderately high Mach number.

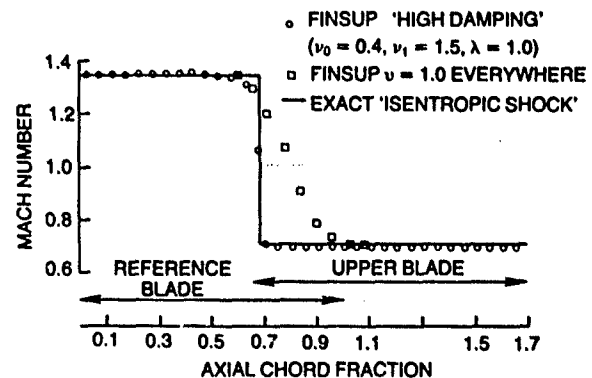


Figure 9 Effect of artificial viscosity on shock smearing

An additional technique used in Whitehead's numerical scheme is the variation of artificial viscosity as convergence proceeds. The values given above are the limiting values as convergence is approached, but considerably greater dissipation is put in at earlier stages. As the solution proceeds, and the position of the smeared shock has been located, the definition sharpens as ν is reduced. A typical convergence history is shown in Figure 10.

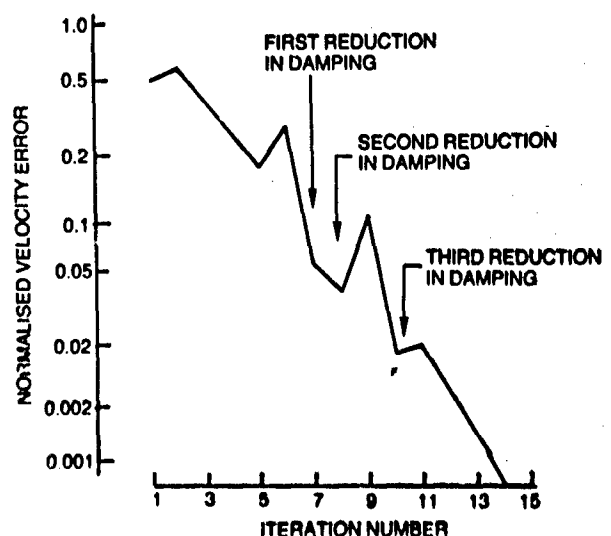


Figure 10 Convergence curve for Whitehead's method

Solution for the unsteady flow

The unsteady flow is determined from the linearized continuity equation (Verdon, equation (64)) with harmonic time dependence:

$$i\Omega\rho + \nabla \cdot h(\rho \nabla \phi + \bar{\rho} \nabla \bar{\phi}) = 0 \quad (14)$$

and from Verdon, equation (57) and (63)

$$\rho = \frac{-\bar{\rho}}{A^2} (i\Omega\phi + \nabla \phi \cdot \nabla \phi) \quad (15)$$

where ρ , ϕ are the perturbed quantities; velocities have been scaled by the steady

inlet speed; $\Omega = \omega(U_{\infty}^2 + V_{\infty}^2)^{-1/2}$, and the unsteady pressure may be obtained from the local sound speed: $p = A^2\rho$. Assuming that the steady flow field has now been determined, the coefficients $\bar{\rho}$, $\nabla\phi$ in equations (14) and (15) governing the unsteady flow are known. Both methods discussed here solve the same differential equations for the unsteady flow but their numerical implementations differ somewhat more than in the steady case.

Whitehead continues with a finite element formulation entirely analogous to his steady solution. The scheme is upwind in a similar manner to the steady flow: the rationale behind this is discussed later in this section. Furthermore his solution to the resulting (complex) linear equations is very close to one iteration of the steady Newton-Raphson scheme. No special treatment of the shock is adopted: it is merely a region of high gradients resulting in 'peaky' unsteady pressures, and the local shape near the shock solution is dependent on the particular choice of viscosity.

By comparison, Caspar & Verdon adopt a different discretization for the unsteady flow. They have a quadratic variation of ϕ over the mesh, and require a least-squares fit for the interpolation to the mesh point values:

$$\delta\phi = \phi - \phi_0 = \sum_{n=1}^N \gamma^n f^n \quad (16)$$

where γ^n are the complex coefficients which define the surface over which $\delta\phi$ is approximated and $\{f^n\}$ are the five interpolating polynomials: $f^1 = \delta\xi$; $f^2 = \delta\eta$; $f^3 = \delta\xi^2$; $f^4 = \delta\xi\delta\eta$; $f^5 = \delta\eta^2$; where $\delta\xi = \xi - \xi_0$ etc.

This approximation to the unsteady potential is applied to a rotated difference scheme following Jameson (1974). The differential operator for the continuity equation for the perturbed quantities (14) is 'split' into streamwise and normal components, L_1 and L_2 , respectively. L_2 is always approximated by central-differencing, whereas the treatment of L_1 depends on local Mach number, and is upwind in supersonic regions.

$$L_1\phi|_{1,j} = L_1\phi|_{1,j} \quad \text{if } M_{1,j} < 1$$

$$= L_1\phi|_{1-1,j} \quad \text{if } M_{1,j} > 1. \quad (17)$$

Unsteady shock waves are captured on the global (cascade) mesh, but then fitted on the local mesh, i.e. the appropriate unsteady shock jump conditions are applied across a grid line (normal to the blade surface) in the local mesh.

Therefore Caspar & Verdon's approach to the unsteady flow differs from Whitehead's in two important features. Firstly the shock fitting means that the correct jump conditions are applied to the unsteady shock reducing concern over the use of an artificial viscosity. Shock fitting can provide an accurate description of the shock jump conditions but it is usually computationally cumbersome because of the difficulties in initially locating the shock. However this difficulty is overcome if the shock can be captured in the steady calculation and then the unsteady shock fitted about this position. This is a useful approach that may be adopted in other methods such as the finite volume schemes discussed in the next section.

Secondly, the discretization for the unsteady flow is not the same as for the steady flow. In some circumstances, this could have undesirable consequences because the computed steady flow will result from a particular discretization and with a different numerical scheme, the perturbation will not be about this solution but about a different unknown state. This will happen to some extent anyway because even with the same numerical scheme the steady state residual will have been set to zero, but when the numerical schemes differ the new unsteady solution will also contain terms correcting the discrepancy between the two. This may be illustrated by supposing that $(\bar{\rho}, \bar{u})$ is the exact solution of the governing equations, and $(\bar{\rho}_u, \bar{u}_u)$ that obtained from a given numerical scheme for example with upwinding. If we write the continuity equation for the unsteady flow

$$\frac{\partial \rho}{\partial t} + \nabla \cdot (\rho \underline{u}) = 0 \quad (18)$$

and put $\rho = \bar{\rho} + \rho'$, $\underline{u} = \bar{\underline{u}} + \underline{u}'$ we obtain

$$\frac{\partial \rho'}{\partial t} + \nabla \cdot (\rho' \bar{\underline{u}} + \bar{\rho} \underline{u}') = -\nabla \cdot (\bar{\rho} \underline{u}'), \quad (19)$$

neglecting quadratic and higher orders in primed quantities. If the time-dependent perturbations are about the numerical approximations $\bar{\rho}_u$, $\bar{\underline{u}}_u$ then the right hand

side would be replaced by $\nabla \cdot (\bar{\rho}_u \bar{\underline{u}}_u)$. Thus in regions where upwinding has significant effects (such as near shocks) the solution contains a response due to the error in the steady approximation. This has been confirmed by numerical experiments using Whitehead's program. In Caspar & Verdon's method, however, this will be most import-

ant close to a shock, and the problem is avoided due to the shock fitting that takes place.

TIME-MARCHING SOLUTIONS OF THE EULER EQUATIONS

We now turn to the second general class of methods, not based on potential flow, but attempting instead to allow for rotational flow and obtain solutions of the Euler equations. The conservation form of Euler's equations for unsteady, inviscid, compressible flow has been given earlier by Verdon (Chapter 11, equations (8), (9), (10)), and may be written for two dimensional flow as

$$\frac{\partial}{\partial t} \underline{U} + \frac{\partial}{\partial x} \underline{F} + \frac{\partial}{\partial y} \underline{G} = 0, \quad (20)$$

where

$$\underline{U} = \begin{pmatrix} \rho \\ \rho u \\ \rho v \\ \rho e \end{pmatrix}$$

$$\underline{F} = \underline{F}(\underline{U}) = \begin{pmatrix} \rho u \\ \rho u^2 + p \\ \rho uv \\ (\rho e + p)u \end{pmatrix}$$

and

$$\underline{G} = \underline{G}(\underline{U}) = \begin{pmatrix} \rho v \\ \rho uv \\ \rho v^2 + p \\ (\rho e + p)v \end{pmatrix}$$

Here the equations are in dimensional form: (u, v) are the velocity components, ρ is the density, p is the static pressure, and e is the specific stagnation internal energy, so that $(e + p/\rho)$ is the stagnation enthalpy. For a perfect gas, the pressure is given by:

$$p = (\gamma - 1)(\rho e - \frac{1}{2}\rho(u^2 + v^2)) \quad (21)$$

where γ is the ratio of specific heats.

In many time-marching solutions of equation (20) for steady flow, the full equations for unsteady flow are solved subject to boundary conditions that do not vary with time. The calculation proceeds until a steady state is reached and the time-dependent terms are approximately zero. The unsteady flow computation may then start with the steady solution 'driven' by unsteady boundary conditions corresponding to either a periodic inflow condition (in the forced response problem), or periodic blade motion (in the flutter case).

As described earlier, it is permissible in calculating flutter thresholds to linearize the equations and boundary conditions. This is not essential in time-marching methods as the calculations may proceed until all flow variables become truly periodic in response to the driving boundary conditions. However, linearization of the moving blade conditions allows the blade to be assumed stationary, and conditions on the unsteady flow may then be

applied at the mean position of the blade. If the motion is not linearized then the blade must be allowed to move and its motion must be large compared to the local mesh size in order to be resolved, or the grid must move with the blades. If a linearized approach is adopted, a harmonic unsteady component of the form $\underline{U}' \exp(i\omega t)$ may be substituted additionally into the equations, and then in principle the time-marching may proceed in the usual way to calculate the (steady) complex amplitude \underline{U}' . This approach has been investigated by Hobson (1976) and also by Ni & Sisto (1976), in a method in which the equations applied to a flat plate cascade are solved in differential form. This class of method is described next, and then we go on to discuss integral (finite volume) methods. A discussion of the implementation of the boundary conditions in both these methods is given in the next Section.

Differential Methods

In a differential method, the system of differential equations are solved using a finite difference scheme on a convenient rectangular grid. Details of such schemes are given for example by Smith (1985), Peyret & Taylor (1985), and Richtmyer & Morton (1967): the application to time-marching has been described by Gopalakrishnan (1973). In general the method involves transforming the physical region (the blade passage) into a rectangular computational domain with the blade surfaces lying along sides of the rectangle. The transformed co-ordinates may be obtained numerically from a potential solution in the physical plane. The differential equations (20) are more complicated when written in terms of the transformed variables, but are solved in the rectangular region by discretizing the equations on the transformed rectangular grid.

Several attempts have been made to solve equations (20) for flutter thresholds using explicit time-stepping schemes, in particular the two-stage predictor-corrector scheme of MacCormack (1976). The scheme is basically of the form of a predictor step:

$$\tilde{\underline{U}}_{ij}^n = \underline{U}_{ij}^n - \Delta t \left(\left(\frac{\partial \underline{F}}{\partial x} \right)_{ij}^n + \left(\frac{\partial \underline{G}}{\partial y} \right)_{ij}^n \right), \quad (22)$$

followed by a corrector step:

$$\underline{U}_{ij}^{n+1} = \frac{1}{2}(\underline{U}_{ij}^n + \tilde{\underline{U}}_{ij}^n) - \frac{1}{2}\Delta t \left(\left(\frac{\partial \underline{F}}{\partial x} \right)_{ij}^n + \left(\frac{\partial \underline{G}}{\partial y} \right)_{ij}^n \right) \quad (23)$$

$$\text{where} \quad \tilde{\underline{F}}_{ij}^n = \underline{F}(\tilde{\underline{U}}_{ij}^n),$$

$$\text{and} \quad \tilde{\underline{G}}_{ij}^n = \underline{G}(\tilde{\underline{U}}_{ij}^n). \quad (24)$$

In the first step one-sided spatial differences are used with the second step then correcting the predicted values using opposite one-sided differences. This gives a method that is second-order accurate overall. Again, suitable 'splitting' of the spatial operators into streamwise

and normal components is possible and this allows the method to be readily combined with one-dimensional characteristic solutions at the boundaries; this will be discussed later.

Preliminary results for this method in subsonic flow have been given for example by Pandolfi (1980) and for quasi three-dimensional transonic flows in fans by Joubert (1984). Joubert used two-dimensional cylindrical co-ordinates, and added a further step to the scheme to allow shock waves to be captured by providing dissipation in the form of a numerical viscosity as described in the previous section. A linearized approach was not used (although the results for bending and torsional motion were shown to be linear and therefore superposable): the results were obtained by allowing the grid to move with the blades. For the example given by Joubert, the computation of unsteady lift and moment coefficients settled down to a periodic solution after about three periods of the blade oscillation.

An explicit MacCormack scheme was also used by Ni & Sisto (1975) in their linearized calculation of flutter over staggered flat plates. Again a rectangular grid was used in the computational domain but the linearization allowed the blade boundary conditions to be applied at the mean position of the blades and the mapping did not change with time.

In explicit methods, the time-step is restricted by the CFL condition (see for example Smith (1985)) which gives a maximum allowable time step limited by the propagation of information in the physical domain. This time step restriction in purely explicit methods led to the development of a 'semi-implicit' method for low frequency applications (Ballhaus, 1978) but difficulties were again experienced near the leading and trailing edges of the aerofoil. Subsequently fully-implicit schemes were developed, most importantly the factored algorithm approach of Beam & Warming (1976), and its developments given in Warming & Beam (1978), which allows the computation to be 'split' into two one-dimensional problems. A non-iterative second-order time-accurate formula may be derived for the solution of equation (20) by first using a trapezoidal formula for the time-differencing to give:

$$\underline{u}^{n+1} - \underline{u}^n - \frac{1}{2}\Delta t \left[\left(\frac{\partial \underline{F}}{\partial x} + \frac{\partial \underline{G}}{\partial y} \right)^n + \left(\frac{\partial \underline{F}}{\partial x} + \frac{\partial \underline{G}}{\partial y} \right)^{n+1} \right] + O(\Delta t^3). \quad (25)$$

and then allowing a local Taylor expansion about \underline{u}^n to obtain \underline{F}^{n+1} and \underline{G}^{n+1} :

$$\begin{aligned} \underline{F}^{n+1} &= \underline{F}^n + A^n(\underline{u}^{n+1} - \underline{u}^n) + O(\Delta t^2), \\ \underline{G}^{n+1} &= \underline{G}^n + B^n(\underline{u}^{n+1} - \underline{u}^n) + O(\Delta t^2) \end{aligned} \quad (26)$$

where A is the matrix $A_{jk}(\underline{u}) = \frac{\partial}{\partial u_k} F_j(\underline{u})$,

$B_{jk}(\underline{u}) = \frac{\partial}{\partial u_k} G_j(\underline{u})$, and $U(t) = U(n\Delta t) = \underline{u}^n$

where Δt is the discrete time increment.

For the Euler equations, $\underline{F} = A\underline{u}$ and $\underline{G} = B\underline{u}$ which simplifies equations (26) so that equation (25) becomes:

$$\begin{aligned} & \left[I + \frac{\Delta t}{2} \left(\frac{\partial}{\partial x} A^n + \frac{\partial}{\partial y} B^n \right) \right] \underline{u}^{n+1} \\ &= \left[I - \frac{\Delta t}{2} \left(\frac{\partial}{\partial x} A^n + \frac{\partial}{\partial y} B^n \right) \right] \underline{u}^n + O(\Delta t^3) \end{aligned} \quad (27)$$

The most important step in the method is the introduction of a third-order term to equation (27) to derive a factored scheme for (27), with the same temporal accuracy:

$$\begin{aligned} & \left(I + \frac{\Delta t}{2} \frac{\partial}{\partial x} A^n \right) \left(I + \frac{\Delta t}{2} \frac{\partial}{\partial y} B^n \right) \underline{u}^{n+1} \\ &= \left(I - \frac{\Delta t}{2} \frac{\partial}{\partial x} A^n \right) \left(I - \frac{\Delta t}{2} \frac{\partial}{\partial y} B^n \right) \underline{u}^n + O(\Delta t^3). \end{aligned} \quad (28)$$

The algorithm (28) can be rewritten in the form:

$$\underline{u}^* = \left(I - \frac{\Delta t}{2} \frac{\partial}{\partial y} B^n \right) \underline{u}^n \quad (29a)$$

$$\begin{aligned} & \left(I + \frac{\Delta t}{2} \frac{\partial}{\partial x} A^n \right) \underline{u}^{**} \\ &= \left(I - \frac{\Delta t}{2} \frac{\partial}{\partial x} A^n \right) \underline{u}^* + O(\Delta t^3) \end{aligned} \quad (29b)$$

$$\left(I + \frac{\Delta t}{2} \frac{\partial}{\partial y} B^n \right) \underline{u}^{n+1} = \underline{u}^{**} \quad (29c)$$

A more general form of the algorithm written in 'delta' form is given by Warming & Beam (1978), where the factorization of equation (25) is written as

$$\begin{aligned} & \left(I + \frac{\Delta t}{2} \frac{\partial}{\partial x} A^n \right) \left(I + \frac{\Delta t}{2} \frac{\partial}{\partial y} B^n \right) \Delta \underline{u}^n \\ &= -\Delta t \left(\frac{\partial \underline{F}}{\partial x} + \frac{\partial \underline{G}}{\partial y} \right)^n + O(\Delta t^3), \end{aligned} \quad (30)$$

where Δ is defined as the forward difference operator

$$\Delta \underline{u}^n = \underline{u}^{n+1} - \underline{u}^n.$$

The factored scheme (30) can be implemented as

$$\left(I + \frac{\Delta t}{2} \frac{\partial}{\partial x} A^n \right) \Delta \underline{u}^* = -\Delta t \left(\frac{\partial \underline{F}}{\partial x} + \frac{\partial \underline{G}}{\partial y} \right)^n, \quad (31a)$$

$$\left(I + \frac{\Delta t}{2} \frac{\partial}{\partial y} B^n \right) \Delta \underline{u}^n = \Delta \underline{u}^*, \quad (31b)$$

$$\underline{u}^{n+1} = \underline{u}^n + \Delta \underline{u}^n, \quad (31c)$$

where $\Delta \underline{u}^*$ is a dummy temporal difference.

The scheme (31) reduces to the form (29) when the assumptions $\underline{F} = A\underline{u}$ and $\underline{G} = B\underline{u}$ are again made, but as it stands it is computationally more efficient. This delta formulation is also used in the factored algorithm for the Navier Stokes equations (Beam & Warming, 1978).

The factored (or alternating-direction (ADI)) scheme reduces the large matrix inversion problem to small bandwidth matrix inversion problems for which much more efficient solution algorithms exist. To produce block tridiagonal matrices, three-point spatial difference approximations

are used. This scheme is non-dissipative and consequently large amplitude oscillations appear in the solution in the neighbourhood of any shock waves. The use of centred differences (to give second order spatial accuracy) necessitates some artificial viscosity to damp spurious numerical oscillations, and to reduce these oscillations a fourth order dissipative term may be added to each of the equations (29) or (31). However Warming & Beam report that this did not eliminate the shock oscillations and considerably greater reduction can be achieved by switching from centred spatial differences to upwind (one-sided) differences whenever the flow is locally supersonic (leading to the solution of block bi-diagonal matrices). Beam & Warming (1976) describe a hybrid scheme that enables this to be done whilst maintaining a proper conservation form of the difference scheme. With this scheme it is shown that fourth order dissipative terms were not required in the shock neighbourhood, although they were required elsewhere.

Solutions of the full unsteady Euler equations for subsonic flow have been obtained using this implicit method by Holtmann, Servaty & Gallus (1984). Their paper also provides comparisons between a MacCormack scheme, an ADI scheme and a characteristics method for computing the transient flow in a duct connected to a steady reservoir, following the rupture of a diaphragm at one end. The resulting one-dimensional wave motion was computed until the steady state was reached. This is a problem that may be solved successfully using the method of characteristics throughout the computational domain, and comparisons were made using MacCormack's method and Beam & Warming's ADI method for the interior. It was found that these methods followed the characteristics solution fairly closely, although inclusion of the dissipative terms in Beam & Warming's algorithm produced a smoother transient flow.

The ADI scheme was therefore combined with appropriate characteristics solutions at the boundaries to calculate bending flutter of a flat plate cascade and a compressor cascade. This work is a development of that of Steger (1978) who obtained solutions of the Euler equations for an oscillating isolated aerofoil using a similar implicit factored algorithm with a time-dependent grid. Whilst it is likely that this is the most ambitious of the published difference methods described, the authors indicate that the computation is very expensive, and it may be that an explicit method would be quicker. In their review of transonic flow past oscillating isolated aerofoils, Tijdeman & Seebas (1980) suggest that for reduced frequencies (based on semi-chord) below 0.2, implicit methods converge faster than explicit methods, but otherwise the numerical effort is about four times less for an explicit method. This value of reduced frequency is close to the lower limit of interest in turbomachine problems.

Steger (1978) also described the application of the method to the 'thin layer' Navier Stokes equations in which the viscous terms are retained only in derivatives normal to the boundary. This approach with an iterative ADI scheme has been used in a forced response problem by Rai (1985) to calculate two-dimensional flow through a rotor-stator stage. Patched and overlaid multiple grids are used in which the patched boundaries are allowed to move relative to each other. This is again computationally expensive, restricting the number of blade passages that can be treated.

Finite Volume Methods

For solution by finite volume schemes, equation (20) is written in integral form (see Verdon, Chapter II, equations (1),(2),(3)) over a stationary finite area Σ :

$$\frac{\partial}{\partial t} \int_{\Sigma} \underline{U} \, dA + \oint_{\delta \Sigma} (\underline{F}_n \underline{x} + \underline{G}_n \underline{y}) \, ds = 0 \quad (32)$$

where (n_x, n_y) are the components of the normal to the boundary curve $\delta \Sigma$. For a given cell denoted by ij , (32) may be approximated by an ordinary differential equation:

$$A_{ij} \frac{d}{dt}(\underline{U}_{ij}) + R_{ij}(\underline{U}) = 0. \quad (33)$$

Here $R_{ij}(\underline{U})$ represents the net flux of conserved quantities out of the cell, which is balanced by the rate of change of \underline{U} within the cell. In predicting steady flows, equation (33) for unsteady flow is solved with steady boundary conditions until the net flux in each cell reduces to zero.

Time-marching solutions of this equation for steady flows can be very efficient, particularly when it is recognised that since only the converged steady solution is required it is not necessary for the calculation to proceed in a 'time-accurate' manner. In explicit schemes, where the time step is restricted by the CFL condition, it is usual to allow the time step to vary over the computational region according to the local CFL number. This, and other features such as multiple grids or the use throughout the calculation of an energy relation restricted to steady flow, means that the transient behaviour of the flow has no physical meaning and the time-marching takes place in 'pseudo-time'. Application of the method to a general unsteady flow requires the removal of these devices, which considerably slows the computations, although of course the steady flow may first be calculated in a 'pseudo-time' manner.

The flux term $R_{ij}(\underline{U})$ in equation (33) may be approximated in different ways depending on the storage scheme within the cell. The choice determines the order of accuracy of the scheme. The differential equation (33) may be solved using standard techniques such as predictor-corrector or

multi-stage Runge Kutta. In the methods developed by Denton (1975, 1983) a more ad hoc scheme is used in which the fluxes $R_{ij}(U)$ in time Δt are calculated and these then determine the changes in conserved quantities U within the cell. These changes are "distributed" by updating the values stored at the cell corners in such a way as to ensure stability. This first-order scheme is modified by second-order correction terms as the solution is approached. In Denton's method for two-dimensional flow the unsteady energy equation is not solved but is replaced by the assumption of constant stagnation enthalpy (or constant rothalpy in quasi three-dimensional flow). For the momentum variables, the downstream nodes are updated with the cell changes but an element of upwinding is introduced depending on the local Mach number by distributing the density changes between upstream and downstream nodes according to a weighting based on the local static temperature. The pressure on a given face of the cell is then also calculated as a weighted average from these densities. Central differences are used to obtain the values at the cell faces, resulting in a method that is second order accurate in space. In common with other methods, further numerical damping is required in order to capture shock waves. In Denton's method this is incorporated as an extra pressure term proportional to the square of the density gradient in the streamwise direction. The resulting method has been successful in predicting steady flows in two-dimensional cascades and is widely used. A boundary layer calculation has been added to the method by Calvert & Herbert (1980).

The method has been extended to three-dimensional flows by Denton himself, and also to periodic unsteady flows by Mitchell (1980) and further developed by Hodson (1984), in attempts to predict a wake-generated unsteady flow. This is a forced response problem in which the blades are assumed to be stationary and an upstream boundary condition corresponding to a time-periodic mass flux is imposed. The flow at inlet is also spatially periodic, not necessarily over the rotor blade spacing. In extending Denton's method to unsteady flow, it is necessary to remove the restrictions which prevent the method being 'time-accurate'. The time step must therefore be the same at all points and also an unsteady energy equation must be re-introduced.

Apparently, attempts to provide a stable differencing scheme for the full set of equations were not successful, and Hodson instead replaced the energy equation by the relation that the convective derivative of entropy is zero (Verdon, Chapter II, equation (14)). Use of this equation does not of course imply that the flow is homentropic, and if a non-uniform source of entropy is present upstream, or is allowed to arise due to dissipation in the numerical scheme as would be the case for a non-uniform strong shock wave, then the downstream distribution of entropy may still be treated correctly. In Hodson's

computation the steady flow was first established and then the unsteady boundary conditions were introduced. Convergence of the program occurred when the flow properties became truly periodic. This did not happen rapidly: for the example given by Hodson it appeared to take at least twenty periods of the wake passing frequency. More recently, a forced response calculation for three-dimensional flow through a turbine stage has been reported by Koya & Kotake (1985). The blade to blade periodicity is again imposed so that only a single blade passage need be considered but in this case both blade rows are included in the computation zone although once more the flow is assumed inviscid.

Independently of the above, solutions of the Euler equations by finite volume techniques have been highly developed in aircraft applications. Some of the most efficient methods are based on the multi-stage Runge Kutta schemes of Jameson, Schmidt & Turkel (1981). In this method centred spatial differences are used and the numerical smoothing required to suppress oscillations in the solution is incorporated explicitly into the model by modifying equation (33) with the addition of a dissipative term. This is constructed so as to be fourth order in smooth regions of the flow but in the neighbourhood of shock waves a second order term is used related to the local pressure difference. This smoothing enables shock waves to be captured fairly cleanly. The revised equation (33) is integrated by multi-stage methods which are simplified versions of standard Runge Kutta schemes designed for stability rather than order of accuracy. Again, there is no concern for 'time-accuracy' in a method devised for steady flow, and convergence is accelerated by the use of multiple grids. These methods were developed originally by Jameson (1979) for potential flow calculations and subsequently applied to solutions of the Euler equations by Ni (1981) and Jameson (1983). The use of multi-grid methods with Lax-Wendroff as well as multi-stage Runge Kutta time-stepping has been investigated in some detail for single aerofoils by Hall (1985).

In these methods developed by Jameson a 'cell-centred' storage scheme is used (as opposed to the 'cell vertex' schemes used by Denton (1983) and Ni (1981)), and quantities required at a face are evaluated as the averages of the values in the cells on either side of the face. This again reduces to a central difference scheme and is second order accurate provided that the grid is smooth enough. Cell vertex schemes are not as restricted to smooth grids and away from shock waves will require less artificial dissipation. They may in particular be expected to be more efficient for three-dimensional grids.

In external aerodynamics, where much of the work is aimed in the long term at predicting three-dimensional flow about complete aircraft under cruise conditions where viscous effects may be negligible,

methods of solution of the Euler equations for inviscid steady flow are well advanced and more recently applications of the method to steady viscous flow have been made (Swanson & Turkel, 1985). In turbo-machine applications, Jameson's methods have been applied to steady cascade aerodynamics by Thompkins and co-workers at MIT, in developments in which the Reynolds averaged Navier Stokes equations have been solved together with a turbulence model. In this work convergence is accelerated by the use of implicit smoothing (Jameson & Baker, 1983) rather than multiple grids, but in common with multigrids the technique is applied to the residuals (changes) in dependent variables and not to the dependent variables themselves, thus reducing in effect as the steady state is approached. Such methods are currently being extended to full unsteady solutions at many centres, although it will of course be some time before they are readily available as design tools.

IMPLEMENTATION OF BOUNDARY CONDITIONS

In a numerical method, boundary conditions must be applied at the edges of the computational zone. In steady flow problems with identical blades, the computational zone extends over a single blade passage and this is usually also the case in unsteady flow. Suitable repeat conditions need to be specified on these boundaries, and also suitable conditions on the solid blade surface. Whilst in analytic solutions of unsteady problems the solution domain may extend to infinity upstream and downstream, a computational domain would normally extend only one or two chord lengths upstream and downstream of the blade row. Again, suitable boundary conditions are needed at the edges of the domain.

The detailed implementation of the boundary conditions depends, of course, on the numerical method employed in solving the equations. However, the physical principles to be considered are the same for all methods, and need to be clearly understood to allow suitable implementation schemes to be developed: an unequivocal statement of the problems which can arise from a negligent treatment of the boundary conditions has been given by Moretti (1969).

Blade surface boundary conditions

In an inviscid model of a real flow, the usual condition is that the velocity normal to the surface is zero, but slip tangential to the surface is allowed. On a stationary wall, this boundary condition is simply $\underline{n} \cdot \underline{V} = 0$, where \underline{n} is the unit vector normal to the wall and \underline{V} is the velocity vector (u, v). In the case of steady potential flow this equation is written as $\underline{n} \cdot \nabla \phi = 0$. In many numerical schemes, this condition is implemented by defining dummy cells outside the computational zone and assigning values to the nodes of the cells such that under the difference scheme concerned

the appropriate conditions are met along the boundary itself. Together with the appropriate Euler equation for momentum, $\underline{n} \cdot \underline{V} = 0$ implies

$$\left| \frac{\partial p}{\partial n} \right| = \kappa \rho (u^2 + v^2) \quad (34)$$

where κ is the curvature of the boundary.

The condition for no flow through a moving surface is obtained by setting the normal component of the fluid velocity equal to the blade velocity at that point:

$$\underline{n} \cdot \underline{V}(\underline{f}) = \underline{n} \cdot \frac{\partial \underline{f}}{\partial t} \quad (35)$$

Here \underline{f} is the displacement of the surface; \underline{V} is given on the wall and is thus evaluated at \underline{f} .

For a fixed mesh, Taylor's theorem may be applied to give values for \underline{V} in terms of its values at the mean displacement, $\underline{f} = 0$, to give $\underline{V}(\underline{f}) = \underline{V} + (\underline{f} \cdot \nabla) \underline{V} + \dots$ (where we adopt the notation that everything is evaluated at $\underline{f} = 0$ unless otherwise stated). If the displacement \underline{f} is small, then equation (35) can be linearized in the usual way by writing $\underline{f} = \underline{f}' \exp(i\omega t)$, $\underline{n} = \underline{n}_0 + \underline{n}' \exp(i\omega t)$, $\underline{V} = \underline{V}_0 + \underline{V}' \exp(i\omega t)$, to give

$$\underline{n}_0 \cdot \underline{V}' = \underline{n}_0 \cdot (i\omega \underline{f}' - (\underline{f}' \cdot \nabla) \underline{V}_0) - \underline{n}' \cdot \underline{V}_0 \quad (36)$$

This is equivalent to Verdon's equation (69), which is written in terms of \underline{r}_0 , the unit vector tangential to the surface:

$$\underline{n}_0 \cdot \underline{V}' = \underline{n}_0 \cdot (i\omega \underline{f}' - (\underline{f}' \cdot \nabla) \underline{V}_0 + (\underline{V}_0 \cdot \underline{r}_0)(\underline{r}_0 \cdot \nabla) \underline{f}'). \quad (37)$$

Other variables required on the blade surface may be similarly written in terms of a Taylor expansion, so that for the surface pressure for example we have

$$p'(\underline{f}) = p' + (\underline{f}' \cdot \nabla) p_0 + O(|\underline{f}'|^2) \quad (38)$$

It is known that difficulties may arise in evaluating (38) when the two terms on the right-hand side of the equation are comparable, in particular when ∇p_0 is

large. This is most likely to be in regions where the aerofoil has large surface curvature, specifically at the leading edge. For oscillating cascades of flat plates (for example Ni & Sisto, 1975), the term is zero. The problem is confined to methods where a linearized solution is sought; most notably the potential methods described earlier. In their solution, Verdon & Caspar (1982) show by reference to a model incompressible problem that the expansion in terms of the blade amplitude is regular provided that the displacement is small compared to the surface radius. They perform inner and outer expansions in the vicinity of the leading edge for the model problem and conclude the need for a local C-type grid to resolve the behaviour around blunt leading edges.

In his potential flow solution, Whitehead

adopts a different approach whereby he retains his original cascade grid, but introduces a modified potential ϕ' given by $\phi' = \phi + \int \nabla \cdot \mathbf{v}$, where $\nabla \cdot \mathbf{v} = \nabla \cdot \mathbf{v}_0$ and ϕ is the unsteady perturbation of Φ . This is equivalent to working in a frame of reference moving with the blade. After some algebra he obtains:

$$p'(\xi) = -\bar{p}(\ln \phi' + (\nabla \cdot \mathbf{v})\phi' - \ln \xi \cdot \bar{\nabla}_0), \quad (39)$$

so that the numerically difficult term has been eliminated. (This modification changes the finite element formulation for ϕ'). It may be noted that this approach cannot readily be applied when the section does not move as a rigid body (Cedar, 1986).

The use of this modified potential is analytically equivalent to allowing the grid to move, and this is the approach adopted in some studies, (for example Holtmann, Servaty & Gallus, (1984) described earlier), following the method developed by Thompson, Thames & Mastin (1977). In this differential method, the physical domain is transformed in the usual way into a rectangular region, and the solution is calculated in the transformed plane with a time-varying co-ordinate transform that ensures that the rectangular grid remains unchanged with time.

'Repeat' boundary conditions

As described earlier, in steady flow computations the streamwise boundaries upstream and downstream of the blades should be identical at corresponding points across the computational domain. In forced response problems it may be necessary to include more than one blade passage (but still an integral number of them). In computations of flutter, the travelling wave nature of the motion around the disc assembly is described by including an interblade phase angle σ in a factor $\exp(i\sigma)$ between the variables from blade to blade. This is applied to the streamwise boundaries of the computational region.

In unsteady flow and during time-marching to a steady solution a wake is present downstream of each blade and it is necessary in some implementations to take specific account of this. An inviscid wake consists of a vortex sheet across which the pressure and velocity normal to the sheet are continuous, but the tangential velocity is discontinuous. In the potential methods discussed earlier, an unsteady wake jump condition is explicitly included of the form; (from Verdon, equation (75)):

$$[\phi]_{\text{wake}} = [\phi]_{\text{t.e.}} \exp(-iNS) \quad (40)$$

where S is the distance from the trailing edge and $(1-u/q_\infty)$ where q_∞ is the downstream steady speed.

In the differential schemes where the equations are solved on a transformed rectangular grid then care is taken to

ensure that the wake discontinuity occurs on the boundary; this enables the discontinuity to be 'fitted' exactly, as is shown for example in the forced response calculation by Erdos, Alzner & McNally (1977) of flow through a fan stage. When a time dependent grid is used (for example Holtmann, Servaty & Gallus, 1984) the grid is adjusted even in computing steady flow to ensure this. Pandolfi (1980) uses techniques analogous to those developed by de Neef & Moretti (1980) for shock fitting. It is also necessary that the Kutta condition is satisfied: in steady flow calculations this is usually interpreted as ensuring that the flow leaves the trailing edge smoothly whilst in unsteady flow it is assumed that the flow is tangential to the upper or lower surfaces depending on the sign of the shed vorticity. In finite volume solutions of the Euler equations, no explicit treatment of the wake is necessary although a sharp velocity discontinuity cannot be realised and the resulting wake will be somewhat smeared; discontinuities at a sharp trailing edge may not be apparent particularly with a cell-centred scheme.

Inflow and outflow boundary conditions

At the inflow and outflow boundaries it is desirable to prevent spurious reflections from the edge of the computational domain, since these contaminate the solution in the interior of the region and considerably delay or even prevent convergence. It is usual to apply non-reflecting boundary conditions by establishing the characteristic form of the equations, and then imposing conditions on those characteristic variables which propagate into the computational zone. Equivalent considerations in analytical aeroacoustics (the radiation condition) lead to choosing the branch of the solution to disallow incoming waves from infinity (see for example Goldstein, Braun & Adamczyk (1977)). It is also usually necessary in implementing the numerical algorithm used in the interior of the computational zone to require values of all variables on the boundary so that all cells may be treated in the same way. This is a quite separate matter from the physical problem we are considering here, and the relevant variables may be extrapolated from values in the interior. The extrapolation has its own problems, in particular stability of the numerical schemes, and this is discussed in some detail by Yee, Beam & Warming (1981) and Gottlieb & Turkel (1978), but is not considered further here.

To establish the relevant characteristic variables, it is necessary to write equation (20) in quasi-linear form

$$\frac{\partial \mathbf{U}}{\partial t} + \mathbf{A} \frac{\partial \mathbf{U}}{\partial x} + \mathbf{B} \frac{\partial \mathbf{U}}{\partial y} = 0 \quad (41)$$

where as before \mathbf{A} is the matrix $\mathbf{A}(\mathbf{U}) = \partial \mathbf{F}_j(\mathbf{U}) / \partial \mathbf{U}_k$ and $\mathbf{B}(\mathbf{U})$ is similarly defined.

For computations of steady flow, it is usual to assume quasi one-dimensional flow

at the inflow and outflow boundaries so that equation (41) may be written

$$\frac{\partial \underline{U}}{\partial t} + A \frac{\partial \underline{U}}{\partial x} = 0. \quad (42)$$

In order to derive the boundary condition, we obtain the left-hand eigensystem of A . The results are familiar if we change the dependent variable from the conservation variables and define \underline{U} simply in terms of density, velocity and pressure i.e.

$$\underline{U} = \begin{pmatrix} \rho \\ u \\ v \\ p \end{pmatrix}. \quad (43)$$

The eigenvalues λ remain

$$(u, u, u \pm a). \quad (44)$$

Assuming that $0 < u < a$, conditions at inflow must be supplied for the characteristic variables corresponding to $\lambda \in \{u, u, u + a\}$; and at outflow for $\lambda = u - a$. At inflow, these eigenvalues relate to entropy and vorticity convecting at the stream speed u , and an incoming acoustic wave propagating at sonic speed a relative to the flow. Similarly the condition at outflow relates to an incoming acoustic wave.

The characteristic form (see for example Richtmyer, 1978, §17.8) of equation (42) is given by

$$\alpha^T \left(\frac{\partial}{\partial t} + \lambda \frac{\partial}{\partial x} \right) \underline{U} = 0 \quad (45)$$

where α is the left hand eigenvector of A corresponding to λ , and T denotes the transpose. With \underline{U} given by equation (43) this leads to

$$a^2 \left(\frac{\partial}{\partial t} + u \frac{\partial}{\partial x} \right) \rho - \left(\frac{\partial}{\partial t} + u \frac{\partial}{\partial x} \right) p = 0$$

$$\left(\frac{\partial}{\partial t} + u \frac{\partial}{\partial x} \right) v = 0$$

and

$$\left(\frac{\partial}{\partial t} + (u+a) \frac{\partial}{\partial x} \right) u \pm \frac{1}{\rho a} \left(\frac{\partial}{\partial t} + (u+a) \frac{\partial}{\partial x} \right) p = 0 \quad (46)$$

corresponding to the eigenvalues (44). It may be noted that only in special circumstances may equations (46) be written simply as

$$\left(\frac{\partial}{\partial t} + \lambda \frac{\partial}{\partial x} \right) w = 0 \quad (47)$$

where w is a straightforward characteristic variable corresponding to λ . If the coefficients in equations (46) are assumed locally constant then the equations may be written in the form (47) with characteristic variables

$$w \in \{(a_0^2 \rho - p), v, (u \pm p/\rho_0 a_0)\}. \quad (48)$$

In these circumstances the required characteristic variable given by (48) is a specified constant (the boundary condition) whilst the remaining characteristic variables may be extrapolated from the interior of the computational zone. The

assumption of locally constant coefficients is only strictly appropriate in a linearized problem, but nevertheless appears to be widely used (Yee, Beam & Warming, 1981). In the linearized problem where the flow field may be decomposed as $\underline{U} = \underline{U}_0 + \underline{U}_1$ etc, the characteristic variables for the unsteady problem are given by equation (48):

$$w_1 \in \{a_0^2 \rho_1 - p_1, v_1, u_1 \pm p_1/\rho_0 a_0\}. \quad (49)$$

Equations (46) also reduce to the form of (47) when the flow is isentropic. In that case the characteristic variables corresponding to $\lambda = u \pm a$ are the well-known Riemann invariants.

In general however the characteristic form cannot be written so simply and the boundary conditions take the form given by Hedstrom, (1979):

$$\alpha^T \frac{\partial \underline{U}}{\partial t} = 0. \quad (50)$$

This leads to boundary conditions at inflow:

$$a^2 \frac{\partial \rho}{\partial t} - \frac{\partial p}{\partial t} = 0 \quad (\text{entropy}) \quad (51)$$

$$\frac{\partial v}{\partial t} = 0 \quad (\text{vorticity}) \quad (52)$$

$$\rho a \frac{\partial u}{\partial t} + \frac{\partial p}{\partial t} = 0 \quad (\text{acoustics}) \quad (53)$$

and at outflow:

$$\rho a \frac{\partial u}{\partial t} - \frac{\partial p}{\partial t} = 0. \quad (\text{acoustics}) \quad (54)$$

In strictly one-dimensional flow with dependent variables (ρ, u, p) then equation (52) is omitted from the boundary conditions.

If we again assume locally constant coefficients then equations (51)-(54) reduce to $\frac{\partial w}{\partial t} = 0$, where w is given by equation (48). In a linearized problem with $\underline{U}_0 + \underline{U}_1 = \underline{U}_0 + \underline{U}' \exp(i\omega t)$, the unsteady boundary conditions reduce to

$$a_0^2 \rho' - p' = 0 \quad (55)$$

$$v' = 0 \quad (56)$$

$$\rho_0 a_0 u' \pm p' = 0. \quad (57)$$

Unfortunately direct implementation of the boundary conditions is not always possible in practice because the relevant characteristic variable or function is not known at the boundary. In particular, at the outflow boundary often only the far field static pressure is known. Whilst the problem is still well-posed with this boundary condition, it does mean that the characteristic variable cannot be specified but must be partially constructed using some values from the interior. In their work on outflow boundary conditions for steady flow solutions, Rudy & Strikwerda

(1980) modify equation (54) to form:

$$\frac{\partial p}{\partial t} - \rho a \frac{\partial u}{\partial t} + \alpha(p - p_\infty) = 0 \quad (58)$$

where α is a chosen constant. Use of equation (58) ensures that at a steady converged state when the time derivatives go to zero, $p = p_\infty$. There are optimal values of α to improve the speed of convergence depending on the Mach number and problem geometry. This method is employed by Jameson, Schmidt & Turkel (1981) with locally constant coefficients $\rho_0 a_0$ and α typically set equal to $1/8$.

A comparison of these boundary conditions applied in a steady flow calculation in a cascade has been given by Berry (1984), and the convergence histories are given in Figure 11. The calculation method is an implicit factored scheme based on Steger, Pulliam & Chima (1980).

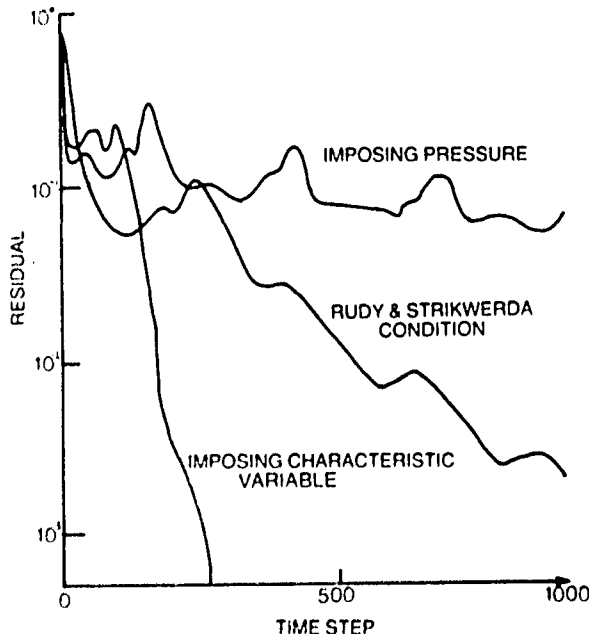


Figure 11 Effect of outflow boundary conditions on convergence history (Berry, 1984)

The conditions derived above are applicable to flows that may be approximated as quasi one-dimensional at the boundary. Whilst this is usually appropriate in computing steady flow, it is desirable for unsteady flow to relax the assumption that \underline{U} is uniform at the boundary and consider the full equation (41). In this case we require the left-hand eigensystem of $\{A + \eta B$ where ξ and η are independent variables. The eigenvalues are

$$\lambda \in \{\xi u + \eta v, \xi u + \eta v, \xi u + \eta v \pm a(\xi) \quad (59)$$

where $\zeta = \sqrt{\xi^2 + \eta^2}$.

The boundary conditions (50) would then take the form:

$$a^2 \frac{\partial \rho}{\partial t} + \frac{\partial p}{\partial t} = 0 \quad (60)$$

$$\eta \frac{\partial u}{\partial t} + \xi \frac{\partial v}{\partial t} = 0 \quad (61)$$

$$\xi \frac{\partial u}{\partial t} + \eta \frac{\partial v}{\partial t} \pm \frac{\zeta}{\rho a} \frac{\partial p}{\partial t} = 0 \quad (62)$$

These boundary conditions have been investigated by Berry (1984) for a flow field which may be linearized as before, with $\underline{U} = \underline{U}_0 + \underline{U}' \exp(i\omega t)$, where it is assumed that \underline{U}_0 is uniform at the boundary. Under this assumption, Berry adopts the interpretation that $\xi = \partial/\partial x$ and $\eta = \partial/\partial y$.

Unfortunately, $\zeta = \sqrt{\xi^2 + \eta^2}$ cannot be given exactly and must be approximated in some way. Berry suggest two approximations taking successive terms in the Taylor series which result in the unsteady boundary conditions:

$$a_0^2 \rho' - p' = 0, \quad (63)$$

$$\frac{\partial}{\partial y} u' + \frac{\partial}{\partial x} v' = 0 \quad (64)$$

and either

$$\rho_0 a_0 \frac{\partial}{\partial x} u' \pm \frac{\partial}{\partial x} p' = 0 \quad (65)$$

which is a first approximation, taking $\zeta = \xi = \partial/\partial x$; or second approximation:

$$\rho_0 a_0 \left(\frac{\partial^2}{\partial x^2} u' + \frac{\partial^2}{\partial x \partial y} v' \right) \pm \left(\frac{\partial^2}{\partial x^2} + \frac{1}{2} \frac{\partial^2}{\partial y^2} \right) p' = 0 \quad (66)$$

These are the two-dimensional equivalents of equations (55)-(57). The conditions were not implemented by Berry in his implicit method but were suggested as being more suitable for an explicit method. It is possible that particularly with the second approximation problems may arise in getting good estimates of the spatial derivatives.

Boundary conditions analytically equivalent to those given in equations (51)-(54) and (63)-(66) may be obtained for the conservation variables $(\rho, \rho u, \rho v, p)$, although the expressions are more complicated: the conditions will of course not be identical once discretized. Analogous boundary conditions were used by Whitehead (1982) in matching his solution to a calculation of the unsteady far field, based on a small perturbation solution of a uniform flow.

APPLICATION OF THE METHODS TO FLUTTER CALCULATIONS

In this section some examples are presented of application of the numerical methods described earlier, but the results presented are regrettably restricted to potential flow calculations. Some results from the method of Caspar & Verdon have been given earlier in this volume by Verdon (Chapter 11) and here we include some additional examples taken from Verdon & Usab (1986). The remaining results given here are obtained from the program "Pinsup" develop-

ed by Whitehead (1982) and Whitehead & Newton (1985). Comparisons are given with linear analytic solutions, such as Goldstein's (1977) normal shock method and its extension to strong oblique shocks (Acton, 1981). However, the real test of any prediction is comparison with experimental data and some cases are shown here. Fransson (1984) has initiated a very useful study by establishing a database of "standard configurations" upon which numerical (and analytical) methods may be assessed. Broadly, his initial findings indicate that although most methods agree for low Mach number flows, there are large discrepancies in the high subsonic, or supersonic regimes even for a flat plate test case.

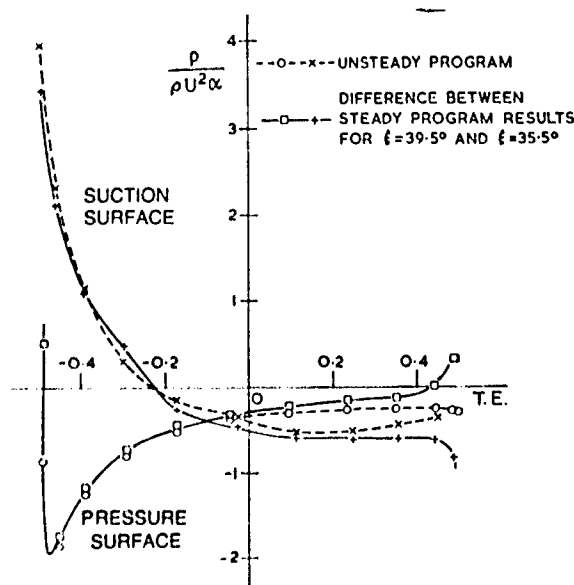


Figure 12 Unsteady pressure coefficient in the low frequency limit (Joukowski profile, stagger angle $\xi = 37.51^\circ$, space-chord ratio $s/c = 0.99$, inlet flow angle $\beta = 53.5^\circ$; torsional motion of amplitude a about mid-chord).

The first two figures show the behaviour of Whitehead's program Finsup in two limiting cases. First, in the low frequency limit for torsional blade motion (as the frequency tends to zero with zero interblade phase angle) in incompressible flow, figure 12 shows that the unsteady solution for a cambered blade agrees well with the difference between two steady solutions obtained for slightly different stagger angles. It may be noted that the unsteady pressure changes rapidly near the blade leading edge, and this is why special treatment is required in that region.

Secondly, in the limit of uniform subsonic flow through a flat plate cascade, the pressures predicted by the finite element method are compared in Figure 13 with those from a linearized theory (Smith, 1971), and this again shows good agreement.

Figures 14 and 15 (taken from Whitehead, 1982) compare Finsup with Caspar and Verdon's finite difference calculation and Atassi's incompressible flow solutions

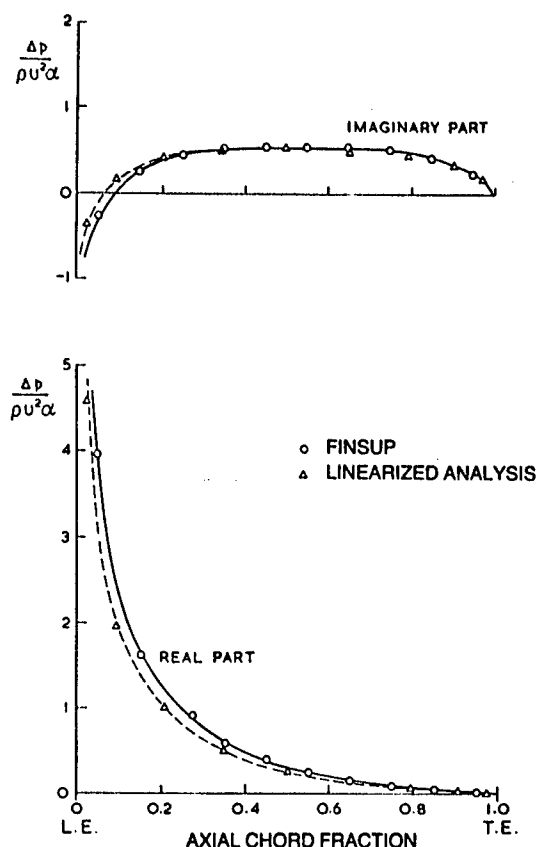


Figure 13 Comparison of the pressure jump across the blade with a linearized analytic solution (Smith, 1971) for unstaggered flat plate cascade (interblade phase angle $\sigma = 30^\circ$, reduced frequency $\omega c/U = 0.5$, $M = 0.8$)

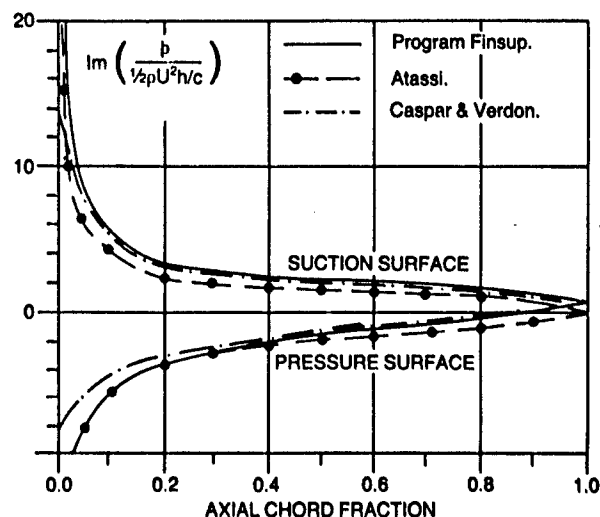


Figure 14 Imaginary part of the unsteady surface pressure coefficient. Flat plate cascade; bending vibration of amplitude h normal to chord; ($s/c = 1$, $\xi = 45^\circ$, $\beta = 45^\circ$, $\omega c/U = 1.0$, $\sigma = 180^\circ$).

(Atassi & Akai, 1978): both examples are at low Mach number, the first corresponds to a flat plate cascade and the second to a cascade of thick aerofoils. All three

methods agree well for the flat plate cascade but for the thick cascade aerofoil Verdon's prediction differs somewhat. (This difference is greater in the real part of the pressure where the method predicts high loading toward the trailing edge, which may be attributed to numerical singularities in the steady gradient terms used in the computation of unsteady pressure.)

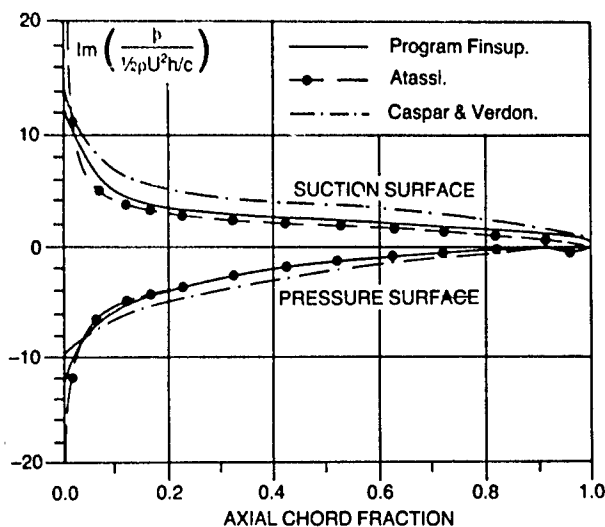


Figure 15 Imaginary part of unsteady surface pressure coefficient. Bi-convex profile, 10% thick, zero camber; bending vibration normal to chord, ($s/c = 1.0$, $\xi = 45^\circ$, $\beta = 47.1^\circ$, $\omega c/U = 1.0$, $\sigma = 180^\circ$).

In Figure 16 the unsteady surface pressure computed by Whitehead's method is compared to Goldstein's normal shock theory for a flat plate cascade in torsional motion, with inlet Mach number $M = 1.34$. In Finsup the parameter μ is used to control the isentropic shock position in the steady flow. It is a measure of the change in potential between inlet and outlet and so is related to the lift generated by the blading. Two finite element solutions are shown: in the first ($\mu = 0.875$) the shock is on or just forward of the pressure surface leading edge; in the second ($\mu = 0.885$) the shock is just within the passage. There is a noticeable difference in the pressure surface unsteady pressures near the leading edge and this highlights the importance of establishing the precise steady flow conditions, and geometry. In an inviscid calculation of a uniform flow in a parallel passage with a normal shock wave, the precise position of the shock is undetermined by the inlet and exit conditions. In Goldstein's analysis therefore a strong shock is assumed to be at the leading edge of each flat plate and lie normally across the passage. On the suction surface immediately ahead of the shock the numerical method differs from the analytic solution: this is probably due to smearing of the shock by artificial viscosity. Discrepancies downstream of the shock may be due to differences in the shock strength cases, since the isentropic jump in Whitehead's method produces a much

lower downstream Mach number; or to the wrong pre-shock conditions - or both. The overall conclusion is that although the trends are similar, the precise details differ considerably.

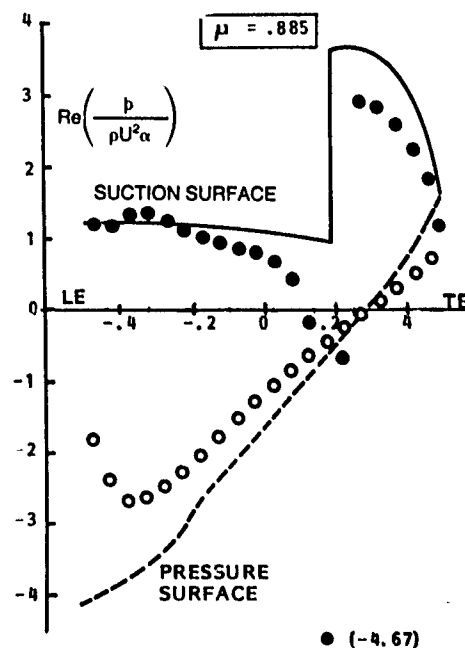
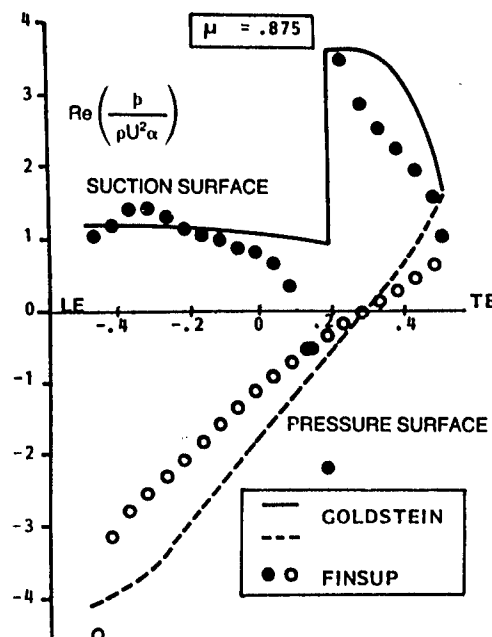


Figure 16 Unsteady surfaces pressure coefficients for torsional motion about mid-chord (Verdon and McCune (1975) cascade, $M = 1.34$)

Comparisons with experimental data are now briefly considered. Figure 17 shows how well Whitehead's method performs on Carta's low Mach number ($M = 0.18$) DCA blade, for which good experimental data are available. Caspar & Verdon's predictions for the same cascade (at a different interblade phase angle) are shown in Figure 18 (taken from Verdon & Usab, 1986). These are also in good agreement with the experimental data. Figure 19 shows an application to the DDA

turbine cascade (Jay, Rothrock, Riffel & Sinnet, 1979) which has thick blades with 110° of turning. The comparison has been made over a range of exit Mach number and interblade phase angle, and this case is typical (rather than showing best agreement), although agreement generally worsens with increasing exit Mach number. Figure 20 shows a second application to a turbine test case which illustrates good agreement with the EPFL test data (Bolcs & Fransson, 1986).

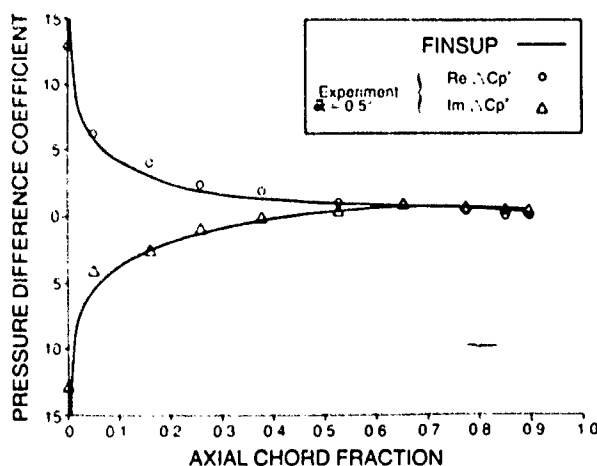


Figure 17 Unsteady pressure distribution for "Standard Configuration 1" (Carta DCA blade, blade incidence $i = 6^\circ$, $\omega c/2U = 0.122$, $\sigma = -45^\circ$).

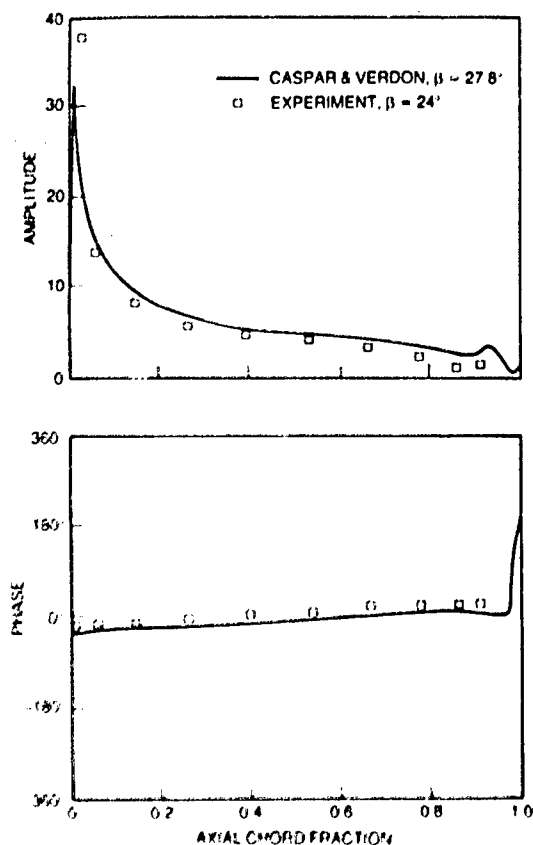


Figure 18 Unsteady pressure difference coefficient for "Standard Configuration 1" ($M = 0.17$, $\omega c/2U = 0.122$, $\alpha = -135^\circ$, $\alpha = 2^\circ$).

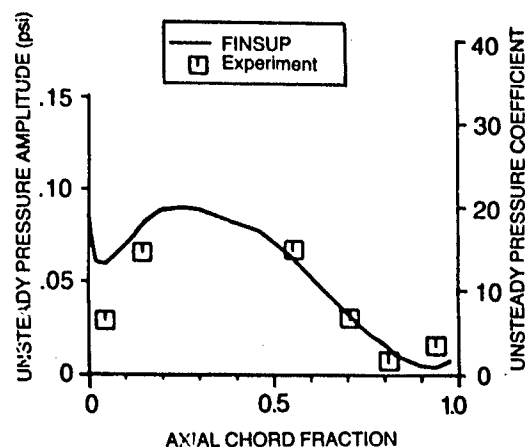


Figure 19 Unsteady suction surface pressures for DDA turbine ($\sigma = -45^\circ$, $M = 0.78$).

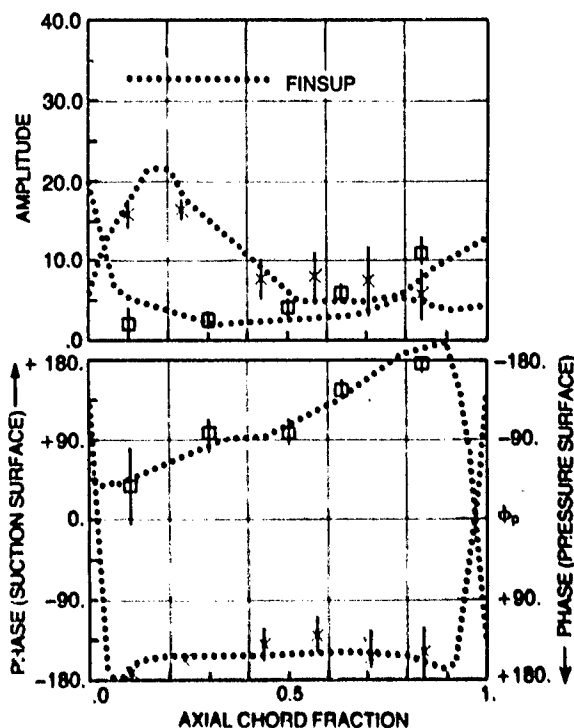


Figure 20 Unsteady surface pressure coefficients for "Standard Configuration 4".

Caspar & Verdon's prediction for "Standard Configuration 5" is shown in Figure 21 where it can be seen that there is significant difference between the amplitude of the predicted pressure difference coefficient and the experimental values. In the experiment only one blade in the cascade was vibrated but in the theoretical modelling only a single value of inter-blade phase angle was used ($\sigma = 180^\circ$).

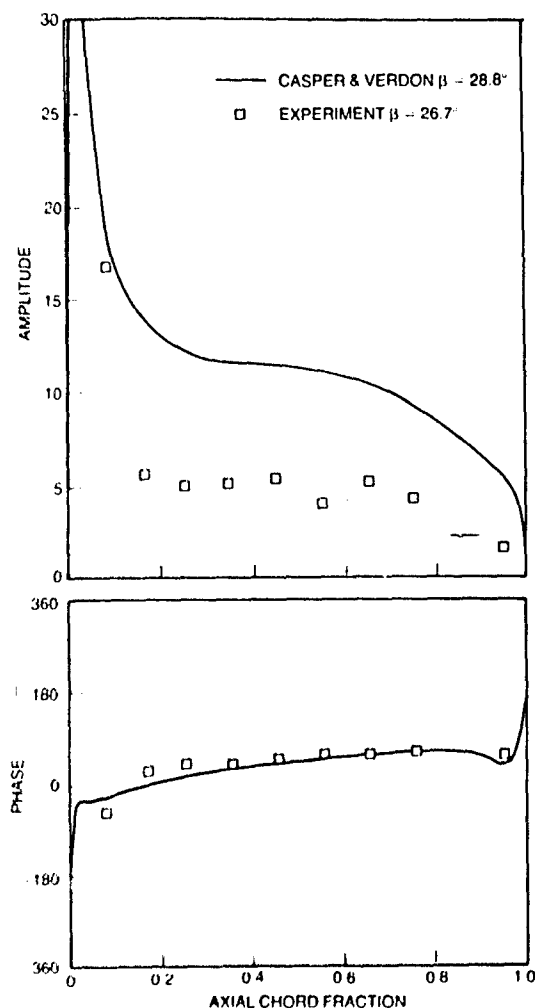


Figure 21 Unsteady pressure difference for "Standard Configuration 5". ($M = 0.5$, $\omega c/2U = 1.02$, $\sigma = 180^\circ$, $\alpha = 0.3^\circ$)

Verdon & Usab also report predictions with measured data for a cascade of symmetric bi-convex aerofoils. When the blades are unloaded in steady flow, inlet Mach number $M = 0.65$, the agreement is moderately good as shown in Figure 22. In the second example shown in Figure 23, in which the steady flow is at incidence with a leading edge shock, the prediction differs considerably from the measured data on the suction surface of the blade.

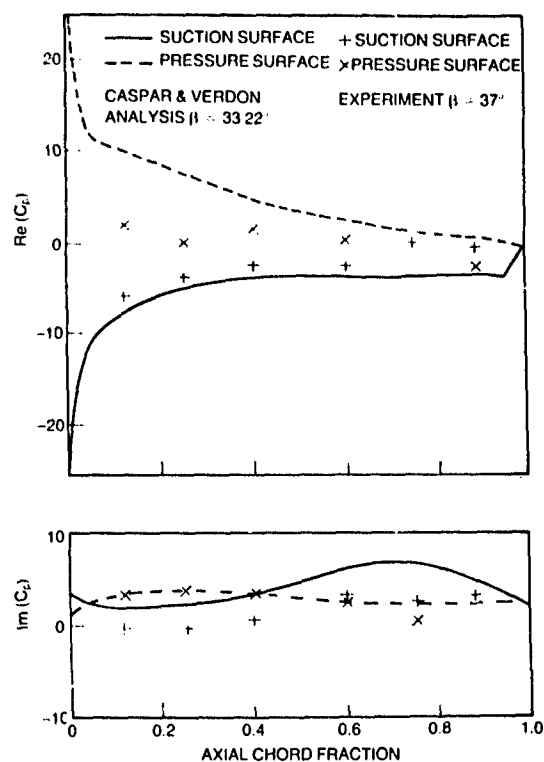


Figure 22 Unsteady pressure coefficient for NASA Lewis Cascade ($M = 0.65$, $\omega = 200$ Hz, $\sigma = 90^\circ$).

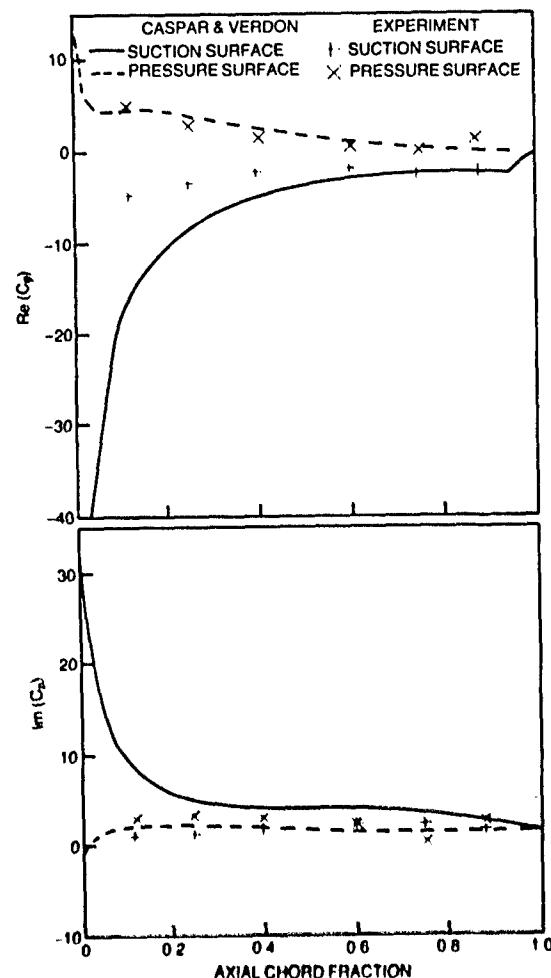


Figure 23 Unsteady surface pressure coefficient for the NASA Lewis Cascade ($M = 0.8$, $\beta = 30^\circ$, $\omega = 200$ Hz, $\sigma = 90^\circ$).

In Figure 24 we return to Finsup and the Carta DCA blade to assess the importance of geometry: the flat plate, zero incidence, case shows a much greater sensitivity to interblade phase angle than does the full geometry solution. This could be important in a stability calculation application to a more marginally unstable blade, where a flat plate calculation might predict instability at $\alpha = 45^\circ$, whereas the full geometry might remain stable. Figure 25 shows that this behaviour is not a general rule, since the situation is reversed for the DDA turbine blade.

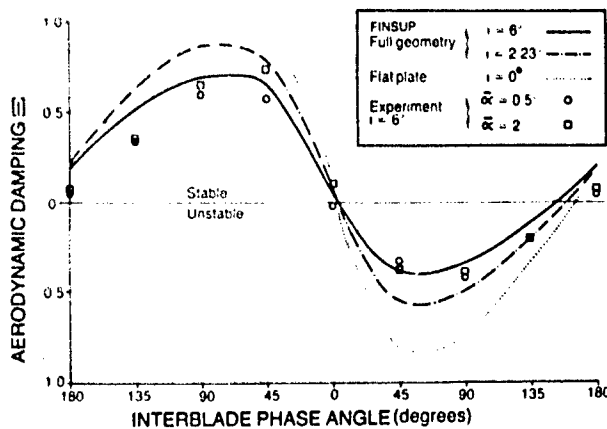


Figure 24 The effect of geometry and incidence on aerodynamic damping for "Standard Configuration 1" (Carta DCA blade, $wc/2U = 0.122$)

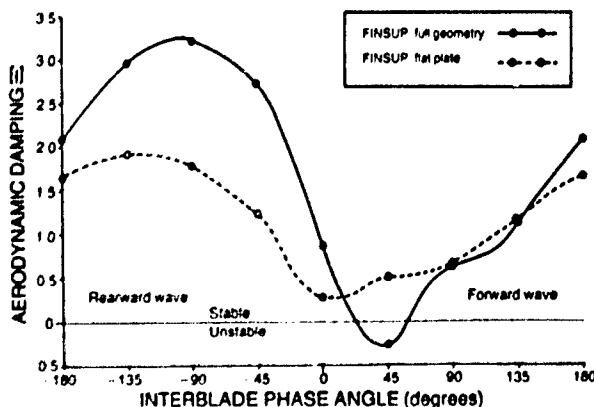


Figure 25 Variation of aerodynamic damping with interblade phase angle (DDA turbine, $wc/2U = 0.273$)

Having presented comparisons with experiment for low and high subsonic Mach numbers there remains the more difficult case of supersonic inlet flow. Fleeter and Jay have shown in chapter VII how Whitehead's method performs for such a flow and they have commented upon why the predictions of each numerical method differ from the measured unsteady pressures. One difficulty in solving an unsteady flow with a shock by a potential method lies in

obtaining the correct mean flow. The steady flow is incorrect in at least three important ways: (i) incorrect shock jump conditions, (ii) no boundary layer growth downstream (especially on the suction surface) and (iii) artificial viscosity giving shock smearing.

The first of these could be tackled by providing an entropy increase such that the potential flow gave the correct Mach number downstream of the shock, (or by changing streamtube height); neither Caspar's nor Whitehead's method has this facility at present. An Euler method would clearly be preferable. To cure the second shortcoming requires either a boundary layer treatment to cope with separated flows or streamtube contraction to provide a passage averaged approximation. The latter technique has been successfully used in Finsup to vary the pressure ratio across the cascade. The third problem remains in Whitehead's method but has been eliminated by Verdon who uses shock fitting in the unsteady calculation to obtain the correct shock jump conditions.

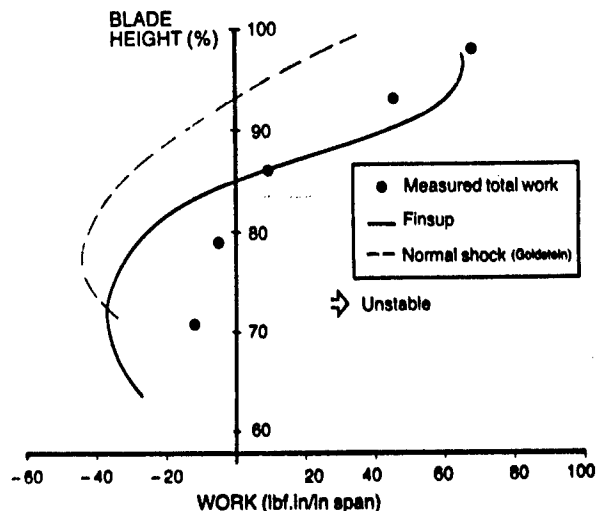


Figure 26 Total unsteady work

The above discussion is entirely concerned with unsteady pressure coefficients, but of course, when the unsteady aerodynamics methods are applied to a complex disc mode (for example for a snubbed (clapped) rotor) it is the overall work or stability which matters. The sensitivity of the predicted overall work to changes in its components requires careful study: it is not enough that the agreement of pressure prediction with experiment is good. What is needed is an objective assessment of the quality of the prediction in the light of the application for which it is to be used. Figure 26 shows the variation of total section work against radius for a model fan (Brooker and Halliwell, (1984)); although Finsup does not agree entirely with the measured data, it is closer than the normal shock predictions. The reason for this is more clearly seen in Figure 27. By running the finite element method for a range of streamtube height ratios, pressure ratio across the cascade is

varied. Results from Finsup are compared with predictions from the normal shock model of Goldstein (1977) and its modification to oblique shocks (Acton, 1981) and a linearization about supersonic uniform flow with unity pressure ratio (referred to as Linsup in the figure), in addition to an experiment at a flutter condition. The source of increasing instability with reducing pressure ratio lies in the contribution to the work integral from the unsteady moment due to torsional motion. It is observed that high pressure ratio leads to a large stable value for this which reduces as the pressure ratio is dropped. This example emphasises the importance of ensuring that mean flow conditions are correctly modelled.

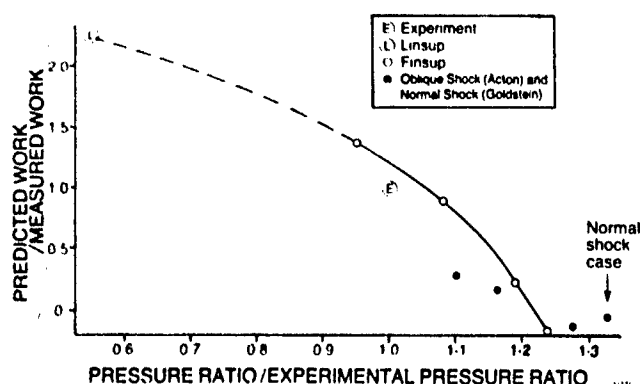


Figure 27 Variation of section unsteady work with pressure ratio

CONCLUDING REMARKS

In this chapter we have concentrated on unsteady methods applicable to turbomachines; a review of progress in external aerodynamics is given by Tijdeman & Seebass (1980). Other reviews of interest are Ballhaus (1978) also concerning transonic flows about aerofoils, and MacCormack & Lomax (1979) who review computational methods in compressible viscous flows.

Much of the work we have described concerns the numerical methods devised to calculate an unsteady flow which has been assumed a small linear perturbation of a non-linear steady potential flow. These are the only methods that are sufficiently well-developed to be used in design calculations even though they are limited by the assumption of potential flow and include a linearization which is only valid if the shock movement is not too large. It is clear that solutions of the Euler equations are to be preferred because they provide a less simplified modelling of the flow. However, although methods to calculate the Euler equations are now well advanced it is only in computing steady flow that they are regarded as sufficiently robust for regular use in design. For unsteady flow most of these methods may be regarded as research tools, even for two-dimensional flow. Happily many of the methods for solution of the Euler equations when developed will be readily extended to include the extra terms necessary for solution of the Navier-Stokes equations, and these methods are under active develop-

ment both for unsteady and three-dimensional flow. The methods are computationally very expensive at present and it will be some time before they are regularly used in design. But as we have seen in the previous section continuing progress is vital to achieve a flexible numerical field method capable of examining all the important flow parameters.

Acknowledgement

The authors wish to thank colleagues at Rolls-Royce plc and Topexpress Ltd for their advice during the preparation of this article. We are particularly grateful to Dr P Stow of Rolls-Royce for his detailed comments. It is published with the permission of Rolls-Royce plc, whose support is gratefully acknowledged.

STALL FLUTTER

F. Sisto

Department of Mechanical Engineering
 Stevens Institute of Technology
 Hoboken, New Jersey 07030
 USA

INTRODUCTION

As with other topics of aeroelasticity in axial turbomachines, the subject of stall (alternatively stalling, stalled) flutter has its roots in antecedent experience related to aircraft wings, control surfaces and propellers (Dowell et. al., 1978). Thus the key characteristic, that this particular self-excited aerelastic instability occurs with a periodic separation of the flow from the airfoil surface, is a carryover from a confirmed type of behavior with isolated airfoils (Studer, 1936) (Victory, 1943).

Two caveats relative to stall flutter in turbomachines must be stated before continuing with the development of this chapter. In the first place the flutter speed of a wing in subsonic flow varies and then typically drops as a continuous function of increasing incidence. The changes become most precipitous as the incidence approaches the value for static stall as defined by maximum lift coefficient. This behavior seems also to be the case in the axial flow compressor stage operating subsonically, although flutter at low incidence (low loading) has not been a problem in practice because the required relative velocities are much higher than those existing in actual machines. Hence, a more cautious description of the stall flutter phenomenon might be flutter at high incidence or at high aerodynamic loading.

The second remark relates to the fact that the axial-flow turbomachine stage is characterized by a multiplicity of airfoils, rather than a single wing, with the unavoidable mutual aerodynamic interference that this implies. This interference may inhibit airfoil stall and delay steady separation to very high incidence, even to the point where the annulus flow may exhibit wall stall before any separation from the airfoils is encountered. The aerodynamic interference will lead also to unsteady separation of the cascaded airfoils and a phasing between the stalling events at adjacent airfoils, or an apparent "propagation" of the unsteady flow perturbations along the cascade, i.e., in the peripheral direction. For these reasons the stalling behavior of isolated airfoils will be referred to only minimally in the sequel.

The flow perturbation zones rotate in the same direction as the rotor, but at a fraction of the rotor speed; hence stator vanes also experience the flow perturbation at a frequency equal to the absolute pattern rotation rate times the number of such zones in the annulus. If the airfoils do not vibrate then this latter behavior is properly termed propagating or rotating stall since it is purely an instability of the flow. However, if

stalling is triggered by oscillatory changes of effective upwash attributable to airfoil vibration*, then cascade flutter is a by-product of the self-excited aeroelastic instability, not its cause. On the other hand, if the airfoils resonate structurally with the frequency of encountering stall zones, this is properly termed an aerodynamically forced vibration. There is obviously a grey area between these types of blade vibration, at the one extreme flutter occurring with temporally uniform onset flow, and at the other extreme resonance occurring upon the coincidence of frequencies.

Propagating stall, or rotating stall, is a subject of considerable importance aside from the possibility of producing a damaging blade resonance. If the frequency of encounter is low compared to the blade natural frequency the blades may flutter within the stall cell where low throughflow velocities exist. If the increase in stall flutter amplitude while residing within the cell is greater than the decay that takes place when the blade is outside the cell, then quite appreciable amplitude and blade stress may build up in a short period of time. There are indications, in fact, that there is an actual flow reversal within strong stall patches, so that the stall flutter alluded to above may occur by separation of the flow from the trailing edge of the profile, which temporarily has become the "leading edge".

Propagating stall cells usually decrease in number as the incidence increases, so that typically one stall cell appears in the flow annulus just prior to encountering surge. This single cell exhibits very large flow perturbations, although the throughflow averaged over the annulus area remains constant with time. At surge the flow in the entire annulus is perturbed at any instant and hence the throughflow varies with time in either an oscillatory or transient fashion, reaching negative values at some instants of time. The periodic loading and unloading of all the blades in a row during surge constitutes an aeroelastic event of considerable importance. Not only is the gas bending load reversed with a frequency of the order of several Hertz, but hundreds of cycles of stall flutter fatigue damage may be accumulated during each of these surge cycles.

The transient counterpart, often termed "hung" stall, is attributed to the pumping system characteristic of the

*Small amplitude vibrations may always be assumed to be present due to turbulence, acoustic radiation, bearing roughness and so forth.

compressor or fan installation (Koff and Greitzer, 1984). In such cases the reduced throughflow velocities may persist indefinitely and, in addition to the transient change in mean aerodynamic loading, appreciable periods of stall flutter self-excitation may be encountered. The subject of blade response to transient stall was broached formally by Sisto (1974) and is currently receiving a great deal of renewed attention.

THE ROLE OF MACH NUMBER

Before proceeding with the quantitative exposition of stalling flutter it should be noted that subsonic relative velocities conventionally are under discussion. Thus even if a transonic axial-flow compressor, fan or turbine is under scrutiny, the stall flutter will occur usually at part-speed operation where the relative velocities are assumed to be subsonic. That some local supersonic flow is necessary for stall flutter to develop, or that there is no such occurrence as subsonic stall flutter, are not supportable statements at present.

Clearly, for some more modern designs, stall flutter may not be explained until the additional instability attendant to shock wave oscillation is considered. However, for low-speed and other designs, "flutter at high incidence" has been recorded where the occurrence of local supersonic Mach numbers could not be observed or justified (Carter and Kilpatrick, 1957). And there are many linear cascade data, including measurements in water tunnels (Yashima, 1977) (Tanida et al., 1963) and in an air tunnel (Arnoldi et al., 1977) showing that negative aerodynamic damping coincident with flow separation in cascaded airfoils occurs with essentially incompressible (i.e., shock-free) flow. Chi and Srinivasan (1984) note that the role of flow separation during subsonic stall flutter needs to be justified; predictions based on compressible separated aerodynamics of Chi (1980) give encouraging agreement with diverse stall flutter experience on a shrouded fan.

In the next Section two exceptional cases of flutter are treated in which the presence of shock waves is of transcendent importance. Following that treatment the remainder of this Chapter will be devoted to stall flutter as ordinarily defined.

CHOKE FLUTTER AND SUPERSONIC STALL FLUTTER

Choke Flutter

This type of flutter (alt. choking flutter, choked flutter) occurs in Region II near the choke line on a typical compressor operating map (see Figure 1 of the first chapter). It is associated with incidence and passage area schedules such that a choked throat is formed, followed by a passage shock downstream of the throat. With relative motion of adjacent blades the shock becomes nonstationary. The subsequent mechanism of the flutter

instability is described qualitatively in Dowell et. al., (1978), including possibly unsteady separation bubbles.

Considering a single airfoil with thickness oscillating in a wind-tunnel of small height, Tanida and Saito (1977) were able to demonstrate both analytically and experimentally that choke flutter is a distinct possibility, critically involving shocks which fluctuate in position and strength. The analysis is based on one-dimensional unsteady flow with oscillation limited to torsion.

An earlier note by Savkar (1976) presented an analysis of the same problem, limited however, to shock-free solution of the linearized equations of transonic flow. In both these references the comparison with the cascade is valid only for unstaggered cascades at $\sigma = 180$ deg. Although other analyses of this problem had been made previously, also showing the possibility of torsional instability at low supersonic Mach numbers, this note presented the first solution of the unsteady transonic equation for the windtunnel (i.e., cascade) problem. In this sense "transonic" is equivalent to "choked" since $M = 1.0$ can be treated for sufficiently high oscillation frequencies.

Micklow and Jeffers (1981) considered a semi-actuator disk representation of phase cascade blade oscillations and developed a choke flutter analysis. Since one-dimensional channel flow connected the upstream and downstream flow fields it was possible to consider flutter modes not only with flexure but with pitching components as well. The method of solution limited the interblade phase angle to $\sigma = \pm 90^\circ$.

Tang and Zhou (1983) used a finite difference method to solve the perturbation equations of an oscillating staggered cascade with finite blade thickness and arbitrary interblade phase angle. The assumed flutter mode was confined to flexure.

In accuracy these choke flutter analyses might be expected to improve with year of publication. Since the possibility of flow separation is not admitted in any of these models, they are most applicable to low values of steady incidence. As noted in other Chapters of this Manual there continues to be a trend in unsteady cascade aerodynamics to treat finite thickness, transonic flow with moving shock waves of variable strength. The analytical treatment of choke flutter in a middle stage represents a point in this parameter space corresponding to the stage operating at or near its choke line. (In a multistage compressor this may not correspond precisely to the choke line for the compressor as a whole). The choke flutter mechanism is comparable to stall flutter in the sense that both phenomena are induced by large flow and loading anomalies, or nonlinearities, controlled predominantly by the time-dependent relative position of adjacent blades. Classical flutter, by

comparison, depends to a greater extent on the relative vibratory velocity of the cascaded airfoils. It is probable that the two phenomena can merge, or coexist, so that shock waves begin to play a role in stall flutter and conversely flow separation is induced by periodic shock movement, with shock-wave boundary-layer interaction and "shock stall".

Experimental documentation of choke flutter is contained in Ellis et. al., (1978), Lubomski (1979), Jutras and Stallone (1980) and Lubomski (1981). The mode is usually flexure but may also be a coupled mode involving some torsion. In this sense the early torsional theories and supporting wind tunnel experiments were not capable of demonstrating flexural choke flutter stemming from the restrictions of the analyses and design of the experimental apparatuses. For this reason the method of Tang and Zhou (1983) is recommended since they assume a flutter mode in flexure.

What is ultimately needed is an extension to cascaded airfoils of the methods used for computing unsteady transonic flow over isolated airfoils using the full Navier-Stokes equations and including the possibility of capturing shocks of variable strength and position. Verdon and Caspar (1984) are in the process of developing such a method, but restricted to inviscid flow. Most likely analyses of this type will prove adequate for choke flutter and system modes instabilities. Continuing to larger negative incidence values a transonic "stall" flutter may occur once again. For this regime a return to the full Navier-Stokes equations becomes necessary in order to treat shock-induced separation. Such methods are currently under development for single airfoils, see Chyu and Kuwahara (1982).

SUPERSONIC BENDING STALL FLUTTER

As indicated by the title, this type of flutter occurs with a combination of high loading (i.e., near the compressor or fan surge line) and high relative Mach number associated with high rotational speed. Adamczyk (1978) and Adamczyk et. al., (1982) have developed an actuator disk quasisteady analysis in two-dimensional flow for supersonic bending flutter and have achieved considerable success in predicting the relative instability in several supersonic fans. Rotor-loss and deviation-angle correlations are obtained for NASA transonic compressor correlations ($M < 1.15$) and together supply the effect of flow separation or "stalling" behavior in the model.

These incremental stagnation pressure and flow angle changes are applied downstream of the actuator disc, the upstream flow being irrotational. By its nature an actuator disc model cannot predict unsteady moments, hence only flexural flutter may be analyzed. Since blade bending (in two orthogonal directions) is observed in this regime this limitation of the analysis is not a detraction although the model would fail to yield a prediction for torsional flutter where this mode of instability was physically

possible. However, since the supersonic bending stall flutter may be expected to occur in unshrouded fan (and possibly in free-standing axial flow turbine) blades at fairly low reduced frequencies, the limitations of quasisteady actuator disc analysis are not entirely debilitating.

The existence of this type of stall flutter is corroborated experimentally by Loiseau and Maquennehan (1976) and seems to require a detached leading-edge bow shock wave which spans the passage to the suction surface of the adjacent blade (compressor convention). Its prediction is best performed using the method of Adamczyk et. al., (1982).

STALL FLUTTER

Nonlinear Phenomena

As contrasted with classical flutter (i.e., flow attached at all times) the mechanism for net energy transfer from the airstream to an oscillating blade need not rely on elastic and/or aerodynamic coupling between two modes, nor upon a phase lag between a displacement and its aerodynamic reaction. These latter effects are necessary in a linear system to account for an airstream doing positive work on a vibrating blade. The essential feature of stall flutter is the nonlinear aerodynamic reaction to the motion of the blades. Coupling and phase lag may alter the results somewhat; the basic instability mechanism and its principal features are explicable in terms of nonlinear normal force and moment characteristics. See Chapter 5 in Dowell et. al., (1978).

In that reference it is shown that analysis of stall flutter of an isolated airfoil based on purely theoretical considerations is not quantitatively useful. Nonetheless such an analysis is instructive, and illuminates the mechanism of instability.

For plunging displacement of a two-dimensional "typical section" it is assumed that the static normal force coefficient, C , including penetration well into the stall regime is given by a polynomial approximation in powers of A

$$C = \sum_{n=0}^{\infty} a(n, \alpha) \tilde{A}^n$$

where \tilde{A} is the instantaneous departure from the steady state value of angle of attack. A is attributable to the plunging velocity acting normal to the onset flow. The mean angle of attack is α . Assuming that the single-valued static characteristic of normal force versus angle of attack continues to be operative in the dynamic application, the work per cycle done by this force acting on the displacement may be calculated and is given by

$$P = \frac{1}{2} \rho V^3 b \left(A(\omega Y/V)^2 + B[(\omega Y/V)^2]^2 + D[(\omega Y/V)^2]^3 + \dots \right)$$

The constants A, B and D depend on α through the a -coefficients of the

C-characteristic, ρ is the fluid density, V is the velocity, ω is the plunging frequency and Y is the amplitude of the bending displacement, y . The cubic dependence of P on V is a natural consequence of the dimensions of power, or work per unit time.

In general A , B and D individually may be either positive or negative. The eight sign combinations are of fundamental interest in describing possible stall flutter behavior. These cases have been sketched in Figure 1a, excluding the case of A , B and D being all negative since this does not lead to flutter.

Cases i and ii are examples of "soft" flutter; given an airstream velocity V and mean incidence α such as to produce values of A , B and D corresponding to cases i or ii, the vibratory amplitude of flutter grows smoothly from zero. In case ii the amplitude of stall flutter reaches a steady value and does not increase further. In either case i or ii a plot of y versus y/ω with time as a parameter produces a "trajectory" of the "characteristic point" that is a spiral departing from the origin at $t = 0$. In case ii the spiral asymptotically approaches a circle for very large time. In the language of nonlinear mechanics the circular path is a "limit cycle" and hence most instances of stall flutter may be termed limit cycle vibrations.

Cases iii and iv describe a type of behavior termed "hard flutter". In these cases when flutter appears as a self-sustaining oscillation, the amplitude jumps to a large finite value. In case iv the motion spirals to a circular limit cycle at a larger stable amplitude in the phase plane (i.e., the y , \dot{y}/ω plane). If the limit cycle is unstable, labelled U on Figure 1a, the slightest perturbation from an initially purely

circular path will result in monotonic spiralling away either to a larger or smaller radius. The examples of stable limit cycles are labelled S. The origin is either stable (hard flutter) or unstable (soft flutter). It is a theorem in nonlinear mechanics that the concentric circular limit cycles of a given system are alternately stable and unstable. See case v.

For torsional flutter the analysis is more complex since the upwash, proportional to the local effective angle of incidence, is compounded from the instantaneous angular displacement plus the instantaneous tangential velocity in a direction normal to the chord. The first effect is independent of chordwise location; the second is linearly dependent upon the distance along the chord from the elastic axis and the angular velocity of vibration. Both incidence components vary harmonically with the flutter frequency and are in quadrature with each other.

As a result, in the analogous modeling of torsional stall flutter (Dowell et. al., 1978) a key difference emerges when compared with bending flutter; an aerodynamic moment appears which is out of phase with the angular velocity of pitch. Torsional stall flutter is therefore found to be a more complex phenomenon, with a greater sensitivity to the time lag between the oscillatory motion and the periodic aerodynamic moment considered as the response. Furthermore, torsional flutter exhibits a strong dependence on the effective position of the axis of twist.

In qualitative terms it is concluded that the behavior in torsional flutter is intermediate between quasisteady behavior and a type of behavior typical

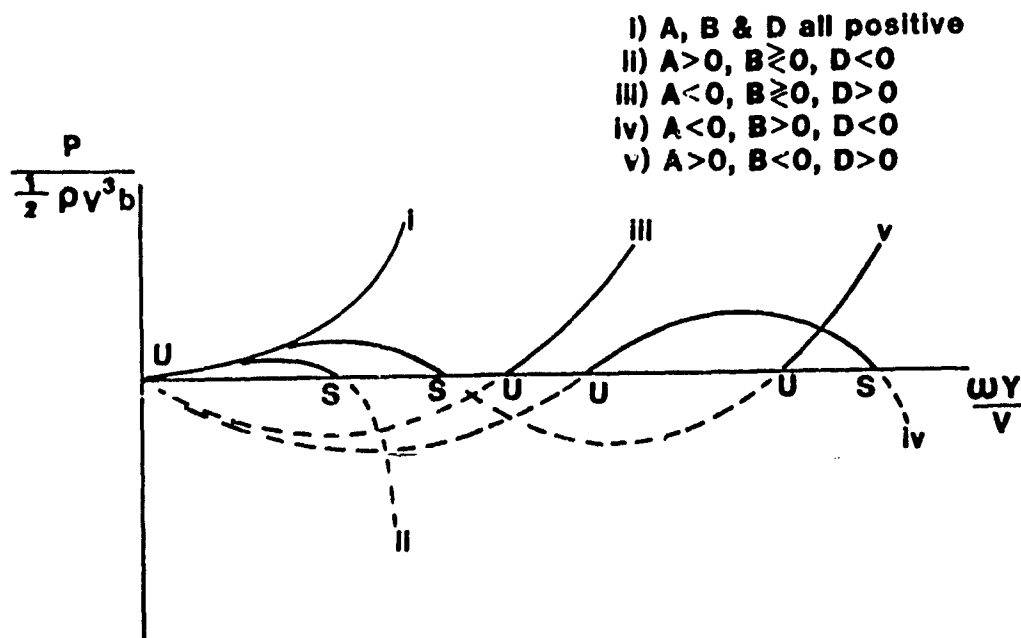


Fig. 1a Aerodynamic Power as a Function of Amplitude of Flutter Motion.

of bending stall flutter, i.e., critical dependence on the local slope of the moment characteristic.

The ability to predict the flutter amplitude or flutter stress stems from the nonlinear nature of stall flutter. By contrast, in linearized formulations of the flutter problem only the stability boundary may be determined. The condition for constant flutter amplitude is that the work per cycle, or power, be null. Finding the roots of the equation $P = 0$ yields the dimensionless flutter amplitude $\omega Y/V$ as a function of the mean incidence α since the "constants" A, B and D are parametric functions of α . A, B and D depend on the point of the C-characteristic chosen for expansion in polynomial of powers of $(\omega Y/V)^2$. In Figure 1b hard and soft flutter amplitudes are displayed as presumed functions of the mean incidence, α . Hard flutter displays a sudden jump to finite amplitude as α achieves a critical value and "quenches" at another lower absolute value of α . The two features taken together produce the characteristic hysteresis loop indicated by the arrows.

Motion in a third degree of freedom is practically important. Oscillatory surging of the blade profile in the chordwise direction can be related to a nonlinear behavior of the aerodynamic drag. Although blades are locally very stiff structurally in the chordwise direction, the drag/surging mechanism will nonetheless be of importance for highly twisted blades where the local surging displacement will be a consequence of the radial distribution of twist and the radial distance from the flexural node. The coupling between vibratory surge displacements and the drag (rotor-loss mechanism) has been considered in the earlier reference to supersonic bending stall flutter (Adamczyk, 1978). Under these circumstances stall flutter with several degrees of freedom may occur. The assumption of a system mode that couples bending-bending-torsion in a prescribed fashion is an example of stall flutter with multiple modal components.

A deficiency in the expository theory outlined here is the absence of frequency dependence in the aerodynamic normal force, moment and drag characteristics, e.g., the C-characteristic in the bending flutter example. The actual characteristics may also be double-valued, having two different magnitudes at the same angle of incidence depending upon the direction of approach. The moving shock waves discussed in the role of Mach number are one cause of such dynamic hysteresis.

The greatest deficiency in this immediate discussion of stall flutter is the fact that the cascade environment has been neglected. Cascaded airfoils stall differently from a single airfoil, not only because of the channeling influence of adjacent blades, but also due to the strong variation of aerodynamic interference with interblade phase angle, σ . The experimental quasisteady moment loops obtained at stall with different σ by Sisto and Ni (1972) demonstrate the effect of cascading on stall.

EMPIRICAL CORRELATIONS

The earliest experimental identification of turbomachinery stall flutter (Shannon, 1945) was in a World War II axial compressor and occurred in the fundamental bending mode of the cantilever rotor blading. Although torsional mode flutter also appeared with substantially lower stresses, the early experience seems to have been predominantly in flexure (Pearson, 1953). Later, as typical cantilever aspect ratio increased, blade thickness decreased and the center of twist moved toward the trailing edge, the torsional mode became flutter-prone at high incidence.

In either fundamental flexure or twist, the earliest attempt at flutter correlation for economy of testing and for subsequent application to design consisted in plotting incidence versus relative velocity at constant levels of flutter stress from experimental data. By assigning a threshold value of alternating root stress for flutter to be present, one of these stress contours became the flutter boundary. Instead of

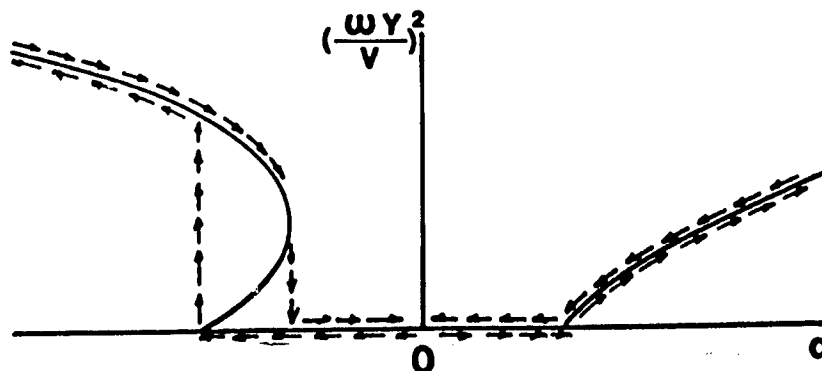


Fig. 1b Hard and Soft Flutter Amplitude Dependence on a Critical Parameter (Mean Incidence)

velocity the nondimensional reduced velocity, $V/(\omega c/2)$, provided a more compact correlation. The tests were usually conducted with single stage rigs and the aerodynamic data set, V and α , were usually measured or inferred at a representative station at 80% span, or thereabouts, of the free-standing rotor blades. In addition to aerodynamic variables, the critical flutter condition is affected by a host of geometric parameters such as stagger, solidity, profile, fixity (or structural restraint) and their radial variations. It is clear therefore that a data base from which one would hope to predict the flutter behavior of a completely new stage design is too large to be economically or physically feasible. The result was that the actual data bases were much more modest and their use was confined to qualitative estimates of expected behavior of stages that were not too radically different from previously tested configurations.

The earliest "design rules" were statements that the reduced velocity based on the semichord should be kept below 1.25 using the torsional frequency and below 5 or 6 in flexure. In these rules there was the implicit assumption that the flutter frequency was equal to the natural frequency of the blade (accounting for centrifugal stiffening if the blade was rotor-mounted). Since blade mass ratios were high and observed flutter frequencies were close to the natural frequencies, this was a reasonable assumption. Later versions of the design rules added correlations with respect to design pressure ratio of the stage, solidity, etc.. However, these were all empirical results, in most instances proprietary, and, in any event, not valid for extrapolation to new conditions.

In Figure 2 a typical single stage experimental correlation is presented.

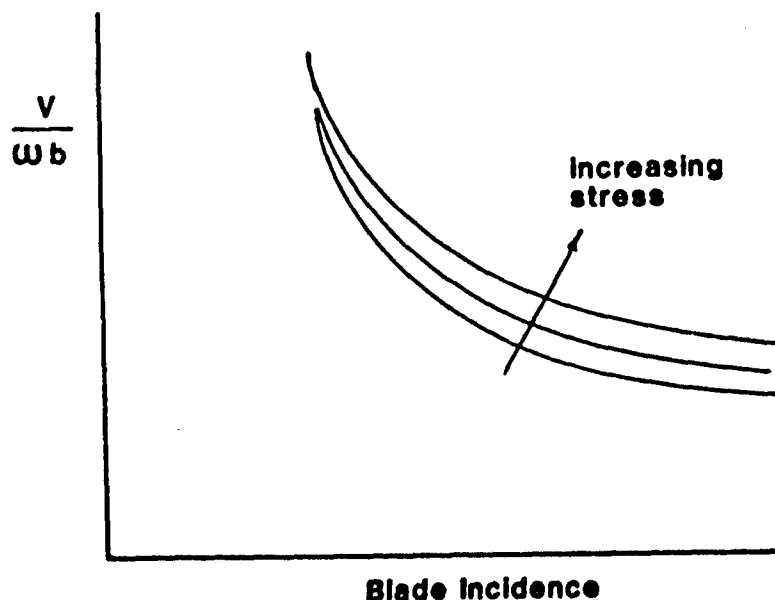


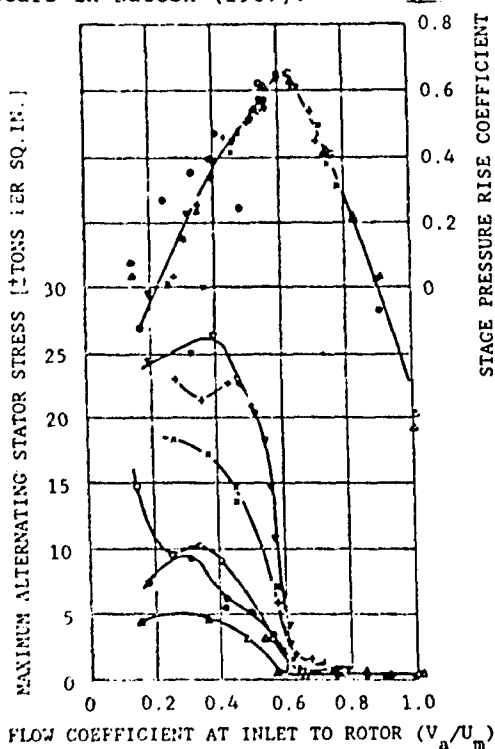
Fig. 2 Experimental Stall Flutter Stress Contours on a Plot of Incidence Versus Reduced Velocity

An important use of these data is the implicit suggestion they contain for corrective design changes. If a compressor is built and encounters stall flutter in a particular front stage, it will usually be beneficial if the stage's operating line can be lowered and/or moved to the left by changes external to the rotor itself, e.g., guide vane or throttle schedules. By the same token on-rotor modifications such as increasing the natural frequency by changing the blade material will move the value of $V/(\omega c/2)$ toward lower stall flutter stress.

Figure 3, taken from Carter and Kilpatrick (1957), shows the experimentally obtained stage pressure rise and stator flutter stress in bending plotted against the flow coefficient in a single stage compressor. The correlation of high stall flutter stress with blade stall (as defined by peak stage pressure rise) is dramatic. Since incidence and flow coefficient are inversely related, the critical dependence of stall flutter on operating near or above the "stalling incidence" is clearly demonstrated. Some mention should be made, particularly in annular cascades, that the stalling incidence measured or inferred from low response instrumentation may mask the fact that the flow velocity vector is fluctuating rapidly between "unstalled" and "fully stalled" values; the stage may be in a rotating stall condition.

In this early experience the flutter mode was usually fundamental bending, the amplitudes were modulated with apparent randomness and non-identical frequencies of adjacent blades were observed. At high stress amplitude, or alternatively when the flutter was predominantly torsional, the frequencies would lock into a common value and then unique interblade phase angles could be defined.

It is most likely that the axial compressor designs whose behavior has been characterized above are subjected to a form of buffeting at high incidence. The turbulent, separated wakes of these low solidity front stages give rise to a blade normal force which contains sufficient energy content at the blade bending frequency for each blade to resonate at its own natural frequency value. At somewhat higher blade bending amplitude, or alternatively if the torsional mode was selected, a "locking in" of shedding and oscillation frequencies occurs for the entire annular cascade. This nonlinear effect of "entrainment of frequency" represents the threshold of true stall flutter. The torsional behavior is more descriptive of modern designs and the increased coherence of the vortex shedding of adjacent blades is also enhanced by the smaller blade spacing (high solidity) of these designs. The trend in compressor airfoil sections toward more rearward, maximum thickness and maximum camber has the effect of displacing the elastic axis (or torsion center) toward the trailing edge. In almost every variety of flutter it has been found that this trend is destabilizing. A particularly clear analytical exposition of the effect of torsion center location for a fully separated flow about a single airfoil appears in Natesh (1967).



Flutter Stresses and Aerodynamic Performance Recorded in Single-stage Compressor Tests

Pressure rise measured from inlet to rotor to exit from stator.

Speed, r.p.m.: Δ 7,500. \diamond 15,000.
 \bullet 10,000. \times 17,500.
 \square 12,500. ∇ 20,000.

Mean air density at inlet to stator
 0.0706 lb. per cu. ft.

Fig. 3 Dependence of Flutter Stress on Stage Pressure Rise Coefficient (Carter & Kilpatrick, 1957)

SEPARATED FLOW MODELS

A number of attempts have been made to capture the essential features of unsteady stalled flow starting from free-streamline theory (Helmholtz or Kirchhoff Flow). In these two-dimensional incompressible models there are usually one or more parameters that are supposedly to be supplied by correlation with key experiments. Usually these parameters will relate to the movement (or non-movement) of the separation and reattachment points on the profile, or closure of the regions of separation. The implication is that in applying the theory to a new design situation the constants are to be supplied by the geometric and aerodynamic parameters of that design as they appear in the correlation.

A substantial number of single airfoil investigations and results are not discussed here because of the strong indication that cascading is the predominant controlling parameter in turbomachine stall flutter. A brief summary of the earliest cascade solution (Sisto, 1967) is given here in order to demonstrate the type of assumptions found to be necessary in order to produce a tractable model.

Considering incompressible flow about a two-dimensional cascade of flat plate airfoils, the minimal empiricism necessary relates to the shape of the separation streamlines and the (assumed constant) pressure within the separated region downstream of each airfoil formed by these streamlines. In turn, the simplest specification is that the separation streamlines emanate from the leading and trailing edges of each profile and that the pressure within the separated "wake", including the complete suction side of each airfoil, is equal to the upstream static pressure. Since the wake boundaries are assumed in the model to extend indefinitely far downstream, this wake configuration is tantamount to assuming a zero steady incidence and an infinitesimally thin wake. That the magnitude of the steady wake pressure may prove to be incorrect is of little direct concern since the unsteady lift and moment acting on the profiles is sought. Of greater concern are the assumptions of constancy of that pressure and of zero mean incidence.

With the previous set of simplifying assumptions the cascade appears as depicted in Figure 4a. The wakes are reduced to semi-infinite slits, the pressure surface of each foil coinciding with the lower edge of the local slit, and the suction surface of each foil lying within the slit but not touching it. With mean mainstream velocity and pressure U, P and perturbations u, v and p , the Euler equations reduce to the Laplace equation for the acceleration potential, or pressure function

$$\phi(x, y, t) = -p(x, y, t)/\rho$$

The boundary conditions are mixed, on the suction surface of each profile $\phi = 0$, whereas the upwash satisfies

$$v_n(x, y) = \partial Y_n / \partial t + U \partial Y_n / \partial x$$

on the pressure surface. The subscript n refers to the n th airfoil and Y_n is its displacement normal to its chord.

The method chosen for the solution makes use of the complex function $W = \phi + i\psi$ and a conformal transformation of the domain from $z = x + iy$ to $\zeta = \xi + i\eta$ such that the entire region exterior to the slits in the z -plane is mapped onto the upper half of the ζ -plane. Figure 4b shows that the images of the wake boundaries and the foil chords lie on the real axis in the ζ -plane in a periodic array with period 2π and with the leading edge of the zeroth foil at the origin.

The boundary and side conditions may now be listed.

- i) The pressure being zero in the wake requires

$$\phi = 0 \text{ for } \eta = 0,$$

$$2n\pi < \xi_c < (2n+2)\pi - \xi_c$$

where ξ_c is the absolute chord-length in the ζ -plane.

- ii) The upwash boundary condition stated in the z -plane is

$$v = \partial Y_n / \partial t + U \partial Y_n / \partial x \text{ for } y = ns \cos \beta \text{ and } ns \sin \beta < x < c + ns \sin \beta.$$

- iii) Replacing the perturbation pressure by ϕ in the Euler equation results in

$$\partial \phi / \partial y = (\partial / \partial t + U \partial / \partial x)^2 Y_n$$

on the same intervals as the second boundary condition.

- iv) The requirement that the pressure perturbations approach zero at great distances from the cascade,

$$\lim_{\eta \rightarrow \infty} W = 0,$$

- v) and the satisfaction of the Kutta condition

$$W(z) \text{ finite for } z = c + ins \exp(-i\beta)$$

completes the statement of the boundary and side conditions. Harmonic time dependence is assumed of the form

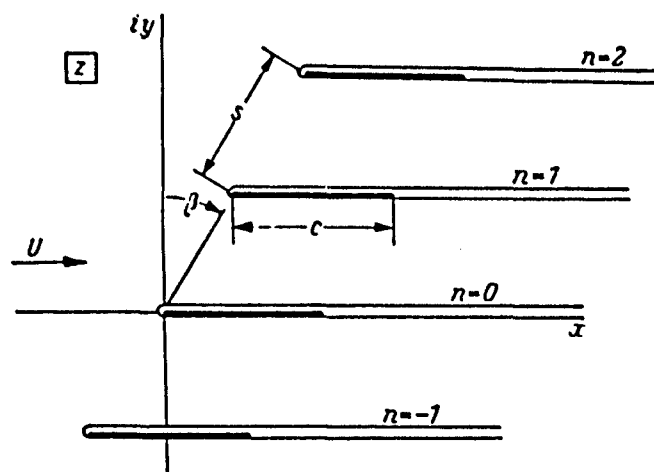


Fig. 4a Physical Plane

$$\phi(\xi, \eta, t) = \bar{\phi}(\xi, \eta) \exp(j\omega t), \text{ etc.}$$

where the barred quantity may be j -complex* to account for phase differences and ω is the common frequency of all blade motions. A further assumption of constant interblade phase angle, σ , between the motion of adjacent blades then takes the form

$$\phi(\xi, \eta, t) = \phi(\xi + 2n\pi, \eta, t + n\sigma/\omega)$$

$$Y_n(t) = Y_0(t) \exp(jn\sigma)$$

Subsequent modification to account for finite thickness of blade and wake provided good correlation with low speed stall flutter experience (private communication from DDA Division of G.M.).

This model was extended by Perumal (1976) to include a fixed point of separation on the suction surface, not necessarily at the leading edge. Yashima and Tanaka (1977) considered a thick, fully separated region of constant shape and obtained the unsteady pressures as a perturbation about the steady flow solution.

Chi (1980) reformulated the problem in terms of two simultaneous integral equations. By eliminating the need for a conformal transformation it was thus

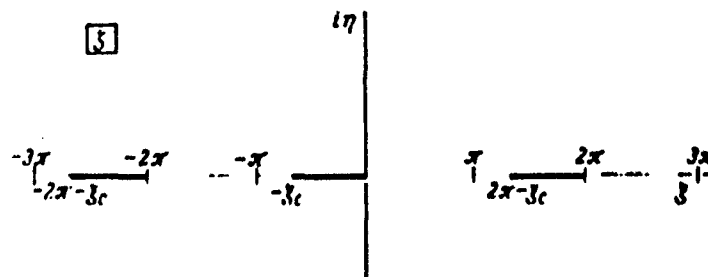


Fig. 4b Transformed Plane.

*The quantities $i = (-1)^{1/2}$ and $j = (-1)^{1/2}$ cannot be mixed; that is ij does not equal -1

possible to treat subsonic compressible flow. Reasonable predictive agreement was obtained with torsional stall flutter data from a high speed fan experiment. Were this work to be extended to include moving in-passage shock waves and time dependent separation, it would constitute the needed analysis for transonic stall flutter alluded to earlier in this chapter.

Attempts to treat moving separation points in cascades have so far not met with success. The single airfoil with suction surface open separation has been reported by Sisto and Perumal (1974) and the leading edge separation bubble with time dependent reattachment is reported in Tokel and Sisto (1978). Although the aerodynamic reactions resulting from these analyses display some validity with respect to experimental comparisons (see Dowell et. al., 1978), they were not extended to cascades of airfoils stemming largely from the difficulty of representing the separation (or reattachment) point movement with an arbitrary inter-blade phase angle. (This specific question is addressed in the closing sections of this chapter.) The criteria for periodic boundary layer separation, gross flow separation with local flow reversal and the formation of vortical structures cannot be satisfactorily predicted other than by addressing the full Navier-Stokes equations or otherwise recognizing the viscous nature of the flow near the profile surface.

Thus, the separated flow models described above are qualitatively interesting and give promise of being useful when the parameters describing separation are known a priori. However, reliable quantitative results cannot be expected without further research to establish the separated flow patterns with more realistic modelling.

RECENT TRENDS

MODERN APPROACH TO STALL FLUTTER

Stall flutter with entirely subsonic flow is now taken to mean that a radical lowering of the flutter speed with increasing incidence brings the critical speed within the realm of attainable values in the compressor. The strong implication is that time-dependent flow separation on the suction surface is present. Without regard to the location of the separation region(s) this fact of separation makes it necessary to recognize the role of fluid viscosity and consider the full Navier-Stokes equations to be governing. In their most general form these equations recognize unsteady time dependence. For sufficiently high Reynolds numbers the onset of turbulent flow, or transition thereto, is beset by the problem of choosing a turbulence model, or turbulent "closure", in order to be able to solve the Navier-Stokes equations. The flow in general is compressible.

These combined difficulties have led investigators to simplify the computational problem in several respects. By confining the effect of viscosity to the neighborhood of the fluid boundaries

(blade surfaces) the boundary layer equations may be applied there. The flow away from the solid surfaces may be considered inviscid and then the "inner" and "outer" flows are solved simultaneously with proper patching conditions (i.e., proper asymptotic behavior for the inner flow). Normally the unsteady boundary layer equation is solvable provided the time dependence of the outer flow is specified; i.e. pressure and velocity at the outer edge of the boundary layer.

This level of simplification has not proven to be sufficient to yield a tractable system of governing equations for cascades with appreciable unsteady flow separation. More recently so-called vortex methods are beginning to be used to model two-dimensional unsteady cascade flows with the effect of viscosity confined to the boundaries and to the diffusion of discrete vortices. As yet these methods have not been applied to the flutter situation where the boundaries are executing small harmonic displacements.

Lewis and Porthouse (1982) describe their vortex method as one of calculating the potential flow past the cascaded profiles under the influence of the mean flow and the previously shed and discretized vorticity distributed throughout the domain. This is followed by calculation of the drift velocity of each free vortex element in the field, and hence its displacement over a time increment t . New elements of free vorticity are shed (over the same time increment) from the separation points. Viscous diffusion calculations result in a random redistribution of all shed vortices and the entire sequence of computations is repeated for each subsequent time step. Stemming from the large computer storage requirements, the small number (3) of blade passages studied and the limited elapsed time, Lewis and Porthouse were not able to detect flow periodicity along the cascade, or propagating stall.

Spalart (1984), using a similar vortex method, couples it to an integral boundary layer solver to determine the instantaneous separation points, and with several other innovations is able to attain a condition of propagation of the stall zones in an infinite two-dimensional linear cascade with periodicity enforced over each subset of either 3, 4 or 5 blades. The solution displays moving separation points with a definite interblade phase angle. Thus the velocity of propagation is predicted.

In executing these vortex methods steps have to be taken to limit the number of discrete vortex "blobs" that can be tracked on the finite computational domain, although periodic extension to produce an infinite two-dimensional cascade does not pose a strong limitation since the induction functions are well known. The discretization scheme is important in limiting this total number of free vortices, as is the consolidation of multiple elements into fewer elements downstream of the cascade. Other details and cautions may be found in the

references. However, the indications are that the method is viable for predicting periodically stalled flow about cascades subject, naturally, to some limitations. A time sequence of instantaneous streamlines in rotating stall is reproduced from Spalart (1984) as Figure 5. The stall cell definition and propagation are dramatically portrayed.

Propagation rates for an imposed wavelength along the cascade can be computed, as well as the critical incidence at which the instability appears. Time dependent components of the aerodynamic moment and normal force can be calculated. By considering multiple wavelengths in successive calculations a stability criterion could be developed relating both propagation rate and wavelength of the stall zones (and hence frequency of encounter) to cascade geometry and incidence.

One limitation is related to accuracy. Since the smallest turbulence scales cannot be modelled and other approximations must be introduced to make the method computationally practical, the precision of the results

is less than desired for application to design. Other limitations are related to assumed flow incompressibility and two-dimensionality; propagating stall in multi-stage machines is known to exhibit strong radial components of velocity.

However, the most important limitation from the vantage point of the aeroelastician is the complete fixity of the airfoils comprising the boundary. In the vortex methods reported, no provision has been made to allow, or prescribe, vibratory displacements. Although the present vortex methods will have some validity for predicting non-resonant (low amplitude) vibration due to propagating stall, they will fail to account for the aeroelastic coupling between blade structure and blade aerodynamics. This coupling is critical for near-resonant forcing and becomes crucial for predicting stall flutter.

In the near term attention should be devoted to refining the vortex method for linear cascades to increase its speed, efficiency and accuracy. Additional model features should be considered that have proven useful in potential,

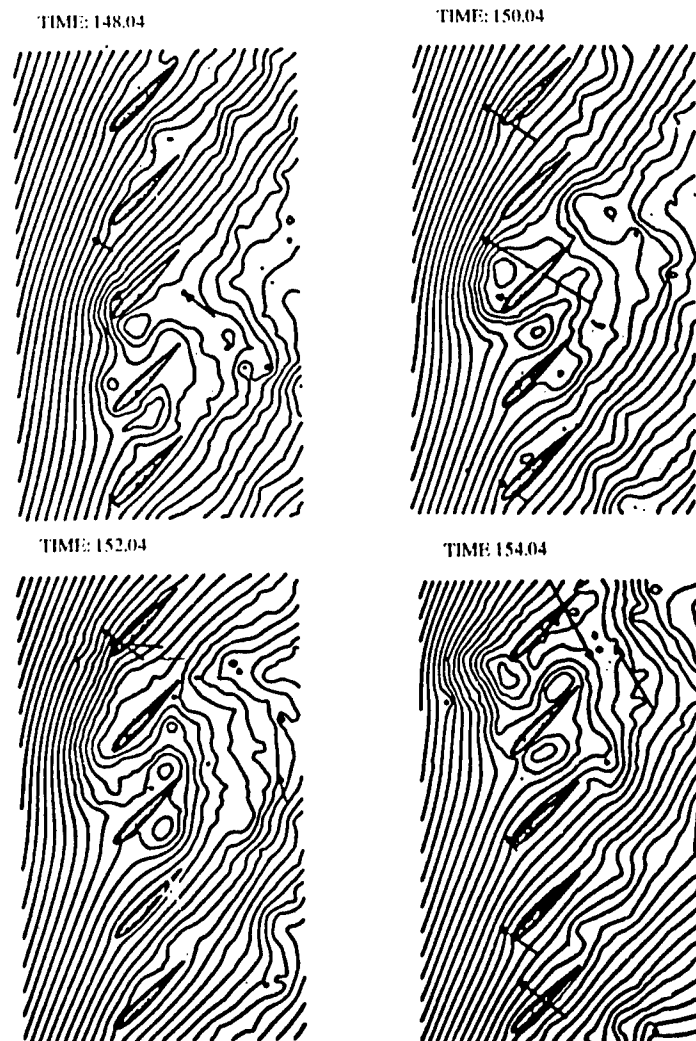


Fig. 5 Streamline Patterns at Four Successive Instants of Time, Showing Stall Propagation, Computed by the Vortex Method (Spalart, 1984)

attached flow. (An example is the use of summed aerodynamic modes to represent a continuous distribution of bound vorticity.) Following this step it is necessary to allow for small harmonic motion of the airfoils in plunge, surge and pitch. How such a computational algorithm could be incorporated into a stall flutter prediction system is speculative. Several possibilities come to mind but these are best left to future research.

CONCLUDING REMARKS

This exposition of stall flutter, and the closely related phenomena of choke flutter and supersonic bending stall flutter, has been largely qualitative of necessity. No purely

analytical method of description leading to completely reliable prediction has evolved between 1945 and 1985. Some semiempirical methods have achieved limited success in isolated instances and the purely experimental methods of prediction (actually verification) are too expensive and therefore considered unsatisfactory. The effective modus operandi has been to use experimental correlations as design criteria followed by a development phase in which perceived deficiencies are corrected.

In the future, with the development of the vortex method and its logical extensions, the engineering aeroelastician charged with stall flutter avoidance may conceivably be more analytical and therefore more cost effective.

UNSTEADY AERODYNAMIC MEASUREMENTS IN FLUTTER RESEARCH

by

Sanford Fleeter
Thermal Sciences and Propulsion Center
School of Mechanical Engineering
Purdue University
West Lafayette, Indiana 47907
USA

Robert L. Jay
Allison Gas Turbines
Division of General Motors
Indianapolis, Indiana 46224
USA

INTRODUCTION

Under certain conditions, a blade row operating in a uniform flow field can enter into a self-excited oscillation known as flutter. The blade motion is sustained by the extraction of energy from the uniform flow during each vibratory cycle, with the flutter frequency corresponding generally to one of the lower blade or coupled blade-disk natural frequencies.

The outstanding feature of flutter is that high stresses exist in the blading, leading to short term, high-cycle fatigue failure. Because flutter is encountered over a relatively wide range of operating conditions, i.e., a flutter boundary, it is a problem which must be solved before continuing in the engine development. The solution often involves rotor blade modifications which decrease engine performance. Hence, the design of flutter free blading in the development of a gas turbine engine is a very significant problem.

Compressor blade failure due to flutter has been recognized as a major problem almost from the beginning of the development of the axial flow compressor. Failures of turbine blading, on the other hand, have generally been associated with aerodynamically induced forced vibrations, although limited cases of flutter in high aspect ratio aft stage blading of power turbines have occurred. However, with the aerodynamic performance design trend toward higher flow velocities, the reduced frequency of turbine blading is approaching that of compressor blades. Also, at these higher velocities, shocks are present in the turbine blade passages. As a result, the flutter of turbine blades, including shock-induced flutter, may become increasingly important.

Until very recently, it was not feasible to develop mathematical models to predict the unsteady aerodynamics appropriate for the various flutter flow regimes. This necessitated the development of empirical design systems for flutter prediction. The limited flutter data available upon which to base these empirical systems were acquired during exploratory component testing directed at measuring aerodynamic performance. As a result, these flutter data tend to be haphazard and somewhat random in nature. If flutter was encountered, the aerodynamic and flutter characteristics, including the incidence angle, were determined. Flutter boundaries were then established for each flow regime by correlating the reduced frequency at a specific blade spanwise location with the

relative Mach number or the incidence angle, for example.

Advances in technology have required the designer to predict the flutter free operating range of new rotor configurations for conditions beyond the experience levels inherent in available design systems. As a result, flutter is often encountered during initial rotor development testing.

To provide the designer with a valid flutter predictive design system, two approaches are being pursued. One approach involves the development of advanced empirical or semi-empirical design systems, accomplished by means of a systematically obtained extensive flutter boundary data bank. The second approach, made possible through the recent advances in capabilities for computational fluid dynamics, involves replacing the empiricism of current design systems with unsteady aerodynamic mathematical models developed from first principles. This requires the acquisition and analysis of unsteady aerodynamic data appropriate for directing the development of these models as well as for determining their validity prior to being implemented in the design system.

EXPERIMENTAL OBJECTIVES

There are a number of different overall objectives which must be considered in defining a flutter experiment. These include: the acquisition and analysis of data to validate and/or to direct the development of advanced models; the generation of a flutter boundary data bank; and the investigation of new concepts to affect the flutter characteristics of a rotor.

Analysis Validation and Direction

The development of an analytically based design system is directly dependent on the availability of models which accurately predict the unsteady aerodynamics in the various flutter regimes. Thus, detailed data are necessary to experimentally determine the range of validity of existing unsteady flow analyses and to direct the development of advanced models. These data must be obtained from experiments which model the fundamental phenomena inherent in turbomachinery flutter. Thus, the parameters which must be modeled characterize both the steady and the unsteady flow fields.

A description of the steady state aerodynamics of a typical inlet stage compressor, mid-stage compressor, and inlet stage turbine are described in the next chapter "Unsteady Aerodynamic Mea-

measurements in Forced Vibration Research." The steady aerodynamic data of interest are the inlet flow field and the detailed blade row characteristics including the surface static pressure distributions and regions of flow separation. These data are acquired with standard steady state instrumentation.

The unsteady data quantify: the harmonic surface pressure distributions and its phase relation to the motion of the blading; the unsteady aerodynamic lift, moment, or aerodynamic damping; and the unsteady characteristics of the separated flow regions. Dynamic instrumentation used to acquire these data include strain gages, light probes, hot-film gages, and miniature high response pressure transducers.

Flutter Boundary Data Bank

The development of an advanced empirical or semi-empirical design system requires an extensive and systematically obtained flutter boundary data bank, with operating conditions and geometries extended well beyond current experience levels. The parameters which must be considered in the data bank include the flutter mode, the reduced frequency, the blade incidence angle or loading, the inlet Mach number, the blade and cascade geometry, the surge and choke margins, the air density ratio, and the temperature.

The primary data of interest quantify the effect of these parameters on the flutter boundary characteristics including: the aerodynamic operating conditions at the flutter boundary, the flutter frequency, and the interblade phase angle. These data are acquired by means of standard instrumentation, including blade mounted strain gages.

Concept Investigations

New or advanced concepts for flutter stability enhancement must be experimentally verified before they can be utilized in an engine design. Depending on the particular concept, the necessary experiments may involve the measurement of the flutter boundary and/or validation of mathematical models.

EXPERIMENTAL FACILITIES AND TECHNIQUES

The overall objectives of the flutter research experiment specify the appropriate facility. Linear cascades, stationary annular cascades, and high speed rotating rigs have been widely utilized. Low speed rotating rigs, although used for forced vibration research, are not used for flutter experiments because they offer no significant advantages over linear cascades. The particular experiment objectives specify the required data and, thus, the necessary instrumentation and experimental techniques.

Flutter Boundary Data

High Speed Rotating Rigs

Full scale, high speed rotating rigs instrumented to establish both the basic

aerodynamic and mechanical conditions, as well as the corresponding flutter boundaries, provide the ultimate in flutter boundary data as well as the final test of advanced concepts. However, such full-scale data are very costly, particularly in a quantity sufficient to provide a minimum data bank. Hence, it is necessary to consider other than full-scale test vehicles.

One alternate test vehicle is a high speed scale model rotor. Certainly, the scale model rotor flutter boundaries are appropriate for use in a flutter data bank if the flutter boundaries correspond to those of the full size rotor. This requires the scaling of the parameters of significance to rotor flutter, including the reduced frequency and the steady aerodynamic performance.

To scale a full size rotor and maintain Mach number similarity, the blading must be geometrically consistent with regard to blade profile, blade angles, solidity, and spanwise thickness-to-chord ratios. If the model and the prototype operate under identical inlet conditions in the same working fluid, then the relationships presented in Table 1 are maintained. As indicated, maintaining Mach number similarity results in a lower Reynolds number for the model. However, as long as the Reynolds number is on the order of 200,000 or greater, no significant losses result. Also, the aeroelastic characteristics of the full size and model blading should be identical as the reduced frequency is unaltered by the scaling.

| Parameter | Full-Size Prototype | Scale Model |
|---------------------|-----------------------------------|-----------------------------------|
| Corrected Mass Flow | W_c | W_c/R^2 |
| Rotor Speed | N | $N \cdot R$ |
| Blade Chord | C | C/R |
| Blade Thickness | T | T/R |
| Blade Span | S | S/R |
| Blade Frequency | F | $F \cdot R$ |
| Mach Number | M | M |
| Relative Velocity | V | V |
| Reduced Frequency | $2 \cdot \pi \cdot C \cdot F / V$ | $2 \cdot \pi \cdot C \cdot F / V$ |
| Reynolds Number | Re | Re/R |

where R is the scale factor, defined as the ratio of the full-size to model rotor tip diameters.

Table 1. Rotating Blade Row Scaling Parameters

The scaling of rotor flutter was experimentally considered by Jay (1975). The objective of these experiments was to determine if a substantially reduced diameter fan (1/5 scale with an 8 in. (20.32 cm) diameter model) would exhibit the same aeroelastic characteristics as the prototype full size fan.

This model fan flutter program demonstrated that excellent correlation between the model and the prototype fan could be obtained with regard to blade natural frequency, fatigue strength, blade frequency variation with rotor speed, static stress field, blade untwist, and aerodynamic performance. The possibility of using such a model for parametrically defining stall flutter boundaries and creating a stall flutter data bank was also indicated. Both the model and the prototype exhibited qualitatively similar first torsion mode stall flutter in the part speed, high loading region of the compressor map, with this model and prototype flutter characterized in terms of reduced frequency and tip Mach number in Figure 1. However, the high amplitude, constant phase torsional stress typical of the supersonic flutter found in the prototype fan was not found in the model fan.

Linear Cascades

For reasons of cost and geometric flexibility, the use of a stationary cascade to parametrically investigate flutter boundaries for a flutter data bank is highly attractive. However, the relation between the flutter boundary determined from a stationary cascade and that for the corresponding rotor must be considered.

The simplest and most convenient cascade experiment to obtain qualitative rotor flutter boundary data involves the free flutter testing of a two dimensional

linear airfoil cascade, with the airfoils modeling the tip section of the rotor blading. The reduced frequency at flutter can be maintained in the cascade. However, because free flutter testing has no provision for maintaining a constant interblade phase angle, the cascade and the corresponding rotor will likely have different interblade phasing.

The free flutter testing of a linear cascade of five airfoils to determine the supersonic unstalled flutter boundaries of a rotor was experimentally investigated by Snyder and Commerford (1974). The data demonstrated non-uniform airfoil phasing as well as a large factor difference, on the order of 2.5, between the fan and the cascade data. This relatively poor correlation is attributable to the nature of free flutter testing in a finite cascade. In particular, the first airfoil is near to an isolated airfoil and, therefore, more stable than an airfoil in an infinite cascade. As a result, this first airfoil does not set up the correct unsteady upstream flow field to the next airfoil in the cascade. As this finite cascade effect progressively decreases through the cascade, it might be overcome by utilizing large numbers of airfoils. However, this is not typically practical in a linear cascade.

Stationary Annular Cascades

A stationary annular cascade eliminates many of the problems associated with using a finite linear cascade to represent a rotor experiencing flutter. The annular cascade not only eliminates the free flutter interblade phasing and the finite cascade considerations, but also offers reduced cost and increased flexibility as compared to a rotor. Thus, it can be used to provide a data bank for the development of engine flutter design criteria.

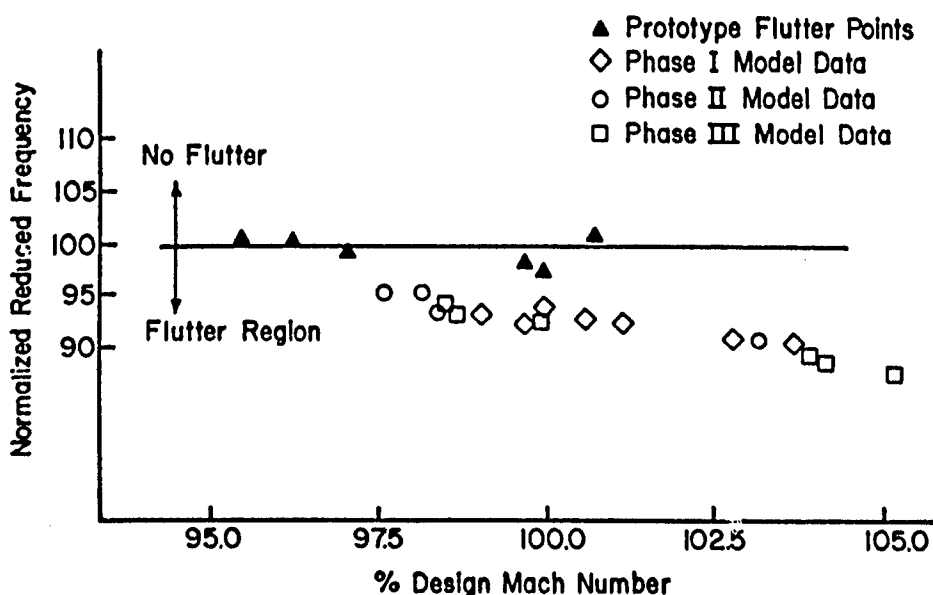


Fig. 1. Operation of Model and Prototype Fans (Jay 1975)

The simulation of rotor flutter with a stationary annular cascade has been addressed by Ellis, Rakowski, and Bankhead (1978) and Jutras, Stallone, and Bankhead (1980). This flutter annular cascade was conceived on the basis of two-dimensional data referenced to the 87.5% span. The cascade aerodynamics and, therefore, the compatible airfoil design, are not truly two dimensional due to the axisymmetric flow field. The primary aerodynamic parameters are controlled to be constant over the outer airfoil half span. These include the cascade loading, the thickness-to-chord ratio, the airfoil camber and solidity, the throat margins and the incidence angle. The airfoil stagger is varied along the airfoil span to provide the desired incidence angle, with the radial variation of the Mach number a result of the facility aerodynamics. To allow precise tuning of airfoil natural frequency while maintaining compatibility with the facility flow field, variations are present in the modeling of the inner half-span of the airfoils, primarily the thickness, chord, and camber.

This annular cascade exhibited a wide range of instabilities, including choke and stall flutter. Excellent correlation was obtained between the annular cascade flutter and that of the modeled rotor, as demonstrated in Figure 2 in terms of Mach number and incidence angle.

Aerodynamic Damping Data

A limitation of flutter boundary testing is that no unsteady data is obtained until flutter is encountered. If the blade row is stable over the test operating conditions, no information about the location of the flutter boundary is obtained.

A method for the direct measurement of aerodynamic damping in stable regions of the rotor performance map was demonstrated using a transonic rotor instrumented with strain gages, Crawley (1982). In this method, an upstream disturbance is created by the interaction of the primary flow with a series of small jets injected normal to the surface of inlet struts. After the sharp termination of this disturbance, the subsequent free vibration ring down of the rotor is a measure of the aerodynamic plus structural damping. Analysis of the strain gage data in terms of multi-blade modes led to a direct measurement of aerodynamic damping for three interblade phase angles, all of which indicated high levels of aerodynamic damping.

Analysis Validation and Direction

In the development of an analytically based design system, it is necessary to experimentally verify the unsteady aerodynamic models. The fundamental dependent variable is the airfoil surface unsteady pressure distributions. Ideally, this experimental verification process is accomplished by correlating predicted complex surface unsteady pressure distributions with analogous data acquired on a rotor blade during flutter. Such rotor flutter unsteady pressure data are difficult and costly to acquire because of the accuracy required for model verification and refinement, and the number of operating conditions, geometrical configurations, and mode shapes of vibration, which must be investigated.

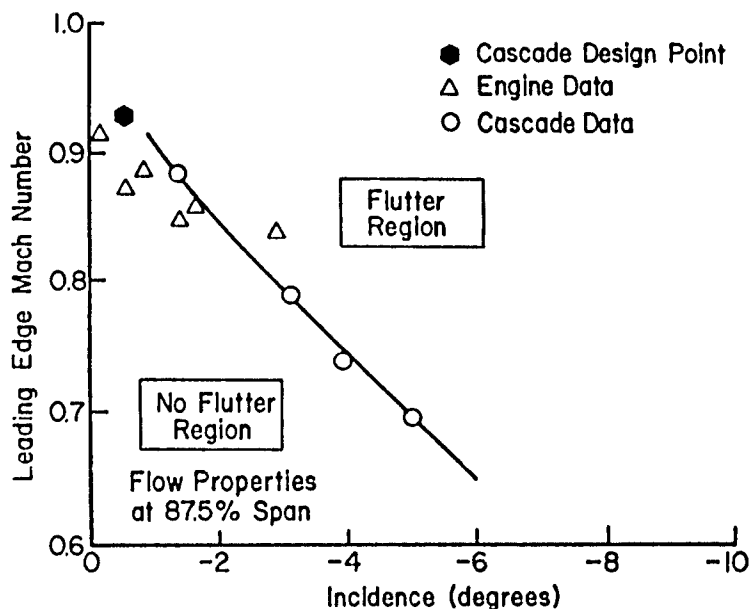


Fig. 2. Comparison of Midstage Verification Annular Cascade Instability Results with Engine Data (Jutras, Stallone, and Bankhead, 1980)

Linear Cascades

Two dimensional controlled oscillating cascade experiments are the most widely used and accurate means for establishing the validity and directing refinements of unsteady aerodynamic flutter models. Cascade experiments provide increased flexibility as compared to rotor investigations in terms of variations in aerodynamic and flow conditions as well as experimental objectives. This increased flexibility introduces complexities in that the oscillating cascade must simulate the significant rotor flutter phenomena.

The simulation of rotor flutter with a finite two dimensional cascade must be carefully considered. In addition to the usual concerns associated with steady cascade testing, there are several additional considerations for unsteady cascade flows. Some airfoils in the cascade may be either more or less stable than others. With a supersonic inlet flow to an airfoil cascade with a large stagger angle, for example, the bow wave from the second airfoil in the cascade will not intersect the first airfoil, Figure 3. Hence, the first airfoil acts as an isolated airfoil. For Mach numbers greater than 1.58, this "isolated" cascaded airfoil is stable at all frequencies of oscillation. Thus, in this case, it is unlikely that the finite cascade corresponds to a section of an infinite cascade where there is no first blade and the aerodynamics and motion of each blade are identical. The airfoil cascade must be a valid representation of the phenomena existing in the rotor blade row, with the unsteady data obtained at the high reduced frequency values corresponding to flutter of the rotor. Ranges of reduced frequency values of significance to rotor flutter are indicated in Table 2. It should be noted that data obtained at lower reduced frequencies and Mach numbers, for example, are still of great value in the assessment of modeling assumptions and predictions.

| Type of Flutter | Reduced Frequency ($k = 2\pi f/V$) |
|---------------------------------------|---|
| Unstalled Supersonic Torsion | 0.7 to 1.3 |
| Supersonic Bending | 0.2 to 0.5 |
| Subsonic/Transonic Torsional Stall | 0.4 to 1.6 |
| Choke Bending | 0.3 to 0.5 |

Table 2. Typical Flutter Reduced Frequency Ranges

Flutter of rotor blades is modeled, both analytically and experimentally, by considering harmonic cascade airfoil oscillations with a constant interblade phase angle. Two experimental approaches are utilized to achieve these controlled airfoil cascade oscillations.

One approach directly simulates the flutter aerodynamic modeling by harmonically oscillating all of the airfoils in the cascade with a constant interblade phase angle. An oscillating centrally located airfoil in the cascade is instrumented to measure the unsteady airfoil surface pressure distributions, the unsteady lift or moment, or the aerodynamic damping. Airfoil cascade driving mechanisms include bar linkage systems, Carta and St. Hilaire (1976), cam arrangements, Boldman and Buggele (1978), and computer controlled electromagnets, Fleeter, et al (1975). The latter drive system is further considered in the next chapter "Unsteady Aerodynamic Measurements in Forced Vibration Research."

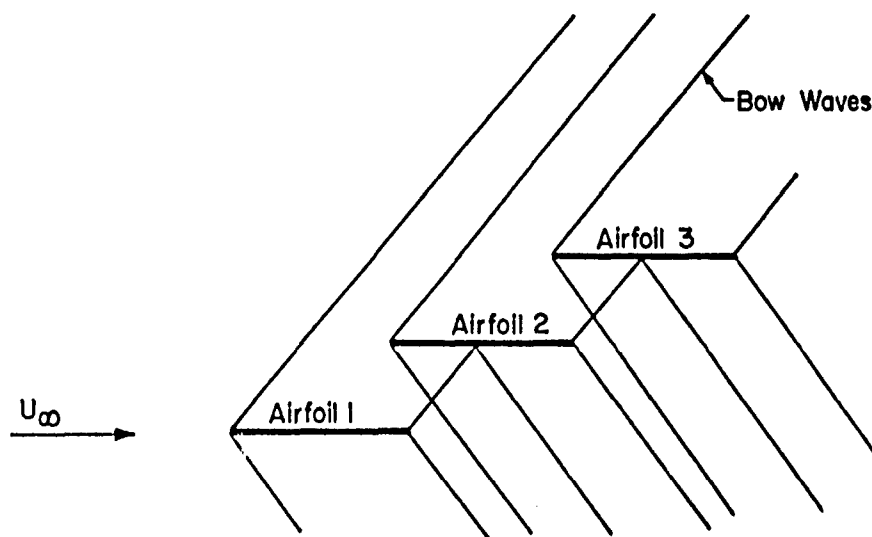


Fig. 3. Supersonic Flow Field Schematic for Large Stagger Angle Cascade

The second approach is based on measuring the airfoil unsteady forces and moments, and the surface unsteady pressure distributions using an influence coefficient technique, Hanamura, Tanaka, and Yamaguchi (1980), and Ewins and Hillary, (1980). This requires the oscillation of only one airfoil in the cascade, i.e., only the center airfoil in the cascade is oscillated with the other airfoils fixed. The unsteady influence coefficients are then determined by measuring the resulting unsteady forces or surface pressure distributions on all of the airfoils in the cascade. The unsteady forces or pressure distributions for any specified interblade phase angle are then determined from these influence coefficients by means of vector addition. Thus, such unsteady data are equivalent to the case where all of the airfoils in the cascade are oscillating with an arbitrary interblade phase angle.

Another consideration is the unsteady cascade periodicity. For example, in a steady cascade flow with a subsonic axial Mach number, the inlet flow conditions to any airfoil passage are determined by the stationary position and profiles of the preceding airfoils relative to the undisturbed flow ahead of the first airfoil, Figure 4. Under this condition, the periodicity in the flow field of succeeding airfoil passages is achieved after a relatively few airfoils. In an unsteady flow, however, the inlet conditions to any airfoil passage depend on both the position and the motion of the preceding airfoils. Analytical results indicate that the number of airfoils required to achieve a periodic unsteady flow field is a function of frequency, even if the motion of the airfoils is uniform with a constant interblade phase angle.

Unsteady cascade periodicity in a subsonic flow field has been addressed, Carta (1982). These experiments involved measuring the unsteady pressure along the leading edge plane of a linear cascade of eleven airfoils oscillating in torsion. Unsteady cascade periodicity was achieved over the range of parameters considered, as indicated in Figure 5.

The objective of the two dimensional cascade experiment must also be considered. For example, if the cascade experiment is intended to provide data solely to validate analyses and quantify significant unsteady flow features not analytically modeled, then the cascade geometry, flow conditions, and reduced frequency do not have to correspond to those of an actual rotor, although it may be desirable. It is only necessary for the cascade experiment to simulate the assumptions inherent in the model and for the reduced frequency to be high enough so that unsteady data, not quasi-steady data, are obtained.

Two dimensional linear cascade experiments can also be used to determine the stability of a rotor. As previously noted, the finiteness of the linear cascade precludes free flutter testing as a means of measuring a rotor flutter boundary. However, if the unsteady aerodynamic work or damping is measured, not the flutter boundary, then the finiteness problem can be overcome and the modeled rotor stability determined. In this case, the two dimensional cascade experiment must model the significant unsteady and steady features of the rotor.

The unsteady features of the rotor can be modeled using a driven oscillating airfoil cascade, appropriate instrumentation, and data acquired over a range of interblade phase angles. Either every airfoil in the cascade can be harmonically oscillated with the interblade phase angle controlled by means of the driving mechanism, or influence coefficients can be measured using a single oscillating centrally located airfoil, with the interblade phasing accomplished analytically.

In addition to simulating the unsteady aerodynamics of the rotor during flutter, it is also necessary that the experiment closely model the rotor operating conditions at the flutter boundary, with the cascade design based on a representative rotor blade section. However, due to the radius change and area convergence of the rotor, it is not possible to maintain the inlet and exit Mach numbers and flow angles in the corresponding two-dimensional cascade.

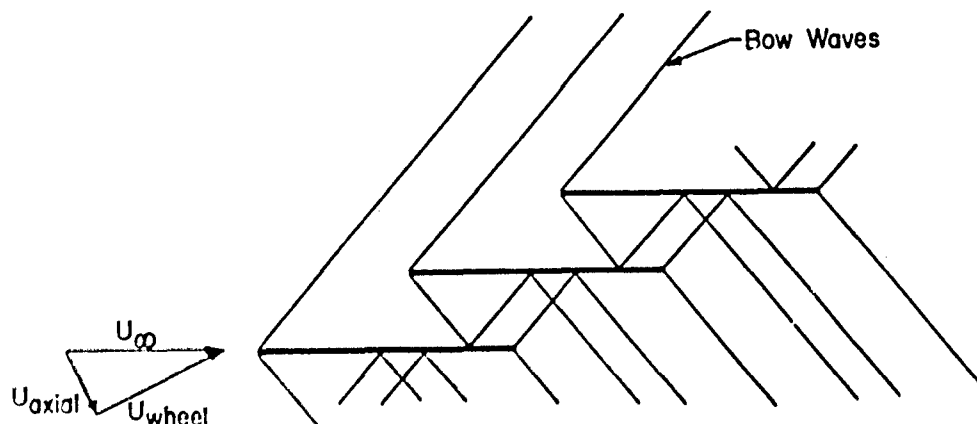


Fig. 4. Cascade Supersonic Inlet Flow with Subsonic Axial Component Schematic

A viable two dimensional cascade representation can be achieved by preserving the critical elements of the rotor section flow field. For supersonic inlet rotor blade sections, the flow field is critically affected by the shock system, and to a much lesser degree by the specific blade geometry. To preserve the shock system, the two dimensional cascade must maintain the corresponding rotor element values of the following parameters: the inlet and exit Mach numbers; the starting margin (A/A^*); and the rotor critical incidence angle, defined as the angle between the upstream air angle and the blade suction surface angle at a point midway between the leading edge and the intersection of the first covered characteristic and the suction surface. The stagger angle, starting margin, deviation criteria and parameters such as the thickness-to-chord distribution, maximum thickness, solidity, and leading edge radius-to-chord ratio are also maintained. This results in a cascade that is representative of the modeled rotor blade section in terms

of Mach number, shock system, and loading distributions, even though the cascade is not a geometrical scale of the rotor section, Riffel and Fleeter (1981).

Instrumentation

Strain gages are the primary sensor to indicate the onset of flutter, as well as the amplitude, frequency, and interblade phase angle of the blade vibration. The strain gage waveform is the result of the response of the airfoil to the instantaneous flow field. Thus, it is indicative of the physical mechanism of the flutter. Also, strain gages can be used to measure the unsteady aerodynamic lift, moment, and damping. However, limitations in the application of strain gages currently exist. In general, strain gage data give no measure of stability prior to the onset of flutter. However, techniques to accomplish this are being developed, Loiseau, Nicolas, and Maquennehan (1980). Also, they cannot measure blade load distributions, although efforts to accomplish this are continuing, Ewins (1980).

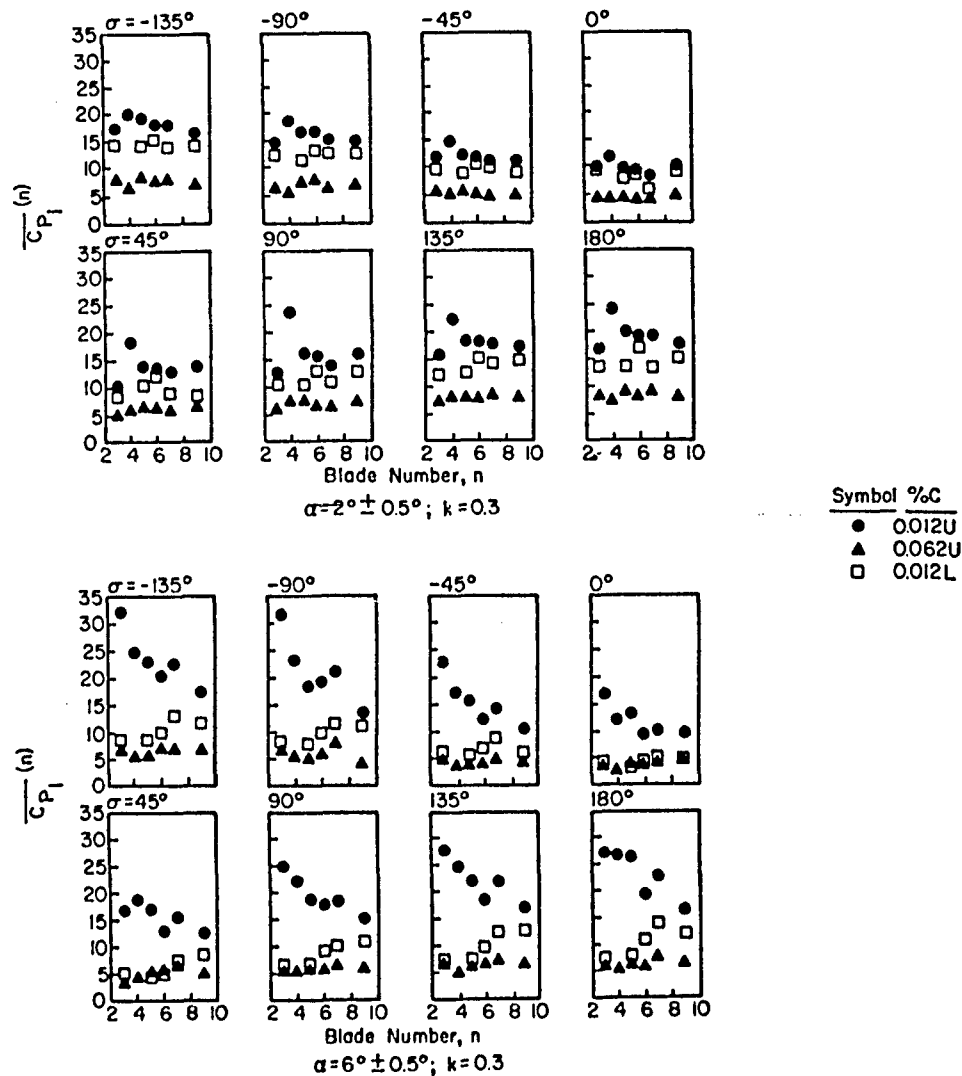


Fig. 5. Airfoil Gapwise Pressure Amplitude for Various Leading Edge Region Chordwise Positions, $\alpha = 2^\circ \pm 0.5^\circ$, $k = 0.3$ (Carta, 1982)

Light probe systems have proven to be invaluable as a supplement to the strain gage in measuring the passage and non-synchronous vibration of every blade in a rotor. This is of particular value in detecting instabilities where there is a high degree of circumferential response variability. A constant spatial interval yields a constant output reflection, but flutter, which involves variable spatial intervals, yields a variable output reflection. Casing mounted light probes are used to measure airfoil tip static and dynamic displacements and have also been used to resolve flutter into its principal bending and torsional contributions, Kurkov and Dicus (1983), Nieberding and Pollack (1977), and Roth (1980). Another optical method to resolve flutter involves the placement of mirrors over several points on a blade surface and illuminating these points with a short duration pulse of laser light once per revolution, Stargardter (1977).

Miniature high response pressure transducers with a flat frequency response in excess of 10 KHz are used to measure unsteady surface pressure distributions. Typically these transducers are embedded in an airfoil, requiring the airfoil surface to be machined. The electromechanical configuration of the pressure transducer is similar to the basic strain gage in that the sensing element consists of a four-arm Wheatstone bridge bonded to a thin flexible diaphragm, Armentrout and Kicks (1979). An extensive calibration is required to account for the effects of centrifugal force on the sensitivity and zero offset of the transducer as well as for the effects of mounting induced strain, Minkin (1976) and Grant and Lanati (1978).

High response hot wires and films are used to measure instantaneous flow velocities, with hot films being more durable but having a decreased frequency response. Films attached directly to a surface measure skin friction, thereby determining the nature of the surface flow. Specifically, the hot film can be used to identify laminar, turbulent, or separated flow, as well as the transition from one flow regime to another.

A more detailed description of hot wires and films, as well as a discussion of the dynamic calibration of pressure transducers is presented in the next chapter "Unsteady Aerodynamic Measurements in Forced Vibration Research."

Data Analysis Techniques

Unsteady flow experiments, including flutter investigations, generate large quantities of data which require high frequency transmission and recording. These data involve a wide band of frequencies, with the amplitude and phase relations between frequency components of importance. Hence, high speed, digital data processing is essential.

Gostelow (1977) described several techniques for the analysis of unsteady turbomachinery data, including the use of signal averaging and fast Fourier Trans-

form (FFT) based computer techniques. Carta and St. Hilaire (1977), Fleeter, Jay, and Bennett (1981), and Capece and Fleeter (1984) utilized similar techniques for unsteady cascade data analysis. Detailed examples of unsteady data acquisition and analysis techniques are presented in the next chapter "Unsteady Aerodynamic Measurements in Forced Vibration Research."

EXPERIMENTAL RESULTS

Positive Incidence Stall Flutter

At subsonic relative Mach numbers, positive incidence stall flutter may occur. It is generally attributed to blade stall and surface flow separation, caused by operating beyond some critical airfoil incidence angle. However, in some instances, it has been reported that the stall flutter boundary has been found near maximum compressor efficiency. This indicates that stalling may not be essential for stall flutter, although it could be the most severe condition.

Bending, torsion, and coupled modes of vibration have been noted when this type of flutter is encountered at part-speed in a high-speed fan, and at or near the design speed in a low or high pressure compressor. In an unshrouded rotor, it is generally unphased at low amplitudes, with the possibility of a constant interblade phase angle at the large amplitudes of vibration which occur deeper into the flutter region. With a shrouded rotor, interblade phasing is enforced by the part-span mechanical ties.

A comprehensive series of experiments directed at investigating the subsonic unsteady aerodynamics of an oscillating airfoil cascade subjected to aerodynamic loading has been performed by Carta and St. Hilaire (1977, 1979). A linear cascade of 11 NACA 65 series airfoils was coherently driven by means of a mechanical linkage system in a sinusoidal torsional motion with an amplitude of 2°. The center airfoil of the cascade was instrumented with miniature high response pressure transducers and hot film gages. The unsteady surface pressure distributions were measured for mean incidence angles to 10°, reduced frequencies to 0.386, and interblade phase angles from -60° to +60°, and analyzed to determine the stability parameters. These include the complex unsteady torsional moment coefficient and the aerodynamic damping.

Aerodynamic loading was found to be significant, with the interblade phase angle the principal parameter affecting stability, Figure 6. Specifically, at the low loading conditions, the reduced frequency had only a small effect on the unsteady aerodynamic moment and damping. However, at high levels of loading, but with no indications of airfoil stall apparent from the steady airfoil surface static pressure data, large reduced frequency effects were evident.

The cascade was unstable over the entire range of loading and reduced frequency values for interblade phase

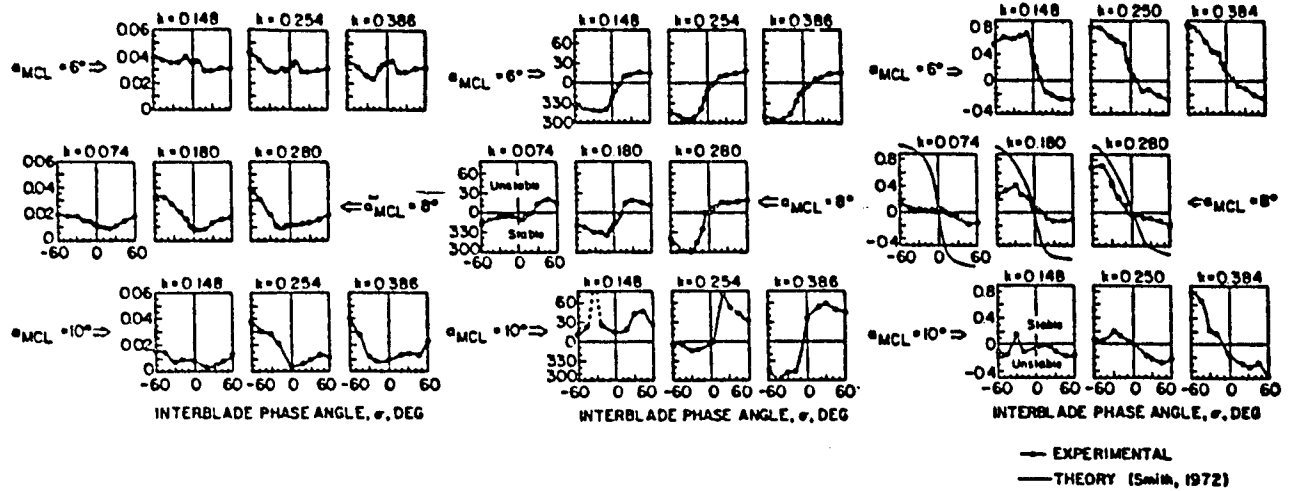


Fig. 6. Variation of First Harmonic Moment and Aerodynamic Damping with Reduced Frequency (Carta and St. Hilaire, 1979)

angles greater than 10° . This result is similar in behavior, but not in magnitude, to predictions from potential flow cascade models and lends support to the previous observation that airfoil stall need not be present for stall flutter. For negative interblade phase angles, cascade stability was more dependent on loading and reduced frequency, conforming more closely with conventional stall flutter behavior. In particular, for interblade phase angles less than 10° , stability increased with frequency and decreased with loading.

The effect of interblade phase angle on the pressure time histories in the leading edge region of the airfoils is shown in Figure 7. As the interblade phase angle increases, the second harmonic of the leading edge pressure response exhibits an increasing dominance. This second harmonic has the characteristics of the loss in suction peak associated with dynamic stall, with the minimum at peak incidence. A com-

parison of Figures 6 and 7 reveals that the onset of instability closely coincides with the second harmonic becoming dominant over the first harmonic for interblade phase angles greater than 5° . Also, there is a phase shift from lead to lag with decreasing interblade phase angle values in the 6.2% chord data, with the cascade instability a direct consequence of this phase shift. Thus, cascade stability is seen to be related to the unsteady aerodynamics in the leading edge region of the airfoil.

The effect of the torsional elastic axis on the unsteady moment of oscillating isolated and cascaded airfoils at high incidence angles with leading edge separation was investigated in a water tunnel by Tanaka, Shinohara, and Hanamura (1976) and Yashima and Tanaka (1977), respectively. A crank mechanism was used to drive the airfoils, with the unsteady forces measured by means of strain gages. They found the critical reduced frequency to be larger for the stalled case than the unstalled one, with the critical re-

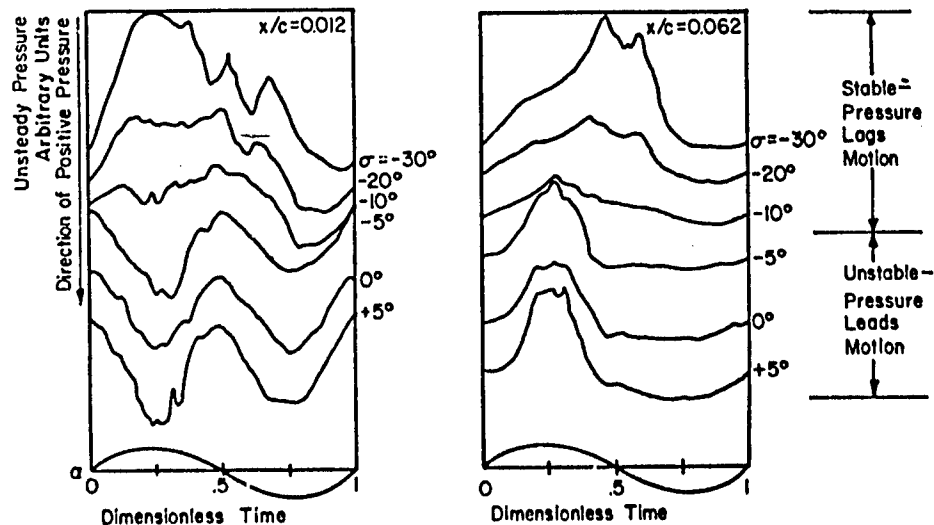


Fig. 7. Time-Averaged Pressure Wave Forms from Airfoil Suction Surface for Several Interblade Phase Angles (Carta and St. Hilaire, 1979)

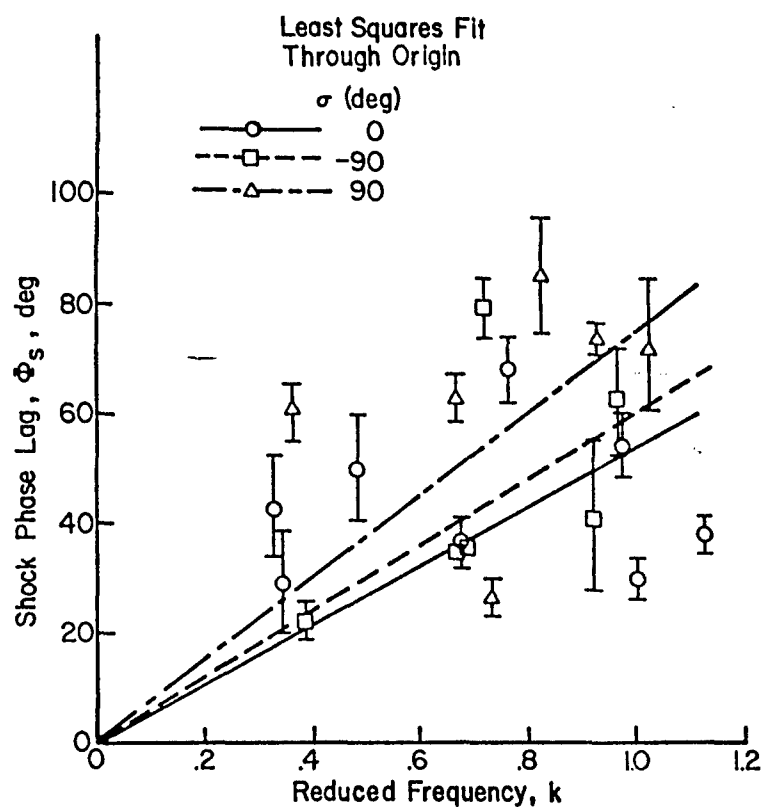


Fig. 9. Shock Phase Lag at Mach = 0.8
(Boldman, Buggele, and Michalson, 1981)

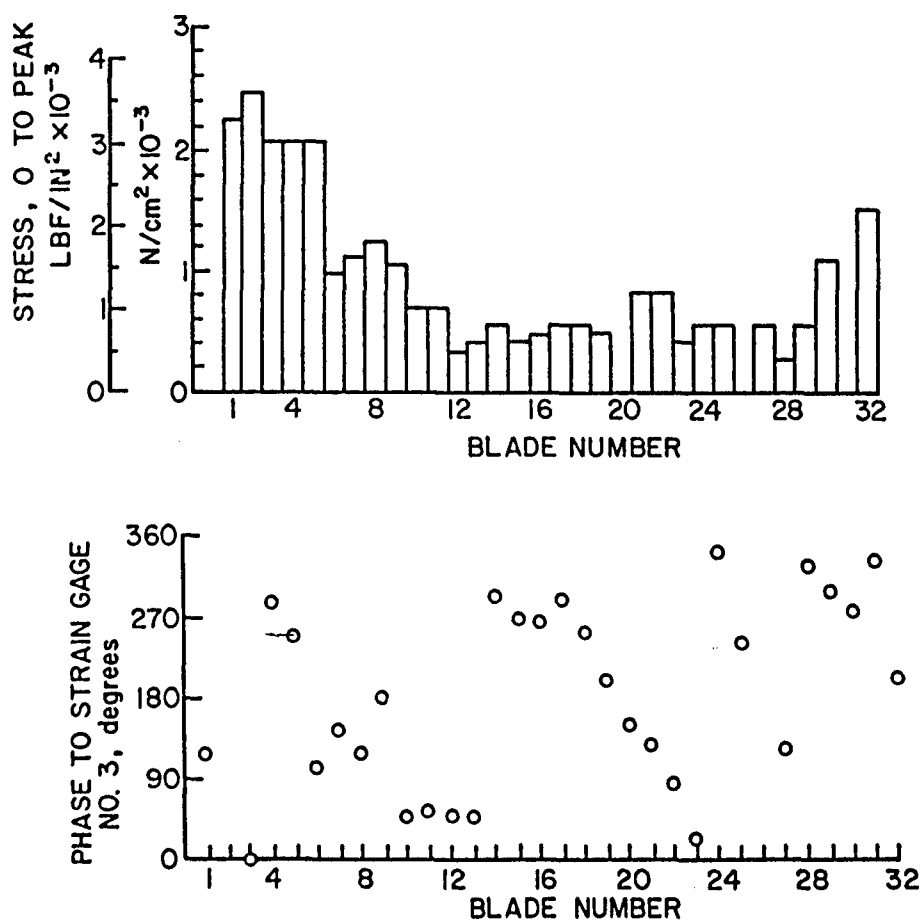


Fig. 10. Blade Flutter Amplitude and Phase Angle for
TS22 at 67% Speed (Stargardt, 1979)

A series of fundamental unsteady aerodynamic experiments to provide data to validate and direct model development in the unstalled supersonic with a subsonic axial component flow regime have been performed. Both torsion and translation mode cascade oscillations have been investigated, with the frequency of oscillation and the interblade phase angle precisely controlled by means of electromagnets under the direction of a minicomputer. The unsteady airfoil surface pressure distributions were measured by means of high response dynamic pressure transducers. These data were analyzed to determine the unsteady pressure magnitude distribution and its phase relation to airfoil motion. The parameters varied included the inlet Mach number, the interblade phase angle, the reduced frequency, and the steady aerodynamic loading.

A cascade of classical airfoils was utilized to obtain fundamental data to verify supersonic inlet flat plate cascade models. These airfoils have a flat suction surface and a wedge-shaped pressure surface. Correlation of the unsteady data obtained for harmonic torsion, Fleeter, et. al., (1977), and translation mode, Fleeter, et. al., (1978), oscillations with predictions obtained from a flat plate supersonic flutter model, Caruthers and Riffel (1980), verified this fundamental model. The torsion mode data were obtained at a reduced frequency of 0.32. These torsional data exhibited excellent correlation with the flat plate predictions on both the pressure and the suction surfaces when the variation in the blade-to-blade amplitude of oscillation was considered, as demonstrated in Figure 11.

The classical airfoil translation mode investigation utilized a graphite/epoxy composite airfoil with a maximum thickness of 0.22 cm (0.087 in.). The composite airfoils enabled a two-dimensional airfoil mode shape to be maintained at a translation reduced frequency of 0.2, a value corresponding to that characteristic of rotors experiencing bending flutter. For example, Figure 12 shows the translation mode shapes for both a steel and a graphite/epoxy composite airfoil. As seen, two-dimensionality in the test section is maintained only with the composite airfoil.

Figure 13 shows the translation mode pressure surface aerodynamic phase lag data correlation with the flat plate theory at an inlet Mach number of 1.35 for two levels of steady aerodynamic loading. These data generally exhibit very good correlation with the flat plate predictions. The phase lag and the unsteady pressure coefficient remain nearly constant between the leading edge and the mid-chord region shock wave intersection location. The theory predicts the intersection location to be at approximately 70% chord, with the unity pressure ratio data indicating the presence of a shock in the region between the 60% and 75% chord transducer locations. The effect of increasing the steady loading is to move the shock intersection forward.

Graphite/epoxy composite airfoils were also utilized to measure the unsteady aerodynamics in experiments which model the geometries and operating conditions of the second stage of the five

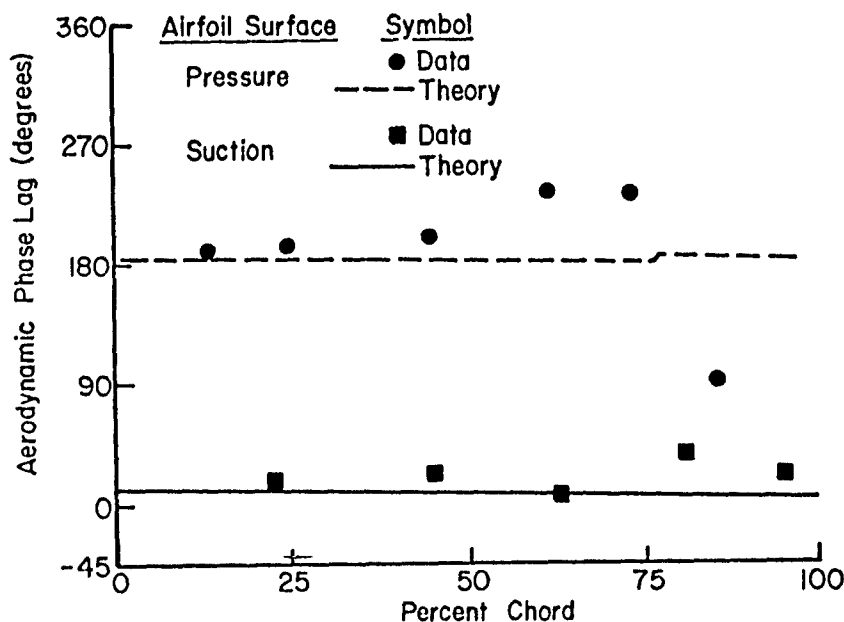


Fig. 11. Classical Airfoil Torsion Mode Aerodynamic Phase Lag Data Correlation for a Mach Number of 1.55, an Interblade Phase Angle of 14.75° and a 1.05:1 Static Pressure Ratio (Fleeter, et al, 1977)

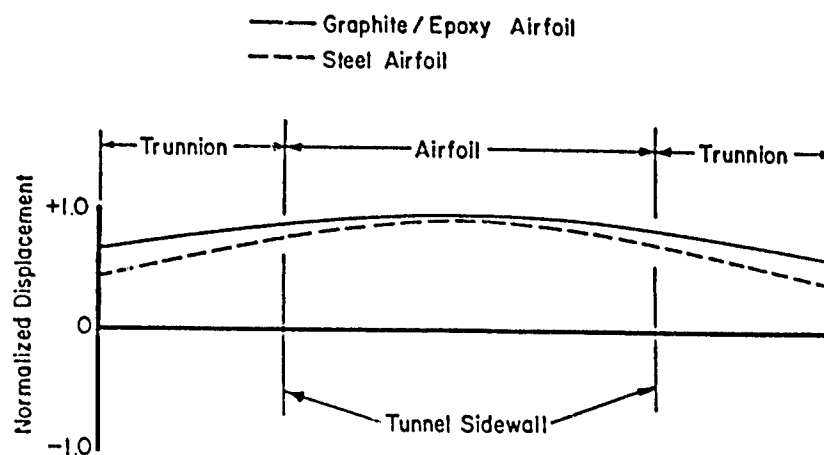


Fig. 12 Composite and Steel Airfoil Predicted Mode Shapes at 300 Hz (Riffel and Fleeter, 1980)

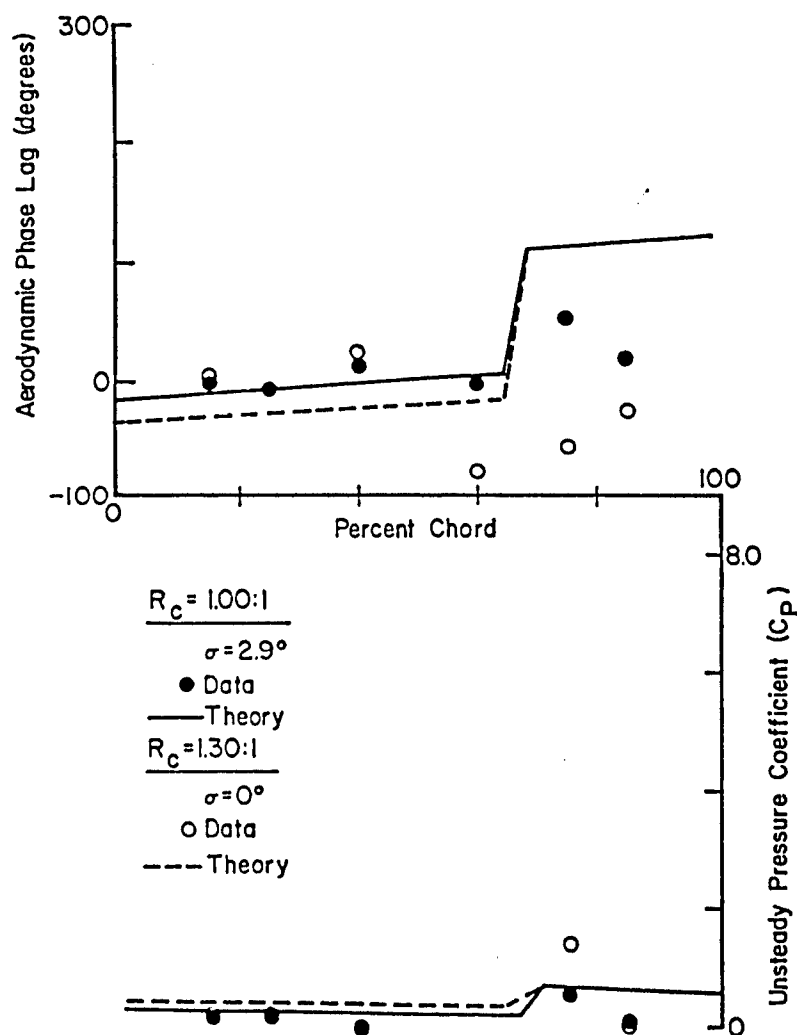


Fig. 13. Pressure Surface Classical Airfoil Translation Mode Results (Fleeter, et al, 1978)

stage TF41-A100 LP-IP compressor rig which experienced torsion mode supersonic flutter and the second stage of the NASA two stage fan which experienced supersonic bending mode flutter, Riffel and Rothrock (June and December, 1980). The pressure ratios investigated correspond to rotor operating points which are: far removed from the flutter boundary, immediately adjacent to the boundary - one inside and one outside the flutter region; and deep into the flutter region.

Figures 14 and 15 present examples of the torsion mode cascade results. Figure 14 shows the effect of cascade loading on the aerodynamic phase lag data. Predictions from the variable amplitude flat plate model are represented by the shaded region. As seen, the correlation is excellent at the low pressure ratio, with the exception of the 40% chord position, where the data indicates the presence of a reflected passage shock wave. As the cascade pressure ratio is increased, the deviation between the prediction and the data increases, particularly over the aft portion of the airfoil behind the reflected shock.

Figure 15 presents the imaginary part of the torsion mode unsteady moment coefficient determined from the surface pressure data. For the lower two pressure ratios, the cascade is stable for all interblade phase angles, in agreement with the rotor test. At the higher two pressure ratios, corresponding to conditions wherein the rotor was immediately adjacent to and deep within the flutter region respectively, the cascade data demonstrate a supersonic unstalled torsion mode flutter region for negative interblade phase angle values. Also, at the highest pressure ratio, the most unstable cascade data point is in agreement with the A100 rotor test data.

Whitehead, et. al., (1976) described an experiment to measure the unsteady torsion moment coefficients on an oscillating flat plate annular airfoil cascade for subsonic and transonic Mach numbers. The sixteen airfoils are driven in torsion at constant interblade phase angles by electromagnetic exciters, with the aerodynamic moment measured by means of strain gages. The data exhibit trendwise agreement with subsonic, Smith (1972), and supersonic, Nagashima (1974), unstalled predictions, although there are differences in magnitude, as seen in Figure 16. However, there are also differences, in some cases substantial, in the values of the moment coefficient measured on different blades.

Halliwell, Newton and Lit (1983) present a comparison of experimental and theoretical results for a transonic research fan vibrating in a coupled flutter mode. The unsteady pressure measurements on the blade surfaces are accomplished by instrumenting two pairs of blades, each defining a blade passage, with high response pressure transducers. On one of these pairs, transducers are installed on the rear half of the blade chord, with the front half of the chord instrumented on the other pair.

Figure 17 shows the correlation of the unsteady pressure amplitude data with three theories: Goldstein, Braun, and Adamczyk (1977), Acton (1981), and Whitehead (1981). As seen, the prediction of both the amplitude and the phase of the surface unsteady pressures is generally good for the supersonic section of the blade. For the subsonic part on the suction surface, the comparison is less favorable. This might be expected due to the limitations of inviscid flow theory. On the pressure surface, the comparisons are reasonably good, except

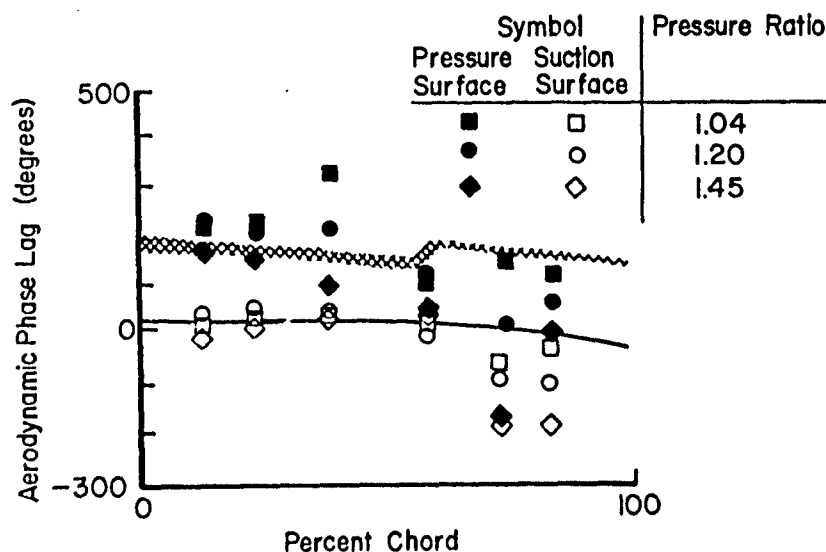


Fig. 14. The Effect of Loading on the Torsion Mode Aerodynamic Phase Lag Data for a -90° Interblade Phase Angle (Riffel and Rothrock, 1980)

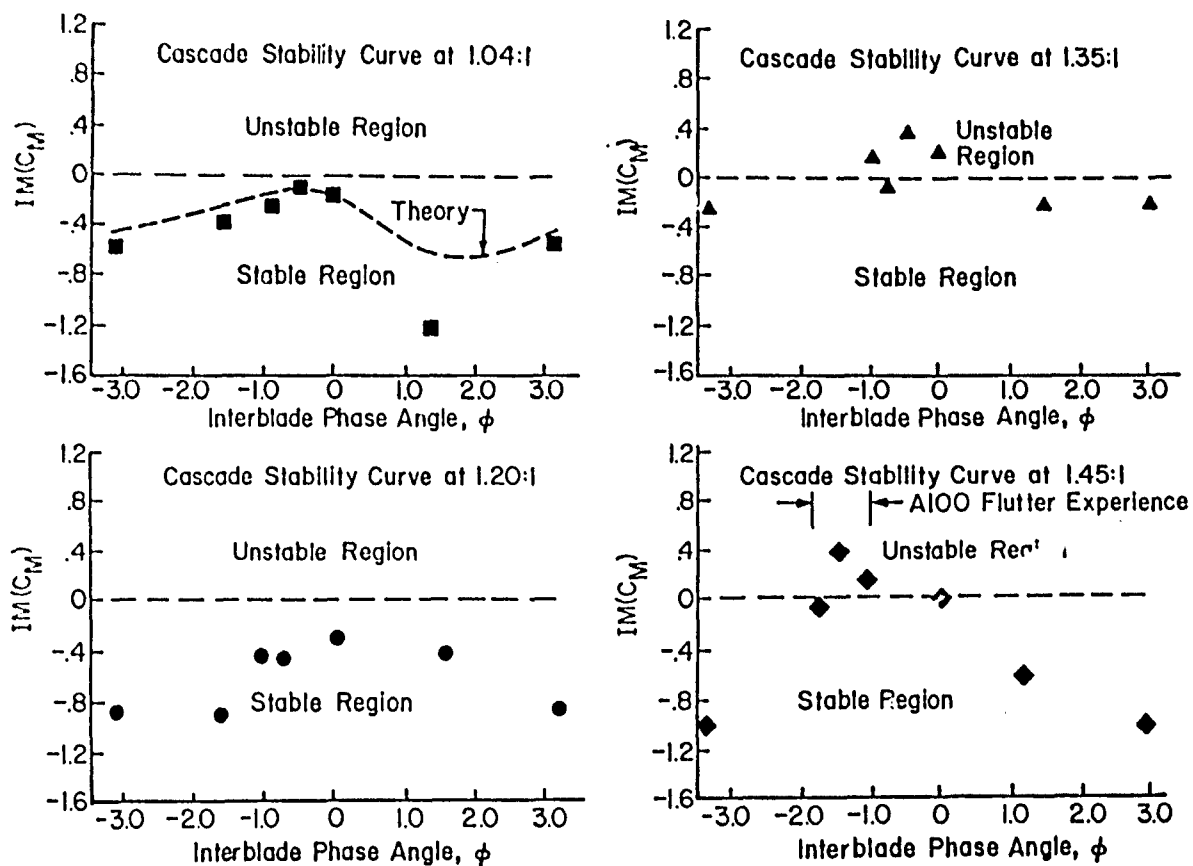


Fig. 15. Torsion Mode Cascade Stability Results (Riffel and Rothrock, 1980)

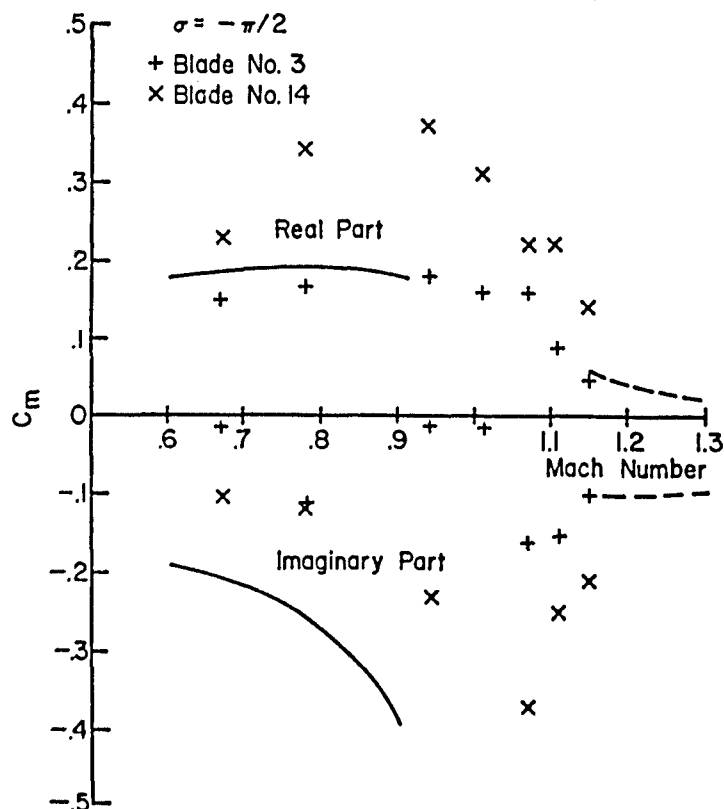


Fig. 16. Unsteady Torsion Moment Annular Cascade Results (Whitehead, et al, 1976)

in the complex flow region just behind the shock. Thus, the role of the shock is seen to be important, both with respect to its steady state position and the unsteady flow changes across it.

Choke and Negative Incidence Flutter

Choking flutter in the bending mode usually occurs at negative incidence angles at a part-speed condition with the blade row operating either subsonically or transonically. In a choked flow condition, the blade passage inlet flow is constrained to pass through a decreased stream area. Thus, Mach numbers which are greater than the inlet Mach number can occur in the blade passage, thereby leading to the possible existence of passage shocks which can cause flow separation or perhaps couple adjacent blades. The physical mechanism of choke flutter is not fully understood. High negative incidence angles and choked flow are both viable candidates. Choke flutter is generally unphased at low ampli-

tudes of vibration, with the possibility of a constant interblade phase angle existing at larger amplitudes.

A study of some of the basic unsteady aerodynamic phenomena of interest to choke flutter in turbomachines has been reported by Tanida and Saito (1976). A single airfoil is mounted between adjustable parallel walls and oscillated in torsion about its midchord in a subsonic flow field.

Typical complex aerodynamic moment data, measured with strain gages mounted on the torsion rod driving system, are presented in Figure 18. The shocks, particularly the weak ones, were observed to oscillate in a somewhat random manner. Thus, these data are averaged over a number of cycles, with the shaded regions indicating the range of data. As seen, the distance to the wall has a significant effect. Thus, these results indicate the possibility of choking flutter in a transonic internal flow.

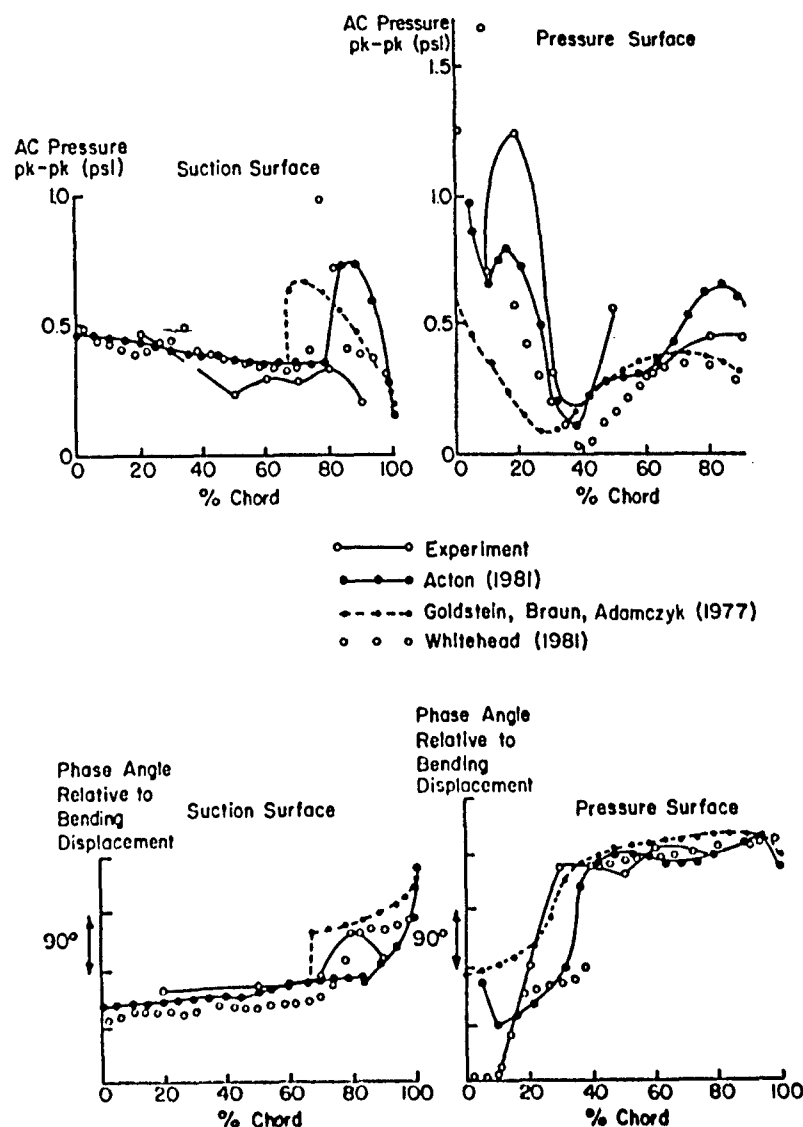


Fig. 17 Comparison of Predicted and Measured Unsteady Pressure (Halliwell, Newton, and Lit, 1983)

An experimental study directed at providing choke and negative incidence flutter boundary information is also being conducted, Jutras, Stallone, and Bankhead (1980). The stationary annular cascade facility previously noted for quantifying stall flutter boundaries is also being used to map the choke and negative incidence flutter boundaries as a function of the following variables: reduced frequency, solidity, incidence, Mach number, air density, and inlet pressure and temperature.

The results indicate definite trends in flutter boundary migration and extent due to blade stiffness (reduced frequency), solidity, and inlet conditions. For both choke and negative incidence flutter, an increase in these parameters was shown to be destabilizing. Figure 19 demonstrates the effect of solidity on both bending and torsion mode choke flutter in terms of the inverse reduced frequency (the reduced velocity) and the incidence angle.

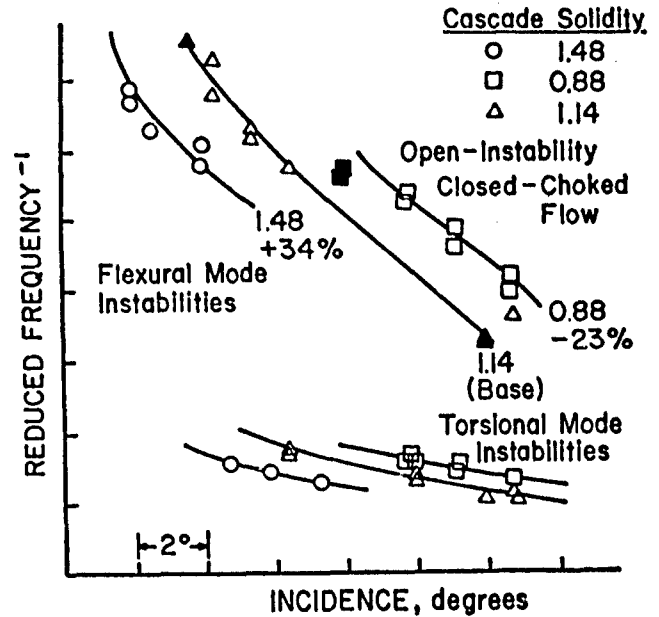


Fig. 19. Choke Flutter Sensitivity to Cascade Solidity (Jutras, Stallone, and Bankhead, 1980)

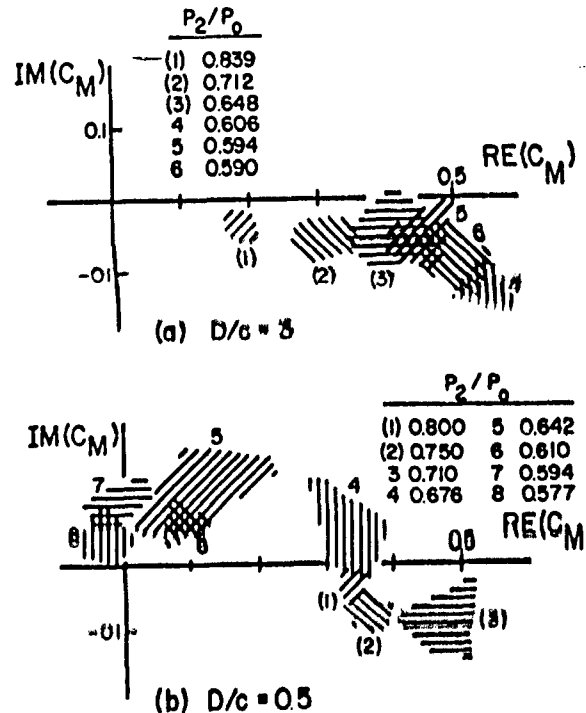
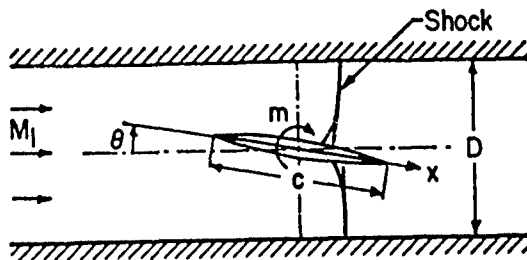


Fig. 18. Choke Torsional Moment Coefficients (Tanida and Saito, 1976)

Turbine Blade Flutter

Although flutter is not currently a problem in turbines, as previously noted, harmonically oscillating data for turbine type airfoils, i.e., thick airfoils with large flow turning, are of fundamental interest with regard to validating and directing analyses.

Rothrock, Jay and Riffel (1982), measured the torsion mode subsonic and transonic unsteady aerodynamics in a linear cascade of five highly cambered, thick, airfoils instrumented with dynamic pressure transducers. Specifically, the effect of steady operating conditions and interblade phase angle on the time variant surface pressure distributions were determined.

Although the unloaded flat plate cascade analysis of Smith (1972) predicted the trendwise variation of the unsteady data on the highly loaded, large turning airfoils, the data consistently exhibited a larger pressure coefficient. Also, the unsteady flow field appeared to be a function of the averaged flow properties rather than the inlet flow conditions, as evidenced by the better phase angle correlation of the data with a meanline analysis. An interesting result was the almost exact correspondence of the in-phase surface pressure trends obtained from quasi-steady data and unsteady data at a reduced frequency of approximately one, Figure 20. Thus, this experiment quantitatively demonstrated the coupling of the steady and unsteady flow fields. Further discussion of this turbine unsteady aerodynamic experiment is found in the next chapter "Unsteady Aerodynamic Measurements in Forced Vibration Research."

SUMMARY

This chapter has considered the various aspects of unsteady aerodynamic flutter experiments. Overall objectives considered included the validation and direction of analyses, the development of a flutter boundary data bank, and concept investigations. Experimental modeling requirements, and the applicability of high speed rotating rigs, stationary annular cascades, and two-dimensional linear cascade facilities, were discussed in terms of these overall objectives. The data requirements, as well as the associated instrumentation and data acquisition and analysis techniques, were considered as a function of particular experiment objectives. Following this, a brief overview of experimental research results for each type of flutter was presented.

In aeroelastic problems of gas turbine engine blading, flutter and forced vibration have a common background. The difference is that flutter is self induced whereas forced vibration is not, and involves a forcing function. As a result, there is a commonality in fundamental research in these two areas. Both are directed toward unsteady aerodynamics, including the measurement of the aerodynamic damping and unsteady surface pressure distributions. This chapter has considered the experimental flutter research. Forced vibrations is discussed in the next chapter "Unsteady Aerodynamic Measurements in Forced Vibration Research."

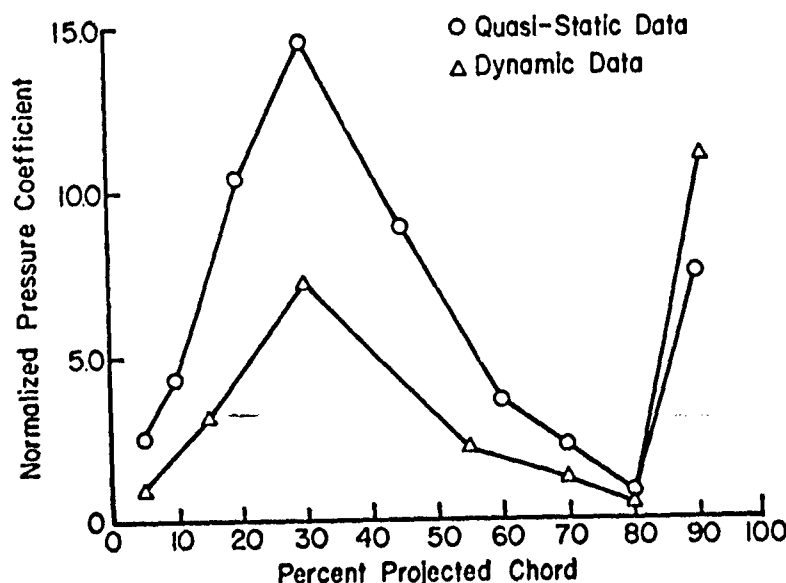


Fig. 20. Comparison of the Quasi-Steady and Unsteady Suction Surface Data for a 2.8 Expansion Ratio (Rothrock, Jay, and Riffel, 1982)

UNSTEADY AERODYNAMIC MEASUREMENTS IN FORCED VIBRATION RESEARCH

by

Robert L. Jay
Allison Gas Turbine Division
of General Motors
Indianapolis, Indiana 46206
USA

Sanford Fleeter
Thermal Sciences and Propulsion
School of Mechanical Engineering
Purdue University
West Lafayette, Indiana 47906
USA

INTRODUCTION

Blade and vane failure due to flutter and forced vibration is a continuing costly problem in turbomachines with resulting time delays, redesigns and part replacement. Flutter, as discussed in the previous chapter entitled, "Unsteady Aerodynamic Measurements in Flutter Research," is defined as the self-excited oscillations of a blade row occurring as the blading extracts energy from a uniform flow field. Forced resonant vibration occurs as a result of non-uniformities in the flow field being periodically applied to the blading at frequencies corresponding to its structural modes of vibration. In this case, the blading dissipates energy into the flow. Since both flutter and forced vibration require quantification of the unsteady aerodynamic loading created by oscillations of the blade row, the experimental efforts described in the previous chapter are useful in describing the aerodynamic damping portion of the forced vibration problem. However, in the forced vibration problem, a quantification of the unsteady loading acting on the blading as a result of a non-uniform flow field must be made.

Research to quantify and understand the mechanisms of forced vibration has required innovative and unique approaches to reproduce the turbomachinery environment and aeroelastic behavior of the component in facilities which allow meaningful measurements of aerodynamic and structural response. This chapter is designed to give those considering involvement in forced vibration research a knowledge of various aspects of such investigations. For those actively pursuing forced vibration research this chapter will serve as a review of the approaches used by others.

The forced vibration problem will first be defined and critical parameters requiring measurement and simulation identified. Four types of experimental facilities which have been useful in investigating the unsteady aerodynamic aspects of forced vibration will be discussed. The advantages and limitations associated with each type of facility will be addressed. Next, a brief review of recent research investigations will be presented for familiarization with each type of facility and methods used to acquire unsteady aerodynamic data. The concerns of data acquisition and calibration will then be examined. This subject is vital to ensure correct acquisition of quality data in a judicious and timely manner. Finally, two examples of recent progress will be reviewed to give

a physical sense of the nature of flutter and forced response investigations.

PROBLEM DEFINED

Forced response is defined as the resulting action of a system due to an input forcing function. A single degree of freedom elastic system can be described by the familiar equation,

$$M\ddot{X} + C\dot{X} + KX = f(t) \quad (1)$$

The response of the system described can be measured in terms of acceleration, velocity or displacement, for different forcing functions $f(t)$. Should the forcing function be periodic at a frequency of f_f , a resonant condition will exist when f_f is equal to the natural frequency of the system. The response of the system at this condition will be dictated by the damping and the magnitude of the forcing function.

Sources

A turbine engine blade has many degrees of freedom, hence many natural frequencies. Additionally, excitation forces which can create resonant response of the blading in their multiple modes of vibration are many. Both periodic and non-periodic, aerodynamically and mechanically induced forces can be present in the turbine engine environment. Non-periodic forces such as foreign object impact and surge can create large harmonic oscillations of the blading in multiple or single modes of vibration. Periodic forces arising from distortion of the aerodynamic field and mechanically induced sources such as tip rub and gear tooth excitation provide the forcing functions necessary to allow blading to operate in resonance.

For this discussion, the forces acting on the blading will be restricted to those aerodynamically induced forces which result from geometrically traceable sources in the aerodynamic flow path. Therefore, by definition the forces created by aerodynamic distorted regions encountered in rotating stall will be excluded, although the techniques to experimentally study these forces are the same as for the forces which will be discussed. The geometrically traceable sources which create distortions in the aerodynamic environment of blading can be identified. Excitations due to adjacent blading rows, differences in the number of upstream blading rows, bleed slots and ports, combustion or burner distortion, and burner cans have been major sources recognized to date.

To illustrate potential resonant conditions due to this class of excitation, Campbell diagrams for an unshrouded inlet fan rotor, a low aspect ratio mid-compressor stage, and an inlet turbine rotor blade are presented in Figures 1, 2, and 3, respectively. As shown in Figure 1, frequencies of a fan rotor blade are such that low engine order excitations (2,3,4 of the fundamental mode) are possible. Inlet struts, if present, can be numbered such that excitations of the first torsional and second bending modes will occur. Chordwise bending mode excitations can result due to the proximity of the downstream vane row. For a midstage rotor blade, the frequencies are higher than the fan stage as illustrated by the proximity of the first bending mode with eighth engine order as shown in Figure 2. Bleed arrangements create second bending mode excitations in this example. Adjacent vane rows provide excitations to the second torsional and chordwise bending modes. In Figure 3, the turbine blade natural modes can be excited by burner distortion, burner patterns resulting from discrete burner cans, and adjacent vane rows.

From these diagrams it is readily seen that aerodynamic distortion from many sources can create potentially hazardous excitations to the rotor blades. Restricting from discussion an over the blade tip bleed slot allows categorization of all the sources into two primary areas, upstream and downstream. Circumferential variation in the aerodynamic state, either upstream or downstream, result in periodic forces being generated on the rotor blading which can create resonant responses of failure level magnitude. This simplistic statement defines the problem which motivates experimentalists and analysts in the area of forced vibration research.

Flow Field, Airfoil Geometry and Mode Shape

Figure 4 presents the requirements for obtaining the necessary aerodynamic parameters needed to address the forced vibration problem. Definition of the spatial variations in the inlet and exit flow fields requires steady flow calculations or measurements, while quantification of the forces acting on the oscillating airfoil requires time based calculations or measurements. To illustrate the various inlet and exit flow fields which must be studied, the resonances for the fan stage rotor, the midstage compressor rotor, and the inlet turbine stage rotor shown in Figures 1, 2, and 3 will be examined.

In Figure 1 resonances occur at speeds below idle, in mid-operational range, and near maximum speed. Figure 5 presents inlet and exit relative velocities (relative to the airfoil section) at these resonances in the hypothetical example. Transonic velocity in these examples implies a Mach number between 0.95 and 1.05. Thus, as the fan rotor encounters various resonant conditions, the attendant relative flow fields range from totally subsonic to totally supersonic at the tip streamline, with mixed subsonic and transonic flow present radially inward from the tip. For the midstage compressor rotor, Figure 2 defines the resonant speeds and Figure 6 the relative velocity flow fields at these resonances. Generally, the tip Mach number will be less than 1.0 due to increased temperature effects resulting from the forward stages compression of the air. In both examples of compressor stages, the inlet and exit absolute velocities are subsonic.

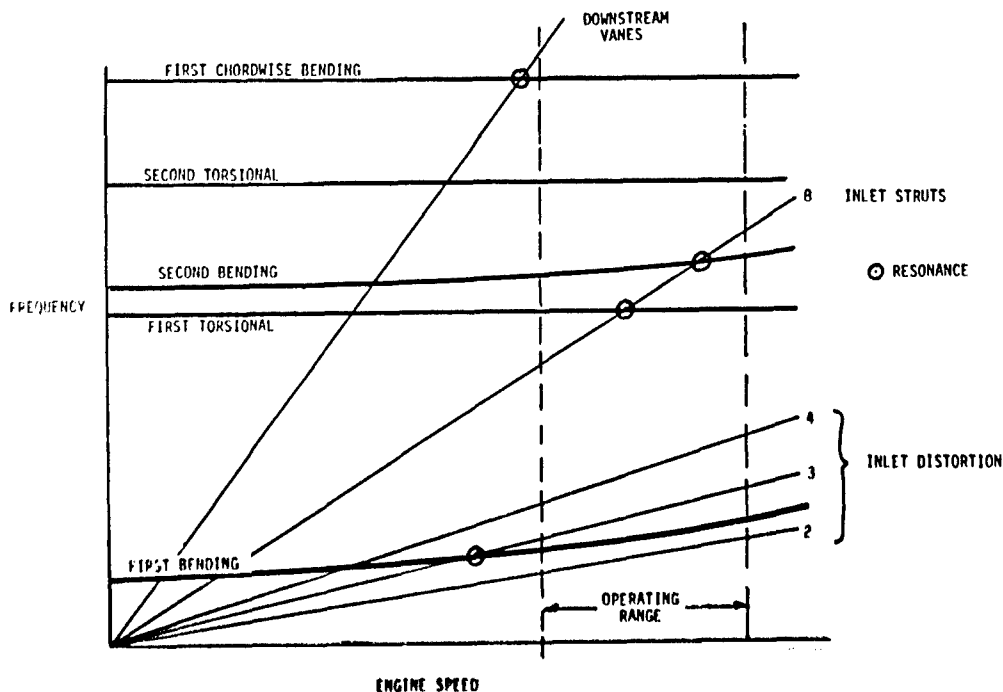


Fig. 1. Typical Campbell Diagram for Unshrouded Inlet Fan Stage.

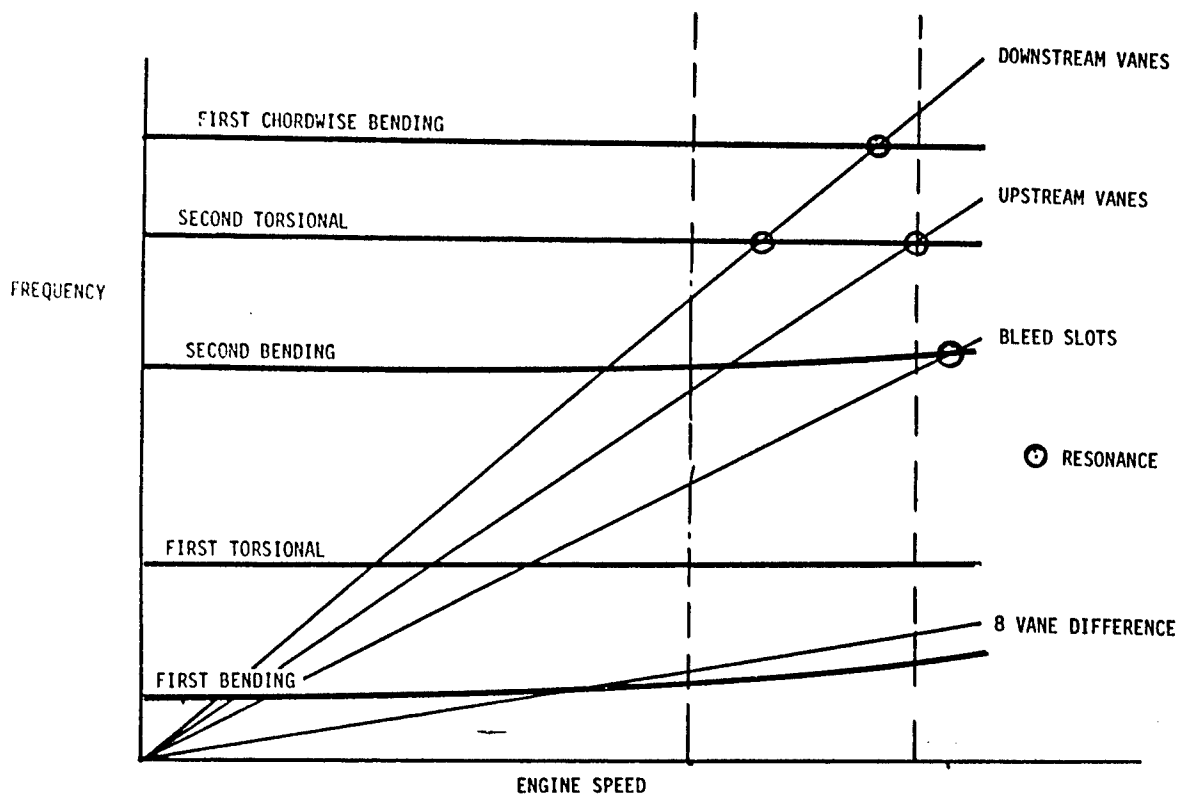


Fig. 2. Typical Campbell Diagram for Low Aspect Ratio Midstage Compressor Rotor Blade

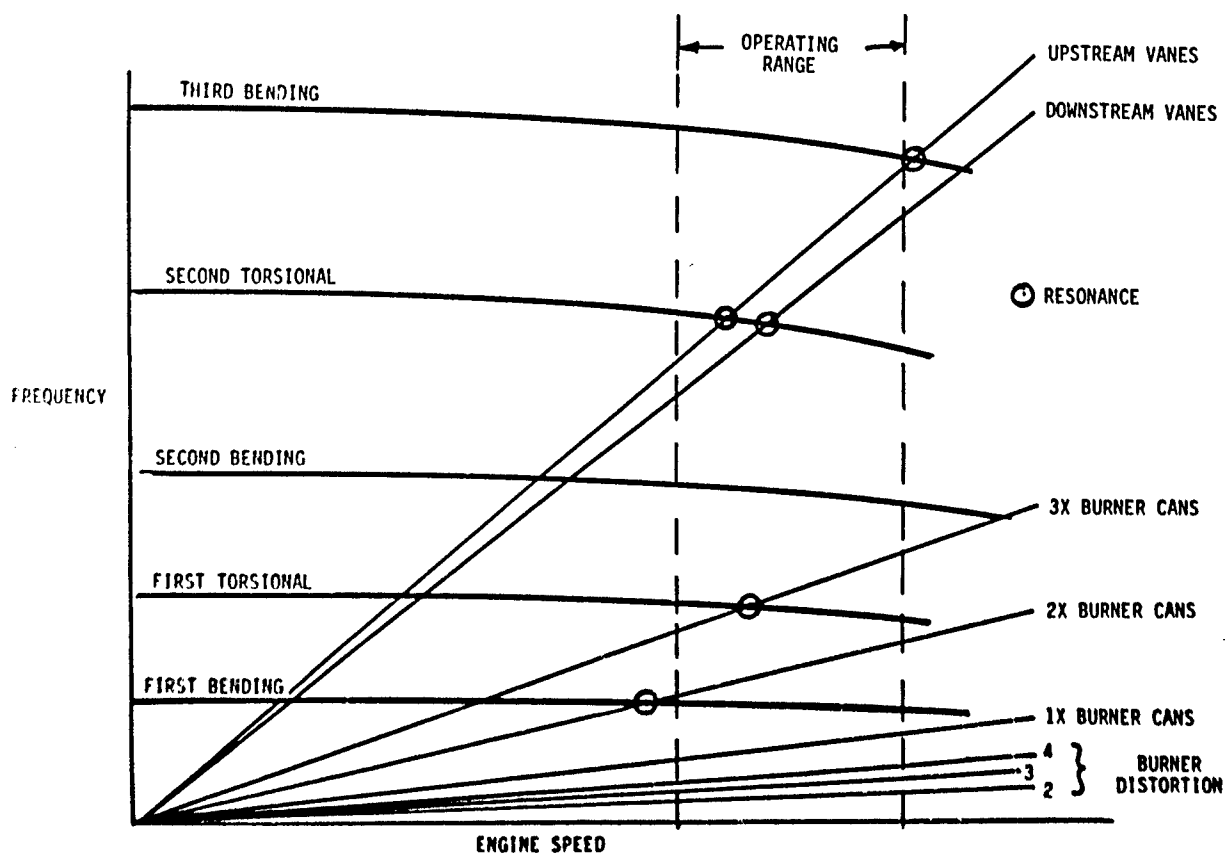


Fig. 3. Typical Campbell Diagram for Inlet Turbine Rotor with Stiff Wheel

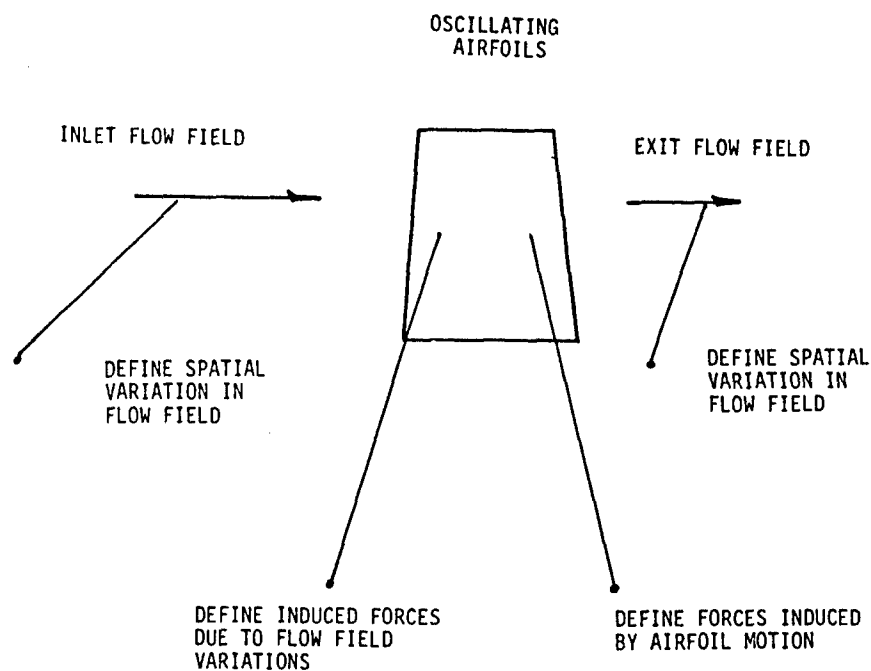


Fig. 4. Requirements for Aerodynamic Quantification of Forced Vibration.

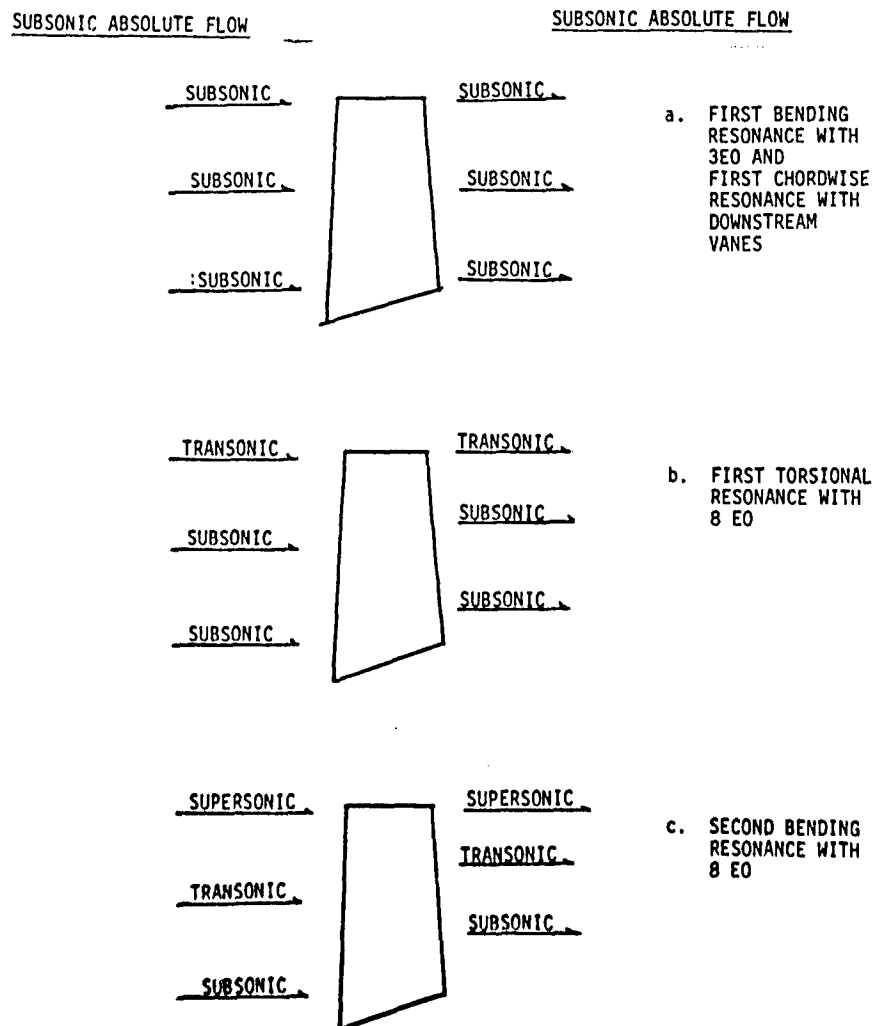


Fig. 5. Transition of Inlet and Exit Relative Flow Fields as Various Resonances occur on Inlet Fan Rotor.

SUBSONIC ABSOLUTE FLOWSUBSONIC ABSOLUTE FLOWSUBSONIC →→ SUBSONICa. SECOND TORSIONAL RESONANCE
WITH DOWNSTREAM VANESSUBSONIC →→ SUBSONICTRANSONIC →→ SUBSONICb. CHORDWISE BENDING, SECOND
TORSIONAL, SECOND BENDING
RESONANCESSUBSONIC →→ SUBSONIC

Fig. 6. Inlet and Exit Relative Flow Fields at Various Resonances of Midstage Compressor Rotor Blade.

ABSOLUTE FLOW: SUBSONIC

ABSOLUTE FLOW:
SUBSONIC
TRANSONIC
SUPERSONIC
(BASED ON NOZZLE
EXPANSION RATIO)

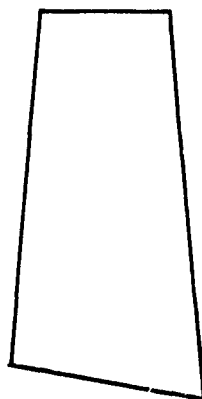
SUBSONIC →→ SUBSONIC, TRANSONIC, OR SUPERSONIC
(BASED ON TURBINE EQUIVALENT
WORK)

Fig. 7. Inlet and Exit Flow Fields at Various Resonances of Inlet Turbine Rotor Blade

The inlet stage turbine rotor resonances shown in Figure 3 can occur in relative velocity flow fields as shown in Figure 7. The exit relative velocity could range from subsonic to supersonic at either idle or high speed based on the particular turbine design. The inlet relative velocity is totally subsonic. Unlike the compressor, the absolute flow at the rotor inlet can range from subsonic to supersonic, again dependent on particular turbine design.

Therefore, referring to Figure 4 which portrays the requirements for aerodynamic quantification of forced response, the inlet and exit flow fields to be examined have been shown to be highly dependent on the particular component of interest. However, not only the flow fields, but also, the blade shapes on the three examples cited are highly varied. For the fan rotor tip section, cambers of slightly negative to slightly positive would not be uncommon. At the pitchline the camber would be on the order of 15 to 30 degrees, while at the hub, camber of up to 50 or 60 degrees would not be unreasonable. For the mid-stage compressor the camber range over the airfoil span would be in the area of 15 to 30 degrees. The inlet turbine rotor blade typically could have between 80 and 130 degrees of turning. Thicknesses of the compressor airfoils at the tip could range between 2.5 and 6 percent of blade chord tapering toward the hub to values of 8 to 14 percent of blade chord. Thickness/chord ratios for an inlet turbine stage could range from 10 to 20 percent based on cooling requirements and other considerations. Identification of blade profiles into categories such as double circular arc, multiple circular arc, and NACA Series 65 is no longer possible due to the arbitrary blade shapes resulting from improved computational codes.

The forces induced on the airfoils by the spatial variations in the inlet or exit flow fields are dependent on both the flow field and blade geometry. The aerodynamic forces created by airfoil motion are also dependent on these parameters and, additionally, the mode shape of a resonant response. Figure 8 presents sketches of modes of vibration discussed in the three example cases. De-

flections in the first four modes pictured can be approximated as in and out of phase rigid body rotations or deflections. The chordwise mode cannot be created by superposition of rigid body rotation and deflection since the mode shape indicates deflection pattern normal to the chord.

Reduced Frequency

Forces induced on the airfoil surfaces by either the spatial variation in the flow field or by oscillations of the airfoil in the airstream are functions of the non-dimensional reduced frequency. The reduced frequency is defined as the product of the airfoil chord and the frequency divided by the relative velocity of the flow. For compressor rotor stages reduced frequencies based on 3/4 span parameters at design speed can range from 0.30 for fundamental mode up to a value of 20 for first chordwise bending modes. Part speed operation can increase these reduced frequencies by virtue of the decrease in relative velocity from design speed. For turbines, reduced frequencies can range over approximately the same range when midspan inlet velocities and chords are used. It must be noted that geometrical considerations such as aspect ratio, spanwise taper of chord and thickness, and other considerations can affect these approximate ranges.

To establish a range of reduced frequencies where forced vibration problems have been noted, several compressor and turbine stages were evaluated. Based on this evaluation, the following ranges are suggested.

| Mode | Reduced frequency range |
|-------------------|-------------------------|
| First bending | 0.30- 2.0 |
| First torsion | 0.8 - 4.0 |
| Second bending | 1.0 - 6.0 |
| Second torsion | 1.6 -10.0 |
| Chordwise bending | 2.0 -20.0 |

These values are for rotating blades. For compressors the values are based on 3/4 span parameters and for turbines, midspan parameters. Coupled wheel-blade modes of most interest, generally will fall into the reduced frequency range encompassed by 0.30 to 6.0.

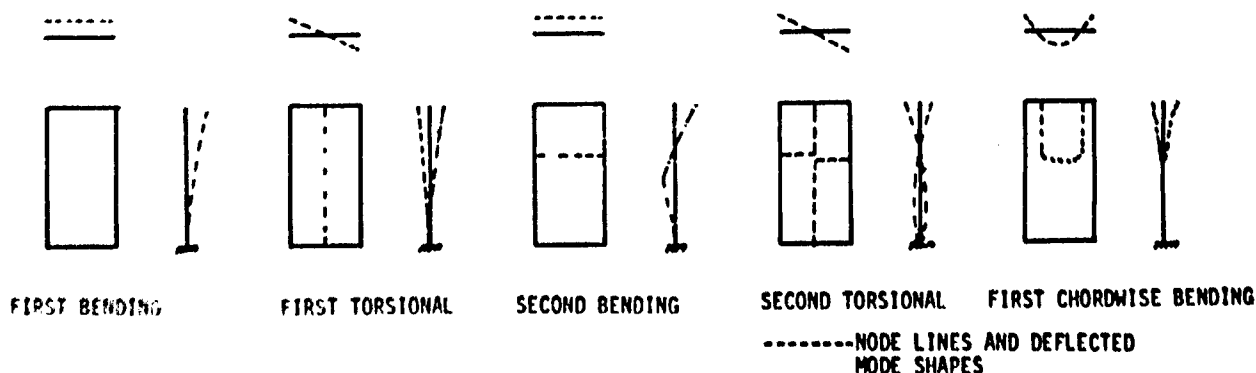


Fig. 8. Pictorial Representation of First Five Modes of Vibration.

For compressor stator vanes, which also experience significant forced vibration problems, reduced frequencies are higher because of the decreased velocities. For this discussion, only the rotating components are considered.

In defining the forced vibration problem in terms of flow fields, blade geometrical considerations, and reduced frequency in various modes, a summary of parameter ranges for investigation can be defined. Table 1 presents such a summary.

Interblade Phase Angle

Having defined the forced vibration problem in terms of these parameters, consider now the type of interactions which can result in spatial variations of the flow fields surrounding a row of rotating airfoils. In Figure 9 are shown the major interactions between rotating blade row and upstream/downstream sources. The potential flow over upstream and downstream stationary vane rows create unsteady disturbances on the airfoils. Likewise, the wakes created by the upstream vane row are convected into the blade row creating a source for unpressures along the rotating airfoil surfaces.

Table 1.
Summary of Parameter Ranges for Forced Vibration Investigations

| Parameter | Compressor | Turbine (inlet stage) |
|-------------------------|-----------------------|-----------------------|
| Absolute velocity | | |
| Inlet | Subsonic | Subsonic - Supersonic |
| Exit | Subsonic | Subsonic |
| Relative velocity | | |
| Inlet | Subsonic - Supersonic | Subsonic |
| Exit | Subsonic - Supersonic | Subsonic - Supersonic |
| Camber | | |
| Hub | <60° | <130° |
| Tip | Near zero - 20° | <80° |
| Thickness/chord | | |
| Hub | 0.14 | |
| Tip | 0.025 | |
| Reduced frequency range | | |
| First bending | 0.30- 2.0 | |
| First torsion | 0.80- 4.0 | |
| Second bending | 1.0 - 6.0 | |
| Second torsion | 1.6 -10.0 | |
| Chordwise bending | 2.0 -20.0 | |

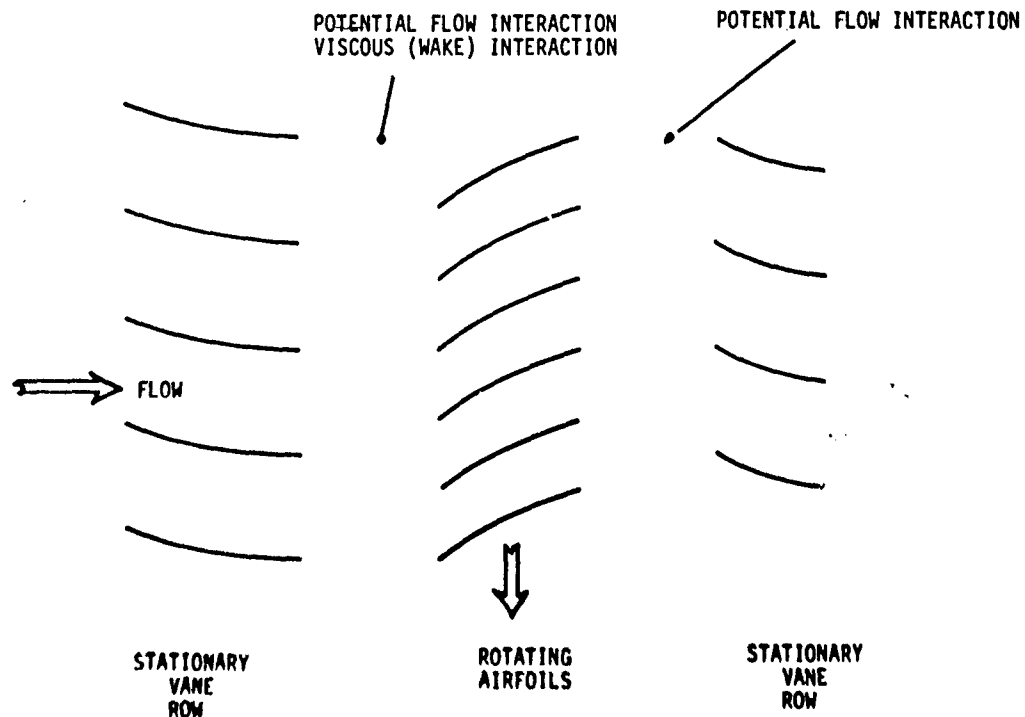


Fig. 9. Interactions Creating Aerodynamic Forces on Rotating Airfoils.

EXPERIMENTAL FACILITY REQUIREMENTS

From the definition of the forced vibration problem presented in the previous section, it is readily obvious that the measurements needed in forced vibration research are most properly made in an operating engine environment. However, this environment is hostile with regard to instrumentation and isolation of parameters is difficult. To circumvent these problems, experimental investigators have turned to specialized facilities and rotating rigs in which the essential features of the flow are preserved, yet the environment and conditions for acquiring meaningful measurements are much more favorable. For purposes of this discussion, four types of experimental facilities are considered: (1) two dimensional rectilinear cascades, (2) stationary annular cascades, (3) low speed rotating rigs and (4) high speed rotating rigs. Advantages and disadvantages of each type of facility will be discussed and their role in defining the aerodynamics of forced response outlined.

In order to define these advantages and disadvantages, it is useful to define two quantities, the aerodynamic gust and

aerodynamic damping. For this discussion, the aerodynamic gust will be defined as the time varying loading of a cascade of arbitrary airfoils which is independent of airfoil movement and which is created by upstream or downstream phased periodic disturbances. The aerodynamic damping will designate the time varying loading of the cascade due to harmonic, phased motions of the airfoils. The superimposing of these two fields then yields the total time-varying aerodynamics in the forced vibration problem.

Linear Cascades

Representation of a spanwise section of a turbomachinery blade by a finite number of two-dimensional airfoil sections has been accomplished in facilities defined herein as linear cascades. The finiteness of the cascade introduces the problem of periodicity, which has been discussed in the previous chapter (Unsteady Aerodynamic Measurements in Flutter Research). Examples of cascades featuring supersonic and subsonic inlet Mach numbers are shown in Figures 12 and 13, respectively. The cascade pictured in Figure 12 was designed to simulate an

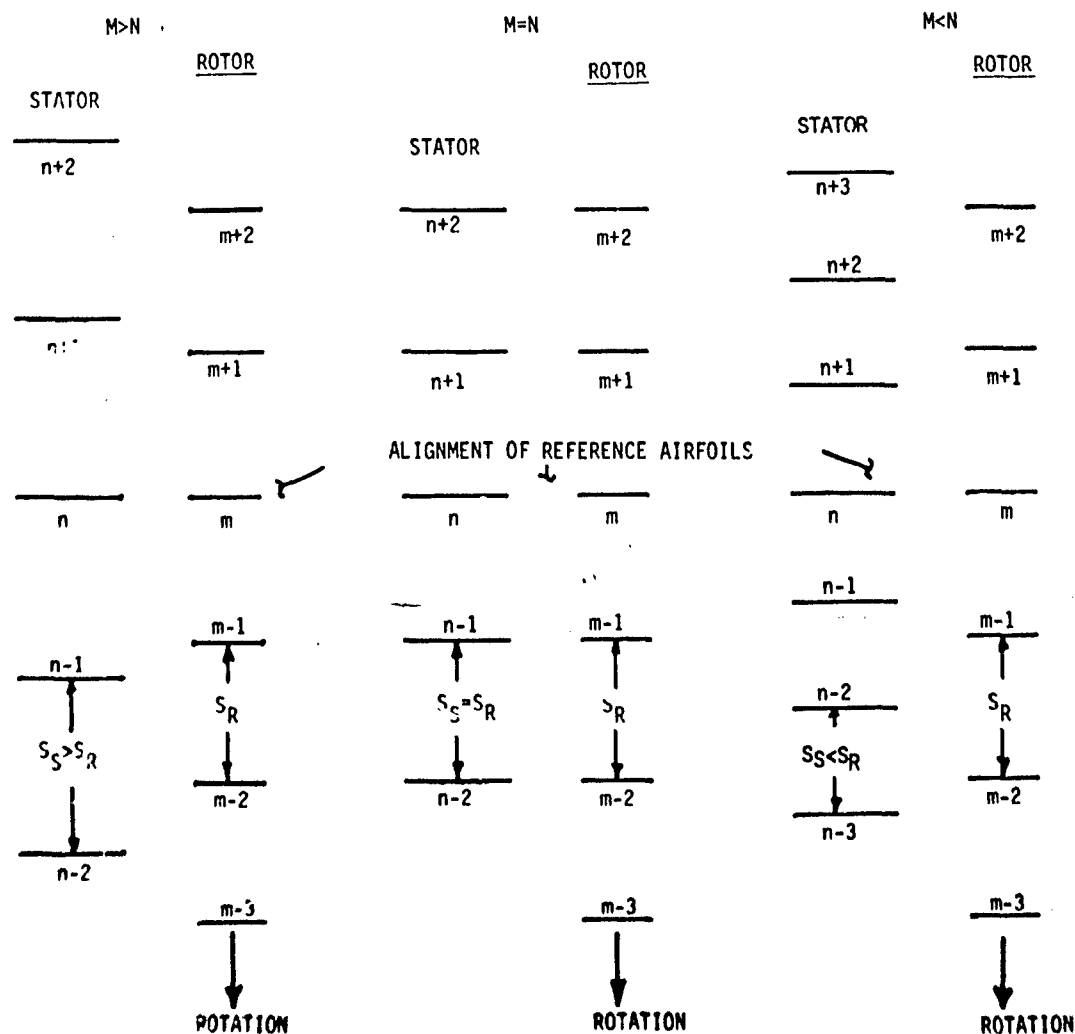


Fig. 11. Phasing Relationships Based on Number of Rotor and Stator Airfoils.

outer span airfoil section of an inlet fan stage, while the cascade pictured in Figure 13 was designed to aerodynamically simulate the mean section of an advanced turbine airfoil design. In both cascades the flow exits the cascade at approximately 3:00 o'clock. For the compressor cascade flow entry is from approximately 9:00 o'clock, while for the turbine cascade the flow enters from approximately 1:00 o'clock. Thus, the flow turning of each cascade is consistent with the engine environment. The cascades are designed to simulate the velocity fields relative to the airfoils. Proper design of upstream nozzles and the ability to control inlet and exit plenum pressures furnish precise control of these velocity fields. Sidewall and nozzle bleeds are used to ensure two dimensional flows through the cascades.

The linear cascade provides an excellent optical path for examining both steady and unsteady effects in the airfoil passages and near their surfaces. Lack of centrifugal and untwist stresses allow static pressure taps or high response pressure transducers to be located much nearer critical leading and trailing edge regions than in a rotating environment. This allows more precise quantification of both the steady and unsteady fields.

Aeroelasticity research in linear cascades has been generally limited to the aerodynamic damping portion of the forced vibration problem. Techniques to oscillate cascaded airfoils at precise frequencies and interblade phase angles

have been developed. Data obtained from high response pressure transducers embedded to preserve airfoil contour have been used to determine aerodynamic damping coefficients as a function of airfoil motion.

The major limitation in obtaining aerodynamic damping data by testing in linear cascades has been proper simulation of reduced frequency. This limitation has arisen due to the spanwise dynamic deflections of the airfoils becoming non two-dimensional, i.e., non-rigid body motions. Also, increasing the reduced frequency by increasing chord lengths presents difficulties in obtaining required tunnel mass flow rates to achieve proper inlet velocities. Decreasing the inlet velocity to increase reduced frequency results in nonconformance to desired test goals.

Achieving proper input gust loading for a linear cascade is extremely difficult, unless extremely low reduced frequency data is desired. A method to oscillate the inlet flow direction at an extremely low frequency and measure the resulting time varying pressures on the airfoil surfaces has been used by Ostidiek (1976). The phasing requirements, as discussed in the previous section, are a prerequisite for proper gust input loading to the cascaded airfoils and are not met in oscillating the inlet velocity angle. To achieve proper phasing of gust loading in the linear cascade would require varying inlet or exit conditions to each airfoil at controlled frequency and phasing.

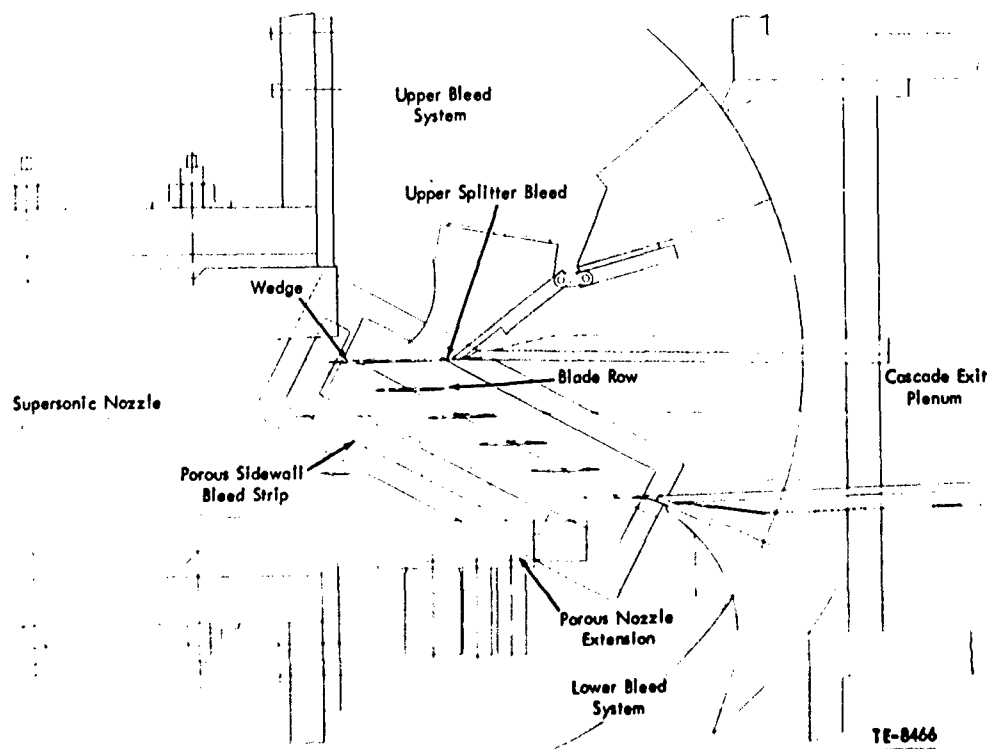


Fig. 12. Schematic of Cascade Facility.

Stationary Annular Cascades

Representation of a spanwise section of a turbomachine blade by stationary airfoils arranged in an annulus has been accomplished in facilities defined herein as stationary annular cascades. The annular arrangement circumvents the periodicity question arising in linear cascades.

Stationary annular cascades can be designed to simulate inlet flows ranging from subsonic to supersonic, depending on the manner in which flow is delivered to the cascade. Annular cascades retain several advantages of the linear cascade such as optical and instrumentation accessibility, centrifugal loading on the airfoils, and control of the velocity fields. However, they suffer from the same type of limitations as do linear cascades, i.e., obtaining proper reduced frequencies at realistic velocities and proper simulation of the gust loading.

Low Speed Rotating Rig

This category is used to define both the rotating blades and stationary vane rows in single or multiple stage test vehicles which have low through flow velocities, with axial Mach numbers in the range of 0.1. Loadings in terms of pressure ratio and equivalent work are usually extremely low. Primary advantages in low speed facilities include optical and instrumentation accessibility, low centrifugal loadings on rotating airfoils, and low horsepower required for drive considerations. In low speed rigs, both upstream and downstream gusts can

be simulated, with the exception of shock impulses from supersonic exit turbine nozzles. Specially fabricated screens, rods, and vane rows can yield variations in gust amplitudes, reduced frequencies, and interblade phasing relative to the rotating airfoils. Variations in numbers of rotor and stator blades can be used to investigate interblade phasing and reduced frequency effects on either the blading of rotor or stator airfoils. Spanwise effects present in rigs of this type present challenges in measurement not encountered in two dimensional linear and annular cascades. The major disadvantage of low speed rigs is the low Mach number range available for investigation.

High Speed Rotating Rig

High speed rotating cascades, which encompass a range from single stage rigs to full engines, are the ideal vehicle in which to make measurements of quantities pertinent to forced vibration under realistic inlet and exit flows, reduced frequencies, and interblade phasing. In this environment, however, optical and instrumentation accessibility present major difficulties. The high centrifugal fields in which the rotating airfoils operate limit locations of instrumentation. Concepts to oscillate airfoils in this environment to obtain aerodynamic damping information require unique attachment designs. Requirements for multi-channel rotating, high speed sliprings to provide transfer of signals and reference power across the stationary to rotating frame of reference introduces additional complexity.

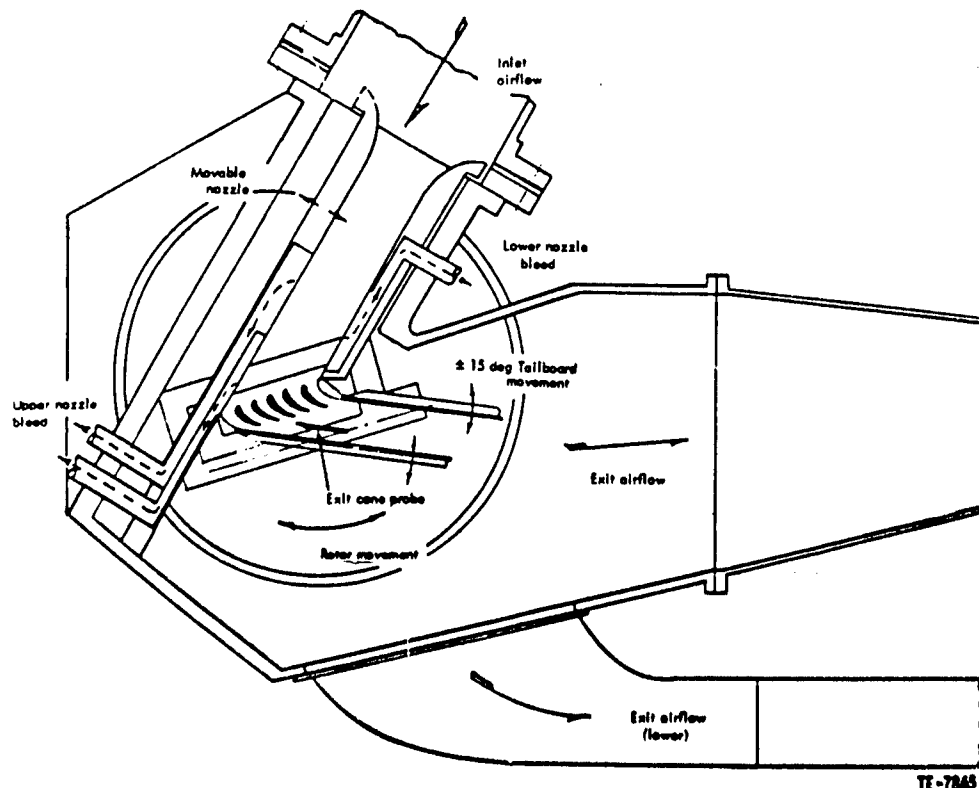


Fig. 13. Schematic of Turbine Rotor Cascade Hardware.

Each type of research facility currently used to obtain experimental data relevant to forced vibration of blading has both advantages and disadvantages. Experimentalists have taken advantage of the uniqueness of each facility and have designed controlled experiments to obtain basic data over parametric ranges offered by the facility. Examples of the forced vibration research being accomplished in the four types of facilities illustrate the discussion presented.

EXPERIMENTAL RESEARCH

In spite of the limitations associated with each type of facility, significant research data have been acquired and measurements made for correlation with theory and experience. Through use of unique and varied driving mechanisms, measurement techniques (pressure, displacement, velocity), flow mediums, visualization methods, and data acquisition and reduction schemes much insight and information on the aerodynamic gust and damping of turbomachine blading has been acquired. The following is a review of a small portion of what has been done to obtain these data in each type of facility.

Linear Cascades

As mentioned earlier Ostdiek (1976) investigated the effects of an oscillating inlet flow at low reduced frequencies on a five bladed cascade. This was done in an attempt to relate the pressure fluctuation on the center airfoil to the varying directional change of the constant magnitude inlet flow. This addresses the input gust loading of the airfoil independent of airfoil movement.

Fleeter (1976a) addressed the aerodynamic damping associated with airfoil motion by controlling the frequency of torsional oscillation and interblade phase angle for a cascade of five blades in a supersonic inlet flow field. Parameters varied were inlet Mach number, interblade phase angle and reduced frequency. Data obtained were the unsteady pressure magnitude and phase by using airfoil embedded dynamic pressure transducers.

Boldman (1978) using a mechanical cam driver to produce precise torsional motion of a single DCA airfoil obtained schlieren motion pictures showing shock patterns moving across the blade. A phase lag (nominally 100°) between the blade motion and response of the flow increased as reduced frequency increased from 1.04 to 1.56.

Aerodynamic evaluation of turbine blade packets in the first three natural modes was carried out by Kovats (1979). Utilizing a shaker to input or absorb energy from the airfoil packets and measuring the resulting power flow allowed quantification of the aerodynamic force in phase with the airfoil motion. He also used interferometry to instantaneously (2×10^{-8} sec) record gas density variations around the first airfoil of the packet. Twenty four records were obtained for the vibration cycle and

were used to obtain aerodynamic damping. A special control circuit was developed to trigger interferograms to be taken at a specified energy flow and at specified airfoil cycle positions.

Loiseau (1980) used measured cascade unsteady pressures from airfoil embedded transducers to calculate aerodynamic damping for comparison with bandwidth damping measurements on the blades of a working compressor. The cascade parameters were set to be similar to those of the compressor and encompassed the stall flutter region, M_n from 0.5 to 1.0. Good agreement in damping was noted at subsonic Mach numbers and at $M_n = 1.0$. However, large differences were obtained in the transonic region after separation incidences had been reached.

ONERA's linear cascade capabilities are described by Szechenyi (1980). Two dimensional periodic flow is simulated for Mach numbers 0.4 through supersonic with variations in Reynolds number obtained by varying tunnel pressure between 1.4 and 3 atmospheres. The cascade consists of six airfoils with the two central airfoils having the ability to vibrate in torsion (75-550Hz) or bending (80-330 Hz) at resonance using a shaker. One of these two airfoils is instrumented with embedded dynamic pressure transducers. Data acquisition and treatment of vibratory motion and pressure measurements is obtained immediately in the form of a print-out.

Steady-state, time-variant and quasi-static pressure data were obtained by Rothrock (1981) from a linear cascade of five turbine airfoils undergoing torsional oscillation. Unsteady pressures were obtained from embedded transducers for six values of interblade phase angle and for four expansion ratios. The major features of the facility are continuous operation for extended periods, mechanized test section for changing cascade incidence, schlieren optical system, wall bleed systems and data acquisition using two digital mini-computers. The drive system is a spring bar and hammer arrangement using an electromagnet on both ends of airfoil trunnions to ensure rigid body motion. The data obtained showed correspondence of surface pressure trends for quasi-static and time-variant testing.

Riffel (1981) presents cascade modeling concepts to preserve the critical values of the flow field for supersonic inlet rotor blade sections. Finite element methods are used to design the airfoil and spring bars to attain appropriate reduced frequencies for torsional and translational modes. The cascade airfoil is designed and fabricated of graphite/epoxy to attain nearly rigid body motions and to reduce the driving force required to attain specified amplitudes.

Unsteady periodicity in a cascade was demonstrated by Carta (1982) through dynamic pressure instrumentation of multiple blades and the sidewall at the airfoil leading edge plane. This cascade consisted of eleven NACA 63-series airfoils oscillating in torsion. A

matrix of 96 data points were obtained based on two incidence angles (2° , 6°), three reduced frequencies (1.44, 0.244, 0.302) and eight interblade phase angles (0° , 45° , 90° , 135° , 180°) at a constant inlet velocity of 200 ft/sec (61 m/sec). Comparison of experimental data with the unsteady Verdon/Caspar (1980) theory for cascaded blades showed excellent agreement.

Stationary Annular Cascades

Addressing the aerodynamic gust, Adachi (1979) used hot wires to measure the steady and unsteady velocity distributions between stator vanes due to wakes produced by moving cylinders upstream. In addition, the above flow field was compared to the measured unsteady force on one stator using twenty four (24) pressure transducers embedded in the airfoil. A photoelectric pickup was used to synchronize the data acquisition to obtain the in-passage velocity distributions at five circumferential positions of the moving cylinder. The output of the pressure transducers was averaged periodically to remove random data extracting the periodic component.

Whitehead (1980) shows good agreement of predictions of force and moment coefficients from a finite element based program with data from an annular turbine blade cascade. The cascade consisted of sixteen (16) airfoils with each blade excited by its own driver. A control system was used to attain constant interblade phase angle between all airfoils. Specifically located strain gages were used to measure moment coefficients based on amplitude and phase from three (3) blades.

A transonic turbine cascade designed to simulate the first three natural modes of vibration of a blade is described by Kirchner (1980). Each blade is excited by its own electromagnetic driver with the capability to prescribe and maintain blade to blade amplitude and interblade phasing for positive aerodynamic damping values. Provision for measurement of unsteady pressure distribution is made on one blade.

Davies (1984) uses interferometry to visualize the shock location and movement on the airfoil around an annular cascade representing a compressor fan blade tip section. This was accomplished by synchronizing the laser pulses to the blade vibration cycle using an electronic triggering system. Individual blade shakers were used to provide specified interblade phase angles and amplitude by means of negative feedback.

Low Speed Rigs

Unsteady pressures on a stator blade row due to the wakes from an upstream rotor were measured by Henderson (1978). The variation of rotor/stator spacing, stator solidity and stator incidence angle were investigated. Recessed pressure transducer data were ensemble averaged to obtain the periodic component. The rotor wake was defined by using a hot film anemometer probe. In addition the unsteady response of the rotor due to the

presence of the stator blades was obtained by strain gage measurements at the midspan of the rotor blade.

Fleeter (1979) measured the unsteady surface pressure distribution near the trailing edge of a classical isolated flat plate, a forty (40) vane classical flat plate stator row and a forty (40) vane cambered NACA Series 65 stator row due to the upstream rotor wake. This was done at reduced frequencies between 14.0 and 20.0. The data acquisition was based on triggered data averaging over four hundred rotor revolutions. During this time eighty (80) to one hundred (100) digitized data points were obtained. The rotor wake was measured using a crosswire probe.

Screens were used by Bruce (1979) to produce sinusoidal axial velocity components of specified number and magnitude to investigate unsteady response of a rotor. Measured values of the unsteady lift force and pitching moment coefficients and their phase angles were obtained by strain gaged sensing elements on one rotor blade. Solidity of the uncambered rotor was varied by choosing 2, 3, 4, 6 or 12 blades. Cascade stagger angle, mean incidence angle and reduced frequency were also varied. A photocell was used to trigger ensemble averaging of the data to eliminate random sources of excitation (i.e., turbulence). This trigger was also used to define phasing between the force and blade response.

Interaction between rotors and stators of a large scale turbine stage was studied by Dring (1981). High response pressure transducers and thin film gages were used on the rotor and stator to identify potential flow and wake effects present. Two rotor-stator axial gaps were investigated. Also studied were the characteristics of the steady flow over the rotor with varying incidences. Fullspan surface flow visualization was obtained by flowing ammonia out of rotor pressure taps with the surface of the rotor covered by Ozalid paper.

Joslyn (1982) used transversing (circumferential and radial) probes to study the flow in a one and one-half stage axial flow turbine model. Three element hot film probes were used to measure instantaneous velocity behind the first vane, first blade and second vane. High response total pressure data were obtained using a transducer mounted in a standard Kiel probe. Unsteadiness and three dimensionality of the flow were investigated.

Using embedded pressure transducers on a rotor airfoil, O'Brien (1982) quantified the unsteady effects of downstream struts (four rotor chord lengths removed) on the rotor. The downstream stator row (one rotor chord length) unsteady effects were also observed.

Capece (1984) conducted an experimental study of the unsteady pressure distributions on the first stage vane row due to upstream rotor wakes. Embedded dynamic pressure transducers were used with data reduction using FFT techniques.

High Speeds Rigs

A single stage axial flow compressor test rig with removable inlet guide vanes is described by Gallus (1979a). This rig was used to investigate blade-stator interaction under subsonic conditions. Measurements of unsteady pressures on the mid-span of rotor and stator blades were accomplished with embedded dynamic pressure transducers. Rotor wake shape (midspan) for points of operation were also measured with a three-hole probe which traversed circumferentially. The data were examined with respect to flow parameters involved (i.e., Mach number, reduced frequency). Gallus (1979b) also obtained schlieren visualization of the flow upstream of a rotor in an axial supersonic compressor stage rig. This was accomplished by a stroboscopic control system. A rig designed to investigate the influence of rotor-blade solidity on the unsteady pressure distribution of a stator at various axial distances downstream is described by Gallus (1981). Rotor wake measurements were made using a traversing three-hole probe. Microphones were employed to measure sound pressure level downstream.

A blow down compressor facility which employs a flow medium of Freon-Argon mixture is presented by Crawley (1980). The ability to drive the twenty-three (23) blades through piezoelectric

crystals to controlled amplitude and phasing is provided. These crystals used as displacement transducers along with strain gage measurements have been used to determine aerodynamic damping by modal analysis. An advantage of using such a facility is the lower centrifugal and bending stresses due to the lower speed of sound and low dynamic pressures. The short test time of eighty (80) ms also increases chances of rotor survival in the event of a flutter instability.

This concludes the survey of some of the work being done using linear and annular cascades, and low and high speed rigs to obtain meaningful measurements of forced vibration and flutter parameters. An additional survey of research activities in the field of unsteady flow has been made by Platzler (1977).

CALIBRATION AND DATA ACQUISITION

In flutter and forced vibration experimental programs described herein and in the previous chapter, a variety of experimental techniques were used by the investigators to acquire time-varying data. Regardless of the technique, common concerns faced by each investigator were those of calibration and data acquisition, both of which must be performed accurately to ensure data quality. These areas will be addressed in the following discussion.

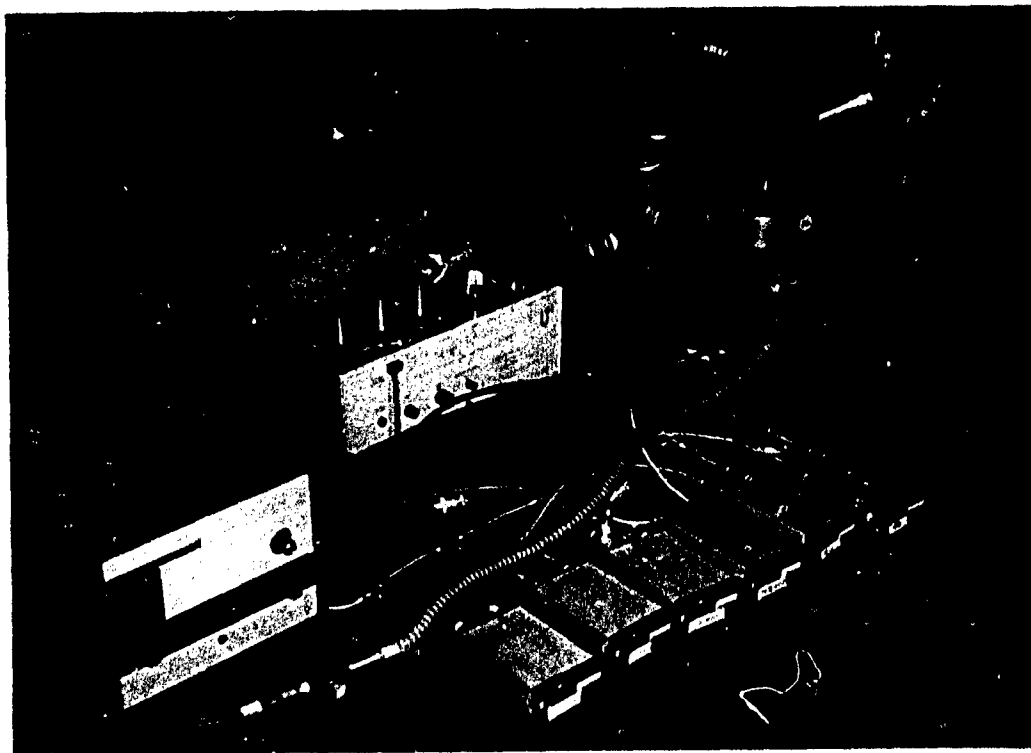


Fig. 14. Setup for Calibration of Hot Wire Instrumentation.

Calibration

Two types of instrumentation, hot wires and high response pressure transducers, form the measurement basis of many investigations of time varying aerodynamics. Thus a general discussion of calibration techniques necessary to ensure data quality from each type will be presented.

Hot Wire Anemometry

Figure 14 presents a photograph of a temperature controlled, airjet system used at Allison to calibrate hot wires for use in several experimental subsonic facilities. Pressurized air, controlled by a throttling valve, flows through a heat exchanger, then through a calibrated orifice. The flow then passes through a converging section, forming a jet of air with known velocity and temperature. Hot wire probes are inserted into the jet. At varying velocities, the output voltages of an anemometry system are recorded. For crossed-wire probes, output voltages for both wires are recorded at varying velocities and probe angles relative to the velocity. The data obtained forms the basis for linearization via the electronic features of the anemometry system, and for corrections to be made in data analysis. Although hot wire anemometry systems, properly tuned, have inherently high frequency response capabilities, the addition of coatings to protect the fragile wires from damage in the operational environment can detrimentally affect their performance.

High Response Pressure Transducers

Techniques for calibration presented herein are discussed using thin line transducers as examples, yet are applicable to high response pressure probes and other pressure measuring devices.

For static calibration of pressure transducers, a tank in which the pressure is variable over the desired working level is commonly used. Output voltages from the pressure transducer are recorded as functions of the tank pressure level and supply voltage to the transducer. Curves constructed yield the sensitivity of the transducer in terms of voltage versus pressure with excitation voltage specified.

High response pressure transducers have inherently high frequency ranges available for accurate measurement, yet the addition of coatings and shields used to protect them from erosion and damage in the operational environment can detrimentally affect their performance. In many instances, the pressure sensitive diaphragm of a transducer is located such that drilled holes, tubes, or cavities connect it to the desired point of measurement. Acoustic transmission and loss through these passages can result in a substantial decrease in the accuracy of pressure measurements. Thus, dynamic calibration of the installed measuring devices is necessary.

*Piezo-electric pressure transducer

To illustrate one technique for obtaining dynamic calibration of installed pressure transducers, an investigation of the effect of a pliable coating over the diaphragm of a thin line high response pressure transducer is informative. Experience with uncoated transducer diaphragms indicated that to increase test longevity of surface mounted transducers, coating of a pliable RTV was needed. The effect of the coating on the measurement accuracy of the transducer was not known, thus an installed dynamic calibration was performed.

This calibration was made using a dynamic pressure generator which is capable of varying the frequency and amplitude of the input pressure signal. This device is basically a siren-tuned oscillator employing a 120-hole rotor wheel controlled by the air pressure level supplied to the inlet. The signal frequency is simply controlled by the rotor angular speed. An axisymmetric contraction horn attached to the stator exhaust serves to focus the pressure signal to the smaller test section. Figure 15 presents a schematic of the system. In the calibration procedure, the input signal was monitored for amplitude and frequency with a piezo-electric reference transducer. This high frequency transducer was dynamically calibrated by the manufacturer over a range of known pressure step inputs. In addition, the transducer was calibrated for lower pressure ranges using a piston-phone acoustic generator. The output signal from the instrumented test blade was monitored and analyzed for signal strength and frequency content. Figure 16 presents the frequency response data for two Kulites* coated with RTV and flush mounted on an airfoil. The amplitude ratios were calculated over a frequency range of 400 to 1000 Hz. The mean RMS amplitude ratio of the Kulite output of the reference output was approximately 0.95 in the test frequency range, and was independent of signal frequency.

Many of the investigations discussed in the section on Experimental Research used thin pressure transducers installed flush or slightly recessed from an airfoil external contour to measure pressure fluctuations arising from induced airfoil motion. Strain gages were used to define the oscillatory motion of the airfoils in order to relate the time varying pressures with the motion. Dependent on the mode shape and frequency investigated, pressure transducers located along the chord of the test airfoils are subjected to varying accelerations, both normal and parallel to the pressure sensitive diaphragm. Dynamic strain fields vary along the span and chord of the airfoils and may induce time varying strains in the pressure transducer, thus leading to erroneous data interpretation. To quantify these effects Allison has used an in-vacuum calibration procedure. This calibration system has been used exclusively on rectilinear cascade airfoils, but the procedure is valid for other non-rotating airfoils.

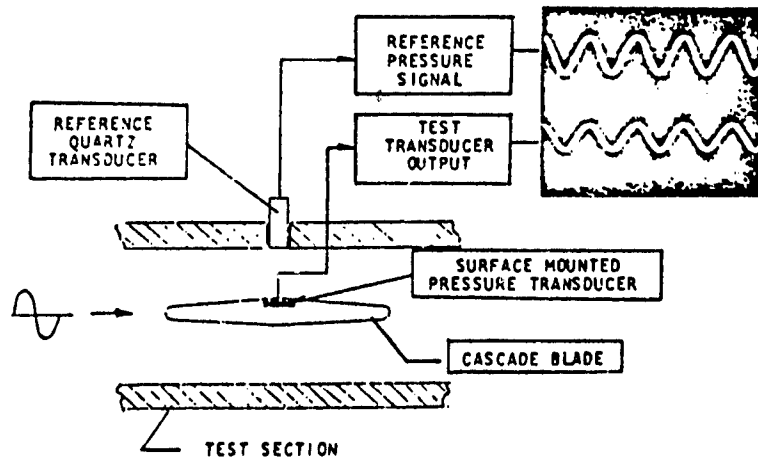
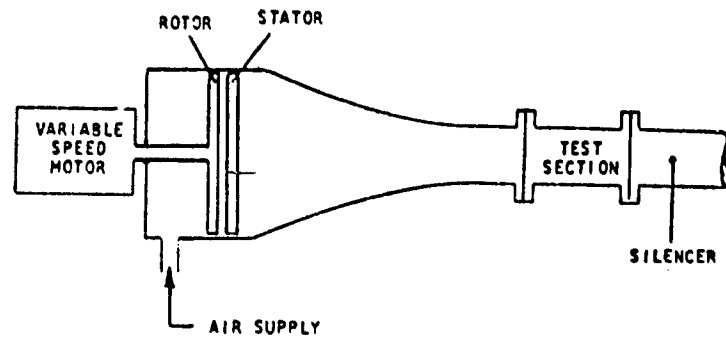


Fig. 15. Dynamic Calibration of Coated Pressure Transducer.

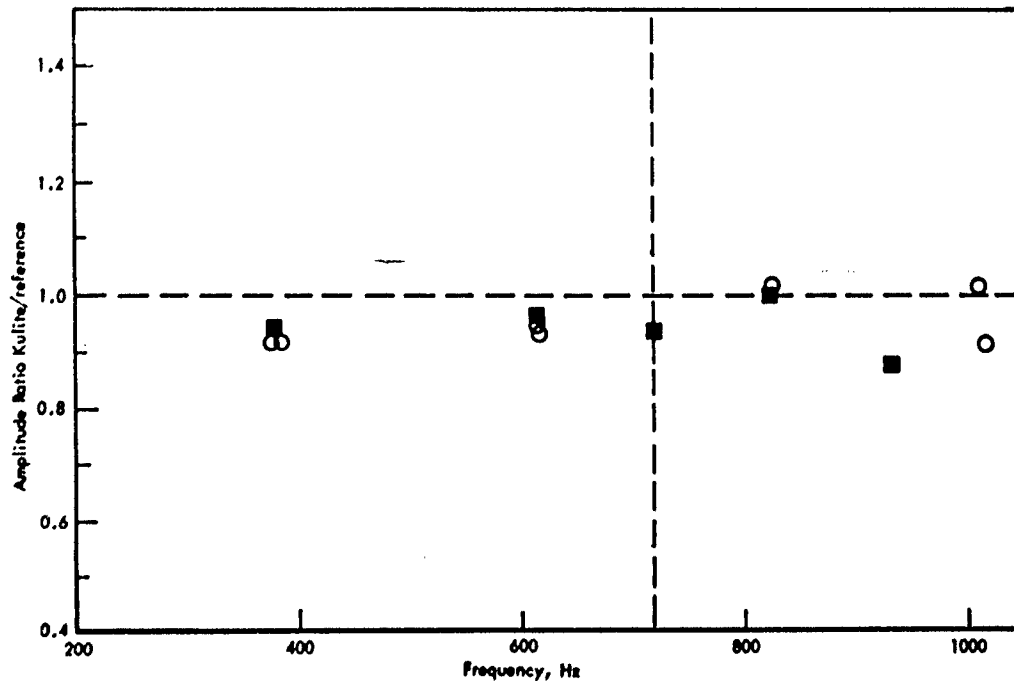


Fig. 16. Frequency Response Data for Kulites coated with RTV.

In obtaining time varying pressures from cascaded airfoils oscillating with coherent phase angles, Allison has used the concept of exciting the airfoils at their resonant frequency. This requires exacting frequency tuning, yet requires minimal power for inducing motion and allows extended frequency ranges to be investigated. In Figure 17, a photograph of a bench rig developed to duplicate the resonant characteristics of a test airfoil when installed in a cascade is shown. Frequency control is via sized torsion rods on either side of the end plates representing the sidewalls of the windtunnel. Excitation at the rigid body rotational natural frequency of the airfoil system is provided by small electromagnets in close proximity to dual driving arms providing torque input to the system. Strain gages, isolated from magnetic induced signals, are located on each torsion rod and are used to define the rotational amplitude of the test airfoil.

For calibration of acceleration and strain effects, the bench rig with the desired pressure instrumented airfoil is placed in a vacuum chamber. Power inputs and instrumentation leadouts are provided across the vacuum to ambient interface. Oscillations of the test airfoil are induced by providing voltages to the electromagnets at the resonant frequency of the system. Voltages from each of the installed pressure transducers are recorded at varying amplitudes. These voltages represent the sum of the accel-

eration and strain induced voltages, since both are functions of the first power of the deflection. Analyses of the signals provided an amplitude and phase calibration of the transducer in terms of airfoil motion. Using this calibration, unsteady pressure data acquired during cascade testing is corrected.

Calibration considerations for installation of high response pressure transducers on rotating airfoils have been reported by Grant and Lanati (1978). Lambourne (1980) presents a discussion on measurements of unsteady pressure in which dynamic calibration concerns are noted. These investigations emphasize the necessity of developing quantitative techniques to ascertain the installed response characteristics of high response pressure transducers.

Data Acquisition

Accurate characterization of the frequency and phase response of the measurement devices must be augmented by a similar characterization of the electronic conditioning necessary to record the desired data. In Figure 18 a dual path data acquisition scheme is illustrated. Conditioning equipment supplies required excitation voltage to the measuring device and provides amplification or attenuation of the time varying signals received from the device. These amplified or attenuated analog signals are processed via digital or analog devices.

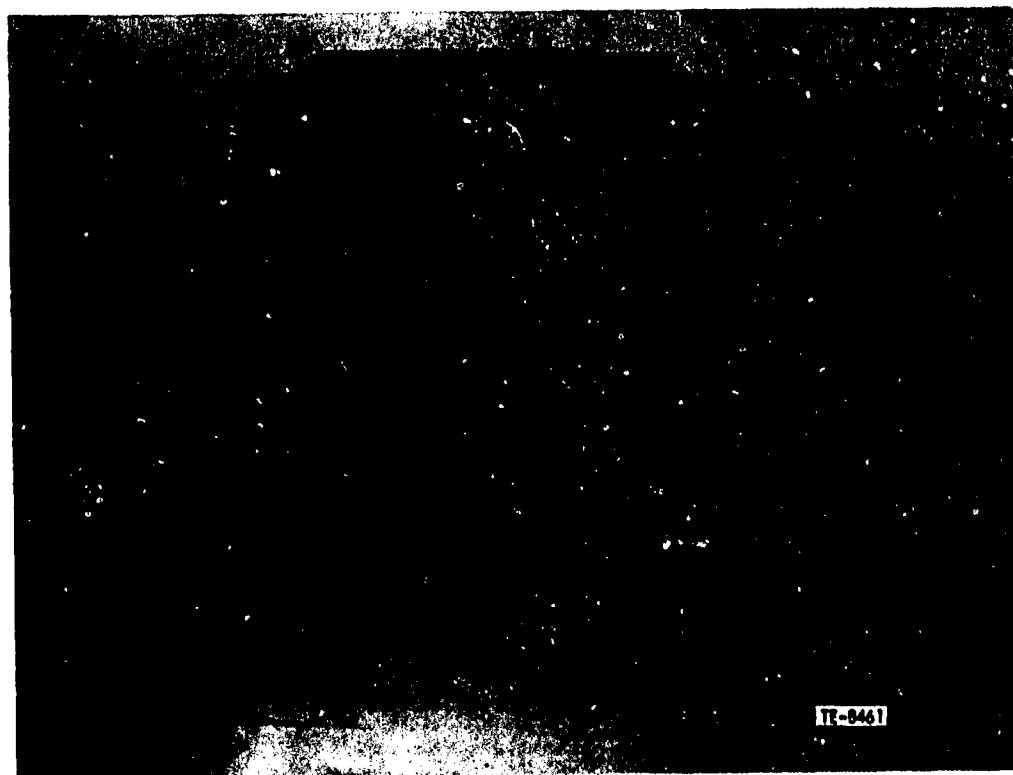


Fig. 17. Hollow Torsion Rod Drive System, Bench Rig.

Paramount among the considerations of each of the elements of an acquisition system is that of desired frequency ranges. Dynamic amplifiers, real time analyzers, and magnetic tape recorders generally have selectable frequency ranges. Analog to digital converters have digitizing rates which create effective frequency ranges. Thus, before final data are acquired, choices concerning the desired frequency range must be made based on expected signal character.

As an example, consider the pressure signal near the leading edge of a stator vane created by the passage of a rotor wake as shown in Figure 19. Harmonic analysis of the indicated raw signal was performed and from the analysis, the amplitude and phase of the first three harmonics were determined and plotted, the first harmonic corresponding to the rotor blade passage frequency. Summing the first three harmonics at each time value yields a fair approximation of the pressure signal, yet true representation was not obtained, indicating a necessity to obtain higher harmonic data. This implied that all systems in the data acquisition system should have frequency ranges at many times the frequency of the rotor blades passage. In this example all acquisition elements were configured such that a frequency range of ten (10) times blade passage frequency was investigated.

A second decision to be made in configuring a data acquisition system to meet a specific experimental requirement is that of on-line or off-line processing. On-line processing has the distinct advantage of providing immediate feedback to the experimentalist for more direct control of the experiment. Yet, in experiments with many parameters to be measured, equipment demands and/or testing times are large, and off-line pro-

cessing is necessary. Consequently, a common compromise is real time analysis of key variables via oscilloscopes and real time analyzers with complete data recordings via a multiple channel tape recorder furnishing off-line analysis capability.

In Figure 18, data in time domain are acquired via the analog-digital converter and oscilloscope (as oscillograph) and, generally, is acquired in the frequency domain via the real time analyzer. Time based data experimental observations such as those recorded by Dring (1981) can be used to provide detailed insight into unsteady flow mechanisms. Frequency domain data has been extensively used to determine the amplitude and phasing of pressure perturbations along oscillating airfoil surfaces in supersonic flutter testing as documented by Fleeter (1976). The choice of using the time or frequency domain for data acquisition, therefore, is dependent on the analysis techniques used in the particular investigation. To illustrate time and frequency domain data, Figures 20 and 21 are presented. These data were acquired from airfoils undergoing excitation from an upstream stator row as reported by Jay (1984). The analog data in Figure 20 is presented as strain gage voltage output versus time. In this figure the sinusoidal characteristics imply blade resonance, and the coherence between the signals from the seven gages imply a phased motion. An expanded cross correlation analysis performed on the same data is shown in Figure 21. In this figure maximum correlation between gages 1 and 8 identifies the resonant frequency and the phase trace identifies the phasing between the signals from the airfoils. For this experiment, on-line monitoring was performed using oscilloscopes and the data shown in Figures 20 and 21 processed off-line.

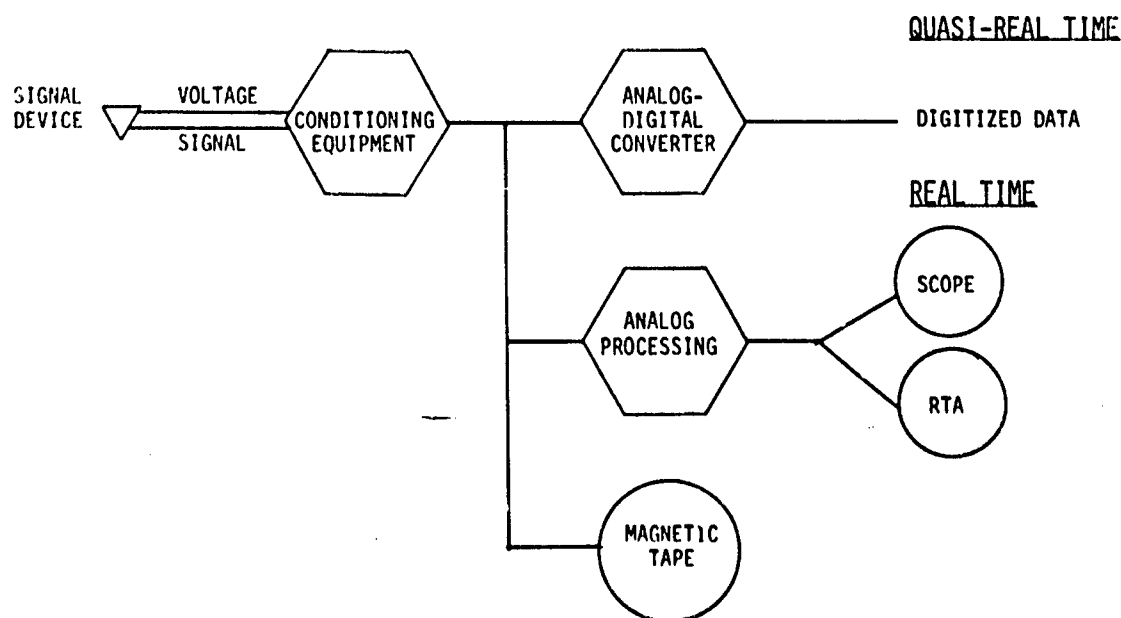


Fig. 18. Schematic of a Dual Path Data Acquisition System.

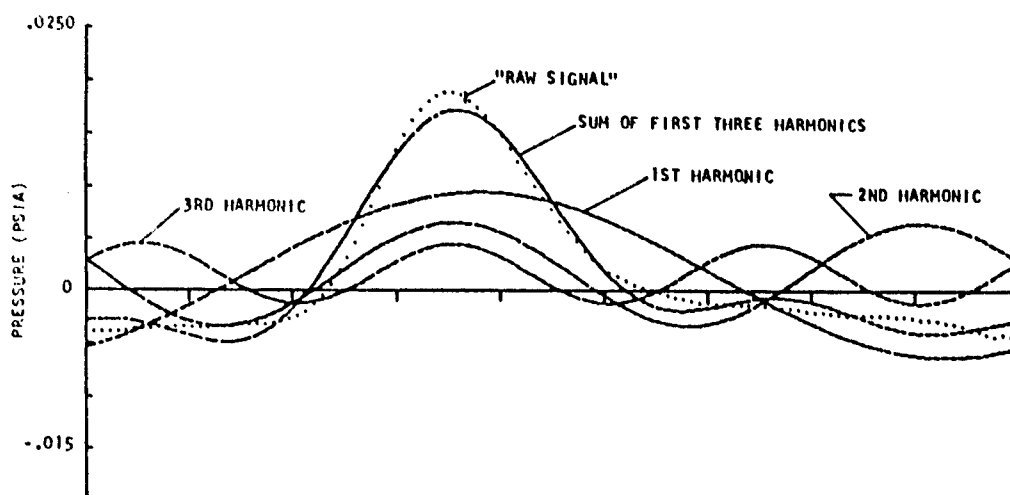


Fig. 19. Example of One Blade Passage Averaged Signal and the First Three Harmonics for the Leading Edge Pressure Surface Transducer.

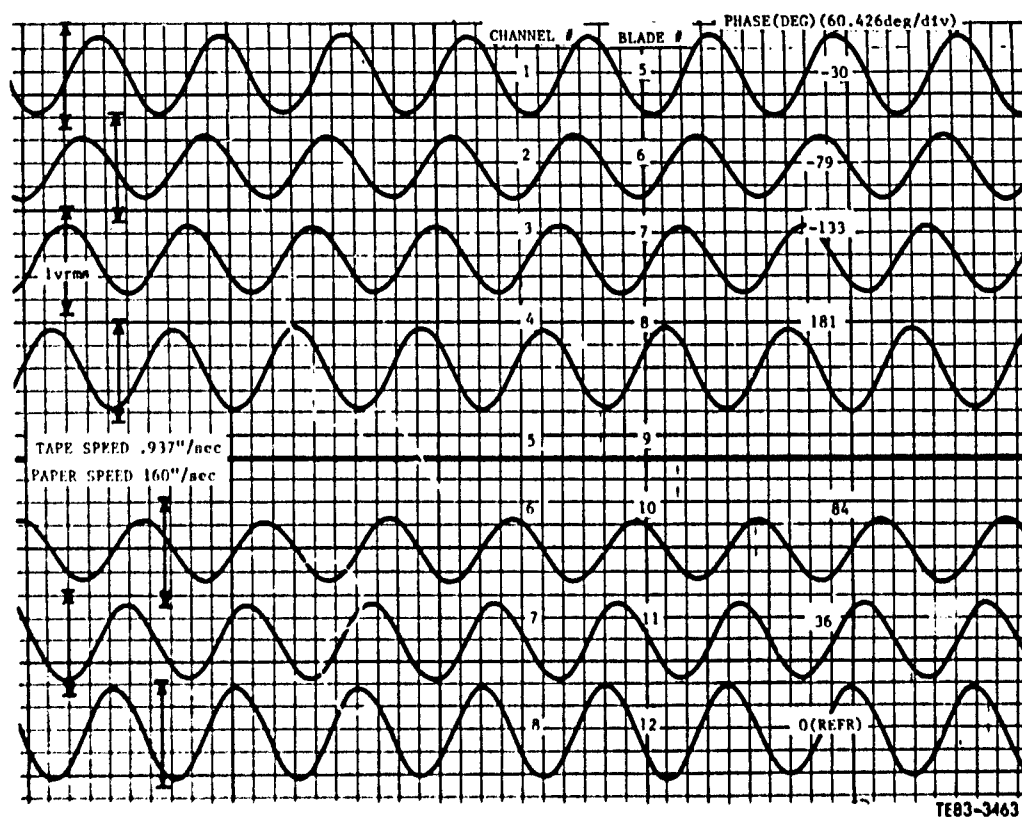


Fig. 20. High Speed Oscillograph at Resonance Peaks.

Currently, the use of computer controlled, high speed analog to digital converters to acquire high response data has been demonstrated to be exceptionally useful in experimental aeroelasticity investigations. Carta (1980) presents a schematic of such a system and defines the effectiveness in terms of experimental guidance and more rapid data processing. Fleeter (1976) presents a discussion of a computer controlled experimental program in which the central feature was a high speed analog to digital converter having a digitizing rate of 100,000 points per second.

Fundamentally, two types of A-D systems are in current use. For this discussion, the two will be referred to as parallel and sequential. A parallel system will be defined as an A-D system with multiple signal inputs and a connector for each input channel. A sequential system will be defined as having multiple signal inputs, but a single time shared converter. The differentiation between data acquired from each of these systems is illustrated in Figure 22.

Operating on identical sinusoidal patterns, the parallel processor acquires data simultaneously from both inputs A and B at time increments of T . The quantity T is the inverse of the digitizing rate as expressed in points per second. In a parallel processor having N inputs and a digitizing rate of M points per second, an acquisition time of T seconds will result in an array of $M \times N \times T$ data points. Each signal would be represented by a vector of $M \times T$ data points.

Assuming that the digitizing rate M , expressed in points per second, is the same for a sequential processor, data as shown in Figure 22b would be acquired. At time equal zero a data point would be converted from signal A, followed by a data point at T later in time from signal B. Thus, the data points from

signals A and B are not acquired at the same instant of time. In a sequential processor having N inputs and a digitizing rate of M points per second, an acquisition time of T seconds results in acquisition of $M \times T$ data points. Each input signal would be represented by $M \times T / N$ data points which would be displaced in time with respect to other signals.

This distinction between the two systems is no hindrance to proper acquisition, yet the manner in which the data is acquired plays an important role in the analyses which must later be performed. Digitizing rates must be specified with regards to both the number of points needed to accurately characterize a signal and the number of points which can be stored via computer memory for digital tape.

The final item to be discussed in the data acquisition system is the magnetic tape record. This recording system finds widespread use because of its capability to faithfully reproduce analog signals to very high frequencies. Recordings of signals provide a capability to recreate events in order to provide additional details, furnish analog data for off-line evaluation, and provide a means to alter the time base of the recorded signals.

In specifying a tape recorder for use in an acquisition system, care must be taken to examine the desired frequency range and the resolution required from the recorded signal. Tradeoffs between frequency response and recording time which are functions of tape speed must be made in experiments where reloading of tape reels is not practical. Phase lag can occur between channels in tape recorders due to head placement. The lag occurring due to this phenomenon is a function of frequency. Therefore, for proper use in experiments when phase determination is desired, reference signals

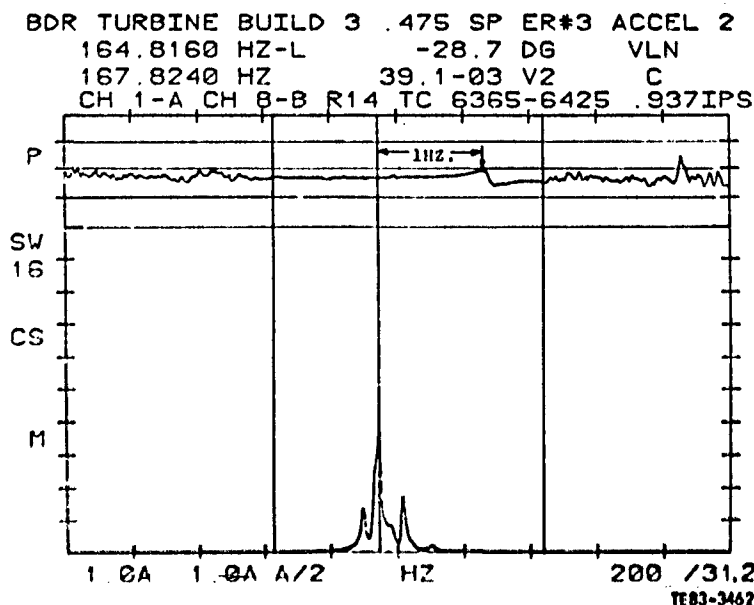


Fig. 21. Expanded Cross Spectrum.

with known phasing can be recorded at the desired frequency and analysis of the recorded signals used to properly compensate for induced phase errors. Resolution and phase checks should be performed at varying voltages and frequencies by inputting known signals, and obtaining playback data for comparison with the input signals. Calibration signals should be placed on each reel of recorded data prior to the data acquisition sequence, providing a reference for data analysis at a later time.

In summary, calibration techniques are necessary to obtain meaningful data from the high response instrumentation used in experimental efforts to understand the physical processes of the forced vibration problem. No one way is the best and only a limited sampling of techniques have been discussed. Special applications of transducers will require special calibration procedures. In establishing data acquisition systems, the obvious primary drivers are those of frequency capabilities and amplitude resolution. Analog and digital systems are capable of obtaining needed data and each experimentalist must choose a system which delivers accurate data in the proper format desired. High speed analog to digital systems controlled by computers with large memories represent the wave of the future, yet by no means do they represent the only way to acquire data necessary to aid in the solution of forced vibration problems.

EXAMPLES OF INVESTIGATIONS REGARDING AERODYNAMIC DAMPING AND GUST LOADING

In this and the previous chapter (Unsteady Aerodynamic Measurements in Flutter Research), discussions of the forced vibration and flutter problems were used to define the aerodynamic parameters and reduced frequencies of concern. The facilities used by various investigators were examined to define the manner by which the facility could be used for gathering appropriate unsteady aerodynamic data. An overview of experimental efforts of those investigators pointed out unique experimental techniques, data acquisition systems, and methods of data analysis. Calibration and data acquisition concerns were presented, since both must be answered to ensure data quality. In this section, a more detailed discussion of experimental efforts to acquire aerodynamic damping and gust loading of airfoils will be presented. For discussion of the aerodynamic damping, important to flutter and forced vibration, efforts involving a linear, two dimensional cascade consisting of five high turning airfoils will be presented. This research reported by Jay (1980) was sponsored by the Department of the Navy through the Naval Air Systems Command. Definition of the experimental program to define the unsteady response of a stator to an upstream gust created by blade wakes will be made. This experimental program was sponsored by the Air Force Office of Scientific Research and has been reported by Fleeter (1976b) and Bettner (1982). In these discussions, the primary thrust will be to describe the techniques used to acquire both steady state and time

varying data and to illustrate the data presentation used for comparison with analytical models.

Aerodynamic Damping Study

Facility Description

A rectilinear turbine cascade facility was conceived and built as a research tool to evaluate the steady aerodynamic characteristics of turbine blade sections having high turning. The facility is a continuous-flow, nonreturn, pressure-vacuum-type wind tunnel; the test section is evacuated by two primary steam ejectors. Up to 10 lbm/sec of filtered, dried and temperature-controlled air can be used.

The major features of this facility include the following:

- o Continuous operation for extended time periods
- o A mechanized test section for changing cascade incidence angle
- o A schlieren optical system for visual observation and photography of the facility in both steady and unsteady operation
- o Bleed systems on all four cascade inlet sidewalls
- o A sophisticated instrumentation system centered around two digital mini-computers

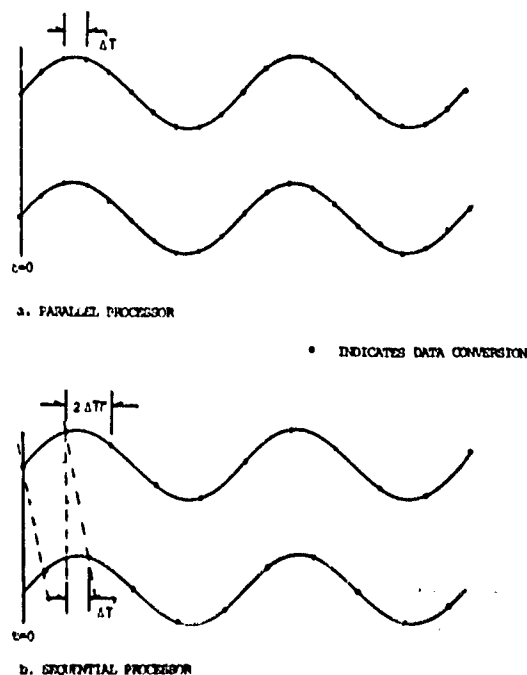


Fig. 22. Illustration of Parallel and Sequential Processors.

In the cascade facility, the entrance flow to the test section is generated by parallel nozzle blocks, (Figures 13 and 23) which set the inlet flow direction. The upper nozzle block is movable to ensure that all the flow is directed through the cascade. The cascade inlet Mach number is determined by the cascade geometry under test.

To aid in the establishment of the cascade inlet periodicity, bleed chambers are provided in the upper and lower nozzle blocks. Adjustments of the bleed rate through these chambers allows the inlet flow field to the cascade to be affected.

Active cascade-inlet sidewall boundary-layer control capability to ensure the two-dimensionality of the cascade flow is effected by the use of suction strips in the cascade sidewalls. Two bleed-hose connections on each strip with separately variable valves provide appropriate bleed flows to the front and rear portions of the sidewall. A third, smaller steam ejector is used to evacuate all of the bleed systems used.

The cascade has dummy end blades presenting one surface to the flow, as shown in Figures 23 and 24. The front dummy blade slides along the movable upper nozzle block as the incidence angle is changed. Adjustable porous tailboards are hinged on the aft ends of the dummy blades, serving to set expansion ratio and exit periodicity. The porous tailboards generate a bleed effect because of the lower exit plenum pressure on their outside surfaces. This bleed

prevents shock wave reflections back into the cascade during transonic exit operation.

For definition of the steady-state operation, static pressure taps are placed on the tunnel sidewalls in the inlet and exit planes of the cascade. Each airfoil passage is so instrumented to allow checks of cascade periodicity, using the static to inlet total pressure ratio. Upstream total pressure and temperature probes are used for definition of the upstream field, and a five hole conical pressure probe is used to scan the exit flow field to establish losses and to check exit flow periodicity.

This specific cascade was designed to obtain the relative flow fields consistent with an advanced design turbine rotor. The inlet Mach number was established as 0.5, while by control of the exit tailboards and exit air valve, exit Mach numbers relative to the airfoils ranging from 0.7 to 1.3 could be obtained.

The ability of the high turning cascade to properly simulate a turbine rotor, coupled with the need to acquire aerodynamic damping measurements in terms of unsteady surface pressures in this flow regime, led to the formulation of an experimental program. Obtaining realistic torsional reduced frequencies for investigation required developing techniques to oscillate the airfoils in phased, harmonic motion. Additionally, designs to incorporate surface pressure transducers were conceived and implemented.

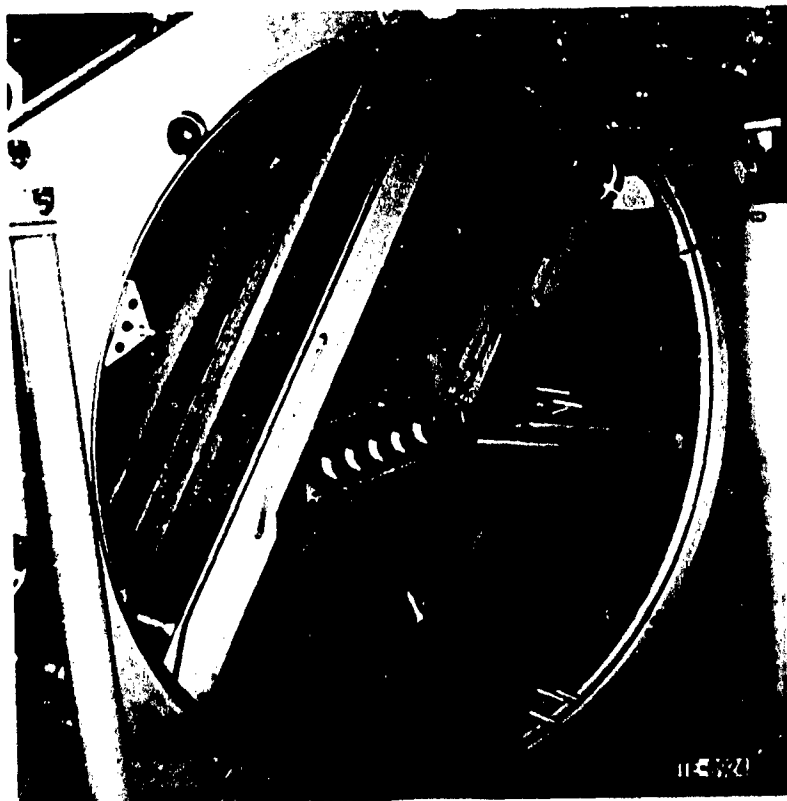


Fig. 23. Photograph of Turbine Rotor Cascade Hardware.

Airfoil Cascade and Instrumentation

The two-dimensional cascade used in this investigation comprises five airfoils that have the profile of a high-turning turbine rotor section. Trunnions were attached to both ends of each airfoil for support in the cascade side-walls. The physical dimensions of the airfoils are a 3.00-inch span, a 2.59-inch chord, a maximum thickness of 0.53 inch, and 112° of turning. The cascade physical parameters are listed in Table 2.

| Table 2. Description of Turbine Airfoil Cascade | |
|--|-------------------|
| Physical Parameters | |
| Chord | 2.59 in. |
| Solidity | 1.891 |
| Setting angle | 25.5 deg |
| Maximum thickness/chord | 0.205 |
| Leading edge radius/chord | 0.024 |
| Trailing edge radius/chord | 0.009 |
| Axial Chord projection | 2.34 in. |
| Torsion axis location | 35.5% (from L.E.) |

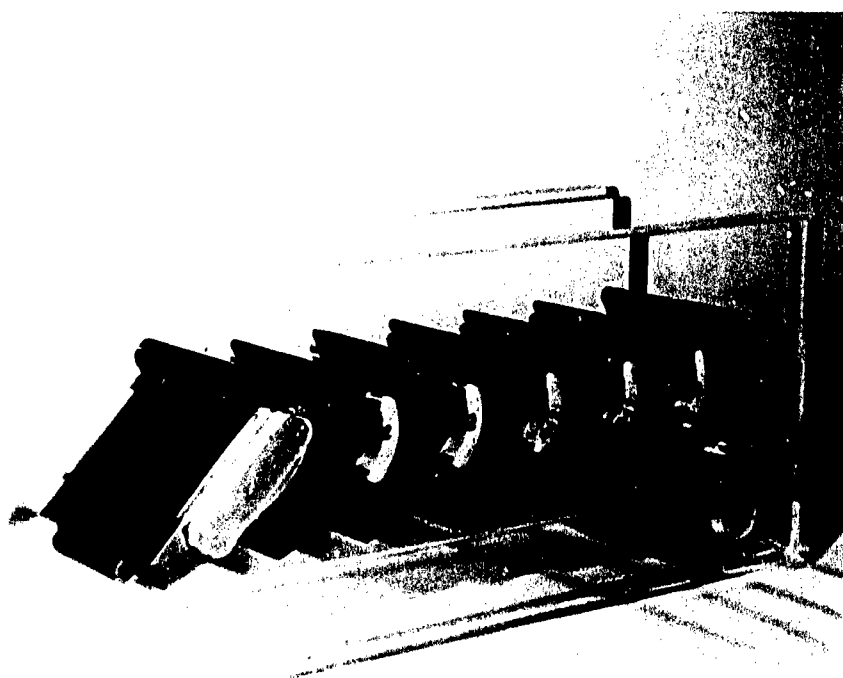
The cascade airfoils consisted of injection-molded fiberglass with a Kevlar outer wrap. Steel trunnions were attached to both ends of each airfoil with screw clamps and pins. These trunnions

were supported in bearings, and the airfoil setting angle was maintained by the clamps of the cascade drive system. Paths for the instrumentation wires and pressure tubes were machined into the blade surface, and the trunnions of the instrumented blades were hollow to allow the wires and tubes to exit the cascade.

For the steady-state testing, the center blade of the cascade was instrumented with nine static pressure taps per surface for definition of the surface pressure distributions. For the time-variant phase of the experiment, the center blade of the cascade was instrumented with 12 miniature high-response Kulite pressure transducers. These Kulites were staggered across the center 50% span of the airfoil, five on the pressure surface and seven on the suction surface. The instrumented airfoil is shown in Figures 25 and 26 for the location of the transducers on the suction and pressure surfaces, respectively.

Oscillation Mechanism

The desired range of reduced frequency for investigation was established by examining resonances of turbines having coupled bending and torsion (blade/disk) modes. From this study a value of reduced frequency in torsion of approximately 1.0 was desired. This led



TE-8925

Fig. 24. Airfoil Cascade in Windows.

to the design of a torsional oscillation system having a resonant frequency of approximately 350 Hz.

An analytical model as shown in Figure 27 was constructed to determine the torsional stiffness required to mount the airfoils to obtain a rigid body torsional (rotational) motion of the airfoil at the prescribed 350 Hz frequency. These requirements could be met by installing precision bearings on each of the airfoil trunnions, providing bearing accommodation and sealing arrangements in the tunnel sidewalls for each airfoil, and by connecting the trunnions to a grounded plate through sized spring bars. To provide the capability to oscillate the airfoil, an arrangement was used whereby electromagnets on each trunnion acted on steel targets located at a fixed distance from the centerline of rotation as established by the bearings. A bench rig used in calibration studies featuring these arrangements is pictured in Figures 28 and 29.

Calibration Procedures

Calibrations were performed before the time-variant data were acquired so that the transfer functions throughout the measurement system could be determined. Included in these calibration measurements were strain gage dynamic

sensitivities, Kulite static sensitivities, Kulite amplitude and phase shift components due to oscillation, amplifier and signal conditioner gains and phase shifts, and phase shifts between channels of the magnetic tape recorder.

For the calibration of the strain gages on the spring bars, the torsion drive system bench rig shown in Figure 29 was used. The system was first tuned to the desired frequency with a specific pair of spring bars, and then the amplitude of the strain gage signal was read by a minicomputer. The amplitude of the blade motion was obtained by using a dial indicator and height gage to measure the difference between the upward peak height of the trailing edge and at-rest position. The difference between the downward peak height and at-rest was similarly obtained. The linear motion at the trailing edge was thus the sum of these measurements, which was converted to torsional amplitude by using the length of the blade from axis to trailing edge. This procedure was repeated for several amplitudes, resulting in a linear plot of voltage versus torsional amplitude. The slope is the sensitivity expressed in mV/V/radian when the bridge voltage is divided out. The sensitivity of each pair of spring bars was calibrated in this fashion. In addition, measurements along the span were used to ensure rigid body rotation.

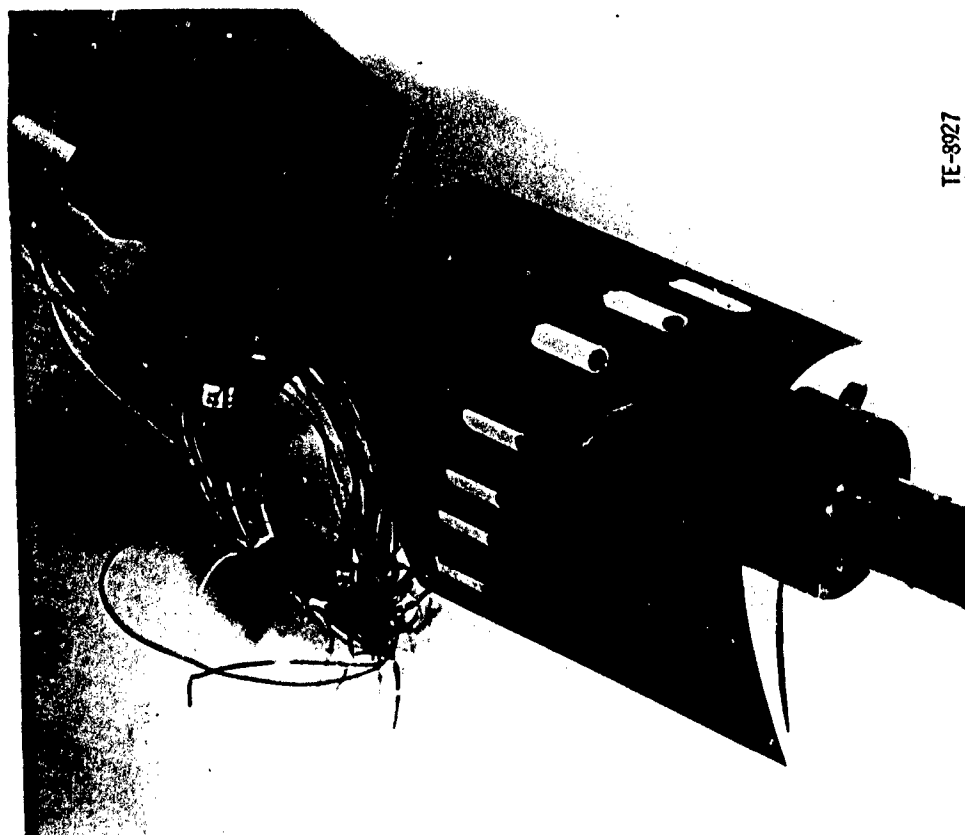


Fig. 25. Kulite Transducer Installation - Suction Surface.

7E-8921

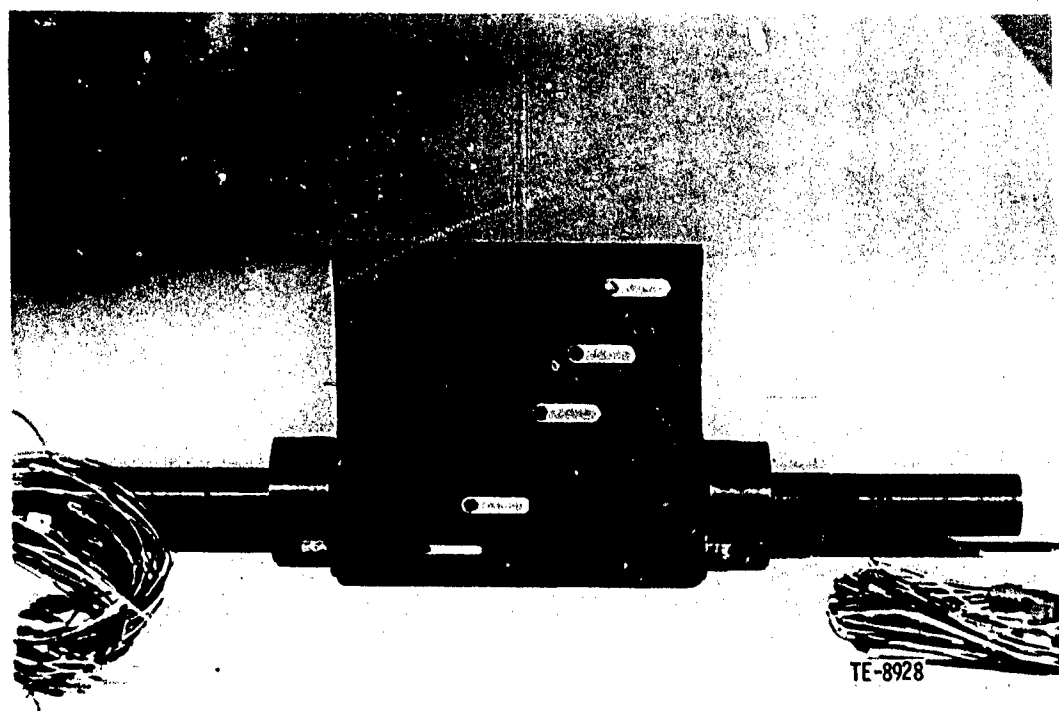


Fig. 26. Kulite Transducer Installation - Pressure Surface.

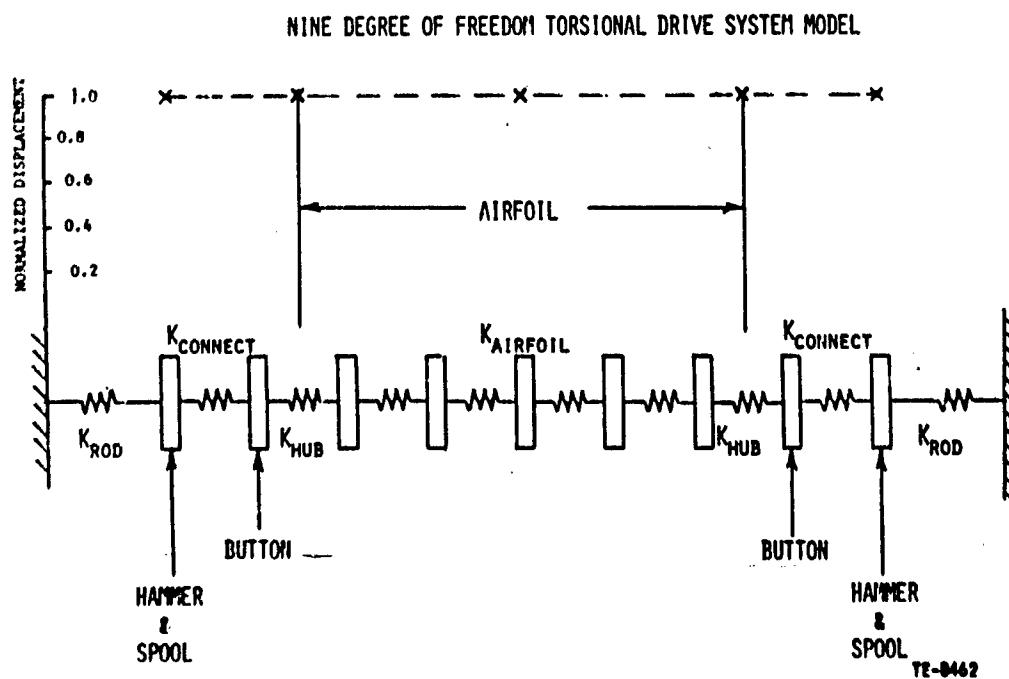


Fig. 27. Torsion Airfoil Analytical Model.

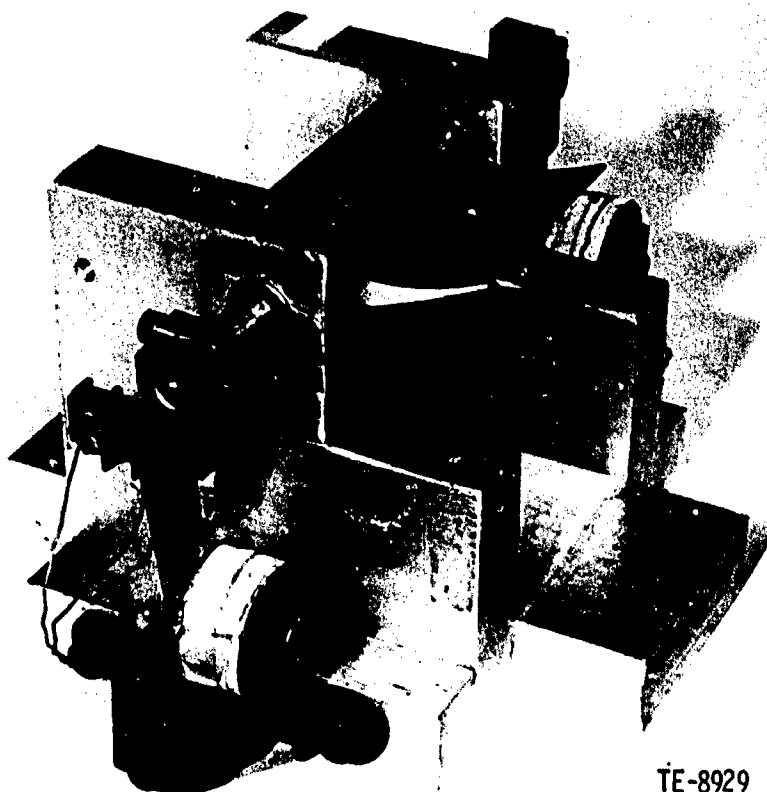


Fig. 28. Torsion Drive System Bench Rig.



Fig. 29. Torsion Drive System Bench Rig.

The Kulite pressure transducer static sensitivities were obtained with a vacuum-jar calibration rig. A quartz manometer-controller was used to evacuate the jar containing the Kulite-instrumented blade to the desired pressure. The d-c voltage output of each Kulite was measured over a range of pressures, resulting in plots of voltage versus pressure. The sensitivities in mV/psi were the slopes of these linear plots. These sensitivities compared closely with manufacturer-supplied data.

A Kulite pressure transducer mounted on an oscillating airfoil is subjected to forces resulting from acceleration of the transducer diaphragm and strain transmitted to the transducer through its mounting as well as to forces from the pressure to be measured. To determine the acceleration/strain contribution to the Kulite signal, the instrumented blade was oscillated in the bench rig in a vacuum. Under these conditions, no pressure-induced signal was present. The remaining signal was therefore the result of acceleration/strain effects alone. The minicomputer was used to measure the amplitude and phase shift of each Kulite signal over a range of rotational blade amplitudes. The data plots of signal versus torsional amplitude were linear. A calibration of acceleration effects was thus obtained and stored in the computer data analysis program to allow corrections to the final data. These effects were less than 5% of a typical pressure measured during time-variant testing.

The transducer mounting technique used for this cascade instrumented airfoil featured a perforated metal screen cover over each transducer, made flush

with the airfoil surface as shown in Figures 25 and 26. This method demonstrated an acceleration sensitivity of approximately half that obtained with an RTV diaphragm coating previously used for cascade airfoils.

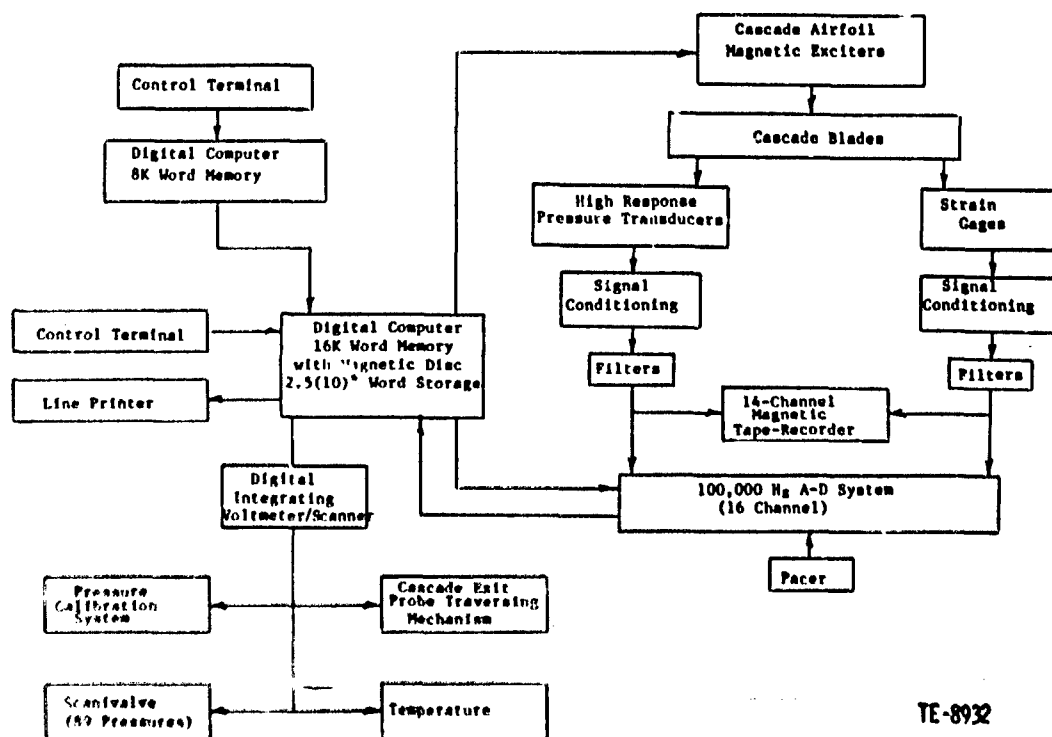
The dynamic response of the blade-mounted Kulites to an oscillating pressure was not obtained. Experience with mounted Kulites had shown that the dynamic characteristics of the Kulites are sufficient for measurements at the frequency used in this testing.

To complete the calibration for the experiment, the gains and phase shifts of all the other electronics were determined and stored in the computer for on-line corrections.

Data Acquisition and Analysis

The primary components of the data acquisition system, including the equipment for on-line and off-line analysis, are shown schematically in Figure 30.

With the tunnel in operation, the steady-state data were measured, using the minicomputer system interfaced with a Scanivalve pressure cabinet and crossbar scanner. Steady-state periodicity was established at the desired expansion ratio, and a cone-probe exit survey was made to yield the aerodynamic performance, wake definition, and mass-averaged properties. Schlieren photographs were also taken at the transonic exit operating points to show trailing edge shock structures. The computer listed each measured pressure, including the surface static pressure of the instrumented center airfoil.



TE-8932

Fig. 30. Schematic of Data Acquisition System.

For the oscillating airfoil testing, the center airfoil was replaced with the airfoil instrumented with high response pressure transducers. Operating conditions as described by the steady-state data obtained previously were re-established and the airfoils were oscillated at varying interblade phase angle with amplitudes controlled consistent with available driving energy. To obtain the phased motion, the 8K Word Memory Computer was programmed to switch power to each pair of electromagnets on each of the five blades in the cascade. Since perfect tuning of the cascade airfoil suspension systems was not possible, each airfoil operated near its resonance frequency. The phase shifts occurring in a lightly damped system in the neighborhood of its resonant peak amplitude resulted in discrepancies in the blade to blade desired interblade phase angles. A cross correlation analysis programmed on the 16K Word Memory Computer was used in conjunction with the sequential A-D system to obtain actual phasing between the blade motions as indicated by the strain gages on each spring bar. This on-line feature allowed phase corrections to be entered via the smaller computer.

After the desired interblade phase angle was established, the signals from the Kulite pressure transducers were recorded on the magnetic tape recorder with a center-blade strain gage signal for phase reference.

The recorded Kulite signals were analyzed off-line with the aid of the analog-to-digital multiplexer and the minicomputer. An averaging technique was used to establish raw signals. These signals were then corrected as described by calibration information. Pressure amplitude and phase angles were thus obtained for each Kulite on the airfoil surfaces.

In the processing of the Kulite signals, a data enhancement scheme was used. A recorded reference signal, the square wave voltage delivered to the electromagnets on the center airfoil, was electronically shaped and provided a trigger to the A-D system. Upon triggering, digitizing of the analog signals was performed over a time period equal to six cycles of oscillation. The digitizing process and the number of points acquired was controlled by the computer. These data were arranged internally in the computer and the computer then initiated acquisition of a similar data set from the taped signals. One hundred data sets were thus acquired, representing samples from different times in the recorded test sequence. Averaging each digitized data point corresponding to a precise time of acquisition and transducer for the 100 samples was accomplished to obtain a six cycle enhanced digital representation of the analog signal. This digital representation was then analyzed using Fourier techniques to furnish both amplitude and phase of all signals referenced to the motion of the center airfoil. All phase and amplitude corrections necessary based on calibration information as described previously were made via the computer to obtain representation of the data in engineering units.

Presentation of Data

To provide experimental data for examination of the adequacy of various analytical models, a presentation format in which normalized pressure coefficients and phase lags for each of the transducers was adopted. The normalized pressure coefficient was defined as the amplitude of the measured unsteady pressure divided by the product of twice the inlet dynamic head and the rotational amplitude of the instrumented airfoil. The phase lag for each transducer was referenced to the motion of the same airfoil. These coefficients and phase lags were plotted versus their position along the projected chord of the airfoil. Typical plots are shown in Figures 31 and 32.

Further data analysis yielded similar plots representing the pressure differences and phasing across the airfoil. Integration of these pressure differences over the chord length could then be accomplished to furnish the unsteady lift and moment coefficients due to the rigid body rotation of the airfoil, and thus determine the aerodynamic damping.

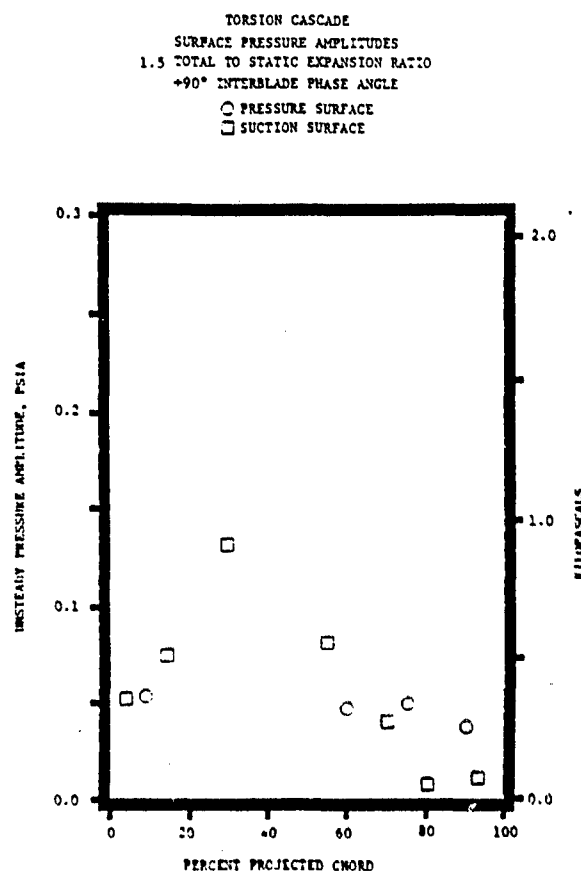


Fig. 31. Normalized Pressure Coefficient.

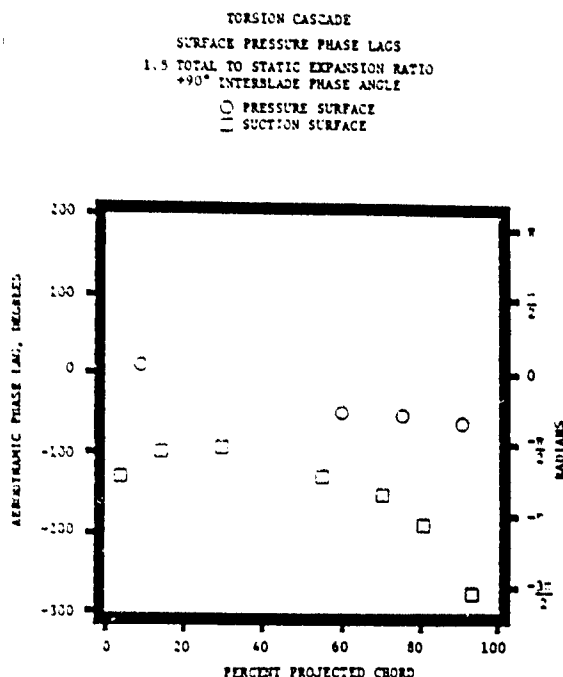


Fig. 32. Phase Lag, Pressure Surface.



Fig. 33. Low Speed Compressor Rig Facility.

Gust Loading of Stator Vane

Facility Description

In this investigation, a Low Speed Compressor Facility (LSCF) was used. The blading and flow path of the LSCF have been designed to reflect realistic aerodynamic values of blockage, blade loading and loss levels, and tip clearance, along with realistic geometric design parameters that are typical of aft stages of modern multistage compressors. Also, the Reynolds number at the compressor inlet is typical of modern compressors, i.e., greater than 200,000. The blading and flow path are physically large enough to allow high-quality, detailed endwall boundary layer measurements to be made over the entire endwall.

Resulting geometric and design point aerodynamic conditions for the low speed compressor, along with representative airfoil geometry, are listed in Table 3. Forty-two blades were used in the rotor design. The design features high camber with fairly large deviation angles near the hub region. Maximum thickness varies from nearly 7% of chord at the hub to 4% at the tip. The blade chord varies linearly with radius and yields a solidity of about 1.6 at the hub to 1.3 at the tip. Blade incidence was set between +1.2 to -1.0 degree limits. Fiberglass material was used for the blade profile and platform. The fiberglass material was molded around a flat steel spar that passed from the tip section of the blade down through the blade and was welded to a steel base plate. The blades are held in the wheel by a T-shaped base arrangement that allows blades to be easily changed in the wheel without disturbing the basic wheel design.

Table 3.
Low Speed Compressor Design Input

| | | |
|---------------------------------|--------|--------|
| Flow rate, $W/\theta/\delta$ | 31.01 | lb/sec |
| Tip speed, U_t/θ | 183.50 | ft/sec |
| Rotational speed, N/θ | 876.30 | rpm |
| Stage pressure ratio, R_c | 1.0125 | |
| Stage efficiency, η_{TT} | 88.1% | |
| Inlet tip diameter, D_t | 48.00 | in. |
| Hub/tip radius ratio, r_h/r_t | 0.80 | |
| Blade span, l | 4.80 | in. |
| Blade chord, C_b | 4.589 | in. |
| Blade aspect ratio | 1.046 | |
| Blade solidity, C_b/s | 1.435 | |
| Vane chord, C_v | 5.089 | in. |
| Vane aspect ratio, l/C_v | 0.943 | |
| Vane solidity, C_v/s | 1.516 | |

Nearly the entire axial length of the flow path features a transparent Plexiglas casing sector that covers a circumferential extent of 108 degrees. This transparent casing permits a utilization of flow visualization techniques.

The assembled test rig with 1.0 aspect ratio blading is shown installed in the test facility in Figure 33. Fore and aft center bodies are supported and, hence, blade and vane end clearances are established by five struts located in the far front of the flow path and five struts located downstream of the stator. The struts are 10% thick 65 series symmetric airfoil contours.

Table 3 shows that both the overall rig and the airfoils are large. The large airfoils permit detailed, accurate studies to be accomplished without having to resort to extreme miniaturization of instrumentation.

Figure 34 illustrates the low speed compressor path, showing the blade and vane locations along with the transparent windows and the arrangement of the rotating components. The flow-path hub/tip radius ratio was held constant at 0.8 for a large distance both upstream of the rotor and down-stream of the stator. This flow-path contour not only simplified inlet and exit station instrumentation design but also provided the axial length upstream of the rotor to dictate the characteristics of the rotor inlet boundary layer.

Vane Design

The vane features a large camber angle variation in the hub region, a radially constant maximum thickness/chord distribution, and incidence that varies from about 0 to -1 deg. Vane solidity varies from 1.68 at the hub to 1.35 at the tip. Forty vanes were incorporated in the stage design. Fiberglass material forms the airfoil profile. It is molded around a steel spar that passes radially through the vane and is welded to the steel trunnion. The vane/casing interface design allows the vanes to be reset over ± 20 deg. from design setting angle. Figure 34 shows the vanes cantilevered from the casing with a stationary endwall under the vane hub. Table 4 summarizes the compressor design by presenting mean-section aerodynamic and geometric design values.

Table 4.
Airfoil Mean-Section Mechanical
and Aerodynamic Characteristics

| Type of airfoil | 65 ser. | 65 ser. |
|------------------------------|---------|---------|
| Chord, C--in. | 4.589 | 5.089 |
| Solidity, $\sigma = C/s$ | 1.435 | 1.516 |
| Camber, ϕ --deg | 20.42 | 48.57 |
| Aspect ratio, AR = L/C | 1.046 | 0.943 |
| Leading edge radius/C | 0.0044 | 0.0049 |
| Trailing edge radius/C | 0.0028 | 0.0030 |
| Inlet angle, β_1 --deg | 59.38 | 37.84 |
| Exit angle, β_2 --deg | 42.41 | 0.00 |
| Loss coefficient, \bar{w} | 0.043 | 0.056 |
| Diffusion factor, D_f | 0.449 | 0.410 |

Steady-State Instrumentation

Steady-state instrumentation consists of multiple-element total pressure rakes distributed circumferentially around the annulus at the stage inlet, stator inlet, and stage exit planes; boundary layer rakes on the hub and tip walls at the rotor inlet and stator exit; multiple-element total temperature rakes at the stator inlet and exit; and static pressure taps distributed around the annulus on the hub and tip walls and axially through the stage. This instrumentation arrangement is illustrated in Figure 35. In addition, 15 static pressure taps are arranged on the tip wall of one stator passage to allow mapping of the vane tip static pressure distribution. The stage inlet total temperature is measured in the plenum chamber located upstream of the flow-path annulus. All of the pressure instrumentation is connected to a six-unit 48-channel Scanivalve, interfaced with a Digitec scanner and driven by a Hewlett-Packard (HP) Model 2117F computer. Differential (0-1.0 psid) Druck pressure transducers are employed in the Scanivalve. A deadweight system provides reference pressures of 0.0, 0.5, and 1.0 psia to the Scanivalve transducers for continuous on-line calibration of the pressure measurement system.

Radial/circumferential hot-wire anemometer surveys are performed in the exit planes of the rotor and stator. In addition, radial/circumferential surveys can be performed at two axial locations inside the stator passage. Streamwise velocity and air angle are determined by positioning the probe at a fixed axial, circumferential, and radial location, and then by yawing the probe until the output voltages of the two hot-wires are the same value. DISA constant-temperature hot-wire anemometry equipment is used. The outputs are linearized and compensated for temperature differences that exist between the velocity calibration jet air stream and the rig flow field environment.

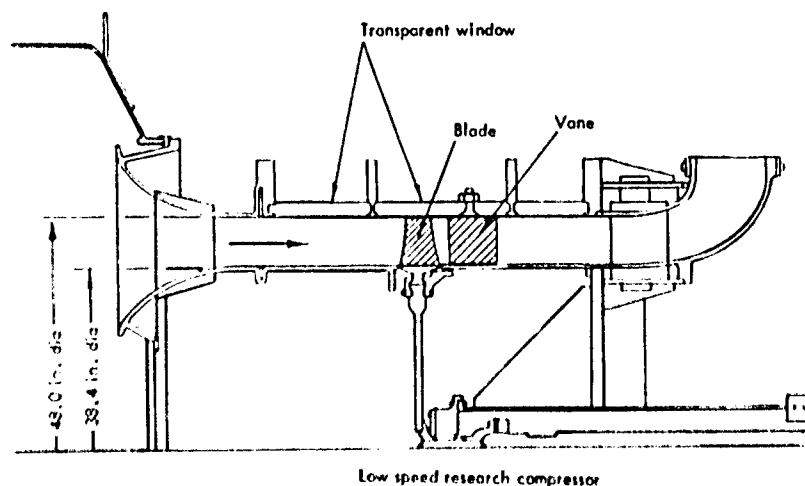


Fig. 34. Low Speed Compressor Flow Path.

TE-9181A

Applicability of LSCF Gust Investigations

This facility was examined relative to its potential in carrying out experimental studies relative to forced vibration, namely the effects of gust loading on the stator vanes created by the rotor wake and the potential interaction effects between the rotor and stator which creates unsteady loading on the rotor airfoils. The large, thick blades and stators were ideal for installing high response pressure transducers and a hot-wire system was available for quantification of the rotor wake velocity defects. The low axial Mach number of approximately 0.1 was viewed as low relative to the data base from engine testing, yet was deemed acceptable since gust data was critically needed to provide an experimental data base for examining the accuracy of analytical models. The blade passage frequency of 630 Hertz yielded a reduced frequency based on the stator vane chord and inlet relative velocity of approximately 14.0, a value consistent with engine experience. Therefore, the LSCF was selected to carry out investigations regarding gust loading of the stator vane and potential interaction effects on the rotor airfoil. In this discussion, only the investigation regarding gust loading will be presented.

Dynamic Instrumentation

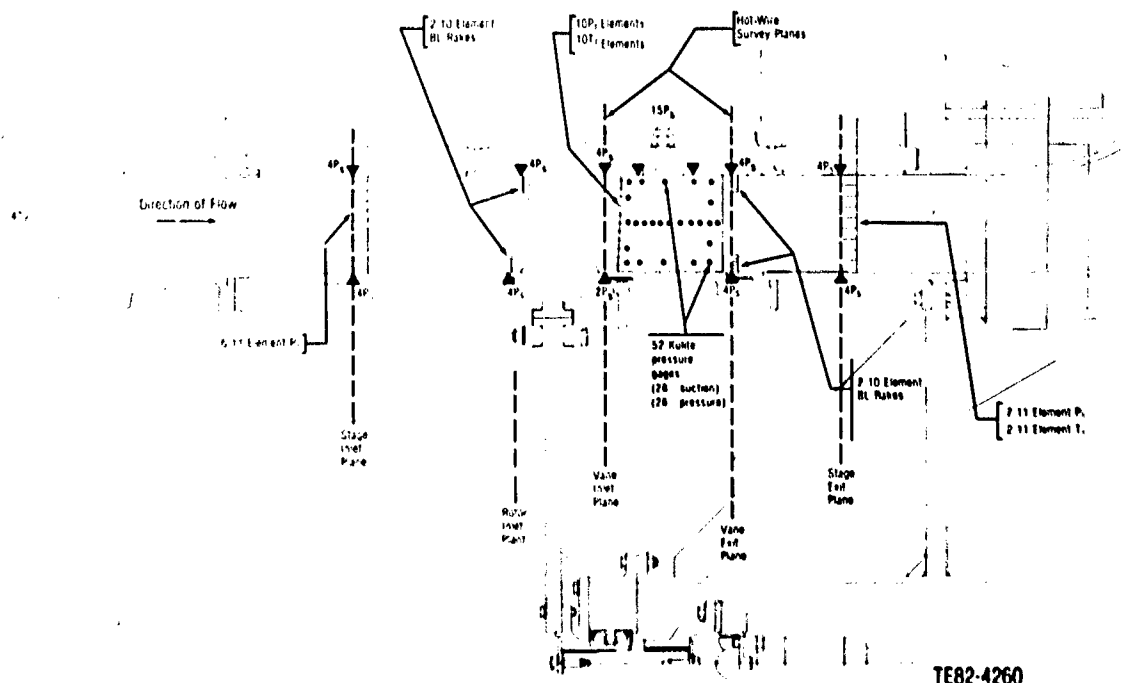
For time-variant measurements on the stator, miniature pressure transducers and a crossed-wire probe were used.

Kulite thin-line transducers were located on the surfaces of four stator airfoils. These transducers were flush-mounted by grooving the surface. The grooves, designed to accommodate the transducer, bonding agent, and lead wires, extend from the particular transducer through the stator trunnion. The grooves are clearly seen in Figure 36 on two of the mean-section instrumented airfoils used in this experimental program. Figure 37 shows the location of Kulite pressure transducers on the hub and tip sections and leading and trailing edge regions of two additional instrumented airfoils. A view of the crossed-wire probe used in the experiment is shown in Figure 38. In this photograph the wire is located near the center span instrumented airfoils.

Data Acquisition System and Calibration

The central element in the acquisition of the time-variant and steady-state data in this experiment is a digital computer with its specialized peripheral hardware. An HP Model 2117F computer operating under RTE1VB software is used with a Preston GMAD-2 analog-to-digital (A/D) conversion system to acquire data at a rate of up to 248,000 points per second. For data acquisition in the steady-state mode, the computer is interfaced with a Digitec scanner, which allows conversion of Scanivalve voltages to appropriate pressures as well as calculation of operating temperatures.

Calibration of the steady-state pressure measuring system is accomplished



TE82-4260

Fig. 35. Steady and Dynamic Instrumentation.

automatically and on-line. A deadweight system provides reference pressures of 0, 0.5, and 1.0 psia to the Scanivalve transducers. When the computer reads these pressures, a linear curve fit is used to establish a calibration curve for each of the six transducers. Then the data channels are interpreted, based on the proper curve. For time-variant pressures, the instrumented stators were placed in a pressure chamber, and five levels of pressure, ranging from 8 psia to slightly above ambient, were used to construct a calibration curve for each of the installed transducers. These curves

were read into the computer for transducer voltage conversions to pressure.

Calibration of the crossed-wire probe is obtained via a controlled temperature air jet capable of furnishing velocities over the range of interest. Data at standard temperature (room ambient) are obtained and represent a baseline velocity versus wire output voltage curve. This curve is linearized electronically using built-in features of the anemometry system. Corrections for temperature are made internally in the computer based on the temperature difference from the baseline value.

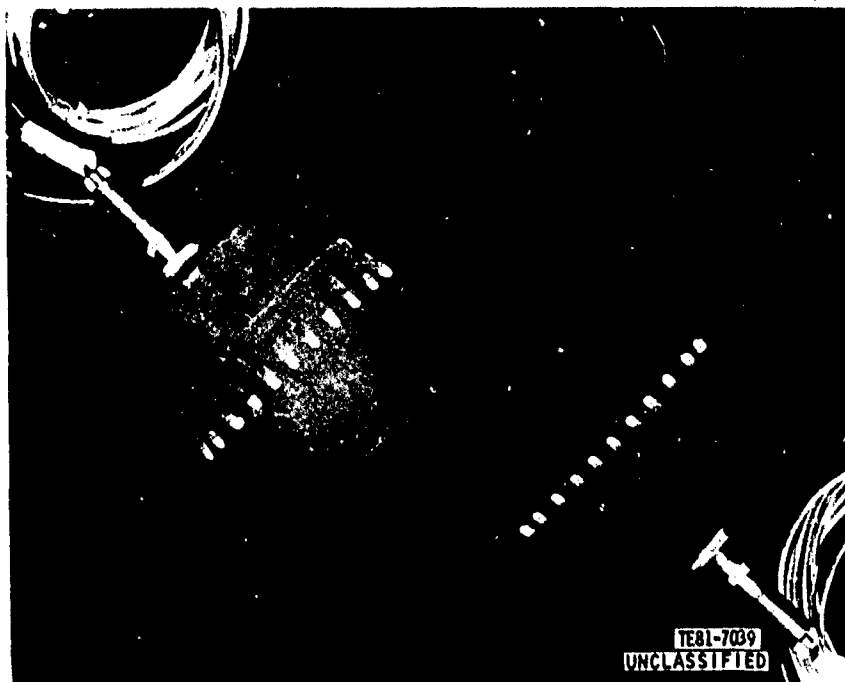


Fig. 36. Vane Mean Section Dynamic Instrument Locations.

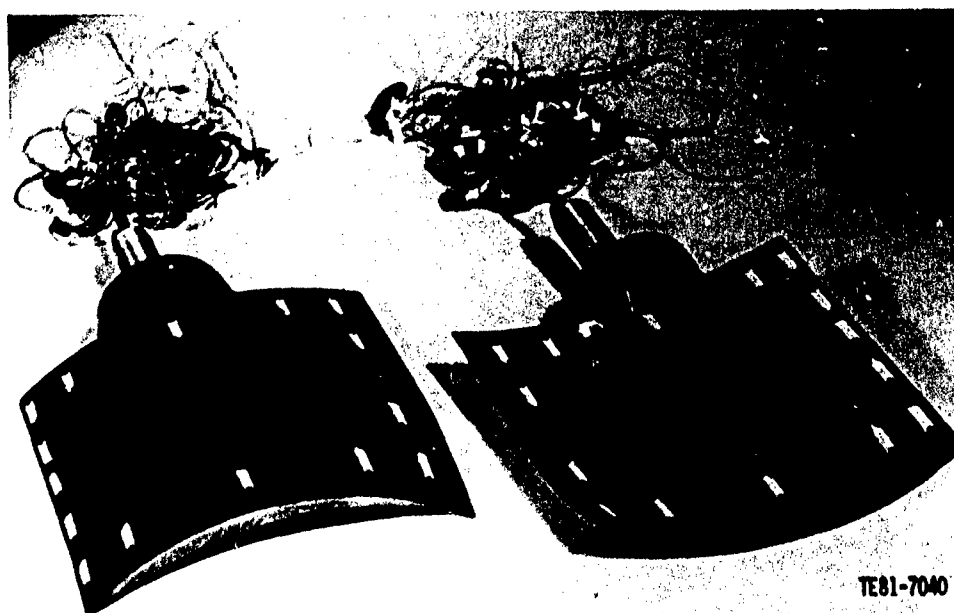


Fig. 37. Radial and Chordwise Suction and Pressure Surface Transducer Instrument Locations.

Calibration of the unsteady pressure transducers electronic network was performed by applying sinusoidal voltages at expected amplitudes from the Kulites over a frequency range of 100 to 10,000 Hertz. This procedure yielded the electronic amplified gains and phase shifts which were later used in data reduction. The A-D connector was calibrated by the same process.

Data Acquisition

The steady-state data acquisition followed the standard compressor evaluation procedure. At a selected corrected speed, the compressor was stabilized for approximately 5 minutes. Following this period, the on-line computer was used to initiate the acquisition of the temperatures and pressures necessary to generate the corrected mass flow rate, overall pressure ratio, and corrected speed. A scanning of the reduced data was then made to assure data uniformity and to ascertain the operating point.

The time-variant data acquisition and analysis technique used was based on a data averaging or signal enhancement concept. The key to such a technique is the ability to sample data at a preset time. For this investigation the signal of interest was generated at the blade passing frequency. Hence, the logical choice for a time or data initiation reference was the rotor shaft and an optical encoder was mounted on the rotor shaft for this purpose. This encoder delivered a square wave voltage signal having a duration of 1.5 microseconds. The computer analog-to-digital converter was triggered from the positive voltage at the leading edge of the pulse, thereby initiating the acquisition of the time unsteady data at the rate of up to 248,000 points per second. The data were

sampled for N blade passages and over M rotor revolutions. These rotor revolutions were not consecutive because a finite time was required to operate on the N blade passage data before the computer returned to the pulse acceptance mode which initiated the gathering of the data.

Preliminary Fourier analysis of the wake data at the blade passage frequency obtained from oscilloscope traces from the hot wires indicated that the fifth harmonic had a content approximately 0.2 of that of the first harmonic (blade passage frequency). Therefore, the sampling rate of the A-D converter was controlled such that at least twenty harmonics of the time varying signals could be acquired. Computer algorithms were established to control the number of data points acquired at varying rotor speeds based on the rotor blade passage frequency, the harmonic resolution desired, and the number of rotor blade passages to be in a sample.

A slight variation in wake profile existed from blade to blade, as determined by examining the averaged data for up to 12 blade passages. At the reduced frequencies of these experiments, the vane surface was influenced primarily by three blade wakes. Hence data was initially acquired for three blade passages. Also, it was found that the unsteady data were essentially unchanged when averaged for 100, 200, or 400 samples. Based on this, 200 rotor samples were used for the dynamic data acquisition. Later studies indicated that only two blade passages were necessary.

From the Fourier analyses performed on the data both the magnitude and phase angles referenced to the data initiation

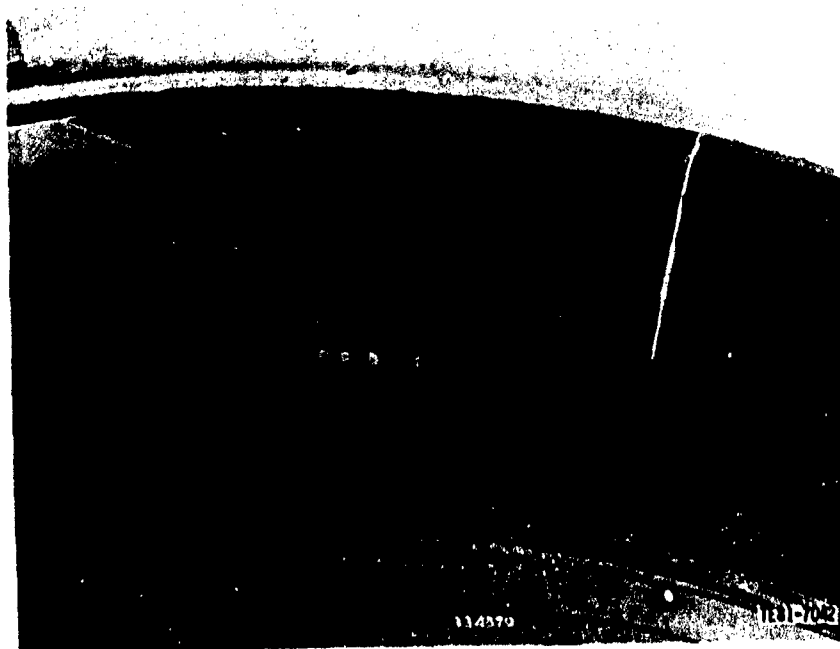


Fig. 38. View of Typical Hot-Wire Installation in Low Speed Compressor Vane Row

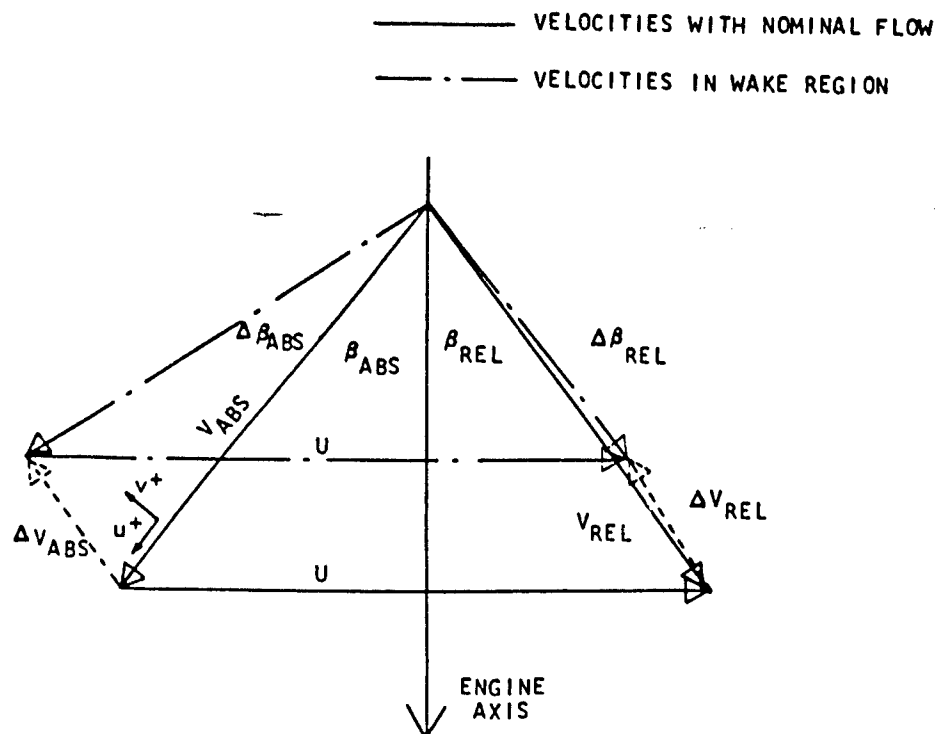
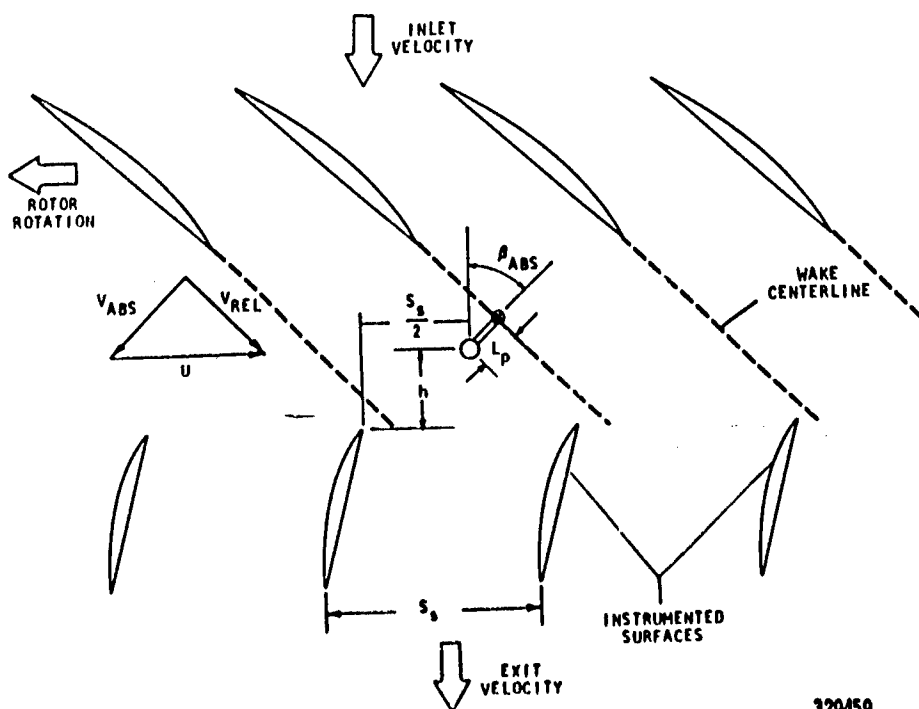


Fig. 39. Reduction in Relative Velocity Created by Blade Wake Creates Corresponding Velocity.



329459

Fig. 40. Schematic of Flow Field used in Dynamic Data Analysis.

pulse were obtained. To then relate the wake generated velocity profiles with the surface dynamic pressures on the instrumented vanes, the rotor exit velocity triangles were examined. Figure 39 shows the change in the rotor relative exit velocity which occurs as a result of the presence of the blade. A deficit in the velocity in this relative frame creates a change in the absolute velocity vector as indicated. This velocity change is measured via the crossed hot-wires. From this instantaneous absolute angle and velocity, the rotor exit relative angle and velocity—and the magnitude and phase of the perturbation quantities are determined.

For wake measurements, the hot-wire probe was positioned between the rotor and stator. To relate the time based events as measured by this hot wire probe to the pressures on the vane surfaces, the assumptions were made that: (1) the wakes were identical at the hot-wire and the stator leading edge planes; (2) the wakes were fixed in the relative frame. Figure 40 presents a schematic of the rotor wakes, the instrumented vanes, and the hot-wire probe. The rotor blade spacing, the vane spacing, the length of the probe, and the axial spacing between the vane leading edge plane and the probe holder centerline are known quantities. At a steady operating point the hot-wire data were analyzed to yield the absolute flow angle and the rotor exit relative flow angle. Using the two assumptions noted, the wake was located relative to the hot wires and the leading edges of the instrumented vane suction and pressure surfaces. From this, the times at which the wake is present at various locations was determined. The incremented times between

occurrences at the hot-wire and the vane leading edge plane were then related to phase differences between the perturbation velocities and the vane surface pressures, using concepts illustrated in a previous section.

To simplify the experiment-theory correlation process, the data were adjusted in phase so that the transverse perturbation was at zero degrees at the vane suction surface leading edge. From the geometry indicated in Figure 40, the time at which this would occur was calculated and transposed into a phase difference. This difference was then used to adjust the pressure data from the suction surface. A similar operation was performed on the pressure surface data so that the surfaces of the vanes were time related; i.e., time relating the data resulted in data equivalent to that for a single instrumented vane. Following this procedure the time varying pressure differences across a single vane at all transducer locations were calculated.

In addition to the unsteady pressure measurements, radial and circumferential scans using the crossed hot wires allowed determination of the complete steady and unsteady velocity fields in the region immediately upstream of the stator row. Illustrations of the steady field in terms of absolute velocity (vane relative velocity) and inlet angle are shown in Figures 41 and 42, respectively. In Figures 43 and 44, the time varying velocity components along and normal to the steady flow vectors are shown. These components represent the harmonic fluctuations occurring at a frequency equal to the rotor blade passage.

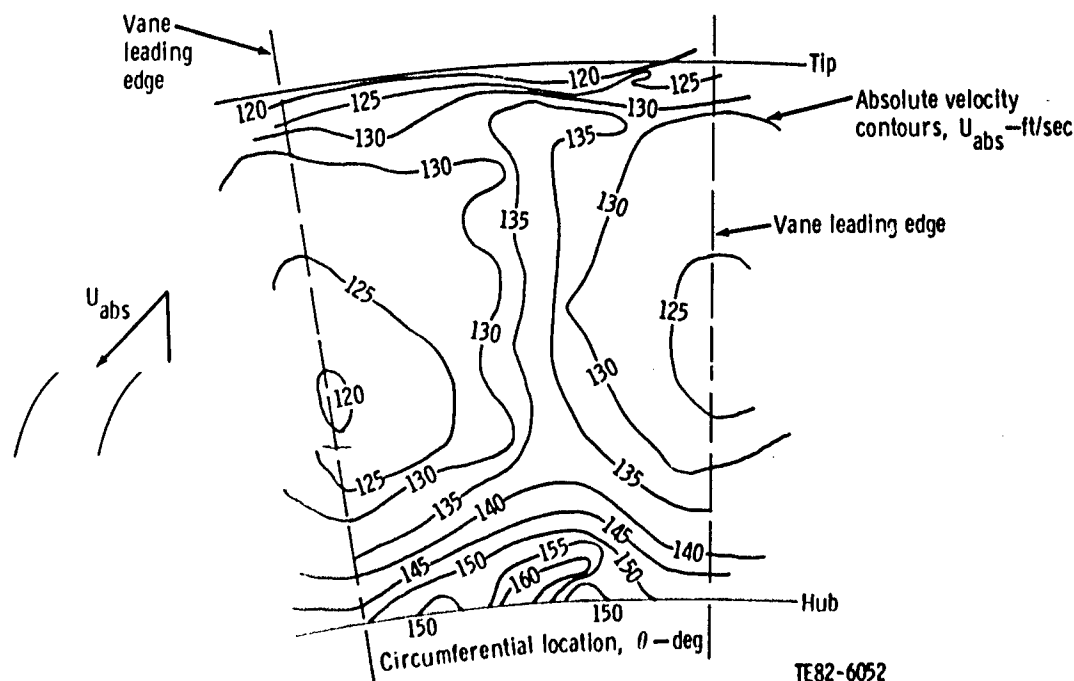


Fig. 41. Vane Leading Edge Absolute Velocity Contours at Near-Design Operating Conditions.

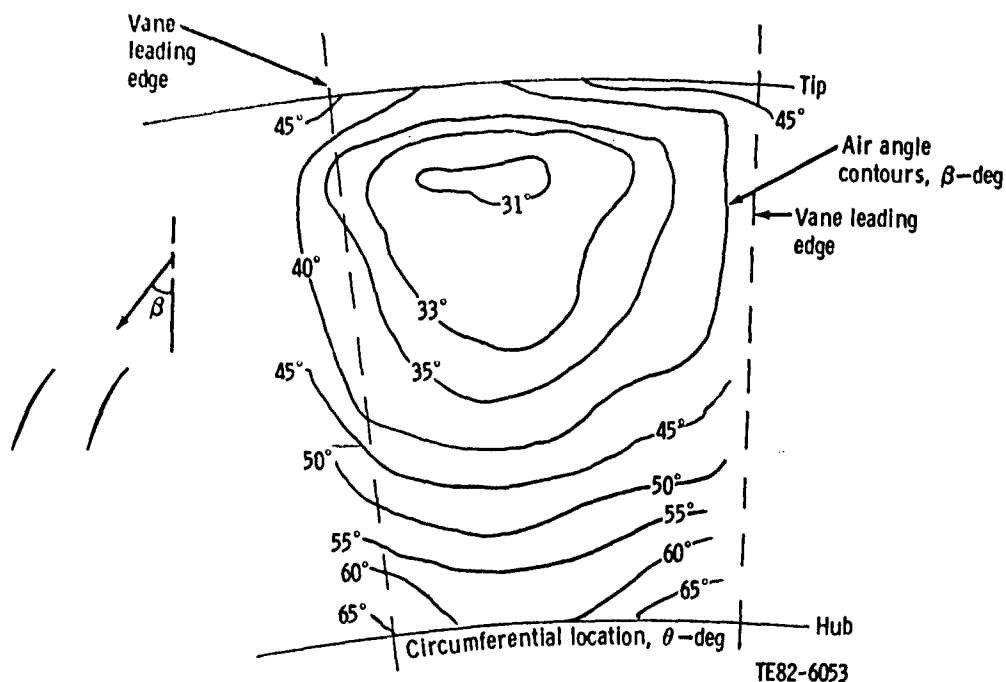


Fig. 42. Vane Leading Edge Air Angle Contours at Near-Design Operating Conditions.

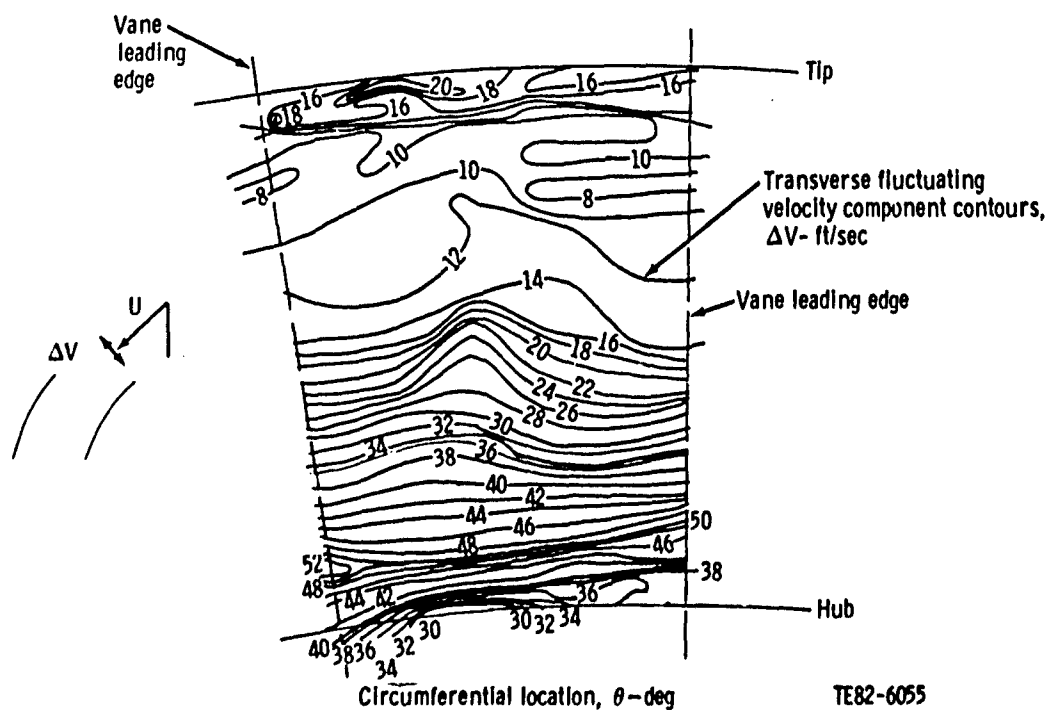


Fig. 43. Vane Lead Edge Streamwise Fluctuating Velocity Component ΔU at Near-Design Operating Condition.

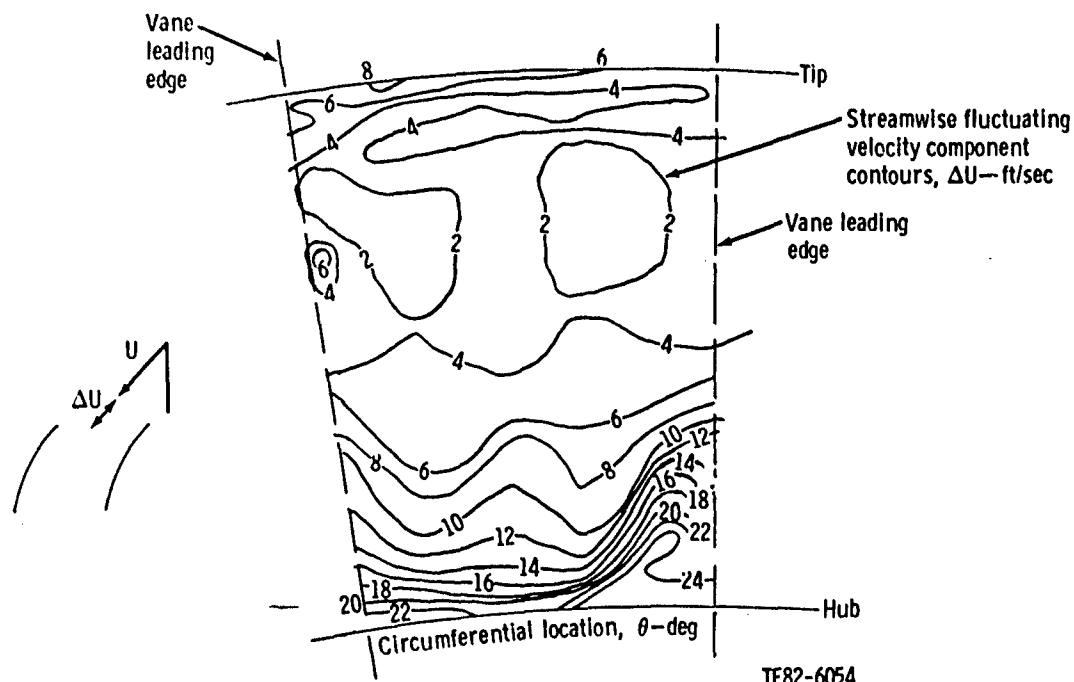


Fig. 44. Vane Leading Edge Transverse Fluctuating Velocity Component ΔV at Near-Design Operating Conditions.

DATA PRESENTATION

For the quantification of the unsteady loading of the stator vane due to the upstream generated wake, the use of normalized pressure coefficients and phase lags allowed the chordwise distribution of unsteady pressures to be described. The normalization was accomplished by dividing the pressure fluctuation magnitudes at particular harmonics of blade passage frequency by the product of twice the stator inlet dynamic head and the appropriate harmonic transverse velocity perturbation expressed as a fraction of the inlet velocity. Typical formats for the presentation of these data are illustrated in Figures 45 and 46 for the pressure and suction surfaces of the transducers located at the stator mid span. Arrangement of data in this form allows analytical predictions to be evaluated on a surface to surface basis. Arrangement of the data in terms of unsteady pressure difference and unsteady lift and moment was also made.

The discussion of these two experimental programs was used to illustrate some, not all, of the concerns involved in the experimental aspects of aeroelasticity pertinent to forced vibration and flutter. Specifically, they were used to provide physical examples which are not always obvious in summary discussions.

SUMMARY

By defining the operating environment of turbomachinery blading in terms of absolute and relative velocity fields, airfoil dynamic mode shapes, and reduced frequency ranges, the applicability of various flow facilities in

establishing critical time varying aerodynamic data needed for the solution of flutter and forced vibration problems was examined. For illustration of pertinent research being accomplished in each type of facility, a sampling of investigations documented in the literature was used. Unique features of data acquisition techniques, methods to induce blade oscillations, and instrumentation concepts were presented to provide an awareness of the different approaches which could be used. Common concerns regarding calibration and data acquisition systems were discussed in a broad overview. The multiple aspects of experimental flutter and forced vibration research were focused by examination of a linear cascade and low speed compressor experimental programs.

From this chapter, a scope of the parametric ranges and the methods which could be used to construct meaningful forced vibration research programs has been established. Supplementary to the coherent gathering of time varying data should be quantification of the steady flow fields in sufficient detail to define wakes, potential disturbances, and the other mechanisms creating spatially oriented disturbances which act to excite blades to resonance, then to failure.

Recommendations for future experimental research could be stated simply as the need to gather data in the correctly simulated operational environment of actual turbomachinery blading. Notable among the experimental programs discussed has been the omission of experimental programs directed toward establishing a data base for blade motions involving chordwise bending. Thus, research in this direction should be accomplished.

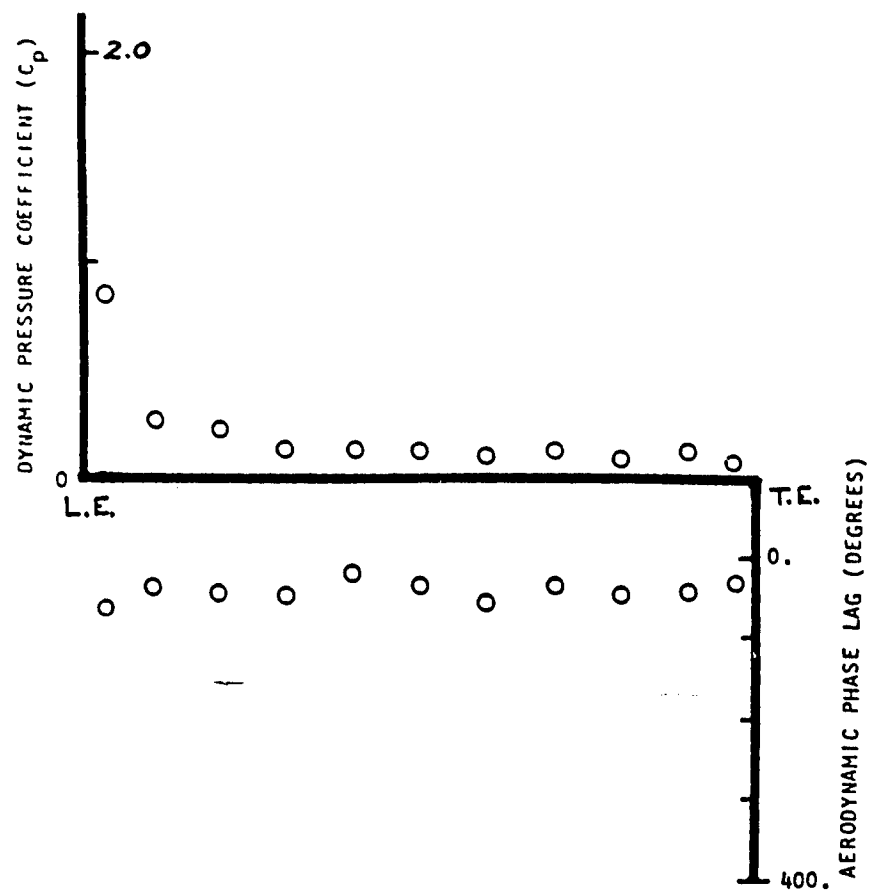


Fig. 45. First Harmonic Pressure Surface Chordwise Dynamic Data.

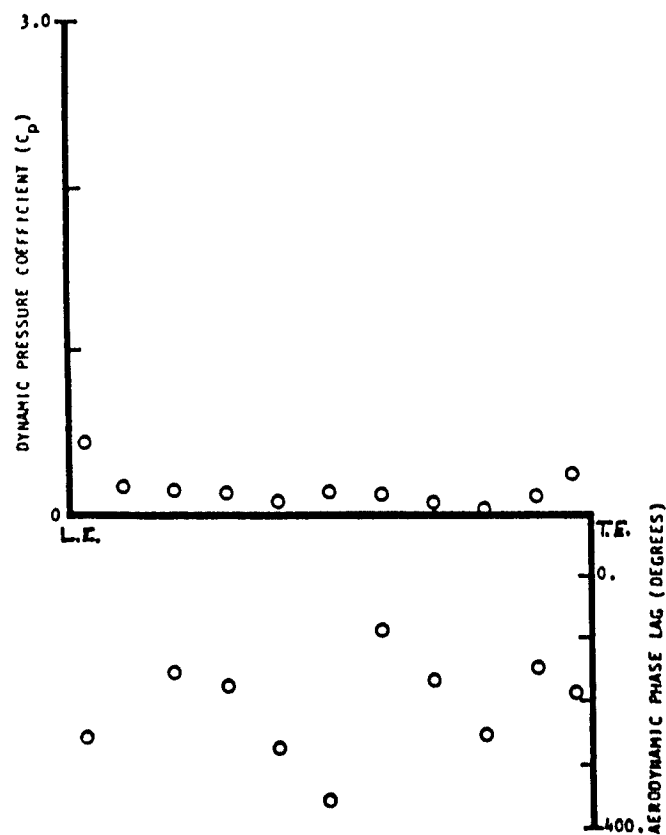


Fig. 46. First Harmonic Suction Surface Chordwise Dynamic Data.

UNDERSTANDING FAN BLADE FLUTTER THROUGH LINEAR CASCADE AEROELASTIC TESTING

Edmond Szechenyi

O.N.E.R.A.
29, Avenue de la Division Leclerc
92320 Chatillon, FRANCE

INTRODUCTION

The development of modern turbo-jet engines is tending increasingly towards the use of inlet fans having blades with sharp leading edges and relatively low natural frequencies of vibration. These characteristics increase the propensity of the blades to flutter.

Tests on actual machines, Loiseau et al (1975), have shown that a variety of blade instabilities can exist. For instance, flutter can occur on one or more blades independently of the neighboring blades of each, or else flutter vibrations can affect all the blades of a rotor which then vibrate as "rotor modes". In this case, the deformations and frequencies of all the blades are the same and they vibrate with a constant relative phase angle.

Fan blade flutter also occurs in different flow regimes. Four different forms of flutter can thus be distinguished, though the differences in some cases might well be rather tenuous.

Fan blade mode shapes are frequently fairly pure in either bending or torsion and flutter in the different flow regimes will usually appear for one or other of those mode as simple degree of freedom flutter.

The four known flutter regimes can be described as follows:

(1) Sub and transonic torsional flutter. This is generally known as stall flutter, but as later descriptions will show, the term "stall" is somewhat incorrect as the flutter is not so much dependent on stall as on flow separation.

Flutter appears when back pressure (angle of attack) is increased. One or more blades will start vibrating at large amplitudes and as back pressure increases still further all the blades will eventually vibrate, possibly according to a rotor mode if they are sufficiently closely tuned in frequency.

(2) Supersonic unstated flow flutter in bending. This form of instability is frequently known as "supersonic stall flutter" but here again the justification of the term "stall" is questionable. The aeroelastic behaviour of a fan under these flow conditions is at present not very well known.

(3) Supersonic started flow flutter in torsion, characteristic of low pressure operation. This instability often determines the operating limit of a fan since its limit crosses the operating line (Fig. 1).

(4) Supersonic started flow flutter in bending, characteristic of the high back pressures approaching the limit of unstated flow. The fundamental mechanism of this instability may well be closely akin to unstated flow flutter (see regime (2) above).

These four distinct forms of fan blade flutter are shown on the typical operating diagram of Figure 1. It must be stressed that there is at present nothing absolute about this classification but that it does seem to encompass the clearly detected forms of flutter occurring in modern fans.

This paper attempts to give some physical insight into the causes and origins of these different flutter regimes. The discussion is based on experimental data obtained in a linear cascade. For sub/transonic flutter the validity of the cascade measurements is tested by comparing these with actual compressor data.

In order to interpret the test results, some understanding of the experimental "philosophy" as well as of the facility used is necessary. These will be described before actually discussing flutter.

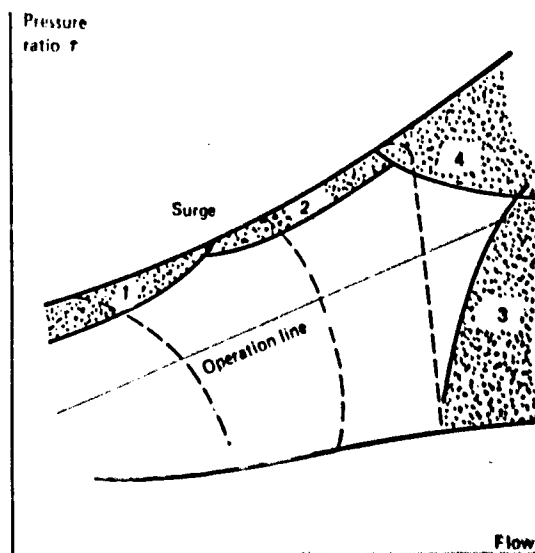


Fig. 1 Mass Flow-Pressure Ratio Field of Compressor. Stability Limits.

AEROELASTIC TESTING

General

Different forms of aeroelastic testing can be employed depending on the purpose of the tests. A manufacturer may wish to predict the flutter behaviour of a future fan while still at the design stage, or else he may require flutter boundaries on an existing machine. In both cases the testing can be relatively simple and limited to the measurement of the free vibrations of the blades as a function of compressor parameters.

However, this form of testing is insufficient for a physical insight into aeroelastic behaviour. This type of research requires that at least some knowledge of the actual aeroelastic forces is obtained.

Aeroelastic testing may be carried out in fixed annular cascades, linear cascades or simply on an existing compressor. Each has its advantages, inconveniences, and applications:

Full compressor rig testing allows for the measuring of the true behaviour of the blades and gives the real flutter limits. Obviously it can in no way be a predictive tool and is thus not applicable in the compressor development stage. Moreover, the complexity of the instrumentation usually limits measurements to blade vibration levels.

Cascades have a more "research and development" vocation. Annular cascades usually consist of a fixed rotor representing the fan to be tested. The blades are instrumented at will (strain gauges, pressure transducers) and in some cases are mounted on electrodynamic shakers so as to enable true aeroelastic measurements, Whitehead et al (1976), Kobayashi (1983), Boelcs and Schlaefli (1984). The inlet flow is given the necessary rotation by means of guide vanes. The advantage of annular cascades over full compressor rigs is that instrumentation is much simpler to implement thus allowing for research studies. On the negative side a number of points can be made: the flow simulation neglects centrifugal effects; aeroelastic measurements on cantilevered blades are not easy to interpret; three-dimensional effects can give an overcomplicated unsteady pressure distribution picture when attempting to obtain some physical insight.

Linear cascades are used exclusively for research and predictions, Boldman et al (1981), Caruthers and Riffel (1980), Arnoldi et al (1977), Rehlitz (1976), Tanaka et al (1984). Blade profiles are two-dimensional and thus results are strictly speaking applicable to only one section of a fan blade. The cascade is by definition finite as against an annular cascade which is infinite as seen by the flow. This need not be a very important handicap if the number of blades in the linear cascade is sufficiently large for all interactive forces to be measured. However, good flow periodicity can be difficult to generate while in an annular cascade perfect periodicity is inherent.

Of the advantages of linear cascades, simplicity overrides all others: simplicity in design; simplicity of instrumentation; simplicity in applying a well-defined vibrational motion to the blades; simplicity in the analysis and interpretation of results. This is what makes the linear cascade the most widely used tool in aerodynamic or aeroelastic turbomachinery research.

Aeroelastic Testing in the Present StudyThe Linear Cascade Facility

In attempting to understand the causes of flutter it is essential to be able to analyze in detail the aeroelastic forces acting on the blades for varying flow parameters. The linear cascade is ideally suited for this purpose.

The linear cascade wind tunnel built at ONERA in 1977 for aeroelastic research is shown in the photograph of Figure 2 and schematically in Figure 3.

The tunnel is of the blow-down type and is connected to a compressed air source at 9 atmospheres. The total volume of the compressed air reservoir is such that test run times in excess of 10 minutes can be achieved at transonic flow speeds.



Fig. 2 View of the Cascade Wind Tunnel.

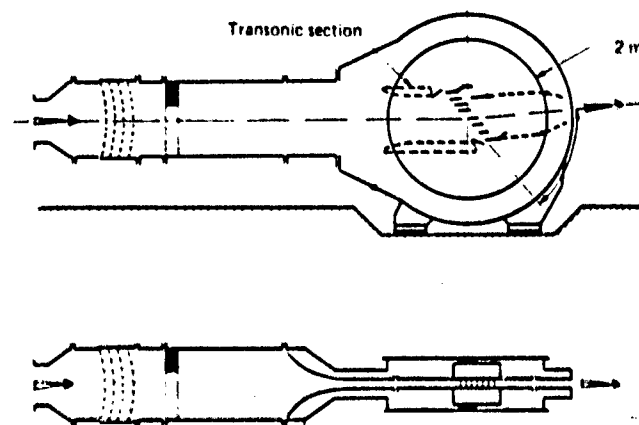


Fig. 3 Schematic View of the Straight Cascade Tunnel.

The linear cascade should simulate the rotor as closely as possible to enable the study of the action of the various parameters on blade stability. The most important and most easily varied parameters are considered here, namely: flow speed, angle of attack (deviation), frequency of vibration, chordwise position of the pitching axis (torsional modes), pressure ratio (for started supersonic flow only).

The wind tunnel can be fitted with three different nozzles: for Mach numbers 1.2 and 1.4, and for sub/transonic flow giving Mach numbers from 0.4 to 1.0.

The facility is so designed that the angle of attack can be adjusted by rotating the entire cascade (with the diffuser) about its center which is set on the leading edge line. This allows variations in the angle of attack while leaving solidity and stagger angle unaltered. Angle of attack variations simulate the effect of choking at the inlet of the compressor at constant turning speeds for subsonic, transonic, and unstarted supersonic flow.

The cascade is composed of from 7 to 9 blades. The blade length (tunnel width) is 120 mm. The chord-length depends on the stagger angle and solidity of the cascade and is normally between 80 and 100 mm.

Principles Underlying Aeroelastic Testing

Aeroelastic forces in a cascade are those induced on a blade by its own vibrating motion or by the vibrations of neighbouring blades.

Aeroelastic measurements yield unsteady coefficients of lift and moment. These are either "direct", as in the case of forces acting on the vibrating blade, or "coupling" coefficients when the influence of the vibration of neighbouring blades is considered.

The aeroelastic force coefficients are determined as the transfer functions between the vibratory motion and the resulting lift, moment or pressure: complex coefficient

$$C = C' + iC'' = - \frac{\int_0^{\infty} F(t) e^{-i\omega t} dt}{(1/2) \rho V^2 S \int_0^{\infty} \psi(t) e^{-i\omega t} dt}$$

where $F(t)$ and $\psi(t)$ are the time histories of the aeroelastic force and of the vibratory motion producing it, respectively.

The imaginary coefficient C'' is the measure of aeroelastic damping. If $C'' < 0$, there is an aeroelastic instability (flutter).

In the present testing technique, the assumption is made that the direct and coupling terms combine linearly so that a vectorial addition of these forces can be made. In other words, one assumes that the principle of superposition is valid. Thus, the total coefficient for a blade in an infinite cascade is:

$$C_T = \sum_{n=-\infty}^{\infty} C_n e^{in\theta}$$

or

$$\text{Re}(C_T) = C_T' = \sum_{n=-\infty}^{\infty} (C_n' \cos n\theta - C_n'' \sin n\theta)$$

$$\text{Im}(C_T) = C_T'' = \sum_{n=-\infty}^{\infty} (C_n' \sin n\theta + C_n'' \cos n\theta)$$

where n is the blade index:

$n = 0$ is the vibrating blade

$n < 0$ are the "upstream" blades

$n > 0$ are the "downstream" blades

C_n is the complex coefficient measured on blade n

θ is the blade-to-blade phase angle.

This assumption considerably simplifies the experimental set-up but above all it allows a more intimate analysis of aeroelastic behaviour as direct and coupling terms are measured and assessed separately. It should also be noted that blade-to-blade phase angle is not an experimental parameter but merely appears in the calculation.

The practical consequence of this assumption is that only one blade must be made to vibrate and only one blade needs to be instrumented in order to measure aeroelastic coefficients. The relative positions of these two blades in the cascade must be variable in order to measure all the terms. When measuring the direct coefficients these two blades are of course one and the same.

In practice the vibrating blade has a fixed position approximately half way down the cascade while the instrumented blade can take up any of the blade positions in the cascade.

If this assumption of superposability were not made, all the blades of the cascade would have to vibrate at exactly the same frequency and amplitude with any given constant blade-to-blade phase angle. Whilst the complexity of the design of such a test rig is tremendous Boldman et al (1981), the tests yield results that do not allow an assessment of the relative importance of direct and coupling terms.

Moreover, it must be stressed that the separation of these components is physically significant as flutter often appears on isolated blades (i.e., flutter where only direct aeroelastic forces act as in the case of mistuned blades).

Superposability may seem to be an unfounded simplifying assumption, but it has been adopted by a number of researchers and notably Hanamura et al. (1980) who demonstrated its validity by theory for an infinite cascade in ideal flow. No absolute proof of its universal validity exists but an experimental verification was made at Mach = 1.4 by making two neighbouring blades vibrate simultaneously

and measuring the total coefficient (C_T) on one of the blades. The result was compared with the calculated total coefficient obtained with only one blade vibrating

$$(C_T = \sum_{n=0}^1 C_n e^{in\theta}).$$

This was done for three blade-to-blade phase angles. The agreement is very good as shown in Figure 4 for two different frequencies of vibration.

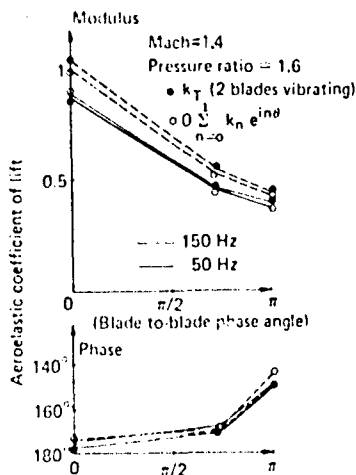


Fig. 4 Comparison between the Measured Aeroelastic Coefficient obtained by Linear Superposition of the Coefficients of the 2 Blades.

Blade Instrumentation

Aeroelastic testing requires the measuring of unsteady forces. This can be performed by a balance or other force transducers, but results cannot yield pressure distributions which are fundamental in an attempt at understanding the aeroelastic phenomena.

Miniature pressure transducers technology is now sufficiently developed to allow reliable good quality unsteady pressure measurement on fixed or vibrating blades. In this study, aeroelastic force measuring instrumentation consists of a set of pressure transducers placed in a single cross-section of the blade. Between 20 and 26 transducers are used depending on the blade profile and on the chord-length. This number is sufficient for a good representation of the unsteady pressure distribution and hence of the lift and moment coefficients obtained by integration.

The transducers employed are manufactured by Kulite. At chordwise positions where the thickness exceeds 2.1 mm standard cylindrical (1.6 mm diameter) transducers are used. For thinner blade

sections a specially designed flat model is used (thickness: 0.5 mm). This transducer can be implanted at blade locations where the thickness is down to 0.6 mm and thus allows measurements very near the leading and trailing edges (Figure 5).

Blade Vibration Mechanism

A complete aeroelastic study on a two-dimensional profile requires separate measurements in the presence of plunging and pitching motion. The frequency of vibration must be such that the reduced frequency (k_R) is the same as that of the normal modes of the fan blades being simulated.

The vibratory motion of the blade must be truly two-dimensional plunging or pitching. Blade deformations must be avoided as far as possible as they produce unwanted three-dimensional effects; the input to the aeroelastic transfer function is then no longer perfectly known or defined.

In practice, the possible ranges of frequency in the facility are approximately:

- pitching motion: from 70 to 600 Hz,
- plunging motion: from 70 to 300 Hz,

giving maximum reduced frequencies of 0.6 and 0.3 in pitching and plunging respectively at a flow speed of Mach = 1.

Blade vibration is obtained by means of four linear hydraulic actuators, two on either end of the vibrating blade (Figure 6). A position control of each actuator is ensured by high frequency servo-valves using a feedback signal delivered by displacement transducers.

The four actuators are made to vibrate with relative amplitudes and phases such as to give the required plunging (all in phase) or pitching motion (two in phase, two in counter-phase).

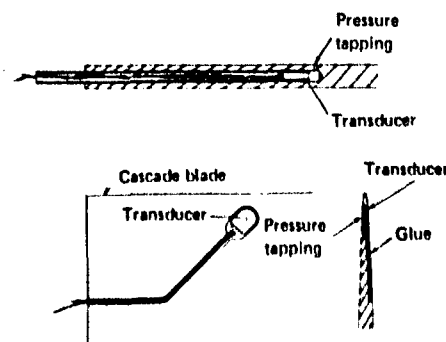


Fig. 5 Pressure Transducer Mountings.

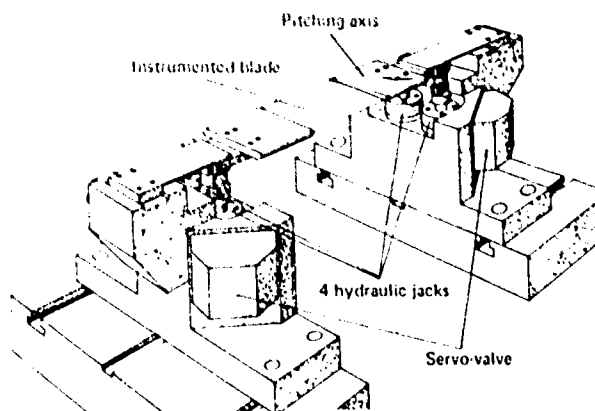


Fig. 6 Blade Vibration Mechanism.

Data Acquisition and Reduction

Wind tunnel data, the vibrational motion of the blade and unsteady pressure measurement are all filtered, simultaneously sampled, multiplexed, digitized, and recorded on disc. Thence, the aerodynamic transfer functions are calculated giving complex lift, moment, and pressure coefficients. The results are immediately available in the form of a print-out. If desired, unsteady pressure distribution plots can be obtained within a few minutes of a test run.

Measurements on a Compressor Blade

Aeroelastic measurements were carried out on one of the fans simulated in the straight cascade. The purpose of this test was to estimate the validity of straight cascade measurements. The suction surface of one blade of the fan was instrumented with a strain gauge and five flat unsteady pressure transducers of the same type as in the straight cascade, discussed in section "Blade Instrumentation". The strain gauge was calibrated to give amplitudes of torsional vibration at the pressure transducer section.

Transfer functions between strain gauge and pressure transducer signals gave the required pressure coefficients which could then be compared to the straight cascade measurements for the same aerodynamic conditions.

This test was limited to sub/transonic flow conditions.

Presentation of Results

The experimental results discussed below are mainly based on the direct coefficients as these illustrate most clearly the aeroelastic phenomena and their dependence on the various compressor parameters. Coupling terms are discussed in so far as their presence influences flutter limits.

All results are shown in the form of complex aeroelastic coefficients (see "Principles Underlying Aeroelastic Testing"). These are generally plotted as modulus and phase diagrams since these usually give the most insight into physi-

cal behavior, though in some cases real and imaginary parts are also given.

The pressure distributions are mostly shown for the blade surface where the main aeroelastic forces are generated. Rarely are both suction and pressure surface distributions given.

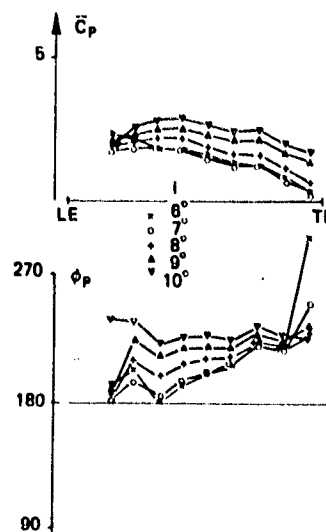
The phase reference for lift and moment is taken so that there is instability for $\pi < \phi < 2\pi$. The phase reference for the pressure coefficients is such that the suction surface pressures ahead of the pitching axis are always dissipative for $\pi < \phi < 2\pi$. Note that for plunging motion the pitching axis is considered to be at infinity downstream.

SUB/TRANSONIC FLOW FLUTTER IN TORSION

General

In this chapter, sub/transonic flutter is analysed. The pressure distributions shown and used for discussion are restricted to the suction surface as the pressure surface values are virtually invariant with the various parameters and thus play no role in the appearance of flutter. An example of pressure surface distributions is shown in Figure 7.

The bulk of the results is for a pitching axis at mid-chord but the effect of the position of this axis is discussed.

Fig. 7 Example of Pressure Surface Distributions at $M = 0.9$.

The Influence of Angle of Attack

Figures 8 and 9 show that, whatever the Mach number or the frequency of vibration, an increasing angle of attack always brings the blade nearer to a condition of instability.

The cause of this is easily understood after examining pressure distributions such as those in Figure 10. One finds that flutter can exist only when the phase distribution has changed its shape.

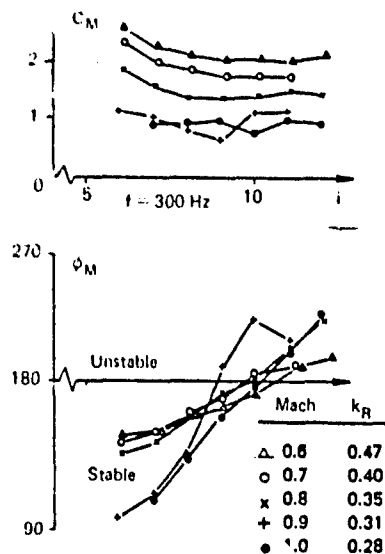


Fig. 8 C_M against Angle of Attack at Different Flow Speeds.

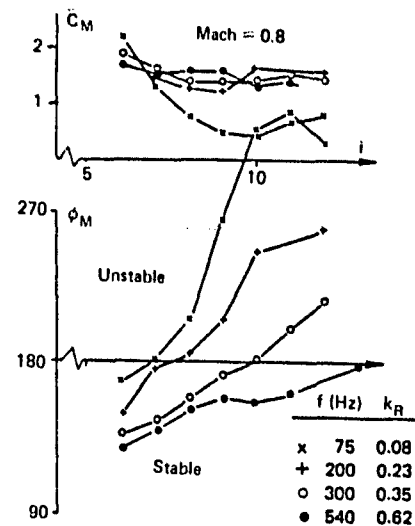


Fig. 9 C_M against Angle of Attack at Different Frequencies of Vibrations.

The theoretical inviscid flow on a flat plate gives a positive slope for the phase distribution curve (propagation from the trailing edge towards the leading edge). In Figure 10, one can see this slope progressively changing as the angle of attack increases to the point where the whole distribution curve has a negative slope (propagation from the leading edge toward the trailing edge).

This change in phase angle brings certain large pressures (e.g. near the leading edge) into a phase quadrant where they act as an exciting force and are thus destabilizing.

Comparisons with steady pressure distributions and surface flow visualizations show that a negative phase distribution slope generally corresponds to an area of flow separation. This is vital information as it shows how stability conditions depend on flow separation and, hence, on the angle of attack.

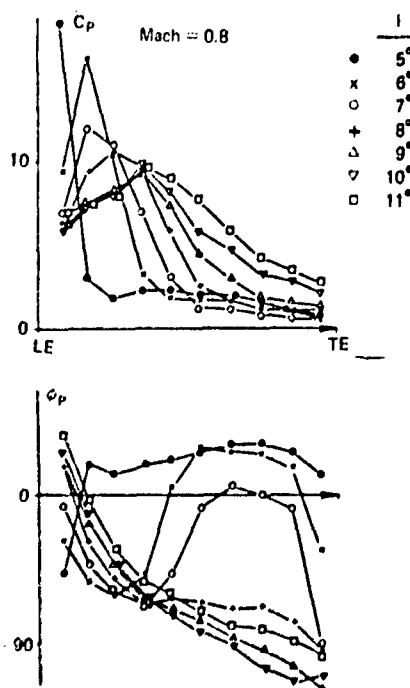


Fig. 10 Pressure Distribution (Upper Surface) for Different Angles of Attack.

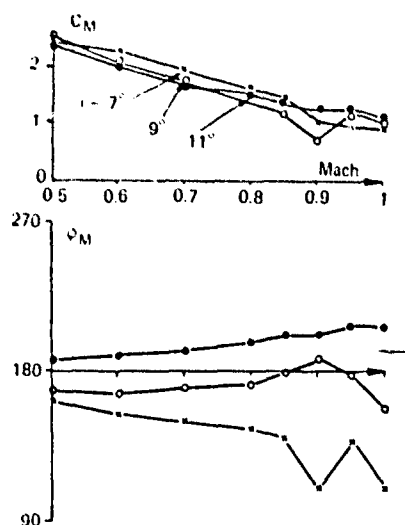
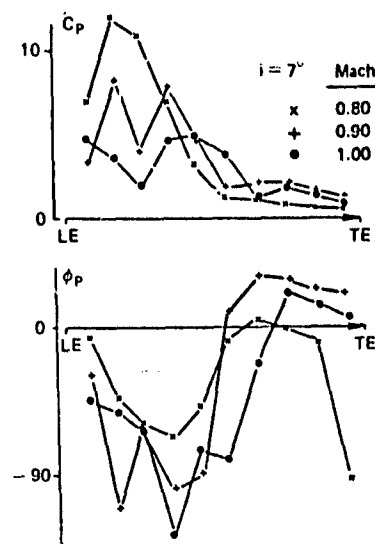
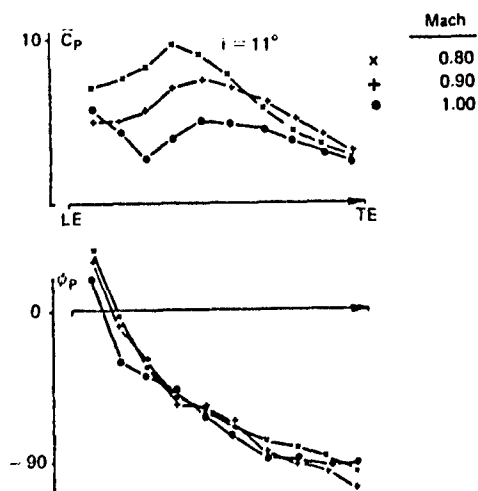
The Influence of Flow Speed

Figure 11 shows typical plots of C_M against Mach number. Three different angles of attack are shown:

- (i) 7° where flow at the leading edge is not separated (save for the usual bubble),
- (ii) 9° where the flow is at the limit of total separation,
- (iii) 11° where the flow is completely separated over the entire chord of the blade.

For all three angles of attack the influence of the flow speed in the subsonic region is monotonic. At transonic speeds the action of shock waves becomes noticeable for angles of attack where flow separation is not complete but at 11° they have no visible influence.

The pressure distributions in Figures 12 and 13 show this even more clearly. At $i=7^\circ$ the flow speed has a strong influence on both modulus and phase while at $i=11^\circ$ (complete flow separation) the influence of Mach number is small on the modulus and insignificant on the phase angles.

Fig. 11 C_M against Mach Number.Fig. 12 Pressure Distribution at Different Flow Speeds and $i=7^\circ$.Fig. 13 Pressure Distribution at Different Flow Speeds and $i=11^\circ$.

The Influence of the Frequency of Vibration

One can see from Figure 9 that stability increases with frequency. This is not due to any important change in the unsteady flow characteristics, but principally to an increasing phase lag. The pressure distributions of Figure 14 are obtained for the same flow conditions but at different frequencies. They show, with increasing frequency, an ever-increasing, negative slope of the phase angle plot.

The Influence on Stability of the Position of the Pitching Axis

Stability is clearly closely dependent on the position of the pitching axis. Figure 15 shows the real and imaginary parts of C_M as a function of the position of the pitching axis (0, 50, and 92% of chord), but they suffice to determine the effect of this parameter.

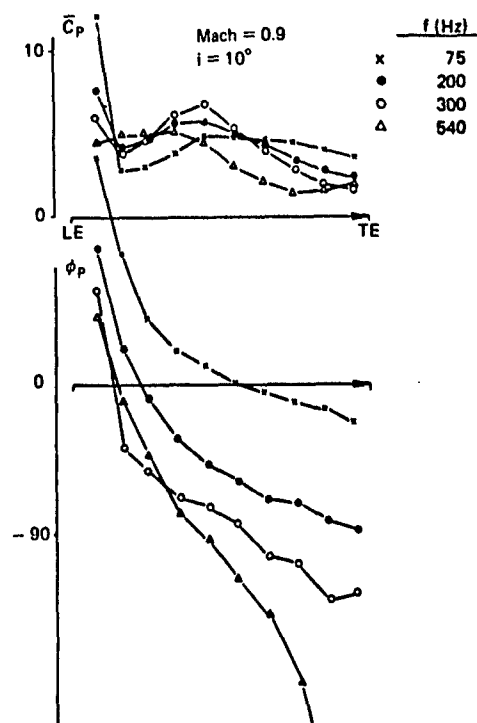


Fig. 14 Pressure Distribution at Different Frequencies.

At small angles of attack the blade is always stable. As this angle increases the blade first becomes unstable for axes located on the upstream half-chord. At high angles of attack (complete flow separation) the blade is unstable for all pitching axes. Figure 16 shows C_M plotted against angle of attack for the three pitching axes.

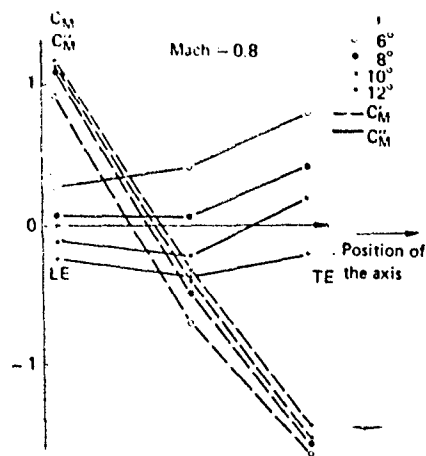


Fig. 15 Components in Phase and in Quadrature as a Function of the Position of the Pitching Axis.

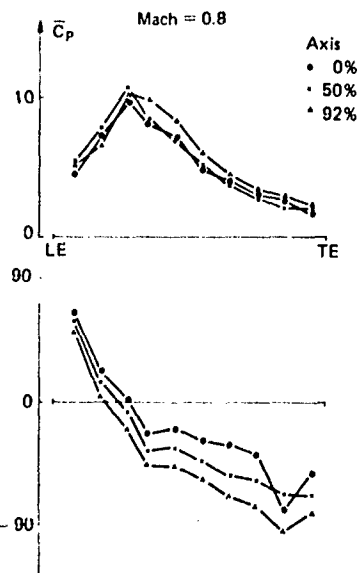


Fig. 17 Unsteady Pressure Distributions for Three Pitching Axes.

It is interesting to note that the pressure distribution (Figure 17) is virtually independent of the position of the pitching axis.

Pitching Axis Prediction by Linear Transposition

It is well known that for flow having linear steady characteristics, the unsteady moment due to pitching about any axis can always be predicted by linear superposition of the moment relative to another axis and the lift due to plunging motion:

$$C_M(a) = C_L(h)x^2 + C_L(o) + C_M(h)x + C_M(o)$$

where $C_M(a)$ is the moment due to pitching about axis a

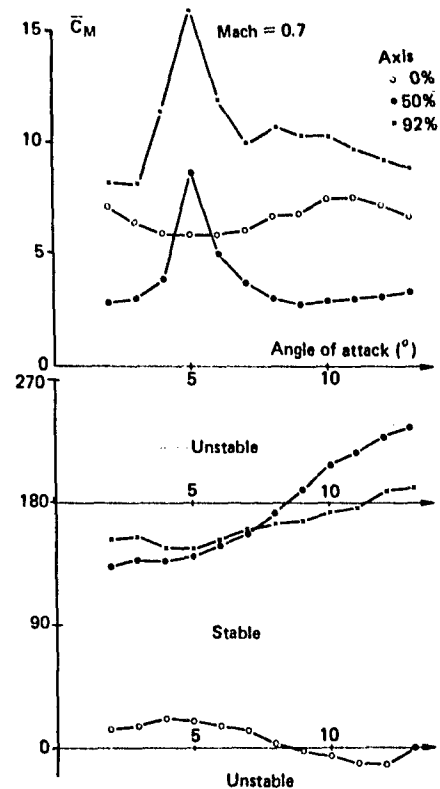


Fig. 16 C_M as a Function of the Angle of Attack at Different Pitching Axes.

$C_M(o)$ and $C_L(o)$ are the moment and lift respectively, induced by pitching about the reference axis

$C_L(h)$ and $C_M(h)$ are the lift and moment respectively, induced by plunging motion

x is the normalized distance between the reference axis (o) and the axis a .

Although the assumption of steady linearity is not verified, the principle of superposition has been tested and it gave the results shown in Figures 18 and 19.

It is clear from these figures that the linear superposition of plunging and pitching gives excellent predictions for any other pitching axis no matter what the angle of attack.

Thus the linear combination is just as valid for completely separated flow as it is for perfect unseparated flow. This is an important result facilitating predictions for true fan blade mode shapes.

Blade-to-Blade Coupling and Total Cascade Coefficients

Figure 20 shows some typical coupling coefficients as a function of the angle of attack. Only the coupling with the immediately adjacent blades was measured (C_{-1} and C_{+1}).

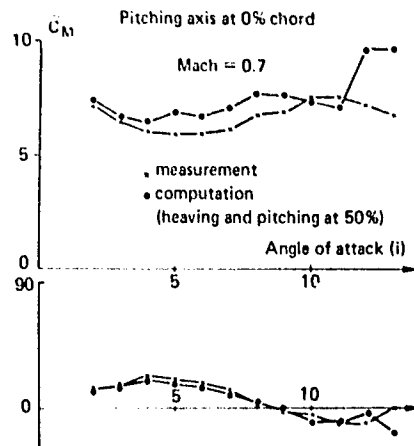


Fig. 18 Comparison between Measurement and Transposition of the Axis by Computation.

From the figure, it is clear that these coefficients are much less sensitive to the angle of attack than in the case of the direct coefficients (C_0). This is also true of the Mach number influence. The effect of frequency is the same as for the direct coefficients, that is, that increasing frequency causes an increasing phase lag.

The total coefficients can be calculated according to the formulae in section "Principles Underlying Aeroelastic Testing". However, the results will depend on the assumed blade-to-blade phase angle, θ . To assess the importance of the coupling terms on cascade stability, it is simplest to assume for each case the value of θ giving the largest coupling effect, i.e., the minimum value of C'' .

Together with the coupling coefficients, Figure 20 also shows C''_{\min} as a function of the angle of attack, resulting from the above computation. It is clear from the figure that C''_{\min} follows the same trend as C_0'' (direct coefficient) relative to the angle of attack. Of course, the flutter limit appears at a much smaller angle of attack but the curve seems to be merely shifted down.

Sub/Transonic Flow Flutter Limits

From the sections "The Influence of Angle of Attack" and "The Influence of Flow Speed", it is clear that the angle of attack at the limit of flutter diminishes with frequency. Strangely enough, at any particular angle of attack this is the only parameter to have a noticeable effect on flutter limits. The effect of flow speed, though not totally negligible, is very weak.

The flutter limit diagram (Figure 21) is thus rather a plot of angle of attack against frequency and not the conventional reduced frequency (k_r); as would normally be expected. The non-dimensional frequency parameter on which the limit of flutter

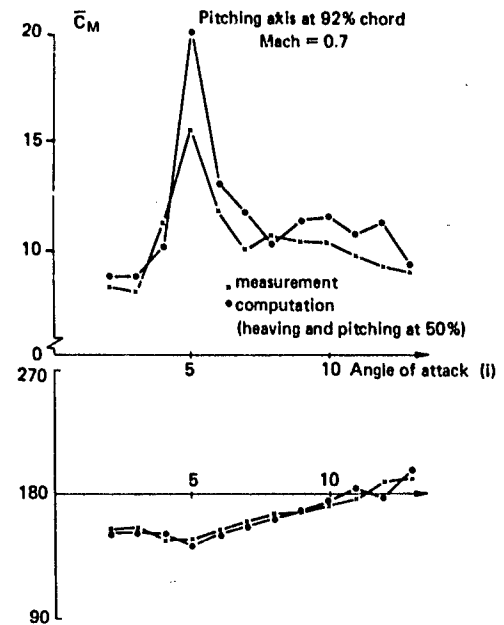


Fig. 19 Comparison between Measurement and Transposition of the Axis by Computation.

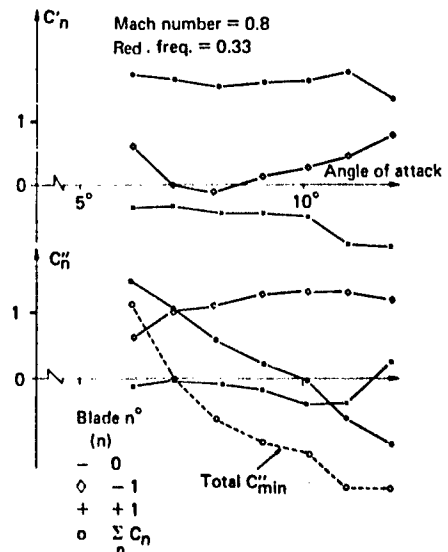


Fig. 20 Direct Coupling and Total Moment Coefficients for Pitching Motion in Sub/Transonic Flow.

depends is some propagation velocity in separated flow which seems only weakly dependent on flow speed. This question needs further investigation.

Conclusions on Sub/Transonic Flutter in Torsion

The principal characteristics of sub and transonic "stall" flutter can be summarized by the following findings:

o The unsteady pressures causing stall flutter of thin compressor blades are mainly situated on the upper surface and on the forward half chord.

o Flutter conditions can only occur when the flow over the blade is completely, or almost separated. Since the conditions enabling flutter are dependent solely on flow separation, they are directly related to the angle of attack.

o When the flow is separated, the presence or absence of flutter depends only on the frequency of vibration. The higher this frequency, the larger the limiting angle of attack.

o A linear superposition of unsteady coefficients obtained with pitching and plunging motions will give correct values for moment coefficients about any other arbitrary pitching axis. This is true at all angles of attack whether the flow is separated or not.

o The name of "stall flutter" for this instability is not strictly correct since flutter depends on flow separation and not on a stall phenomenon.

SUPERSONIC STARTED FLOW FLUTTER

General

Flutter is known to appear separately for torsional and bending modes, the former at low and the latter at high pressure ratios. These two forms of flutter are studied separately with pitching and plunging vibrations respectively at a Mach number of 1.4.

A brief description of steady flow at this Mach number and at different pressure ratios is necessary in order to understand the flutter conditions discussed below.

In started supersonic flow the angle of attack is unique and is given by the slope of the suction surface near the leading edge. The flow determined by the upstream Mach number and by this angle of attack is identical in each channel and thus constitutes a periodic flow pattern.

The pressure ratio plays a fundamental role in shaping the steady flow field. Figure 22 shows typical steady flow configurations for four values of pressure ratio. These patterns were determined in the cascade by means of shadowgraph views. The leading edge shock wave reflects on the suction surface of the neighboring "upstream" blade while the suction surface trailing edge shock reflects on the pressure surface of the "downstream" blade. As the pressure ratio (compression) increases, the reflected leading edge shock and the suction surface trailing edge shock both progressively straighten and finally coalesce and move up to the channel throat. This occurs at the limit of started flow; any attempt at increasing the pressure ratio beyond this point causes the flow to become unstalled and the flow in the channel becomes totally subsonic.

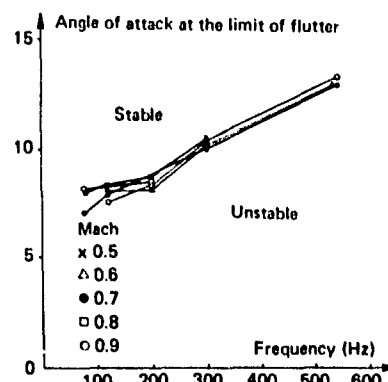


Fig. 21 Typical Sub/Transonic Torsional Flutter Limits Considering "Direct" Terms Only.

The positions of the various shock waves and of their reflections are obviously sensitive to variations in Mach number and pressure ratio and are thus sources of pressure fluctuations when the blades vibrate.

Figures 23 a and b show the suction and pressure surface steady pressure distributions for the four examples of Figure 22.

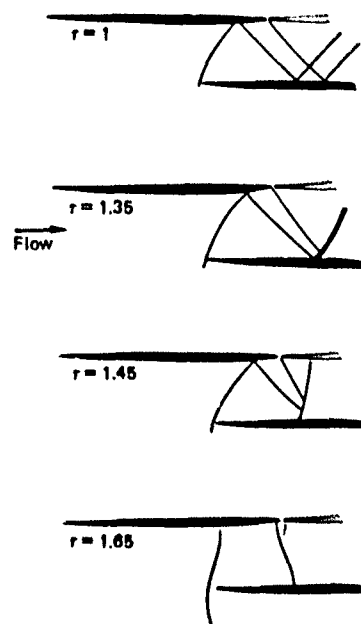


Fig. 22 Shock Wave Patterns at Different Pressure Ratios.

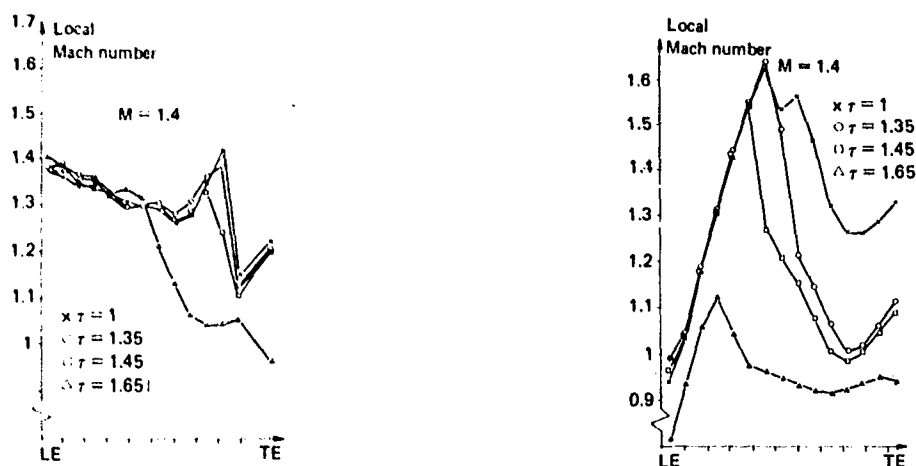


Fig. 23 (a) Steady Pressure Distribution - Suction Surface;
(b) Steady Pressure Distribution - Pressure Surface.

The Nature of the Flutter and the Influence of Pressure Ratio

Pitching Motion

Figure 24 shows the influence of pressure ratio on the direct and coupling moment coefficients. It is clear that the direct coefficients (vibrating blade) are by far the most influenced by pressure ratio. This is confirmed by the plotting of the smallest value (most unstable) of the total coefficient C_T against pressure ratio (Figure 24) after the calculation presented in "Principles Underlying Aeroelastic Testing". The total curve runs virtually parallel to that of the direct coefficient.

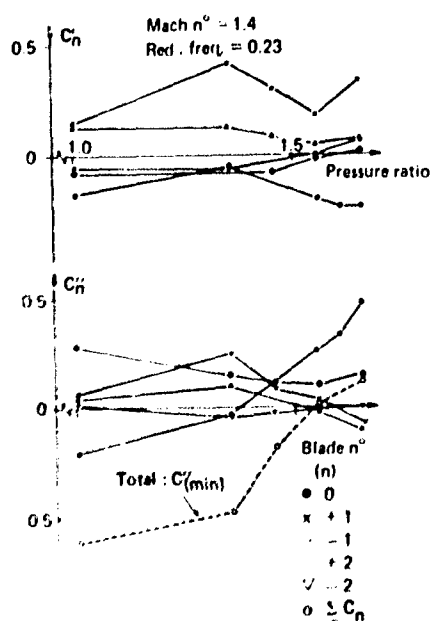


Fig. 24 Direct, Coupling and Total Moment Coefficient for Pitching Moment in Supersonic Started Flow.

A better understanding of the physical grounds for this flutter is gained through the study of unsteady pressure distributions. Practically, this means the evaluation of a vast amount of data (local pressures for each blade), but experience has shown, as in subsonic flutter, that the change from flutter conditions to no flutter and vice-versa is essentially governed by the direct coefficients. The pressure distributions on the vibrating blade can thus give reasonably adequate insight into the physical phenomena.

Figures 25 and 26 show suction and pressure surface pressure coefficient distributions in the form of modulus and phase. According to the quadrant in which the phases of the pressures are situated, the contributing moment is either exciting or damping (see figures).

The pressure surface (Figure 25) shows no particular overall tendency toward damping or excitation and the pressure ratio does not have a marked effect. However, the suction surface (Figure 26) shows a very large unsteady pressure near the trailing edge with a phase angle always situated in an exciting quadrant. As pressure ratio increases the magnitude of this trailing edge pressure drops rapidly. It is clear that the main contribution to flutter conditions for $x < 1.6$ is this large trailing edge pressure.

A glance at Figure 22 shows that this very large unsteady pressure is situated at the foot of the trailing edge shock. The movement of the shock with blade vibrations and the magnitude of the pressure difference across the shock are the factors determining the magnitude of the unsteady pressure. The fact that the position of the pressure peak does not vary with pressure ratio confirms the responsibility of the trailing edge shock wave.

Thus, one can safely conclude that the upper surface trailing edge shock motion is the primary motor of pitching flutter in supersonic started flow.

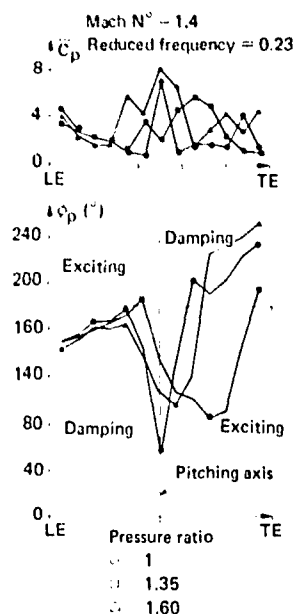


Fig. 25 Unsteady Pressure Distribution for Pitching Motion - Pressure Surface.

Plunging Motion

The aeroelastic behavior in plunging is quite different from that in pitching (above); however, the participation of the coupling terms relative to the direct terms in the total coefficient is very similar.

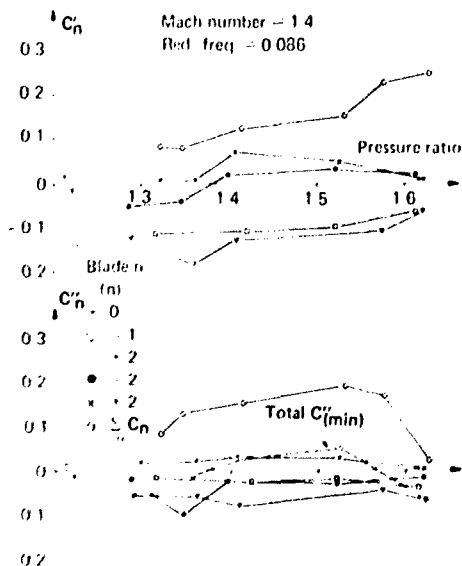


Fig. 27 Direct, Coupling and Total Lift Coefficients for Plunging Motion in Supersonic Started Flow.

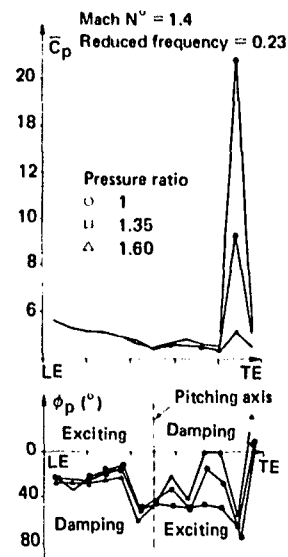


Fig. 26 Unsteady Pressure Distribution for Pitching Motion - Suction Surface.

Figure 27 (like Figure 24) shows a very much more marked effect of varying pressure ratio on the direct coefficients than on the coupling terms. This is, of course, reflected in the total minimum coefficient which (like in pitching) behaves very much in the same way relative to pressure ratio as the direct coefficients.

The total minimum coefficient curve shows possible flutter limits for $\tau < 1.38$ and $\tau > 1.58$. As for pitching motion, the direct coefficient pressure distribution will be studied in order to understand the source of flutter.

Figures 28 and 29 show the suction and pressure surface distributions respectively.

Figure 28 illustrates clearly the approach of flutter as the pressure ratio increases: the phase angle reaches into the exciting quadrant while the corresponding pressure peak is large. This pressure peak does not have the same origin as in the case of pitching: it is the point of impact of the reflection of the leading edge shock wave produced by the neighboring blade. Judging from this figure alone, the blade should become increasingly stable as the pressure ratio decreases. This is true to a point: a look at Figure 29 shows an increasingly greater portion of the pressure surface pressure distribution in the exciting quadrant with diminishing pressure ratio. The rapid change of phase near the leading edge is due to the position of the recompression shock on the pressure surface. As this shock wave moves aft with decreasing pressure ratio, the extent of the exciting zone increases and flutter conditions once again appear.

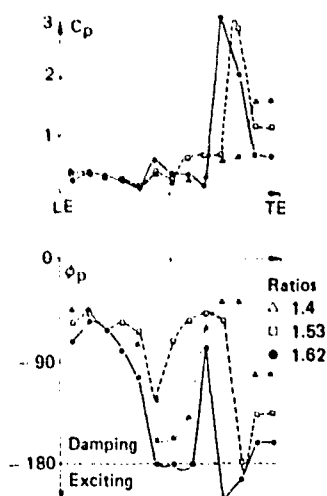


Fig. 28 Unsteady Pressure Distribution for Plunging Motion - Suction Surface.

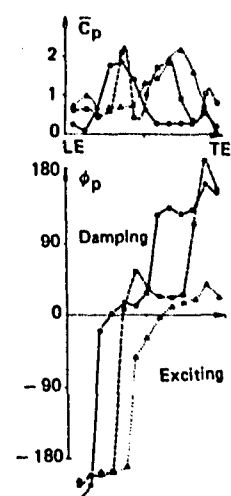


Fig. 29 Unsteady Pressure Distribution for Plunging Motion - Pressure Surface.

The Influence of Frequency

-For the case of pitching motion, Figure 30 shows the direct coefficient as a function of frequency. This parameter introduces a time (or phase) lag so that the pressure ratio range showing flutter conditions will progressively shrink with increasing frequency.

-The effect of frequency on flutter conditions in plunging motion is virtually negligible as illustrated by Figure 31. There is a noticeable influence on the magnitude of the coefficient but the phase angle remains practically speaking constant.

Conclusions on Flutter in Started Supersonic Flow

The characteristics of flutter in started supersonic flow depend on the mode of vibration concerned:

-Pitching flutter occurs at low pressure ratios and disappears as this parameter increases. The flutter is mainly due to the movement of the suction surface trailing edge shock wave, induced by the pitching motion. As pressure ratio increases the shock foot has probably an increasingly stable position and thus generates less unsteady destabilizing pressures.

-Plunging flutter is found at both high and low pressure ratios. At high pressure ratios the main cause is the motion of the impinging shock wave originating from the leading edge of the neighboring "upstream" blade. This effect disappears at lower pressure ratios where a weaker destabilizing process takes over on the pressure surface. This is due to the aftward movement of the final recompression shock wave with decreasing pressure ratio.

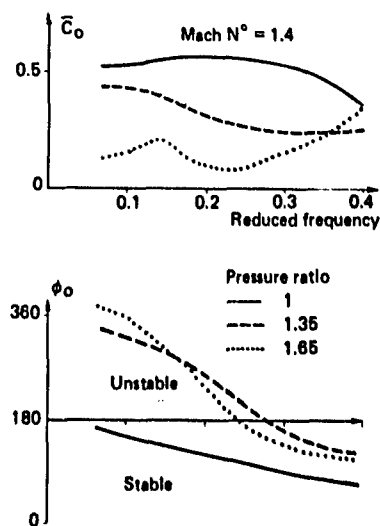


Fig. 30 Direct Moment Coefficient for Pitching Motion.

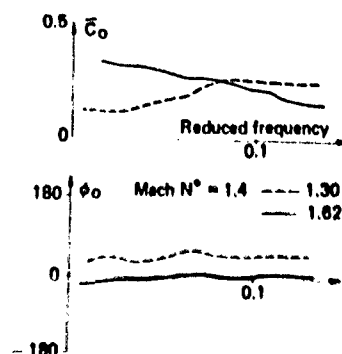


Fig. 31 Direct Lift Coefficient for Plunging Motion.

The effect of frequency on flutter limits is important in the case of pitching. An increasing phase lag with increasing frequency reduces the likelihood of flutter. In plunging, frequency has little influence on flutter limits.

SOME IDEAS ON SUPERSONIC UNSTARTED FLOW FLUTTER

Good periodicity in a linear cascade for unstarted supersonic flow is very difficult to obtain. However, it was achieved across four adjacent blades, but to date only one preliminary aeroelastic test has been carried out with plunging motion.

Results obtained seem to indicate that the most significant aeroelastic behavior appears on the aft half-chord of the suction surface at the point where the bow shock of the "downwind" blade reflects.

The aeroelastic pressure measurements show:

- on the suction surface, a distribution having a very similar character to that of started supersonic flow with plunging motion (see Figure 28);

- on the pressure surface, a distribution closely akin to the case of transonic flow (Figure 7). This is not surprising, as the pressure surface is totally subsonic.

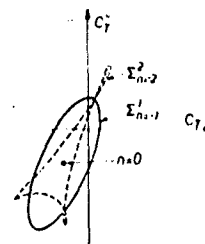
One can tentatively conclude that unstarted flow flutter will essentially resemble started supersonic flow high pressure ratio bending flutter. This conclusion would be, in fact, quite logical since started supersonic flutter appears as pressure ratio rises and the flow approaches the limit of started flow conditions. A certain continuity would not be surprising. However, more measurements and a much more profound analysis are required before definite conclusions can be drawn.

CASCADE RESULTS AND PREDICTIONS

The Relative Importance of Cascade Effects on Flutter, Szechenyi (1983)

The above results show that coupling coefficients can be of the same order of magnitude as direct coefficients, in particular for neighboring blades (C_{11}). These terms can thus largely contribute to the presence of flutter.

However, it is clear that flutter is neither entirely nor even essentially an unsteady cascade effect, since all the studied forms of blade flutter can exist as single-degree-of-freedom single-blade instabilities. The blade-to-blade coupling effects appear as vectorial additions (to the single blade forces) which either increase or reduce stability, according to the blade-to-blade phase angle.



Mach $N^\circ = 1.4$
Reduced frequency = 0.23
Pressure ratio = 1

Fig. 32 Total Moment Coefficient for $0 \leq \theta < 2\pi$ in Pitching Motion.

Figure 32 illustrates this very simply. Here are two results for supersonic bending with C'' plotted against C' for $0^\circ < \theta < 360^\circ$. The combined effect of five blades (C_0, C_{11}, C_{12}) has been accounted for. The points around the loops are for the different blade-to-blade phase angles and the single point inside each loop is the direct value. Experience shows that the usual parameters (frequency, angle of attack, Mach number, pressure ratio) have a much more significant influence on the position of the direct coefficient point than on the size of the loops. Hence, the parameter dependence of the direct forces is the principal factor leading to flutter conditions.

In an actual compressor, the real effect of the coupling terms will depend largely on the frequency tuning of the blades. The above discussion, of course, supposes perfect tuning.

Mistuning is a frequently employed method for attempting to avoid flutter problems and this can, in fact, be a very powerful tool. However, it has a severe limitation in that mistuning can change or shrink a loop such as in Figure 32 but can never change its position relative to the axes of the figure. In other words, a case with single-blade flutter cannot be remedied by mistuning. Theoretical studies on mistuning, as for example by Crawley and Hall (1984), have come to this same conclusion.

Comparison between Linear Cascade and Actual Fan Measurements

One blade of the fan simulated in the sub/transonic flutter research reported in the section "SUB/TRANSONIC FLOW FLUTTER IN TORSION" was instrumented with five pressure transducers in the same manner as the linear cascade blade (see "Measurements on a Compressor Blade").

Pressure measurements on the compressor blade can be compared directly with those obtained in the linear cascade wind tunnel. The results are presented in the same form, that is, modulus and phase of the complex pressure coefficients.

The maximum frequency of vibration in the cascade is, in fact, approximately 30% lower than the first torsional natural frequency of the fan blade.

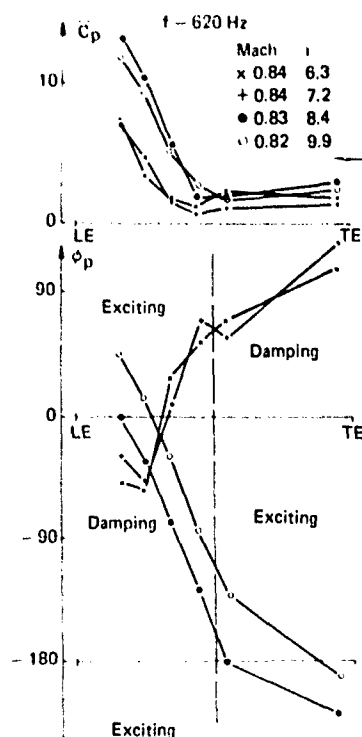


Fig. 33 Pressure Distributions on a Blade in a Compressor

A comparison of pressure distributions at Mach 0.8 in Figures 33 (fan) and 34 (cascade) shows very similar shapes. The pressure levels are equivalent and the change of shape of the phase curve (positive slope becoming negative) occurs at about the same angle of attack: between 7 and 8°.

The comparison at transonic speeds (Figures 35 and 36) gives rise to the same comments as above but the phase curves for the compressor are noticeably less steep than those for the cascade (faster propagation) and particularly on the downstream half-chord. This difference, though seemingly not very significant from a qualitative point of view, is all the more important in that the frequency of vibration of the fan blade is higher than that in the cascade and should logically produce a greater phase lag (see "Presentation of Results").

This phase discrepancy on the downstream half-chord has obviously some influence on stability limits. However, in all cases the actual fan is more stable than cascade measurement predictions.

Use of Cascade Data for Fan Blade Flutter Predictions

The application of cascade test result to a real compressor can, at the present time, only be made by strip theory. Aerodynamic damping can be obtained fairly simply from cascade results by the following equation:

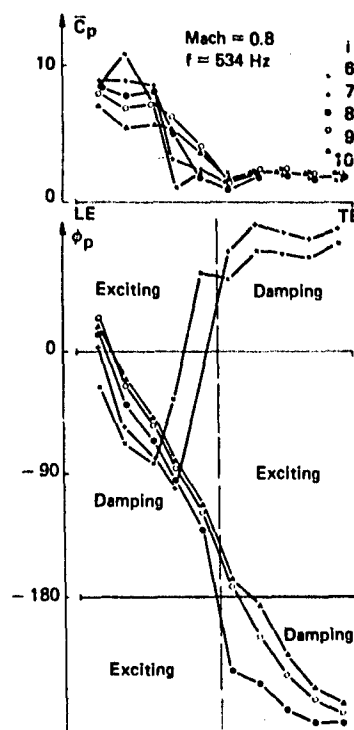


Fig. 34 Pressure Distributions on a Blade in the Wind Tunnel.

$$\zeta = \frac{\pi \rho l}{2 \mu N} \sum_{j=1}^N \frac{b_j^2 \alpha_j^2}{k_{Rj}} C_{L,Mj}''$$

where N is the number of strips.

A comparison between aerodynamic damping measured directly on a fan blade and the above calculations based on linear cascade measurements was made for subsonic flow. The result presented in Figure 37 shows that qualitative predictions are generally good. Predicted damping values are close for Mach = 0.8 but are always lower than those actually measured. This discrepancy may well be due to the pressure distribution differences shown in "Comparison between Linear Cascade and Actual Fan Measurements" above.

THE FUTURE

The physical understanding of fan blade flutter can be considered at different levels. A straightforward parametric study of aeroelastic damping will give some insight into parameter dependence but cannot reveal the aerodynamic behavior leading to this dependence. Aeroelastic pressure distributions go a step further and give some understanding of the aerodynamics behind the aeroelastic behavior. This is the state of the art described in this article. One could go further by looking at the causes of the observed aeroelastic behavior. For instance, in the case of subsonic flow, it is clear that flutter conditions are created when the direction of propagation on the suction surface is reversed; but what causes this change of direction when the flow separates?

There is some way to go yet before fully understanding all the underlying mechanisms of fan blade flutter.

Research must progress in this direction in order to give a physical background to the development of theoretical predictive tools and in order to establish reliable flutter free design criteria.

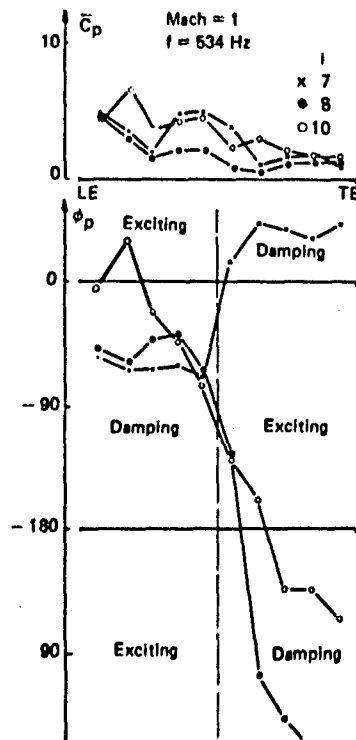


Fig. 36 Pressure Distributions on a Blade in the Wind Tunnel

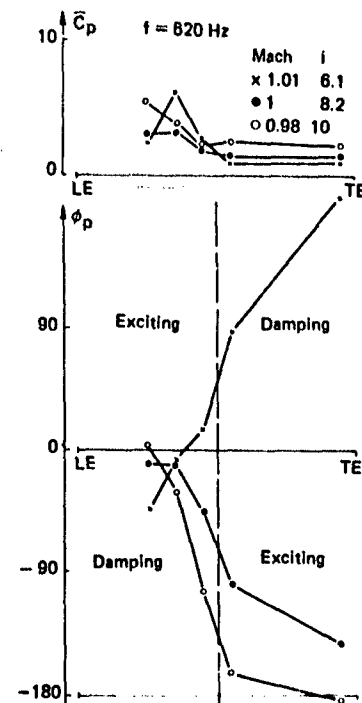


Fig. 35 Pressure Distributions on a Blade in a Compressor

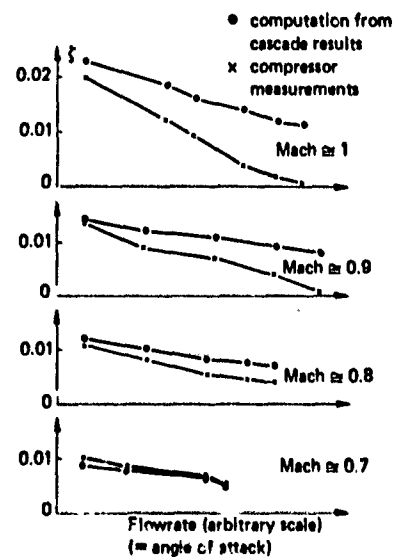


Fig. 37 Aerodynamic Damping as a Function of Flow Rate (Angle of Attack). Comparison between Compressor and Linear Cascade.

UNSTEADY AERODYNAMIC MEASUREMENTS ON ROTORS

by

Heinz E. Gallus
Institut für Strahlantriebe
und Turboarbeitsmaschinen
RWTH Aachen, FRG

INTRODUCTION

From the above chapters on "Unsteady Aerodynamic Measurements in Forced Vibration Research" and "Unsteady Aerodynamic Measurements in Flutter Research," respectively, it has become obvious that four types of experimental facilities are in use to simulate and investigate the unsteady aerodynamic aspects of forced vibration and flutter in axial-flow turbomachines. These are

- Linear Cascades
- Stationary Annular Cascades
- Low Speed Rotating Rigs
- High Speed Rotating Rigs.

These test facilities have been developed in order to overcome the difficulties due to accessibility problems in real machines. Moreover, they make it easier to isolate and vary the major parameters of importance. Most experimental studies have been conducted in linear cascades. They represent a spanwise section of a turbomachinery blading by a finite number of two-dimensional airfoils. Linear cascades provide the most convenient and cost-effective way to study subsonic, transonic, and supersonic flow phenomena and to vary the profile and cascade parameters. Further advantages are the easy access for flow visualization and the accommodation of large blade dimensions for detailed measurements of the steady and unsteady effects in the blade passages and on the blade surfaces. The limitations of linear cascades arise from the difficulty to achieve flow periodicity with a finite blade number and to produce the proper input gust loading or simulation of the reduced frequency necessary to obtain the desired aerodynamic damping data.

Several successful applications of linear and stationary annular cascades in the field of flutter investigations have been described in the previous chapters. However, with regard to forced vibration research both types of cascades imply limitations in obtaining proper reduced frequencies at realistic velocities and satisfactory simulation of the gust loading. The latter is defined as the time varying motion-independent aerodynamic loading of a cascade of airfoils which is created by upstream or downstream moving periodic disturbances. The physics of this interaction can be studied by arranging rotating blade rows and stationary vane rows in "rotating rigs" similar to their arrangement in real turbomachines, but with the advantage of being able to make use of scale model rotors and stages and of special rig constructions which provide easy access for all the instrumentation needed to identify and quantify the events in spatial unsteady

flow fields. Variations in gust amplitudes, reduced frequencies, and interblade phasing relative to the rotating airfoils can be realized quite easily. Using various numbers of rotor and stator blades permits the investigation of interblade phasing and reduced frequency effects on both the blading of rotor and stator airfoils. Rotating rigs also allow the experimental analysis of spanwise effects which are of increasing influence for large aspect ratio twisted bladings with highly varying inlet and exit flow fields along the blade span including tip leakage and secondary flow effects due to viscous flow. Another very important advantage of rotating rigs is the possibility of studying periodical flow separation and stall effects which may cause large dynamic blade loads. These studies are necessary to improve the mathematical modelling of the complex three-dimensional, viscous, unsteady flows which occur in the real turbomachine and to obtain the rotor and stator blade surface loads. However, these studies require -in addition to the techniques for unsteady flow measurements in stationary cascades presented in the preceding chapters -further efforts to measure the unsteady flow on the rotor and in the rotating frame of reference, respectively. This chapter is restricted to these very difficult measurements. An attempt will be made to give an overview of the various techniques and their application in selected examples. In view of the great amount of available material, a certain selectivity is unavoidable.

OBJECTIVES OF EXPERIMENTAL ROTOR AND STAGE UNSTEADY AERODYNAMIC RESEARCH

The major objectives of experimental aeroelastic research in turbomachines are:

- a. flutter measurements
- b. forced vibration measurements including
 - aerodynamic gust measurements
 - aerodynamic damping measurements
 - measurements of both effects occurring simultaneously.

Such measurements serve to provide the designer with advanced empirical or semi-empirical design systems, e.g., with a systematic flutter boundary data bank. However, it is more helpful and, indeed, also applicable to other than aeroelastic problems, such as noise, performance, and efficiency questions, to develop less empirically based prediction methods that can be utilized outside the limits of available experience. The recent advances in computational fluid dynamics encourage efforts to develop unsteady aerodynamic

models which also account for viscous flow have been neglected up to now.

Therefore, detailed unsteady aerodynamic measurements in rotors and rotating rigs which simulate the environment of the real machine are, although very costly, unavoidable for both guiding the development of satisfactory models and proving their validity. In many cases, disagreements between such measurements and predictions from simplified mathematical models are due to the omission of major features of the blade row phenomena occurring in the real machine.

From this point of view, a number of additional objectives of unsteady aerodynamic measurements in rotors and stages become important. They cover the whole range of parameters influencing the steady and unsteady spatial viscous flow field around rotor and stator blades. Some of them are listed below:

- blade row interactions (potential flow and viscous (wake) interaction)
- rotor and stator blade wake transport and decay
- unsteady boundary layers, flow separation and stall behavior, transition to rotating stall
- endwall influences and secondary flow effects
- turbulence effects
- shock/boundary-layer interaction
- unsteady aerodynamic blade forces and moments
 - on the fixed blading due to gust loads
 - on the vibrating blading in uniform inlet flow (aerodynamic damping/flutter)
 - on the vibrating blading with gust loads.

Representative measurements are often taken at the midspan section or at 75 percent span. However, in low pressure axial-flow compressor or turbine stages the airfoil and cascade geometry of the adjacent blade rows (spanwise taper of chord, thickness, and stagger) as well as the aerodynamic gust loads vary considerably from hub to tip. Therefore, for the solution of the forced response problem these spanwise variations have to be taken into account. Similarly, the blade deflections caused by the surface pressure loads show strong spanwise variations for the various natural blade modes.

In addition to these spanwise changes in geometry and gust loads further considerable variations may occur in the spanwise distribution of

- dynamic boundary layer behavior and position of separation along the airfoils
- shock position and shock/boundary layer interaction in the case of transonic or supersonic flow.

All this information is needed for the whole operating range. The resulting time-dependent spanwise aerodynamic load distribution - as demonstrated in Fig. 1 - can then be introduced as time-dependent forcing function into the equation of motion of the elastic blade system. At resonant conditions, i.e., equal frequencies of the forcing function and one of the natural blade frequencies, the response of the system will be governed by the damping forces. The knowledge of maximum stress levels at resonant conditions is a major requirement due to the inability of avoiding all the resonant conditions in a multi-stage compressor. Therefore, intolerably high stress levels have to be eliminated by design changes.

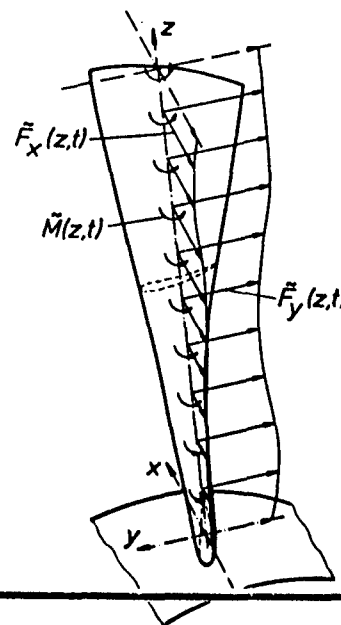


Fig. 1. Spanwise Unsteady Aerodynamic Airfoil Load Distribution

In this chapter, the discussion of measurements in rotors and rotating rigs will be restricted mainly to aerodynamic measurements and, in a few cases, to blade vibration measurements as they affect the unsteady flow field and, therefore, influence aerodynamic damping or flutter.

Surely, this approach to improve the prediction methods and models by measurements in rotating test rigs with blade operating environments, representing those in the real machine, is a very difficult and costly one. However, it will ultimately save a lot of money because the number of required experimental steps in the development of an acceptable prototype can be reduced. Many such efforts have already been reported in the open literature. Several examples of utilized rotating test rigs, measurement techniques as well as achieved results will be presented in the following sections in order to provide an overview of the state-of-the-art.

MEASUREMENT TECHNIQUES ON ROTORS OF TURBOMACHINES

The study of the unsteady flow, forced vibration, aeroelastic damping and flutter in rotating blade rows requires

- techniques to measure the vibration of rotating blades, i.e. mode shapes, amplitudes and angles of displacement, as well as
- techniques to investigate the unsteady aerodynamics of the flow leading to forced vibration and flutter.

This can be accomplished by measuring either on the rotor itself, i.e., in the rotating frames of reference, or in the stationary frame by using highly sensitive fast response techniques.

Rotating frame measurements need a reliable data transfer out of the rotating to the stationary frame. Transfer problems arising from low signal to noise ratios can be overcome by providing both signal conditioning and amplification on board the rotor. Subsequently, the high level signals can be transmitted to the data system via low-noise slip ring devices or by radio-telemetry, Lakshminarayana et al (1980), O'Brien et al (1974), Adler (1978), Kemp (1978), Jones (1970). To compare unsteady flow data with time-averaged values in the

relative flow field of the rotor, pneumatically measured signals from rotating probes or pressure taps on the rotor blade surface are usually transmitted out of the rotor by a rotating scanivalve system.

TECHNIQUES FOR DISPLACEMENT AND VIBRATION MEASUREMENT ON ROTOR BLADES

The widely used technique of applying strain gauges together with slip rings has been documented in many publications. A short review of this technique has been presented by F.O. Carta and R.L. O'Brien (1980). Although this technique has proved its usefulness to monitor the alternating stresses on rotating and stationary bladings or the onset of flutter, the strain gauge provides no information on the vibration mode involved or on the deformation mode shape of the blade. In particular, it cannot detect the blade surface load distribution. For the determination of deformation mode shapes optical methods have been developed. Stargardt (1977) measured the deflections of a rotating fan blade with embedded mirrors on the blade. The key to the method is the unique blade and disk deflection occurring with any of the potential motions. Detailed data on the blade and disk vibration mode shapes of fans up to 2.2 m diameter has been measured by Hockley et al. (1978) who used double pulse laser holography. Both axial and tangential components of the blade

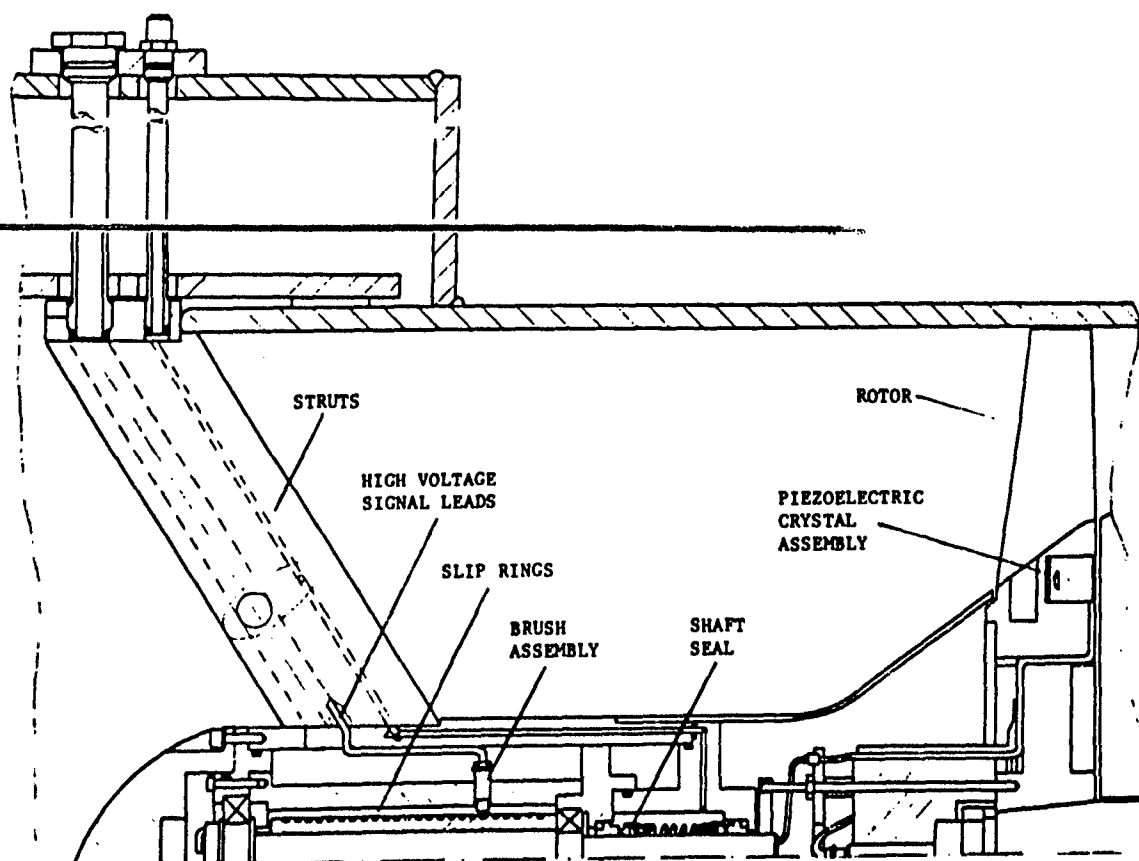


Fig. 2. Cut-away view of the test section, showing the rotor and piezo-electric crystal assemblies, the center-body, and support struts (from Crawley 1982).

and tangential components of the blade mode shape were obtained by taking holograms from two directions. The analysis of the holograms was performed with the aid of a computer linked television system which generated the required blade mode shapes directly from the photographs of the hologram reconstructions. The applicability of these methods is limited to fans or isolated rotor bladings. Neiberding and Pollack (1977) worked on optical detection of blade flutter. They used a casing optics systems to accurately detect the passage of blade leading and trailing edges. The importance of vibration measurements on rotor blades by optical probes from the casing is also emphasized by H. Roth (1980). Kurkov (1980) performed flutter spectral measurements using case-mounted pressure transducers.

Aerodynamic damping measurements using a specially instrumented version of the MIT Transonic Compressor were performed and reported by E.F. Crawley (1982). In runs at the operating point, the rotor was aerodynamically excited by a controlled two-per-revolution fixed upstream disturbance. Analysis of the data in terms of multiblade modes led to a direct measurement of aerodynamic damping for three interblade phase angles. Fig. 2 shows a cut-away view of the rotor, shaft, and forward centerbody. Aeroelastic testing was conducted in the MIT Blowdown Compressor facility, providing quasi-steady flow conditions in the test section for a limited period of time. In aeroelastic studies, a 24 channel slip ring assembly is housed in a centerbody supported by three struts ahead of the rotor. The above mentioned time varying upstream disturbance was created by the interaction of the primary flow with a series of small jets injected normal to the surface of streamlined struts upstream of the rotor. Thus, the symmetric disturbance along the struts causes a region of velocity defect behind the injector. The disturbance was terminated at 100 msec after test start and could be shut off within 1 msec, thus providing a well defined and sharp termination of the upstream disturbance. Fig. 3 shows a detail of Fig. 2, concerning the rotor instrumentation. Piezo-electric displacement transducers were mounted on the disk recording the local displacement of each of the 23 blade roots. In addition, 4 strain gauges measured the blade response in bending. The transducer signals could be calibrated linearly against tip displacement for each of the natural blade modes. Thus, one independent displacement measurement per blade is provided. From these data and from the structural analysis of the MIT Rotor, it was possible to resolve the multiblade modal response of the blade-disk modes associated with one family of circumferential modes. The response to forced vibration at the design point due to upstream disturbances was investigated. After sharp termination of the disturbance, the subsequent free vibration ring downstream of the rotor served as a measure of the aerodynamic plus structural damping. Additionally, the aerodynamic response of the rotor to the disturbance was investigated by use of high frequency response wall static pressure transducers upstream of the rotor indicating the

increase of the local bow shock strength when the blade passes through the region of velocity defect in the disturbed flow.

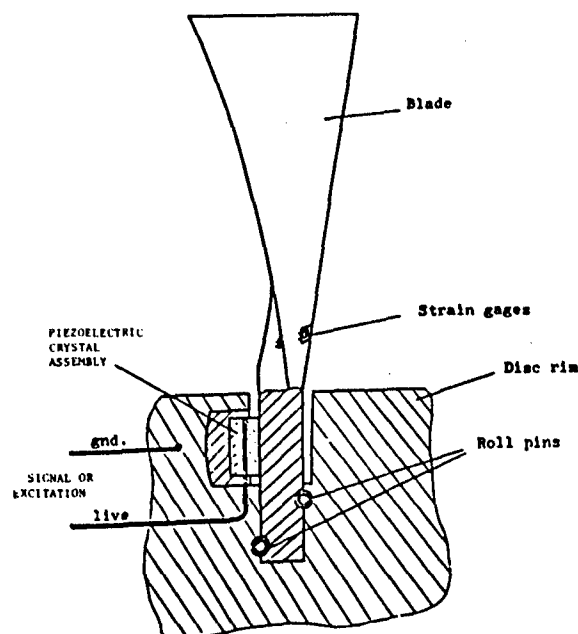


Fig. 3. Details of root attachment showing the location of the piezoelectric displacement transducer (from Crawley 1982).

TECHNIQUES FOR UNSTEADY FLOW MEASUREMENT ON ROTORS

In principle, the majority of unsteady flow measuring methods on rotors can be classified as follows:

- a. Measurements by direct physical connections of a high response measuring element to the measurement point, such as
 - high response pressure transducers
 - high response hot wires or hot films that can be used both on rotor blade and passage end wall surfaces to detect surface distributions. They can also be introduced into probes and mounted to probe holders that can be shifted in the rotating or stationary frame of reference to provide unsteady flow data of the blade passage and the flow field in front and aft of the blade row. Since such probes and, in particular, the probe holders intrude into the flow field it must be required that these instruments are kept as small in size as feasible.
- b. Optical methods of flow measurement and visualization, such as
 - Flow Visualization, e.g., by smoke or dye injection
 - Gas Fluorescence
 - Schlieren - or Shadowgraph Methods
 - Holographic Interferometry
 - Laser Velocimetry

These non-intrusive measurement systems have many advantages, as will be indicated in the next section by presenting some typical examples of performed measurements. However, there are also limitations that make it necessary to use the measuring techniques of the first category as well.

In the next section, a short review of the various methods mentioned above is presented and the pertinent literature is cited, so that the reader may consult these publications for details of the measuring devices, calibration procedures, data acquisition and processing.

EXAMPLES FOR THE APPLICATION OF UNSTEADY FLOW MEASURING TECHNIQUES ON ROTOR

During the last three decades, great progress in the field of microelectronics, particularly high frequency response microsensors as well as electronic data acquisition and evaluation, has led to significant improvements in the measurement of the unsteady flow and blade vibrations in the rotating frame. In this chapter it will only be feasible to select some typical examples of key measurements which provide a physical understanding of the complicated three-dimensional, viscous unsteady flow in blade passages and of the structural dynamic response in the forced vibration problem. Experimental blade flutter investigations on rotors will be excluded here because they were already dealt with in the previous chapter on "Unsteady Aerodynamic Measurements in Flutter Research."

UNSTEADY BLADE STATIC PRESSURE MEASUREMENTS

The development of miniature, high response pressure transducers which are small enough to be embedded in the surface of the blade has generated great progress in unsteady aerodynamic investigations. Arranging several of these transducers around the airfoil enables one to measure unsteady surface blade loads and to obtain information on the forcing function in the forced vibration problem. Parallel use of pneumatic pressure taps on the surface of an adjacent rotor blade allows one to compare unsteady and steady static pressure distributions on the airfoil.

The electromechanical configuration of the pressure transducers and their installation in slots or grooves which have to be provided in the blade surface, is well-known from the literature, Carta & O'Brien (1980), Gallus (1975), and will not be repeated here. However, it should be remarked that such grooves and inner holes in rotor blades can reduce the blade strength considerably. This causes a certain limitation in the use of this technique on high-speed rotors. Therefore, new attempts should be made to provide a type of surface-film pressure transducer which can be fixed onto the blade surface without grooves but which is thin enough not to disturb the surface conditions on the airfoil.

Unsteady static blade pressure measurements are in use for flutter investigations on isolated fans as well as for

the determination of aerodynamic blade forces due to rotor-stator interaction.

Increasing knowledge of the physics of rotor-stator interaction and improved mathematical models to predict the time-dependent flow field as well as the induced dynamic blade forces are fundamental objectives of unsteady aerodynamic research. Rotor-stator interactions are an inherent property of turbomachines due to the relative motion of blade rows. Even if viscous effects, such as wakes, could be neglected, the relative motion of blade rows produces a periodically fluctuating flow field around the airfoils and induces dynamic forces on the airfoil surfaces. These potential flow interactions of blade rows (rotor-stator or counter-rotating rotors) are quite amenable to two-dimensional flow calculations using the cascade flow model which is obtained by unwrapping an annulus of infinitesimal radial height from the flow passage of an axial-flow turbomachine. It is well-known that this potential-flow interaction causes dynamic blade forces upstream and downstream which are very strong in the case of very small axial gaps between the blade rows but which rapidly diminish with increasing axial blade row distances. This effect, well explained by potential flow theory, has also been measured in various investigations of axial-flow compressor and turbine stages.

In addition to potential-flow interaction, wake flow interaction has to be considered in order to determine the aerodynamic load of an airfoil. Assuming uniform machine inlet flow, except for the first upstream rotor blade or stator vane row, all subsequent rows of airfoils are exposed to a periodically unsteady inlet flow field due to the wakes created by the upstream blade or vane rows. These wakes are convected into the downstream row creating unsteady pressure distributions along the airfoil surfaces.

Fig. 4 displays the scaled midspan section of a subsonic axial-flow compressor stage investigated by Gallus et al. (1980). Four pressure transducers were integrated into the suction surface of a rotor blade and three into the pressure surface. In Fig. 5 the local time histories of the fluctuating portions of the static airfoil surface pressures are plotted versus time for one blade passing period both with the inlet guide vanes being present and removed. For the latter case, the dashed lines indicate that there exists a slight periodic upstream influence of the stator vanes on the rotor blades due to potential flow interaction, although, as can be seen from Fig. 4, the axial gap between rotor exit and stator inlet is large (30.5 mm) compared to the axial chord of the stator vane (61.9 mm). At this rotor part speed of only 6500 rpm, i.e., about 68 percent of the nominal speed (9500 rpm), the strain gauges at the rotor blade root indicated no noticeable vibrations. Due to the wakes of the inlet guide vanes, the peak local pressure fluctuation of about 2000 Pascal appears at position RS1 located on the rotor blade suction surface close to the leading edge. The electrical signals of the high response pressure transducers (Kulite) were transferred from the rotating frame

to the stationary frame by a slipping transmitter. The local time-averaged static airfoil surface pressures at rotor-blade midspan were determined by an array of pneumatic static pressure taps. In this case, the pneumatic pressure signal transfer from the rotating to the stationary frame was achieved by means of a rotating Scanivalve system on the rotor shaft. The centrifugal effect on the columns of air in the rotating piping between pressure tap location and rotor shaft axis was taken into account by an appropriate correction of the measured pressure values. These measurements on a rotor blade surface were described by Gallus et al. (1978). Machine data, details of the measuring device, and data acquisition were reported by T. Wallmann (1980).

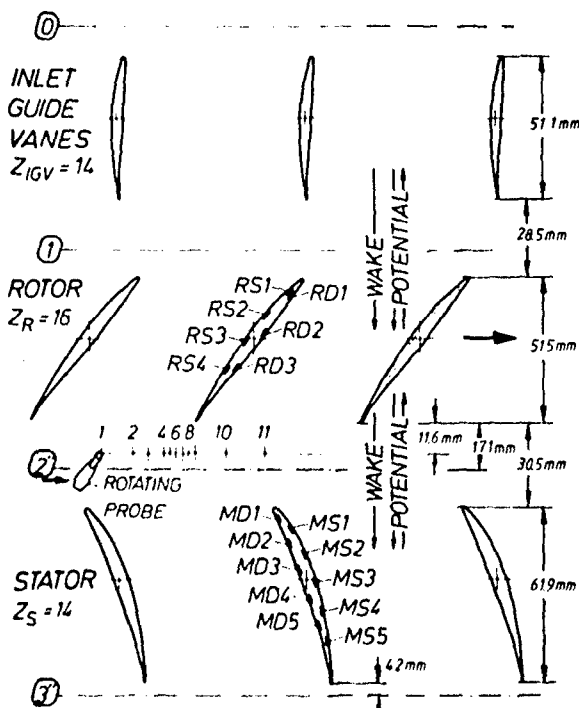


Fig. 4. Scaled midspan section of a subsonic axial-flow compressor stage (from Gallus et al. 1980)

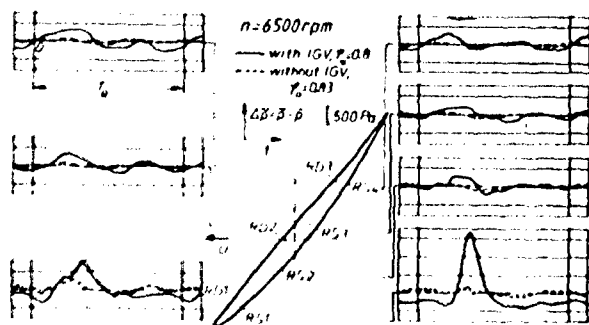


Fig. 5. Fluctuating portions of static rotor airfoil pressures deviating from local time-averaged values, plotted versus time of one blade passing period. Full lines correspond to IGV's mounted, dashed lines to IGV's removed (from Gallus et al. 1980)

Attempts have been made to calculate the unsteady pressure distributions due to wake interaction, e.g., by Naumann and Yeh (1973), Lotz (1965), and Henderson (1972). Gallus et al. (1981) applied these prediction methods to the axial-flow compressor stage without IGV's, as shown in Fig. 4, and compared with measured unsteady static airfoil pressure distributions on the stator vanes. The results are presented in Fig. 6 in terms of Fourier coefficients of the lift fluctuation plotted versus the harmonic components. From this comparison it becomes obvious that with respect to the first and second harmonic components the predicted values are only in very rough agreement with the measurements. For flow rates between 0.8 to 0.7, predicted and measured coefficients differ even more. Fig. 6 also includes the comparison with results predicted by the potential flow interaction theory according to Lotz (1965). For very large axial spacing between rotor and stator, the potential flow interaction is negligibly small.

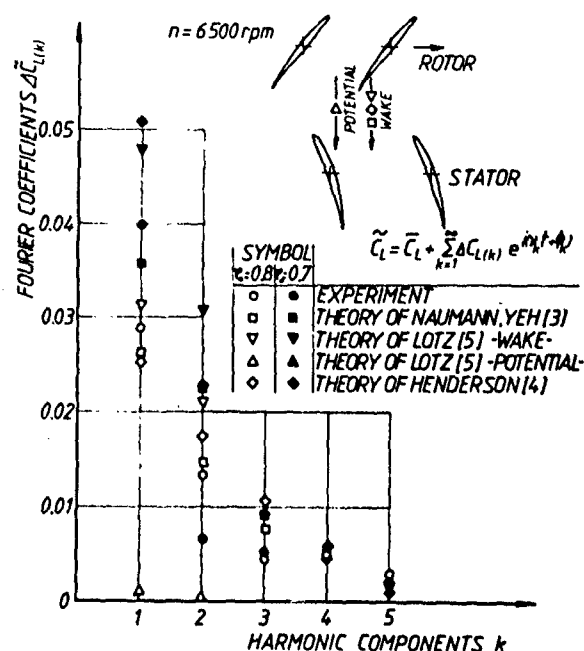


Fig. 6. Analysis of rotor-stator interaction for flow rate coefficients of 0.8 and 0.7 (from Gallus et al. 1981)

In the mean time, improved computational methods based on the solution of the two-dimensional unsteady Euler equation have been established to predict the aerodynamic blade forces caused by the measured unsteady inlet flow conditions, such as velocity and angle distribution in the periodic upstream wake flow, e.g., by Ispas et al. (1980). This requirement makes it necessary to know the wake flow field downstream of stator and rotor blade rows either by measurements or by computational approaches.

Measurements of the wake flows, in particular the study of their differing character and decay downstream of rotor blades and stator vanes, have been conducted by various authors with the aid of rotating pneumatic or rotating as well as stationary probes provided with high response pressure transducers or hot wires, and by laser velocimetry, respectively. These techniques will be considered in the following sections.

Dring et al. (1982) studied the aerodynamic interaction between the rotor and stator airfoils of a large scale axial turbine stage. The data included measurements of the time-averaged and instantaneous surface pressures, and was acquired with rotor-stator axial gaps of 15 and 65 percent of axial chord. Fig. 7 shows the airfoil geometry and the transducer locations. The measured results reveal the upstream potential flow influence of the rotor on the stator as well as the downstream potential flow and wake influences of the stator on the rotor, as presented in Fig. 8, where the stator and rotor unsteady pressure envelopes are plotted in addition to the time-averaged static pressure distribution.

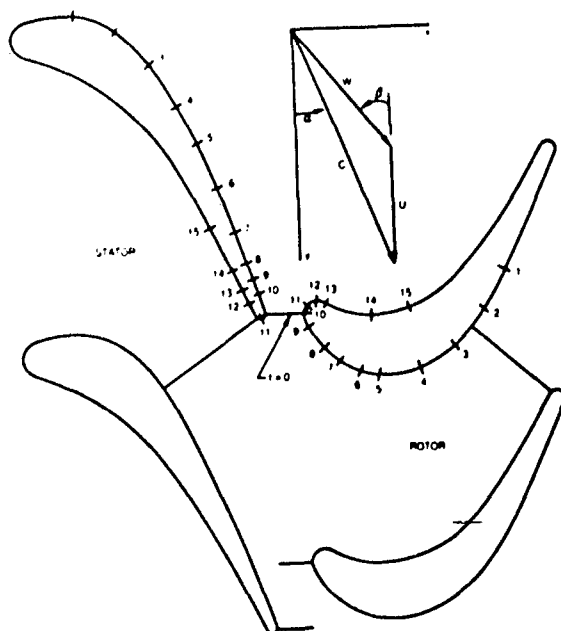


Fig. 7. Turbine stage at 15 percent axial gap (Kulite sites) (from Dring et al. 1982)

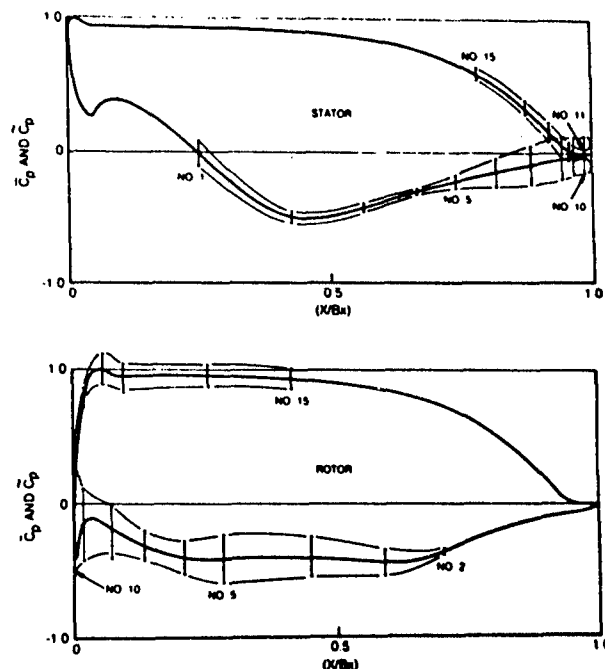


Fig. 8. Stator and rotor unsteady pressure envelopes, 15 percent gap, $(C_X/U) = 0.78$ (from Dring et al. 1982)

Beside these high response blade static pressure measurements there are also results from thin film gauge measurements on stator and rotor blades reported by Dring et al. (1982). Samples of the rotor thin film gauge data for the three rotor inlet flow angles (35, 40, and 45 degrees) are presented in Fig. 9 for the 15 percent gap. Data are shown for sites 5 and 7 located on the suction surface toward the leading edge. For the rotor, periodic events occurred at the stator passing frequency. It becomes obvious that the strong unsteadiness at site 7 near the leading edge is greatly reduced at site 5 further downstream. At both sites, regions of large random fluctuation due to the turbulence in the stator wake are superimposed on the periodic fluctuation. Zones of smaller randomness increased with reduced turning. The reduced leading edge overspeed produced a laminar boundary layer on the rotor suction surface which was periodically interrupted by the impingement of the turbulent upstream stator wake. The periodic oscillation between laminar and turbulent boundary layer flow on the rotor suction surface was found in good agreement with similar observations mentioned in the literature.

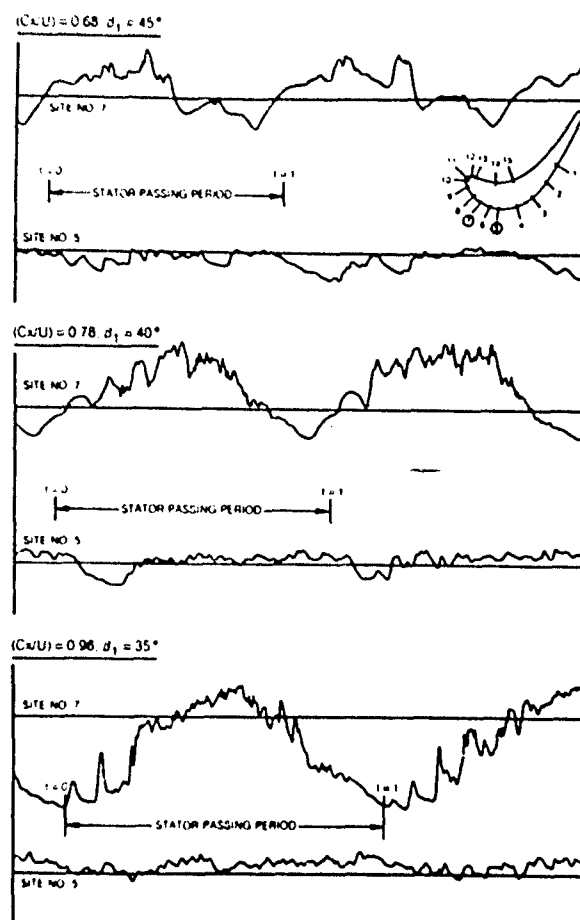


Fig. 9. Rotor thin film data, 15 percent gap (from Dring et al. 1982)

The influence of both the axial gap between rotor and stator and the rotor-stator blade number ratio on the aerodynamic blade load measured with high response pressure transducers has also been investigated by Grollius (1981) and Gallus et al. (1982).

W. F. O'Brien et al. (1980) used on-rotor high response transducers for their study of distorted inflow behavior on the dynamic response of the flow over the rotor blades. A rotating telemetry system provided the data transfer.

HIGH RESPONSE PRESSURE TRANSDUCERS FOR UNSTEADY PRESSURE FIELD MEASUREMENTS ON THE CASING WALL

This technique is favoured for the study of rotating stall and for the determination of shock-wave configurations at the tip of trans- or supersonic compressor bladings.

Larguier (1980) reports on a rotating stall study with 26 piezoelectric ceramic pressure transducers mounted in a casing zone located in the rotor section. As long as no rotating stall cells appear, each of these transducers emits a signal periodically modulated by the passage of the rotor blades. When rotating stall occurs the passage of the separated zone in front of a transducer causes a considerable change of response and a reduction

of the amplitude of the modulation due to the blade passage, while the mean pressure level varies. From the measurement of instantaneous pressure distributions on the casing wall, the evolution of the pressure distribution on the rotor blade tip airfoils at various times during the passage of the rotating stall cell could be deduced.

Bohn (1977), Gallus et al. (1977) and Broichhausen (1981) used high response pressure transducers distributed along the rotor and stator casing wall of an axial-flow supersonic compressor stage to study the unsteady upstream influence of the stator on the rotor blade tip flow. During low-speed operation with subsonic axial flow velocity in the gap between rotor and stator, the rotor flow pattern is influenced by the axial retroaction of the stator. The downstream interaction between rotor and stator along the casing wall was investigated, too, to determine the influence of the relative rotor position on the wall pressure distribution at the entrance of the stator. It was remarkable that the maximum amplitude of the static pressure fluctuation due to rotor blade passing amounted to 65 percent of the amplitude of the mean static pressure.

Figs. 10a and 10b, taken from Larguier (1980), show results from high response wall pressure measurements which were performed on a model of a supersonic compressor at ONERA. The casing wall of the rotor section was equipped with 12 piezoelectric ceramic pressure transducers to produce pressure diagrams as a function of time. Fig. 10b presents the isobar map developed from pressure recordings including the drawing of shock waves as detected by schlieren photographs.

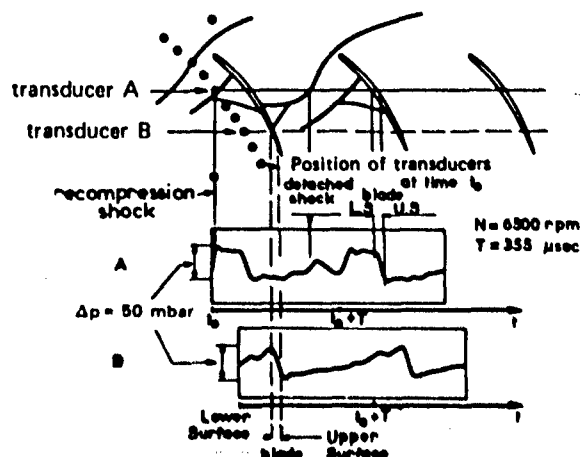


Fig. 10a. Transducer arrangement and relative position of rotor at time of measurement triggering. Examples of recordings. (from Larguier 1980)

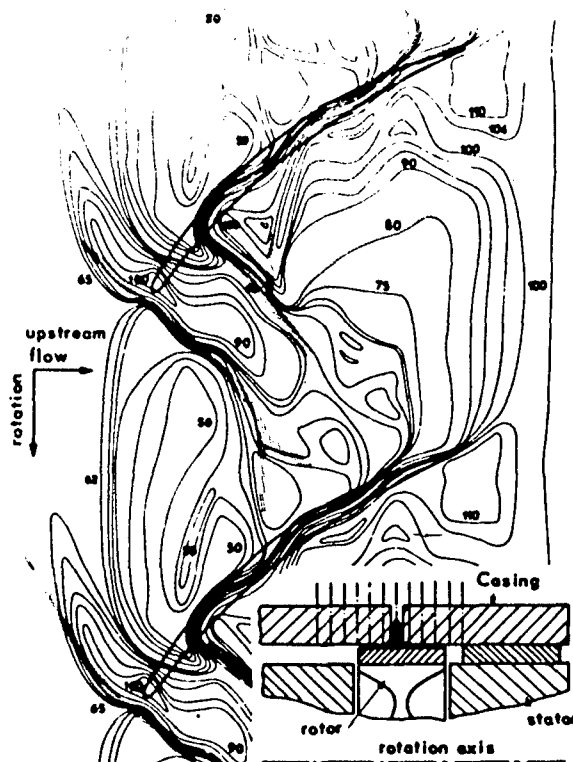


Fig. 10b. Chart of isobars along the casing wall (mbar). Comparison with shock waves observed by schlieren photography (shaded zones). (from Larguier 1980)

ROTOR FLOW FIELD AND ROTOR WAKE STUDIES WITH THE AID OF ROTATING PROBES

This category of measurements is restricted to moderate rotor speeds because of the enormous centrifugal forces acting on sensors, probes, and probe holders, on the one hand, and the increasing interaction with and disturbance of the flow field to be measured, on the other. Hence, this technique has predominantly been applied to low speed test rigs and isolated rotors. Nevertheless, most of the knowledge about the complicated phenomena in rotor blade passages as well as in the rotor wake flow measured in the rotating frame of reference has been gathered with the aid of this technique.

B. Lakshminarayana (1980) presented an extensive review of the various probe designs in his keynote paper contributed to the Symposium on "Measurement Methods in Rotating Components of Turbomachinery" at the 1980 Joint Fluids Engineering and Gas Turbine Conference in New Orleans. Various rotating probe traverse mechanisms, probe types and sensors developed in research laboratories all over the world are described in this review paper. It includes a detailed survey of the transfer of pressure data from a rotating to a

stationary system by means of pressure transfer devices, such as scanivalves or rotating transducers converting the pressure into an electrical signal in the rotor frame of reference. References to the most widely used methods for the transfer of electrical data from rotating transducers such as pressure transducer, hot wire, strain gauge, and thermocouple via mercury slipring unit or telemetry system are listed. The reader also finds a comprehensive survey of the various types and essentials of hot wire and pressure probe measuring techniques for the experimental analysis of rotor passage and exit flow.

In the following paragraphs, examples of the rotating probe measuring technique and some selected results taken from the literature will be cited.

Very detailed information on an axial flow research compressor facility designed for flow measurement in rotor passages has been presented by B. Lakshminarayana (1980). In this facility, Sitaram et al. (1981) used conventional probes, such as five-hole, disc, and spherical pitot-static probes to determine the three-dimensional flow field in a rotor passage.

Because of the extraordinary difficulties to traverse such types of probes in a rotating passage, in particular at high circumferential speeds, and due to the blockage effect of such probes in case of a comparatively small passage area, most of the measurements with rotating probes concentrated on the investigation of the relative flow field downstream of the rotor blade trailing edge. Many mid-span and fullspan measurements of this kind have contributed to the analysis of the complicated flow field aft of a rotor showing considerable radial flow effects. Circumferential and radial probe traversing as well as measurements at various axial stations enable one to study secondary flow and mixing effects as well as the tip clearance influence. Maps of the rotor exit flow vectors and relative total pressure contours can be obtained for an axial measuring station, and from their changes at various downstream stations the decay of the wakes and the overall downstream behavior of the relative flow field can be determined. Such a detailed experimental analysis is recognized to be a powerful tool for improved designs and advanced computational methods for flow prediction. As an example of excellent work with this technique, there are to be mentioned the investigations of an axial compressor rotor in a large scale rotating rig by R. P. Dring et al. (1979, 1981). Fig. 11 demonstrates the radial-circumferential distribution of the relative total pressure coefficient measured by a rotating five-hole probe at a downstream distance of 10 percent of the mid-span axial chord. The rotor exit flow vectors corresponding to Fig. 11 are shown in Fig. 12. Such results of measurements are suitable to test the quality of computational prediction methods. These investigations also included the measurement of the rotor wake deformation with varying flow rate coefficient.

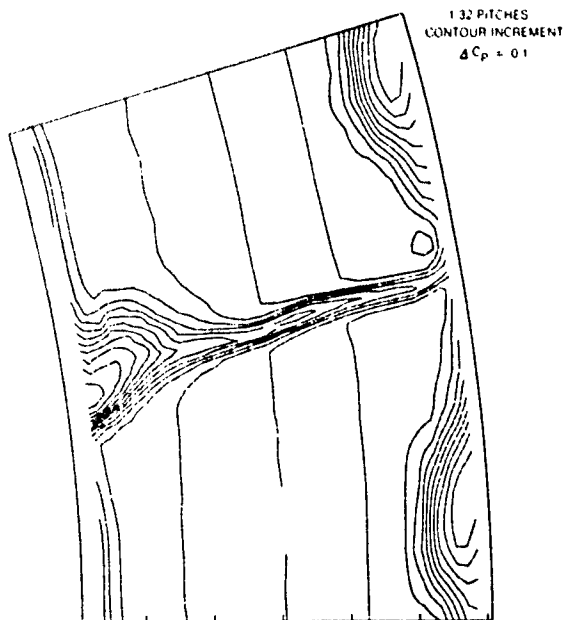


Fig. 11. Total pressure contours, 30% aft, $(C_X/U_m) = 0.85$ (from Dring et al. 1981)

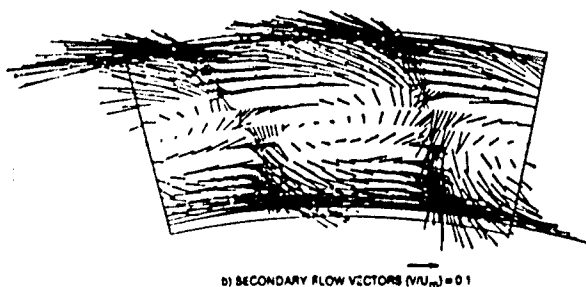


Fig. 12. Relative flow speed contours and secondary flow vectors relative to core flow, $\phi = 0.85$ (from Dring et al. 1981)

Wake deformation and wake transport are well-known to directly influence the unsteady static pressure distribution in the downstream blade row. Therefore, the flow in the airfoil wake has been a favorite subject of numerous experimental attempts to describe the wake behavior downstream of rotor and stator blades. Investigations conducted by Thompson and Kerrebrock (1975), Reynolds and Lakshminarayana (1980), Reynolds et al. (1979), Ravindranath and Lakshminarayana (1979), Raj and Lakshminarayana (1976), Hirsch and Kool (1977), Kool et al. (1978), Gallus (1975), Gallus (1979) have revealed remarkable features of the rotor wake flow, such as large radial velocities in the wakes, local regions of large radial flows near endwalls, similarity of wake

profile shape, asymmetry of wake velocity profiles with decreasing flow rate coefficient, symmetric and asymmetric wake radial velocity profiles. These studies will contribute to an improved analytical modelling of the wake influence, e.g., on the unsteady aerodynamic blade load of the downstream blade row. Among others, Fleeter et al. (1978, 1980), Gallus (1975), Gallus et al. (1980), Ispas et al. (1980) investigated the unsteady aerodynamic response of compressor stators generated by rotor wakes. Gallus et al. (1982) included the decay of rotor wakes due to increasing axial gaps as well as the influence of various rotor-stator blade number ratios into their experimental program.

Figs. 13 and 14 demonstrate wake flow measurements by a rotating pneumatic three-hole probe, Gallus (1979), Wallman (1980).



Fig. 13. Rotating three-hole pneumatic probe traversed during rotation behind the rotor trailing edge as indicated in Fig. 4. The photo includes a view of the high response pressure transducers at midspan. (from Gallus 1979)

Knauf and Gallus (1984) measured the unsteady aerodynamic response of vibrating stator vanes to upstream rotor wakes at midspan.

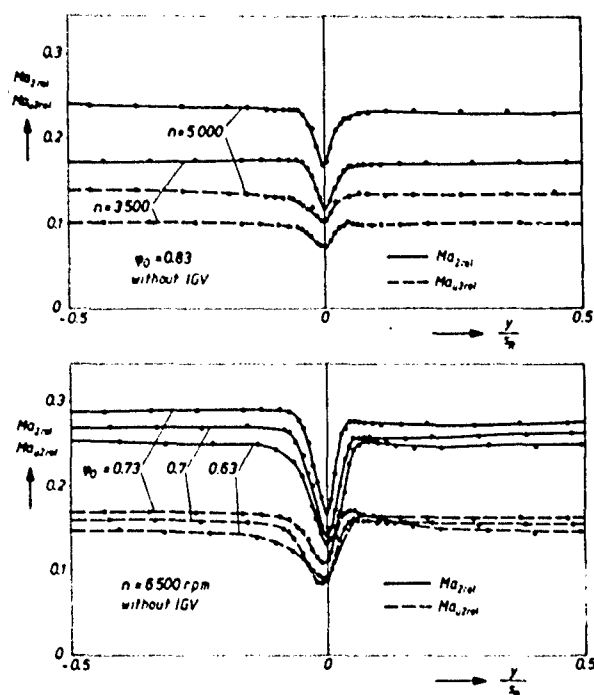


Fig. 14. Wake flow measurements with rotating probe shown in Fig. 13. The upper part demonstrates the influence of rotor speed, the bottom part depicts the wake shape deformation due to decreasing flow coefficient from 0.73 to 0.63 (from Gallus 1979).

Unsteady flow effects in the rotating frame of reference can, for instance, be detected by use of high response pressure transducers or hot wires on a rotating probe. Fig. 15, taken from Gallus et al. (1980) and Wallman (1980) shows a photo of a compressor rotor additionally provided with a Kiel type probe integrated semiconductor transducer that can be traversed to detect the wake transport from inlet guide vanes through the rotor blade passage, and periodic rotor blade flow separation, respectively; see also Fig. 4.

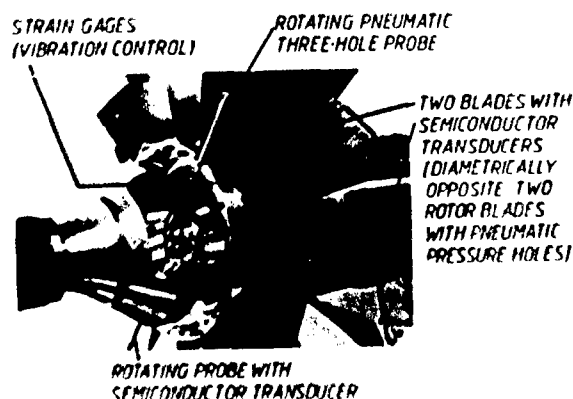


Fig. 15. Photo of the instrumentation for on-rotor measurements in a high speed axial compressor stage (from Gallus et al. 1980)

Ravindranath and Lakshminarayana (1979) applied rotating tri-axial hot wire probes to investigate the structure and decay characteristics of turbulence behind a compressor rotor. Matsuuchi and Adachi (1983) presented measurements of the three-dimensional unsteady flow inside a rotor blade passage of an axial flow fan. These measurements were made with a single hot wire probe rotating with the rotor.

MEASUREMENT OF THE ROTOR FLOW BY HIGH RESPONSE STATIONARY PROBES

This field of measurement problems is mainly covered by two techniques:

- stationary hot wire technique, and
- stationary high response pressure probes.

There are two methods available to apply the stationary hot wire technique to flow measurements at the rotor exit or inlet. The first method uses a three sensor wire whereas the second utilizes a single sensor which is rotated about its own axis. To separate the periodic and random components from the measured signal, a periodic sampling and averaging technique is employed in both cases. Lakshminarayana (1981) presented a detailed introduction to these techniques. The stationary hot wire technique has been used widely for the study of isolated rotor wake flows and the fluctuating flow fields in the gaps between the blade rows, respectively. Because of the smallness of the sensors compared with the high response pressure probes, the hot wire technique is favoured for flow field measurements in stator vane passages. For example, Fig. 16, taken from Gallus and Hoenen (1983), gives a view of the local fluctuation of the rotor exit flow angle in a stator midspacing position of the probe at three various spanwise locations, plotted versus time of one blade passing period. The operating point corresponds to unthrottled flow at about 37 percent of the design speed of the axial flow compressor stage. Fig. 17 demonstrates already large local fluctuations of the radial flow angle for the same operating point, showing maximum amplitude at mid-span. These measurements were performed with the aid of a three-sensor hot wire probe that was also used to determine the spanwise distribution of the degree of turbulence in the planes 1, 2, and 3 in Fig. 18. This figure also includes the data measured by a one-sensor probe that cannot include the radial component which is of considerable influence in the rotor exit flow.

The following examples demonstrate the use of high response pressure transducers in stationary probes, such as the data in Fig. 19 obtained from a stationary Kiel type probe provided with a semiconductor transducer for time-dependent spanwise total pressure measurements of the rotor exit flow, Wallmann (1980), Gallus and Hoenen (1983).

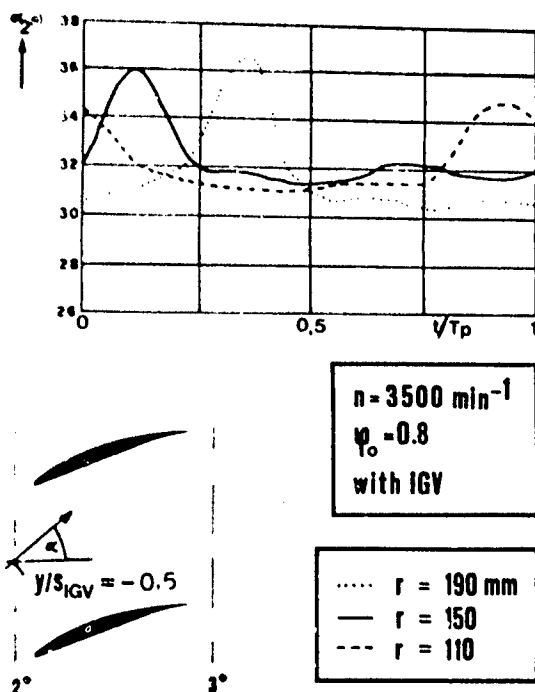


Fig. 16. Time-dependent rotor exit flow angle measured at three different spanwise locations in a mid-spacing position of the three-sensor hot wire probe (plane 2*) (from Gallus and Hoenen 1983)

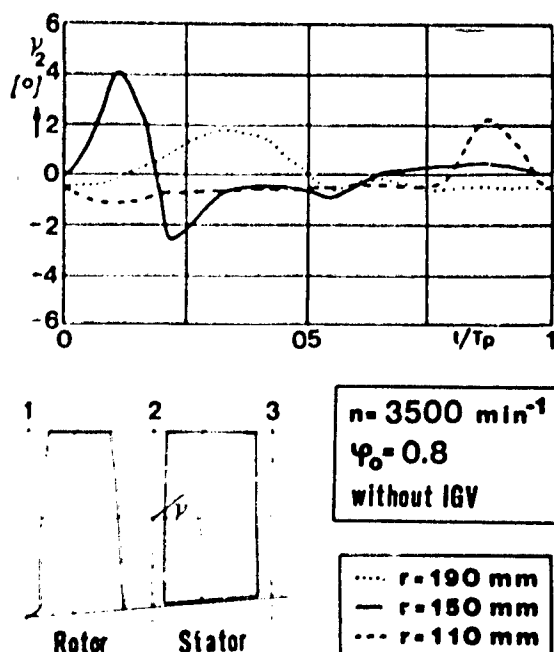


Fig. 17. Time-dependent rotor exit flow angle measured at three different spanwise locations and plotted versus time of one rotor blade passing period. The three-sensor hot wire probe was positioned in the center of the spacing between two stator vanes. (from Gallus and Hoenen 1983)

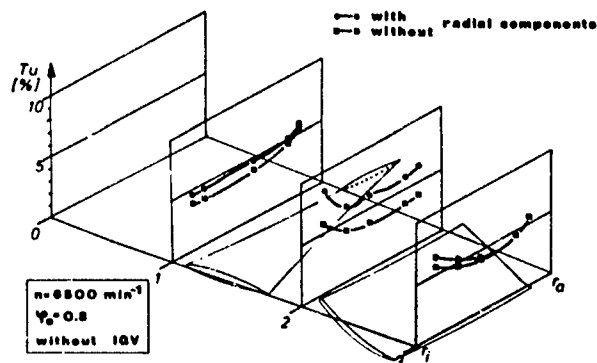


Fig. 18. Spanwise distributions of turbulence in the stations 1, 2, and 3 of an axial-flow compressor stage, measured by one-sensor and three-sensor probes (from Gallus and Hoenen 1983).

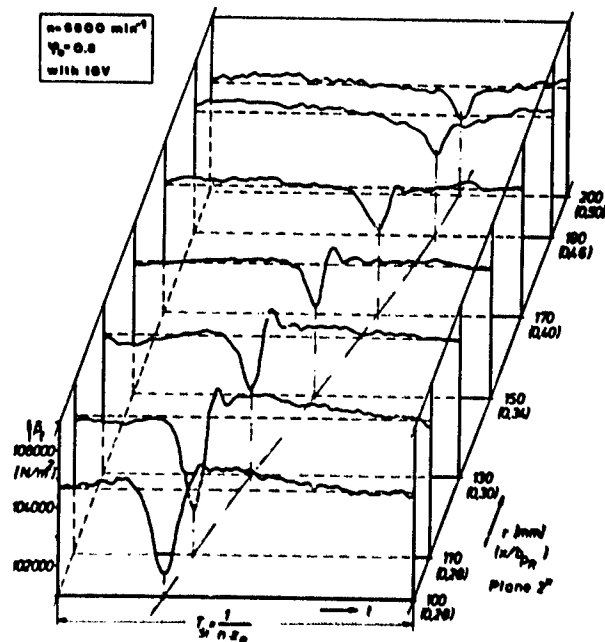


Fig. 19. Spanwise time-dependent total pressure distribution downstream of the compressor rotor shown in Fig. 15, at a rotor speed of 6500 rpm and a flow coefficient of 0.8 (from Gallus and Hoenen (1983)).

Shreeve and Neuhoﬀ (1984) reported on the development of a Dual Probe Digital Sampling (DPDS) technique. Two probes of different design are mounted circumferentially separated in the case wall 14 percent of tip chord downstream of the trailing edge of a supersonic compressor rotor. These probes can be translated radially and also rotated around their tips. Both probes are provided with Kulite transducers in the probe tips. Due to the different probe geometry the dependence of the outputs of the two probes on Mach number, pitch and yaw angle is quite different. While the Type A probe is a good indicator of the Mach number, and independent of pitch angle, the Type B probe is suitable to measure the pitch angle. The probe outputs are sampled at the same point in the rotor frame of reference, at delayed times, with the probes set to nine angles with respect to their axes. One sample of each probe is taken per rotor revolution, thus yielding a sample rate equivalent to the rotor speed. A procedure analogous to the calibration procedure used for multi-sensor probes is applied to the dual probe system to derive Mach number and flow angles from the two arrays of nine measurements. Neuhoﬀ et al. (1986) demonstrated the capability of this technique to resolve the radial as well as tangential and axial velocity components of the flow field in a high speed compressor rotor including the wake regions.

Kerrebrock et al. (1980) describe a spherical probe having five surface mounted silicon pressure sensors as shown in Fig. 20. From the five pressure signals of this probe the stagnation and the static pressures, Mach number and flow angles in two planes could be determined. All diaphragms are well upstream of the separation point on the sphere, so that Reynolds number effects are weak. The authors present details of the calibration of the probe due to steady-state tests. The well-known problems with respect to thermal drift of the semi-conductor transducers could be overcome by compensation methods. This miniature high frequency response probe proved its reliability in the MIT Blowdown Compressor Facility.

OPTICAL METHODS FOR ROTOR FLOW INVESTIGATIONS

These methods play a very important role in the investigation of rotor flows. Some of them can also be used at high-speed operation in the trans- and supersonic flow regime where flow field measurements by rotating probes become rather problematic due to strong aerodynamic interactions with the flow, on the one hand, and due to mechanical difficulties with sensors, probes, and probe holders, on the other.

A very comprehensive survey of non-intrusive optical measuring techniques appropriate for turbomachine application was presented by Meyer (1980). His review paper briefly includes the description of the physical principles of the various techniques.

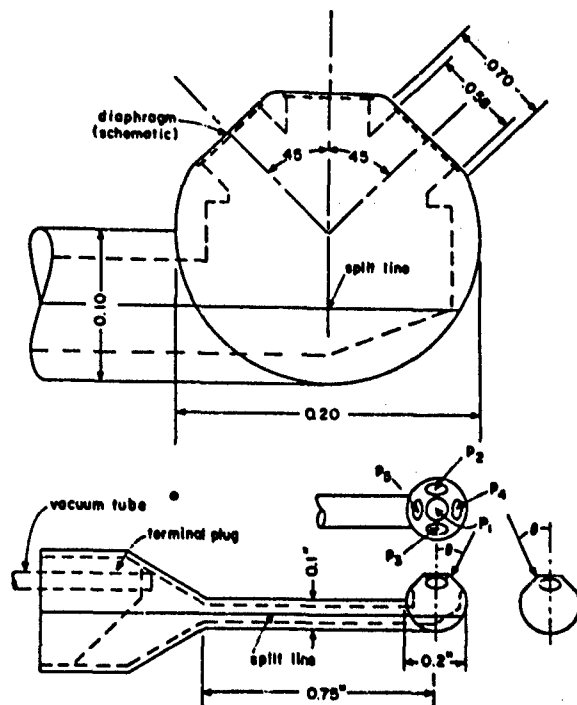


Fig. 20. Miniature high frequency sphere probe with five semi-conductor pressure transducers (from Kerrebrock et al. 1980)

This section will only select and describe some representative applications of the various optical techniques used for unsteady flow investigations in rotors and rotating rigs.

FLOW VISUALIZATION

Flow visualization is one of the most instructive methods for the understanding of complicated fluid dynamic problems. In particular, it offers the observation of unsteady flow effects in the whole flow field at one sight. For instance, particle injection such as smoke or dye allows the study of flow separation or vortex shedding phenomena. However, these tracing techniques are restricted to low velocity flows with low turbulence level. Increasing turbulence and flow velocity leads to an outwash of the traces due to diffusion of the particles into the surrounding flow.

Surface painting techniques are in use to locate boundary-layer transition and separation. Dring and Joslyn (1981) report on the flow visualization of surface streamlines on rotating turbine blades in a large scale test rig. They utilized the ammonia-oxalid technique developed by Ruden (1944) and by Johnston (1964). It consists of attaching a piece of Oxalid paper onto the airfoil surface immediately downstream of a pressure tap location. When ammonia is slowly discharged from the tap, it reacts with the paper leaving a dark streakline indicating the blade surface flow direction.

SCHLIEREN AND SHADOWGRAPH TECHNIQUES

These techniques are well-known from windtunnel investigations of linear cascades. During the last two decades attempts have been made to extend their application to steady and unsteady flow measurements in trans- and supersonic compressor rotors and stages. Buskies (1969) succeeded in developing a Schlieren-technical method for the flow analysis in a stationary annular supersonic compressor cascade. Parallel light from a light source passed a cylindrical lens system in front of a casing window and was directed normal to the polished hub surface and reflected back the same way. Thus, the light passes the flow passage in both directions integrating three-dimensional effects of the flow field along the blade height. However, in case of large hub-to-tip ratios these three-dimensional effects are rather small.

This technique has been extended at ONERA by Fabri (1971), Fertin (1974), LeBot and Larguier (1976) and at the

Technical University of Aachen to the steady and unsteady flow measurements in supersonic axial-flow compressor stages. It has proved useful in many respects, such as the experimental analysis of the structure, periodicity and stability of shock waves in supersonic rotors and stators, rotor-stator interaction, shock/boundary-layer interaction and shock-oscillations (Dettmering (1969), Gallus et al. (1977), Broichhausen and Gallus (1981)). The schlierenoptical measuring system is shown in Fig. 21. A flash lamp is used as a light source and operated by a stroboscope. The latter is triggered from a rotor blade in order to provide a steady view of the unsteady rotor and stator flow at a certain rotor-stator position. Phase shifting of the stroboscopic flash enables one to obtain stationary pictures of all the instantaneous flow events within a blade passing period of the rotor blade. Slow motion observation of the unsteady flow can be achieved by detuning the stroboscope frequency and recording with the aid of a video-camera.

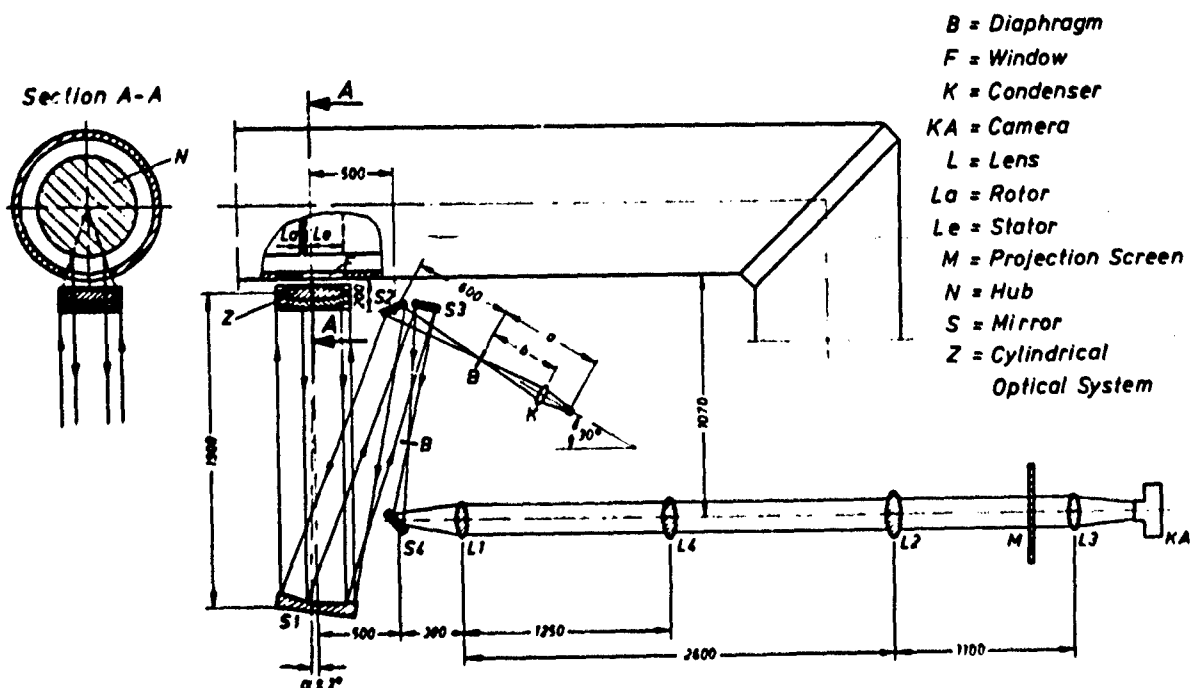


Fig. 21. Schlieren optical system for flow visualization in supersonic compressor stages (from Gallus 1975).

This technique has been used to investigate the structure of the rotor bow waves in comparison with a theoretical analysis (Gallus et al. (1977), Broichhausen and Gallus (1981)). Fig. 22 demonstrates the blade-row interaction of the rotor on the stator at two different rotor positions, Gallus et al. (1977b).

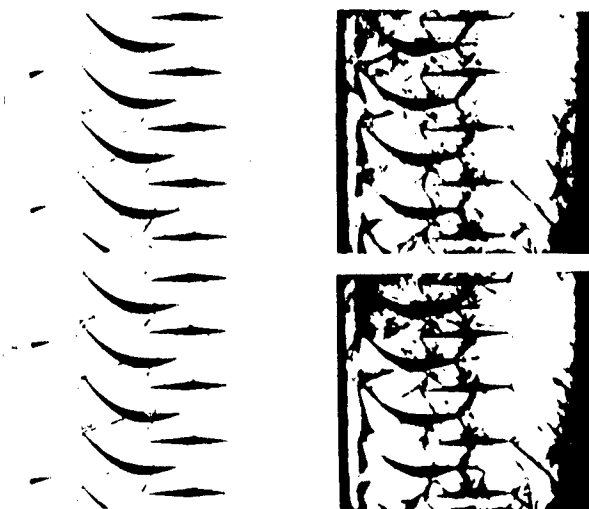


Fig. 22. Schlieren visualization of the rotor-stator flow interaction in a supersonic compressor stage (from Gallus et al. 1977)

This Schlieren-optical investigation of the unsteady flow in various supersonic axial-flow compressor stages up to a static pressure ratio of 3.2 has been augmented by measuring techniques, such as use of high response pressure transducers on the side-walls and stator blade surfaces as well as Kiel-type and wedge-type probes provided with semi-conductor transducers.

GAS FLUORESCENCE TECHNIQUE

This technique has been developed at MIT by Epstein (1977) and Epstein et al. (1979) to determine the instantaneous intrablade static density. The gas fluorescence technique is particularly well suited to studying shock structures in transonic compressors. One individual measurement yields density data from a complete blade-to-blade flow area, and allows an accurate determination of shock position and strength. Epstein and Kerrebrock (1979) presented a detailed analysis of the passage as well as the bow shock strengths obtained for a compressor rotor with tip Mach number of 1.2 and a stagnation pressure ratio near 1.6 using this technique. Thompkins and Epstein (1976) as well as Haymann-Haber and Thompkins (1980) compared the experimental results with computational solutions.

HOLOGRAPHIC INTERFEROMETRY

In the early 70's, NASA initiated activities to apply pulsed laser holographic interferometry to the analysis of shock patterns in axial-flow transonic compressor rotors, Benser et al (1974),

Hantman et al. (1973), Wuerker et al. (1973). One of the holographic techniques developed in this program is illustrated in Fig. 23, taken from Hantman et al. (1973). It shows the optical flow path of the object beam entering through a small window in the casing of the transonic fan rig. The diffuse light is reflected from the stationary hub surface just ahead of the rotor inlet towards the blade tip section and passes through a further window in the casing onto the holographic plate. The reference beam was contained in an associated holocamera. The test rotor was a highly loaded fan with a design tip speed of about 550 m/s and a pressure ratio up to 2.3. To obtain the holograms the laser is pulsed twice at a time interval between 5 and 10 microseconds. During this interval of time the density field within the blade passage moves by 5 to 10 percent of the blade spacing. Due to the double exposure a differential interferogram of the density variation is obtained which is made visible by reconstruction of the hologram.

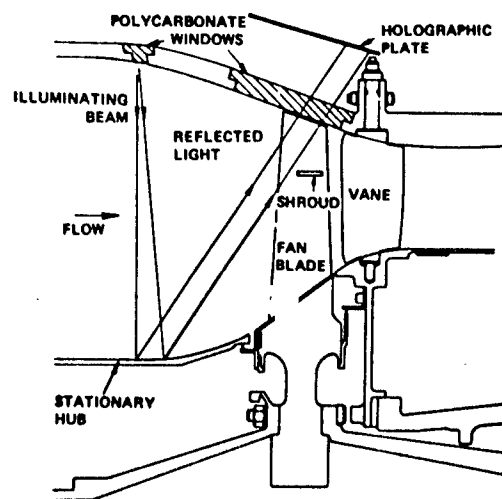


Fig. 23. Optical paths of reflected light holography in a transonic fan rig (from Hantman et al. 1973)

The advantages of holographic interferometry for turbomachinery application can be seen, first of all, in obtaining three-dimensional flow data by a single measurement. Decreased optical precision of the test section windows and other optical components does not affect the measuring accuracy. On the other hand, the difficulties of this technique in its application to turbomachinery become obvious in the rather limited accessibility to the flow field and in the extensive quantitative analysis of the measurements. The latter can also be affected by machine vibrations.

LASER VELOCIMETRY

This measuring technique has been developed to a very high standard, and its successful use in turbomachinery has already been proved in various applications. Detailed information about these

developments can be found in two extensive review papers by W. McNally (1976) and P. Runstadler (1976). More recent surveys of the state-of-the-art of laser velocimetry were presented by several authors at the 1980 Joint Fluids Engineering and Gas Turbine Conference in New Orleans.

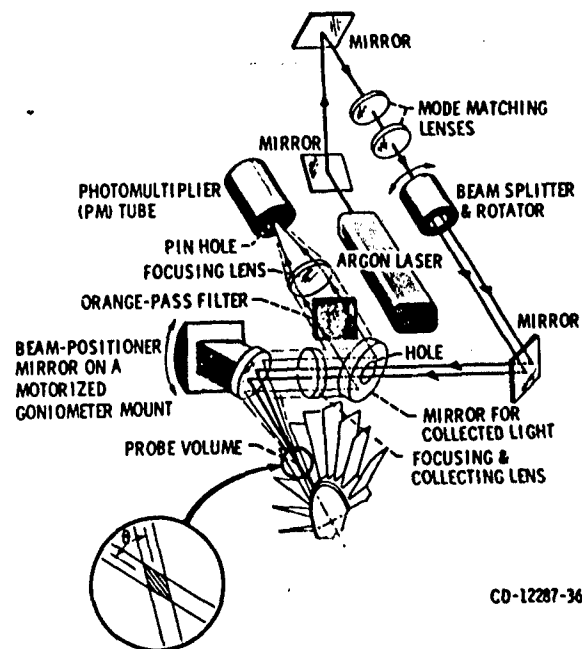
Various publications confirm the increasing success of the laser velocimetry for measurements on rotors. In 1972, Wisler and Mossey (1977) reported on measurements within a compressor rotor passage using the Laser Doppler Velocimeter. In 1976, Wisler (1976), presented a paper on the application of this technique on shock wave and flow velocity measurements in a high speed fan rotor.

Schodl (1977a, 1977b, 1980) described the development of the Laser-Two-Focus Velocimetry at DFVLR. Eckhardt (1976) presented the results of the first detailed flow field measurements with this technique within a high-speed centrifugal compressor impeller. L2F-measurements in a transonic axial-flow compressor were published by Weyer and Dunker (1977).

Laser velocimetry has turned out to become the main tool for flow field research in high-speed rotors. Nevertheless, there are still some problems associated with accessibility difficulties in high-speed turbomachines, background noise in narrow blade passages and near walls, flow seeding, and time and expense required to make the measurements. Recently, good progress has been achieved to overcome or reduce some of these problems. Various authors presented excellent contributions to the current developments at the 1980 Joint Fluids Engineering and Gas Turbine Conference in New Orleans.

Powell et al. (1980) present results that demonstrate the anemometer's capability in flow mapping within a transonic axial-flow compressor rotor. Typically, a velocity profile, derived from 30000 measurements along 1000 sequential circumferential positions covering 20 blade passages, can be obtained in 30 seconds. To allow flow measurements near the rotor hub and the casing window fluorescent seed particles are used. Figs. 24 and 25 illustrate the optical layout as well as a block diagram of the anemometer.

Schodl (1980) reports on further successful work to improve the signal-to-noise ratio and to shorten the measuring time by multi-window operation and simplification of mean value calculation and error estimation. As an example of the improvements achieved by using the advanced automated L2F-technique, he compares the measuring time for the test case shown in Fig. 26. Due to the automated measuring procedure the time needed for the same number of data could be reduced by a factor of 12. Due to the improved optics the minimum distance of approaching a wall could be reduced to about 0.5 mm.



CD-12287-36

Fig. 24. Optical layout of laser anemometer (from Schodl 1977)

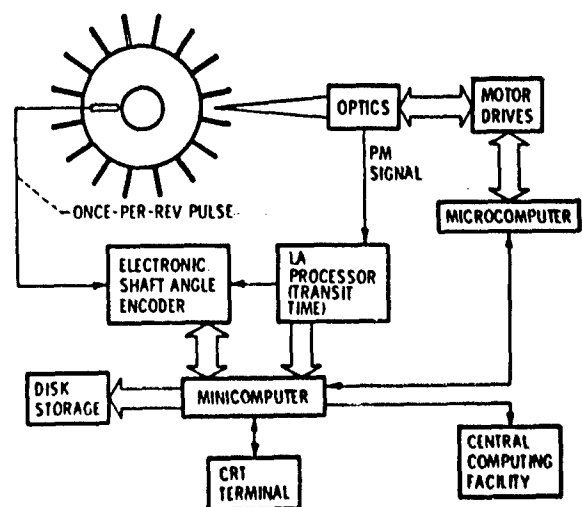


Fig. 25. Block diagram of complete Laser anemometer (from Schodl 1977)

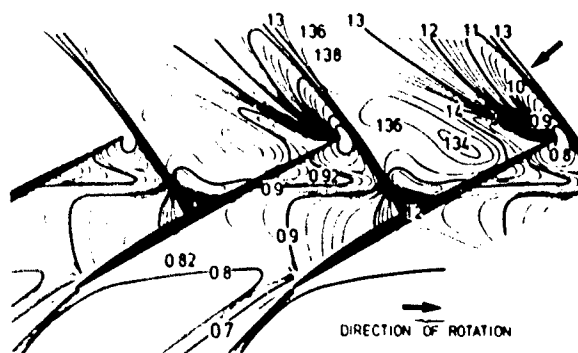


Fig. 26. Lines of constant relative Mach number through the blade passage at 89% blade height (100% speed) (from Schodl 1980)

At the same symposium, Strazisar and Powell (1980) reported on laser anemometer measurements in a transonic axial-flow compressor rotor. The flow phenomena investigated include flow variations from passage to passage, the three-dimensionality of the rotor shock system, as shown in Fig. 27, three-dimensional flows in the blade wake, and the development of the outer endwall boundary layer.

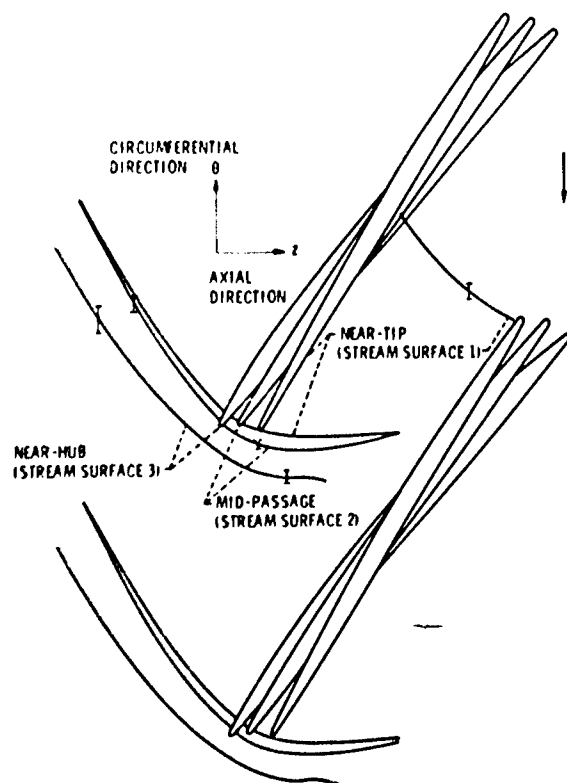


Fig. 27. Three-dimensional structure of the rotor shock system, 100 percent speed (from Strazisar et al. 1980)

Comparative experimental and computational studies, such as those by Dunker et al. (1977) and McDonald et al. (1980), show the increasing quality of this experimental tool to support the development and improvement of computational methods that are capable to achieve a satisfactory approach to the prediction of the complex real flow field in turbomachines.

Recent L2F-measurements in high-speed turbine rotors have shown that the experimental analysis of the exceedingly complicated unsteady secondary flow in such a rotor blade passage has become feasible. Binder (1985), Binder et al. (1985) investigated the effect of wakes on the unsteady turbine rotor flow, and turbulence production due to secondary vortex cutting within the rotor blade channel.

Förster and Mach (1985) succeeded in calculating the individual particle paths from these measurements and traced the progress of fluid filaments through the rotor passage. They could show that the boundaries between wake and core flow segments in the front part of the rotor agree closely with the distribution of turbulent energy, whereas three-dimensional effects play a major role towards the rear part, as can be seen from Fig. 28. The unsteady flow through the rotor was calculated from the measured data and demonstrated in a color film.

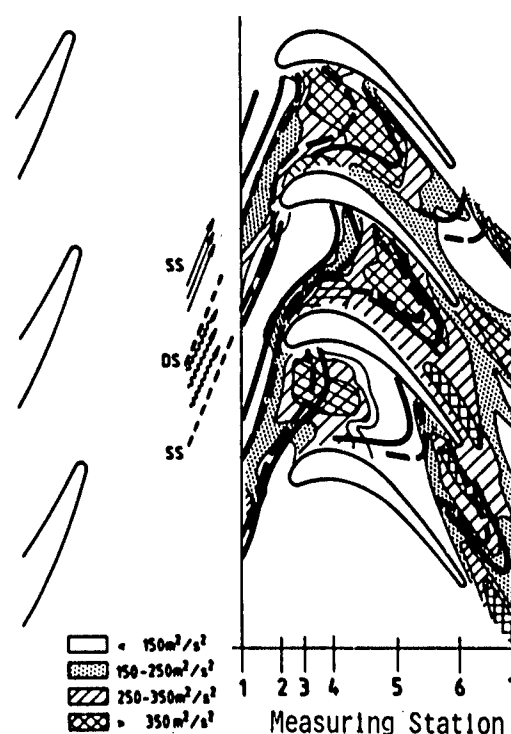


Fig. 28. Comparison of convective deformation of fluid filaments with instantaneous distribution of turbulent kinetic energy $c_t \text{ (m}^2/\text{s}^2\text{)}$ (from Förster and Mach 1985)

The few selected examples presented in this section confirm the great progress of laser velocimetry in turbomachinery application, especially for rotor flow analysis.

SUMMARY

This chapter intended to give a review of the wide variety of fluid and structural measurements on rotors which are available at the present time. Methods of flow visualization in the complex flow passages have always been important for the understanding of the flow characteristics and for the development of design criteria. The evolution from smoke flow and similar methods to those involving Schlieren and laser holography represents a range from rather simple to very sophisticated quantitative measurement techniques. A number of methods to obtain dynamic pressure and flow conditions on rotors are now rather commonly applied. Obviously, detailed structural dynamic analysis and unsteady flow analysis methods are now becoming available to be applied in conjunction with the measurements to analyze and improve given

designs. Results from the measurements can be taken as inputs to analysis methods or for the purpose of verifying their accuracy. To predict the occurrence of flutter, it is necessary to know from either computational or experimental analysis the unsteady aerodynamic forces and the structural motion. For resonant vibration, the magnitude of the driving force has to be determined, too. These requirements include advances in the three-dimensional viscous flow analysis by computational and experimental approaches. As was pointed out in the discussion of the experimental methods utilized for unsteady high speed rotor flow measurements, continued improvement of the nonintrusive measurement techniques will be necessary. Unsteady flow measurement techniques should also be extended to high temperature regions. Data handling systems should be improved.

REFERENCES

- ABBOTT, I.H. and VON DOENHOFF, A.E. 1959 Theory of Wing Sections, Dover Publ., New York.
- ABRAMOWITZ, M. and STEGUN, I.A. 1969 Handbook of Mathematical Functions. National Bureau of Standards. Applied Mathematical Series 55.
- ACTON, E. 1981 Unsteady Flow in a Supersonic Cascade with Strong Oblique Leading Edge Shocks. Topexpress Ltd.
- ADACHI, T. and MURAKAMI, Y. 1979 Three-Dimensional Velocity Distribution Between Stator Blades and Unsteady Force on a Blade Due to Passing Wakes. JSME, Vol. 22, No. 170, pp. 1074-1082.
- ADAMCZYK, J.J. 1975 The Passage of a Distorted Velocity Field through a Cascade of Airfoils. In Unsteady Phenomena in Turbomachinery, AGARD-CP-177, Paper No. 31.
- ADAMCZYK, J.J. 1978 Analysis of Supersonic Stall Bending Flutter in Axial-Flow Compressor by Actuator Disc Theory. NASA. Tech. Paper 1345.
- ADAMCZYK, J.J. and GOLDSTEIN, M.E. 1978 Unsteady Flow in a Supersonic Cascade with Subsonic Leading Edge Locus. AIAA Journal, Vol. 16, No. 12, pp. 1248-1254.
- ADAMCZYK, J., GOLDSTEIN, M., and HARTMAN, M. 1982 Supersonic Unstalled Flutter. NASA TM 79001.
- ADAMCZYK, J.J., STEVENS, W., and JUTRAS, R. 1982 Supersonic Stall Flutter of High-Speed Fans. Trans. ASME Journal of Engineering for Power, Vol. 104, No. 3, pp. 675-682.
- ADLER, A. 1978 Telemetry for Rotating Measurements on Turbomachinery, ASME Paper No. 78-GT-105.
- AKAI, T.J. and ATASSI, J. 1981 Stability and Flutter of Turbine Blades at Low Speed. In Aeroelasticity in Turbomachines, Proceedings of the 2nd International Symposium Held in Lausanne, Sept. 1980, Editor: P. Suter, Juris-Verlag Zurich, pp. 187-202.
- ARIS, A. 1962 Vectors, Tensors and the Basic Equations of Fluid Mechanics. Prentice-Hall.
- ARMENTROUT, E.C. and KICKS, J.C. 1979 Pressure Instrumentation for Gas Turbine Engines - A Review of Measurement Technology. Trans. ASME Journal of Engineering for Power, Vol. 101, No. 3, pp. 373-383.
- ARMSTRONG, E.K. and STEVENSON, R.E. 1960 Some Practical Aspects of Compressor Blade Vibrations. Journal Royal Aerospace Society, Vol. 64, No. 591, pp. 117-130.
- ARMSTRONG, E.K. and WILLIAMS, D.D. 1966 Some Intake and Maldistribution Effects on Compressor Rotor Blade Vibration, Journal of Sound and Vibration, Vol. 3, No. 3, pp. 340-354.
- ARNOLDI, R.A., CARTA, F.O., NI, R.H., DALTON, W. N. and ST. HILAIRE, A. O. 1977 Analytical and Experimental Study of Subsonic Stall Flutter. AFOSR-TR-77-0854.
- ASHLEY, H. and LANDAHL, M. 1965 Aerodynamics of Wings and Bodies. Addison-Wesley.
- ATASSI, H. and AKAI, T.J. 1978 Effect of Blade Loading and Thickness on the Aerodynamics of Oscillating Cascades. AIAA 16th Aerospace Science Meeting. Paper No. 78-227.
- ATASSI, H. and AKAI, T.J. 1980 Aerodynamics and Aeroelastic Characteristics of Oscillating Loaded Cascades at Low Mach Number.
PART I: Pressure Distribution, Forces and Moments
PART II: Stability and Flutter Boundaries, Trans. ASME Journal of Engineering for Power, Vol. 102, No. 2, pp. 344-356.
- BALLHAUS, W.F. 1978 Some Recent Progress in Transonic Flow Computations. In (Wirz, H. J. and Smolderen, J. J., eds) Numerical Methods in Fluid Dynamics, Hemisphere Publishing Corporation, U.S.A.
- BEAM, R.M. and WARMING, R. F. 1976 An Implicit Finite-Difference Algorithm for Hyperbolic Systems in Conservation-Law Form. Journal of Computational Physics, Vol 22, pp. 87-110.
- BEAM, R.M. and WARMING, R. F. 1978 Implicit Factured Schemes for the Compressible Navier Stokes equations, AIAA journal, Vol. 14, No. 4, pp. 393-402.
- BENDAT, J.S. and PIERSALL, A.D. 1971 Random Data. Wiley Interscience, John Wiley and Sons, Inc.
- BENSER, W.A., BAILEY, E.E., GELDER, T.F. 1974 Holographic Studies of Shock Waves Within Transonic Fan Rotors, NASA-TMX-71430, 1974.

- BERRY, P.E. 1984 Computation of Unsteady Flow in a Blade Passage. Paper presented at the Symposium on Unsteady Aerodynamics of Turbomachines and Propellers, Engineering Department, University of Cambridge, U.K., September 1984.
- BETTNER, J.L. 1982 Influence of Blade Tip Clearance on Aerodynamically Induced Vibration. Final Report for Air Force Office of Scientific Research, Contract F49620-80-C-0078.
- BILLINGTON, A.E. 1949 Aerodynamic Lift and Moment for Oscillating Airfoils in Cascade. Report E.63, Aeronautical Council of Scientific & Industrial Research, Australia.
- BINDER, A. 1985 Turbulence Production Due to Secondary Vortex Cutting in a Turbine Rotor, ASME, Paper 85-GT-193.
- BINDER, A., FORSTER, W., KRUSE, H., ROGGE, H. 1985 An Experimental Investigation into the Effect of Wakes on the Unsteady Turbine Rotor Flow, ASME Journal of Engineering for Power, 107, 1985, pp. 458-466.
- BISPLINGHOFF, R.L. and ASHLEY, H. 1962 Principles of Aeroelasticity. John Wiley and Sons, New York.
- BISPLINGHOFF, R.L., ASHLEY, H. and HALFMAN, R.L. 1955 Aeroelasticity. Addison-Wesley Publishing Co., Reading, Mass.
- BOHN, D. 1977 Untersuchung zweier verschiedener axialer Ueberschallverdichterstufen unter besonderer Berücksichtigung der Wechselwirkungen zwischen Lauf- und Leitrad, Diss. RWTH Aachen.
- BOELCS A. and FRANSSON, T. (Editors) 1986 Aeroelasticity and Turbomachines: Comparison of Theoretical and Experimental Cascade Results. Communication de Laboratoire de Thermique Appliquée et de Turbomachines No. 16, EPFL, Lausanne, Switzerland.
- BOELCS A. and SCHLAEFLI, D. 1984 Flutter Phenomena in a Transonic Turbine Cascade. Symposium on Unsteady Aerodynamics of Turbomachines, Cambridge 1984.
- BOLDMAN, D.R. and BUGGELE, A.E. 1978 Wind Tunnel Tests of a Blade Subjected to Midchord Torsional Oscillation at High Subsonic Stall Flutter Conditions. NASA TM 78998.
- BOLDMAN, D.R., BUGGELE, A.E. and MICHALSON, G.M. 1981 Stall Flutter Experiment in a Transonic Oscillating Linear Cascade. NASA TM 82655.
- BRIDGE, J.F. and ANGRIST, S.W. 1962 An Extended Table of Roots of $J'_n(x)Y'_n(\beta x) - J'_n(\beta x)Y'_n(x) = 0$. Mathematics of Computation, Vol. 16, No. 78, pp. 198-204.
- BRIX, C.W. and PLATZER, M.F. 1974 Theoretical Investigation of Supersonic Flow Past Oscillating Cascades with Subsonic Leading Edge Locus. Washington, D.C., AIAA Paper No. 74-141.
- BROICHHAUSEN, K.D. 1981 Theoretische und Experimentelle Untersuchung eines Ueberschallverdichter-Laufrades mit querschnittsstabilisiertem Verdichtungsstoss, Diss. RWTH Aachen.
- BROICHHAUSEN, K.D., GALLUS, H.E. 1981 Theoretical and Experimental Analysis of the Flow Through Supersonic Compressor Stages, AIAA-81-0067, January 1981.
- BROOKER, M.J. AND HALLIWELL, D.G. 1984 A Comparison of Measured and Predicted Surface Pressure on a Fan Blade in Supersonic Unstalled Flutter. Paper presented at the Symposium on Unsteady Aerodynamics of Turbomachines and Propellers, Engineering Department, University of Cambridge, U.K., September
- BRUCE, E.P. 1979 Axial Flow Rotor Unsteady Performance. Naval Seas Systems Command, TM 79-149.
- BUBLITZ, P. 1976 Experimental Aeroelastic Investigation on a Cascade in a Compressible Flow. DFVLR Report No. DLR-FB-76-60.
- BUBLITZ, P. 1976 Experimental Aeroelastic Investigations on a Cascade in Compressible Flow. Rev. Française de Mécanique, IUTAM Symposium on Aeroelasticity in Turbomachines, pp. 143-150.
- BUSCHIES, U.-H. 1969 Beitrag zur Untersuchung Rotationssymmetrischer Tandemgitter für Ueberschallströmung, Diss. RWTH Aachen.
- CALVEPT, W.J. and HERBERT, M.V. 1980 An Inviscid-Viscous Interaction Method to Predict the Blade-Blade Performance of Axial Compressors. N.G.T.E. Memorandum No. 80012.
- CAMPBELL, W. 1924 Protection of Steam Turbine Disc Wheels from Axial Vibration. ASME Paper No. 1920.

- CAPECE, V.R. and FLEETER, S. 1984 First Stage Stator Vane Unsteady Aerodynamic Response in a Multi-Stage Compressor. AIAA-84-1209, June 1984.
- CARSTENS, V. 1981 Unsteady Pressure Distributions in a Cascade taking into Account Profile Thickness and Steady Circulation. In Aeroelasticity in Turbomachines Proceedings of the Second International Symposium Held in Lausanne, Sept. 1980, Editor: P. Suter, Juris-Verlag-Zurich, pp. 65-83.
- CARTA, F.O. 1957 Unsteady Aerodynamic Theory of a Staggered Cascade of Oscillating Airfoils in Compressible Flow. United Aircraft Research Rept. R-0582-19, E. Hartford.
- CARTA, F.O. 1966 Coupled Blade-Disk-Shroud Flutter Instabilities in Turbojet Engine Rotors. ASME Paper No. 66-WA/GT-6.
- CARTA, F.O. 1967 Coupled Blade-Disk-Shroud Flutter Instabilities in Turbojet Engine Rotors. Trans. ASME Journal of Engineering for Power, Vol. 89, No. 3, pp. 419-426.
- CARTA, F.O. 1974 Analysis of Oscillating Pressure Data Including Dynamic Stall Effects. NASA CR-2394
- CARTA, F.O. 1982 Unsteady Gapwise Periodicity of Oscillating Cascade Airfoils. ASME Paper No. 82-GT-286.
- CARTA, F.O. 1982 An Experimental Investigation of Gapwise Periodicity and Unsteady Aerodynamic Response in an Oscillating Cascade. NASA Contractor Report 3513. Contract NAS3-22018.
- CARTA, F.O. 1983 Unsteady Aerodynamics and Gapwise Periodicity of Oscillating Cascaded Airfoils. Trans. ASME Journal of Engineering for Power, Vol. 105, No. 3, pp. 565-574.
- CARTA, F.O., O'BRIEN, R.L. 1980 Unsteady Aerodynamic Measurement Techniques for Turbomachinery Research, Keynote Paper presented to ASME Joint Fluids Engineering and Gas Turbine Conference, New Orleans, 1980, pp. 177-185.
- CARTA, F.O. and ST. HILAIRE, A.O. 1976 An Experimental Study on the Aerodynamic Response of a Subsonic Cascade Oscillating Near Stall. Project SQUID TR-UTRC-2-PU.
- CARTA, F.O. and ST. HILAIRE, A.O. 1977 Experimentally Determined Stability Parameters of a Subsonic Cascade Oscillating Near Stall. ASME Paper No. 77-GT-47.
- CARTA, F.O. and ST. HILAIRE, A.O. 1979 Effect of Interblade Phase Angle and Incidence Angle on Cascade Pitching Stability. ASME Paper No. 79-GT-153.
- CARTA, F.O. AND O'BRIEN, R.L. 1980 Unsteady Aerodynamic Measurement Techniques for Turbomachinery Research Measurement Methods in Rotating Components of Turbomachinery. ASME Joint Fluids Engineering and Gas Turbine Conference, New Orleans, Edited by B. Lakshminarayana and P. Runstadler, pp. 177-185.
- CARTER, A.D.S. 1953 Some Preliminary Notes on the Flutter of Axial Compressor Blades. N.G.T.E. Memorandum No. M. 181.
- CARTER, A.D.S. 1955 A Theoretical Investigation of the Factors Affecting Stalling Flutter of Compressor Blades. N.G.T.E., A.R.C. Technical Report No. R. 172, C.P. No. 265.
- CARTER, A.D.S. and KILPATRICK, D.A. 1957 Self-Excited Vibration of Axial-Flow Compressor Blades. Proceedings of the Institution of Mechanical Engineers. Vol. 171, pp. 245-281.
- CARTER, A.D.S., KILPATRICK, D.A., MOSS, C.E. and RITCHIE, J. 1955 An Experimental Investigation of the Blade Vibratory Stresses in a Single-Stage Compressor. N.G.T.E., A.R.C. Technical Report No. 4. 174, C.P. No. 266.
- CARUTHERS, J.E. 1976 Theoretical Analysis of Unsteady Supersonic Flow Around Harmonically Oscillating Turbofan Cascades. Ph.D. Thesis. Georgia Institute of Technology.
- CARUTHERS, J.E. 1981 Aerodynamic Analysis of Cascaded Airfoils in Unsteady Rotational Flow. In Aeroelasticity in Turbomachines, Proceedings of the 2nd International Symposium Held in Lausanne, Sept. 1980, Editor: P. Suter, Juris-Verlag Zurich, pp. 31-64.
- CARUTHERS, J.E. and RIFFEL, R.E. 1980 Aerodynamic Analysis of a Supersonic Cascade Vibrating in a Complex Mode. Journal of Sound and Vibration, Vol. 71, No. 2, pp. 171-184.
- CASPAR, J.R. 1983 Unconditionally Stable Calculation of Transonic Potential Flow through Cascades using an Adaptive Mesh for Shock Capture. Trans. ASME A: Journal of Engineering for Power, Vol. 105, No. 3, pp. 504-513.

- CASPAR, J.R. and VERDON, J.M. 1981 Numerical Treatment of Unsteady Subsonic Flow Past an Oscillating Cascade. AIAA Journal, Vol. 19, No. 12, pp. 504-513.
- CEDAR, R.C. 1986 The Development of a Finite Element Method for the Analysis of Steady and Unsteady Turbomachinery Blade Flow. PhD thesis, Cranfield Institute of Technology, U.K.
- CHI, M.R. 1980 Unsteady Aerodynamics in Stalled Cascade and Stall Flutter Prediction. ASME Paper 80-C2/Aero-1.
- CHI, R.M. and SRINIVASAN, A.V. 1984 Some Recent Advances in the Understanding and Prediction of Turbomachine Subsonic Stall Flutter. ASME Paper 84-GT-151.
- CHORIN, A.J. 1973 Numerical Study of Slight Viscous Flow, Journal of Fluid Mechanics, Vol. 37, Pt IV, pp. 785-796.
- CHORIN, A.J. 1980 Vortex Models and Boundary Layer Instability. SIAM, J. Sci. Stat. Comput., Vol. 1, pp. 1-21.
- CHYU, W.J. and KUWAHARA, K. 1982 Computations of Transonic Flow over an Oscillating Airfoil with Shock-Induced Separation. AIAA 20th Aerospace Science Meeting, Paper No. AIAA-82-0350.
- COLLAR, A.R. 1946 The Expanding Domain of Aeroelasticity. J. Royal Aero. Soc., L, August, pp. 613-636.
- CRAWLEY, E.F. 1982 Aerodynamic Damping Measurements in a Transonic Compressor. ASME Paper 82-GT-287.
- CRAWLEY, E.F. and HALL, K.C. 1985 Optimization and Mechanism of Mistuning in Cascades. Journal of Engineering for Gas Turbines and Power, V. 107, N2, pp. 418-426, 1985.
- CRAWLEY, E.F., KERREBROCK, J.L. and DUGUNDJI, J. 1980 Preliminary Measurements of Aerodynamic Damping of a Transonic Compressor Rotor. PP. 263-271, Measurement Methods in Rotating Components of Turbomachinery, Library of Congress Catalog Card Number 79-57425.
- DAVIES, M.R.D. and BRYANSTON-CROSS, P.J. 1984 Holographic Measurements and Theoretical Predictions of the Unsteady Flow in a Transonic Annular Cascade. ASME 84-GT-174.
- DENTON, J.D. 1975 A Time Marching Method for Two- and Three-Dimensional Blade to Blade Flows, A.R.C., R & M No. 3775.
- DENTON, J.D. 1983 An Improved Time Marching Method for Turbomachinery Flow Calculation. Journal of Engineering for Power, Vol 105, pp. 514-524.
- DETTMERING, W. 1969 Entwicklungsschritte zur Ueberschallverdichterstufe, Rheinisch-Westfälische Akademie der Wissenschaften, Vortrag Nr. 226, Westdeutscher Verlag.
- DOWELL, E.H., CURTISS, H. C. JR., SCANLAN, R.H. and SISTO, F. 1978 A Modern Course in Aeroelasticity. Sijthoff & Noordhoff, The Netherlands.
- DRING, R.P., JOSLYN, H.D. 1981 Measurement of Turbine Rotor Blade Flows, Trans. ASME, April 1981, Vol. 103, pp. 400-405.
- DRING, R.P., JOSLYN, H.D., HARDIN, L.W. 1975 Experimental Investigation of Compressor Rotor Wakes, United Technologies Research Center, East Hartford, Technical Report No. 123, September 1975.
- DRING, R.P., JOSLYN, H.D., HARDIN, L.W. 1981 An Investigation of Axial Compressor Rotor Aerodynamics, Trans. ASME, Paper No. 81-GT-56.
- DRING, R.P., JOSLYN, H.D., HARDIN, L.W. and WAGNER, J.H. 1981 Research on Turbine Rotor-Stator Aerodynamic Interaction and Rotor Negative Incidence Stall. Final Report, AFWAL-TR-81-2114.
- DRING, R.P., JOSLYN, H.D., HARDIN, L.W., WAGNER, J.H. 1982 Turbine Rotor-Stator Interaction, Trans. ASME, Journal of Engineering for Power, pp. 729-742, Vol. 104, October 1982.
- DUGUNDJI, J. & BUNDAS, D.J. 1983 Flutter and Forced Response of Mistuned Rotors using Standing Wave Analysis. AIAA Paper 83-084.
- DUNKER, R.J., STRINNING, P.E., WEYER, H.B. 1977 Experimental Study of the Flow Field Within a Transonic Axial Compressor Rotor by Laser Velocimetry and Comparison With Through-Flow Calculations, ASME Paper No. 77-GT-28.
- DEPPAND, W.F. Aerodynamic Theory, 1934. Julius Springer, Berlin, Vol. 2, p. 91.
- OWIGHT, H.B. 1948 Table of Roots for Natural Frequencies in Coaxial Type Cavities. Journal of Mathematics and Physics, Vol. 27, No. 1, pp. 84-89.

- ECKHARDT, D. 1976 Detailed Flow Investigations Within a High-Speed Centrifugal Compressor Impeller, *Journal of Fluids Engineering*, Vol. 98, No. 3, September 1976, pp. 390-402.
- EHLERS, F.E. and WEATHERILL, W.H. 1982 A Harmonic Analysis Method for Unsteady Transonic Flow and Its Application to the Flutter of Airfoils. NASA CR 3537.
- ELLIS, D.H., RAKOWSKI, W.J. and BANKHEAD, H. R. 1978 A Research Program for the Experimental Analysis of Blade Instability. AIAA Paper 78-1089.
- EMMONS, H.W., PEARSON, C.E., & GRANT, H.P. 1955 Compressor Surge and Stall Propagation. *ASME Transaction*, 27, 2, pp. 455-469.
- EPSTEIN, A.H. 1977 Quantitative Density Visualization in a Transonic Compressor Rotor, *ASME Journal of Engineering for Power*, Vol. 99, July 1977, pp. 460.
- EPSTEIN, A.H., KERREBROCK, J.L., THOMPSON, W.T. 1979 Shock Structure in Transonic Compressor Rotors, *AIAA Journal*, April 1979.
- ERDELYI, A. 1956 Asymptotic Expansions. Dover Publications.
- ERDOS, J. I. and ALZNER, E. 1977 Numerical Solution of Periodic Transonic Flow through a Fan Stage, *AIAA journal*, Vol. 15, No. 11, pp. 1559-1568.
- EWINS, D.J. 1973 Vibration Characteristics of Bladed Disc Assemblies. *Journal of Mechanical Engineering Sciences*, Vol. 15, No. 3, pp. 165-186.
- EWINS, D.J. 1974 Vibration Modes of Mistuned Bladed Disks. *Trans. ASME Journal of Engineering for Power*, Vol. 98, No. 3, pp. 349-354.
- EWINS, D.J. and HILLARY, M.B., 1981 A Method for Force Determination from Vibration Response Measurements. In *Aeroelasticity in Turbomachines*, Proceedings of the 2nd International Symposium Held in Lausanne, Sept. 1980, Editor: P. Suter, Juris-Verlag Zurich, pp. 263-284.
- FABRI, J. 1971 La visualisation de l'écoulement dans un compresseur axial supersonique, *L'Aeronautique et l'Astronautique*, No. 32, 1971, pp. 3-11.
- FERTIN, G. 1974 Recording of Schlieren Pictures for Flow Visualization in Rotating Machines, *ONERA, T.P. NO. 1396*.
- FLEETER, S. 1979 Trailing Edge Conditions for Unsteady Flows at High Reduced Frequency. AIAA 79-0152.
- FLEETER, S. 1979 Aeroelasticity Research for Turbomachine Applications. *Journal of Aircraft*, Vol. 16, No. 5, pp. 320-326.
- FLEETER, S., BENNETT, W.A., JAY, R.L. 1980 The Time-Variant Aerodynamic Response of a Stator Row Including the Effects of Airfoil Camber, *Trans. ASME, Journal of Engineering for Power*, April 1980, Vol. 102, pp. 334-343.
- FLEETER, S., JAY, R.L. and BENNETT, W.A. 1976 Compressor Stator Time-Variant Aerodynamic Response to Upstream Rotor Wakes. Final Report for Air Force Office of Scientific Research, Contract F44620-74-C-0065.
- FLEETER, S., JAY, R.L., BENNETT, W. A. 1978 Rotor Wake Generated Unsteady Aerodynamic Response of a Compressor Stator, *Trans. ASME*, October 1978, Vol. 100, pp. 664-675.
- FLEETER, S., JAY, R.L. and BENNETT, W.A. 1981 Wake Induced Time-Variant Aerodynamics Including Rotor-Stator Axial Spacing Effects. *ASME Journal of Fluids Engineering*, Vol. 103, No. 1, pp. 59-66.
- FLEETER, S., McCLURE, R.B., HOLTMAN, R.L. and SINNET, G.T. 1975 Supersonic Inlet Torsional Cascade Flutter. *AIAA Journal of Aircraft*, Vol. 12, No. 8, pp. 664-669.
- FLEETER, S., NOVICK, A.S., RIFFEL, R.E. and CARUTHERS, J.E. 1976 An Experimental Determination of the Unsteady Aerodynamics in a Controlled Oscillating Cascade. *ASME Paper 76-GT-17*.
- FLEETER, S., NOVICK, A.S., RIFFEL, R.E. AND CARUTHERS, J.E. 1977 An Experimental Investigation of the Unsteady Aerodynamics in a Controlled Oscillating Cascade. *Trans. ASME Journal of Engineering for Power*, Vol. 99, No. 1, pp. 88-96.
- FLEETER, S., RIFFEL, R.E., LINDSEY J.H. and ROTHROCK, M.D. 1978 Time-Variant Translational Mode Aerodynamics of a Classical Transonic Airfoil Cascade. *AGARD Propulsion and Energetics Panel, Symposium on Stresses, Vibrations, Structural, Integration and Engine Integrity*, CP-248.
- FORD, R.A.J. and POORD, C.A. 1979 An Analysis of Aeroengine Fan Flutter using Twin Orthogonal Vibration Modes. *ASME Paper 79-GT-126*.
- FORSTER, W., MACH, K. 1985 Unsteady Flow in a Turbine Rotor, *VDI-Berichte 572.2*, 1985, pp. 273-292.

- FRANSSON, T.H. and SUTER, P. 1983 Two-Dimensional and Quasi Three-Dimensional Experimental Standard Configuration for Aeroelastic Investigations in Turbomachine-Cascades. Report LTA-TM-83-2, Ecole Polytechnic Federale de Lausanne.
- FRANSSON, T.H. 1984 Two-Dimensional and Quasi Three-Dimensional Experimental Standard Configurations for Aeroelastic Investigations in Turbomachine-Cascades. Paper presented at the Symposium on Unsteady Aerodynamics of Turbomachines and Propellers, Engineering Department, University of Cambridge, U.K., September.
- FUNG, Y.C. 1955 An Introduction to the Theory of Aeroelasticity. John Wiley and Sons, New York.
- FUNG, K.Y., YU, N.J., and SEEBASS, R. 1978 Small Unsteady Perturbations in Transonic Flows. AIAA Journal, Vol. 16, No. 8, pp. 815-822.
- GALLUS, H.E. 1975 Results of Measurements of the Unsteady Flow in Axial Subsonic and Supersonic Compressor Stages, AGARD, CP No. 177, Monterey, 1975.
- GALLUS, H.E. 1979 High Speed Blade-Wake Interactions, AGARD-LS "Unsteady Flow in Turbomachines," von Karman Institute for Fluid Dynamics, Belgium, Mitteilung Nr. 79-11, Institut für Strahlantriebe und Turboarbeitsmaschinen, RWTH Aachen.
- GALLUS, H.E., BOHN, D., BROICHHAUSEN, K.D. 1977 Measurements of Quasi-Steady and Unsteady Flow Effects in a Supersonic Compressor Stage, Trans. ASME, Journal of Engineering for Power, October 1977, Vol. 99, pp. 537-544.
- GALLUS, H.E., BOHN, D. and BROICHHAUSEN, K.D. 1979 Unsteady Upstream Effects in Axial-Flow Supersonic Compressor Stages. ASME 79-GT-55.
- GALLUS, H.E., GROLLIUS, H. and LAMBERTZ, J. 1981 The Influence of Blade Number Ratio and Blade Row Spacing on Axial-Flow Compressor Stator Blade Dynamic Load and Stage Sound Pressure Level. ASME 81-GT-165.
- GALLUS, H.E., GROLLIUS, H. and LAMBERTZ, J. 1982 The Influence of Blade Number Ratio and Blade Row Spacing on Axial-Flow Compressor Stator Blade Dynamic Load and Stage Sound Pressure Level. Trans. ASME Journal of Engineering for Power, Vol. 104, No. 3, pp. 633-641.
- GALLUS, H.E., HOENEN, H. 1983 Measurement of 3-D Unsteady Flow Downstream of Rotor and Stator Blades in Axial-Flow Compressors, 1983 Tokyo Intern. Gas Turbine Congress, 83-Tokyo-IGTC-68.
- GALLUS, H.E., LAMBERTZ, J. 1981 Gestaltungsrichtlinien zur Reduzierung von Schaufelschwingungsanregungen infolge instationärer Schaufeldruckverteilungen, Forschungsbericht Nr. 3076 des Landes NRW, Westdeutscher Verlag GmbH, Leverkusen - Opladen.
- GALLUS, J.E., LAMBERTZ, J., WALLMANN, TH. 1978 Experimentelle Untersuchung der Relativstroemung im Laufrad einer Axialverdichterstufe, Forschungsbericht des Landes NRW Nr. 2711, Westdeutscher Verlag GmbH, Leverkusen - Opladen.
- GALLUS, H.E., LAMBERTZ, J. and WALLMANN, TH. 1979 Blade Row Interaction in an Axial-Flow Subsonic Compressor Stage. ASME 79-GT-92.
- GALLUS, H.E., LAMBERTZ, J., WALLMANN, TH. 1980 Blade Row Interaction in an Axial-Flow Subsonic Compressor Stage, Journal of Engineering for Power, January 1980, Vol. 102, pp. 169-177.
- GARRICK, I.E. and RUBINOW, S.I. 1946 Flutter and Oscillating Air Force Calculations for an Airfoil in Two-Dimensional Supersonic Flow. NACA Report 846.
- GOLDSTEIN, M.E. 1975 Cascade with Subsonic Leading-Edge Locus. AIAA Journal, Vol. 13, No. 8, pp. 1117-1118.
- GOLDSTEIN, M.E. 1976 Aeroacoustics, McGraw-Hill Publishing Company.
- GOLDSTEIN, M.E. 1978 Unsteady Vortical and Entropic Distortions of Potential Flows Round Arbitrary Obstacles. Journal of Fluid Mechanics, Vol. 89, Part 3, pp. 433-468.
- GOLDSTEIN, M.E., BRAUN, W. and ADAMCZYK, J.J. 1977 Unsteady Flow in a Supersonic Cascade with Strong In-Passage Shocks, Journal of Fluid Mechanics, Vol. 83, Part 3, pp. 569-604.
- GOLDSTEIN, M.E. 1979 Turbulence Generated by the Interaction of Entropy Fluctuations with Non-Uniform Mean Flows. Journal of Fluid Mechanics, Vol. 93, Part 2, pp. 209-224.
- GOPALAKRISHNAN, S. 1973 (a) Fundamentals of Time-Marching Methods; (b) Application of the Time-Dependent Technique to Turbomachinery Cascades. Papers presented at the von Karman Institute for Fluid Dynamics, Lecture Series 59, May 21-25.

- GORELOV, D.N. 1966 Oscillations of a Plate Cascade in a Transonic Gas Flow, *Mekhanika Zhidkosti i Gaza*, Vol. 1, No.1, pp. 69-74.
- GOSTELOW, J.P. 1977 A New Approach to the Experimental Study of Turbomachinery Flow Phenomena. *Trans. ASME Journal of Engineering for Power*, Vol. 99, No. 1, pp. 97-105.
- GOSTELOW, J.P. 1984 *Cascade Aerodynamics*. Pergamon Press.
- GOTTLIEB, D. and TURKEL, E. 1978 Boundary Conditions for Multistep Finite-Difference Methods for Time-Dependent Equations. *Journal of Computational Physics*, Vol. 26, pp. 181-196.
- GRAHAM, R.W. and COSTILOW, E.L. 1965 Compressor Stall and Blade Vibration. Chapter XI in *Aerodynamic Design of Axial-Flow Compressors*, NACA SP-36.
- GRANT, H.P. and LANATI, G.A. 1978 Instrumentation for Measuring the Dynamic Pressure on Rotating Compressor Blades. NASA CR-159466.
- GREITZER, E.M. 1985 An Introduction to Unsteady Flow in Turbomachines. In *Thermodynamics and Fluid Mechanics of Turbomachinery*, Proceedings of a NATO Advanced Study Institute, Martinus Nijhoss.
- GROLIUS, H. 1981 Experimentelle Untersuchung von Rotornachlaufzellen und deren Auswirkungen auf die dynamische Belastung axialer Verdichter- und Turbinengitter, Diss. RWTH Aachen.
- HABASHI, W.G., HAFEZ, M.M., and KOTIUGA, P.L. 1985 Computation of Choked and Supersonic Turbomachinery Flows by a Modified Potential Method. *AIAA Journal*, Vol. 23, No. 2, pp. 214-220.
- HAFEZ, M.M. and LOVELL, D. 1983 Entropy and Vorticity Corrections for Transonic Flows. AIAA 6th Computational Fluid Dynamics Conference; Paper No. 83-1926.
- HAFEZ, M.M., RIZK, M.H., and MURMAN, E.M. 1977 Numerical Solution of the Unsteady Transonic Small-Disturbance Equations. Paper presented at the 44th meeting of the AGARD Structures and Materials Panel, Lisbon, Portugal, April 17-22.
- HALFMAN, R.L., JOHNSON, H.C. and HALEY, S.M. 1951 Evaluation of High Angle of Attack Aerodynamic-Derivative Data and Stall-Flutter Prediction Techniques. NACA TN 2533.
- HALL, M.G. 1985 Cell Vertex Multigrid Schemes for Solutions of the Euler Equations. Paper presented at Conference on Numerical Methods for Fluid Dynamics, University of Reading, U.K. April 1-4. To be published in *Procs, IMA Conference Series*, Oxford University Press.
- HALLIWELL, M.A. 1976 The Characteristics, Prediction and Test Analysis of Supersonic Flutter in Turbofan Engines. *Vibrations in Rotating Machinery Conference*, C186/76, pp. 181-185.
- HALLIWELL D.G., NEWTON, S.G. and LIT, K.S. 1983 A Study of Unsteady Pressures Near the Tip of a Transonic Fan in Unstalled Supersonic Flutter. *ASME Symposium on Vibrations of Bladed Disk Assemblies*.
- HAMAMOTO, I. 1960 Minute Harmonic Oscillations of a Flat Plate Cascade in Transonic Flow, *Proceedings of the 10th Japan National Congress for Applied Mechanics*, pp. 227-231.
- HANAMURA, Y., TANAKA, H. and YAMAGUCHI, K. 1980 A Simplified Method to Measure Unsteady Forces Acting on the Vibrating Blades in Cascade. *Bulletin of the JSME*, Vol. 23, No. 180.
- HANTMAN, R.G., BURR, R.J., ALWANG, W.G., WILLIAMS, M.C. 1973 Application of Holography to the Determination of Flow Conditions within the Rotating Blade Row of a Compressor, NASA CR-121112, July 1973.
- HAYMANN-BAHER, G., THOMPSON, W.T. 1980 Comparison of Experimental and Computational Shock Structure in a Transonic Compressor Rotor, *ASME Paper No. 80-GT-81*.
- HE, L. and ZHOU, S. 1984 Numerical Prediction of Transonic Stall Flutter in Axial Compressors. *Cambridge Symposium Proceedings: Unsteady Aerodynamics of Turbomachines and Propellers*, pp. 119-128.
- HEDSTROM, G.W. 1979 Nonreflecting Boundary Conditions for Nonlinear Hyperbolic Systems. *Journal of Computational Physics*, Vol. 30, pp. 222-237.
- HENDERSON, R.E. 1972 The Unsteady Response of an Axial Flow Turbomachine to an Upstream Disturbance, Ph.D. Diss., Engineering Department, University of Cambridge.
- HENDERSON, R.E. and FRANKE, G.P. 1978 Investigation of the Unsteady Pressure Distribution on the Blades of an Axial Flow Fan. Final Report for NASA Grant No. NGR 39-009-275.

- GORELOV, D.N. 1966 Oscillations of a Plate Cascade in a Transonic Gas Flow, *Mekhanika Zhidkosti i Gaza*, Vol. 1, No.1, pp. 69-74.
- GOSTELOW, J.P. 1977 A New Approach to the Experimental Study of Turbomachinery Flow Phenomena. *Trans. ASME Journal of Engineering for Power*, Vol. 99, No. 1, pp. 97-105.
- GOSTELOW, J.P. 1984 *Cascade Aerodynamics*. Pergamon Press.
- GOTTLIEB, D. and TURKEL, E. 1978 Boundary Conditions for Multistep Finite-Difference Methods for Time-Dependent Equations. *Journal of Computational Physics*, Vol. 26, pp. 181-196.
- GRAHAM, R.W. and COSTILOW, E.L. 1965 Compressor Stall and Blade Vibration. Chapter XI in *Aerodynamic Design of Axial-Flow Compressors*, NACA SP-36.
- GRANT, H.P. and LANATI, G.A. 1978 Instrumentation for Measuring the Dynamic Pressure on Rotating Compressor Blades. NASA CR-159466.
- GREITZER, E.M. 1985 An Introduction to Unsteady Flow in Turbomachines. In *Thermodynamics and Fluid Mechanics of Turbomachinery*, Proceedings of a NATO Advanced Study Institute, Martinus Nijhoff.
- GROLIUS, H. 1981 Experimentelle Untersuchung von Rotornachlaufzellen und deren Auswirkungen auf die dynamische Belastung axialer Verdichter- und Turbinengitter, Diss. RWTH Aachen.
- HABASHI, W.G., HAFEZ, M.M., and KOTIUGA, P.L. 1985 Computation of Choked and Supersonic Turbomachinery Flows by a Modified Potential Method. *AIAA Journal*, Vol. 23, No. 2, pp. 214-220.
- HAFEZ, M.M. and LOVELL, D. 1983 Entropy and Vorticity Corrections for Transonic Flows. *AIAA 6th Computational Fluid Dynamics Conference*; Paper No. 83-1926.
- HAFEZ, M.M., RIZK, M.H., and MURMAN, E.M. 1977 Numerical Solution of the Unsteady Transonic Small-Disturbance Equations. Paper presented at the 44th meeting of the AGARD Structures and Materials Panel, Lisbon, Portugal, April 17-22.
- HALFMAN, R.L., JOHNSON, H.C. and HALEY, S.M. 1951 Evaluation of High Angle of Attack Aerodynamic-Derivative Data and Stall-Flutter Prediction Techniques. NACA TN 2533.
- HALL, M.G. 1985 Cell Vertex Multigrid Schemes for Solutions of the Euler Equations. Paper presented at Conference on Numerical Methods for Fluid Dynamics, University of Reading, U.K. April 1-4. To be published in *Procs, IMA Conference Series*, Oxford University Press.
- HALLIWELL, M.A. 1976 The Characteristics, Prediction and Test Analysis of Supersonic Flutter in Turbofan Engines. *Vibrations in Rotating Machinery Conference*, Cl86/76, pp. 181-185.
- HALLIWELL D.G., NEWTON, S.G. and LIT, K.S. 1983 A Study of Unsteady Pressures Near the Tip of a Transonic Fan in Unstalled Supersonic Flutter. *ASME Symposium on Vibrations of Bladed Disk Assemblies*.
- HAMAMOTO, I. 1960 Minute Harmonic Oscillations of a Flat Plate Cascade in Transonic Flow, *Proceedings of the 10th Japan National Congress for Applied Mechanics*, pp. 227-231.
- HANAMURA, Y., TANAKA, H. and YAMAGUCHI, K. 1980 A Simplified Method to Measure Unsteady Forces Acting on the Vibrating Blades in Cascade. *Bulletin of the JSME*, Vol. 23, No. 180.
- HANTMAN, R.G., BURR, R.J., ALWANG, W.G., WILLIAMS, M.C. 1973 Application of Holography to the Determination of Flow Conditions within the Rotating Blade Row of a Compressor, NASA CR-121112, July 1973.
- HAYMANN-BAHER, G., THOMPSON, W.T. 1980 Comparison of Experimental and Computational Shock Structure in a Transonic Compressor Rotor, *ASME Paper No. 80-GT-81*.
- HE, L. and ZHOU, S. 1984 Numerical Prediction of Transonic Stall Flutter in Axial Compressors. *Cambridge Symposium Proceedings: Unsteady Aerodynamics of Turbomachines and Propellers*, pp. 119-128.
- HEDSTROM, G.W. 1979 Nonreflecting Boundary Conditions for Nonlinear Hyperbolic Systems. *Journal of Computational Physics*, Vol. 30, pp. 222-237.
- HENDERSON, R.E. 1972 The Unsteady Response of an Axial Flow Turbomachine to an Upstream Disturbance, Ph.D. Diss., Engineering Department, University of Cambridge.
- HENDERSON, R.E. and PRANKE, G.F. 1978 Investigation of the Unsteady Pressure Distribution on the Blades of an Axial Flow Fan. Final Report for NASA Grant No. NGR 39-009-275.

- HIRSCH, CH., KOOL, P. 1977 Measurement of the Three-Dimensional Flow Field Behind an Axial Compressor Stage, Trans. ASME, Vol. 99A, 1977, p. 168.
- HOBSON, P.E. 1976 Numerical Methods for Calculating Unsteady Flows in Subsonic and Supersonic Turbomachinery Cascades. A.R.C., C.P. No. 1348.
- HOCKLEY, B.S., FORD, R.A.J., FOORD, C.A. 1978 Measurement of Fan Vibration Using Double Pulse Holography, ASME Paper No. 78-GT-111.
- HOBSON, H.P. 1984 An Inviscid Blade to Blade Prediction of a Wake Generated Unsteady Flow. ASME Paper No. 84-GT-43.
- HOLTMAN, H., SERVATY, S. and GALLUS, H.E. 1984 Computation of the Subsonic Flow Field Through Oscillating Compressor and Turbine Cascades. Paper presented at the Symposium on Unsteady Aerodynamics of Turbomachines and Propellers, Cambridge, U.K., September.
- HONDA M. 1960 Theory of a Thin Wing in a Shear Flow. Proceedings Royal Society of London, Series A, No. 264, pp. 372-394.
- HONDA M. 1961 Theory of Shear Flow through a Cascade. Proceedings Royal Society of London, Series A, No. 265, pp. 46-70.
- HOUNJET, M.H.L. 1981 Transonic Panel Method to Determine Loads on Oscillating Airfoils with Shocks. AIAA Journal, Vol. 19, No. 5, pp. 559-566.
- HUPPERT, M.C. and BENSER, W.A. 1953 Some Stall and Surge Phenomena in Axial-Flow Compressors. J. Aero. Sci., 20, 12, pp. 835-845.
- HUPPERT, M.C., CALVERT, H.F. and MEYER, A.J. 1954 Experimental Investigation of Rotating Stall and Blade Vibration in the Axial-Flow Compressor of a Turbojet Engine. NACA RM E54A08.
- ISPAS, I., GROLIUS, H., GALLUS, H.E. 1980 Über den Einfluss von Nachlaufedellen auf die instationäre Druckverteilung an den nachfolgenden Schaufelreihen in Axialverdichtern und Axialturbinen, VDI-Berichte No. 361, pp. 33-43.
- IURA, T. and RANNIE, W.D. 1953 Observations of Propagating Stall in Axial-Flow Compressors. California Institute of Technology Mechanical Engr. Dept. Lab. Report No. 4, Pasadena.
- JAMESON, A. 1974 Iterative Solution of Transonic Flows over Airfoils and Wings including Flows at Mach 1. Comm. Pure and Applied Maths, Vol. 27, p. 283.
- JAMESON, A. 1979 Acceleration of Transonic Potential Flow Calculations on Arbitrary Meshes by the Multiple Grid Method. AIAA Paper No. 79-1458.
- JAMESON, A. 1983 Solution of the Euler Equations for Two-Dimensional Transonic Flow by a Multigrid Method. Applied Mathematics and Computation, V. 13, No. 3-4, pp. 327-358.
- JAMESON, A. and BAKER, T. J. 1983 Solution of the Euler Equations for Complex Configurations, AIAA-Paper 83-1929.
- JAMESON, A., SCHMIDT, W., and TURKEL, E. 1981 Numerical Solutions of the Euler Equations by Finite Volume Methods Using Runge-Kutta Time-Stepping Schemes. AIAA Paper No. 81-1259.
- JAY, R.L. 1975 Subscale Flutter Testing of TF-41-A-100 LP1 Blades. AFAPL-TR-75-82.
- JAY, R.L. and BURNS, D.W. 1983 Bladed Disk Response Study. Final Report Number AFWAL-TR-83-2050 under Air Force Contract F33615-79-C-2045.
- JAY, R.L., McBAIN, J.C. and BURNS, D.W. 1984 Structural Response Due to Blade Vane Interaction. Journal of Engineering for Gas Turbines and Power, Vol. 106, No. 1, pp. 50-60.
- JAY, R.L., ROTHROCK, M.D., RIFFEL, R.E. and SINNET, G. T. 1979 Time-Variant Aerodynamics for Torsional Motion of Large-Turning Airfoil. Final Report for Naval Air Systems Command, Contract N00019-79-C-0087, D.D.A. EDR No. 10192, DDA. EDR No. 10192.
- JEFFERS, J.D., II, MAY, A. and DESKIN, W.J. 1978 Evaluation of a Technique for Predicting Stall Flutter in Turbine Engines, NASA Report CR-135423.
- JEFFERS, J.D., II and MPECE, C.E.JR. 1975 F100 Fan Stall Flutter Problem Review and Solution. AIAA Journal of Aircraft, Vol. 12, No. 4, pp. 350-357.
- JORSTON, J.P. 1964 A Wall-Trace Flow Visualization Technique for Rotating Surfaces in Air, ASME Journal of Basic Engineering, 1964, p. 907.
- JONES, L.N. 1970 Telemetry of Engine Rotor Test Data, Conference on "Methods of Transmitting Signals from Rotating Plant," Central Electricity England, Research Laboratories, Leatherhead, England.

- JONES, D.I.G., HENDERSON, J.P., and ROGERS L.C. 1979 Viscoelastic Damping in USAF Applications. AGARD Conference Proceedings No. 277, Damping Effects in Aerospace Structures, Williamsburg, VA, 1983.
- JONES, W.P. (ed) 1961 Manual on Aerolasticity. AGARD Publication, Paris.
- JOSLYN, H.D., DRING, R.P. and SHARMA O.P. 1983 Unsteady Three-Dimensional Turbine Aerodynamics, Trans. ASME Journal of Engineering for Power, Vol. 105, No. 2, pp. 322-331.
- JOUBERT, H. 1984 Supersonic Flutter in Axial Flow Compressors. Paper presented at the Symposium on Unsteady Aerodynamics of Turbomachines and Propellers, Cambridge, U.K., September.
- JUTRAS, R.R., STALLONE, M.J. and BANKHEAD, H.R. 1980 Experimental Investigation of Flutter in Mid-Stage Compressor Designs. AIAA Paper 80-0786, pp. 729-740.
- JUTRAS, R., CHI, M., and FROST, R. 1982 Experimental Analysis of Blade Instability - A Flutter Data Correlation for Turbomachinery Blading. AFWAL-TR-82-2008.
- KAJI, S. 1980 Flutter of Linear Cascade in Compressible Flow, Paper C282/80 I. Mech. E. Conference in Churchill College, Sept. 1980.
- KAJI, S. and OKAZAKI, T. 1970 Propagation of Sound Waves through a Blade Row, I. Analysis Based on the Semi-Actuator Disk Theory. Journal of Sound and Vibration, Vol. 11, No. 3, pp. 339-353.
- KAJI, S. and OKAZAKI, T. 1970 Propagation of Sound Waves through a Blade Row, II. Analysis Based on the Acceleration Potential Method. Journal of Sound and Vibration, Vol. 11, No. 3, pp. 355-375.
- KAJI S. and OKAZAKI, T. 1972 Cascade Flutter in Compressible Flow. Trans. JSME Vol. 38, No. 309, pp. 1023-1033.
- KAJI, S., TAKATA, H. and NIWA, N. 1981 Three-Dimensional Analysis of Cascade Flutter in Parallel Shear Flows. In Aeroelasticity in Turbomachines, Proceedings of the Second International Symposium Held in Lausanne, September 1980, Editor: P. Suter, Juris-Verlag-Zurich, pp. 357-370.
- KANTROWITZ, A. 1946 The Supersonic Axial-Flow Compressor, NCA Rep. 974.
- KARMAN, Th. von and TSIEN, H.S. 1945 Lifting-Line Theory for a Wing in Non-Uniform Flow. Quarterly of Applied Mathematics, Vol. 3, No. 1, pp. 1-11.
- KAZA, K.R.V. and KIELB, R.E. 1982 Flutter and Response of a Mistuned Cascade in Incompressible Flow. AIAA Journal, 20, 8, pp. 1120-1127.
- KAZA, K.R.V. and KIELB, R.E. 1984 Flutter of Turbofan Rotors with Mistuned Blades. AIAA Journal, 22, 11, pp 1618-1625.
- KEMP, R.E. 1978 Closed-Coupled Telemetry for Measurements on Gas Turbines, Instrumentation Technology, September 1978.
- KERLICK, G. D. and NIXON, D. 1982 A High-Frequency Transonic Small Disturbance Code for Unsteady Flows in a Cascade. AIAA/ASME 3rd Joint Thermophysics, Fluids, Plasma and Heat Transfer Conference; Paper No. 82-0955.
- KERREBROCK, J.L., EPSTEIN, A.H., THOMPSON, W.T. 1980 A Miniature High Frequency Sphere Probe, ASME Joint Fluids Engineering and Gas Turbine Conference, New Orleans, 1980, pp. 91-98.
- KIKUCHI, M. 1980 Interaction of Supersonic Linear Cascade with Sinusoidally Distorted Flow between Two Parallel Plates (in Japanese). Transactions of the Japan Society of Mechanical Engineers, Series B, Vol. 46, No. 412, pp. 2247-2256.
- KIKUCHI, M. 1981 Flutter Characteristics of Supersonic Linear Cascade Between Two Parallel Plates (in Japanese). Transactions of the Japan Society of Mechanical Engineers, Series B. Vol. 47. No. 421, pp. 1671-1680.
- KILPATRICK, D.A. and BURROWS, R.A. 1958 Aspect-Ratio Effects on Compressor Blade Flutter. Brit. A.R.C. Report R. & M. No. 3103.
- KIRSCHNER, A., FOSCO, B. and MULLER, E. 1981 Control of Vibration in Aeroelastic Cascade Experiments. In Aeroelasticity in Turbomachines, Proceedings of the 2nd International Symposium Held in Lausanne, Sept. 1980, Editor: P. Suter, Juris-Verlag-Zurich, pp. 285-296.
- KLOPPER, G. H. and NIXON, D. 1984 Nonisotropic Potential Formulation for Transonic Flows. AIAA Journal, Vol. 22, No. 6, pp. 770-776.
- KNAUF, W., GALLUS, H.E. 1984 Techniques for Measuring Blade Forces and Damping in Oscillating Axial-Flow Compressor Blade Rows, Symposium Proceedings "Unsteady Aerodynamics of Turbomachines and Propellers," Cambridge, England, September 1984.

- KOBAYASHI, J. 1983 Measurement of Unsteady Pressure Distribution on Oscillating Airfoils in a Turbine Annular Cascade. International Gas Turbine Congress, Tokyo 1983.
- KOCH, W. and MOHRING, W. 1983 Eigensolutions for Liners in Uniform Mean Flow Ducts, AIAA Journal, Vol. 21, No. 2, pp. 200-213.
- KOFF, S.G. and GREITZER E.M. 1984 Stalled Flow Performance for Axial Compressors - I: Axisymmetric Characteristics, ASME Paper 84-GT-93.
- KOOL, P., DE RUYCK, J., HIRSCH, CH. 1978 The Three-Dimensional Flow in an Axial Plane Downstream of a Compressor Rotor, ASME Paper 78-GT-66.
- KOVASZNAVY, L.S.G. 1953 Turbulence in Supersonic Flow. Journal of Aeronautical Sciences, Vol. 20, No. 10, pp. 657-674.
- KOVATS, Z. 1979 Dynamic Cascade Facility and Methods for Investigating Flow-Excited Vibration and Aerodynamic Damping of Model Low-Pressure Blade Groups, ASME 79-WA/GT-6.
- KOYA, M. and KOTAKE, S. 1985 Numerical Analysis of Fully Three-Dimensional Periodic Flows through a Turbine Stage. ASME Journal of Engineering for Gas Turbines and Power, Vol. 107, No. 4, pp. 945-952.
- KURKOV, A.P. 1980 Flutter Spectral Measurements Using Stationary Pressure Transducers, ASME Joint Fluids Engineering and Gas Turbine Conference, New Orleans, 1980, pp. 225-234.
- KURKOV, A.P. 1980 Flutter Spectral Measurements Using Stationary Pressure Transducers Measurement Methods in Rotating Components of Turbomachinery. Trans. ASME Journal of Engineering for Power, Vol. 103, No. 2, pp. 461-467.
- KURKOV, A.P. 1981 Measurement of Aerodynamic Work During Fan Flutter. NASA TM-82-652 for 1981 ASME Winter Annual Meeting.
- KURKOV, A.P. 1981 Flutter Spectral Measurements using Stationary Pressure Transducers. ASME Journal of Engineering for Power, 103, 2, pp. 461-467.
- KURKOV, A.P. 1983 Measurement of Aerodynamic Work During Fan Flutter. Trans. ASME Journal of Engineering for Power, Vol. 105, No. 1, pp. 204-211.
- KURKOV, A. and DICUS, J. 1978 Synthesis of Blade Flutter Vibrating Response Using Stationary Transducers. ASME Paper No. 78-GT-160.
- KUROSAKA, M. 1974 On the Unsteady Supersonic Cascade with a Subsonic Leading Edge - An Exact First Order Theory: Parts 1 and 2. Trans. ASME A: Journal of Engineering for Power, Vol. 96, No. 1, pp. 13-31.
- KUROSAKA, M. 1978 Three-Dimensional Refraction Effect Upon Unsteady Oscillating Airfoils in Supersonic Flow. General Electric Company Report, SRD-78-063.
- KUROSAKA, M. and BUELFELT, I.H. 1978 Suppressive Effect of Liners on Supersonic Compressor Flutter, General Electric Company Report, SRD-78-063.
- LAKSHMINARAYANA, B. 1980 An Axial Flow Research Compressor Facility Designed for Flow Measurement in Rotor Passages, ASME Joint Fluids Engineering and Gas Turbine Conference, New Orleans, 1980, pp. 31-42.
- LAKSHMINARAYANA, B. 1981 Techniques for Aerodynamic and Turbulence Measurements in Turbomachinery Rotors, Trans. ASME, Journal of Engineering for Power, April 1981, Vol. 103, pp. 374-392.
- LAKSHMINARAYANA, B., RUNSTADLER, P., Editors 1980 Measurement Methods in Rotating Components of Turbomachinery, ASME, Joint Fluids Engineering and Gas Turbine Conference, New Orleans, 1980.
- LAMBOURNE, N.C. 1980 Experimental Techniques in Unsteady Aerodynamics Reference 10. AGARD Report No. 679, Special Course on Unsteady Aerodynamics.
- LANDAHL, M. 1961 Unsteady Transonic Flow. Pergamon Press.
- LANE, P. 1956 System Mode Shapes in the Flutter of Compressor Blade Rows. Journal of the Aeronautical Sciences, Vol. 23, No. 1, pp. 54-66.
- LANE, P. and FRIEDMAN, M. 1958 Theoretical Investigation of Subsonic Oscillatory Blade-Row Aerodynamics. NACA TN 4136.
- LANGUIER, R. 1980 Experimental Analysis Methods for Unsteady Flows in Turbomachines, ASME Joint Fluids Engineering and Gas Turbine Conference, New Orleans, pp. 71-80.
- LeBALLZUK, J.C. 1984 Numerical Viscid-Inviscid Interaction in Steady and Unsteady Flows. In Numerical and Physical Aspects of Aerodynamic Flows II, (ed. T. Cebeci), Springer-Verlag, pp. 259-284.

- LE BOT, Y., LARGUIER, R. 1976 Characterisation experimentale des Ecoulements Internes dans les Turbomachines, Revue Francaise des Mecanique, No. 57, 1976, pp. 5-14.
- LEWIS, R.I. and PORTHOUSE, D.T.C. 1982 A Generalized Numerical Method for Bluff Body and Stalling Aerofoil Flow. ASME paper 82-GT-70. London.
- LIGHTHILL, M.J. 1958 Fourier Analysis and Generalized Function, Cambridge University Press.
- LILLEY, G.M. 1952 An Investigation of the Flexure-Torsion Flutter Characteristics of Airfoils in Cascade. Report. No. 60, The College of Aeronautics, Cranfield.
- LOCK, R.C. and FIRMIN, M.C.P. 1982 Survey of Techniques for Estimating Viscous Effects in External Aerodynamics. In Proc. of the IMA Conf. on Numerical Methods in Aeronautical Fluid Dynamics, (ed. P. L. Roe), Academic Press, pp. 337-430.
- LOISEAU, H. LEPOING G., and MAQUENNEHAN B. 1975 Recherches exploratoires sur l'aeroelasticite des aubes de turbomachines. AGARD Meeting on Unsteady Effects in Turbomachiens, Monterey 1975.
- LOISEAU, H. and MAQUENNEHAN, B. 1976 Aeroelastic Instabilities in Compressors and Wind Tunnel Tests of Straight Cascades, Revue Francaise de Mecanique, Numero Special, pp. 157-167.
- LOISEAU, H., NICOLAS, J. and MAQUENNEHAN, B. 1981 Measurement and Prediction of the Aerodynamic Damping of Compressor Blades. In Aeroelasticity in Turbomachines, Proceedings of the 2nd International Symposium Held in Lausanne, Sept. 1980, Editor: P. Suter, Juris-Verlag-Zurich, pp. 399-408.
- LOTZ, M. 1965 Erregung von Schaufelschwingungen in axialen Turbomaschinen durch die benachbarten Schaufelgitter, Diss. TU Muenchen.
- LUBOMSKI, J.F. 1979 Characteristics of Aeroelastic Instabilities in Turbomachinery - NASA Full Scale Engine Test Results. NASA T.M. 79805.
- LUBOMSKI, J.F. 1981 Status of NASA Full-Scale Engine Elasticity Research. NASA T.M. 81500.
- MACCORMACK, R.W. 1976 An Efficient Numerical Method for Solving the Time-Dependent Compressible Navier-Stokes Equations at High Reynolds Number. NASA Technical Memorandum X-73,129.
- MACCORMACK, R.W. and LOMAX, H. 1979 Numerical Solutions of Compressible Viscous Flows. Annual Review of Fluid Mechanics, Vol. 11, pp. 289-316.
- MARTENSEN, E. 1959 Calculation of Pressure Distribution over Profiles in Cascade in Two-Dimensional Potential Flow, by means of a Fredholm Integral Equation, Arch. Rat. Mech. Anal. Vol 3., No. 3, pp. 235-270. (See NASA TT F-702 for English Translation.)
- MATSUUCHI, K. AND ADACHI, T. 1983 Measurement of the Three-Dimensional Unsteady Flow Inside a Rotor Blade Passage of an Axial-Flow Fan, Tokyo, IGTC-67.
- McCROSKEY, W.J. et al. 1980 Dynamic Stall on Advanced Airfoil Sections. Paper No. 80-1, Proceedings 36th Annual Forum American Helicopter Society, Washington.
- McCUNE, J.E. 1958 A Three-Dimensional Theory of Axial Compressor Blade Rows - Application in Subsonic and Supersonic Flows. Journal of the Aerospace Sciences, Vol. 25, pp. 544-560.
- McCUNE, J.E. 1958 The Transonic Flowfield of an Axial Compressor Blade Row. Journal of the Aerospace Sciences, Vol. 25, pp. 616-626.
- MCDONALD, P.W., BOLT, C.R., DUNKER, R.J., WEYER, H.B. 1980 A Comparison Between Measured and Computed Flow Field in a Transonic Compressor Rotor, ASME Paper No. 80-GT-7.
- McNALLY, W.D. 1976 Review of Experimental Work on Transonic Flow in Turbomachinery, SQUID Workshop on "Transonic Flow Problems in Turbomachinery," Hemisphere Publishers, 1976, pp. 457-484.
- McNALLY, W.D. and SOCKOL, P.M. 1981 Computational Methods for Internal Flows with Emphasis on Turbomachinery. NASA Tech. Memo. 82764.
- MEHALIC, C.M., DICUS, J.H. and KURKOV, A.P. 1977 Effect of Pressure and Temperature on the Subsonic Stall Flutter Region of a YF100 Engine. NASA TMX 73785.
- MEHALIC, C.M., HURRELL, G.H., DISCUS, J.H. LUBOMSKI, J.F., KURKOV, A.P. and EVANS, D.G. 1977 Experimental Results and Data Format of Preliminary Fan Flutter Investigation Using YF100 Engine. NASA TM X-3444, Washington.

- MELNIK, R.E. 1980 Turbulent Interactions on Airfoils at Transonic Speeds - Recent Developments. AGARD Symposium on Computation of Viscous-Inviscid Flows, AGARD-CP-291; Paper No. 10.
- MENDELSON, A. 1949 Aerodynamic Hysteresis as a Factor in Critical Flutter Speed of Compressor Blades at Stalling Conditions. Journal of the Aerospace Sciences, Vol. 16, No. 11, pp. 645-652.
- MICKLOW, J. and JEFFERS, J. 1981 Semi-Actuator Disc Theory for Compressor Choke Flutter. NASA Contractor Report 3426.
- MIKOLAJCZAK, A. A. 1975 The Practical Importance of Unsteady Flow. Unsteady Phenomena in Turbomachinery, AGARD CP-177; Paper No. 1.
- MIKOLAJCZAK, A.A., ARNOLDI, R., STARGARDTER, H. and SNYDER, L.E. 1975 Advances in Fan and Compressor Blade Flutter Analysis and Predictions. AIAA Journal of Aircraft, Vol. 12, No. 4, pp. 325-332.
- MILES, J.W. 1959 The Potential Theory of Unsteady Supersonic Flow. Cambridge University Press.
- MINKIN, H.L. 1976 Performance of Some Miniature Pressure Transducers Subjected to High Rotational Speeds and Centripetal Accelerations, ISA ASI 76317.
- MITCHELL, N. 1980 Time Marching Method for Unsteady Two-Dimensional Flow in a Blade Passage. Int. J. Heat and Fluid Flow, Vol. 2, No. 4, pp. 205-220.
- MORETTI, G. 1969 Importance of Boundary Conditions in the Numerical Treatment of Hyperbolic Equations. The Physics of Fluids, Vol 12, Supplement II, pp. 13-20.
- NAGASHIMA, T. 1974 The Vibration of Compressor and Turbine Blade in Compressible Flow. Ph.D. Thesis, Cambridge University, CUED.
- NAGASHIMA, T. and WHITEHEAD, D.S. 1974 Aerodynamic Forces and Moments for Vibrating Supersonic Cascades of Blades. Cambridge University CUEDA/A-Turbo/TR59.
- NAGASHIMA, T. and WHITEHEAD, D.S. 1978 Linearized Supersonic Unsteady Flows in Cascades. Aeronautical Research Council, R&M 3811.
- NAMBA, M. 1969 Theory of Transonic Shear Flow Past a Thin Aerofoil. Journal of Fluid Mechanics, Vol. 36, Part 4, pp. 759-783.
- NAMBA M. 1969 Lifting-Surface Theory for Cascade of Blades in Subsonic Shear Flow. Journal of Fluid Mechanics, Vol. 36, Part 4, pp. 735-757.
- NAMBA, M. 1972 Lifting Surface Theory for a Rotating Subsonic or Transonic Blade Row. Aeronautical Research Council, R&M 3740.
- NAMBA, M. 1976 Lifting Surface Theory for Unsteady Flows in a Rotating Annular Cascade, Proceedings of IUTAM Symposium on Aeroelasticity in Turbomachines, Paris, Revue Francaise de Mecanique, Special issue, pp. 39-46.
- NAMBA, M. 1977 Three-Dimensional Analysis of Blade Force and Sound Generation for an Annular Cascade in Distorted Flows. Journal of Sound and Vibration, Vol. 50, No. 4, pp. 479-508.
- NAMBA, M. 1986 Three-Dimensional Unsteady Flow in Axial Turbomachines, Naval Post-graduate School Report, NPS67-86-001.
- NAMBA, M. and ABE, T. 1984 Unsteady Aerodynamic Forces on Supersonic and Transonic Annular Cascades Interacting with Distorted Inlet Flows. In Unsteady Aerodynamics of Turbomachines and Propellers, Proceedings of the 3rd International Symposium held in Cambridge, Sept. 1984, published by Cambridge University Engineering Department, pp. 205-226.
- NAMPA, M. and FAN, F. D. 1985 Unsteady Aerodynamic Characteristics of a Supersonic Cascade of Swept Blades. Proceedings of the 7th International Symposium on Air Breathing Engines held in Beijing, Sept. 1985, pp. 679-686.
- NAMBA, M. and FUKUSHIGE, K. 1980 Application of the Equivalent Surface Source Method to the Acoustics of Duct Systems with Non-Uniform Wall Impedance. Journal of Sound and Vibration, Vol. 73, Part 1, pp. 125-146.
- NAMBA, M. and ISHIKAWA, A. 1983 Three-Dimensional Aerodynamic Characteristics of Oscillating Supersonic and Transonic Annular Cascades. Trans. ASME Journal of Engineering for Power, Vol. 105, No. 1, pp. 138-146.
- NAMBA, M. YAMASAKI, N., and KURIHARA, Y. 1984 Some Three-Dimensional Effects on Unsteady Aerodynamic Forces on Oscillating Cascades, *ibid.*, pp. 217-230.
- NATESH, M. S. 1967 Torsional Instability of Fully Stalled Airfoil (or Supercavitating Hydrofoil). Trans. ASME Journal Engineering for Industry, Vol 89, No. 4, pp. 671-682.

- NAUMANN, H., YEH, H. 1973 Lift and Pressure Fluctuations of a Cambered Airfoil Under Periodic Gusts and Applications in Turbomachinery, Trans. ASME, Journal of Engineering for Power, 1973, pp. 1-10.
- de NEEF, T. and MORETTI, G. 1980 Shock Fitting for Everybody. Computers and Fluids, Vol. 8, No. 3.
- NEIBERDING, W.C., POLLACK, J.L. 1977 Optical Detection of Blade Flutter, ASME Paper No. 77-GT-66 and NASA TM 73573, March 1977.
- NEUHOF, F., SHREEVE, R.P., FOTTNER, L. 1986 Evaluation of the Blade-to-Blade Flow from a High Speed Compressor Rotor, ASME Paper No. 86-GT-117.
- NI, R.H. and SISTO, F. 1975 Numerical Computation of Nonstationary Aerodynamics of Flat Plate Cascades in Compressible Flow. ASME Paper No. 75-GT-5.
- NI, R.H. 1979 A Rational Analysis of Periodic Flow Perturbation in Supersonic Two-Dimensional Cascade. Trans. ASME A: Journal of Engineering for Power, Vol. 101, No. 3, pp. 431-439.
- NI, R.H. 1981 A Multiple Grid Scheme for Solving the Euler Equations. AIAA Paper No. 81-1025.
- NISHIYAMA, T. and KOBAYASHI, T. 1977 Unsteady Aerodynamic Theory for Subsonic Cascade between Parallel Walls, 1st Report, Unsteady Responses in Periodically Varying Gust (in Japanese). Transactions of the Japan Society of Mechanical Engineers, Vol. 43, No. 370, pp. 2175 - 2181, 2nd Report, Flutter Characteristics, pp. 2188-2198.
- O'BRIEN, W.F., COUSINS, W.T., SEXTON, M.R. 1980 Unsteady Pressure Measurements and Data Analysis Techniques in Axial-Flow Compressors, ASME Joint Fluids Engineering and Gas Turbine Conference, New Orleans, pp. 195-202.
- O'BRIEN, W.F., MOSES, H.L., CARTER, H.R. 1974 A Multichannel Telemetry System for Flow Research on Turbomachine Rotors, ASME Paper No. 74-GT-112, March 1974.
- O'BRIEN, W.F. and REIMERS, S.L. 1982 Measurement of Unsteady Pressures on Fan Blades: Rotor-Downstream Strut Interaction. NASA Workshop, A Status Report on Flight Effects on Fan Noise.
- OKUROUNMU, O. and McCUNE, J. E. 1974 Lifting Surface Theory of Axial Compressor Blade Rows, Part I - Subsonic Compressor. AIAA Journal, Vol. 12, pp. 1363-1371; Part II - Transonic Compressor, pp. 1372-1380.
- OSTDIEK, F.R. 1976 A Cascade in Unsteady Flow. AFAPL-TR-76-115.
- OSWATITSCH, K. and KEUNE, F. 1955 The Flow Around Bodies of Revolution at Mach Number 1. Proceedings of the Conference on High Speed Aeronautics, Polytechnic Institute of Brooklyn.
- PANDOLFI, M. 1980 Numerical Experiments on Unsteady Flows through Vibrating Cascades. Proc Symposium 'Aeroelasticity in Turbomachines'. EPFL, Lausanne, pp. 211-228.
- PEARSON, H. 1953 The Aerodynamics of Compressor Blade Vibration. Fourth Anglo-American Aeronautical Conference, London, pp. 127-162.
- PERUMAL, P.V.K. 1976 Thin Airfoil in Eddy Array and Part-Stalled Oscillating Cascade. Ph.D. Thesis, Stevens Institute of Technology.
- PEYRET, R. and TAYLOR, T. D. 1983 Computational Methods for Fluid Flow. Springer Verlag New York Heidelberg Berlin.
- PIGOTT, R. and ABEL, J.M. 1973 Vibrations and Stability of Turbine Blades at Stall. Trans. ASME Journal of Engineering for Power, Vol. 96, No. 3, pp. 201-208.
- PINES, S. 1958 An Elementary Explanation of the Flutter Mechanism. Proceedings of the National Specialists Meeting on Dynamics and Aeroelasticity, Institute of the Aeronautical Sciences, Fort Worth, Texas, pp. 52-58.
- PISTOLESI, E. 1937 On the Calculation of Infinite Cascades of Thin Aerofoils, Aerotecrica, Roma. Vol. 17, p. 484.
- PLATZER, M.F. 1975 Transonic Blade Flutter: A Survey, Shock and Vibration Digest, Vol. 7, No. 7, pp. 97-106.
- PLATZER, M.F. 1977 Unsteady Flows in Turbomachines - A Review of Current Developments. In AGARD-CP-227 Unsteady Aerodynamics, Ottawa.
- PLATZER, M.F. 1978 Transonic Blade Flutter: A Survey of New Developments, Shock and Vibration Digest, Vol 10, No. 9, pp. 11-20.
- PLATZER, M.F. 1982 Transonic Blade Flutter: A Survey of New Developments, Shock and Vibration Digest, Vol. 14, No. 7, pp. 3-8.

- PLATZER, M.F., CHADWICK, W.R., and SCHLEIN, P.B. 1976 On the Analysis of the Aerodynamic and Flutter Characteristics of Transonic Compressor Blades. *Revue Francaise de Mecanique*. Numero Special 1976. pp. 65-72.
- POWELL, J.A., STRAZISAR, A.J., SEASHOLTZ, R.G. 1980 Efficient Laser Anemometer for Intra-Rotor Flow Mapping in Turbomachinery, ASME Joint Fluids Engineering and Gas Turbine Conference, New Orleans, 1980, pp. 157-164.
- RAI, M. M. 1985 Navier-Stokes Simulations of Rotor-Stator Interaction Using Patched and Overlaid Grids, AIAA Paper 85-1519, July 1985.
- RAJ R., LAKSHMINARAYANA, B. 1976 Three-Dimensional Characteristics of Turbulent Wakes Behind Rotors of Axial Flow Turbomachinery, *Journal of Engineering for Power*, Vol. 98, April 1976, pp. 218-228.
- Lord RAYLEIGH 1926 *The Theory of Sound*. Dover Publications 1945.
- RAVINDRANATH, A., LAKSHMINARAYANA, B. 1979 Mean Velocity and Decay Characteristics of the Near- and Far-Wake of a Compressor Rotor Blade of Moderate Loading, ASME Paper 79-GT-202.
- REISSNER, E. 1949 Boundary Value Problems in Aerodynamics of Lifting Surfaces in Non-Uniform Motion, *Bull. Am. Math. Soc.* Vol. 55, p. 825.
- REISSNER, E. 1951 On the Application of Mathieu Functions in the Theory of Subsonic Compressible Flow Past Oscillating Aerofoils, 1951. NACA Tech. Note 2363.
- REYNOLDS, B., LAKSHMINARAYANA, B. 1980 Blade Loading and Spanwise Effects on the Near and Far Wake Characteristics of Compressor Rotor Blade, AIAA Paper 80-0201.
- REYNOLDS, B., LAKSHMINARAYANA, B., RAVINDRANATH, A. 1979 Characteristics of the Near Wake of a Compressor Rotor, AIAA Journal, Vol. 17, No. 9, September 1979, pp. 959-967.
- RICHTMYER, R.D. 1978 *Principles of Advanced Mathematical Physics*, Vol. 1. Springer Verlag.
- RICHTMYER, R.D. and MORTON, K.W. 1986 *Difference Methods for Initial Value Problems*. 2nd Edition, Interscience Publishers, U.S.A.
- RIFFEL, R.E. and ROTHROCK, M.D. 1980 Experimental Determination of Unsteady Blade Element Aerodynamics in Cascades - Torsion Mode Cascade Final Report. NASA CR-159831.
- RIFFEL, R.E. and ROTHROCK, M.D. 1980 Experimental Determination of Unsteady Blade Element Aerodynamics in Cascades. NASA CR-1651.
- RIFFEL, R.E. and ROTHROCK, M.D. 1980 Experimental Determination of Unsteady Blade Element Aerodynamics in Cascades - Translation Mode Cascade Final Report. NASA CR-165166.
- RIFFEL, R. and FLEETER, S. 1981 Experimental Modeling of Unstalled Supersonic Turbofan Flutter. AIAA Journal of Aircraft, Vol. 18, No. 9, pp. 718-724.
- ROTH, H. 1980 Vibration Measurements on Turbomachine Rotor Blades with Optical Probes, ASME Joint Fluids Engineering and Gas Turbine Conference, New Orleans, 1980, pp. 215-224.
- ROTHROCK, M.D., JAY, R.L., and RIFFEL, R.W. 1981 Time-Variant Aerodynamics of High-Turning Blade Elements, ASME 81-GT-123, March 1981.
- ROTHROCK, M.D., JAY, R.L. and RIFFEL, R.E. 1982 Time-Variant Aerodynamics of High-Turning Blade Elements. *Trans. ASME Journal of Engineering for Power*, Vol. 104, No. 2, pp. 412-419.
- ROWE, J.R. and MENDELSON, A. 1955 Experimental Investigation of Blade Flutter in an Annular Cascade. NACA TN 3581.
- RUDEN, P. 1944 Investigation of Single Stage Axial Fans, NACA RM No. 1062, April 1944.
- RUDY, D.H. and STRIKWERDA, J.C. 1980 A Nonreflecting Outflow Boundary Condition for Subsonic Navier-Stokes Calculations. *Journal of Computational Physics*, Vol. 36, pp. 55-70.
- RUGGERI, R.S. and BENSER, W.A. 1974 Performance of a Highly Loaded Two-stage Axial-Flow Fan. NASA TM X-3076.
- RUNSTADLER, P.W.J. 1976 Special Applications and New Technical Aspects of Laser Anemometry, *Proceedings of the ISL/AGARD Workshop on Laser Anemometry*, R 117/76, May 1976, pp. 465-486.

- SALAÜN, P. 1974 Pressions aerodynamiques instationnaires sur une grille annulaire en écoulement subsonique. Publication ONERA N°158.
- SALAÜN, P. 1976 Flutter Instability in an Annular Cascade. Proceedings of IUTAM Symposium on Aerolasticity in Turbomachines, Paris, Revue Francaise de Mechanique, Special issue, pp. 35-38. —
- SALAÜN, P. 1978 Theorie linearisee de l'ecoulement plan supersonique instationnaire a travers une grille. La Recherche Aerospatiale N° 1978-3, pp. 125-132.
- SALAÜN, P. 1979 Flutter Instabilities in an Annular Cascade with Supersonic Relative Flow. ONERA Publication No. 1979-3.
- SALAÜN, P. 1986 Three-Dimensional Unsteady Flow in Axial Turbomachines, Naval Postgraduate School Report, NPS67-86-002.
- SAVKAR, S.D. 1976 A Note on Transonic Flow Past a Thin Airfoil Oscillating in a Wind Tunnel. Journal Sound and Vibration, Vol. 42, No. 2, pp. 195-207.
- SCANLAN, R.H. and ROSENBAUM, R. 1951 Introduction to the Study of Aircraft Vibration and Flutter. The Macmillan Company, New York.
- SCHLEIN, P. 1975 A Study of Unsteady Transonic Interference Effects, Ph.D. Thesis, Naval Postgraduate School.
- SCHNEIDER, P. 1980 Analysis of J85-21 Compressor Aerodynamic Flutter Data. NASA CR 159795.
- SCHNITTGER, J.R. 1954 Single Degree of Freedom Flutter Compressor Blades in Separated Flow. Journal Aerospace Sciences, Vol. 21, No. 1, pp. 27-36.
- SCHNITTGER, J.R. 1955 The Stress Problem of Vibrating Compressor Blades. Journal Applied Mechanics, Vol. 22, No. 1, pp. 57-64.
- SCHODL, R. 1974 Laser-Dual-Beam Method for Flow Measurements in Turbomachines, ASME Paper No. 74-GT-157.
- SCHODL, R. 1977 Laser-Two-Focus Velocimetry (L2F) for Use in Aero-Engines, AGARD-LS-No. 90.
- SCHODL, R. 1977 Entwicklung des Laser-Zwei-Fokus-Verfahrens fuer die beruehrungslose Messung der Stroemungsvektoren, insbesondere in Turbomaschinen, Diss. RWTH Aachen.
- SCHODL, R. 1980 A Laser-Two-Focus (L2F) Velocimeter for Automatic Flow Vector Measurements in the Rotating Components of Turbomachines, ASME Journal of Fluids Engineering, Vol. 102, No. 4.
- SCHODL, R. 1980 A Laser-Two-Focus (L2F) Velocimeter for Automatic Flow Vector Measurements in the Rotating Components of Turbomachines, ASME Joint Fluids Engineering and Gas Turbine Conference, New Orleans, 1980, pp. 139-148.
- SHANNON, J.F. 1945 Vibration Problems in Gas Turbine, Centrifugal and Axial Flow Compressors. Brit. A.R.C. R & M 2226.
- SHREEVE, R.P., NEUHOFF, F. 1984 Measurements of the Flow from a High-Speed Compressor Rotor Using a Dual-Probe Digital Sampling (DPDS) Technique, ASME Journal of Engineering for Power, Vol. 106, April 1984, p. 336.
- SISTO, F. 1952 Flutter of Airfoils in Cascade. Doctoral Dissertation, Massachusetts Institute of Technology.
- SISTO, F. 1953 Stall Flutter in Cascades. Journal of Aerospace Sciences, Vol. 20, No. 9, pp. 598-604.
- SISTO, F. 1955 Unsteady Aerodynamic Reactions of Airfoils in Cascade. Journal of Aerospace Sciences, Vol. 22, No. 5, pp. 297-302.
- SISTO, F. 1967 Linearized Theory of Nonstationary Cascades at Fully Stalled or Supercavitated Conditions. ZAMM, Vol. 47, No. 8, pp. 531-542.
- SISTO, F. 1968 Aeroelasticity of Fans and Compressors. Proceedings of the AGARD Propulsion and Energetics Panel Meeting, Toulouse.
- SISTO, F. 1974 Aeromechanical Response. Proceedings of AGARD Lecture Series No. 72, London, 4.1-4.13.
- SISTO, F. 1978 Aeroelasticity in Turbomachines. In A Modern Course in Aeroelasticity (ed. E. H. Dowell), Sijthoff and Noordhoff, pp. 383-409.
- SISTO, F. and CHANG, A.T. 1981 The Influence of Gyroscopic Forces on the Dynamic Behavior of Rotating Blades. 5th Int. Symposium on Airbreathing Engines, Feb 16-20, Bangalore.

- SISTO, F. and NI, R. 1972 Quasi-Static Moment Measurements for Airfoils in an Annular Cascade. AIAA Journal of Aircraft, Vol. 9, No. 4, pp. 298-305.
- SISTO, F. and PERUMAL, P.K.V. 1974 Lift and Moment Prediction for an Oscillating Airfoil with a Moving Separation Point. ASME Paper No 74-GT-28.
- SISTO, F. and PERUMAL, P.K.V. 1974 Lift and Moment Prediction for an Oscillating Airfoil with a Moving Separation Point. Trans. ASME Journal of Engineering for Power, Vol. 96, No. 4, pp. 372-378.
- SITARAM, N., LAKSHMINARAYANA, B., RAVINDRANATH, A. 1981 Conventional Probes for the Relative Flow Measurement in a Turbomachinery Rotor Blade Passage, Trans. ASME, Journal of Engineering for Power, Vol. 103, No. 2, April 1981, pp. 406-414.
- SMITH, G.D. 1985 Numerical Solution of Partial Differential Equations. 3rd Edition, Clarendon Press, Oxford, U.K.
- SMITH, S.N. 1971 Discrete Frequency Sound Generation in Axial Flow Turbomachines. University of Cambridge Report CUED/A-Turbo/TR 29.
- SMITH, S.N. 1971 Discrete Frequency Sound Generation in Axial Flow Turbomachines, ARC R&M 3709.
- SNYDER, L.E. 1972 Supersonic Unstalled Torsional Flutter, in Aeroelasticity in Turbomachinery. (S. Fleeter, ed.) Proceedings of Project SQUID. Workshop held at Detroit Diesel Allison, Indianapolis, Project SQUID, Office of Naval Research, pp. 164-195.
- SNYDER, L.E., and Commerford, G. L. 1974 Supersonic Unstalled Flutter in Fan Rotors: Analytical and Experimental Results. Trans. ASME Journal of Engineering for Power, Series A, Vol. 96, No. 4, pp. 379-386.
- SOHNGEN, H. 1953 Luftkrafte an einem schwingenden Schaufelkranz kleiner Teilung, Zeit. Ang. Math. U. Phys. Vol. 4, 1953, p. 267.
- SPALART, P.R. 1984 Two Recent Extensions of the Vortex Method. AIAA Paper. No. AIAA-84-0343. Reno.
- SRINIVASAN, A.V., ED., 1976 Structural Dynamic Aspects of Bladed Disk Assemblies. Proc. ASME Winter Annual Meeting, New York.
- SRINIVASAN, A.V. 1980 Influence of Mistuning on Blade Torsional Flutter. NASA CR-165137, August.
- SRINIVASAN, A.V., CUTTS, D. G. and SRIDHAR, S. 1981 Turbojet Engine Blade Damping. NASA CR-165406.
- STARGARDTER, H. 1977 Optical Determination of Rotating Fan Blade Deflections. Trans. ASME Journal of Engineering for Power, Vol. 99, No. 2, pp. 204-210.
- STARGARDTER, H. 1979 Subsonic/Transonic Stall Flutter Study. Final Report. NASA CR-165256, PWA 5517-31.
- STEGER, J.L. 1978 Implicit Finite-Difference Simulation of Flow about Arbitrary Two-Dimensional Geometries. AIAA Journal, Vol. 16, No. 7.
- STEGER, J.L., PULLIAM, T.H., AND CHIMA, R.V. 1980 An Implicit Finite Difference Code for Inviscid and Viscous Cascade Flow. AIAA 13th Fluid and Plasma Dynamics Conference, Paper No. 80-1427.
- STRADA, J.A., CHADWICK, W.R., and PLATZER, M.F. 1979 Aeroelastic Stability Analysis of Supersonic Cascades. Trans. ASME, Jour. Eng. for Power, Vol. 101, pp. 533-541.
- STRAZISAR, A.J., POWELL, J.A. 1980 Laser Anemometer Measurements in a Transonic Axial Flow Compressor Rotor, ASME Joint Fluids Engineering and Gas Turbine Conference, New Orleans, 1980, pp. 165-176.
- STUDER, H.L. 1936 Experimentelle Untersuchungen uber Flugschwingungen. Mitteilungen aus dem Institut fur Aerodynamik, Eidgenossische Technische Hochschule, Zuerich, 4/5.
- SURAMPUDI, S.P. and ADAMCZYK, J.J. 1984 Unsteady Transonic Flow in Cascades. Cambridge Symposium Proceedings: Unsteady Aerodynamics of Turbomachines and Propellers, pp. 255-260.
- SURAMPUDI, S.P. and ADAMCZYK, J.J. 1986 Unsteady Transonic Flow over Cascade Blades. AIAA Journal, V. 24, N. 2, pp 293-302.
- SWANSON, R.C. and TURKEL, E. 1985 A Multistage Time-Stepping Scheme for the Navier-Stokes Equations. AIAA 23rd Aerospace Sciences Meeting, Paper No. 85-0035.
- SZECHENYI, E. 1984 Fan Blade Flutter - Single Degree of Freedom Instability or Blade to Blade Coupling? International Gas Turbine Congress, Houston, ASME Paper 85-GT-216.

- SZECHENYI, E. and FINAS, R. 1980 Aerolasticity Testing in a Straight Cascade Wind Tunnel. In Aeroelasticity in Turbomachines, Proceedings of the 2nd International Symposium Held in Lausanne, Sept. 1980, Editor: P. Suter, Juris-Verlag-Zurich, pp. 143-150.
- TANAKA, H., SHINOHARA, K. AND HANAMURA, Y. 1976 Comparison Between Theoretical and Experimental Results of Torsional Stall Flutter of an Airfoil. IUTAM Symposium on Aeroelasticity in Turbomachines, Paris.
- TANAKA, H., YAMAMOTO, K., and FUJIMOTO, I. 1984 Unsteady Aerodynamic Response of Cascade Blades in Pitching Oscillations with Flow Separation. Symposium on Unsteady Aerodynamics in Turbomachines, Cambridge.
- TANG, Z.M. and ZHOU, S. 1983 Numerical Prediction of Choking Flutter of Axial Compressor Blades. AIAA Paper 83-006.
- TANIDA, Y., HATTA, K. and ASANUMA, T. 1963 Experimental Study on Flutter in Cascading Blades. Bull. J.S.M.E., Vol. 6, No. 24, pp. 736-743.
- TANIDA, Y. and OKAZAKI, T. 1963 Stall-Flutter in Cascade. (First Report, Translatory Vibration of Cascade Blades as Treated by Semi-Actuator Disc Method, Part 1.) Bull. J.S.M.E., Vol. 6, No. 24, pp. 744-752.
- TANIDA, Y. and OKAZAKI, T. 1963 Stall-Flutter in Cascade. (Second Report, Translatory Vibration of Cascade Blades as Treated by Semi-Actuator Disc Method, Part 2.) Bull. J.S.M.E. Vol. 6, No. 4, pp. 753-758.
- TANIDA, Y., and OKAZAKI, T. 1968 Stall-Flutter in Cascade. (Third Report, Arbitrary Mode Vibration of Cascade Blades as Treated by Semi-Actuator Disc Method.) Bull. J.S.M.E. Vol. 11, No. 48. pp. 1115-1134.
- TANIDA, Y. and SAITO, Y. 1976 A Study on Choking Flutter. IUTAM Symposium on Aeroelasticity in Turbomachines, Paris.
- TANIDA, Y. and SAITO, Y. 1977 On Choking Flutter. Journal of Fluid Mechanics 82, pp. 179-191.
- TANIDA, H., SHINOHARA, Y. and HANAMURA, Y. 1976 Comparison Between Theoretical and Experimental Results of Torsional Stall Flutter of an Airfoil. IUTAM Symposium on Aeroelasticity in Turbomachines, 81-88, Paris
- TEIPEL, I. 1962 "Ein Charakteristikenverfahren zur Berechnung der verallgemeinerten ebenen Flatterluftkrafte," Z. f. Flugwiss., 10, pp. 374-379.
- THEODORSEN, T. 1935 General Theory of Aerodynamic Instability and the Mechanism of Flutter. NACA Report 496.
- THOMPSON, W.T., EPSTEIN, A.H. 1976 A Comparison of the Computed and Experimental Three-Dimensional Flow in a Transonic Compressor Rotor, AIAA Paper 76-368, July 1976.
- THOMPSON, W.T., KERREBROCK, J.L. 1975 Exit Flow from a Transonic Compressor Rotor, Mass. Inst. of Tech., Gas Turbine Lab., Report No. 123, September 1975.
- THOMPSON, W.T., TONG, S.S., BUSH, R.H., USAB, W.J., and NORTON, R.J.G. 1983 Solution Procedures for Accurate Numerical Simulations of Flow in Turbomachinery Cascades. AIAA Paper No. 83-0257.
- THOMPSON, J.F., THAMES, F.C., and MASTIN, C.W. 1977 Boundary Fitted Curvilinear Coordinate Systems for Solution of Partial Differential Equations on Fields Containing any Number of Arbitrary Two-Dimensional Bodies. NASA-CR 2729.
- TIJDEMAN, H. 1977 Investigations of the Transonic Flow Around Oscillating Airfoils. National Aerospace Laboratory Rep. NLR TR 77090-U.
- TIJDEMAN, H. and SEEBASS, R. 1980 Transonic Flow Past Oscillating Airfoils. Annual Review of Fluid Mechanics, Vol. 12, pp. 181-222.
- TOKEL, H. and SISTO, F. 1978 Dynamic Stall of an Airfoil with Leading Edge Bubble Separation Involving Time-Dependent Reattachment. ASME Paper NO. 78-GT-94.
- TROHA, W. and SWAIN, K. 1976 Composite Inlays Increase Flutter Resistance of Turbine Engine Fan Blades. ASME Paper 76-GT-29.
- VERDON, J.M. 1973 The Unsteady Aerodynamics of a Finite Supersonic Cascade with Subsonic Axial Flow. Journal of Applied Mechanics, Vol. 95, Transactions of the ASME, Series E, Vol. 40, No. 3, pp. 667-671.
- VERDON, J.M. 1977 Further Developments in the Aerodynamic Analysis of Unsteady Supersonic Cascades, Part 1: The Unsteady Pressure Field, and Part 2: Aerodynamic Response Predictions. Trans. ASME Journal of Engineering for Power, Vol. 99, No. 4, pp. 509-525.

- VERDON, J.M., ADAMCZYK, J.J., and CASPAR, J.R. 1975 Subsonic Flow Past an Oscillating Cascade with Steady Blade Loading - Basic Formulation. In Unsteady Aerodynamics (ed. R. B. Kinney), II, pp. 827-851.
- VERDON, J.M. and CASPAR, J.R. 1980 Subsonic Flow Past an Oscillating Cascade with Finite Mean Flow Deflection. AIAA Journal, Vol. 18, No. 5, pp. 540-548.
- VERDON, J.M. and CASPAR, J.R. 1982 Development of a Linear Aerodynamic Analysis for Unsteady Transonic Cascades. NASA Contractor Report 168038.
- VERDON, J.M. and CASPAR, J. R. 1982 Development of a Linear Unsteady Aerodynamic Analysis for Finite-Deflection Subsonic Cascades. AIAA Journal, Vol. 20, No. 9, pp. 1259-1267.
- VERDON, J.M. and CASPAR, J.R. 1984 A Linearized Unsteady Aerodynamic Analysis for Transonic Cascades. Journal of Fluid Mechanics, Vol. 149, pp. 403-429.
- VERDON, J.M. and McCUNE, J.E. 1975 Unsteady Supersonic Cascade in Subsonic Axial Flow, AIAA Journal, Vol. 13, No. 2, pp. 173-201.
- VERDON, J.M. and USAB, W.J. Jr. 1986 Application of a Linearized Unsteady Aerodynamic Analysis to Standard Cascade Configurations, NASA-CR-3940.
- VICTORY, M. 1943 Flutter at High Incidence. Brit. A.R.C. R & M 2048.
- VOGELER, K. 1984 The Unsteady Pressure Distribution on Parabolic Profiles in a Finite Cascade Oscillating in Supersonic Flow. Cambridge Symposium Proceedings: Unsteady Aerodynamics of Turbomachines and Propellers, pp. 171-190.
- WALLMANN, TH. 1980 Experimentelle Untersuchung zur Wechselwirkung zwischen stehenden und umlaufenden Schaufelreihen einer Unterschall-Axialverdichterstufe, Diss. RWTH Aachen.
- WARMING, R.F. and BEAM, R.M. 1978 On the Construction and Application of Implicit Factored Schemes for Conservation Laws, SIAM/AMS Proceedings Vol. 11, pp. 85-129.
- WEYER, H.B. 1980 Optical Methods of Flow Measurement and Visualization in Rotors, ASME Joint Fluids Engineering and Gas Turbine Conference, New Orleans, 1980, pp. 99-110.
- WEYER, H.B., DUNKER, R.J. 1977 Dual Beam Laser Anemometry Study of the Flow Field in a Transonic Compressor, Secondary Flows in Turbomachines, AGARD-CP-214, 1977, pp. 8.1-8.11.
- WHITEHEAD, D.S. 1959 The Vibration of Cascade Blades Treated by Actuator Disc Methods, 1959. Proc. I. Mech. E. Vol. 173, p. 555.
- WHITEHEAD, D.S. 1960 Force and Moment Coefficients for Vibrating Aerofoils in Cascade. British A.R.C. R & M No. 3254.
- WHITEHEAD, D.S. 1962 Bending Flutter of Unstalled Cascade Blades at Finite Deflection, R. & M. 3386.
- WHITEHEAD, D.S. 1966 Effect of Mistuning the Vibration of Turbomachine Blades Induced by Wakes. J. of Mechanical Engineering Science, 8, 1, pp. 15-21.
- WHITEHEAD, D.S. 1970 Vibration and Sound Generation in a Cascade of Flat Plates in Subsonic Flow. Cambridge University Engineering Department Report CUED/A-Turbo/TR 15.
- WHITEHEAD, D.S. 1973 The Effect of Compressibility on Unstalled Torsional Flutter, R. & M. 3754.
- WHITEHEAD, D.S. 1980 Unsteady Aerodynamics in Turbomachinery. In Special Course on Unsteady Aerodynamics, AGARD Report No. 679.
- WHITEHEAD, D.S. 1981 Program FINSUP Steady and Unsteady Flow in Cascades by a Finite Element Method. CUED/A-Turbo/TR105.
- WHITEHEAD, D.S. 1982 The Calculations of Steady and Unsteady Transonic Flow in Cascades. Cambridge University Engineering Department Report CUED/A-Turbo/TR 118.
- WHITEHEAD, D.S. 1986 An Actuator Disc Analysis of Unsteady Subsonic Cascade Flow. Jour. Sound Vib. Expected to be published Sept. 1986.
- WHITEHEAD, D.S. and DAVIES, M.R.D. 1983 An Actuator Disc Analysis of Unsteady Supersonic Cascade Flow, Journal of Sound and Vibration, Vol 88, No. 2, pp. 197-206.
- WHITEHEAD, D.S. and GRANT, R.J. 1980 Force and Moment Coefficients for High Deflection Cascades. In Aeroelasticity in Turbomachines, Proceedings of the 2nd International Symposium Held in Lausanne, Sept. 1980, Editor: P. Suter, Juris-Verlag Zurich, pp. 85-128.

- WHITEHEAD, D.S. and NEWTON, S.G. 1985 A Finite Element Method for the Solution of Two-Dimensional Transonic Flows in Cascades. International Journal for Numerical Methods in Fluids, Vol. 5, pp. 115-132.
- WHITEHEAD, D.S., WATSON, P.J., NAGASHIMA, T. and GRANT, R.J. 1976 An Experiment to Measure Moment Coefficients for Aerofoils Oscillating in Cascade. IUTAM Symposium on Aeroelasticity in Turbomachines, Paris.
- WHITHAM, G.B. 1974 Linear and Nonlinear Waves. John Wiley and Sons.
- WILLIAMS, M.H. 1979 Linearization of Unsteady Transonic Flows Containing Shocks. AIAA Journal, Vol 17, No. 4, pp. 394-397.
- WISLER, D.C. 1976 Shock Wave and Flow Velocity Measurements in a High Speed Fan Rotor Using the Laser Velocimeter, ASME Paper No. 76-GT-49, March 1976.
- WISLER, D.C., MOSSEY, P.W. 1977 Practical Application of LV Systems to Aero-Engine Research and Development, AGARD-LS-No. 90.
- WILLIAMS, M.H. 1979 Linearization of Unsteady Transonic Flows Containing Shocks. AIAA Journal, Vol 17, No. 4, pp. 394-397.
- WOODS, L.C. 1955 Unsteady Plane Flow Past Curved Obstacles with Infinite Wakes. Proceedings Royal Society A, 229, 152-180.
- WOODS, L.C. 1956 Aerodynamic Forces on an Oscillating Aerofoil Fitted with a Spoiler. Proceedings Royal Society A, 239, 328-337.
- WUERKER, R.F., KOBAYASHI, R.J., HEFLINGER, L.O. 1973 Application of Holography to Flow Visualization within Rotating Compressor Blade Row, NASA CR-121264.
- YAMASAKI, N. and NAMBA, M. 1982 Effect of Sound Absorbing Wall Linings on Aerodynamic Forces of a Subsonic Vibrating Cascade. Memoirs of the Faculty of Engineering, Kyushu University, Vol. 42, No. 4, pp. 251-278.
- YAMASAKI, N. and NAMBA, M. 1982 Theory of an Oscillating Cascade in an Incompressible Shear Flow (in Japanese). Transactions of the Japan Society of Mechanical Engineers, Series B. Vol. 48, No. 436, pp. 2415-2422.
- YASHIMA, S. and TANAKA, H. 1977 Torsional Flutter in Stalled Cascade. ASME Paper 77-GT-72.
- YEE, H.C., BEAM, R.M., and WARMING, R.F. 1981 Stable Boundary Approximations for a Class of Implicit Schemes for the One-Dimensional Inviscid Equations of Gas Dynamics. AIAA Paper No. 81-1009.
- YU, N.J., SEEBASS, A.R., and BALLHAUS, W.F. 1978 Implicit Shock-Fitting Scheme for Unsteady Transonic Flow Computations. AIAA Journal, Vol. 16, No. 7, pp. 673-678.

| REPORT DOCUMENTATION PAGE | | | |
|--|--|--|---|
| 1. Recipient's Reference | 2. Originator's Reference AGARD-AG-298 Volume 1 | 3. Further Reference ISBN 92-835-1543-9 | 4. Security Classification of Document UNCLASSIFIED |
| 5. Originator | Advisory Group for Aerospace Research and Development North Atlantic Treaty Organization 7 rue Ancelle, 92200 Neuilly sur Seine, France | | |
| 6. Title | AGARD MANUAL ON AEROELASTICITY IN AXIAL-FLOW TURBOMACHINES. VOLUME 1: UNSTEADY TURBOMACHINERY AERODYNAMICS | | |
| 7. Presented at | | | |
| 8. Author(s)/Editor(s) M.F.Platzer and F.O.Carta, Editors | 9. Date March 1987 | | |
| 10. Author's/Editor's Address See Flyleaf | 11. Pages 276 | | |
| 12. Distribution Statement | This document is distributed in accordance with AGARD policies and regulations, which are outlined on the Outside Back Covers of all AGARD publications. | | |
| 13. Keywords/Descriptors | | | |
| Acoustics of turbomachines Aeroelasticity Blade flutter Cascade calculation Flutter research | | Rotor aerodynamics Stall flutter Turbomachines Unsteady Aerodynamics Vibration | |
| 14. Abstract | | | |
| <p>This volume reviews the unsteady aerodynamics portion of aeroelasticity in axial-flow turbomachines. It contains 11 well coordinated chapters prepared by 11 different authors and co-authors. Most methods discussed are still limited to two-dimensional cascade flow. The current status of knowledge of three-dimensional flow and some viscous flow effects are also incorporated, while methods for computing unsteady boundary layer effects are just being developed and left out. Included are some chapters on numerical methods for unsteady transonic flow, for unsteady aerodynamics and aeroelastic measurement techniques, and for experimental results on cascades and rotors. A second volume for the structural dynamics portion (AG 298/2) will follow next year.</p> <p>This AGARDograph was prepared at the request of the Propulsion and Energetics Panel and of the Structures and Materials Panel of AGARD.</p> | | | |

| | | | |
|--|--|--|--|
| <p>AGARDograph No.298 Volume 1 Advisory Group for Aerospace Research and Development, NATO AGARD MANUAL ON AEROELASTICITY IN AXIAL-FLOW TURBOMACHINES. VOLUME 1: UNSTEADY TURBOMACHINERY AERO-DYNAMICS M.F.Platzer and F.O.Carta, Editors Published March 1987 276 pages</p> <p>This volume reviews the unsteady aerodynamics portion of aeroelasticity in axial-flow turbomachines. It contains 11 well coordinated chapters prepared by 11 different authors and co-authors. Most methods discussed are still limited to two-dimensional cascade flow. The current</p> <p>P.T.O.</p> | <p>AGARD-AG-298 Vol.1</p> <p>Acoustics of turbomachines Aeroelasticity Blade flutter Cascade calculation Flutter research Rotor aerodynamics Stall flutter Turbomachines Unsteady aerodynamics Vibration</p> | <p>AGARDograph No.298 Volume 1 Advisory Group for Aerospace Research and Development, NATO AGARD MANUAL ON AEROELASTICITY IN AXIAL-FLOW TURBOMACHINES. VOLUME 1: UNSTEADY TURBOMACHINERY AERO-DYNAMICS M.F.Platzer and F.O.Carta, Editors Published March 1987 276 pages</p> <p>This volume reviews the unsteady aerodynamics portion of aeroelasticity in axial-flow turbomachines. It contains 11 well coordinated chapters prepared by 11 different authors and co-authors. Most methods discussed are still limited to two-dimensional cascade flow. The current</p> <p>P.T.O.</p> | <p>AGARD-AG-298 Vol.1</p> <p>Acoustics of turbomachines Aeroelasticity Blade flutter Cascade calculation Flutter research Rotor aerodynamics Stall flutter Turbomachines Unsteady aerodynamics Vibration</p> |
| <p>AGARDograph No.298 Volume 1 Advisory Group for Aerospace Research and Development, NATO AGARD MANUAL ON AEROELASTICITY IN AXIAL-FLOW TURBOMACHINES. VOLUME 1: UNSTEADY TURBOMACHINERY AERO-DYNAMICS M.F.Platzer and F.O.Carta, Editors Published March 1987 276 pages</p> <p>This volume reviews the unsteady aerodynamics portion of aeroelasticity in axial-flow turbomachines. It contains 11 well coordinated chapters prepared by 11 different authors and co-authors. Most methods discussed are still limited to two-dimensional cascade flow. The current</p> <p>P.T.O.</p> | <p>AGARD-AG-298 Vol.1</p> <p>Acoustics of turbomachines Aeroelasticity Blade flutter Cascade calculation Flutter research Rotor aerodynamics Stall flutter Turbomachines Unsteady aerodynamics Vibration</p> | <p>AGARDograph No.298 Volume 1 Advisory Group for Aerospace Research and Development, NATO AGARD MANUAL ON AEROELASTICITY IN AXIAL-FLOW TURBOMACHINES. VOLUME 1: UNSTEADY TURBOMACHINERY AERO-DYNAMICS M.F.Platzer and F.O.Carta, Editors Published March 1987 276 pages</p> <p>This volume reviews the unsteady aerodynamics portion of aeroelasticity in axial-flow turbomachines. It contains 11 well coordinated chapters prepared by 11 different authors and co-authors. Most methods discussed are still limited to two-dimensional cascade flow. The current</p> <p>P.T.O.</p> | <p>AGARD-AG-298 Vol.1</p> <p>Acoustics of turbomachines Aeroelasticity Blade flutter Cascade calculation Flutter research Rotor aerodynamics Stall flutter Turbomachines Unsteady aerodynamics Vibration</p> |

NATO  OTAN

7 rue Ancelle · 92200 NEUILLY-SUR-SEINE

FRANCE

Telephone (1)47.38.57.00 · Telex 610 176

**DISTRIBUTION OF UNCLASSIFIED
AGARD PUBLICATIONS**

AGARD does NOT hold stocks of AGARD publications at the above address for general distribution. Initial distribution of AGARD publications is made to AGARD Member Nations through the following National Distribution Centres. Further copies are sometimes available from these Centres, but if not may be purchased in Microfiche or Photocopy form from the Purchase Agencies listed below.

NATIONAL DISTRIBUTION CENTRES

BELGIUM

Coordonnateur AGARD – VSL
Etat-Major de la Force Aérienne
Quartier Reine Elisabeth
Rue d'Evere, 1140 Bruxelles

CANADA

Defence Scientific Information Services
Dept of National Defence
Ottawa, Ontario K1A 0K2

DENMARK

Danish Defence Research Board
Ved Idraetsparken 4
2100 Copenhagen Ø

FRANCE

O.N.E.R.A. (Direction)
29 Avenue de la Division Leclerc
92320 Châtillon

GERMANY

Fachinformationszentrum Energie,
Physik, Mathematik GmbH
Kernforschungszentrum
D-7514 Eggenstein-Leopoldshafen

GREECE

Hellenic Air Force General Staff
Research and Development Directorate
Holargos, Athens

ICELAND

Director of Aviation
c/o Flugrad
Reykjavik

ITALY

Aeronautica Militare
Ufficio del Delegato Nazionale all'AGARD
3 Piazzale Adenauer
00144 Roma/EUR

LUXEMBOURG

See Belgium

NETHERLANDS

Netherlands Delegation to AGARD
National Aerospace Laboratory, NLR
P.O. Box 126
2600 AC Delft

NORWAY

Norwegian Defence Research Establishment
Attn: Biblioteket
P.O. Box 25
N-2007 Kjeller

PORTUGAL

Portuguese National Coordinator to AGARD
Gabinete de Estudos e Programas
CLAFAP
Base de Alfragide
Alfragide
2700 Amadora

TURKEY

Milli Savunma Başkanlığı (MSB)
ARGE Daire Başkanlığı (ARGE)
Ankara

UNITED KINGDOM

Defence Research Information Centre
Kentigern House
65 Brown Street
Glasgow G2 8EX

UNITED STATES

National Aeronautics and Space Administration (NASA)
Langley Research Center
M/S 180
Hampton, Virginia 23665

THE UNITED STATES NATIONAL DISTRIBUTION CENTRE (NASA) DOES NOT HOLD STOCKS OF AGARD PUBLICATIONS, AND APPLICATIONS FOR COPIES SHOULD BE MADE DIRECT TO THE NATIONAL TECHNICAL INFORMATION SERVICE (NTIS) AT THE ADDRESS BELOW.

PURCHASE AGENCIES

National Technical
Information Service (NTIS)
5285 Port Royal Road
Springfield
Virginia 22161, USA

ESA/Information Retrieval Service
European Space Agency
10, rue Mario Nikis
75015 Paris, France

The British Library
Document Supply Division
Boston Spa, Wetherby
West Yorkshire LS23 7BQ
England

Requests for microfiche or photocopies of AGARD documents should include the AGARD serial number, title, author or editor, and publication date. Requests to NTIS should include the NASA accession report number. Full bibliographical references and abstracts of AGARD publications are given in the following journals:

Scientific and Technical Aerospace Reports (STAR)
published by NASA Scientific and Technical
Information Branch
NASA Headquarters (NIT-40)
Washington D.C. 20546, USA

Government Reports Announcements (GRA)
published by the National Technical
Information Services, Springfield
Virginia 22161, USA



Printed by Specialised Printing Services Limited
40 Chigwell Lane, Loughton, Essex IG10 3TZ